

UNCLASSIFIED

AD NUMBER

AD464018

LIMITATION CHANGES

TO:

Approved for public release; distribution is unlimited.

FROM:

Distribution authorized to U.S. Gov't. agencies and their contractors; Specific Authority; MAY 1965. Other requests shall be referred to Arnold Engineering Development Center, Arnold AFS, TN.

AUTHORITY

AEDC ltr 18 Jan 1966

THIS PAGE IS UNCLASSIFIED

AEDC-TR-65-117

- cy 6
JUN 16 1965
NOV 18 1965
JAN 11 1967
DEC 19 1972
MAR 12 1976



A STUDY OF OPTICAL SYSTEM CONCEPTS AND HIGH INTENSITY LIGHT SOURCES FOR SOLAR RADIATION SIMULATION

Halbert Fischel

Messinger Consultants Co.

and

Roger R. Hughes

Honeywell Inc.

May 1965

PROPERTY OF U. S. AIR FORCE
AEDC LIBRARY
AF 40(600)1000

**ARNOLD ENGINEERING DEVELOPMENT CENTER
AIR FORCE SYSTEMS COMMAND
ARNOLD AIR FORCE STATION, TENNESSEE**

This document has been approved for public release
and its distribution is unlimited. (Ref BSC/TR-15-5
AD-A011700
26 Jul 1975)

NOTICES

When U. S. Government drawings, specifications, or other data are used for any purpose other than a definitely related Government procurement operation, the Government thereby incurs no responsibility nor any obligation whatsoever, and the fact that the Government may have formulated, furnished, or in any way supplied the said drawings, specifications, or other data, is not to be regarded by implication or otherwise, or in any manner, licensing the holder or any other person or corporation, or conveying any rights or permission to manufacture, use, or sell any patented invention that may in any way be related thereto.

Qualified users may obtain copies of this report from the Defense Documentation Center.

References to named commercial products in this report are not to be considered in any sense as an endorsement of the product by the United States Air Force or the Government.

A STUDY OF OPTICAL SYSTEM CONCEPTS
AND HIGH INTENSITY LIGHT SOURCES
FOR SOLAR RADIATION SIMULATION

Halbert Fischel

and

Roger R. Hughes

This document has been approved for public release
and its distribution is unlimited.

Ref DDC/ TR-75/5
AD A011700
1st July 1975

FOREWORD

This work was performed for the Arnold Engineering Development Center, Air Force Systems Command, Arnold Air Force Station, Tennessee, 37389, under Contract AF 40(600)-1069, Solar Radiation Simulation Optical Systems Studies, Program Element 62405334/8952, Task 895211.

All items compared in this report were commercial items that were not developed or manufactured to meet Government specifications, to withstand the tests to which they were subjected, or to operate as applied during this study. Any failure to meet the objectives of this study is no reflection on any of the commercial items discussed herein or on any manufacturer.

The study described herein was conducted at Honeywell Inc., California Ordnance Center, West Covina, California, under the direction of R. C. Cooke, Project Manager. Personnel contributing to the research effort and to the preparation of this report include H. Fischel, Associate Consultant, Messinger Consultants Co., San Marino, California, R. R. Hughes, Development Engineer, R. A. Griest, Jr., Senior Development Engineer, and D. R. Cole, Senior Technical Writer, all of Honeywell Inc.

This report has been assigned Honeywell Technical Document No. H-6152-19.

The reproducibles used in this reproduction of this report were supplied by the author.

This technical report has been reviewed and is approved.

G. MacFARLANE
Sqdn Ldr, RCAF
Technology Division
DCS/Plans and Technology

DONALD D. CARLSON
Colonel, USAF
DCS/Plans and Technology

ABSTRACT

The study described herein has been made to evaluate three new high-powered arc sources as possible radiation sources for a large modular solar simulator. The three sources are (1) the Vortex Stabilized Radiation Source developed by Giannini Scientific Corp. (Plasmadyne); (2) the Fluid Transpiration Arc developed by Vitro Laboratories; and (3) the High Intensity Carbon Arc developed by RCA Service Co.

From data supplied by Arnold Engineering Development Center (AEDC), the radiation characteristics of the sources have been studied to determine the spectral properties of the radiation from each source, and to permit derivation of mathematical expressions for the radiance distribution of each source.

A careful review of the nature of solar radiation and of the theory of energy transfer in optical systems has been conducted. On the basis of this review and the source radiance functions derived in the source study, several optical system concepts for solar radiation simulation have been synthesized and analyzed for use with each source. The optical concepts studied range from simple parabolic collimators and uncollimated projection modules to systems consisting of trains of conic section reflectors and modifications thereto.

TABLE OF CONTENTS

SECTION	PAGE
1 INTRODUCTION	1
2 SUMMARY	2
3 PROBLEM SUMMARY AND ORGANIZATION	6
4 TECHNICAL DISCUSSION	9
4.1 Some Specific Properties of Solar Radiation	9
4.2 Basic Optical Concepts	13
4.3 Thermodynamics of Incoherent Radiation	21
4.4 Uniformity Criteria and Optical Parametric Determinants	30
4.5 Theoretical Basis of the Source Representation	43
4.5.1 Nature of the Radiation Field Produced by a Light Source	43
4.5.2 Nature of the Source Representation	46
4.6 Energy Tracing	54
5 SOURCE STUDY	56
5.1 Data Required for Representing a Source	56
5.1.1 Introduction	56
5.1.2 Distribution of Radiation About the Source . . .	56
5.1.3 Brightness Distribution	59
5.1.4 Source Spectrum	61
5.2 Analyses of the Directional Radiative Characteristics of the Various Sources	63
5.2.1 Vortex Stabilized Radiation Source (VSRS) . . .	63
5.2.2 Fluid Transpiration Arc (FTA)	88
5.2.3 High Intensity Carbon Arc	101
5.3 Spectral Analyses	110
5.3.1 Criteria Used for the Spectral Analyses	110
5.3.2 Spectral Analyses of Optical Materials	117
5.3.3 Spectral Analyses of the Various Sources . . .	134
6 OPTICAL SCHEMATA	179
6.1 Summary of Modular Schemata to be Studied	179
6.2 Uncollimated Systems	181
6.3 Collimated Systems	181
6.3.1 General Characteristics	181
6.3.2 Hexagonal Array of Paraboloidal Reflectors .	183
6.3.3 Optical Subsystems	183

Table of Contents (Continued)

SECTION	PAGE
6 (Cont)	6.3.4 On-Axis versus Off-Axis Systems 197 6.3.5 Shadowing and Fill-In Systems 200 6.3.6 Modular Arrangements 203
7	BASIC ANALYSES OF THE VARIOUS OPTICAL SCHEMATA 208 7.1 Introduction 208 7.2 Source Representation 208 7.2.1 Radiance Distribution 208 7.2.2 Source Size 211 7.2.3 Micro-Brightness 213 7.3 Modular Array of Uncollimated Projection Systems 213 7.3.1 Introduction 213 7.3.2 System Performance Analysis 216 7.3.3 Analysis of Results 244 7.4 Modular Array of Simple Paraboloids 245 7.4.1 Statement of the Problem 245 7.4.2 The Near-Field Small Source Approximation 247 7.4.3 Parameters and Nomography 252 7.4.4 Numerical Results 257 7.4.5 Summary 284 7.5 Unmodified Conic Section Optical Systems 286 7.6 Modified Conic Section Optical Systems 297 7.6.1 Fresnel Collection Devices 297 7.6.2 Multifaceted Transfer Systems 299 7.6.3 Source Aperture Conjugation 304 7.6.4 Condenser Lens Assembly Analysis 315 7.6.5 Aconic Reflector(s) Analysis 326 7.7 Re-Reflection Analysis 367 7.7.1 Off-Axis Collimators 367 7.7.2 On-Axis Collimators 371
8	CONCLUSIONS 379 8.1 Source Data Analyses 379 8.1.1 Radiance 379 8.1.2 Radiative Efficiency 380 8.1.3 Spectral Distribution 380 8.2 Optical System Concepts 381 8.2.1 Hexagonal Array of Projectors 381 8.2.2 Hexagonal Array of Paraboloids or Modules Consisting of Conic Section Reflectors 382 8.2.3 Modified Conic Section Systems 383 8.2.4 Comparison of Efficiencies of Various Optical Systems 384 8.2.5 On-Axis versus Off-Axis Collimators 387 8.3 Recommendations 387

Table of Contents (Continued)

		PAGE
APPENDIXES		
I	COMPUTER PROGRAMS FOR OPTICAL DESIGN AND ANALYSIS	390
II	SPECTRAL FILTRATION	395
III	SINGLE SURFACE COLLECTOR FOR COSINE OUTPUT FROM A SPHERICAL INPUT	399

LIST OF TABLES

		PAGE
TABLE		
5-1	Tabulation of VSRS Intensity Distribution Data as Obtained from Plasmadyne	64
5-2	Report and Table and/or Figure from Which the Data Listed in Table 1 was Obtained	65
5-3	Relative Radiance Distribution of the VSRS for Various Operating Conditions	67
5-4	Average Relative Radiance Distributions of the VSRS with a 12 mm Electrode Gap and an Axial Bore Anode or Recessed Plate Anode	68
5-5	Absolute Radiance Distribution of the VSRS for Various Operating Conditions (As Corrected)	78
5-6	Collection Efficiency for the VSRS	87
5-7	Radiance Measurements for the Fluid Transpiration Arc (by Vitro Laboratories)	88
5-8	Radiance of the Fluid Transpiration Arc (As Corrected)	92
5-9	Defining Parameters for the Representation of the 37.5 KW Fluid Transpiration Arc	103
5-10	Dissipative Efficiencies of the Various Optical System Configurations Studied as a Function of the Thickness of the Refractive Material (Spectral Criterion II)	123
5-11	Percent of energy in each indicated wavelength, band of the solar spectrum and of the source spectrums required, after spectral filtration, for each indicated optical system configuration (Spectral Criterion III)	135
5-12	Relative Intensity in each indicated wavelength band of the solar spectrum and of the source spectrums required, after spectral filtration for each indicated optical system configuration (Spectral Criterion III)	136
5-13	Percent of Energy in each indicated wavelength band of the Solar Spectrum and the source spectrum required, after filtration, for each indicated optical system configuration (Spectral Criterion IV)	140

List of Tables (Continued)

TABLE		PAGE
5-14	Relative Intensity in each indicated wavelength band of the solar spectrum and of the source system required, after spectral filtration, for each indicated optical system configuration (Spectral Criterion IV)	140
5-15	Percent of energy in each indicated wavelength band of the solar spectrum and of the source spectrum required, after spectral filtration, for each indicated optical system configuration (Spectral Criterion V)	144
5-16	Relative Intensity in each indicated wavelength band of the Solar Spectrum and the source spectrum required, after spectral filtration, for each indicated optical system configuration (Spectral Criterion V)	145
5-17	Identification of the Various Spectrums considered for the Vortex Stabilized Radiation Source	149
5-18	Percent of Energy in each indicated wavelength band of the Solar Spectrum and Spectrums, I, IV, V, and VII of the Vortex Stabilized Radiation Source (Spectral Criterion IV) . . .	151
5-19	Relative Intensity in each indicated wavelength band of the Solar Spectrum and Spectrums I, IV, V, and VII of the Vortex Stabilized Radiation Source (Spectral Criterion IV) . . .	152
5-20	Percent of Energy in each indicated wavelength band of the Solar Spectrum and Spectrums VIII and IX of the Vortex Stabilized Radiation Source (Spectral Criterion V)	158
5-21	Relative Intensity in each indicated wavelength band of the Solar Spectrum and Spectrums VIII and IX of the Vortex Stabilized Radiation Source (Spectral Criterion V)	159
5-22	For each indicated optical system configuration, the Maximum Efficiency with which Spectrums I, IV, V, VII, VIII, or IX of the VSRS can be filtered to match the source spectrums required, after spectral filtration, in order to match the Solar Spectrum	163
5-23	Maximum and Probable Dissipative Efficiencies of the indicated Source, Optical-System, Spectral-Filter Combinations	165
5-24	Percent of Energy and Relative Intensity in Each Indicated Wavelength band of the Indicated Radiation Sources (Spectral Criterion III)	175
5-25	Maximum efficiency with which the spectrums of the indicated sources can be filtered to match the source spectrums required, after spectral filtration, for each indicated optical system configuration (Spectral Criterion III)	176
5-26	Maximum and Probable Dissipative Efficiencies of the indicated Source, Optical-System, Spectral-Filter Combinations	177

List of Tables (Continued)

		PAGE
7-1	Uniformity Calculations for an Hexagonally Arranged Array of Parabolic Reflectors	267
7-2	Geometrical and Performance Parameters of the Various Source, Parabolic-Reflector Systems which, when arranged in an hexagonal array, provide a mean intensity of 0.260 watts/sq. cm (Venus Orbit Intensity) and $\pm 10\%$ Uniformity	285

LIST OF ILLUSTRATIONS

		PAGE
FIGURE		
4-1	Schematic Representation of Field Angle and Collimation Angle	10
4-2	Albedo Radiation Geometry	12
4-3	Aperture and Field	14
4-4	Aperture and Field Transfer	16
4-5	Equivalent Solar Disc	17
4-6	Lines of Constant Relative Intensity from Fully Driven 2.5 KW Hg-Xe Lamp Microbrightness Study	19
4-7	Source and Target Elements	24
4-8	Lambertian Source and Symmetric Field	28
4-9	Flux Concentration	29
4-10	Collimator Schematic	34
4-11	Spherical Abberation	37
4-12	Conjugated Optical Train	41
4-13	Schematic Representation of Radiation Fields	45
4-14	Source Emission Characteristics	48
4-15	Schematic Representation of Radiant Energy Transfer by an Optical System	49
5-1	Schematic Representation of the Experimental Technique Suggested for Measuring the Distribution of Radiation about a Light Source	57
5-2	Average Relative Radiance of the VSRS with a 12 mm Electrode Gap and an Axial Bore Anode or Recessed Plate Anode (Linear Plot)	69
5-3	Average Relative Radiance Distribution of the VSRS with a 12 mm Electrode Gap and an Axial Bore Anode or Recessed Plate Anode (Polar Plot)	70

List of Illustrations (Continued)

FIGURE			PAGE
5-4	Average Relative Radiance of the VSRS with a 6 mm Electrode Gap and a Recessed Plate Anode (Linear Plot)	71	
5-5	Average Relative Radiance of the VSRS with a 6 mm Electrode Gap and a Recessed Plate Anode (Polar Plot)	72	
5-6	Relative Radiated Power Distribution of the VSRS with a 12 mm Electrode Gap and an Axial Bore Anode or Recessed Plate Anode	74	
5-7	Relative Radiated Power Distribution of the VSRS with a 6 mm Electrode Gap and a Recessed Plate Anode	76	
5-8	Radiative Efficiency of the VSRS as a Function of Input Power	79	
5-9	Radiance of the VSRS with a 12 Millimeter Electrode Gap and a Recessed Plate Anode Before and as Modified by a Conical Reflecting Surface on the Cathode	81	
5-10	Approximation, Using Straight Lines, of the Radiance of the VSRS With a 12-Millimeter Electrode Gap and a Recessed Plate Anode Before and as Modified by a Conical Reflecting Surface on the Cathode	82	
5-11	Collection Efficiency for the Vortex Stabilized Radiation Source	85	
5-12	Radiative Efficiency of the Fluid Transpiration Arc as a Function of Input Power (as corrected)	91	
5-13	Lines of Constant Relative Brightness of the 37.5 KW Fluid Transpiration Arc (Side View)	94	
5-14	Approximation of the Lines of Constant Relative Brightness of the 37.5 KW Fluid Transpiration Arc (Side View)	96	
5-15	Graphical Approximation of a Line of Constant Relative Brightness with Two Ellipses	97	
5-16	Approximation of the Lines of Constant Relative Brightness of the 37.5 KW Fluid Transpiration Arc (Front View)	100	
5-17	Approximation to the Brightness Distribution Seen Across the Front View of the Fluid Transpiration Arc (37.5 kilowatts) .	102	
5-18	Superimposed Horizontal and Vertical Scans - Intensity in mw/cm ² of 35-kw Unshielded Carbon Arc at Radius of 6 feet	105	
5-19	Intensity in mw/cm ² of Shielded 75-kw Carbon Arc at Radius of 6 feet	106	
5-20	Intensity in mw/cm ² of Unshielded 75-kw Carbon Arc at Radius of 6 feet	109	
5-21	Absorptance of Evaporated Gold and Evaporated Silver	113	
5-22	Absorptance of Evaporated Copper, Evaporated Aluminum and Aluminum Paint	114	

List of Illustrations (Continued)

FIGURE		PAGE
5-23	Spectrum of Fluid Transpiration Arc When Operated at 37.5 KW (Spectral Criterion II A)	116
5-24	Reflectance As a Function of Wavelength for Evaporated Aluminum	121
5-25	Summary Calculation of Source Spectrum Required for an Optical System of 3 Evaporated Aluminum Mirrors and 4 Lenses of Corning Fused Silica Code 7940, Suprasil, or Ultrasil (Total Thickness of 4 Inches)	124
5-26	Summary Calculation of Source Spectrum Required for an Optical System of 3 Evaporated Aluminum Mirrors and 4 Infrasil Lenses (Total Thickness of 4 Inches)	125
5-27	Transmittance, including surface reflections, of 1 cm thicknesses of Suprasil and Infrasil	126
5-28	Initial Calculation of Source Spectrum Required for an Optical System of 3 Evaporated Aluminum Mirrors and 4 Infrasil Lenses (Total Thickness of 8 Inches)	127
5-29	Summary Calculation of Source Spectrum Required for an Optical System of 3 Evaporated Aluminum Mirrors and 4 Infrasil Lenses (Total Thickness of 8 Inches)	128
5-30	Summary Calculation of Source Spectrum Required for an Optical System of 4 Evaporated Aluminum Mirrors and 4 Infrasil Lenses (Total Thickness of 4 Inches)	129
5-31	Summary Calculation of Source Spectrum Required for an Optical System of 4 Evaporated Aluminum Mirrors and 4 Infrasil Lenses (Total Thickness of 8 Inches)	130
5-32	Variation, With Total Thickness of Infrasil, of the Source Spectrum Required for an Optical System of 3 Evaporated Aluminum Mirrors and 4 Infrasil Lenses (Spectral Criterion II B)	132
5-33	Variation, With Total Thickness of Infrasil, of the Source Spectrum Required for an Optical System of 4 Evaporated Aluminum Mirrors and 4 Infrasil Lenses (Spectral Criterion II B)	133
5-34	Solar Spectrum (Spectral Criterion III)	137
5-35	Source Spectrums Required, After Spectral Filtration for Optical Systems Consisting of Three Aluminum Mirrors and Four Infrasil Lenses (Spectral Criterion III)	138
5-36	Source Spectrums Required, after Spectral Filtration, for Optical Systems Consisting of Four Aluminum Mirrors and Four Infrasil Lenses (Spectral Criterion III)	139
5-37	Solar Spectrum (Spectral Criterion IV)	141

List of Illustrations (Continued)

FIGURE		PAGE
5-38	Source Spectrums Required, After Spectral Filtration, for Optical Systems Consisting of Three Aluminum Mirrors and Four Infrasil Lenses (Spectral Criterion IV)	142
5-39	Source Spectrums Required, After Spectral Filtration, for Optical Systems Consisting of Four Aluminum Mirrors and Four Infrasil Lenses (Spectral Criterion IV)	143
5-40	Solar Spectrum (Spectral Criterion V)	146
5-41	Source Spectrums Required, After Spectral Filtration, for Optical Systems Consisting of Three Aluminum Mirrors and Four Infrasil Lenses (Spectral Criterion V)	147
5-42	Source Spectrums Required, After Spectral Filtration, for Optical Systems Consisting of Four Aluminum Mirrors and Four Infrasil Lenses (Spectral Criterion V)	148
5-43	Spectrum I of the Vortex Stabilized Radiation Source (Spectral Criterion IV)	153
5-44	Spectrum IV of the Vortex Stabilized Radiation Source (Spectral Criterion IV)	154
5-45	Spectrum V of the Vortex Stabilized Radiation Source (Spectral Criterion IV)	155
5-46	Spectrum VII of the Vortex Stabilized Radiation Source (Spectral Criterion IV)	156
5-47	Spectrums I, IV, V, and VII of the Vortex Stabilized Radiation Source (Spectral Criterion IV)	157
5-48	Spectrum IX of the Vortex Stabilized Radiation Source (Spectral Criterion IV)	160
5-49	Spectrum VIII of the Vortex Stabilized Radiation Source (Spectral Criterion V)	161
5-50	Spectrums VIII and IX of the Vortex Stabilized Radiation Source (Spectral Criterion V)	162
5-51	Spectrum of High Intensity Carbon Arc (Spectral Criterion 11A)	166
5-52	Spectrum of High Intensity Carbon Arc (Spectral Criterion II B)	167
5-53	Spectrum of High Intensity Carbon Arc (Spectral Criterion III)	168
5-54	Spectrum of Fluid Transpiration Arc When Operated at 37.5 KW (Spectral Criterion II A)	169
5-55	Spectrum of Fluid Transpiration Arc When Operated at 37.5 KW (Spectral Criterion II B)	170
5-56	Spectrum of Fluid Transpiration Arc When Operated at 37.5 KW (Spectral Criterion III)	171
5-57	Spectrum of Fluid Transpiration Arc When Operated at 29.1 KW (Spectral Criterion II A)	172

List of Illustrations (Continued)

FIGURE		PAGE
5-58	Spectrum of Fluid Transpiration Arc When Operated at 29.1 KW (Spectral Criterion 11B)	173
5-59	Spectrum of Fluid Transpiration Arc When Operated at 29.1KW (Spectral Criterion III)	174
6-1	Optical System Concepts	180
6-2	Basic Collector Types.	186
6-3	A Fresnel Collector	188
6-4	A Multifaceted Collector	189
6-5	Source Aperture Transfer Optics	191
6-6	Basic Collimator Types	198
6-7	On- and Off-Axis Collimators	199
6-8	Collection Fill-In Optical Systems	202
6-9	Collimator Fill-In Optics	204
6-10	Staggered Array of Collimators	205
6-11	An Off-Axis Modular System	207
7-1	Projection Module Systems	214
7-2	Schematic Representation of the Geometric Relationships which Govern the Transfer of Radiation from an Array of Projectors to a Target Position	217
7-3	Schematic Representation of a Projector System	227
7-4	Hexagonal Array of Projectors.	233
7-5	J versus γ for $\Theta = 5.73^\circ$	239
7-6	J versus γ for $\Theta = 11.42^\circ$	240
7-7	J versus γ for $\Theta = 22.62^\circ$	241
7-8	J versus γ for $\Theta = 53.13^\circ$	242
7-9	Projection Module Design Concept.	246
7-10	Schematic Representation of the Geometry of a Paraboloidal Reflector	248
7-11	Source Radiance Distribution Required for Absolute Uniformity Across the Aperture of a Parabolic Reflector	251
7-12	R versus R for a Simple Spherical Source and a 1° Field Angle.	259
7-13	R versus R for a Simple Spherical Source and a 2° Field Angle.	260
7-14	\bar{R} versus R for a Simple Spherical Source and a 3° Field Angle	261
7-15	\bar{R} versus R for a Combination Source and a 3° Field Angle	262
7-16	\bar{R} versus n_c for a Simple Spherical Source and a 1° Field Angle.	263

List of Illustrations (Continued)

FIGURE	PAGE
7-17 \bar{R} versus η_c for a Simple Spherical Source and a 2° Field Angle	264
7-18 \bar{R} versus η_c for a Simple Spherical Source and a 3° Field Angle	265
7-19 \bar{R} versus η_c for a Combination Source and a 3° Field Angle	266
7-20 R versus α for the Basic VSRS and the Modified VSRS (Approximate)	281
7-21 Conic Section Optical Systems	287
7-22 Ellipsoidal Reflector Parameters	288
7-23 Hyperboloidal Reflector Parameters	288
7-24 Multifaceted Concepts	301
7-25 Aperture and Field Stop Mapping	306
7-26 Spherical Aberration of the Pupil Planes (Distortion)	309
7-27 Pincushion Distortion	310
7-28 Solid Angle Transfer at Cardinal Points. Schematic	311
7-29 Conic Section Optical System with Condenser Lenses	316
7-30 Theoretical and Compromise Relationships Between $\sin \phi_2$ and $\sin \phi_3$ for a Condenser Assembly Design	322
7-31 Desired Compromise and Specified Minimum Values of $\sin \phi_3$ as a Function of $\sin \phi_2$ for Condenser Assembly Design	323
7-32 Desired Compromise and Specified Maximum Values of $\sin \phi_2$ and $\sin \phi_3$ as a function of $\sin \phi_2$ for Condenser Assembly Design	324
7-33 Parameters of a Modified Cassegrainian Collimator for a System Using Condenser Lenses	328
7-34 Plot of r^2 vs. $\cos \alpha$ for Original and Modified Optical Systems	341
7-35 Uniformity vs. Aperture Radius for Original and Modified Design	342
7-36 Residual Spherical Abberation in a Corrected Optical System	343
7-37 Modified Cassegrainian Collimator for a System without Condenser Lenses	346
7-38 Collector and Paraboloid	357
7-39 Parameters of a Two-Element Collector	361
7-40 Collector Fill-in System	366
7-41 Graphical Ray Trace of Re-Reflection by Paraboloidal Reflector Module	368
7-42 Graphical Ray Trace of Images of Object Surfaces in the Test Volume as Formed by a Paraboloidal Reflector	369

List of Illustrations (Continued)

FIGURE		PAGE
7-43	Graphical Ray Trace of Re-Reflection by a Cassegrainian System Module	370
7-44	Case 1 - Diffuse Object	372
7-45	Case 2 - Specular Object	376
III-1	Parameters of a Single-Surface Collector	400
III-2	Schematic Representation of a Collector Which Collects Radiation Between 40° and 180° of the Axis and Whose Output Radiance Distribution is a Cosine Function Within 65° of the Axis	403
III-3	Schematic Representation of a Collector Which Collects Radiation Between 45° and 180° of the Axis and Whose Output Radiance Distribution is a Cosine Function Within 65° of the Axis	404
III-4	Schematic Representation of a Collector Which Collects Radiation between 50° and 180° of the Axis and whose Output Radiance Distribution is a Cosine Function Within 65° of the Axis	405
III-5	Schematic Representation of a Collector Which Collects Radiation Between 55° and 180° of the Axis and Whose Output Radiance Distribution is a Cosine Function Within 65° of the Axis	406
III-6	Schematic Representation of a Collector Which Collects Radiation Between 60° and 180° of the Axis and Whose Output Radiance Distribution is a Cosine Function Within 65° of the Axis	407
III-7	Schematic Representation of a Collector Which Collects Radiation Between 65° and 180° of the Axis and Whose Output Radiance Distribution is a Cosine Function Within 65° of the Axis	408
III-8	Schematic Representation of a Collector Which Collects Radiation Between 70° and 180° of the Axis and Whose Output Radiance Distribution is a Cosine Function Within 65° of the Axis	409

Glossary of Radiometric Terms as Used in This Report

Brightness	-	Power radiated by a source per unit surface area per unit solid angle. Typical units: watts/sq cm-steradian, symbol: B
Flux	-	Energy radiated per unit time; power. Typical units: watts. Symbol F
Flux density	-	Radiant energy density per unit time; intensity. Typical units: watts/sq. cm. Symbol E
Intensity	-	Energy density per unit time. Typical units: watts/sq. cm. Symbol E
Power	-	Energy per unit time. Typical units: watts. Symbol P
Radiance	-	Power radiated by a source per unit solid angle. Typical units: watts/steradian. Symbol I

SECTION 1

INTRODUCTION

Solar radiation is one of the most important parameters to be simulated in an aerospace environmental facility. The Arnold Engineering Development Center has recently supported research directed toward the development of high-powered arcs, suitable for use as sources for solar simulation. These sources and their developers are: the Vortex Stabilized Radiation Source, Giannini Scientific Corporation (Plasmadyne); the Fluid Transpiration Arc, Vitro Laboratories; and the High Intensity Carbon Arc, RCA Service Co. It is important to determine the applicability of these sources to the simulation of solar radiation, to the extent possible in their present state of development. It is also important to determine which, if any, of the sources may have a marked superiority for the application from the standpoint of the optical designer.

Accordingly, the purposes of this study were to synthesize and analyze various optical system configurations to determine those best suited for the simulation of solar radiation; to analyze, on the basis of data furnished by AEDC, the radiation characteristics of the three sources; and to determine relative performance factors of the three sources when used in combination with the most promising optical systems. The study described herein was conducted between 23 August 1963 and 25 January 1965, by Honeywell Inc., California Ordnance Center, West Covina, California under Contract AF40(600)-1069.

SECTION 2

SUMMARY

The properties of the solar radiation field are defined in detail and their relationship to uniformity and total intensity are obtained. The thermodynamics of radiant energy transfer in optical systems is discussed as it relates to the various optical system requirements and solar radiation field characterization.

The relationship between physical source parameters and optical parameters is obtained and it is shown that the field angle which is required for a given solar simulator optical system design is a function of (1) physical source parameters, particularly brightness, (2) optical system dissipative efficiency, and (3) desired intensity.

As a result of the theoretical analysis, a very important criterion is obtained which describes, in terms of the radiance of the source, the optical system requirements for ultimate beam uniformity. In addition to the total intensity and efficiency relationships upon which basic system parameters are based, additional system parameters are defined by this uniformity criterion, which is referred to as the "Normal Illuminance Criterion". It is seen that, by virtue of this criterion, strict limitations are imposed upon optical system parameters. The constraints obtained thereby form the essence of the optical system design in each of the cases presented. In addition, the theoretical analysis provides a basis for calculating the transfer of radiant energy through optical systems, and a description of a computer program (denoted the "Energy Trace Program") based upon this analysis is given in Appendix I. (The "Energy Trace Program" is primarily utilized in the final design effort for theoretical testing of a specific optical system design.) This computer program is based upon a source representation whereby the actual source brightness distribution is approximated by a combination of Lambertian surface radiators (surfaces of constant brightness) of various geometrical shapes.

In the section dealing with the source studies, the most important radiometric characteristics and parameters of a source (namely the radiance, brightness distribution, and spectrum) are discussed and techniques are suggested whereby these characteristics and parameters may be experimentally determined and represented. The physical and optical properties of various materials are discussed and analyzed to define the source spectrums required, after spectral filtration, for optical systems consisting of various combinations of these materials to provide output radiation whose spectrum matches the solar spectrum.

It is shown that the choice of optical materials is dependent on the spectrum specification and, for the spectrum specification which divides the solar spectrum between 0.2 micron and 3.0 microns into 19 wavelength bands, each of which contains approximately the same fraction of the solar energy, the most appropriate optical materials are (1) evaporated aluminum for the reflecting surfaces and (2) optical quality fused quartz (fused silica) for the refracting components. The maximum spectral filtration efficiency for the various combinations of source spectrums and optical materials is determined. In addition to the spectral analysis, the data provided concerning the Vortex Stabilized Radiation Source, the Fluid Transpiration Arc, and the High Intensity Carbon Arc are analyzed to define equations which describe the radiance distribution for each source. These equations are subsequently integrated to determine the total power radiated by each source for each set of operating conditions and, from this, the radiative efficiency of each source for each set of operating conditions is calculated. These equations are also used both for estimates of collection efficiency, (i. e., the fraction of the radiated power which can be collected and utilized by each optical system concept), and for defining criteria for the design of an optical system to provide uniformity. The data concerning the brightness distribution of the Fluid Transpiration Arc is also analyzed and a mathematical representation of this source is generated in order to illustrate, by example, the concepts involved.

A classification scheme has been devised for organizing the various optical concepts into an orderly arrangement for systematic analysis. The organization of these optical concepts is described in section 6. An effort has been made to include representative examples of each of the possible optical concepts for the purpose of solar simulation optical system design. Every possible system design, of course, is not included in the study; however, it is felt that a comprehensive sampling of the various possibilities is included. All optical system designs are based on the modular concept and are adapted for suitable arrangement in a multi-modular array of either a hexagonal pattern or, alternatively, in a square pattern (which may be more convenient, geometrically, in the case of modules of off-axis design).

In the basic analysis of the various optical schemes in section 7, several assumptions are made with regard to the source representation for the purpose of a first order analysis. First, it is assumed that the source is spherically symmetric unless otherwise indicated in the analysis itself. It is further assumed, except as indicated, that the source is of negligible extension (size). The purpose of these assumptions is to facilitate the analysis of the optical concepts and to relate the results most directly to optical properties, without undue influence of the source characterization. An analysis is performed to determine how variations in the radiation distribution across the aperture of a single module relate to variations in the distribution of the radiation provided by the total system array as a function of distance from the array. It is seen that there is a fairly close relationship between uniformity across the module

aperture and uniformity within the target volume of the total array; however, the averaging effect of distance from the array can be used to relax the actual uniformity requirements for the individual modules.

Based upon the general analysis of the modular system and its uniformity requirements, an analysis of a hexagonal array of projectors is performed, and it is found that the uniformity obtaining from such an array is a function of the packing density of modules. The relationship between the average intensity in the target volume and the individual module power levels is also determined. A hexagonal array of parabolic reflectors is analyzed, and it is found that reasonable uniformity can be obtained from such an array for limited module efficiencies. Quantitative results are obtained for each of the three light sources as employed in a hexagonal array of parabolic reflectors and these values are compared.

In view of the results obtained from the array of simple parabolic reflectors, a study is made of more complex systems involving extensive combinations of conic section reflectors and it is shown that these are entirely equivalent to the case of the parabolic collimator. Attention is then turned to modifications of the simple conic section reflector system.

Since much of the non-uniformity is introduced in the collection components, efforts are made to modify the collection system in terms of Fresnel collection devices, and it is shown that these are quite impractical because of severe losses in overall efficiency for the system.

The multi-faceted concept is also investigated and it is shown that a multi-faceted mirror component, or pebble bed, located at the position of the hyperboloid of a Cassegrainian collimator is not so good a choice as a multi-faceted relay lens located at the entrance pupil of the collimator. Parametric equations are determined which define the conditions which must be observed in order to successfully employ either multi-faceted device to smooth the distribution across the final beam, although, as further investigations reveal, such a device may be unnecessary because of a high probability that modifications of the conic section mirror elements alone will prove adequate.

A typical example of the aperture transfer concept is investigated in which a multi-axis collection system images the source several times upon itself in different orientations to achieve a smooth intensity distribution at the field element (the aperture plane) of the module optical system. This plane is then imaged by a projection lens upon the collimator aperture which delivers the actual collimated beam. Such a system is probably feasible, but is better suited to large single module systems which make use of many sources and collectors. (A source-collector bank is most useful when lamp mixing is desired.) Next, the insertion of a condenser lens system in the conjugate train

of elements is studied and it is found that additional control over the distribution of the beam may be obtained, although the additional collection efficiency made possible is largely offset by the additional absorption of the condenser lens elements.

Finally, an investigation is made to determine the feasibility of modifying the conic section mirror surfaces to achieve the additional compensation needed in the optical system design. This is done, in conjunction with the use of a condenser lens system, by defining the techniques for modifying the hyperbolic surface in the Cassegrainian collimator and then compensating for the spherical aberration so introduced by modifying the parabolic element. Because the use of aconic reflectors appears to be a feasible approach for compensation of variations introduced by the collection optics when used in conjunction with the condenser elements, effort is then made to define these surfaces without the use of the condenser elements. A method is derived for defining such surfaces and it is indicated that a closed solution for the evaluation of these surfaces for any given source radiance distribution is feasible. Quantitative results were not obtained to define the aconic surfaces which would be used with each of the three sources under consideration; however the behavior of the defining equations indicates that further study of these systems is warranted.

An analysis of re-reflection from system collimators is made for both the on-axis and off-axis cases and it is found that, for collimators whose focal lengths are in the order of 1/20 of the throw distance to the target, the intensity of returned radiation is on the order of only a few percent of the simulated solar intensity. In the case of properly designed off-axis modules, no energy reflected from the target is returned to the target by the collimators.

SECTION 3

PROBLEM SUMMARY AND ORGANIZATION

An appreciation of the importance of solar radiation as a principal factor in the total heat balance of a space vehicle has been well established. When considering the simulation of solar radiation as an integral part of the space environmental program, it is important to clearly define the specific properties which characterize solar radiation and the degree to which they must be reproduced in the testing environment. The exact nature of the testing rationale and its objective will bear heavily upon each specification of solar simulator performance requirements and although development of specifications is not a part of the present study, the precise physical definition of solar radiation and its proper mathematical description will be of concern. How this definition, as well as source characteristics, relates to optical design and parameterization is one of the most fundamental problems which must be dealt with.

Many difficulties have been encountered in the past several years with regard to the simulation of solar radiation and these encompass a number of problems which have heretofore received little attention in optical engineering. They can be divided conveniently into two categories; design analysis and component fabrication. Although the latter is by no means the less serious and must be taken into consideration in all phases of evaluation, this program is directed primarily toward the former. The study is conducted with particular emphasis upon uniformity, collimation, proper field angle, adequate intensity, cold black space, solar spectrum, efficiency, reliability, and functional utility as characteristics which, in themselves, do not make the basic problems underlying their realization immediately apparent. For example, the need to obtain a specified level of intensity which is uniform over any normal flat plane independent of depth in a finite volume, imposes important restrictions on any optical system. Collimation, when rigorously defined, is seen to be a fundamental requirement for some concepts, while for others it is not necessary. Proper field angle, adequate intensity, and efficiency are seen to be inextricably tied together on the basis of fundamental principles. Cold black space simulation can be achieved to varying degrees depending upon the design of the optical system and associated cooling provisions. Spectral match is a problem common to all designs although compensation to improve it may be more convenient in one design than another.

The purpose of this study, and the problems with which it deals, can be summarized as the requirement for synthesizing and analyzing various source, optical-system configurations with respect to the characteristics mentioned

above, and for considering the equally important problems of reliability, functional utility, and feasibility of construction of any given design. It will be seen that the representation of the light source in the analysis is of paramount concern and will receive much attention in what follows.

Performance requirements initially established as design goals for the concepts to be analyzed in this study are as follows:

1. Intensity.

- a. Adjustable from 0.5 to 1.0 solar constants (0.140 w/cm^2)
- b. Capable of accepting a source to provide Venus orbit solar intensity

2. Field Angle

As small as possible to closely reproduce the angle subtended by the sun at earth distance (32 minutes of arc)

3. Collimation

As required to provide uniformity with respect to test volume depth.

4. Uniformity

Uniform to within $\pm 5\%$ as measured by a sensor 1 cm by 1 cm over any plane cross section at distances varying from 40 to 170 feet.

5. Spectrum

Match Johnson curve as follows:

<u>Spectral Range</u> (Microns)	<u>Band Width</u> (Microns)	<u>Tolerance</u> (Per Cent)
0.2 - 3.0	0.02	± 20
0.2 - 0.8	0.2	± 8
0.8 - 2.0	0.3	± 8
2.0 - 3.0	0.5	± 8

The analysis was conducted in accordance with the following organization:

1. Sources were classified into two types; single-ended and double-ended.
2. Mathematical representation of radiation sources was then divided into first order effects (radiance distribution), higher order and off-axis effects (micro-brightness distribution), and spectrum.

3. The optical module was generalized and divided into three mutually exclusive functional sub-systems; collection, transfer, and collimation or projection.

4. A flexible classification of optical schemata was outlined. The criterion for a distinct category is based upon the particular analysis involved and how far its results extend over a given set of optical designs. Certain equivalences were noted among some system types, thereby lumping them into the same category as characterized by the basic underlying analytical relationships.

5. The synthesis of optical designs and parameters and the analysis of performance characteristics was carried out, for the most part, on a first order basis as this is generally adequate for the determination of feasibility and for purposes of evaluation.

6. The modular concept itself was studied and the effects peculiar to, and problems associated with, such a scheme were determined on a quantitative basis. As a result of this study, it is possible to set criteria for individual module performance as a function of total system requirements.

7. Finally, specific source characteristics were related to the surviving optical designs on a first order basis and mutual compatibility evaluated. Numerical examples for specific cases are presented.

This report is organized in the following manner:

Section 4 discusses the basic principles governing the analytical methods used in this study. In addition to providing a solid foundation for the results derived therefrom, sufficient detail is presented to enable the reader to apply the techniques employed here to many individual cases which require special application or variation of method.

Section 5 discusses radiation source studies, including a discussion of the specific source characteristics which must be experimentally determined, suggested experimental techniques, and an analysis and reduction of the data provided concerning the three sources considered for application to the analysis of the various optical system concepts.

Section 6 discusses optical system classification. This section serves as an introduction and index to the general optical systems analyses of Section 7.

Section 7 consists of detailed analyses of pertinent optical systems or representative examples of a general scheme.

Section 8 provides a summary discussion of results, conclusions, and recommendations.

SECTION 4

TECHNICAL DISCUSSION

The following discussion will analyze the nature of the study and design task, and will explain some of the important related concepts. The discussion will begin with a careful definition of the terms which apply to radiation and optical parameters.

4.1 SOME SPECIFIC PROPERTIES OF SOLAR RADIATION

Perhaps the most important first step in approaching the solar radiation simulator design problem is to examine the nature of the radiation field which is to be simulated. Some of the specific properties which must be considered are collimation, field angle, uniformity, intensity and spectrum.

Before stating the design goals concerning these properties, it is instructive to consider first the concepts of collimation and field angle and their relationship to uniformity. To collimate means to render parallel and collimation is often confused with the concept of field angle. Field angle has to do with the angular subtense of the source at a receiving target, whereas collimation angle refers to the angular subtense of the receiving target at the source. For example, consider the case where a 20-foot-diameter satellite is located 93 million miles from the sun (in the vicinity of the orbit of the Earth). In this case, the field angle subtended by the sun at any position on the surface of the satellite is 32 minutes of arc while the collimation angle subtended by the satellite at any position on the surface of the sun is extremely small (approximately 1.4×10^{-8} minutes of arc); hence the term collimated. The total collimation angle subtended by the Earth at the sun is approximately 0.3 minute of arc. The field angle and collimation angle subtended by and at the sun, at and by Earth and Venus are schematically represented in figure 4-1.

Perhaps the best way to gain an appreciation of the concept of collimation is to think of the continuum of spherical wave fronts emanating from the sun's surface. The intensity on a spherical wave front decreases inversely with the square of its radius of curvature. By the time these wave fronts reach the vicinity of the Earth, they have a radius of curvature of approximately 93 million miles and any 20-foot-diameter section of any such wave front is essentially flat. Thus, solar radiation at the earth, within any reasonable volume, consists of a continuum of nearly plane waves contained within a field angle of 32 minutes of arc. It is therefore adequate, for the purpose of this study, to think of the sun as being infinitely far away and providing exactly plane wave radiation at the Earth, thereby providing uniform radiation intensity throughout the finite volume of interest.

The distinction between collimation and field angle should not be considered trivial; whereas the effects of collimation error can cause wide

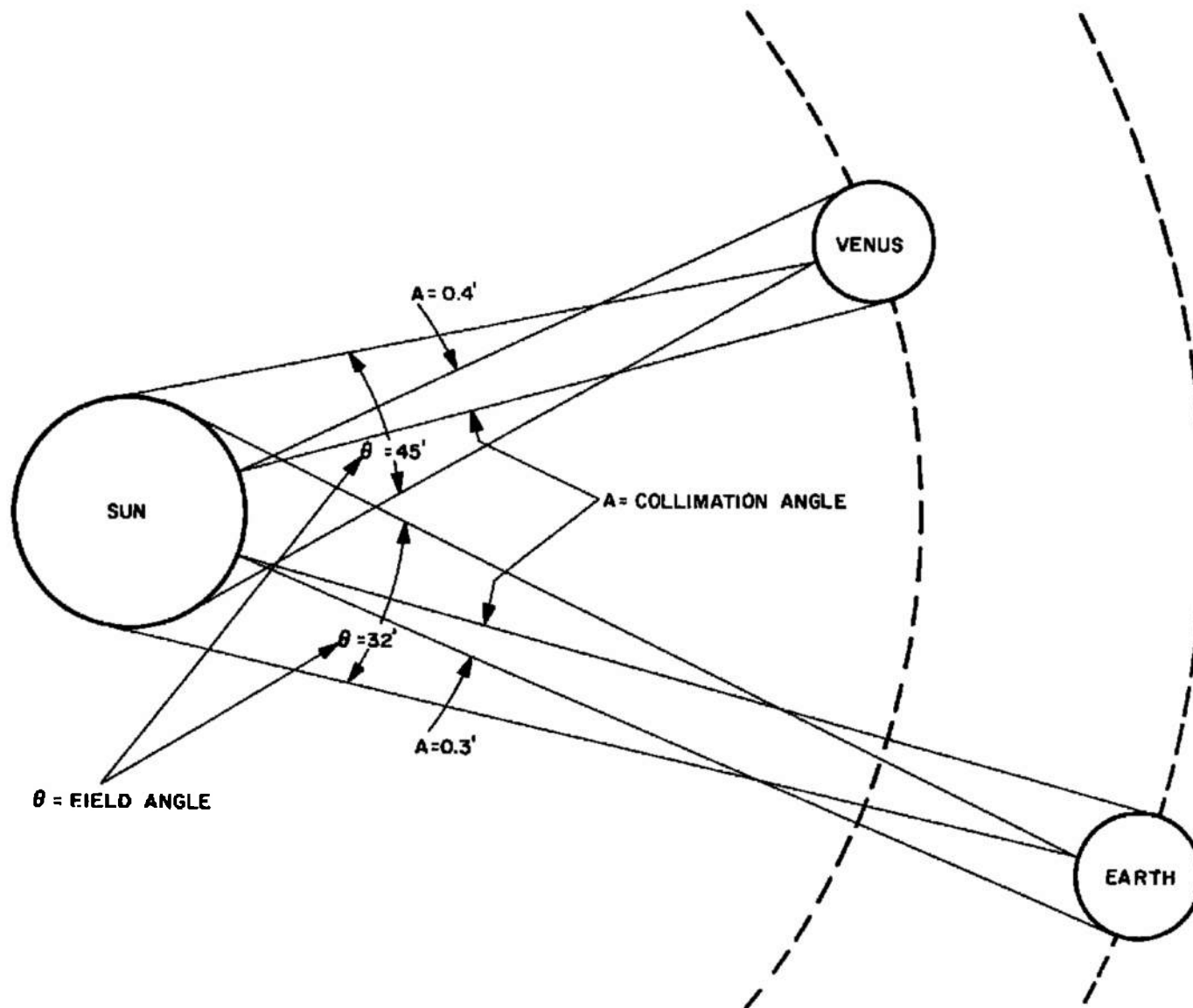


Figure 4-1. Schematic Representation of Field Angle and Collimation Angle

variation in intensity within a target volume, the field angle may have any value without affecting the uniformity. To illustrate this latter point, consider planetary radiation or albedo, as illustrated in figure 4-2. Here the field angle subtended by the earth is very large and, for a 100-mile orbit, is about 155 degrees. However, the angle subtended by a 20-foot satellite (the collimation angle), even at the nadir (the closest point on the earth), is only 10 seconds of arc for a 100-mile orbit. This means that the radiation striking the satellite is flat to within 10 seconds of arc across the entire aperture to the volume. By simulator standards, this is highly collimated, and uniformity would easily obtain throughout the volume enclosing the satellite since the inverse square falloff in about 20 feet at a distance of 100 miles is quite insignificant, about 0.01 percent. Thus, it is not the field angle which controls uniformity in depth but rather the planeness (collimation) of the incident radiation.

It is shown later that the choice of field angle ("decollimation angle" or non-parallelism) is not open to convenience or disposition, but is constrained by the source characteristics. Except for dissipative losses, field angle is even independent of optical design. Thus, any two optical systems with the same number of reflecting and refracting interfaces and, therefore, nearly the same dissipative losses, must be designed for the same field angle if they are both to provide the same intensity using the same source. This is an example of only one of many design constraints.

Some of the specific properties of solar radiation which the radiation field produced by the solar radiation simulator must closely approximate are:

1. Intensity Produced by the Sun.
 - a. Intensity at the Earth's orbit is 0.140 watts-per-square-centimeter.
 - b. Intensity at the orbit of Venus is 0.260 watts-per-square-centimeter.
2. Field Angle Subtended by Solar Radiation.
 - a. The sun subtends 32 minutes of arc at the Earth's orbit.
 - b. The sun subtends 45 minutes of arc at the orbit of Venus.
3. Collimation of Solar Radiation.
 - a. Within any reasonable volume of simulation, the collimation angle is zero.
4. Uniformity of Solar Radiation.
 - a. Within any reasonable volume of simulation, the radiation is uniformly distributed.
5. Solar Spectrum.
 - a. The solar spectrum will be represented according to the data given in Table 16-8, Reference 1.

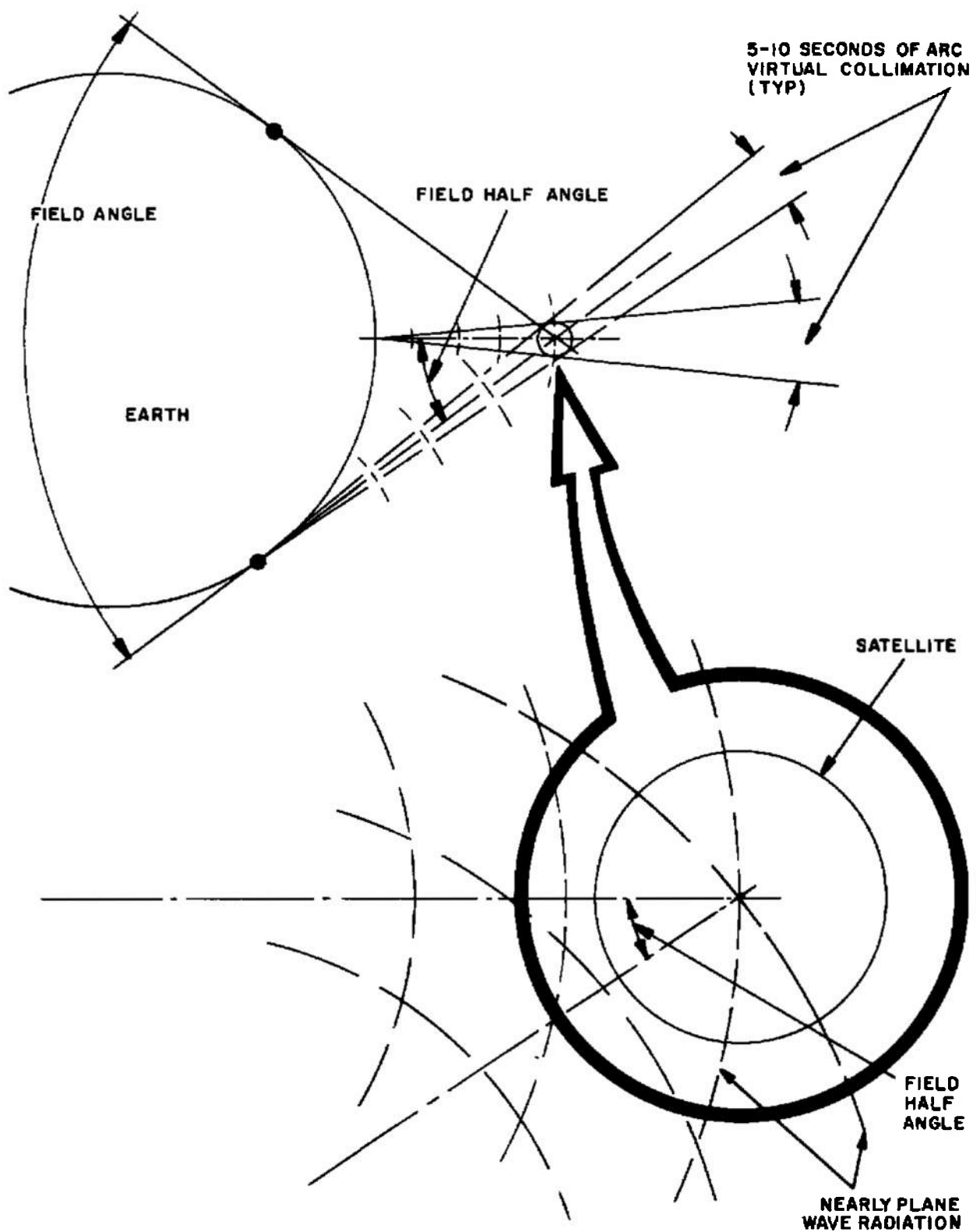


Figure 4-2. Albedo Radiation Geometry

4.2 BASIC OPTICAL CONCEPTS

There are a number of concepts and subtleties concerning the nature and relationship of the optical components which require considerable attention as they form the foundation upon which most optical designs are based. In order that the subsequent discussion on radiation transfer may be properly presented, it is best to define certain basic optical concepts in order to ensure that they are mutually and accurately understood.

First, several fundamental optical principles will be clarified, namely the concepts of field, aperture, vignetting, and conjugate planes. Referring to figure 4-3, it is seen that the field of an optical system is understood to be the angle subtended by the image or the object, whether or not either is at infinity as measured from the effective position of the lens. The assumption, which is indeed a valid one, is that all optical systems can be viewed as equivalent to a single, thick lens, or "black box" as it were, separating planes of effective entry and exit. The aperture of the optical system is the effective size of the lens such that all points within this dimension may view all points of the field. For example, when looking up to view the sun, the field of view is the 32 minutes of arc that the sun subtends in the sky, and the aperture of the system is the pupil of the eye which restricts its lens, acting as a telescope in this case.

These concepts lead, inevitably, to the problem of vignetting. Thus, if there is more than one lens in an optical system, the effective aperture of the optical system must be determined in a complicated way. Some lenses may have their edges somewhat vigneted, while others do the vignetting. In the case of off-axis systems, the resulting vignetting becomes even more complicated; one side of one lens may vignette the opposite side of another lens from one direction of the field, while the reverse is true for another direction in the field. In any case, the concept of vignetting and the understanding of where effective stops in an optical system occur is of paramount importance for understanding the way in which a field of view is generated in an optical system.

When the black box which contains the equivalent optical system for a complicated optical train, is closely examined internally, it shows many positions at which a given object or plane is imaged over and over again. This repetitious imaging is sometimes quite necessary in order to accomplish transfer of radiation within the limitations imposed. For example, submarine periscopes reimagine the field of view many times before it is finally presented to the viewer. In any case, the need to refer to the transfer of image, aperture, or field stop positions periodically down the optical train will present itself regularly in the following discussion.

Having established these definitions, they may now be used to illustrate some properties of special importance in an optical system. For this purpose consider the perhaps oversimplified, but nevertheless typical, collimating optical

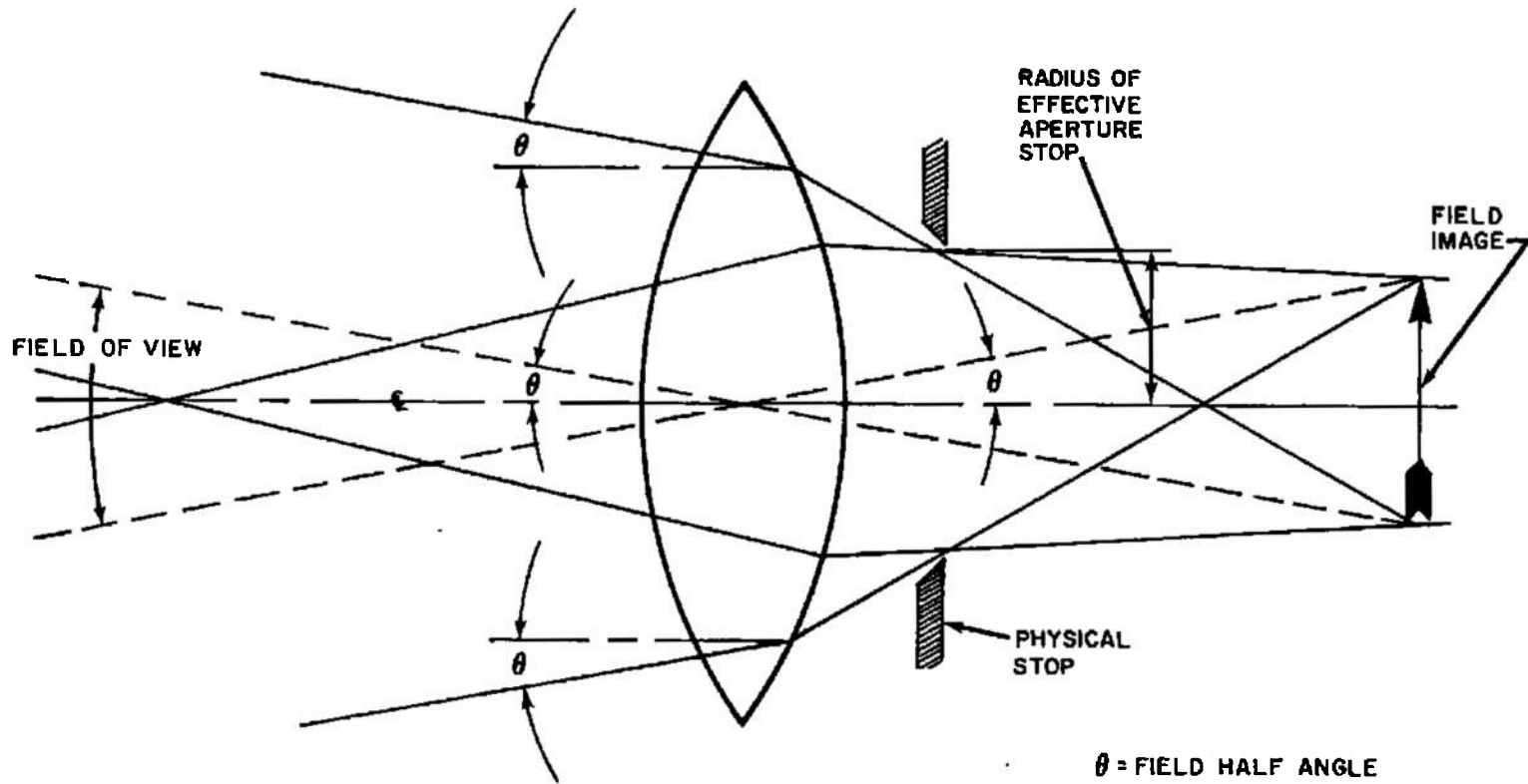


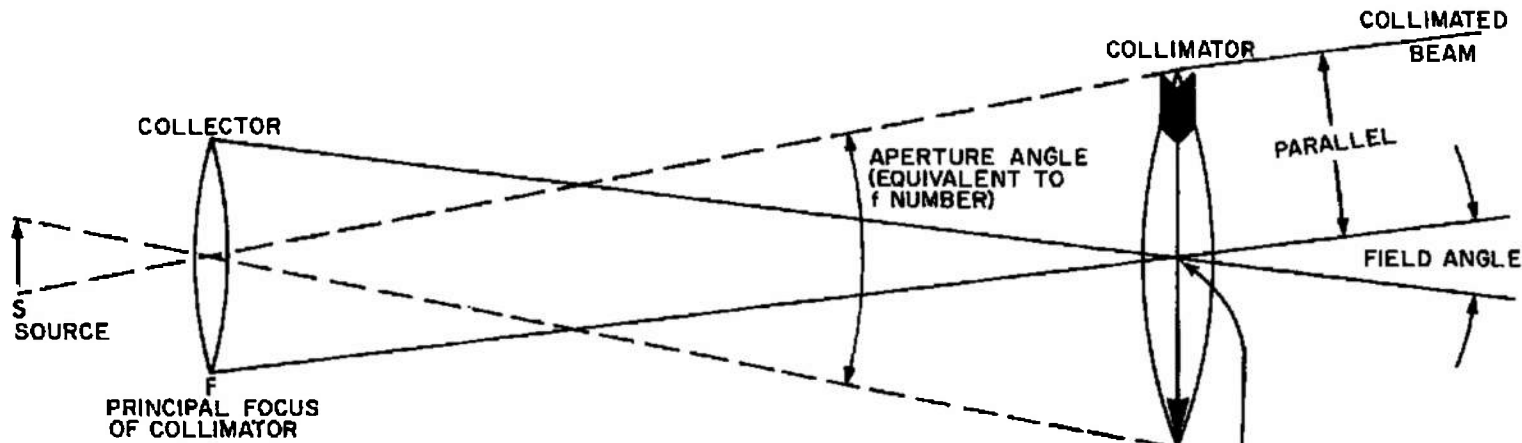
Figure 4-3. Aperture and Field

system illustrated in figure 4-4. In part A of figure 4-4, a simple collecting lens is shown gathering light from the source, S. The collecting lens images the source into a collimating lens, and it is seen that the transfer of source boundaries proceeds from the source itself through the optical train and reestablishes the source at the collimating lens position. In addition, the collecting lens is shown to be at the principal focus of the collimating lens, position F. The following situation is evident: because there is no light outside the source boundaries, the source becomes the aperture for the collimated beam; that is, the source is the aperture stop for the system and the collimating lens need be no larger than the source image at the position of the collimating lens. On the other hand, the collecting lens at position F becomes the effective illuminated disc determining the field angle for the collimating lens. To summarize the properties of this system then, the source geometry limits the aperture of the system and the collector geometry limits the field of the system.

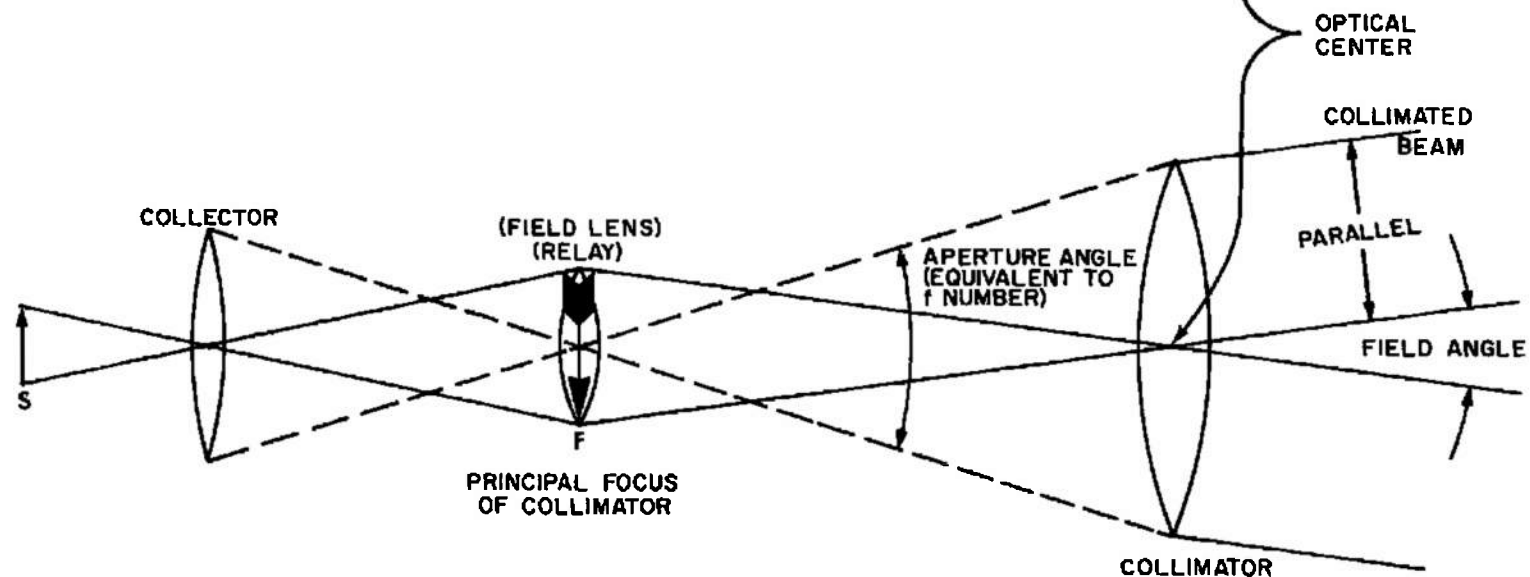
In part B of figure 4-4, the collecting lens forms an image of the arc at position F of the collimator, rather than in the collimating lens itself. At this position a field lens is placed which images the collecting lens onto the collimator lens. This is an extra lens, its only purpose is to avoid vignetting by matching the boundary of the collecting lens with that of the collimating lens. Clearly, in this case, it is either the source geometry or the image of that geometry which determines the field of the collimation system. The aperture of that system is determined by the aperture of the collection system. With regard to the way in which the energy of the source is collected and transferred through the system, two entirely different situations are evident and it is well to gain a firm understanding of the significance of this difference.

Figure 4-5 shows a simple collimator (telescope in reverse) with the source at its principal focus. It is convenient to imagine looking into the collimator from a position in the collimated field. If this were a solar simulator this position would be equivalent to viewing the sun directly from space. Depending upon the position of the eye (P_1 or P_2) various parts of the collimating aperture contribute energy to the pupil. However, the angle over which this energy is contributed (the field angle) is always the same so long as there is no vignetting by the edge of the collimator. It will be seen that this constant field angle is synonymous with beam uniformity. Thus, when looking into the collimating lens, the source imaged at infinity is seen, but it is still visible in all its detail. This concept is illustrated by showing how the head and tail are actually visible from all parts of the field even though the light is parallel from each position on the source.

In this respect, a collimator is equivalent to an eyepiece in a telescope or microscope which forms a real image at some position down the tube. The eyepiece then takes this real image and collimates the light coming from it. When the eye looks into an eyepiece, the eye's lens refocuses the collimated light onto the retina and the image is seen. The reason eyepieces are



A. SOURCE APERTURE CONJUGATION



B. SOURCE FIELD CONJUGATION

Figure 4-4. Aperture and Field Transfer

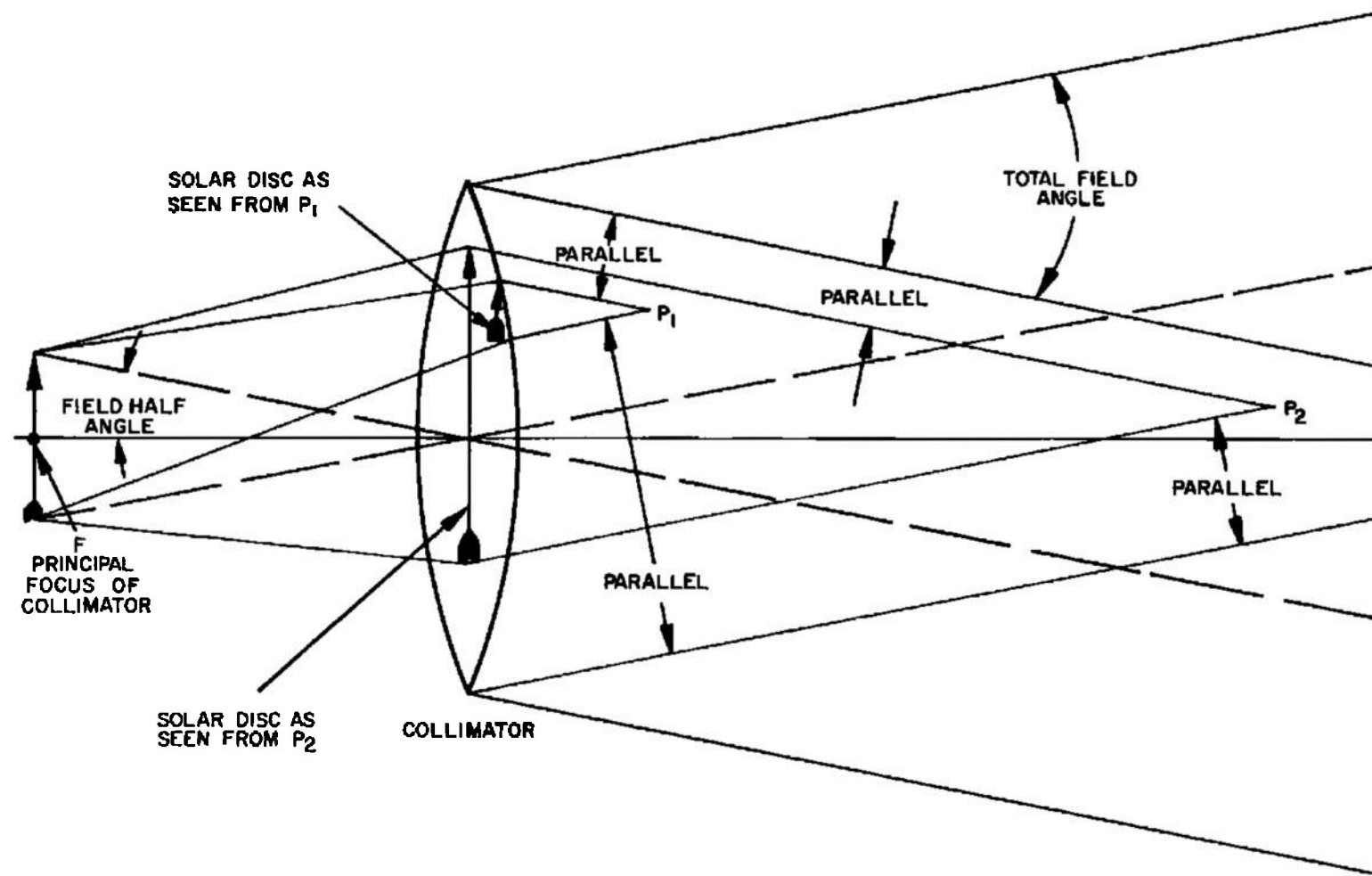


Figure 4-5. Equivalent Solar Disc

designed to image the real image formed by a telescope or microscope virtually at infinity is that the eye is most relaxed when viewing objects at great distances. A collimating optical system is nothing, then, but a huge eyepiece looking ultimately at the source or the real source image as the case may be. It will be convenient to draw upon this concept later when the radiometry of optical systems is discussed.

In the light of these concepts, the difference between the manner in which radiation is transferred through the two illustrations in figure 4-4 can be understood. Thus, looking into the collimator and viewing the radiation field in part A of figure 4-4, one would see the collecting lens appear as an illuminated disc at every point in the test area. In addition, each point in the test area would receive radiation from a corresponding point on the source. The interpretation of this is that every part of the collecting lens is seen at every point in the test area, but only certain parts of the source are seen at corresponding parts in the test area, due to the one-to-one mapping relationship between the two.

On the other hand, in part B of figure 4-4, there is the opposite condition. Because it is the image of the source itself that comprises the illuminated field seen in the collimator, the entire source appears as the illuminated disc. Thus, every point of the source contributes energy to every point in the test area and a one-to-one mapping of apertures now exists between the collecting lens and the collimator.

The bifurcation of optical radiative transfer processes illustrated in the foregoing paragraphs is strictly an artificial one designed to emphasize the diverse nature of the phenomenon. In fact, the transfer process may be viewed either as a separate or intermingled mapping of field and aperture but always with the consideration of both the geometrical and directional properties of light. These concepts are requisite to an understanding of the factors affecting beam uniformity and chromatic homogeneity. The arrangement illustrated in part A of figure 4-4, referred to hereafter as aperture transfer, shows the arc image to be mapped one-to-one onto the final beam aperture. This implies that the beam will carry with it all the nonuniformities which the arc possesses. For example, a map of the microbrightness distribution of a typical 2.5-kw xenon high pressure arc lamp is shown in figure 4-6 and is seen to be highly nonuniform. Studies show that, as might be expected, the spectral content of various positions on some arcs are also strongly different. Thus, a one-to-one correspondence of source geometry with the collimator aperture seems, at first glance, highly undesirable. Perhaps blending of the radiation at some position where the source image may be affected can alleviate this situation, but this is a problem requiring considerable further study. In any case, it would be imprudent to propose such a system without admitting to the major difficulties carried with it.

On the other hand, the arrangement described in part B of figure 4-4 referred to hereafter as field transfer, shows the collector to be isomorphic

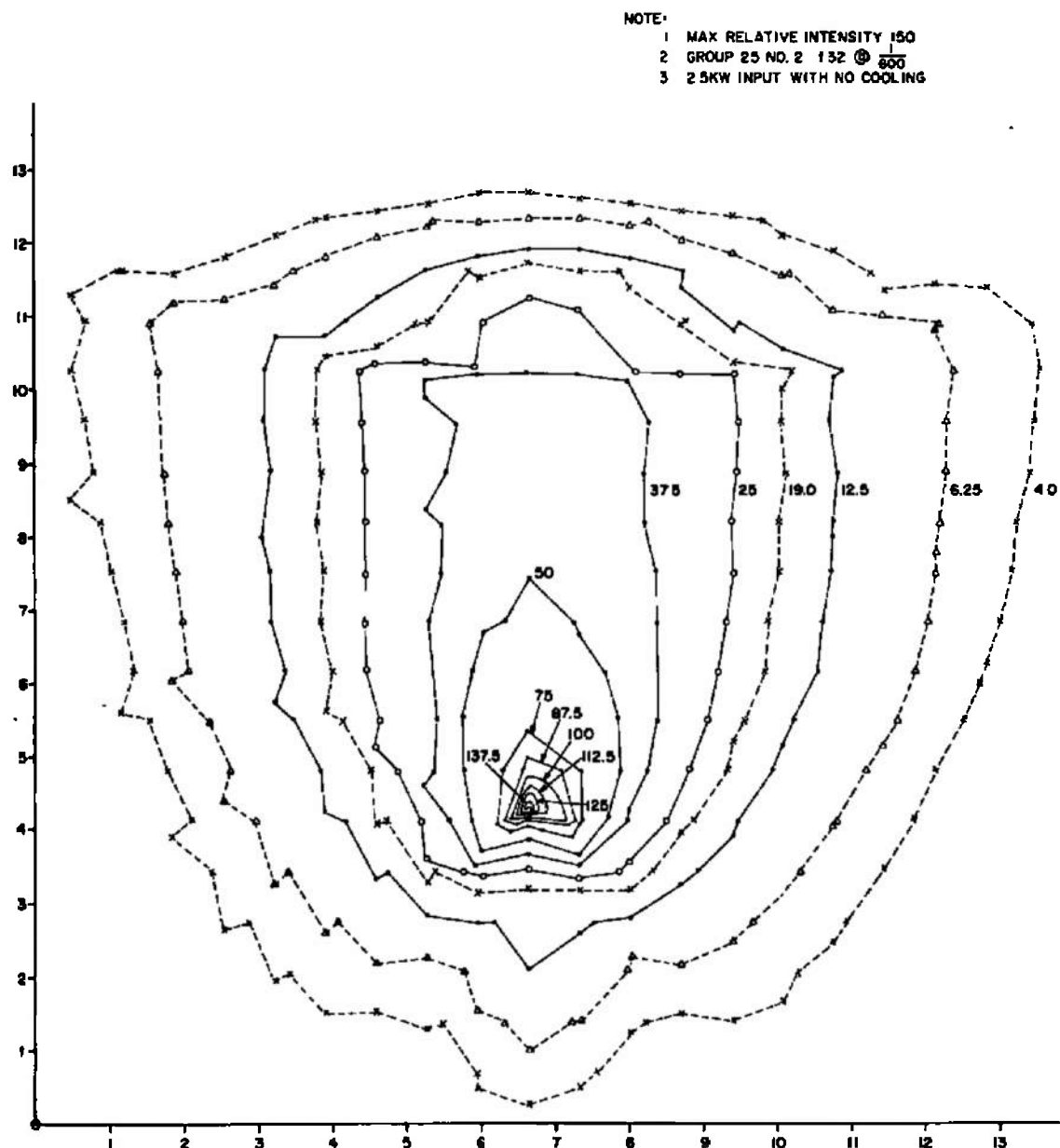


Figure 4-6. Lines of Constant Relative Intensity from Fully Driven 2.5 KW Hg-Xe Lamp Microbrightness Study

to the collimator aperture. Because virtually every point of the arc illuminates any given point on the collector, it appears that the smooth and spectrally homogeneous flux distribution which is obtained makes the problem of establishing uniformity over the collimator aperture considerably simpler. In the case of a simple lens it does; in practice, however, the lamps and collectors are arranged axially in a manner which puts a dark spot in the center of each collector. If the collector apertures are mapped onto the collimator aperture, there will be a hole in the beam.

Clearly, the two extremes represented in parts A and B, above, carry with them distinctly separate difficulties. The possibility of using neutral density or even chromatic shaping of the source images in order to correct the difficulty with the scheme in part A deserves consideration. Also, the possibility of using exotic optical components and filling the radiation gap inherent in the scheme of part B exists. On the other hand, the concept of intermingled mapping of field and aperture alluded to above, contains a whole spectrum of solutions between the extremes of A and B. It is seen that if the cross section of the beam issuing from the source collection is examined, its character changes from a uniform doughnut of light at the collector lens (actually the lens is an aspheric mirror) to a solid nonuniform patch of light at the source image. Thus, an arrangement which employs an optimum position for establishing ultimate beam uniformity might be selected.

The entire problem of beam uniformity and spectral homogeneity is a most complex one since many factors contribute to nonuniformities in the beam, several of which have already been mentioned. Another important one is the inherent falloff in intensity from the axis to the edge of virtually all collimators. It will be shown in the subsequent discussion that a judicious choice of parameters in the collimation system can reduce this inherent falloff to negligible proportions. However, all of this advantage can be lost entirely if the design is not properly coordinated with the optics involved in transferring the radiation from the source to the collimator.

Thus it can be seen that the importance of these geometrical concepts of radiative transfer in an optical system and their many ramifications with respect to ultimate system performance and the degree to which specific requirements may be met cannot be overemphasized.

4.3 THERMODYNAMICS OF INCOHERENT RADIATION

This section will begin with a discussion of some general principles which lead to a consistent system of radiometric definitions, often confused in engineering literature. It will then be shown how the defining equations impose certain restrictions upon optical system parametric relationships and, together with additional conditions of uniformity and the like, lay the foundation for an efficient method of component and system design.

As usual, the starting point in matters of energy transfer is with the conservation laws which in this case will be based upon radiometric expressions of the first and second laws of thermodynamics. It should be emphasized that the subject is incoherent radiation and its corresponding time-averaged quantities. This is because both the sun and the light sources available for use in solar simulation operate under the influence of spontaneous rather than stimulated emission and thus radiation from any given electromagnetic oscillator is equally probable in all directions. Further, statistical methods may be used to average over a large number of oscillators and assign the thermodynamic properties of the aggregate to the radiation they produce without being concerned about interference effects. That thermodynamically conserved parameters are assigned to the radiation itself goes to the very core of our purpose here.

To this end consider a group of oscillators with a statistical frequency distribution $W_n = 2\pi\nu_n^2$. In accordance with Planck's radiation law² the total energy per unit volume is given by

$$E = Nh\nu \sum_{n=1}^{\infty} \left(n - \frac{1}{2}\right) W_n \quad (4-1)$$

where

N = Volumetric oscillator density

h = Planck's constant

ν = dominant frequency of the interval

The expression for the entropy of this system based upon a normal distribution as first derived by Planck is

$$S = kN \left\{ \left[\left(\frac{E}{Nh\nu} + \frac{1}{2} \right) \log \left(\frac{E}{Nh\nu} + \frac{1}{2} \right) \right] - \left[\left(\frac{E}{Nh\nu} - \frac{1}{2} \right) \log \left(\frac{E}{Nh\nu} - \frac{1}{2} \right) \right] \right\} \quad (4-2)$$

²superscripts refer to List of References following the text.

where k is Boltzman's constant.

The ground state for each oscillator at 0°K is

$$E_0 = \frac{h\nu}{2} \quad (4-3)$$

The volumetric energy density per unit frequency interval available for radiation in all directions with a velocity c is called the brightness B_{ν} and because of equation (4-3) is given by

$$B_{\nu} = E - NE_0 \quad (4-4)$$

Dimensionally B_{ν} is energy per unit volume per unit frequency times velocity. It is identical with the Poynting vector \vec{P}_{ν} derivable from Maxwell's equations describing the energy flow in an electromagnetic wave front and given by

$$\vec{P}_{\nu} = \frac{1}{2} (\vec{E}_{\nu} \times \vec{H}_{\nu}^*)$$

where \vec{E}_{ν} is the electric field amplitude and \vec{H}_{ν}^* is the complex conjugate of the magnetic field amplitude. \vec{P}_{ν} is therefore a time averaged vector quantity and its divergence is isomorphic with B_{ν} , i.e.,

$$\nabla \cdot \vec{P}_{\nu} = \vec{B}_{\nu}$$

Combining equations (4-4) and (4-1)

$$\frac{E}{h\nu} - \frac{N}{2} = \sum_{n=1}^{\infty} (n-1) N_n = \frac{B_{\nu}}{h\nu} \quad (4-5)$$

where N_n is the number of oscillators in each state. Now consider the flow of a single photon in a radiation field with a volumetric energy flow density of U . The cross-sectional area occupied by the photon is λ^2 where λ is its wavelength. Its corresponding energy is $h\nu$. Moving with a velocity of c it therefore occupies a volume in unit time of $\lambda^2 c$. Thus

$$U = \frac{h\nu}{\lambda^2 c} \quad (4-6)$$

Using similar logic with unit cross-sectional area traveling with velocity c in unit time the volume is c and the total energy, cU . Since there are $h\nu$ parcels of energy per oscillator the total photon flux per unit time per unit cross-sectional area is:

$$N = \frac{cU}{h\nu} \quad (4-7)$$

Combining (4-6) and (4-7) gives

$$N = \frac{c h \nu}{h \nu \lambda^2 c} = \frac{1}{\lambda^2} = \frac{\nu^2}{c^2} \quad (4-8)$$

It is now a simple matter to insert equations (4-5) and (4-8) into (4-2) and obtain an expression for the entropy of electromagnetic radiation in terms of its brightness. The result is:

$$S = \frac{k\nu^2}{c^3} \left\{ \left[\left(1 + \frac{c^2 B_\nu}{h\nu^3} \right) \log \left(1 + \frac{c^2 B_\nu}{h\nu^3} \right) \right] - \left[\left(\frac{c^2 B_\nu}{h\nu^3} \right) \log \left(\frac{c^2 B_\nu}{h\nu^3} \right) \right] \right\} \quad (4-9)$$

Although this expression is of little more than academic interest for our purposes it does point up the important concept that the parameter B_ν or its spectrally integrated equivalent B is conserved in accordance with the second law of thermodynamics and that it can only be altered by irreversible processes involving conversion of radiant energy to heat. An important distinction between dissipative losses in an optical system, involving such things as transmission and reflectivity as opposed to non-dissipative losses such as collection efficiency or vignetting is therefore made. The former is denoted by k , the system transmittance, and it is considered separately due to its effect on the otherwise conserved parameter B . In fact, in most of what follows the parameter B is understood to be kB , that is, already attenuated by transmission losses.

Having established the parameter B as a metric of radiation entropy, now consider the first law of thermodynamics dealing with the conservation of energy. Referring to figure 4-7, where \hat{r} is a unit vector which defines the direction of radiation propagation from dS to dA , the energy radiated by a surface element $d\vec{S}$ in the direction \hat{r} is proportional to the projection of $d\vec{S}$ in the direction \hat{r} . The energy density decreases in proportion to the square of the distance from $d\vec{S}$ and finally the amount captured by the target element dA is in proportion to the projection of $d\vec{A}$ in the direction $-\hat{r}$. The proportionality constant is B or the total energy available from all the radiators on $d\vec{S}$ in all directions. The element of flux, therefore, radiated by $d\vec{S}$ and captured by $d\vec{A}$ is given by

$$d^2 F = B \left[\frac{(d\vec{S} \cdot \hat{r})(d\vec{A} \cdot \hat{r})}{(nR\hat{r}) \cdot (nR\hat{r})} \right] \quad (4-10)$$

MEDIUM OF REFRACTIVE INDEX, n

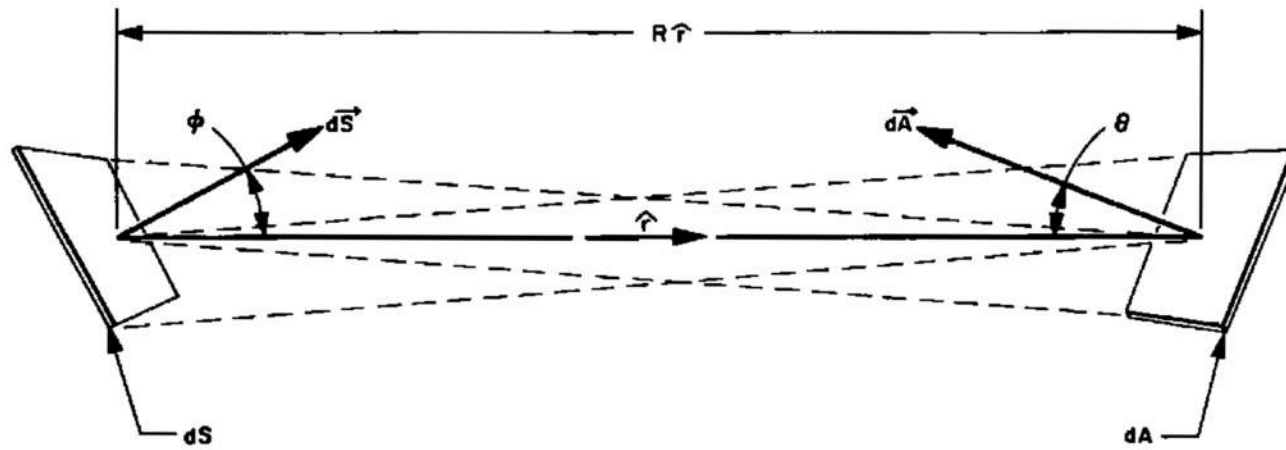


Figure 4-7. Source and Target Elements

In this expression B may or may not be a function of \hat{r} . If it is not, the source element $d\vec{S}$ is considered to be Lambertian.* The quantity $nR\hat{r}$ is the optical path length by which the inverse square falloff is measured. Equation (4-10) contains the basis upon which most of the ensuing theory and radiometric definitions are based. It is seen that equation (4-10) has inherent in it a symmetry involving either one of two solid angles

$$d\omega = \frac{d\vec{A} \cdot \hat{r}}{(nR\hat{r}) \cdot (nR\hat{r})} \quad (4-11)$$

or

$$d\Omega = \frac{d\vec{S} \cdot \hat{r}}{(nR\hat{r}) \cdot (nR\hat{r})} \quad (4-12)$$

Now defining I as the power radiated from the source per unit outward solid angle $d\omega$; from equation (4-10)

$$\frac{d^2 F}{d\omega} = dI = Bd\vec{S} \cdot \hat{r} \quad (4-13)$$

This is the familiar parameter, radiance, analogous to candle power except for the latter's reference to visual response. The power radiated or received per unit area by an element of area will be denoted by E and called flux density or intensity. For a target element $d\vec{A}$, equations (4-10) and (4-13) give

$$dE = \frac{d^2 F}{dA} = \left[\frac{dI}{(nR\hat{r}) \cdot (nR\hat{r})} \right] \cos \theta \quad (4-14)$$

where θ is the angle normal to the target element makes with the direction to the source element. Thus the surface flux density of the wave-front emanating from a source is the latter's radiance divided by the square of the distance from the source to the wave-front. This is based upon the intensity law of geometrical optics calculated from the eikonal or optical path function which satisfies the general differential equation

$$(\nabla \rho)^2 = n^2$$

where n is the index of refraction of the medium. The surfaces of constant ρ are the so-called wave-fronts (actually surfaces of constant spatial phase). These may be determined by calculating optical path lengths of rays traced from a given source point. In its most general form, the ratio of intensities at two positions along an optical ray path is given by the

*A surface whose emittance is independent of direction with respect to the surface normal.

integral³

$$\frac{E_2}{E_1} = \frac{n_2}{n_1} \exp \left[- \int_{s_1}^{s_2} \frac{\nabla^2 \rho}{n} dS \right] \quad (4-15)$$

where the optical path is measured along s and n is allowed to vary continuously. Between any two phase surfaces in a medium of constant n and separated by a path length L , one has

$$\frac{E_2}{E_1} = \frac{R_1 R_1'}{L^2} \quad (4-16)$$

where R_1 and R_1' are the meridional and sagittal radii of curvature of the first phase or wave-front and L is the optical path to the second wave-front. The parameter $\frac{1}{R_1 R_1'}$, where R and R' are the principal radii of the wave-front, is known as the Gaussian curvature or second curvature of the surface. For a spherical wave-front, $R = R'$ yielding the inverse square law

$$E = \frac{I}{R^2} \quad (4-17)$$

where I is the source radiance and E is the intensity on the wave-front of radius R . In practice the Gaussian curvature of the wave-front at a given target point as traced from a given source point would be calculated. Knowing I from the source for the corresponding direction in space would yield the intensity contribution to that target point from the source point considered. When it is necessary to account for the finite extension of the source, the difficulties inherent in this process are enormous. For example, the inability to determine, in advance, that a given direction from a source position will end at a fixed target point makes complicated and time consuming interpolation necessary. This combined with the requirement for a realistic integration throughout the source volume poses a formidable computational task. On the other hand, by starting at a target position and integrating over the radiation field impinging thereon, the problem could be many times simplified since all contributions would be referred to the same point. To do this equation (4-12) for the inward solid angle $d\Omega$ is substituted into equation (4-10) to give

$$dE = \frac{d^2 F}{dA} = B d\Omega \cos \theta \quad (4-18)$$

It will be shown in the discussion concerning the source representation that it is possible to determine the value of B for all directions over which $d\Omega$ is to be integrated. Further, in the discussion concerning energy

tracing, it will be seen that modern and altogether reasonable computer techniques make it possible to calculate the radiant intensity at any position due to radiation transferred through complicated optical systems, on the basis of the concept embodied in equation (4-18).

There are certain important results with regard to axially symmetric radiation fields and Lambertian radiators which may be obtained by applying equation (4-10). Consider, as in figure 4-8, a source element of area dS which radiates symmetrically with respect to its surface normal $d\vec{S}$. If the source element is Lambertian, its brightness B is independent of direction and the total flux density E_s on the surface of the source element may be calculated as follows:

From the geometry of figure 4-8, it is known that

$$d\vec{S} \cdot \hat{r} = dS \cos \phi$$

where \hat{r} is a unit vector in the direction ϕ with respect to the surface normal $d\vec{S}$ of the source element. Combining this relationship with equations (4-10) and (4-11) gives

$$d^2F = B \cos \phi dS d\omega$$

Since the source element dS is assumed to radiate symmetrically with respect to its surface normal, then the outward element of solid angle $d\omega$ may be defined as

$$d\omega = 2\pi \sin \phi d\phi$$

Combining these latter two equations yields

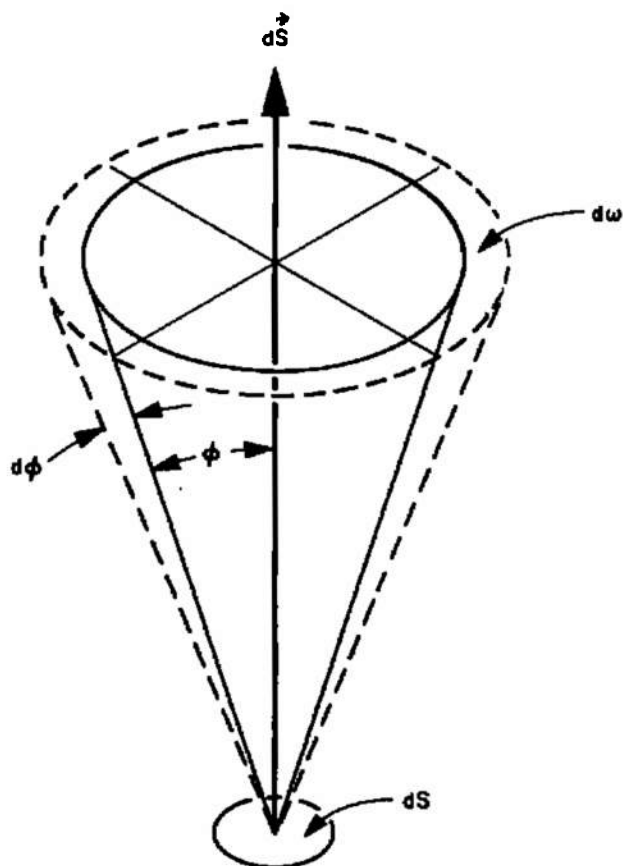
$$d^2F = 2\pi B dS \sin \phi \cos \phi d\phi \quad (4-19)$$

Since the source element radiates into a hemisphere, the total flux density E_s on the surface of the source element is given by

$$E_s = \int_0^{\frac{\pi}{2}} \frac{d^2F}{dS} = 2\pi B \int_0^{\frac{\pi}{2}} \sin \phi \cos \phi d\phi = \pi B \quad (4-20)$$

i.e., the intrinsic brightness B of a Lambertian surface is its total surface flux density divided by π .

Placing this surface element, as in figure 4-9, with its normal coincident with the optic axis of a condenser optical system which collects radiation to the angle Φ , integrating equation (4-19) from 0 to Φ gives the energy collected as:



dS is an element of source area

\vec{dS} is the surface normal of dS

$d\omega$ is an axially symmetric element of solid angle
 $d\omega = 2\pi \sin\phi d\phi$

Figure 4-8. Lambertian Source and Symmetric Field

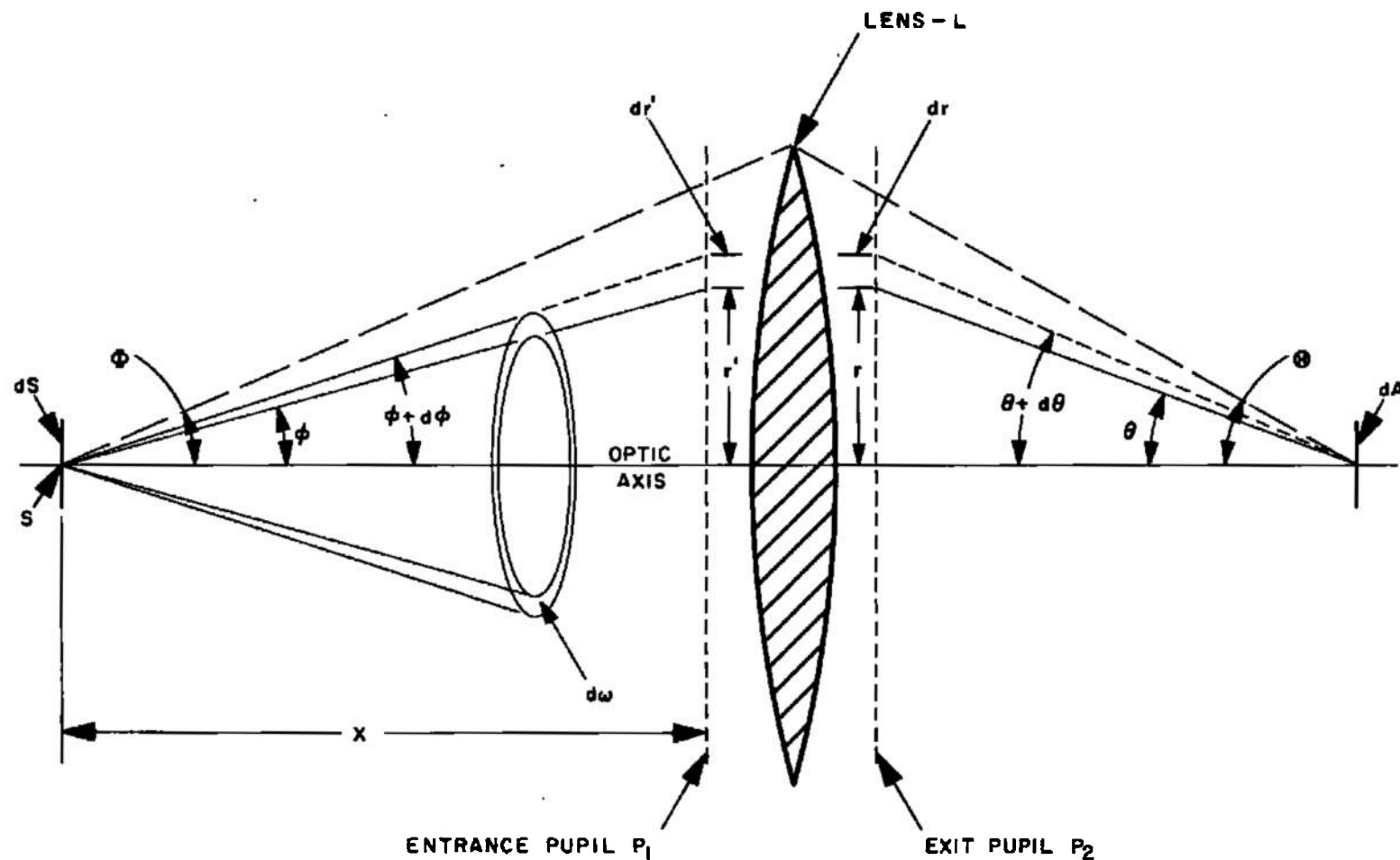


Figure 4-9. Flux Concentration

$$dF = \pi BdS \sin^2 \Phi \quad (4-21)$$

If the convergence angle to the image is Θ , then in accordance with Abbe's sine condition, the ratio of image area dA to source area dS is

$$dA = dS \frac{\sin^2 \Phi}{\sin^2 \Theta} \quad (4-22)$$

Assuming all of dF is contained in dA , then combining equations (4-21) and (4-22), the flux density E_i in the image is

$$E_i = \frac{dF}{dA} = \pi B \sin^2 \Theta \quad (4-23)$$

Thus, for a continuous symmetric field and a Lambertian source, the flux density in the image is dependent only upon the convergence angle and not upon the collection angle. Also from equations (4-20) and (4-23):

$$\frac{E_i}{E_s} = \sin^2 \Theta$$

Since $\sin \Theta$ cannot exceed unity, it is impossible for the intensity of the image to exceed that of the source, no matter what concentrating optical system is employed. This is merely another way of saying that the temperature of the radiation cannot be raised with a passive system.

4.4 UNIFORMITY CRITERIA AND OPTICAL PARAMETRIC DETERMINANTS

In the preceding discussion, it has been shown how basic radiometric principles have already begun to set the framework upon which all optical system designs for solar simulation must be based. By further appeal to these general principles criteria may be defined which must be met in order to achieve a uniform distribution of radiation across the output beam from an optical system. These criteria may, in turn, be used to synthesize the appropriate optical system design. To present the concepts with a minimum of mathematical complexity, the following treatment deals with axially symmetric systems having simply connected boundaries.

Referring to figure 4-9, lens L represents an equivalent "black box" optical system with entrance and exit pupil planes denoted by P_1 and P_2 respectively. (Actually, the term "plane" is a misnomer since the entrance and exit pupils are more generally curved surfaces). Assume that the light source is located at S so that it radiates symmetrically with respect to the axis of the optical system. Considering the axially symmetric element of solid angle $d\omega$ between ϕ and $\phi + d\phi$, the energy dF'

incident upon the element of area dP_1 in the entrance pupil between r' and $r' + dr'$ is

$$dF' = I_\phi d\omega = 2\pi I_\phi \sin \phi d\phi \quad (4-24)$$

where I_ϕ is the source radiance in the direction ϕ . The flux density E' on the element of area dP_2 , is

$$E' = \frac{dF'}{dP_2} = \frac{dF'}{2\pi r' dr'} = I_\phi \left(\frac{\sin \phi d\phi}{r' dr'} \right) \quad (4-25)$$

The flux density E on an element of area dP_2 in the exit pupil between r and $r + dr$ is given by

$$E = \frac{dF}{dP_2} = \frac{dF}{2\pi r dr} \quad (4-26)$$

where dF is the energy incident upon the element of area dP_2 . If the optical system is so defined that all of the flux incident upon the element of area dP_2 in the exit pupil must first pass through the element of area dP_1 in the entrance pupil, then, defining k as the transmittance of the optical system along the optical path from dP_1 to dP_2 ,

$$dF = k dF' \quad (4-27)$$

Substituting equations (4-24) and (4-26) into equation (4-27) yields the relationship

$$E = k I_\phi \left(\frac{\sin \phi d\phi}{r dr} \right) \quad (4-28)$$

From the inverse square law, equation (4-17), the intensity on the entrance pupil at the optic axis is (denoting paraxial *values with the subscript "0")

$$E_0' = \frac{I_0}{X^2} \quad (4-29)$$

where x is the distance from the source to the entrance pupil. If M is now defined as the paraxial magnification between the pupil planes, then

$$dP_{1_0} = M^2 dP_{2_0} \quad (4-30)$$

Dividing equation (4-27) by equation (4-30) now yields

*"paraxial" refers to the limiting values determined for the various parameters along the optic axis. For example, the paraxial magnification of a lens is defined as the ratio of the sine of the angle between the optic axis and a ray entering the lens arbitrarily close to the optic axis, to the sine of the angle which the ray makes with the optic axis after passing through the lens.

$$\frac{dF_o}{M^2 dP_{2_o}} = \frac{k_o dF'_o}{dP'_{1_o}} \quad (4-31)$$

From equations (4-25) and (4-26), equation (4-31) resolves to

$$\frac{E_o}{M^2} = k_o E'_o \quad (4-32)$$

Substituting equation (4-29) gives

$$E_o = k_o I_o \left(\frac{M^2}{X^2} \right) \quad (4-33)$$

If R is now defined as the relative intensity in the exit pupil at a distance r from the optic axis, then from equations (4-28) and (4-33)

$$R = \frac{E}{E_o} = \frac{X^2 k I_o \sin \phi d\phi}{M^2 k_o I_o r dr} \quad (4-34)$$

If the relative transmittance \bar{k}_ϕ and the relative radiance \bar{I}_ϕ are defined such that

$$\bar{k}_\phi = \frac{k}{k_o} \quad (4-35)$$

and

$$\bar{I}_\phi = \frac{I_\phi}{I_o} \quad (4-36)$$

and the following identities are used:

$$\sin \phi d\phi = - d(\cos \phi) \quad (4-37)$$

$$r dr = \frac{1}{2} d(r^2) \quad (4-38)$$

then equation (4-34) may be converted to

$$R = \frac{E}{E_o} = -2 \bar{k}_\phi \bar{I}_\phi \left(\frac{X^2}{M^2} \right) \left[\frac{d(\cos \phi)}{d(r^2)} \right] \quad (4-39)$$

It is instructive to examine the behavior of equation (4-39) for a specific source configuration. For example, consider the case of a flat, Lambertian source so oriented that it is normal to the optic axis. For a flat, Lambertian source, $\bar{I}_\phi = \cos \phi$ and since, by definition

$$-2 \cos \phi d(\cos \phi) \equiv d(\sin^2 \phi) \quad (4-40)$$

then from equation (4-39), assuming that the transmittance of the optical system is constant ($k_\phi = 1$) for all ϕ ,

$$R = \left(\frac{X^2}{M^2} \right) \left[\frac{d(\sin^2 \phi)}{d(r^2)} \right] \quad (4-41)$$

This is the expression used by Luneberg⁴ to design condenser lenses for projection systems which incorporate flat filament lamps in order to achieve uniform illumination of the film gate. Since this study must deal with collimating optical systems, consider now the case, represented schematically in figure 4-10, where a source, located a distance f from the entrance pupil of an optical system, radiates symmetrically with respect to the optic axis into the entrance pupil. Assume that the optical system is so defined that it collimates (makes parallel) the radiation which it collects from the source. By definition, the paraxial magnification M between the pupil planes of a collimating optical system is unity and f is, by definition, the effective focal length of the optical system. Further, since $f = X$, equation (4-39) may be written, for a collimating optical system, as

$$R = \frac{E}{E_0} = -2 \bar{k}_\phi \bar{I}_\phi f^2 \left[\frac{d(\cos \phi)}{d(r^2)} \right] \quad (4-42)$$

This equation, which is denoted as the "Normal Illuminance Criterion", can be used in many ways. For example, to analyze a given collimating optical system to determine the distribution of light across its exit pupil, it is necessary only to trace rays from the source at several angles ϕ and note the distance r from the optic axis at which each intersects the exit pupil. If a plot of $\cos \phi$ versus r^2 is then prepared, the relative intensity distribution across the exit pupil can be determined by examining the slope of this curve as a function of r . If \bar{I}_ϕ and/or \bar{k}_ϕ are not unity, the appropriate correction must, of course, be incorporated.

It should be noted that the above formulation did not take into account effects due to finite extension of the source. For small field angles (on the order of 2° to 5°), these higher order terms are not negligible, but they are small in comparison to the dominant first order effect represented by equation (4-42). In fact, this simple, preliminary analytical procedure is the most rapid and powerful technique available for gaining a comprehensive knowledge of the properties of a given optical system design.

By definition: $r=r'$

55

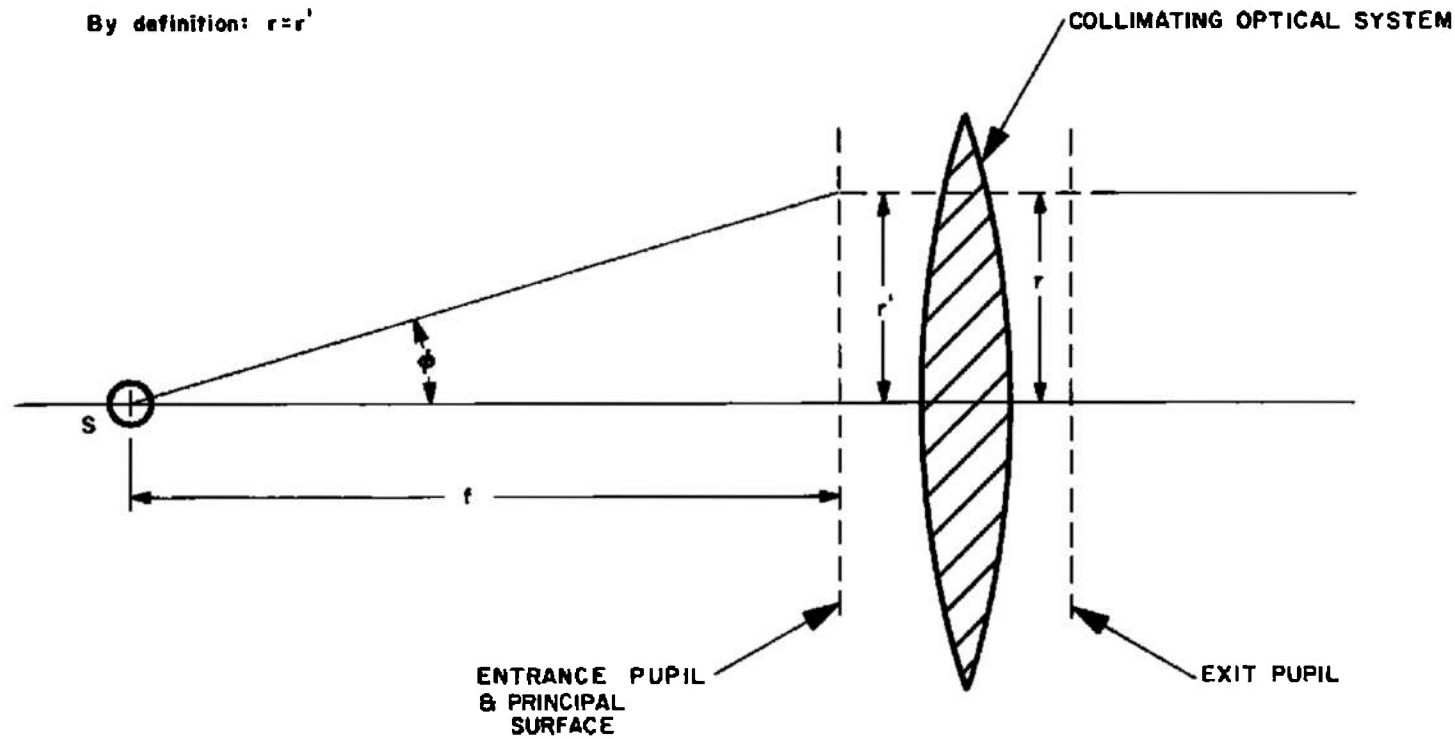


Figure 4-10. Collimator Schematic

On the basis of the preceding, two of the most fundamental relationships which must govern the design of any collimating optical system generated for the purpose of solar simulation may be defined. Since, for a collimating optical system, M is by definition unity and f , the effective focal length, is identically the distance from the source to the entrance pupil along the optic axis, then from equation (4-33)

$$f = \sqrt{\frac{k_o L_o}{E_o}} \quad (4-43)$$

where, again, L_o is the axial radiance of the source, k_o is the axial transmittance of the optical system, and E_o is the axial intensity in the exit pupil. It is imperative that it be recognized that the effective focal length of the optical system is a function only of these three thermodynamic parameters. Thus, it is unnecessary to know what type of optical system is employed except for the purpose of estimating the axial transmittance, (which can be determined from the number of air-glass interfaces, the number of reflecting surfaces, and the approximate total thickness of glass along the axis).

Taking into account the physical size of the source from which the axial radiance L_o is considered to emanate, it is possible to calculate the field angle subtended by the radiation emanating through the axial position in the exit pupil of any optical system since it is equal to that subtended by the source at a distance X . Thus, regardless of the design details of the optical system, so long as it provides a continuous field, then:

$$\sin\left(\frac{\Theta}{2}\right) = \frac{D}{2X} \quad (4-44)$$

where Θ is the total field angle and D is the effective diameter of the source. In the case of a collimating optical system ($f = X$), the field angle Θ is given by

$$\Theta = 2 \arcsin\left(\frac{D}{2f}\right) \quad (4-45)$$

These equations hold, of course, only on axis and the field is axially symmetric only if the source is also axially symmetric. However, by virtue of the principle expressed in equation (4-18) and its integration as seen in equation (4-23), the solid angle

$$\Omega = \pi \sin^2\left(\frac{\Theta}{2}\right) \quad (4-46)$$

must be preserved for all positions across the aperture no matter how the shape of the field may be altered by off-axis aberrations and foreshortening. This statement assumes that the entire source can be seen everywhere in the aperture and that the distribution of B in the simulated solar

field is unaltered. This is never exactly the case as the source is seen from different directions in different parts of the aperture of the optical system; in addition, the microbrightness distribution of a source is generally a function of the direction of view. Thus, Ω in equation (4-46) is not conserved exactly; however, the deviations involved are refinements to be made after such a condition has been approached.

The effects of optical system aberrations can be determined on the basis of the foregoing theory, as is traditional in optical design, by using only information gained from rays either paraxial or passing through the axis. As an example consider the effects of spherical aberration which is the only aberration that does not go to zero for points on axis and has a profound effect on depth-of-field uniformity. Hence, it would be useful to have a method of calculating this effect and isolating its contribution. To this end examine figure 4-11. If X' is the distance from the test plane to the paraxial image of the source, and $\Delta y'$ is the blur circle radius resulting from spherical aberration in the zone of radius r , then

$$r = \Delta y' - X' \tan \theta \quad (4-47)$$

Substituting this into equation (4-39) yields

$$R = -2\bar{k}_\phi \bar{I}_\phi \left(\frac{X^2}{M^2} \right) \left\{ \frac{d(\cos \phi)}{d \left[(\Delta y' - X' \tan \theta)^2 \right]} \right\} \quad (4-48)$$

Holding X' constant,

$$R = -2\bar{k}_\phi \bar{I}_\phi \left[\frac{X^2}{M^2 (X')^2} \right] \left\{ \frac{d(\cos \phi)}{d \left[\left(\frac{\Delta y'}{X'} - \tan \theta \right)^2 \right]} \right\} \quad (4-49)$$

From paraxial theory, any pair of conjugate planes can be referred to any other pair of conjugate planes having magnification M , in which case the magnification is given by

$$M' = \frac{MX'}{X} \quad (4-50)$$

Thus, equation (4-49) may be written

$$R = \bar{k}_\phi \bar{I}_\phi \left(\frac{2}{M'^2} \right) \left\{ \frac{d(-\cos \phi)}{d \left[\left(\frac{\Delta y'}{X'} - \tan \theta \right)^2 \right]} \right\} \quad (4-51)$$

where

- M' = the magnification between the source and its image
- ϕ = initial slope angle subtended at the center of the source by a ray proceeding to some zone at the entrance pupil
- $\Delta y'$ = spherical aberration along that ray at the source image

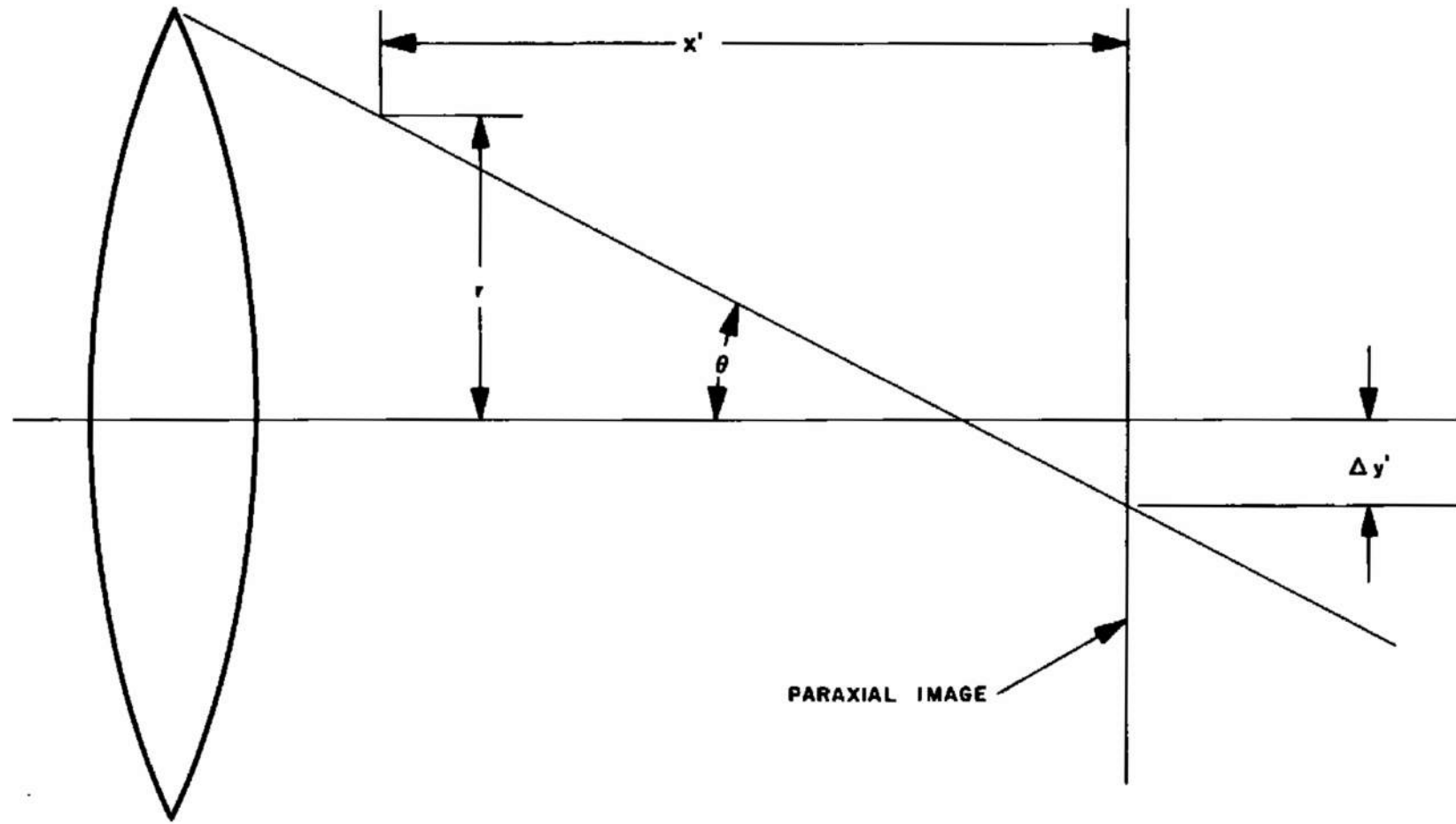


Figure 4-11. Spherical Abberation

Θ = slope angle of the same ray as it proceeds toward its image
 X' = distance from exit pupil (equivalent to an arbitrary position
 in the beam leaving the optical system.)

In a collimating optical system, the latter parameter (X') does not exist except in the presence of spherical aberration. It can now be concluded that, if the spherical aberration is corrected, $\Delta y' = 0$, and R is accordingly independent of X' . This may be interpreted to mean that correction of spherical aberration in the optical system serves to make the light distribution independent of the exact position of the target plane. Inasmuch as a small uniform source was assumed, this independence does not extend to the region of the image of a real source. Nevertheless, it is obvious from this result that one of the most important conditions to be imposed upon the optical design is freedom from spherical aberration.

Now consider whether freedom from other aberrations is a necessity for the realization of uniformity either in depth or across a plane. This may be determined from the following example of how the above theory may be used in the synthesis of optical system parameters. Consider a flat source ($\bar{I} = \cos \phi$) located at the first principal focal point of a collimating optical system and oriented normal to the latter's optic axis. The appropriate form of equation (4-41) would be (assuming the relative transmittance \bar{k} as unity and again defining f as the effective focal length)

$$R = f^2 \left[\frac{d(\sin^2 \phi)}{d(r^2)} \right] \quad (4-52)$$

Setting the expression identically equal to unity for all applicable values of r and ϕ yields

$$\int d(r^2) = f^2 \int d(\sin^2 \phi) \quad (4-53)$$

Integration of equation (4-53) yields

$$\frac{r}{\sin \phi} = f = \text{constant} \quad (4-54)$$

Equation (4-54) tells exactly how a ray entering the optical system must be related to the corresponding exiting ray. Furthermore, this equation is the classical expression for an optical system which is completely free of coma. Again, a condition has been defined where freedom from an optical aberration is a requisite for uniformity.

Now consider equation (4-42), the equation which has been denoted as the "Normal Illuminance Criterion". Integration by parts yields

$$\int d(r^2) = -2f^2 \int \bar{k}_\phi \bar{I}_\phi d(\cos \phi) \quad (4-56)$$

$$r^2 = -2f^2 \left\{ \left(\bar{k}_\phi \bar{I}_\phi \cos \phi \Big|_0^\phi \right) - \int_0^\phi \cos \phi \left[\frac{d(\bar{k}_\phi \bar{I}_\phi)}{d\phi} \right] d\phi \right\} \quad (4-57)$$

Along the optical axis, $\phi = 0$, $\bar{I}_\phi = \bar{I}_0 = 1$, and $\bar{k}_\phi = \bar{k}_0 = 1$. Therefore

$$r^2 = 2f^2 \left\{ 1 - \bar{k}_\phi \bar{I}_\phi \cos \phi + \int_0^\phi \left[\frac{d(\bar{k}_\phi \bar{I}_\phi)}{d\phi} \right] \cos \phi d\phi \right\} \quad (4-58)$$

If the source radiance is assumed to be spherically symmetric, then $\bar{I}_\phi = 1$. Further, if the transmittance across the aperture of the optical system is assumed constant, then $\bar{k}_\phi = 1$. Under these conditions, equation (4-58) reduces to

$$\frac{r^2}{2(1 - \cos \phi)} = f^2 = \text{constant} \quad (4-59)$$

Obviously expressions (4-54) and (4-59) represent two distinctly different conditions on the optical design, the former being freedom from coma while the latter requires coma of a prescribed form and degree. This result illustrates one of the most important facts affecting the design of optical systems for solar simulators; namely, that the design criteria are vitally dependent upon the absolute and relative source characteristics. Further, these criteria result in an optical design problem which is totally different from that usually encountered in lens design (i.e., the greatest possible suppression of all optical aberrations) in that certain aberrations must be deliberately introduced (within prescribed limits as determined by source radiometry) in order to achieve ultimate beam uniformity. This is not surprising since the latter objective certainly has nothing to do with image resolution, which was demanded for virtually all past lens design problems. Accordingly, there is very little past experience upon which to draw for the solution of what is clearly a non-trivial problem. (The treatment of the remaining optical aberrations such as astigmatism, field curvature, and distortion follows similar lines. But, as they are not used directly in the design of the optics, their complexities are omitted from the present discussion.)

When designing an optical system for solar radiation simulation, it is convenient to use an alternative form of equation (4-42). When a train of optical components is involved, such as is shown in figure 4-12, each optical component is joined to the next one through their mutual conjugate foci. The source S is placed at the first focal point and repetitively re-imaged at S_1, S_2 , etc. Equation (4-42) relates the initial angle ϕ_1 from the source to the final height r in the collimator aperture (exit pupil). The zonal magnification m_i of each optical component between the source and the collimator is defined by

$$m_i = \frac{\sin \phi_i}{\sin \phi_{i+1}} \quad (4-60)$$

and the zonal focal length z of the collimator is defined by

$$z = \frac{r}{\sin \phi_n} \quad (4-61)$$

The initial angle ϕ_1 is related to the angle ϕ_n through the equation

$$\frac{\sin \phi_1}{\sin \phi_n} = \prod_{i=1}^n m_i \quad (4-62)$$

Combining equations (4-61) and (4-62) to eliminate $\sin \phi_n$ yields

$$r = \frac{z \sin \phi_1}{\prod_{i=1}^n m_i} \quad (4-63)$$

Squaring equation (4-63) yields

$$r^2 = \frac{z^2 (1 - \cos^2 \phi_1)}{\prod_{i=1}^n m_i^2} \quad (4-64)$$

Since z and m_i are constant for any given ray, equation (4-64) may be differentiated to obtain

$$\frac{d(\cos \phi_1)}{d(r^2)} = - \left[\frac{\prod_{i=1}^n m_i^2}{2z^2 \cos \phi_1} \right] \quad (4-65)$$

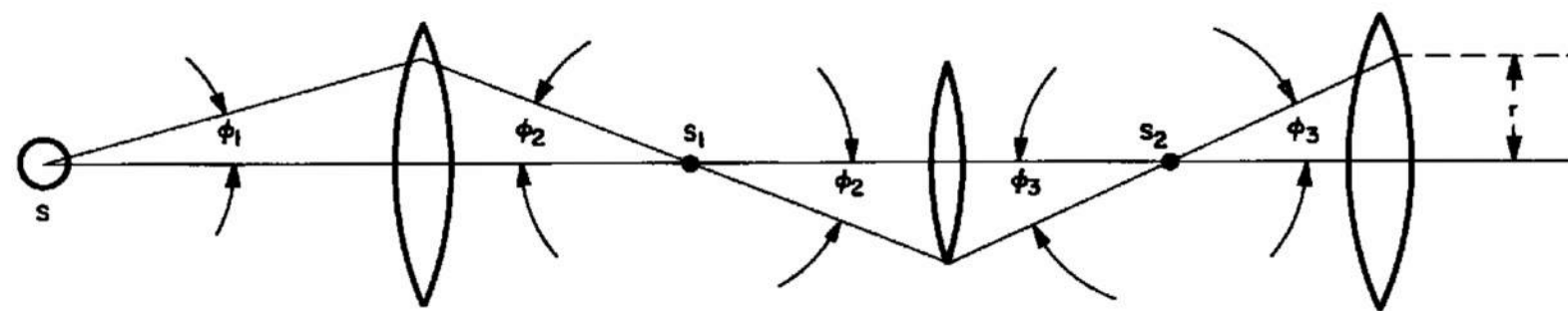


Figure 4-12. Conjugated Optical Train

Substituting equation (4-65) into equation (4-42) gives

$$R = \left(\frac{\bar{k} \bar{I} f^2}{z^2 \cos \phi_1} \right) \prod_{i=1}^n m_i^2 \quad (4-66)$$

In the limit (along the optic axis) as r and ϕ_1 approach zero, R , \bar{k} , and \bar{I} approach unity, z approaches ρ (the paraxial focal length of the collimator), and m_i approaches M_i (the paraxial magnification of the i^{th} component in the optical train). Thus

$$\lim_{r \rightarrow 0} R = \lim_{\phi_1 \rightarrow 0} \left(\frac{\bar{k} \bar{I} f^2}{z^2 \cos \phi_1} \right) \prod_{i=0}^n m_i^2 = \frac{f^2}{\rho^2} \prod_{i=1}^n M_i^2 = 1 \quad (4-67)$$

Therefore

$$f = \frac{\rho}{\prod_{i=1}^n M_i} \quad (4-68)$$

Substituting equation (4-68) into equation (4-42) yields the desired alternative form of equation (4-42)

$$R = \left[\frac{-2\bar{k} \bar{I} \rho^2}{\prod_{i=1}^n M_i^2} \right] \left[\frac{d(\cos \phi_1)}{d(r^2)} \right] \quad (4-69)$$

which gives the necessary information in terms of the paraxial focal length ρ of the collimator and the paraxial magnifications M_i of the n optical components between the source and the collimator. The condition for uniformity is obtained by holding $R = 1$ for all values of ϕ_1 and r . Finally, note that equation (4-68) is a classical optical formula (paraxial magnification condition) which relates the paraxial focal length ρ of one component in the optical system to the paraxial magnifications M_i of the remaining components in the optical system and the effective focal length f of the total system. Thus, equation (4-68) is obviously one more condition which ties the system parameters together.

4.5 THEORETICAL BASIS OF THE SOURCE REPRESENTATION

Perhaps the most important consideration in the design of a solar radiation simulation system is the nature of the radiation field produced by the light source to be used in the system. The problem of characterizing this radiation field reduces, for the purpose of this study, to the generation of an analytical source representation from which the radiant energy intensity produced by the source, optical-system combination at any position in the target volume can be calculated. The purpose of the following is, therefore, (1) to discuss the nature of the radiation field produced by a light source, (2) to define a method whereby this radiation field can be uniquely characterized, and (3) to define the source parameters and characteristics from which a source representation can be generated.

4.5.1 Nature of the Radiation Field Produced by a Light Source

The generation of a source representation begins with an analysis to determine the nature of the radiation field which it must characterize. To illustrate the concepts involved, consider first the scalar field potential on an arbitrary surface which surrounds a point source. The eikonal function $\rho(x, y, z)$ can be defined on such a surface; and by the solution of the equation

$$(\nabla \rho)^2 = n^2 \quad (4-70)$$

for the stated boundary condition, where n is the index of the medium, the function ρ can be determined on any other arbitrary surface, provided the latter is simple and surrounds the source. The direction of propagation of the radiation is normal to the surfaces defined by

$$\rho(\vec{r}) = \text{constant} \quad (4-71)$$

and, in the case of a point source, these surfaces are the family of concentric spheres centered about the source. The ratio of the intensities $\frac{E_2}{E_1}$ for any two positions s_1 and s_2 on the ray in the direction \vec{r} is given by

$$\frac{E_2}{E_1} = \frac{n_2}{n_1} \exp \left[- \int_{s_1}^{s_2} \frac{\nabla^2 \rho}{n} ds \right] \quad (4-72)$$

Thus, if the radiation intensity and direction of propagation are known for all points on an arbitrary surface which surrounds the source, these same quantities may be determined at any other point in space. Therefore, the radiation field produced by a point source may be characterized

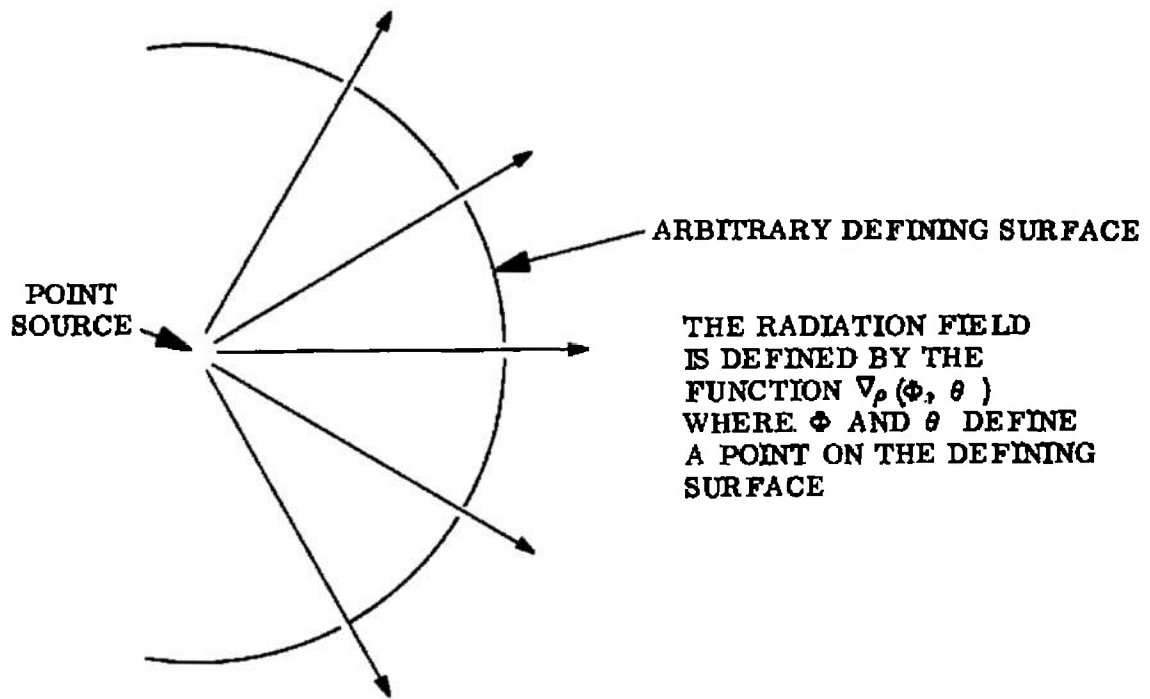
by the simple vector point function $\nabla\rho(\Phi, \Theta)$ where Φ and Θ are the independent parameters on the defining surface.

Because the radiation field is, in reality, the result of many incoherent sources within the arc (which may be considered as a continuum of point sources), it is not possible to characterize the total radiation field with the simple vector-point function noted above. Instead, as a result of this more complicated situation, the radiation field produced by the arc may be considered as the continuum of the radiation fields produced by the continuum of point sources within the arc. Therefore, the radiation field is a continuum defined by the function $\nabla\rho(\Phi, \Theta, \Phi', \Theta')$ where Φ and Θ are the parameters which specify a point on the defining surface, as above, and Φ' and Θ' are independent parameters which determine a direction with respect to the surface at that point. In essence, this means that when the source is finite, the radiation field produced by the source is completely determined only when the polar distribution of energy apparently emanating from each point on the defining surface has been determined. This situation is represented schematically in figure 4-13.

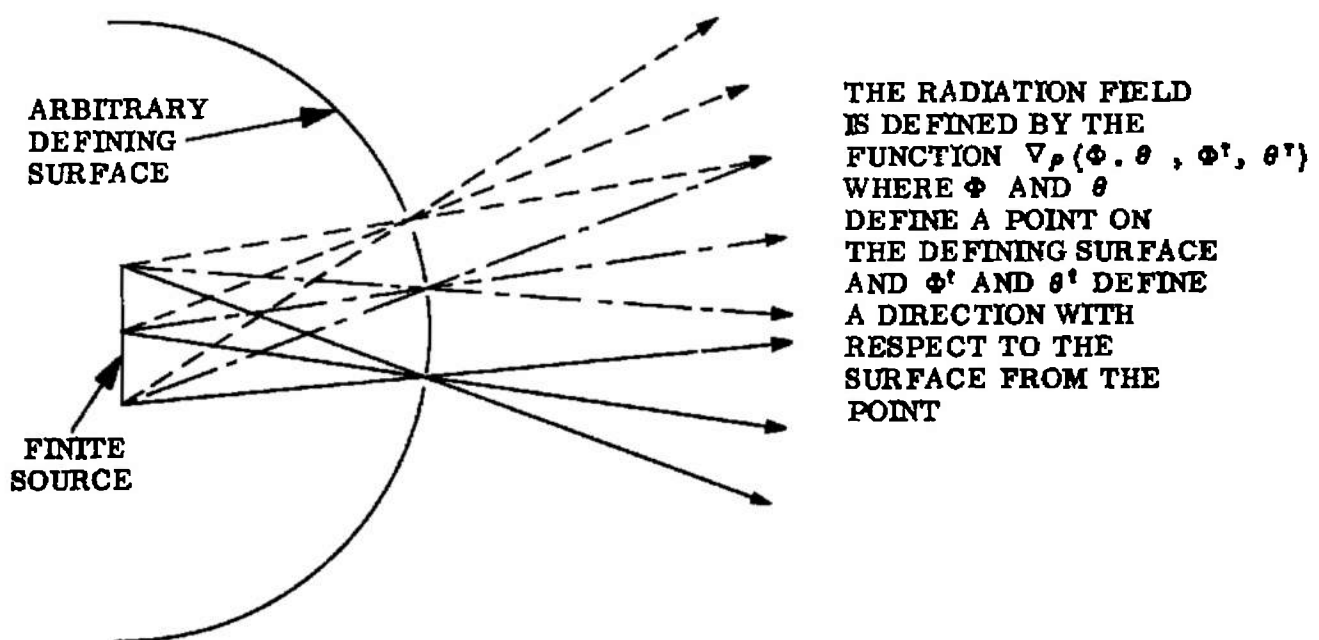
If the assumption is now made that, in all optical systems treated in this study, the distribution of light is sufficiently represented by the classical approximation of geometrical optics and that all variations in the intensity distribution resulting from instantaneous diffraction and interference are nullified by the time average of the field intensity, then the problem resolves to one of characterizing the radiation field by defining the time-averaged polar distribution of radiation apparently emanating from each point on an arbitrary reference surface which surrounds the source. On the basis of this assumption, the choice of a source representation becomes quite arbitrary; although the radiation field produced by a given source is unique, a given radiation field can result from any number of source characteristics. This latter point will be further discussed below, in the treatment of the nature of the source representation.

One additional parameter should be considered in this discussion of the nature of the radiation field, namely the total energy radiated by a given source per unit time. In any radiation field, the total energy E radiated by the source per unit time is given by

$$E = \int_V \nabla \cdot \vec{P} dV \quad (4-73)$$



VIEW A: THE RADIATION FIELD PRODUCED BY A POINT SOURCE



VIEW B: THE RADIATION FIELD PRODUCED BY A FINITE SOURCE

Figure 4-13. Schematic Representation of Radiation Fields

where the divergence of \vec{P} , the Poynting vector, is integrated over all space. If the source is finite, V is bounded. Thus, if \vec{P} is specified only on a surface S which surrounds the source and contains the volume V , energy is conserved and Green's Theorem may be applied, which gives

$$E = \int_V \nabla \cdot \vec{P} dV = \int_S \hat{n} \cdot \vec{P} dS \quad (4-74)$$

where \hat{n} is the unit vector normal to the element of area, dS , on the surface. From this equation, it can be seen that the energy E radiated per unit time may be obtained by integrating the normal component of \vec{P} over the entire surface. Also, since the surface S may be chosen anywhere, as long as it surrounds the source, then \vec{P} must be defined everywhere. The conclusion is, therefore, that the total power output of a given source may be obtained by integrating the simple polar distribution of radiation intensity.

4.5.2 Nature of the Source Representation

In order to generate a source representation, it is first necessary to consider how radiation is transferred from a source to a surface, which resolves, basically, into a consideration of one of the most important concepts in illumination engineering, namely that of source brightness (the energy radiated per unit area per unit solid angle). The definition of source brightness given in most optical texts⁶ is derived from the fact that the energy flux through an element of solid angle which is traced through an optical system must be constant, disregarding irreversible dissipative factors. In general, however, there will be irreversible losses of energy due to absorption and scattering of radiation; and it is convenient to consider the problem of radiation transfer in terms of an alternative parameter, namely the apparent brightness B' , the proportionality constant of equation (4-10)

$$d^2 F = B' \left[\frac{(d\vec{S} \cdot \hat{r}) (d\vec{A} \cdot \hat{r})}{(nR\hat{r}) \cdot (nR\hat{r})} \right] \quad (4-10)$$

where \hat{r} is the unit vector which defines the direction of radiation propagation from dS to dA , n is the index of refraction of the medium through which the radiation passes, and $nR\hat{r}$ defines the optical path length from dS to dA . (The parameter $nR\hat{r}$ also represents the absolute value of the eikonal of the phase surface at dA). Since the source brightness is altered only by irreversible dissipative factors in the optical path, equation (4-10) can be evaluated at any position in an optical system provided that B' is defined as

$$B' = B \prod_{i=1}^m k_i = KB \quad (4-75)$$

where the k_i are the transmittances and reflectances of the m components encountered along the optical path from the source to dA , B is the intrinsic brightness of the source element dS , and K is the fraction of the energy emitted by (or through) the source element dS in the direction \hat{r} which is incident upon the target element dA .

An additional aspect of source brightness must be stressed at this point: with the single exception of an opaque black body (Lambertian radiator), the brightness of an element of area dS on the source surface has a functional dependence on direction \hat{r} . This directional dependence of brightness can arise from two conditions. First, if the source is not opaque, it can be imagined as consisting of a volumetric distribution of point sources with the apparent brightness observed at an elemental area on the source surface being a function of the number of point sources which can be seen through the element of source surface area dS in the direction of view \hat{r} . Second, if the source is opaque and displays either metallic or dielectric properties, there will be an apparent variation in brightness across the source due to the fact that the reflectance (and therefore the emittance as one minus the reflectance) varies as the Fresnel coefficients in accordance with Maxwell's equations. In both cases, the apparent brightness will be greatest in the direction toward the center of the source volume (where the elements of source surface area are seen at normal incidence) and will decrease toward the edges (which are seen at grazing incidence). See figure 4-14. Since in the first case some radiation originates in the interior of the source while in the latter case all of the radiation comes from the source surface, these two cases are quite different with regard to the spatial phase distributions in the interior of the source. However, in both of these cases, the brightness distribution across the source appears to be non-uniform in a similar manner and, as only the time-averaged brightness distribution of the source as it appears to and through the optical system is of interest, it is not necessary to distinguish between these two effects. It is only necessary to generate a source representation whose exterior appearance approximates that of the source.

One way that the exterior appearance of the source may be approximated is to represent the source as a series of non-intersecting mutually transparent Lambertian surfaces, each with an assigned brightness factor as shown schematically in figure 4-14. Since the Lambertian surfaces are mutually transparent, the apparent brightness of an element of area on the outermost surface is equal to the sum of the brightness factors assigned to those surfaces which can be seen through the element of area on the outermost surface. In order to define the techniques whereby such a source representation can be generated as well as to further clarify the concept of source brightness and its relationship to energy transfer, consider the case represented schematically in figure 4-15, where an optical system (the entrance and exit pupils of which are indicated) is used to transfer radiant energy from the source onto a plane located a distance D_p from the exit pupil of the optical system. (The unit

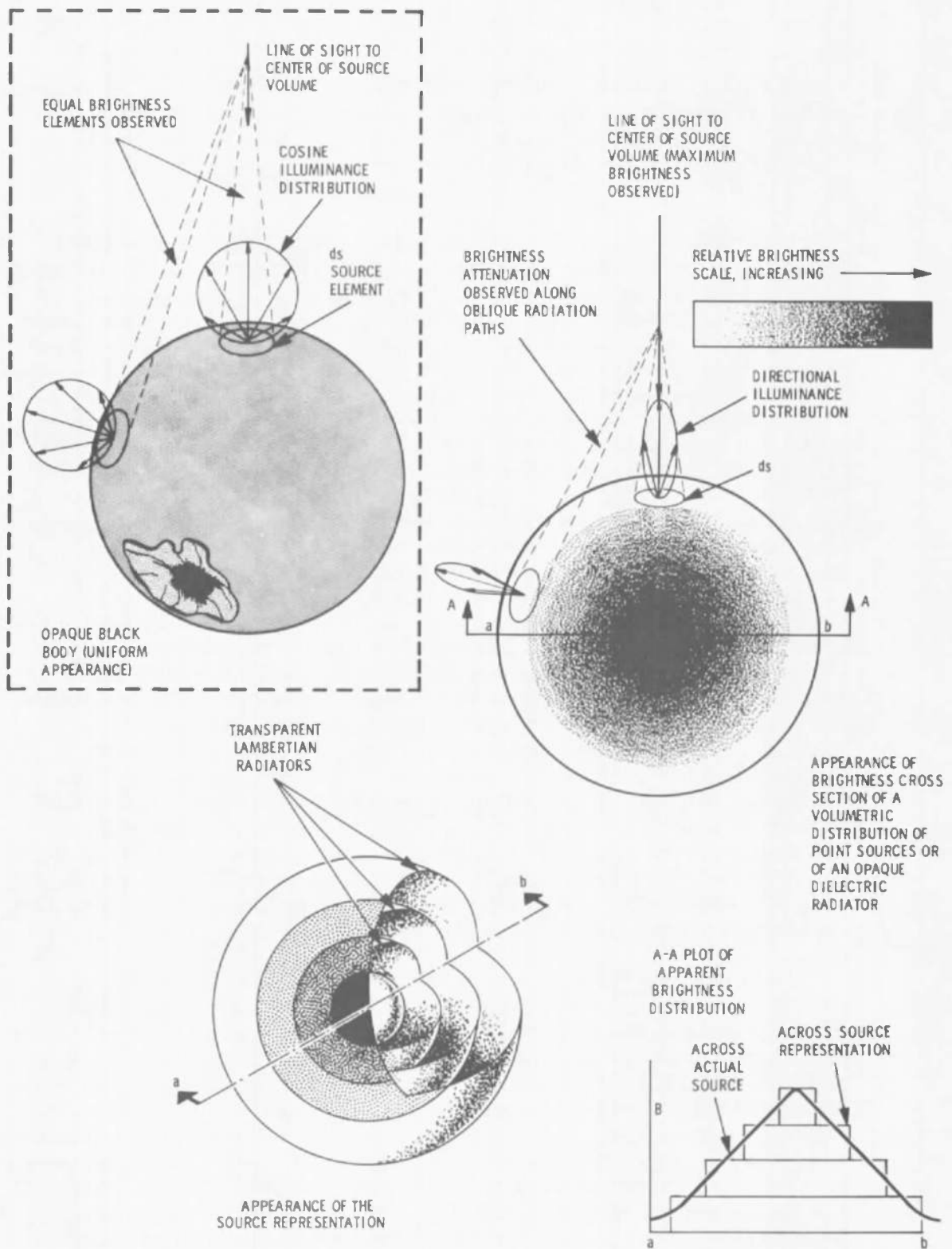


Figure 4-14. Source Emission Characteristics

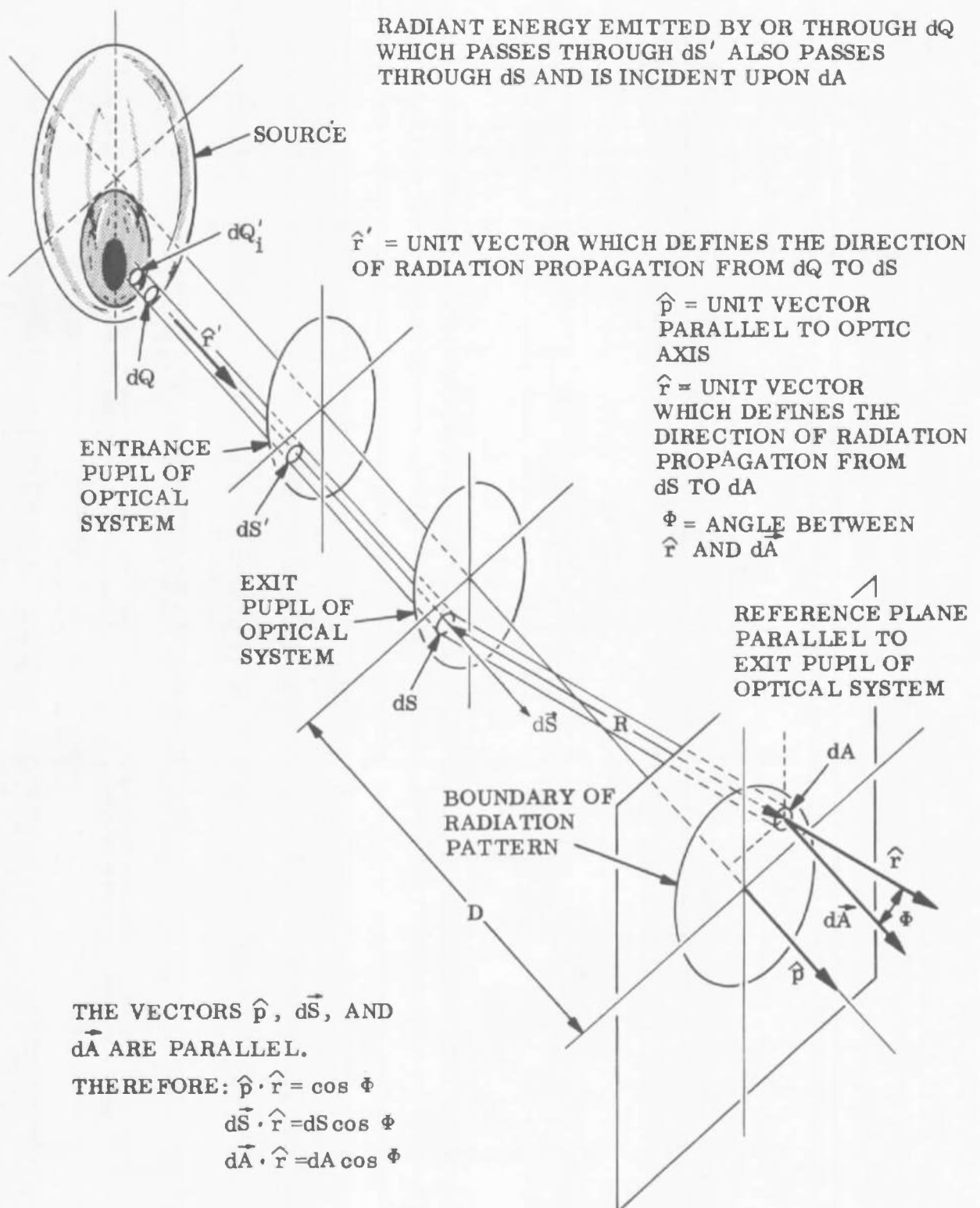


Figure 4-15. Schematic Representation of Radiant Energy Transfer by an Optical System

vector \hat{p} defines the optic axis of the optical system.) If d^2F is defined as the fraction of the element of flux which is emitted through the element of area dS in the exit pupil in the direction defined by the unit vector \hat{r} and which is then incident upon the element of area dA in the reference plane, if $nR\hat{r}$ is defined as the optical path length from dS to dA , if Φ is defined as the angle between \hat{r} and \hat{dA} , and B' is defined as the apparent brightness of dS as seen from dA , since the index of refraction $n=1$ in space and the vectors \hat{p} , dS and dA , are parallel

$$\hat{p} \cdot \hat{r} = \cos \Phi \quad (4-76)$$

$$d\vec{S} \cdot \hat{r} = dS \cos \Phi \quad (4-77)$$

$$d\vec{A} \cdot \hat{r} = dA \cos \Phi \quad (4-78)$$

$$D = R \cos \Phi \quad (4-79)$$

then from equation (4-10)

$$d^2F = B' \left[\frac{dA dS \cos^2 \Phi}{R^2} \right] = B' \left[\frac{dA dS \cos^4 \Phi}{D^2} \right] \quad (4-80)$$

If dE is defined as the flux density on dA due to the element of flux d^2F , then

$$dE = \frac{d^2F}{dA} = B' \left[\frac{dS \cos^4 \Phi}{D^2} \right] \quad (4-81)$$

If K and B are defined respectively as the transmittance and the source brightness along the optical path from dQ through dS' and dS to dA , then equation (4-81) may be written

$$dE = KB \left[\frac{dS \cos^4 \Phi}{D^2} \right] \quad (4-82)$$

If dW is now defined so that

$$dW = d\vec{S} \cdot \hat{r} = dS \cos \Phi \quad (4-83)$$

then, defining Θ as the angle measured in the plane normal to \hat{dA} , which, with Φ defines the direction of \hat{r} , then dW may be expressed as

$$dW = R^2 \sin \Phi d\Phi d\Theta \quad (4-84)$$

If $d\Omega$ is defined as the element of solid angle which dS , and therefore dW , subtends at dA

$$d\Omega = \frac{dW}{R^2} = \sin \Phi d\Phi d\Theta \quad (4-85)$$

$$d\Omega = \frac{d\vec{S} \cdot \hat{r}}{R^2} = \frac{dS \cos \Phi}{R^2} = \frac{dS \cos^3 \Phi}{D^2} \quad (4-86)$$

Because there is only one element of area dQ on the surface of the source which can be seen from the position dA through a given element of area dS in the exit pupil of any optical system, it is possible, on the basis of equations (4-82), (4-85) and (4-86), to state three forms of the general equation which define the transfer of radiant energy from a source through an optical system to a surface. In terms of the previously defined parameters, the radiant energy intensity E on the element of area dA is

$$E = \frac{1}{D^2} \int KB \cos^4 \Phi dS \quad (4-87)$$

$$E = \int KB \cos \Phi d\Omega \quad (4-88)$$

$$E = \iint KB \sin \Phi \cos \Phi d\Phi d\Theta \quad (4-89)$$

If the optical system is used to image the source on the reference plane of figure 4-15 so that the element of area dQ on the source surface is imaged on an element of area dA , then dQ is the only part of the source which can be seen from dA through any element of area dS in the exit pupil. If the entrance and exit pupils of the optical system are chosen small enough to permit K , B and Φ to be considered constant, equation (4-87) may be integrated to establish the relationship between B and E . Therefore

$$B \approx \frac{D^3 E}{KS \cos^4 \Phi} \quad (4-90)$$

The quantity B thus represents the source brightness of an element of area dQ on the source surface in a direction \hat{r}' and has been defined on the basis of the radiation apparently emitted by dQ in the direction \hat{r}' . In reality, however, this radiation may have been emitted through dQ , originating at some position (or positions) dQ'_i in the direction \hat{r}' , as indicated in figure 4-15. Therefore, if there are n positions dQ'_i of brightness ΔB_i which can be seen through dQ in the direction \hat{r}' and if each surface is transparent to the radiation emitted by the other surfaces, then the brightness B of the element of area dQ on the source surface in the direction \hat{r}' is given by:

$$B = \sum_{i=1}^n \Delta B_i \quad (4-91)$$

It is this fact which suggested the method used for representing the source.

In order to represent a given source, first assume that the source consists of n closed surfaces (e.g.: ellipsoids, spheres, etc.), none of which intersect. Assume further that each of these surfaces is a Lambertian radiator of brightness ΔB . The geometry of the outermost surface is now defined so that it is of the same shape and size as the source. If the source is imaged onto a plane and the brightness distribution is determined by applying equation (4-90), a directional brightness factor $B_1 \hat{r}_1$ may be assigned to each element of area dQ on the outermost surface of the source representation. If an integer m_1 is now defined so that

$$\vec{m}_1 = \frac{B_1 \hat{r}_1}{\Delta B} \quad (4-92)$$

then m_1 is identically equal to the number of Lambertian surfaces of brightness ΔB which can be seen through dQ in the direction \hat{r}_1 . Thus, if j directional brightness factors $B_j \hat{r}_j$ are determined from j different directions for each element of area dQ on the outermost surface of the source representation, the geometry of the remaining surfaces may be determined through a consideration of the corresponding values of m_j over the surface.

The source brightness B of an element of area dQ on the source surface in a direction \hat{r} may then be determined from the source representation by determining how many of the Lambertian surfaces of brightness ΔB can be seen through the corresponding element of area dQ on the outermost surface of the source representation in the direction \hat{r} . If N surfaces can be seen, then

$$B = N \Delta B \quad (4-93)$$

It can be seen, therefore, that the radiation field thus characterized by the source representation approaches that produced by the source in reality as $\Delta B \rightarrow 0$ (and $N \rightarrow \infty$) as a limit.

An additional parameter which is extremely useful in determining and representing the source characteristics is the source radiance (energy radiated per unit solid angle). The source radiance I is related to the brightness B of an element of area dS on the surface of the source through the equation

$$I = \int B(d\vec{S} \cdot \hat{r}) \quad (4-94)$$

where \hat{r} is again the unit vector which defines the direction of radiation propagation from dS to a target element of area dA . The source radiance can also be defined in terms of the average source brightness B seen through the solid angle Ω subtended by the source at the target element dA . Thus

$$I = \bar{B} D^2 \Omega = \bar{B} Q \quad (4-95)$$

where D is the distance from the center of the source to the target element and Q is the projected area of the source as seen from the target element. It can be shown that B and Q may be considered constant for any given direction from the center of the source so long as the distance D is large with respect to the source dimensions. Therefore, assume that the source radiance I is a constant in any given direction from the source center in order to establish the relationship between radiance I and intensity E as measured by a detector of finite size.

In terms of the source radiance I , the element of flux dF from the source which is incident upon an element of area dA a distance R from the source center is

$$dF = I \frac{(dA \cdot \hat{r})}{R^2} = I \frac{dA \cos \phi}{R^2} \quad (4-96)$$

If a detector of area $\pi \rho^2$ is used to measure the intensity, then $dA = 2\pi \rho d\rho$. Since $\rho = R \sin \phi$, then

$$dF = 2\pi I \sin \phi \cos^2 \phi d\phi \quad (4-97)$$

If the detector is small enough that the radiance I can be considered constant across its surface, then the total flux incident on the detector is given by

$$F = \frac{2}{3} \pi I (1 - \cos^3 \Phi) \quad (4-98)$$

where Φ is the half angle subtended by the detector at the source center. Thus, since the intensity E measured by the detector is

$$E = \frac{F}{A} = \frac{F}{\pi \rho^2} = \frac{F}{\pi \sin^2 \Phi} \quad (4-99)$$

the relationship between the source radiance and the measured intensity is given by

$$E = \left(\frac{I}{R^2} \right) \left[\frac{2(1 + \cos \Phi + \cos^2 \Phi)}{3(1 + \cos \Phi)} \right] \quad (4-100)$$

Therefore, so long as the detector is chosen small enough that the radiance across its surface can be considered constant, equation (4-100) may be approximated by

$$I \approx ER^2 \quad (4-101)$$

(For a Φ of 10° , this would result in an error of less than 0.76% in the calculated value of the radiance which is far less than the probable magnitude of the error which would be introduced by other factors.)

4.6 ENERGY TRACING

An analytical technique which has proved invaluable in predicting the performance characteristics of various optical systems proposed for solar radiation simulation is that of energy tracing. This technique is based upon a consideration of how radiant energy is transferred to a position in the target volume. To illustrate the concepts upon which the energy tracing rationale is based, suppose that the size and shape of the exit pupil of a given source, optical-system combination as seen from a given target point are known. (This is tantamount to saying that all the directions in space through which light proceeds to the target point from the entire source can be accounted for; thus, the field of energy flux through that point is established.) Defining Ω as the solid angle (the field) subtended by the exit pupil at the target point, the radiant intensity E on an element of area located at the target point is given by

$$E = \int B \cos \psi d\Omega \quad (4-102)$$

where B is the brightness of that portion of the source which can be seen through an element of solid angle $d\Omega$ and ψ is the angle of incidence of the radiant flux contained within $d\Omega$. If ϕ and θ are defined as the direction angles of a spherical coordinate system (ϕ being measured with respect to the polar axis) which is centered at the target point and whose polar axis lies in the plane of the element of area (θ being measured with respect to this plane), then it may be specified that

$$\cos \psi = \sin \phi \sin \theta \quad (4-103)$$

$$d\Omega = \sin \phi d\phi d\theta \quad (4-104)$$

Substituting equations (4-103) and (4-104) into equation (4-102) gives

$$E = \iint B \sin^2 \phi \sin \theta d\phi d\theta \quad (4-105)$$

If the source is Lambertian then, by definition, the brightness B is constant over the field and the radiant intensity E can be determined by integrating equation (4-105) over those values of ϕ and θ which are contained

within the solid angle Ω subtended by the exit pupil. Thus, since the radiation field produced by the source may be completely characterized (except for phase and state of polarization) by representing the source as a series of Lambertian surfaces, the total intensity on the target element of area may be represented as the sum of the intensity contributions from each surface of the source representation, thereby reducing the problem to one of determining the boundaries of the exit pupil seen for each surface of the source representation from the target element of area in order to establish the limits of integration for equation (4-105). The most direct method (and the most convenient and practical from the computer standpoint) whereby the integration limits can be established consists of (1) subdividing the field into many small elements of solid angle $\Delta\Omega = \sin\phi \Delta\phi \Delta\theta$, (2) tracing the central ray of each element of solid angle from the target element of area through the optical system to the vicinity of the source, and (3) testing to determine which (if any) surfaces of the source representation intersect this central ray. An outline of that part of the field through which each surface of the source representation can be seen from the target element of area (and thus the field through which light, originating at each surface of the source representation, is incident upon the target element of area) may be quickly established by this process, thereby permitting the numerical evaluation of equation (4-105) for each source surface. The energy tracing rationale may be summarized as follows:

1. The radiation field produced by any random incoherent light source may (ignoring interference, polarization, and coherence effects) be represented as the sum of those radiation fields produced by a series of successively contained Lambertian radiators which are self-opaque and whose radiation fields are mutually independent.
2. From any given position in the target volume, the boundaries of the exit pupil seen for each surface of the source representation (and thus the field subtended by the radiation from each surface of the source representation) may be determined by tracing rays from the target position through the optical system to the vicinity of the source and determining which, if any, of the surfaces of the source representation are intersected by each ray.
3. Because of the assumption that the radiation fields produced by the Lambertian surfaces of the source representation are mutually independent, then the brightness seen from the target position in any given direction is equal to the sum of the brightness factors for each of those surfaces of the source representation which are intersected by a ray traced from the target position.

A computer program, ENERGY, developed to exploit the techniques described above is discussed in Appendix I.

SECTION 5

SOURCE STUDY

5.1 DATA REQUIRED FOR REPRESENTING A SOURCE

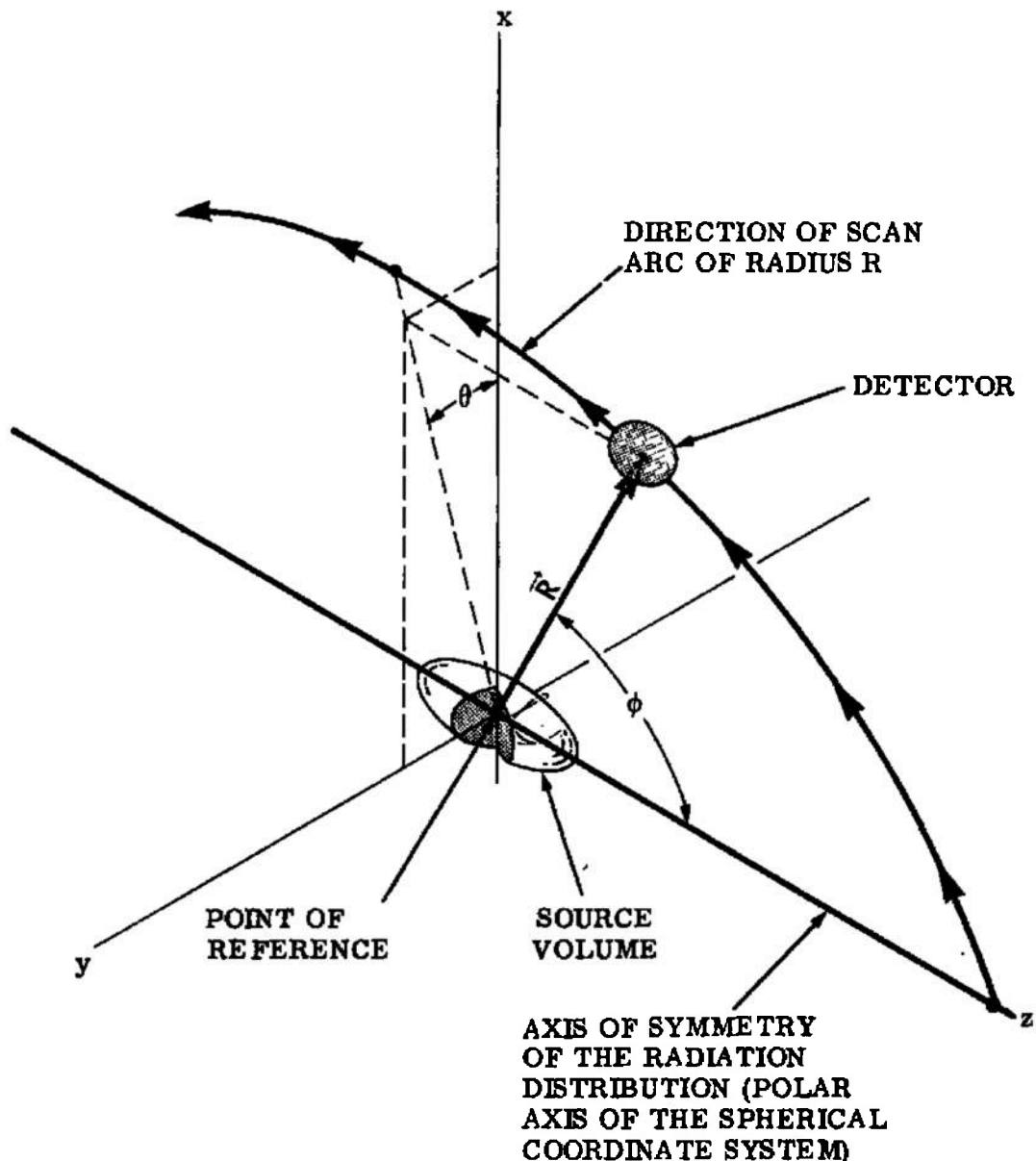
5.1.1 Introduction

In order to design a solar radiation simulation system, it is first necessary to determine the radiative characteristics of the source to be used in the system. Specifically, this information is used to select the most appropriate combination of materials for fabrication of the optical system components, to estimate the spectral filtration requirements, to size and locate the collection optics of a solar simulator module for maximum collection efficiency, to generate a design for the optical system, and to calculate the probable system performance. The directional radiative characteristics can be determined through a study of (1) the physical geometry of the source (e.g., the dimensions and locations of the electrodes), (2) the distribution of radiation about the source, (3) the brightness distribution seen over the surface of the arc from various directions. Information is also required concerning (4) the source spectrum in order to select the most appropriate combination of materials for use in fabricating the optical system and to estimate the spectral filtration requirements.

Information concerning the first of these four categories, namely the physical geometry of the source, can best be supplied in the form of dimensional drawings which show the size, shape, and location of all of those source components which protrude into the radiation field and thus produce shadowing. The remaining three categories and the experimental techniques suggested for determining the information required for each of them are discussed in the following paragraphs.

5.1.2 Distribution of Radiation about the Source.

The suggested experimental setup for measuring the distribution of radiation about the source is represented, schematically, in Figure 5-1 and is described below. Before making any experimental measurements concerning the distribution of radiation about the source, it is first necessary to locate the source within an appropriate spherical coordinate system. The first step in determining this frame of reference consists of locating the point of reference (the origin of the spherical coordinate system of Figure 5-1) with respect to the physical geometry of the source. In theory, the origin of the spherical coordinate system should be so positioned that, if detectors are located at several positions around the



EXPERIMENTAL TECHNIQUE: FOR VARIOUS VALUES OF θ , A BLACK DETECTOR OF KNOWN SENSITIVE AREA IS MOVED TANGENT TO THE SURFACE OF A HYPOTHETICAL SPHERE OF RADIUS R CENTERED ABOUT THE KNOWN REFERENCE POINT. THE RADIANT INTENSITY (WATTS/UNIT AREA) IS RECORDED AS A FUNCTION OF ϕ FOR EACH VALUE OF θ .

Figure 5-1. Schematic Representation of the Experimental Technique Suggested for Measuring the Distribution of Radiation about a Light Source

source and the direction of the normal to the sensitive area of each detector is determined for that angular orientation at which the detector indicates maximum incident flux, then all such normals have a common intersection at the origin of the spherical coordinate system. However, since the radiant intensity sensed by a detector varies with the cosine of the angle of incidence, should the detector be tilted as much as 8° with respect to the direction of the incident flux, the error introduced would still be less than 1%. It is therefore sufficient to choose the point of reference so that it is located at some convenient position near the center of the brightest region of the arc.

Since the origin of the spherical coordinate system is fixed once the location of the point of reference is specified, it then remains only to orient the coordinate system so that its polar axis coincides with the axis of symmetry of the radiation distribution.

In most cases, if the physical geometry of the source is symmetrical about some axis, the radiance is a symmetric function about the same axis which is apparently the case with both the Vortex Stabilized Radiation Source and the Fluid Transpiration Arc, and the physical axis of symmetry and the axis of symmetry of radiation distribution (the polar axis of the spherical coordinate system of figure 5-1) coincide. In those cases where the physical geometry of the source is not symmetrical about some axis (as is the case with the High Intensity Carbon Arc), then (1) the orientation of the polar axis is arbitrarily specified on the basis of convenience and preliminary measurements are taken concerning the distribution of radiation about the source, (2) the axis of symmetry of the radiation distribution is then determined through an analysis and interpretation of this data (an example of this procedure is given in the discussion of the High Intensity Carbon Arc), (3) the spherical coordinate system is then re-oriented so that its polar axis coincides with the axis of symmetry of radiation distribution, and (4) final measurements concerning the distribution of radiation about the source are then taken in terms of the re-oriented spherical coordinate system. (Although it is not absolutely necessary that measurements concerning the distribution of radiation about the source be taken with respect to a spherical coordinate system whose polar axis coincides with the axis of symmetry of the radiation distribution, the use of such a frame of reference greatly facilitates the subsequent data analysis.)

In measuring the distribution of radiation about the source, the sensitive area of the detector is located with respect to the spherical coordinate system so that, for a given value of Θ , it may be moved (for values of ϕ from 0° to 180°) tangent to the surface of a hypothetical sphere of radius R centered about the point of reference. To minimize errors in measurement, the sensitive area of the detector should subtend an angle of less than 2° at the point of reference and should be maintained within 5° of perpendicular with respect to the radius vector \vec{R} .

(see figure 5-1), the source should subtend an angle of less than 2° at the detector, and the experimental setup should incorporate appropriate masking to shield the detector from radiation emanating from outside the arc. The detector used for these measurements should be calibrated in absolute photometric units, e.g., watts-per-square-centimeter, and should be insensitive to variations in the spectrum between 0.25 micron and 2.50 microns (e.g., a thermopile type). The following information is required in order to completely specify the distribution of radiation about the source for any given set of operating conditions:

1. The location and orientation of the spherical coordinate system to which the experimental measurements are referenced should be specified with respect to the physical geometry of the source.
2. The type of detector used for the measurements, the size of its sensitive area, and the distance R from the detector to the point of reference should be specified.
3. The intensity E_ϕ sensed by the detector at each position should be converted to units of radiance I_ϕ (i.e., watts-per-steradian) in accordance with the equation

$$I_\phi = E_\phi R^2 \quad (5-1)$$

4. For each chosen value of Θ , the radiance I_ϕ should be tabulated and plotted as a function of ϕ . (I_ϕ versus ϕ for several values of Θ are required in order to determine the symmetry and stability of the radiation field.)

5.1.3 Brightness Distribution.

Measurement of the brightness distribution over the surface of the arc may be accomplished by imaging the arc on a plane, and measuring the radiant energy intensity distribution throughout the image. It is suggested that these measurements be made in accordance with the following considerations:

1. The entrance pupil of the optical system should subtend an angle of less than 1.2° from the source. (This corresponds to a 10-millimeter diameter aperture located 19 inches from the source.)
2. The magnification should be no less than 25x. (This corresponds to a projection distance of approximately 40 feet for a 19-inch focal length lens).
3. The arc should not subtend a total field angle of more than 4° at the entrance pupil of the optical system. (With a 19-inch

focal length lens and a magnification of 25x, arcs less than approximately 35 millimeters in diameter will satisfy this condition.)

1.38"

4. The optics used for imaging the arc should be of high quality since a lens of low quality, though it may produce an acceptable optical image, is liable to scatter a considerable amount of energy. (An example of a good quality lens system is the Goertz Red Dot Artar, f:11, 19-inch focal length).

5. Rather than determine the spectrally integrated brightness distribution, it is suggested that several essentially monochromatic brightness distributions be determined for a given image through the use of filters with a narrow bandpass (10 millimicrons to 50 millimicrons). The location of the bandpass is arbitrary but should be restricted to those regions where the source spectrum is not varying rapidly. Because of the field restriction noted above, the brightness may be considered directly proportional to the intensity; it is therefore suggested that each monochromatic distribution be expressed in terms of relative intensity. (Later, these can be related in absolute terms through a study of the source radiance and spectrum rather than attempting to calibrate the transmission characteristics of the optical system.) For consistency of measurement, it is suggested that the size of the detector aperture be so chosen that it corresponds to approximately $(0.08\text{mm})^2 = 0.0064$ square millimeters on the source. (For a magnification of 25x, this would be a detector aperture of 4 square millimeters.)

How

the smaller the
signal the
larger the
detector

The following information is required in order to completely specify the brightness distribution over the arc for each set of operating conditions.

For each direction in which the arc is imaged, the monochromatic relative intensity distribution throughout the image should be determined for several regions of the spectrum. (Five regions would be desirable; initially two or three are adequate). One convenient method of presenting this information would be in the form of a grid pattern with the relative intensity at each position in the image noted at a corresponding position in the grid. Each grid pattern should also include information concerning the region of the spectrum which the pattern represents, the relationship between the dimensions of the pattern and the actual dimensions of the source (this is required in order to determine the size of the arc), and the direction in which the source was imaged. In terms of the spherical angles of figure 5-1, the arc should be imaged in at least two directions:

Direction #1	$\phi = 90^\circ$	$\Theta = 0^\circ$
Direction #2	$\phi = 90^\circ$	$\Theta = 90^\circ$

For verification purposes, it is desirable that the arc be imaged in several other directions also, and that corresponding monochromatic relative intensity distributions be determined. While these directions are quite arbitrary, the following directions are suggested for the two types of radiation source under consideration, within the limit(s) dictated by shadowing by the electrode(s):

1. Single-Ended Source: For $\Theta = 0^\circ$ and $\Theta = 90^\circ$, the suggested values of ϕ are 0° , 30° , 60° , 90° , and 110° (this assumes that the electrode is located in the direction $\phi = 180^\circ$ from the chosen point of reference).
2. Double-Ended Source: For $\Theta = 0^\circ$ and $\Theta = 90^\circ$, the suggested values of ϕ are 30° , 60° , 90° , 120° , and 150° .

5.1.4 Source Spectrum

For the initial study of the source, one integrated source spectrum is required. This spectrum should be measured in the same direction from the source as for one of the basic microbrightness measurements, i.e., $\phi = 90^\circ$ and either $\Theta = 0^\circ$ or $\Theta = 90^\circ$ (figure 5-1). For the final study of the source, observations of the spectrum from both of these directions and one additional direction, e.g., $\phi = 30^\circ$ or 60° and $\Theta = 0^\circ$ or 90° , are desirable. If the highest possible accuracy is to be obtained, only the following requirements must be satisfied:

1. Resolution: If the source spectrum is measured as a continuum, the spectrometer employed must possess the ability to resolve all of the spectral lines present; if the lines are not resolved, a large proportion of the energy contained in each is smeared into the continuum radiation energy in a disproportionate manner by the action of the instrument⁷, giving a correspondingly false indication of the amount of energy available. Alternatively, the source spectrum may be determined by dividing the wavelength range into a series of discrete wavelength bands $\Delta \lambda_i = \lambda_i - \lambda_{i-1}$ (none of which overlap) and measuring the energy within each bandwidth; this technique also carries a resolution requirement since the bandwidths chosen must be in accordance with those of the most stringent spectrum specification to which the solar radiation simulator that utilizes the source is to be designed. (Although a grating spectrometer has the highest resolving power, it is not essential that this type of instrument be employed if the resolution requirement can be met.)
2. Detector: Since the system (spectrometer and detector) is calibrated against a standard radiation source, it is not necessary to use a detector which has a black response. It is more appropriate to divide the spectrum into regions, basing the choice of the

detector to be used in each region upon the sensitivity required and the dynamic response characteristics of the various detectors. Low-noise, high-dynamic-range detectors, such as a 1P21 or 1P28 photomultiplier tube for the visible region and a PbS semiconductor for the infrared region, should be used for maximum sensitivity. If sensitivity is still too low, conversion of the sensor dc signal to an ac signal by "chopping" at the entrance slit will permit relatively easy amplification of the detector output to a suitable level. It should be noted that, in particular, thermocouple-type detectors are not suitable because of their low dynamic range.

3. Detector Location: Since the sensitivity of the detector may vary across its surface, the detector must be so located that the same area on its surface is uniformly illuminated for all wavelengths. If the entrance slit of the spectrometer is uniformly illuminated for all wavelengths, the exit slit will also be uniformly illuminated for all wavelengths. It is therefore recommended that the entrance slit be uniformly illuminated and the detector be mounted directly at the exit slit.
4. Optics: In order to provide for uniform illumination of the entrance slit of the spectrometer for all wavelengths, no imaging optical system should be present in the radiation path between the source and the entrance slit. Even the tedious calibration of the transmittance of such an optical system is not sufficient, because vignetting by the entrance slit due to chromatic and other aberrations in the optical system can cause serious errors. Furthermore, the introduction of such an optical system implies the introduction of a corresponding optical system into the radiation path between the exit slit and the detector in order to provide for uniform illumination of the sensitive area of the detector, thus compounding the possible sources of error.

5.2

ANALYSES OF THE DIRECTIONAL RADIATIVE CHARACTERISTICS OF THE VARIOUS SOURCES.

Analyses were conducted of the distribution of radiation about the Vortex Stabilized Radiation Source, the Fluid Transpiration Arc, and the High Intensity Carbon Arc, in order to define the most appropriate expression for the radiance of each. The radiative efficiency of each source was also estimated. In addition, for the Fluid Transpiration Arc, a mathematical source representation was generated in order to illustrate the procedure discussed in Section 4. The analyses, as conducted for each source, are summarized below.

5.2.1

Vortex Stabilized Radiation Source (VSRS).

The analysis of the data provided concerning the distribution of the radiation emitted by the Vortex Stabilized Radiation Source (Plasmadyne) was conducted from the standpoints of radiative efficiency and collection efficiency as follows:

5.2.1.1

Radiance and Radiative Efficiency.

Since the average intensity produced by the solar simulator must be variable, and since the optical system design must be generated on the basis of a specific distribution of radiation about the source, the first step in the determination of the radiative efficiency of the Vortex Stabilized Radiation Source (VSRS) consisted of an analysis to determine how the relative distribution of radiation about the VSRS varies as the conditions under which it is operated are varied. To this end, the VSRS was located in the spherical coordinate system of figure 5-1 such that the origin of the coordinate system was centrally located between the electrodes with the axis of symmetry of the VSRS horizontal and along the polar axis. ϕ was then defined as the angle between a radius vector and the polar axis, measured with respect to the direction of the anode. Θ was defined as the angle between vertical and the projection of the radius vector into the plane perpendicular to the polar axis. The data listed and identified by number in table 5-1 was then compiled as a function of ϕ from the reports indicated in table 5-2 (the data was assumed to be symmetrical with Θ).

By definition, the source radiance I_ϕ is given by

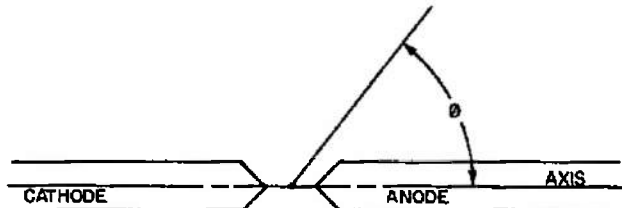
$$I_\phi = E_\phi R^2 \quad (5-2)$$

where E_ϕ is the intensity measured a distance R from the origin of the spherical coordinate system in any direction ϕ . If I_0 is defined as the radiance in the direction $\phi = 90^\circ$, then the relative radiance \bar{I}_ϕ

Table 5-1. Tabulation of VSRS Intensity Distribution Data
as Obtained from Plasmadyne

Polar Radiance Distribution
Vortex Stabilized Radiation Source
100% Argon

- \oplus 12mm Electrode Gap
- * 6mm Electrode Gap
- Axial Bore Anode
- Recessed Plate Anode



Tabulation of Data from Plasmadyne's Reports

Distribution Identification Number	1	2	3	4	5	6	7	8	9	10
Console Input Power (Kilowatts)	\oplus <input type="checkbox"/>		\oplus <input type="checkbox"/>		\oplus <input type="checkbox"/>	\oplus <input type="checkbox"/>		*	<input checked="" type="checkbox"/>	\oplus <input checked="" type="checkbox"/>
Volts	11.2	11.4	15.6	15.9	17.8	19.0	19.4	10.5	16.8	17.0
Amperes	100	100	150	150	150	200	200	200	200	200
Pressure (Atmospheres)	13.6	13.6	13.6	13.6	14.3	13.6	13.6	14.1	14.1	14.2
INTENSITY MEASUREMENTS E_ϕ										
Watts/Sq.Cm. $\times 100\text{Cm.}$										
30°	0.0057	0.0090	0.0092	0.0141	0.0075	0.0127	0.0202	---	0.0076	0.0070
45°	0.0132	0.0210	0.0209	0.0329	0.0206	0.0307	0.0486	0.0008	0.0274	0.0275
60°	0.0185	0.0292	0.0297	0.0464	0.0282	0.0420	0.0665	0.0089	0.0380	0.0384
75°	0.0220	0.0345	0.0351	0.0550	0.0345	0.0493	0.0781	0.0174	0.0472	0.0475
90°	0.0261	0.0410	0.0414	0.0653	0.0401	0.0582	0.0922	0.0256	0.0563	0.0566
105°	0.0266	0.0420	0.0425	0.0670	0.0407	0.0597	0.0947	0.0272	0.0580	0.0584
120°	0.0272	0.0430	0.0438	0.0686	0.0408	0.0597	0.0947	0.0310	0.0604	0.0604
135°	0.0276	0.0438	0.0438	0.0696	0.0407	0.0615	0.0973	0.0355	0.0612	0.0613
150°	0.0254	0.0397	0.0374	0.0588	0.0289	0.0517	0.0820	0.0337	0.0422	0.0425
Radiative Efficiency	21.9%	34.1%	24.9%	38.6%		28.8%	44.6%	21.6%	31.1%	

Table 5-2.. Report and Table and/or Figure from Which the Data Listed in Table 1 was Obtained

AEDC-TDR-64-165 - Study of Radiation from Vortex Stabilized Arcs by D. G. Van Ornum of Plasmadyne Corp., Technical Documentary Report No. AEDC-TDR-64-165, August 1964

10MS014-1033 - Tenth Monthly Progress Report dated 23 January 1964 by Plasmadyne Corp.

11MS024-1033 - Eleventh Monthly Progress Report dated 19 February 1964 by Plasmadyne Corp.

Distribution Identification Number	Report	Table and/or Figure
1	AEDC-TDR-64-165	Figure 16
2	10MS014-1033	Table 1
3	AEDC-TDR-64-165	Figure 16
4	10MS014-1033	Table 2
5	AEDC-TDR-64-165 11MS024-1033	Figure 17 Figure 5
6	AEDC-TDR-64-165	Table 11 and Figure 16
7	10MS014-1033	Table 3
8	AEDC-TDR-64-165	Table 13 and Figure 19
9	AEDC-TDR-64-165	Table 12
10	AEDC-TDR-64-165	Figure 18

in any direction ϕ is given by

$$\bar{I}_\phi = \frac{I_\phi}{I_0} = \frac{E_\phi R^2}{E_0 R^2} = \frac{E_\phi}{E_0} \quad (5-3)$$

Thus, in order to obtain the relative radiance about the VSRS for each of the various indicated operating conditions, the intensity measurements of Table 5-1 need only to be normalized with respect to intensity measured at $\phi = 90^\circ$ for each operating condition. The values thus obtained for the average normalized radiance \bar{I}_ϕ as a function of ϕ are listed in table 5-3. The average normalized radiance and the maximum deviation therefrom (which, in all probability, represents experimental error) was then determined for the two sets of operating conditions indicated in table 5-4. The slightly larger percentage deviation of distribution No. 5 (17.8-kilowatt, Axial Bore Anode, 12 mm electrode gap, 14.3 atmospheres pressure) from the average distribution determined for a VSRS with an Axial Bore Anode and a 12 mm electrode gap operated at 13.6 atmospheres pressure is probably due to both experimental error and the accuracy with which it was possible to tabulate the data from the figures referenced in table 5-2. It may therefore be assumed that the relative radiance distribution around a VSRS with a given anode configuration and electrode gap does not vary with variations in input power or pressure within the ranges of input power and pressure for which data has been provided. The analysis of the relative radiance distribution thus resolves to a study of the three configurations of the VSRS for which data is available, namely the VSRS with (1) an axial bore anode and 12 mm electrode gap, (2) a recessed plate anode and 12 mm electrode gap, and (3) a recessed plate anode and 6 mm electrode gap. Linear and polar plots of the relative radiance versus ϕ are given, respectively, in figures 5-2 and 5-3 for the first two configurations and in figures 5-4 and 5-5 for the last configuration.

The radiative efficiency η is given by

$$\eta = \frac{P_r}{P_0} \quad (5-4)$$

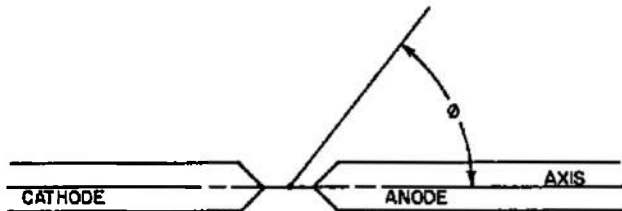
where P_0 is the input power and P_r is the power radiated between ϕ_{\min} and ϕ_{\max} . Since P_0 is known, the problem of determining the radiative efficiency resolves to defining a method whereby P_r may be determined. If $d\Omega$ is defined as an element of solid angle through which a source radiance I_ϕ is seen, then

$$P_r = \int I_\phi d\Omega = \iint I_\phi \sin \phi d\phi d\theta \quad (5-5)$$

Table 5-3. Relative Radiance Distribution of the VSRS for Various Operating Conditions

Polar Radiance Distribution
Vortex Stabilized Radiation Source
100% Argon

- \oplus 12mm Electrode Gap
- $*$ 6mm Electrode Gap
- Axial Bore Anode
- Recessed Plate Anode



Identification Number	1	2	3	4	5	6	7	8	9	10
Console Input Power (Kilowatts)	\oplus <input type="checkbox"/>		\oplus <input type="checkbox"/>		\oplus <input type="checkbox"/>	\oplus <input type="checkbox"/>		*	<input checked="" type="checkbox"/>	\oplus <input checked="" type="checkbox"/>
Volts	11.2	11.4	15.6	15.9	17.8	19.0	19.4	10.5	16.8	17.0
Amperes	100	100	150	150	150	200	200	200	200	200
Pressure (Atmospheres)	13.6	13.6	13.6	13.6	14.3	13.6	13.6	14.1	14.1	14.2

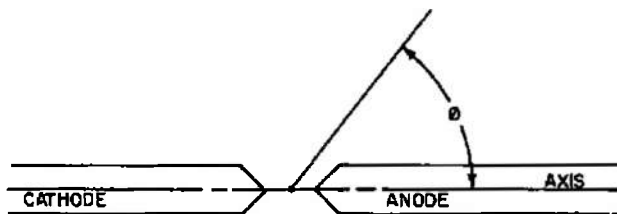
RELATIVE RADIANCE \bar{I}_ϕ
Values Normalized with Respect to Radiance at $\phi = 90^\circ$

30°	0.2184	0.2195	0.2222	0.2159	0.1870	0.2182	0.2191	---	0.1350	0.1237
45°	0.5057	0.5122	0.5048	0.5023	0.5137	0.5275	0.5271	0.0313	0.4867	0.4859
60°	0.7088	0.7122	0.7174	0.7106	0.7032	0.7216	0.7213	0.3477	0.6750	0.6784
75°	0.8429	0.8415	0.8478	0.8423	0.8603	0.8471	0.8471	0.6797	0.8384	0.8392
90°	1.0000	1.0000	1.0000	1.0000	1.0000	1.0000	1.0000	1.0000	1.0000	1.0000
105°	1.0192	1.0244	1.0266	1.0260	1.0150	1.0258	1.0271	1.0625	1.0302	1.0318
120°	1.0421	1.0488	1.0580	1.0505	1.0175	1.0258	1.0271	1.2109	1.0728	1.0671
135°	1.0575	1.0683	1.0580	1.0658	1.0150	1.0567	1.0553	1.3867	1.0870	1.0830
150°	0.9732	0.9683	0.9034	0.9005	0.7207	0.8883	0.8894	1.3164	0.7496	0.7509
Scale Factor I_0	261	268 [†]	414	427 [†]	401	582	603 [†]	256	563	566

[†] As corrected.

Table 5-4. Average Relative Radiance Distributions of the VSRS with a 12 mm Electrode Gap and an Axial Bore Anode or Recessed Plate Anode

Average Normalized Polar Radiance Distribution
 Vortex Stabilized Radiation Source
 100% Argon



Axial Bore Anode 12 mm Electrode Gap 13.6 Atmospheres Pressure			Recessed Plate Anode 12 mm Electrode Gap	
ϕ	Average Normalized Radiance	Maximum Percentage Deviation (Percent)	Average Normalized Radiance	Maximum Percentage Deviation (Percent)
30°	0.2189	+1.51 -1.37	0.1294	±4.37
45°	0.5133	+2.77 -2.14	0.4863	±0.08
60°	0.7153	+0.88 -0.91	0.6767	±0.25
75°	0.8448	+0.36 -0.39	0.8388	±0.05
90°	1.0000	±0.00	1.0000	±0.00
105°	1.0249	+0.22 -0.56	1.0310	±0.08
120°	1.0421	+1.53 -1.56	1.0700	±0.27
135°	1.0603	+0.75 -0.26	1.0850	±0.18
150°	0.9205	+5.73 -3.50	0.7503	±0.09

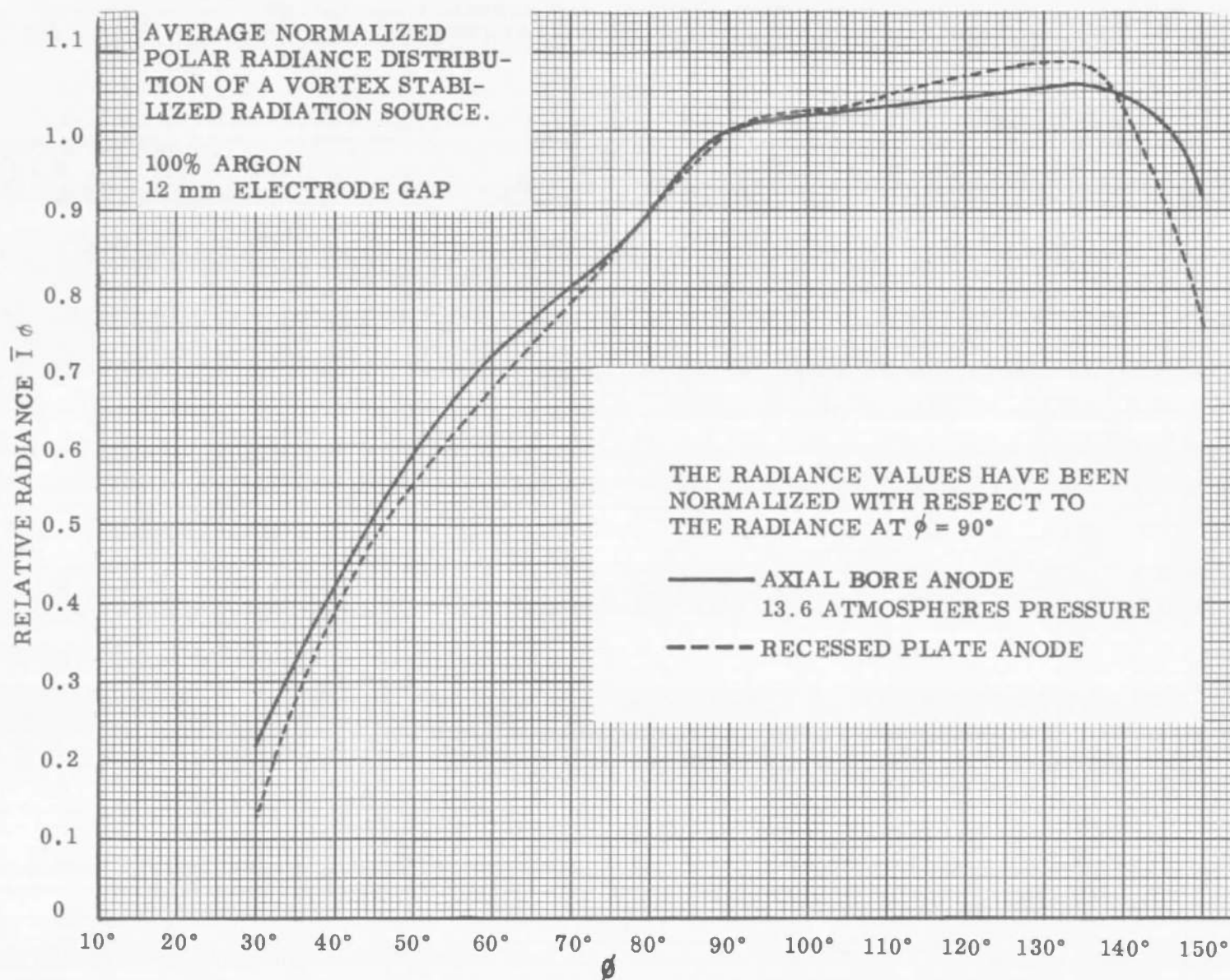


Figure 5-2. Average Relative Radiance of the VSRS with a 12 mm Electrode Gap and an Axial Bore Anode or Recessed Plate Anode (Linear Plot).

THE RADIANCE VALUES HAVE BEEN
NORMALIZED WITH RESPECT TO
THE RADIANCE AT $\phi = 90^\circ$

VORTEX STABILIZED RADIATION
SOURCE
100% ARGON
12 mm ELECTRODE GAP

70

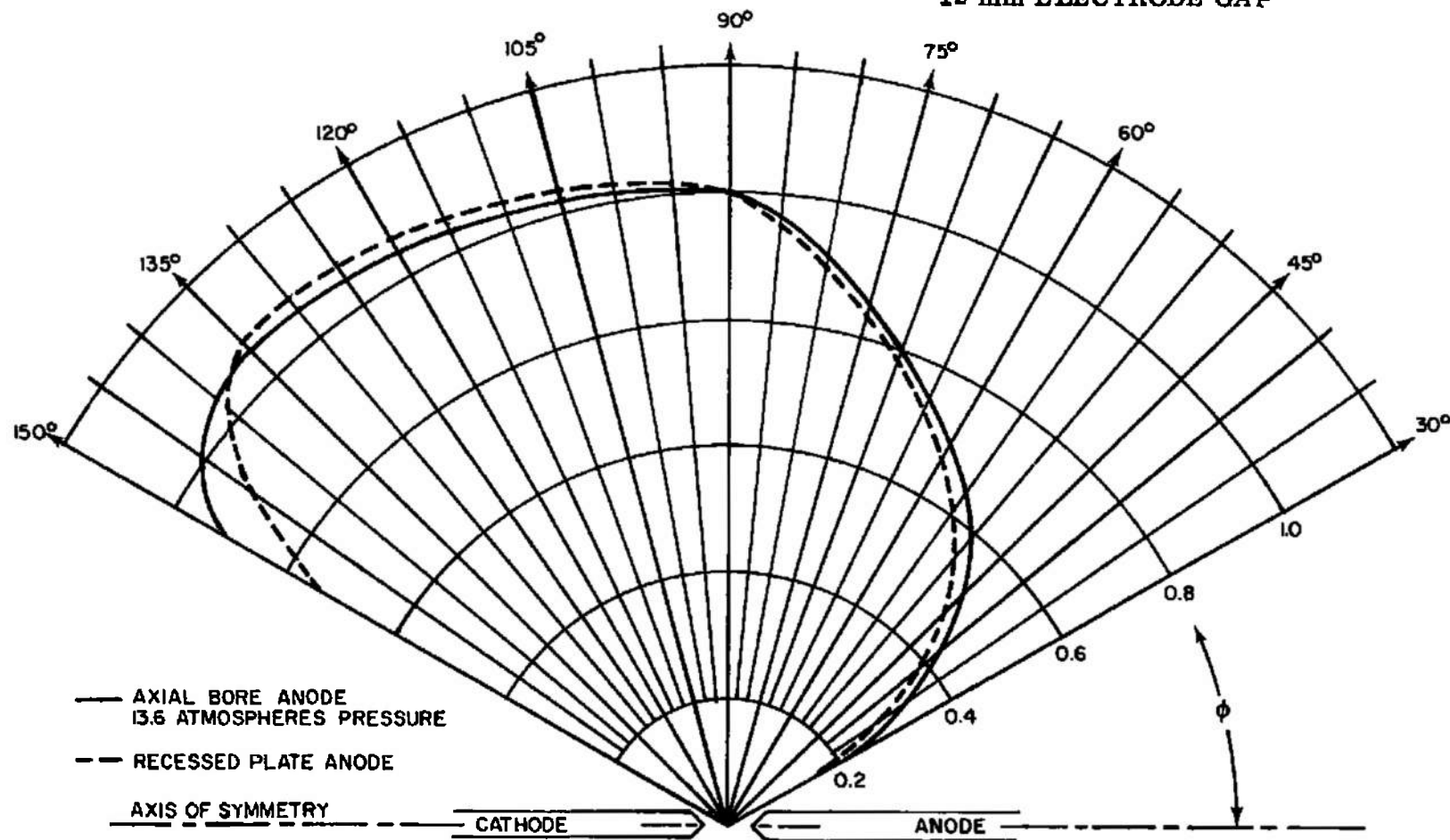


Figure 5-3. Average Relative Radiance Distribution of the VSRS with a 12 mm Electrode Gap and an Axial Bore Anode or Recessed Plate Anode (Polar Plot)

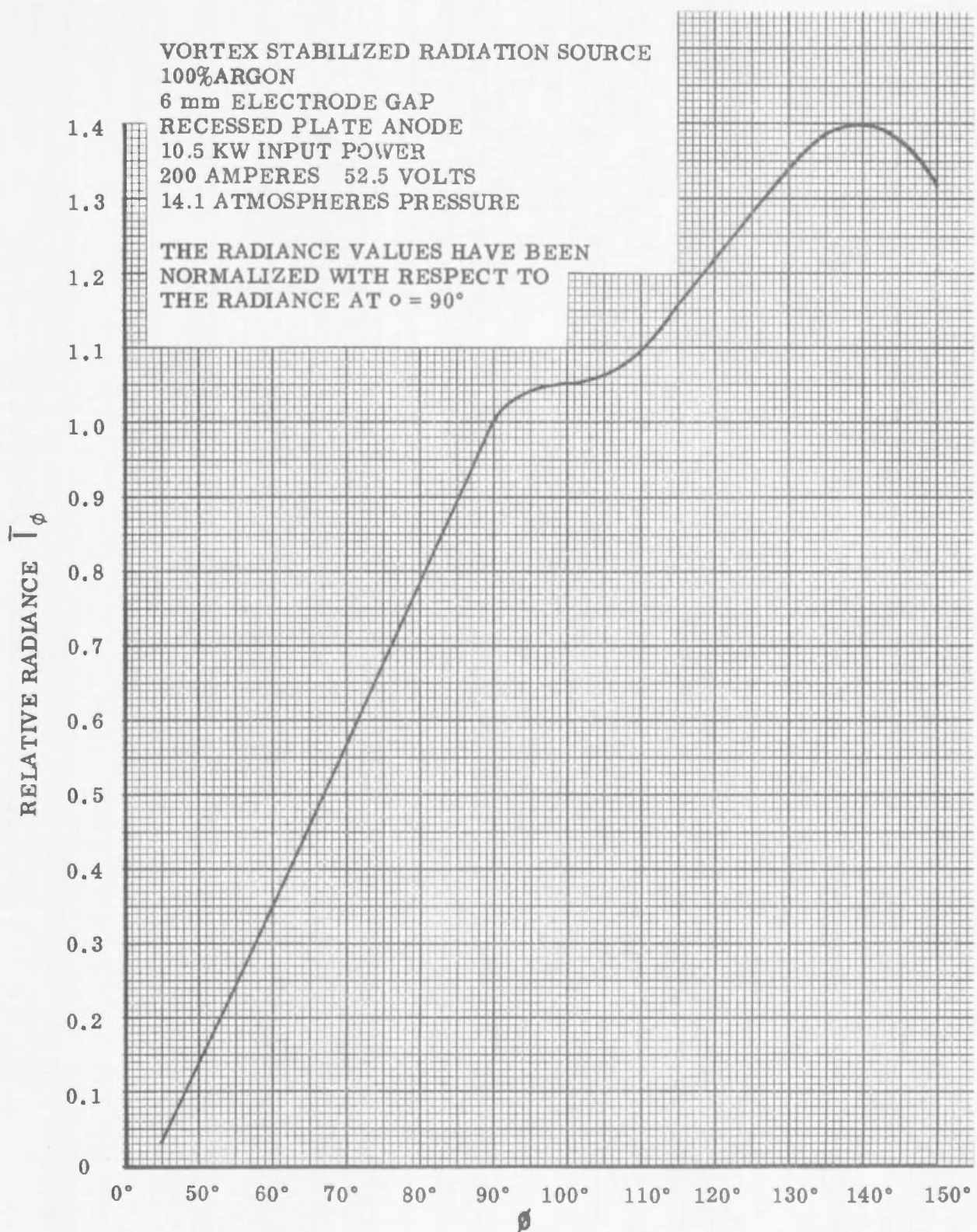


Figure 5-4. Average Relative Radiance of the VSRS with a 6 mm Electrode Gap and a Recessed Plate Anode (Linear Plot)

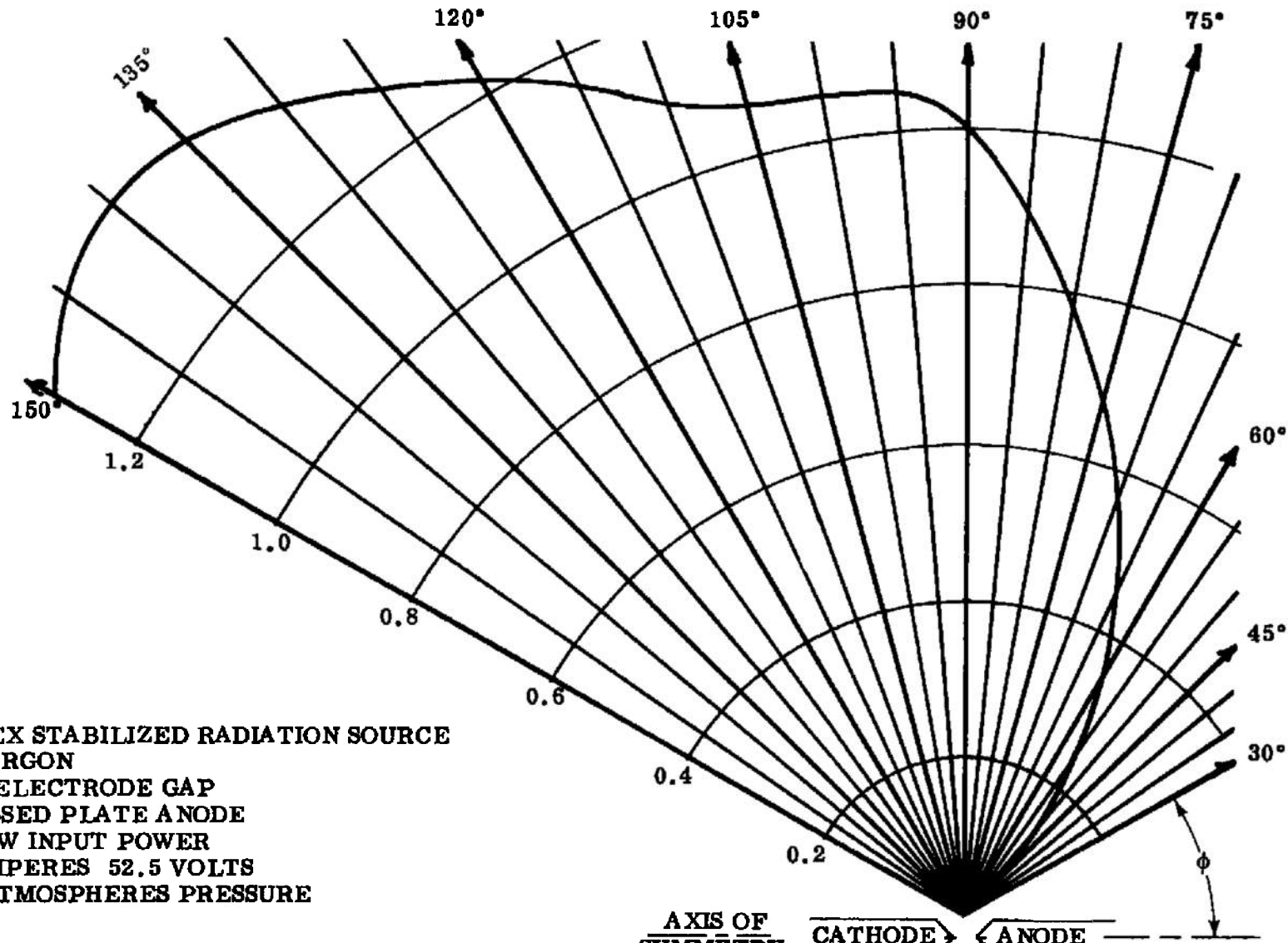


Figure 5-5. Average Relative Radiance of the VSRS with a 6 mm Electrode Gap and a Recessed Plate Anode (Polar Plot)

Since it has been assumed that the radiation distribution is symmetrical about the polar axis, then I_ϕ is independent of Θ and equation (5-5) may be integrated with respect to Θ . Further, if I_0 is again defined as the source radiance in the direction $\phi = 90^\circ$, then from equation (5-5)

$$P_r = 2\pi I_0 \int_{\phi_{\min}}^{\phi_{\max}} \frac{I_\phi}{I_0} \sin \phi d\phi$$

$$= 2\pi I_0 \int_{\phi_{\min}}^{\phi_{\max}} \bar{I}_\phi \sin \phi d\phi \quad (5-6)$$

Since the relative radiance \bar{I}_ϕ in any direction ϕ for a given configuration of the VSRS apparently does not vary with the input power or pressure within the ranges of input power and pressure for which data is available, the relative radiance distributions of figures (5-2), (5-3), (5-4) and (5-5) can be used to determine the radiated power P_r and the resulting radiative efficiency. That is, equation (5-6) may be graphically integrated by plotting $\bar{I}_\phi \sin \phi$ versus ϕ for each configuration of the VSRS and determining the area under each curve between ϕ_{\min} and ϕ_{\max} . Plots of $\bar{I}_\phi \sin \phi$ versus ϕ are shown for the two VSRS anode configurations with a 12 mm electrode gap in figure 5-6 and for the Recessed Plate Anode with a 6 mm electrode gap in figure 5-7. Figure 5-6 also includes a plot of $\bar{I}_\phi \sin \phi$ versus ϕ for a uniformly radiating spherical source (the dotted curve). This latter plot was used to determine the scale factor which relates area to radiated power. This scale factor was determined as follows.

Since for a uniformly radiating spherical source $\bar{I}_\phi = 1$, then equation (5-6) may be directly integrated and it can be seen that the power radiated by a uniformly radiating spherical source is $4\pi I_0$. If A is defined as the area under the dotted curve of Figure 5-6 (the plot of $\bar{I}_\phi \sin \phi$ versus ϕ for a uniformly radiating spherical source), then the scale factor S , which relates the area A to the radiated power $4\pi I_0$, is given by

$$S = \frac{4\pi I_0}{A} \quad (5-7)$$

VORTEX STABILIZED RADIATION SOURCE
100% ARGON
12 mm. ELECTRODE GAP

AREA UNDER CURVES:
SPHERICAL SOURCE = 28.648
AXIAL BORE ANODE = 21.65
RECESSED PLATE ANODE = 21.40
SHADED SQUARE = 1.00

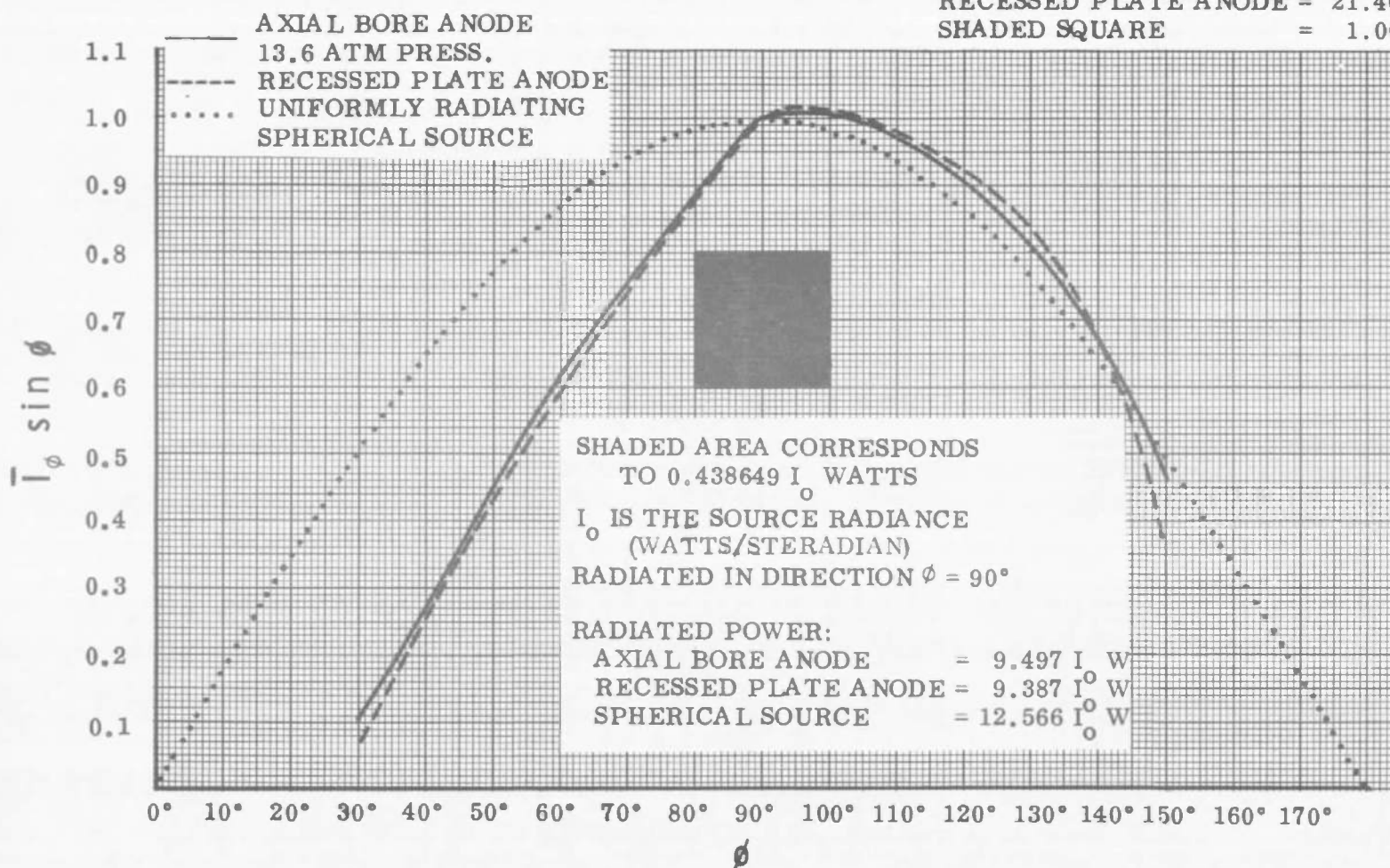


Figure 5-6. Relative Radiated Power Distribution of the VSRS with a 12 mm Electrode Gap and an Axial Bore Anode or Recessed Plate Anode

Although A may be directly measured from figure 5-6, it may also be directly calculated. Defining

$$x = a\phi$$

$$y = b \left(\frac{I_\phi}{I_0} \right) \sin \phi = b \bar{I}_\phi \sin \phi$$

where x and y are plotted in terms of unit length along the abscissa and ordinate, respectively, and a and b are scale factors. In figure 5-6, it can be seen that when $\phi = 180^\circ = \pi$ radians, then $x = 9$ inches. Also, when $\bar{I}_\phi \sin \phi = 1$, then $y = 5$ inches. Therefore

$$a = \frac{9}{\pi}$$

$$b = 5$$

To calculate A for a uniformly radiating source $\bar{I}_\phi = 1$

$$A = \int y dx = ab \int \sin \phi d\phi = 2ab = \frac{90}{\pi} \text{ square inches}$$

Substituting for A in equation (5-7) the scale factor S is

$$S = \frac{4\pi I_0}{\left(\frac{90}{\pi}\right)} = \left(\frac{4\pi^2}{90}\right) I_0 = 0.438649 I_0 \text{ watt-per-square inch}$$

The unit area for which this scale factor was determined is indicated by the shaded square in figures 5-6 and 5-7. The power radiated by each of the three VSRS configurations can be determined from the equation

$$P_r = S A_V = 0.438649 I_0 A_V \quad (5-8)$$

where A_V is the measured area under the appropriate curve between ϕ_{\min} and ϕ_{\max} . The values of A_V and $S A_V$ for the three VSRS configurations are noted on figures 5-6 and 5-7.

The values of I_0 at $\phi = 90^\circ$ for each of the distributions of table 5-1 and the corresponding value of the radiated power P_r and the radiative efficiency η were calculated, using equations (5-2), (5-8) and (5-4) respectively, and the values of the radiative efficiency thus determined were found to closely correspond to the radiative efficiency values listed in table 5-1 which were calculated by Plasmadyne. However, the attempt to establish the relationship

VORTEX STABILIZED RADIATION SOURCE

100% ARGON

6 mm ELECTRODE GAP

RECESSED PLATE ANODE

10.5 KW INPUT POWER

200 AMPERES 52.5 VOLTS

14.1 ATMOSPHERES PRESSURE

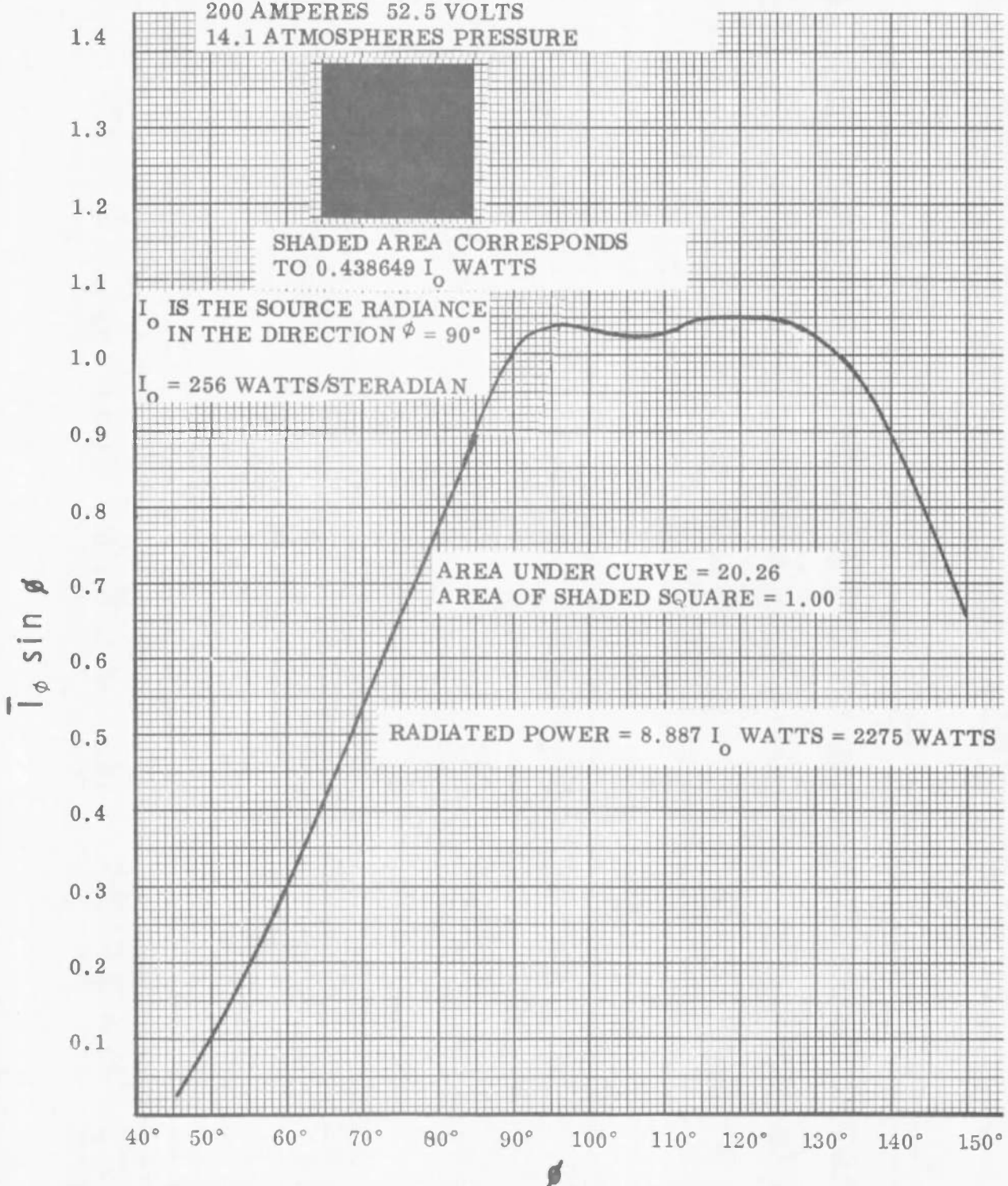


Figure 5-7. Relative Radiated Power Distribution of the VSRS with a 6 mm Electrode Gap and a Recessed Plate Anode

between input power P_o and radiative efficiency η (through a plot of η versus P_o) led to the conclusion that, at least in the case of the VSRS with an axial bore anode and a 12 mm electrode gap, there is a serious discrepancy in the data used to determine the absolute radiance I_o in the direction $\phi = 90^\circ$. After reviewing the reports referenced in table 5-2, it has been concluded that the data for distributions No. 1, 3, 5, 6, 8, 9, and 10 is probably correct. However, there is, in all probability, an error in the data for distributions No. 2, 4, and 7 obtained from Plasmadyne's Tenth Monthly Progress Report 10MS014-1033, due to the techniques employed in calibrating the detector, which could have resulted in the tabulated intensity values being uniformly too high.

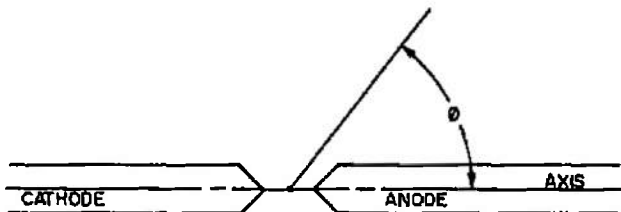
Before discussing this probable source of error, it is convenient to first determine the probable magnitude of the total error. This error factor can easily be determined through consideration of a plot of radiative efficiency versus input power, by making the assumptions that (1) the radiative efficiency is a smoothly varying function of the input power, and that (2) the radiative efficiency values calculated for distributions No. 1, 3, and 6 are correct. That is, it is possible to determine, through a process of successive approximations, the magnitude of the error factor ϵ which, when multiplied by the erroneous radiative efficiency values, gives corrected values of the radiative efficiency for distributions No. 2, 4, and 7 which, when plotted together with the radiative efficiency values calculated for distributions No. 1, 3, and 6 as a function of input power, result in the smoothest curve. The magnitude of the error factor thus determined is $\epsilon = 0.654$. The plot of radiative efficiency versus input power, as corrected, is shown in figure 5-8. A tabulation of the corrected values of the source radiance, in watts-per-steradian, is given in table 5-5. The indicated values of I_o listed in table 5-3 were also corrected by this error factor.

As noted above, the probable source of error in the intensity measurements for distributions No. 2, 4, and 7 lies in the techniques used to calibrate the Reeder Thermocouple employed as a detector. This is evidenced by the fact that if these measurements are uniformly reduced by a factor of 0.654, the resulting values of the radiant efficiency, when plotted together with the radiant efficiency values determined for distributions No. 1, 3, and 6 as a function of input power, lie on a smooth curve (figure 5-8). This indicates that the scale factor determined by Plasmadyne using the calibration techniques discussed in their Tenth Monthly Progress Report (10MS014-1033), was too high by a factor of 1.53. There are at least two major objections which can be offered to the calibration techniques employed by Plasmadyne in measuring distributions 2, 4 and 7. First, the fact that most (if not all) detectors vary in sensitivity over their surface, coupled with the fact that (because

Table 5-5. Absolute Radiance Distribution of the VSRS for Various Operating Conditions (As Corrected)

Polar Radiance Distribution
Vortex Stabilized Radiation Source
100% Argon

- \oplus 12 mm Electrode Gap
- * 6 mm Electrode Gap
- \square Axial Bore Anode
- \blacksquare Recessed Plate Anode



Identification Number	1	2	3	4	5	6	7	8	9	10
Console Input Power (Kilowatts)	\oplus \square		\oplus \square		\oplus \square	\ominus \square		*	\blacksquare	\oplus \blacksquare
Volts	11.2	11.4	15.6	15.9	17.8	19.0	19.4	10.5	16.8	17.0
Amperes	100	100	150	150	150	200	200	200	200	200
Pressure (Atmospheres)	13.6	13.6	13.6	13.6	14.3	13.6	13.6	14.1	14.1	14.2
ABSOLUTE RADIANCE I_ϕ Watts/Steradian										
30°	57	59 [†]	92	92 [†]	75	127	132 [†]	---	76	70
45°	132	137 [†]	209	215 [†]	206	307	318 [†]	8	274	275
60°	185	191 [†]	297	303 [†]	282	420	435 [†]	89	380	384
75°	220	226 [†]	351	360 [†]	345	493	511 [†]	174	472	475
90°	261	268 [†]	414	427 [†]	401	582	603 [†]	256	563	566
105°	266	275 [†]	425	438 [†]	407	597	619 [†]	272	580	584
120°	272	281 [†]	438	449 [†]	408	597	619 [†]	310	604	604
135°	276	286 [†]	438	455 [†]	407	615	636 [†]	355	612	613
150°	254	260 [†]	374	385 [†]	289	517	536 [†]	337	422	425
Radiative Efficiency	22.1%	22.3% [†]	25.2%	25.5% [†]	21.4%	29.1%	29.5% [†]	21.7%	31.5%	31.3%

[†]As corrected

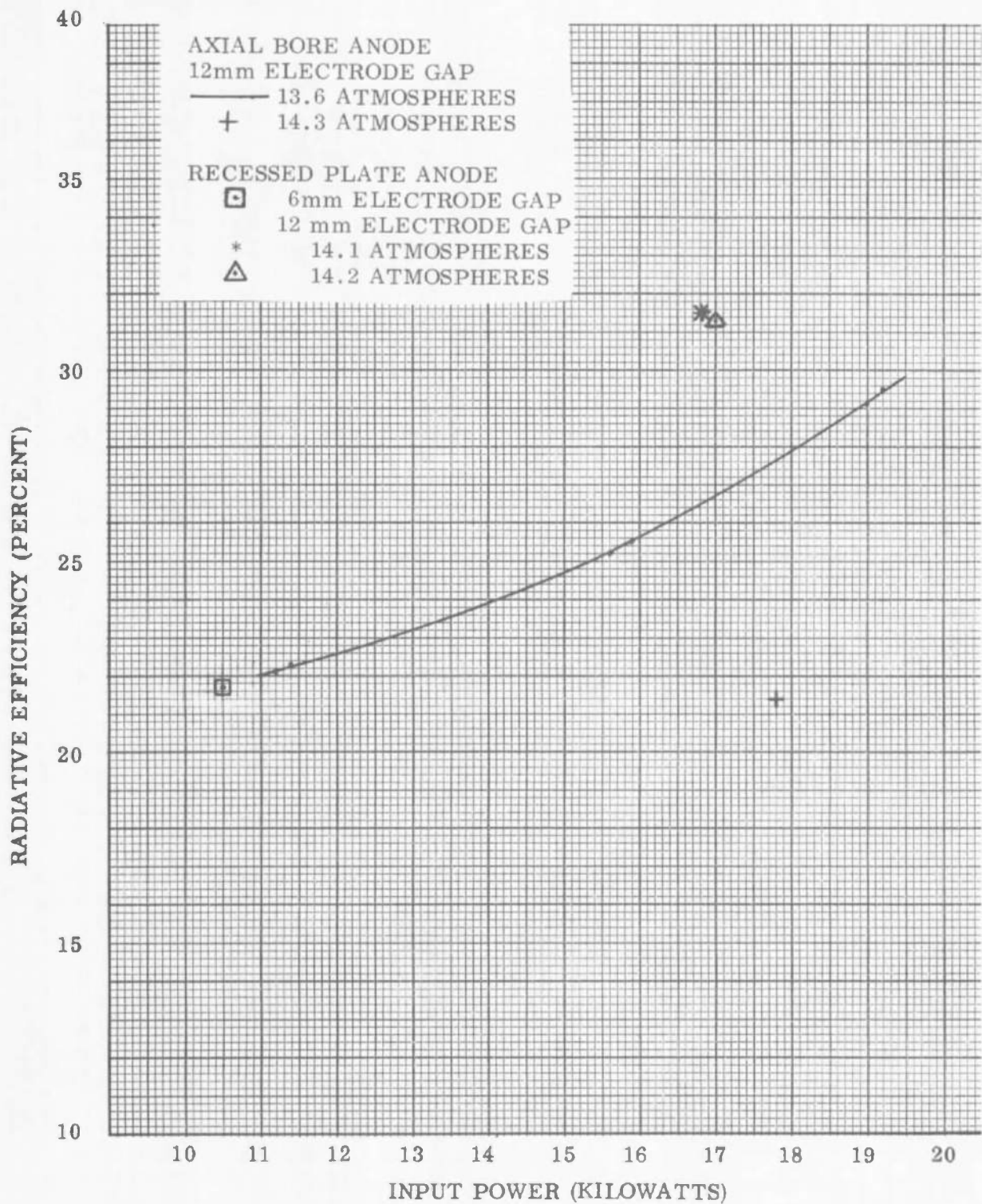


Figure 5-8. Radiative Efficiency of the VSRS as a Function of Input Power

the filament was imaged on the thermocouple) the intensity distribution was, in all probability, very nonuniform, could have introduced a significant error. Second, the assumption that the total transmission of the two mirrors used to image the filament was 0.85 implies that the average transmission of each mirror must be 92.2% for the spectrum of the calibrated tungsten filament, which seems rather hopeful. (If the total error is due only to the assumed value of transmission, the real total transmission of the two mirrors would have been 55.59%, implying a real transmission of 74.56% for each mirror, which seems rather low.) Unfortunately, it is not possible to determine quantitatively the exact (or probable) source (or sources) of error which may (or may not) be inherent in the available data.

The radiance distribution of the VSRS with a 12 millimeter electrode gap and a recessed plate anode (as determined previously and which, for convenience, will be denoted as the radiance distribution of the Basic VSRS) is plotted as the solid curve in figure 5-9 and may be closely approximated by three straight lines as indicated by the solid curve in figure 5-10. The equations which define these three straight lines are as follows (ϕ is expressed in degrees)

Between $\phi = 30^\circ$ and $\phi = 45^\circ$

$$\bar{I}_\phi = \frac{0.07}{3} (\phi - 23.5714) \quad (5-9)$$

Between $\phi = 45^\circ$ and $\phi = 90^\circ$

$$\bar{I}_\phi = \frac{0.1}{9} \phi \quad (5-10)$$

Between $\phi = 90^\circ$ and $\phi = 135^\circ$

$$\bar{I}_\phi = \frac{0.007}{3} (\phi - 338.5714) \quad (5-11)$$

The dotted curve in figure 5-9 represents how the radiance distribution of the Basic VSRS may be modified by incorporating a conical or near conical reflecting surface as part of the cathode and was generated from data included in figure 40 of AEDC-TDR-64-165. This distribution (which, for convenience, we will denote as the radiance distribution of the Modified VSRS) may also be closely approximated by three straight lines as indicated by the dashed curve of figure 5-10. The equations which define these three straight lines are as follows (ϕ is expressed in degrees)

Between $\phi = 30^\circ$ and $\phi = 45^\circ$

$$\bar{I}_\phi = \frac{0.07}{3} (\phi - 23.5714) \quad (5-12)$$

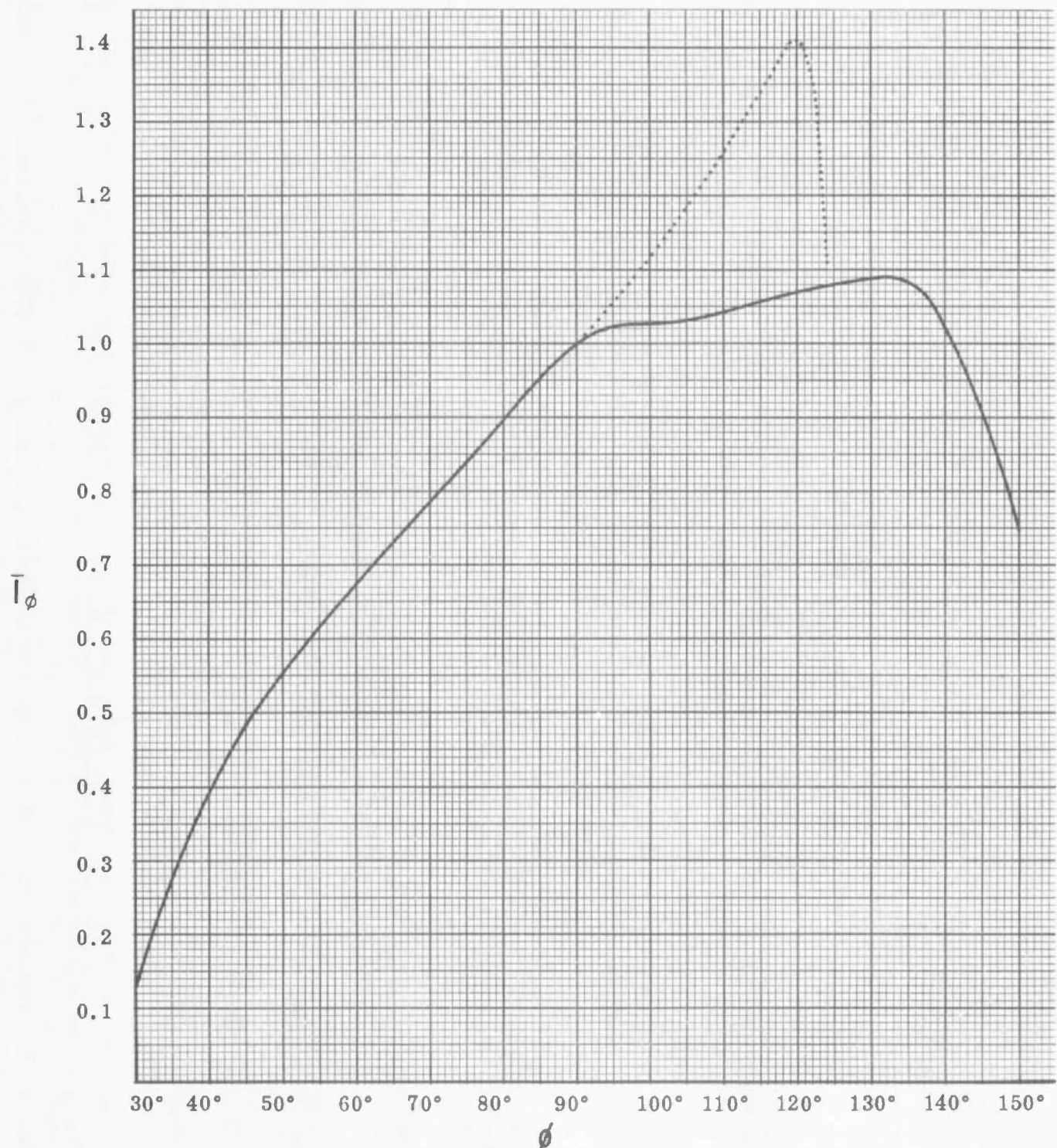


Figure 5-9. Radiance of the VSRS with a 12 Millimeter Electrode Gap and a Recessed Plate Anode Before, and as Modified by a Conical Reflecting Surface on the Cathode

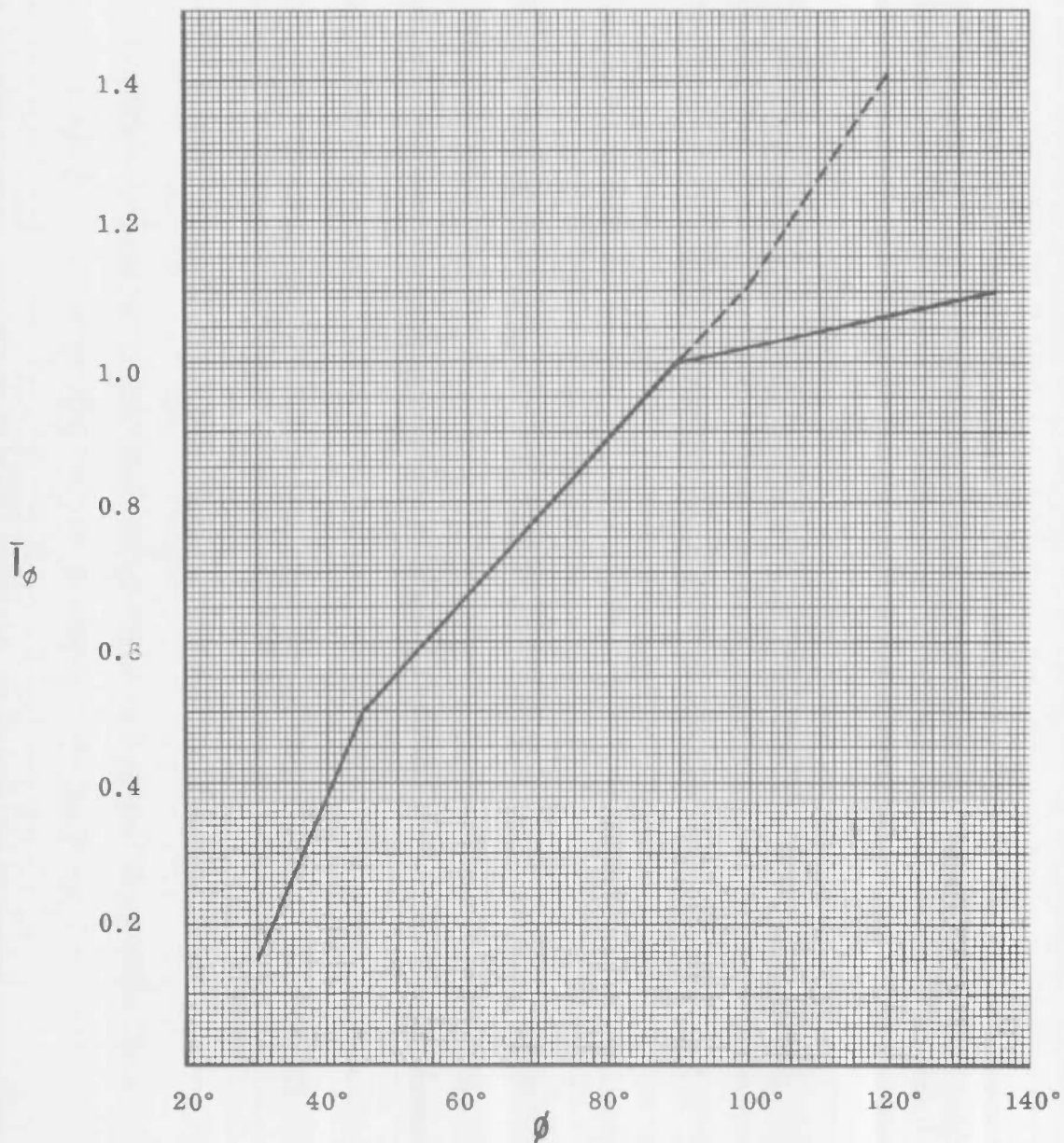


Figure 5-10. Approximation, Using Straight Lines, of the Radiance of the VSRS With a 12-Millimeter Electrode Gap and a Recessed Plate Anode Before and as Modified by a Conical Reflecting Surface on the Cathode

Between $\phi = 45^\circ$ and $\phi = 100^\circ$

$$\bar{I}_\phi = \frac{0.1}{9} \phi \quad (5-13)$$

Between $\phi = 100^\circ$ and $\phi = 120^\circ$

$$\bar{I}_\phi = 0.015 (\phi - 26) \quad (5-14)$$

Since equations (5-9) through (5-14) are all of the form

$$\bar{I}_\phi = S(\phi + K) \quad (5-15)$$

then the power radiated by either of these VSRS configurations into the solid angle for which each radiance function is defined may be determined by substituting equation (5-15) into equation (5-6) and integrating over the appropriate range of ϕ . Thus, again defining I_0 as the source radiance in the direction $\phi = 90^\circ$, the power radiated between ϕ_a and ϕ_b is

$$P = 2\pi I_0 (SQ) \int_{\phi_a}^{\phi_b} (\phi' + \frac{K}{Q}) \sin \phi \, d\phi \quad (5-16)$$

where ϕ is expressed in degrees, ϕ' is ϕ expressed in radians, and Q is the conversion factor, i.e.,

$$Q = \frac{\phi}{\phi'} = \frac{180}{\pi} \quad (5-17)$$

Integrating equation (5-16) gives

$$P = 2\pi I_0 S \left[\left(\frac{180}{\pi} \right) (\sin \phi_b - \sin \phi_a) - (\phi_b + K) \cos \phi_b + (\phi_a + K) \cos \phi_a \right] \quad (5-18)$$

The total power P_B radiated by the Basic VSRS between 30° and 135° is

$$P_B = I_0 (0.3345 + 3.3930 + 4.6634) = 8.3909 I_0 \quad (5-19)$$

where $0.3345 I_o$ is the power radiated between 30° and 45° , $3.3930 I_o$ is the power radiated between 45° and 90° , and $4.6634 I_o$ is the power radiated between 90° and 135° . In figure 5-6, the area under the curve plotted for the VSRS with a recessed plate anode and a 12 millimeter electrode gap between 30° and 135° is 19.188 which corresponds to a total radiated power of $8.4166 I_o$. This is only 0.3% larger than that determined using the straight line approximation, and the validity of the straight line approximation is thus established.

The total power P_M radiated by the Modified VSRS between 30° and 120° is

$$P_M = I_o (0.3345 + 4.5446 + 2.5771) = 7.4562 I_o \quad (5-20)$$

where $0.3345 I_o$ is the power radiated between 30° and 45° , $4.5446 I_o$ is the power radiated between 45° and 100° , and $2.5771 I_o$ is the power radiated between 100° and 120° .

5.2.1.2 Collection Efficiency

It can be stated, in general, that the larger the solid angle through which radiation is collected by an optical system, the more difficult it becomes to generate a detailed optical system design which will meet a given set of performance requirements. For this reason it is improbable that an optical system can be designed for a solar radiation simulator which will collect all of the energy radiated by the VSRS although it is desirable, from an efficiency standpoint, that as much of the radiant energy as possible be collected within such optical and physical restrictions as are imposed by the optical system geometry.

The collection efficiency analysis was performed to establish graphical and tabular data from which the efficiency with which a given optical system will collect radiant energy from each VSRS configuration can be quickly determined, given the solid angle subtended by the collector at the source center. For this analysis, it was assumed that the collector will be located symmetrically about the axis of symmetry of the VSRS such that it subtends a total solid angle Ω given by

$$\Omega = 2\pi (\cos \phi_{\min} - \cos \phi_{\max}) \quad (5-21)$$

where ϕ is again an angle measured from the axis of symmetry of the VSRS from the direction of the anode as illustrated, schematically, in figure 5-11. The solid angle Ω was divided into increments $\Delta\Omega_n$ given by

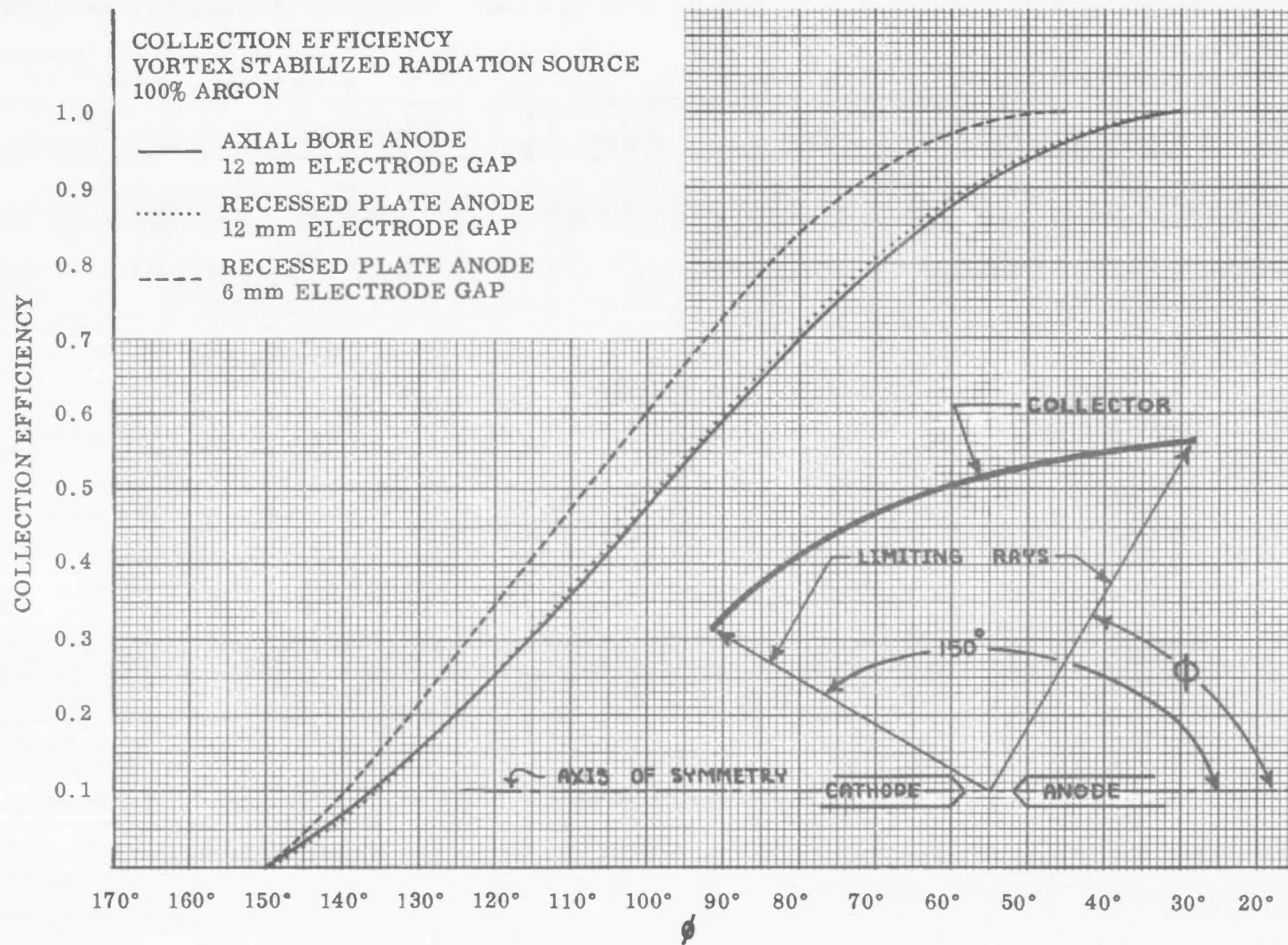


Figure 5-11. Collection Efficiency for the Vortex Stabilized Radiation Source

$$\Delta\Omega_n = 2\pi [\cos\phi_n - \cos(\phi_n + \Delta\phi)] \quad (5-22)$$

and, specifying that $\Delta\phi = 5^\circ$, the percent of the total power radiated by each VSRS configuration which is radiated into each increment of solid angle $\Delta\Omega_n$ was determined from figures 5-6 and 5-7 and is tabulated in table 5-6. (It was assumed that each VSRS configuration radiates only into the solid angle Ω defined by the range of ϕ for which the appropriate curve is plotted in figure 5-6 or 5-7).

The only geometry which seems feasible for use as a collector for the VSRS is a hemi-ellipsoidal reflector. Although a decision as to the location of the collector (whether it should be concave about the anode or the cathode) can only be made after considering the source radiance distribution in terms of the requirements dictated by the remainder of the optical system, it can be seen in figures (5-6) and (5-7) that all three VSRS configurations radiate more than 50% of their power output into the solid angle for which ϕ is greater than 90° . This indicates that, for maximum collection efficiency, the collector should be located so that it is concave about the cathode as represented, schematically, in figure (5-11). Thus, in order to represent collection efficiency as a function of ϕ , the collector was defined as being an ellipsoidal reflector located so that it is concave about the cathode with its primary focus centered between the electrodes. It was further assumed that there is an axially symmetric hole in the reflector which subtends a total angle of 60° at the primary focus. Finally, it was defined that the collector is axially symmetric, subtends the solid angle Ω_Σ at its primary focus, and thus collects all of the radiant energy emitted into Ω_Σ where

$$\Omega_\Sigma = 2\pi (\cos\phi_n - \cos 150^\circ) \quad (5-23)$$

Thus, as ϕ_n varies, Ω_Σ varies, and the collection efficiency as a function of ϕ_n can be determined from figures 5-6 and 5-7. The collection efficiency as a function of ϕ for the three VSRS configurations, as thus determined, is tabulated in table 5-6 and plotted in figure 5-11.

Table 5-6. Collection Efficiency for the VSRS

Vortex Stabilized Radiation Source
100% Argon

$$\Delta\Omega_n = 2\pi (\cos \phi_n - \cos \phi_{n-1}) \text{ Steradians}$$

$$\Omega_\Sigma = 2\pi (\cos \phi_n - \cos \phi_1) \text{ Steradians}$$

		Percent of the radiant energy contained within the indicated axially symmetric solid angle Ω					
		Recessed Plate Anode					
		12 mm Electrode Gap		6 mm Electrode Gap			
n	ϕ_n	Within $\Delta\Omega_n$	Within Ω_Σ	Within $\Delta\Omega_n$	Within Ω_Σ	Within $\Delta\Omega_n$	Within Ω_Σ
1	150°	0.00	0.00	0.00	0.00	0.00	0.00
2	145°	3.03	3.03	2.68	2.68	4.45	4.45
3	140°	3.59	6.62	3.47	6.15	5.18	9.64
4	135°	4.09	10.71	4.19	10.34	5.81	15.45
5	130°	4.49	15.20	4.68	15.02	6.19	21.64
6	125°	4.82	20.01	5.05	20.07	6.42	28.06
7	120°	5.09	25.11	5.30	25.37	6.47	34.52
8	115°	5.32	30.43	5.51	30.89	6.47	40.99
9	110°	5.51	35.94	5.67	36.55	6.42	47.40
10	105°	5.66	41.60	5.77	42.32	6.38	53.73
11	100°	5.75	47.35	5.86	48.19	6.37	60.10
12	95°	5.81	53.16	5.92	54.11	6.42	66.51
13	90°	5.82	58.98	5.90	60.01	6.33	72.84
14	85°	5.69	64.87	5.70	65.71	5.85	78.69
15	80°	5.34	70.01	5.37	71.09	5.12	83.81
16	75°	4.92	74.98	4.96	76.05	4.40	88.22
17	70°	4.54	79.47	4.51	80.56	3.68	91.89
18	65°	4.18	83.65	4.08	84.64	2.95	94.84
19	60°	3.78	87.43	3.63	88.27	2.23	97.08
20	55°	3.35	90.78	3.18	91.45	1.57	98.64
21	50°	2.86	93.65	2.71	94.16	0.95	99.59
22	45°	2.36	96.00	2.24	96.40	0.41	100.00
23	40°	1.85	97.85	1.74	98.14	---	---
24	35°	1.33	99.18	1.21	99.36	---	---
25	30°	0.82	100.00	0.64	100.00	---	---

5.2.2 Fluid Transpiration Arc (FTA)

5.2.2.1 Radiance and Radiative Efficiency.

Because of the experimental set-up used by Vitro Laboratories in their study of the Fluid Transpiration Arc (FTA), the radiance could be measured in only two directions for each set of operating conditions. Locating the FTA in the spherical coordinate system of figure 5-1 so that the polar axis coincided with the axis of symmetry of the electrodes, these directions were $\phi = 0^\circ$ and $\phi = 90^\circ$. The data concerning the radiance of the FTA in these two directions for three sets of operating conditions for which data was supplied is listed in table 5-7.

Table 5-7. Radiance Measurements for the Fluid Transpiration Arc (by Vitro Laboratories)

I_0 = Radiance in the direction $\phi = 0^\circ$

I_{90} = Radiance in the direction $\phi = 90^\circ$

Input Power to FTA *	19.0 kilowatts	29.1 kilowatts	37.5 kilowatts
Volts *	-	56	75
Amperes *	-	520	500
Gas *	100% Argon	100% Argon	100% Argon
Gas Pressure *	Atmospheric	100 psig	200 psig
I_0 (watts/steradian) *	390	1300	1900
I_{90} (watts/steradian) *	355	1170	1825
A	0.9103	0.9000	0.9605
B	0.0897	0.1000	0.0395
Power radiated into a Hemisphere	2340 watts	7760 watts	11700 watts
Radiative Efficiency	12.3%	26.7%	31.2%

* Parameters included in data obtained from Vitro Laboratories.

A simple function which suggests itself to define the radiance I_ϕ of the FTA in a direction ϕ is

$$I_\phi = a + b \cos \phi \quad (5-24)$$

From equation (5-24), it can be seen that when $\phi = 0^\circ$ then $I_0 = a + b$, and when $\phi = 90^\circ$ then $I_{90} = a$. Equation (5-24) can also be written in the normalized form as

$$I_\phi = I_0 (A + B \cos \phi) \quad (5-25)$$

where

$$A = \frac{a}{I_0} = \frac{I_{90}}{I_0} \quad (5-26)$$

$$B = \frac{b}{I_0} = \frac{I_0 - I_{90}}{I_0} \quad (5-27)$$

and this more convenient equation will be used to represent the radiance throughout the remainder of this discussion. The values of A and B for each set of operating conditions for which data was provided are listed in table 5-7.

The power P_r radiated by the FTA for each set of operating conditions can be determined by evaluating the following equation through the solid angle within which the radiance is represented by equation (5-25). That is,

$$P_r = \int_0^\Omega I_\phi d\Omega = 2\pi I_0 \int_0^\Phi (A + B \cos \phi) \sin \phi d\phi \quad (5-28)$$

which, when integrated, yields

$$P_r = \pi I_0 [2A(1 - \cos \Phi) + B \sin^2 \Phi] \quad (5-29)$$

Although the data provided does not indicate what the value Φ should be, the physical geometry of the FTA indicates that as Φ increases beyond 90° the electrodes will begin to obstruct radiation. It will, therefore, be assumed that the radiance of the FTA is represented by equation (5-25) only when $90^\circ \geq \phi \geq 0^\circ$ and that no useful energy is radiated for ϕ greater than 90° . Thus, it may be specified that $\Phi = 90^\circ$, in which case equation (5-27) becomes

$$P_r = \pi I_0 (2A + B) \quad (5-30)$$

Using this equation, the power radiated by the FTA into the hemisphere defined by $\phi \leq 90^\circ$ was determined for each set of operating conditions. These values, together with the corresponding values of the radiative efficiency, are listed in table 5-7.

It would seem that the ratio $\frac{I_{90}}{I_0} = A$ should be either a constant

or a smoothly increasing or decreasing function of the input power. (From the optical design standpoint, it would be desirable if A were constant.) Although there is insufficient data to draw any certain conclusion in this regard, it appears from the data in table 5-7 that this is not the case. However, the magnitude of this apparently random variation in A with variation in input power is small enough that it could be due only to experimental error and, making this assumption, corrected values \bar{A} and \bar{B} , may be defined by determining the average values of A and B , respectively, Thus

$$\bar{A} = 0.9236$$

$$\bar{B} = 0.0764$$

and it may be assumed that the radiance distribution of the FTA is independent of input power and is given by

$$I_\phi = I_0 (\bar{A} + \bar{B} \cos \phi) = I_0 (0.9236 + 0.0764 \cos \phi) \quad (5-31)$$

(The validity of this assumption must, of course, be investigated prior to the detailed design of a solar radiation simulation optical system which is to incorporate the FTA.)

The corrected values of the power P_r radiated into a hemisphere and the corresponding values of the radiative efficiency η_r , determined by representing the radiance of the FTA according to equation (5-31), are tabulated, together with a list of parametric definitions and relationships, in table 5-8. The radiative efficiency of the FTA, as corrected, is plotted as a function of input power in figure 5-12.

The physical situation described by equation (5-31) can arise from several conditions. For example, such a radiance function would result if the source consisted of a combination of a uniformly radiating sphere of radiance $\bar{A} I_0$ and a flat Lambertian Radiator (a disk) of radiance $I_0 \bar{B} \cos \phi$. This radiance function could also result if the source were a Lambertian radiator, e.g., an ellipsoid, whose projected area in each direction ϕ is a function of $(\bar{A} + \bar{B} \cos \phi)$. The actual physical conditions which, for the FTA, result in the radiance function described by equation (5-31), can be determined from an analysis of the micro-brightness

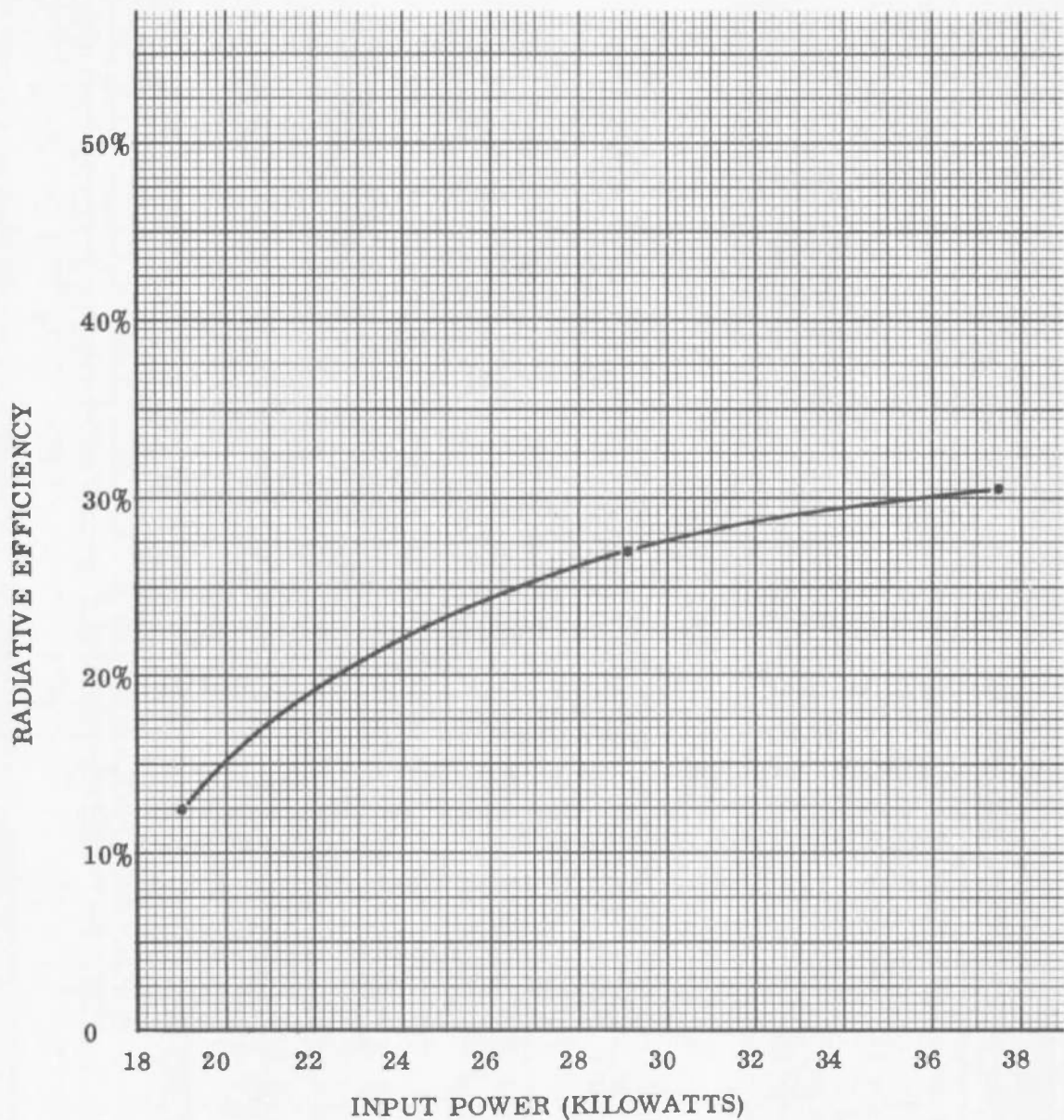


Figure 5-12. Radiative Efficiency of the Fluid Transpiration Arc as a Function of Input Power (as corrected)

Table 5-8. Radiance of the Fluid Transpiration Arc (As Corrected)

Parametric Definitions:

I_o	= Axial Radiance (toward $\phi = 0^\circ$) of FTA
P_o	= Input Power to FTA
P_r	= Power Radiated by FTA into a Hemisphere ($\phi \leq 90^\circ$)
η_r	= Radiative Efficiency of the FTA
\bar{A}	= 0.9236
\bar{B}	= 0.0764
I_ϕ	= $I_o (\bar{A} + \bar{B} \cos \phi)$
P_r	= $\pi I_o (2\bar{A} + \bar{B}) = 6.0432 I_o$
η_r	= $\frac{P_r}{P_o}$

P_o	19.0 kilowatts	29.1 kilowatts	37.5 kilowatts
I_o	390 watts/steradian	1300 watts/steradian	1900 watts/steradian
P_r	2357 watts	7856 watts	11482 watts
η_r	12.4%	27.0%	30.6%

distribution and will be discussed in the presentation of the mathematical representation of the FTA which follows:

5.2.2.2 Mathematical Representation of the FTA

Data concerning the relative micro-brightness distribution of the 37.5-kilowatt FTA was provided for two directions of view, namely a front view ($\phi = 0^\circ$) and a side view ($\phi = 90^\circ$). This data was supplied for each view in the form of a grid pattern (as described in the section dealing with the suggested experimental techniques) where the relative brightness values at various positions in the arc image were noted at the appropriate positions in the grid. The scale factor relating the

size of each grid to the real dimensions of the arc was also supplied. The relationship between the relative brightness values supplied for the front view with respect to the relative brightness values supplied for the side view was unknown.

As the first step in generating the mathematical representation of the FTA, a preliminary analysis of the data for the front view was conducted. From this analysis it was adjudged that, within the limits of accuracy to which the micro-brightness distribution was known and could be represented, the micro-brightness distribution of the FTA could be assumed to be symmetrical about the physical axis of symmetry of the electrodes.

As the second step in generating the mathematical representation of the FTA, the data for the side view of the FTA was analyzed in detail to determine, as closely as possible, the contours of various lines of constant relative brightness. Fourteen lines of constant relative brightness were determined, beginning with a relative brightness of 2.0 for the outermost line. The remaining lines were then plotted for increments in the relative brightness of 2.0 from the preceding line. The lines of constant relative brightness thus determined are shown in figure 5-13. (For identification purposes, these lines were numbered from 1 to 14, where line 1 is the outermost line and has the smallest relative brightness and line 14 is the innermost line and has the highest relative brightness. Thus, the relative brightness value for which the n th line was plotted is $2n$.) The relative brightness value for which each line was plotted is noted on figure 5-13.

The next step in generating a mathematical representation of the FTA consisted of approximating the shape of the lines of constant relative brightness and the area enclosed by each with some analytic function from which a mathematical expression for an axially symmetric surface could be generated. To this end, it was specified that, whenever possible, a line of constant relative brightness would be approximated by an ellipse defined by the equation (in a Z , R coordinate system)

$$\frac{(Z - D)^2}{a^2} + \frac{R^2}{b^2} = 1 \quad (5-32)$$

where Z is measured along the axis of symmetry, a and b are the semi-axes of the ellipse (along the Z -axis and R -axis, respectively), and D is the displacement of the ellipse center from the reference position chosen as the origin of the coordinate system. Further, it was specified that, if it was adjudged that the shape of a line of constant relative brightness was such that it could not be adequately approximated with a

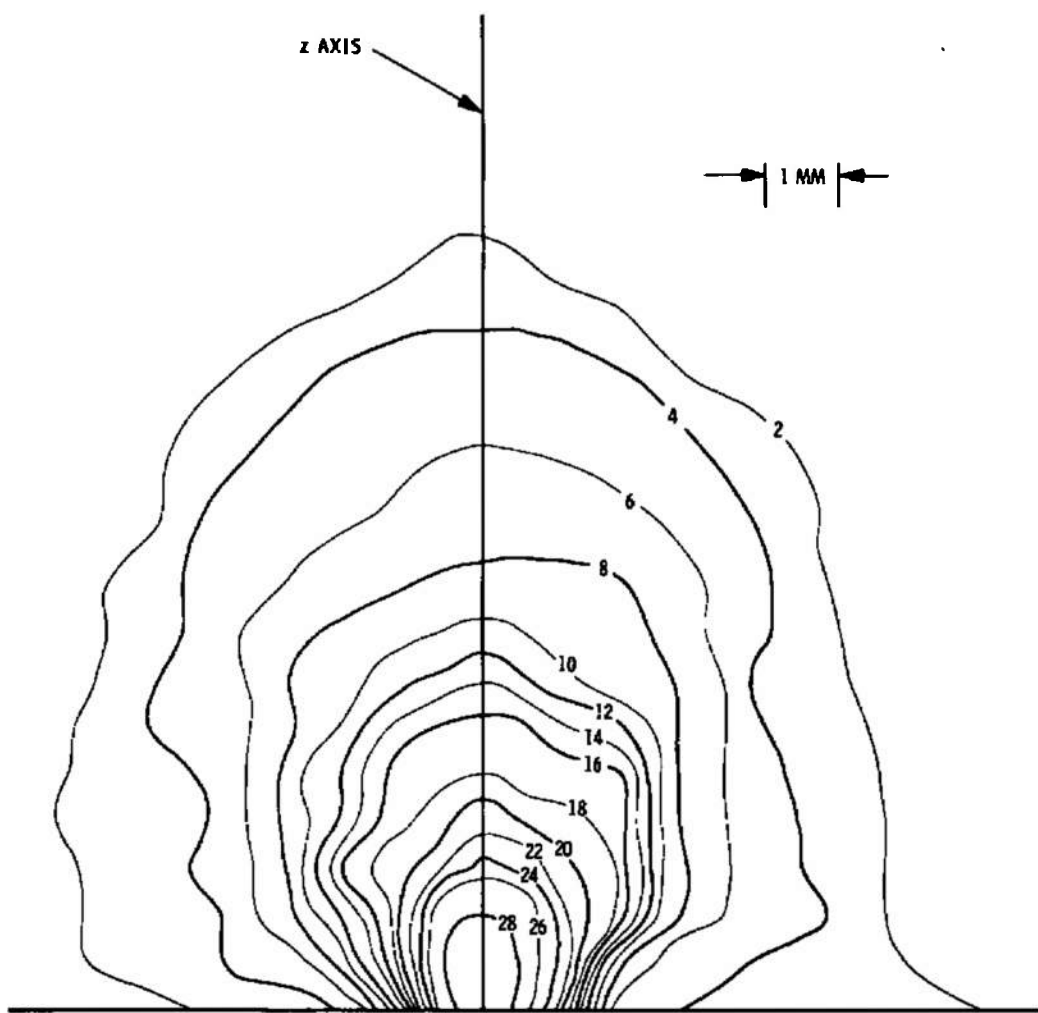


Figure 5-13. Lines of Constant Relative Brightness of the 37.5 KW Fluid Transpiration Arc (Side View)

single ellipse, the line of constant relative brightness could be approximated with a combination of two ellipses or with a combination of an ellipse and a hyperbola, provided that the combination is so defined that the two curves are tangent at a specified boundary position. Using this criterion, the curves of figure 5-14 were determined. From figure 5-14, it can be seen that constant relative brightness lines 2 through 14 were approximated with ellipses. However, in order to adequately approximate line 1, it was necessary to use a combination of two ellipses. The procedure used to define these ellipses is illustrated in figure 5-15 and is described below:

To fit Ellipse A:

Using graphical methods, a portion of an ellipse (the curve AHB of figure 5-15) is chosen which is a good approximation to the line of constant relative brightness between the points A and B. The line A B defines the boundary between the two ellipses and is located a distance T from the center of Ellipse A. The equation which defines this ellipse is, in terms of the parameters of figure (5-15)

$$\frac{(Z - D_1)^2}{a_1^2} + \frac{R^2}{b_1^2} = 1 \quad (5-33)$$

The distance R_0 from the axis to the point B (where $Z = D_1 - T$) is, from equation (5-33)

$$R_0 = b_1 \sqrt{1 - \frac{T^2}{a_1^2}} \quad (5-34)$$

The slope $\left(\frac{dR}{dZ}\right)$ of Ellipse A at point B is

$$\frac{dR}{dZ} = \frac{-b_1^2 (Z - D_1)}{a_1^2 R} = \frac{b_1^2 T}{a_1^2 R_0} \quad (5-35)$$

To fit Ellipse B

It now remains to determine an ellipse which is tangent to Ellipse A at points A and B and which passes through the point C on the line of constant relative brightness. The equation which defines this ellipse in terms of the parameters of figure 5-15 is

$$\frac{(Z - D_2)^2}{a_2^2} + \frac{R^2}{b_2^2} = 1 \quad (5-36)$$

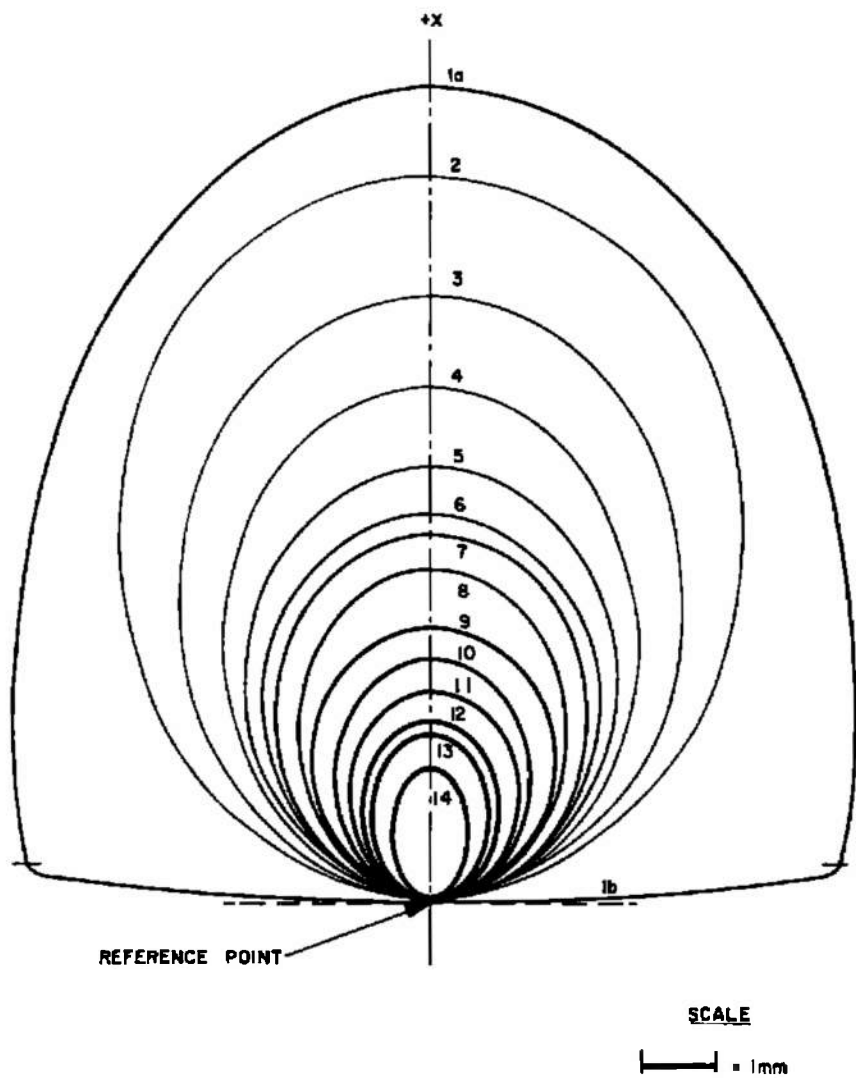
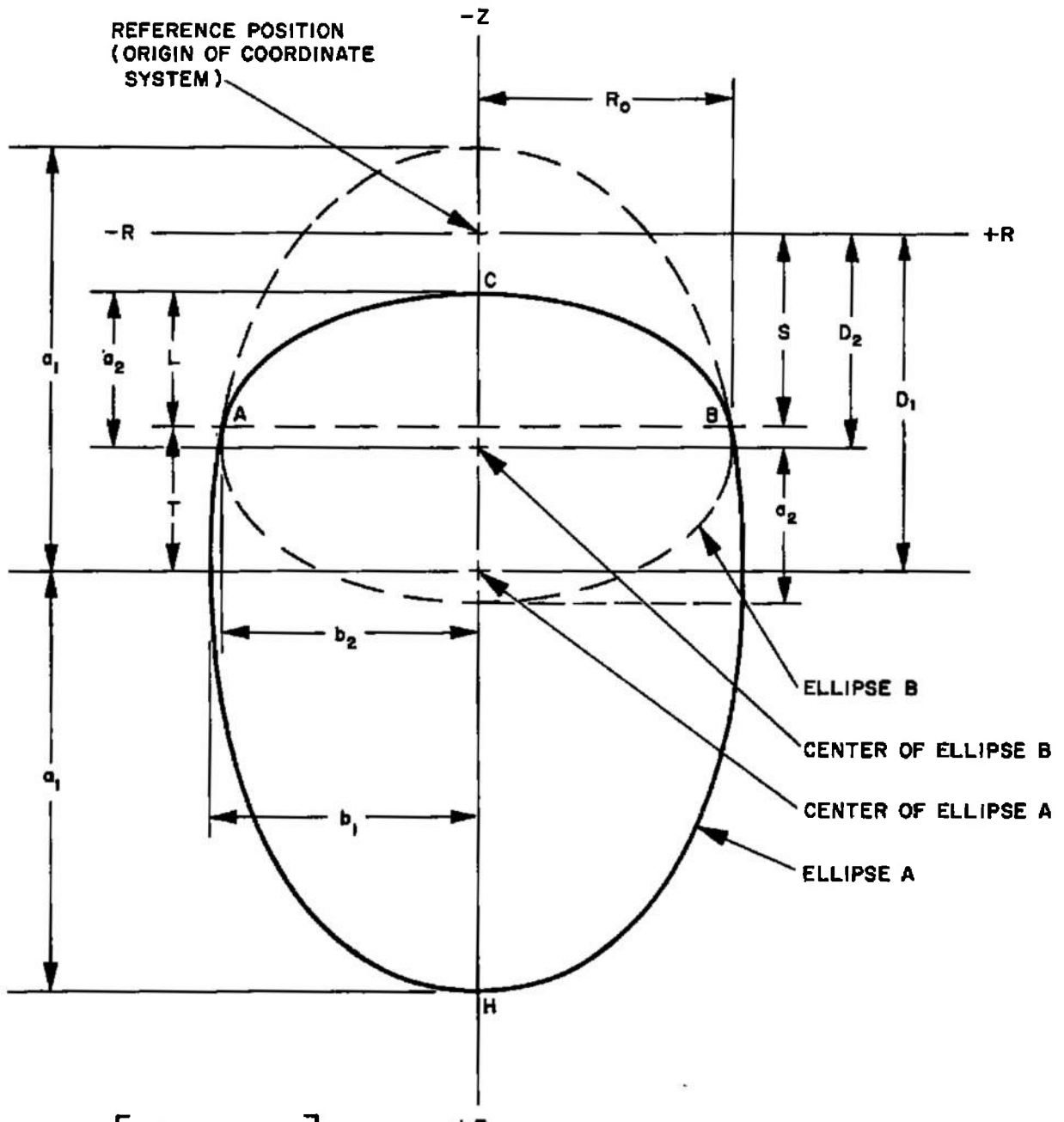


Figure 5-14. Approximation of the Lines of Constant Relative Brightness of the 37.5 KW Fluid Transpiration Arc (Side View)



$$a_2 = L \left[\frac{\frac{a_1^2 - T(L+T)}{a_1^2}}{\frac{a_1^2 - T(2L+T)}{a_1^2}} \right]$$

$$D_2 = D_1 - T - L + a_2$$

$$S = D_1 - T$$

$$b_2 = \frac{a_2 b_1}{a_1} \sqrt{\frac{T}{a_2 - L}}$$

VALUES OF a_1 , b_1 , D_1 , L AND T ARE
DETERMINED GRAPHICALLY

**Figure 5-15. Graphical Approximation of a Line of Constant
Relative Brightness with Two Ellipses**

Defining L as the distance from C to line AB , the slope $\left(\frac{dR}{dZ}\right)$ of Ellipse B at point B (where $Z = D_2 - a_2 + L$ and $R = R_0$) is

$$\frac{dR}{dZ} = \frac{-b_2^2 (Z - D_2)}{a_2^2 R} = \frac{b_2^2 (a_2 - L)}{a_2^2 R_0} \quad (5-37)$$

Since the two ellipses are tangent to each other at their points of intersection (points A and B), then from equations (5-35) and (5-37)

$$\frac{b_1^2 T}{a_1^2} = \frac{b_2^2 (a_2 - L)}{a_2^2} \quad (5-38)$$

Substituting equation (5-34) into equation (5-36) yields (since $Z = D_2 - a_2 + L$)

$$\frac{(L - a_2)^2}{a_2^2} + \frac{b_1^2}{b_2^2} \left(1 - \frac{T^2}{a_1^2}\right) = 1 \quad (5-39)$$

Solving equations (5-38) and (5-39) simultaneously for a_2 gives

$$a_2 = L \left[\frac{a_1^2 - T (L + T)}{a_1^2 - T (2L + T)} \right] \quad (5-40)$$

which value may then be used to determine b_2 and D_2 using the following equations

$$b_2 = \frac{a_2 b_1}{a_1} \sqrt{\frac{T}{a_2 - L}} \quad (5-41)$$

$$D_2 = D_1 - T - L + a_2 \quad (5-42)$$

Equation (5-41) was obtained from equation (5-38). Equation (5-42) was obtained from the geometry of figure 5-15.. Also, from figure 5-15 , the distance S from the reference position to line AB is

$$S = D_1 - T \quad (5-43)$$

Thus, by graphically determining the magnitudes of a_1 , b_1 , D_1 , L and T and by solving equations (5-40) through (5-43) a smooth curve can be defined (as a combination of two ellipses) which closely approximates the line of constant relative brightness.

Since the micro-brightness distribution is symmetric about the axis of symmetry of the electrodes, the appearance of the FTA does not vary with θ . This fact may be simulated, mathematically, by specifying that $R = \sqrt{x^2 + y^2}$ which, when substituted into the equation of each line (or portion of a line) of constant relative brightness of figure 5-48 results in the equation

$$\frac{(Z - D)^2}{a^2} + \frac{(x^2 + y^2)}{b^2} = 1 \quad (5-44)$$

which is the defining equation of an ellipsoid of revolution. The micro-brightness distribution is then approximated by (1) specifying that each surface so defined is Lambertian and radiates energy independently of the other surfaces and then (2) assigning the proper brightness value to each surface. This latter procedure, i.e., the assignment of a brightness value to each surface, consists of defining a step function which closely approximates the brightness distribution seen across the FTA from any direction. To this end consider the micro-brightness distribution of the FTA as seen from the front.

It was previously stated that a preliminary analysis of the micro-brightness distribution of the FTA as seen from the front indicated that this distribution is axially symmetric. In order to represent this distribution in terms of the surfaces defined by equation (5-44), a series of concentric circles of radius b_i was defined where b_i is the semi-minor axis of the i^{th} ellipse of figure 5-14. (For line 1, which is a combination of two ellipses, the value taken for b_1 was the semi-minor axis of ellipse 1A since it represents the maximum radius of line 1.) These circles were then superimposed upon the data concerning relative micro-brightness distribution across the FTA as seen from the front and the relative brightness represented by each circle was determined. These circles and the relative brightness value determined for each are shown in figure 5-16.

The step function used to initially approximate the brightness distribution across the source was

$$I_\phi = S_\phi \left[\frac{3}{2} \bar{B}_1 \Delta A_1 + \left(\frac{3\bar{B}_n - \bar{B}_{n-1}}{2} \right) A_n \right. \\ \left. + \frac{1}{4} \sum_{i=2}^{n-1} (3\bar{B}_{i+1} + \bar{B}_{i-1}) \Delta A_i \right] \quad (5-45)$$

where: I_ϕ = radiance of the FTA in the direction ϕ
 B_i = relative brightness value of the i^{th} line
 A_i = projected area of the i^{th} surface in the direction ϕ
 S_ϕ = scale factor to convert relative to absolute brightness
 $\Delta A_i = A_i - A_{i+1}$

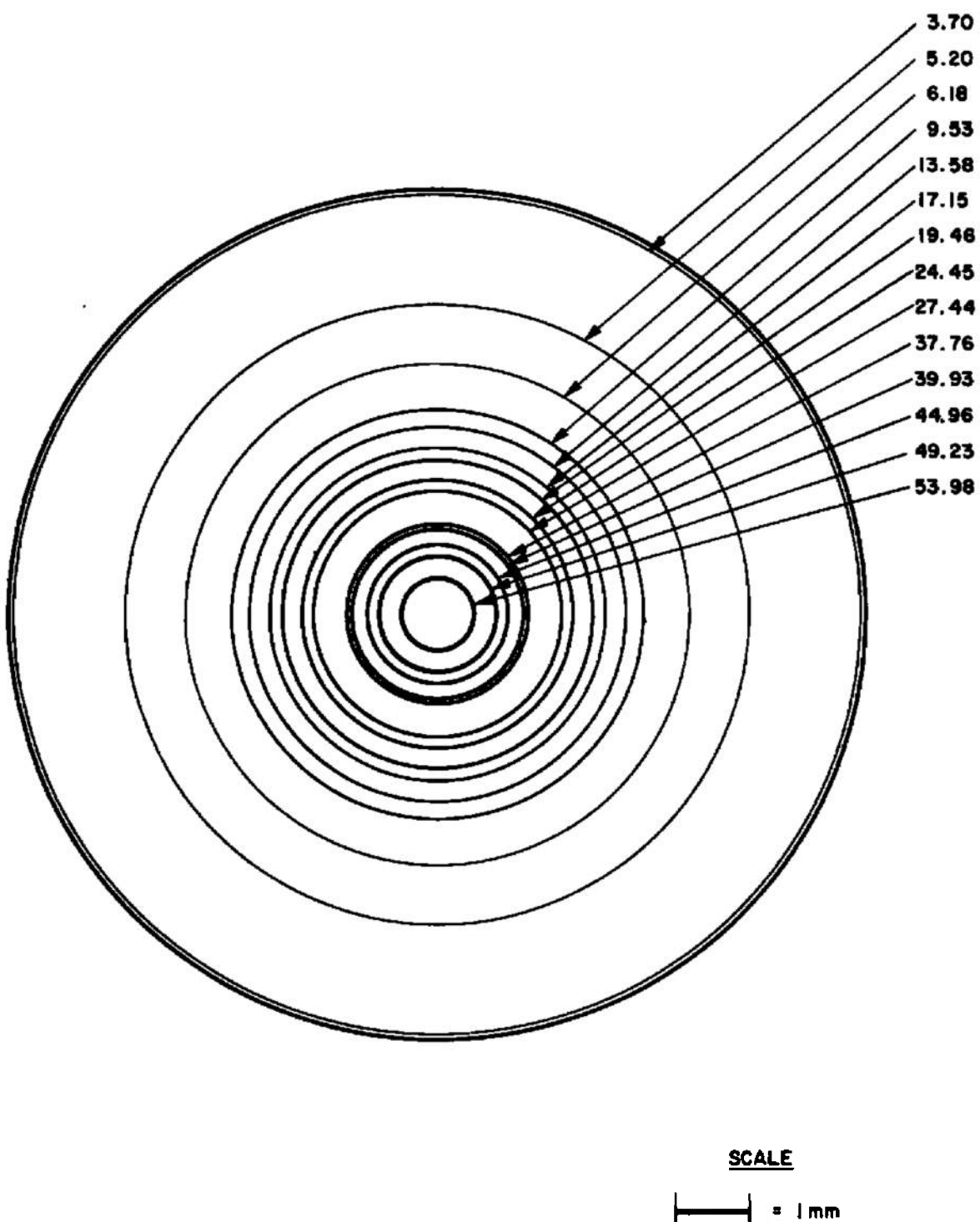


Figure 5-16. Approximation of the Lines of Constant Relative Brightness of the 37.5 KW Fluid Transpiration Arc (Front View)

Since all of the parameters of equation (5-45) are known with the exception of S_1 , equation (5-45) can be solved to determine the appropriate scale factor for each view. The scale factor was then multiplied by the relative brightness factor assigned to each ΔA , and the resulting approximation functions for the two views were analyzed with respect to each other and with respect to the micro-brightness distributions which each represented. The brightness factors were then adjusted as indicated by the analysis and the distributions were re-analyzed. Through successive approximations, step functions were defined for each view which were adjudged to closely approximate the micro-brightness distribution seen across the FTA from each direction.

The solid line plotted in figure 5-17 represents the step function defined to represent the brightness distribution across the FTA as seen from the front. The dashed line indicates the brightness distribution which would result if the surfaces of the FTA representation were assigned the brightness factors determined from the step function defined for the side view. The fact that the FTA appears brighter from the front indicates that the FTA representation must also include a combination of flat, axially symmetric Lambertian radiators. As was noted previously, this is also indicated by equation (5-31) which describes the radiance of the FTA. This increase in the maximum brightness over that seen from the side could result from any of a combination of several conditions. For example, the increase in brightness could be the result of radiation emitted and/or reflected by the electrodes. In any case, this additional radiation apparently emanates from the vicinity of the electrode surface and is described by a cosine radiance function. Therefore, to complete the generation of the FTA representation, a combination of flat axially symmetric Lambertian radiators was defined and brightness factors were assigned to each on the basis of the difference between the two functions. This planar portion of the FTA representation was located (in the vicinity of the surface of the electrodes) at the origin of the coordinate system used to define the ellipsoids of the volumetric portion of the FTA representation. In figure 5-14, the location of the planar portion is indicated by the dashed straight line.

The parameters which define the mathematical representation of the Fluid Transpiration Arc are listed in table 5-9.

5.2.3 High Intensity Carbon Arc

5.2.3.1 Radiance

Analysis of the carbon arc with a view toward establishing an approximate mathematical description of the radiance distribution for any given power level proved to be extremely difficult on the basis of the

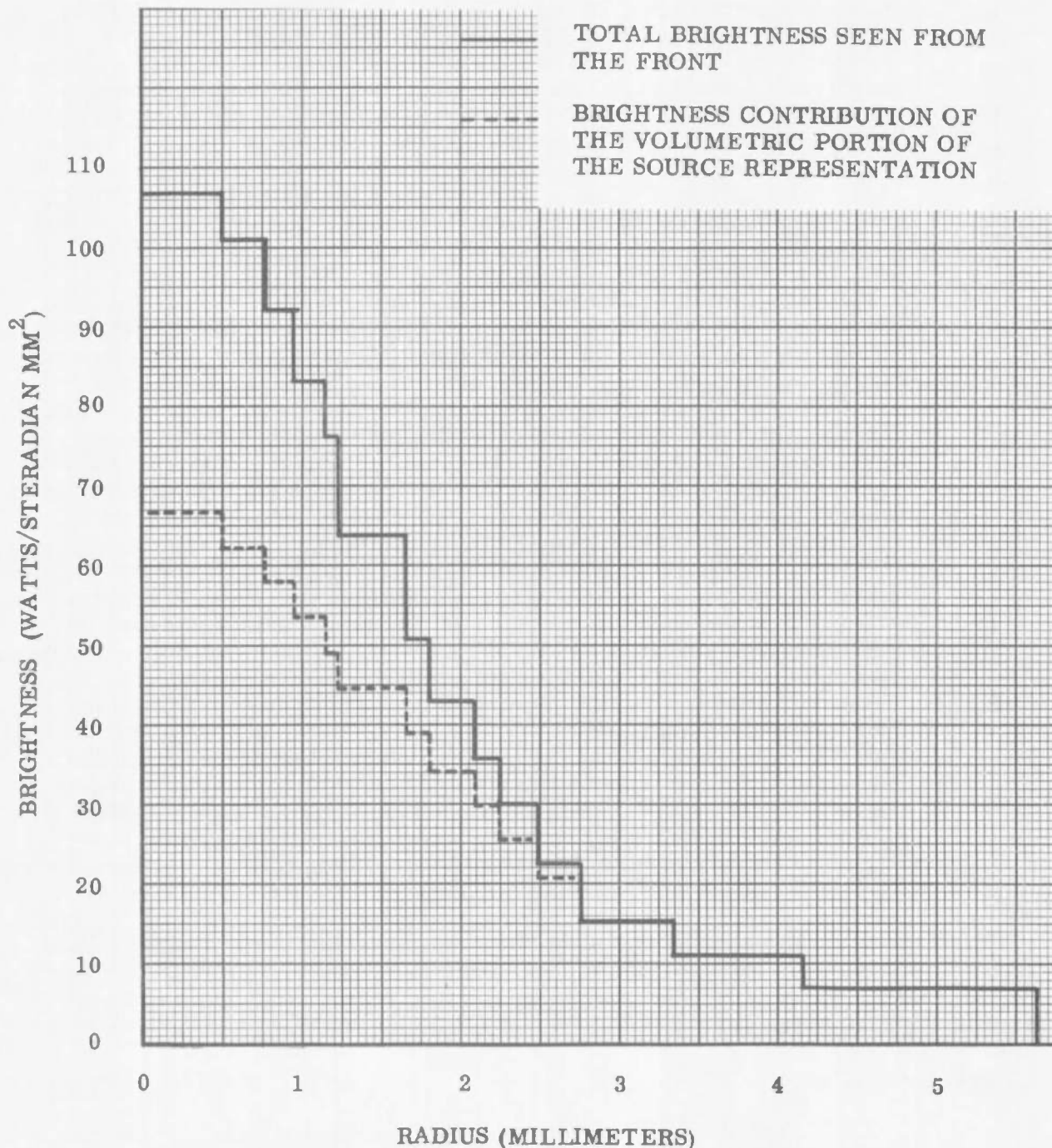


Figure 5-17. Approximation to the Brightness Distribution Seen Across the Front View of the Fluid Transpiration Arc (37.5 kilowatts)

Table 5-9. Defining Parameters for the Representation of the 37.5 KW Fluid Transpiration Arc.

Equation for a surface of the Volumetric Portion:

$$\frac{(Z - D_i)^2}{a_i^2} + \frac{x^2 + y^2}{b_i^2} = 1$$

Equation for a surface of the Planar Portion⁺:

$$x^2 + y^2 = b_i^2$$

Surface Number <i>i</i>	Millimeters			Brightness of Surface (Watts/Steradian· mm ²)	
	Semi-Axis (in xy Plane) <i>b_i</i>	Semi Axis (along z-axis) <i>a_i</i>	Displace- ment of Ellipse Cen- ter <i>D_i</i>	Volumetric Portion	Planar Portion ⁺
* A ₁	5.63	8.24	2.68	7.000	0
B	5.4253	0.44712	0.44712		
2	4.16	4.84	4.84	4.054	0
3	3.34	4.04	4.04	4.316	0
4	2.76	3.42	3.42	5.354	1.907
5	2.48	2.88	2.88	4.836	2.643
6	2.24	2.56	2.56	4.260	1.508
7	2.08	2.44	2.44	4.375	2.777
8	1.80	2.22	2.22	4.950	2.863
9	1.66	1.81	1.81	5.297	7.745
10	1.22	1.60	1.60	4.605	7.629
11	1.14	1.39	1.39	4.375	2.679
12	0.94	1.20	1.20	4.605	4.506
13	0.78	1.08	1.08	4.145	4.685
14	0.50	0.86	0.86	4.605	1.053

* The boundary between the two ellipsoids of Surface No. 1 is located at $Z = 0.44$ millimeters

+ The Planar Portion is located at $Z = 0$

data available. For most power levels there was only one set of data provided on which to base the analysis. In the one case (35-kilowatt operation) where two sets of data were available, one from a set of horizontal scans, and one from a set of vertical scans, correlation between the two sets was poor. Figure 5-18 shows the two sets of data superimposed.

What small degree of symmetry could be established appeared to be roughly circular, although the axis of radiation symmetry was in no case coincident with the anode axis of symmetry, nor was it consistently located with respect to that axis. In most cases the major deviation from circular symmetry was an elongation in the vertical direction, figure 5-19, which amounts to a distribution such that \bar{I}_ϕ along a vertical meridian is more nearly spherical than \bar{I}_ϕ along a horizontal meridian. (See figure 5-1 for a definition of the coordinate system implied.) Complicating this interpretation, however, is the fact that in the case of the 35 kw operation where there are two sets of data from scans taken in different directions, the data is apparently elongated in the direction of the scan (figure 5-18). This may indicate that at least part of the apparent asymmetry is due to the data-taking techniques, or to characteristics of the radiometer used, although there is far too little data available on which to base a positive conclusion.

In order to make the most out of what was available, it was decided to characterize the carbon arc radiance by an approximate mathematical relationship derived from the most smoothly symmetrical sets of data available. With this approach, the data for the shielded 75-kilowatt arc was analyzed, figure 5-19. It was further decided, rather arbitrarily, that at least as a first approximation, circular symmetry about the best axis of radiation symmetry could be assumed, i.e., \bar{I}_ϕ independent of Θ . While this assumption cannot be wholly justified from the data available, it does not require the assignment of an unreasonably large experimental error factor to make the data compatible with the assumption. If a pair of axes, one vertical and one horizontal, are drawn through the approximate center of symmetry and if the circular symmetry assumed is based on the distribution along the vertical axis, a distribution between that of a sphere, $\bar{I}_\phi = 1$, and the cosine function, $\bar{I}_\phi = \cos \phi$ results. If the symmetry is based on distribution along the horizontal axis, the distribution falls between that of the cosine and a cosine square relationship, $\bar{I}_\phi = \cos^2 \phi$. Finally, if the circularly symmetrical distribution is based on an intensity vs. angular position relationship that is the average of the values for the two axes, the result is very close to the cosine relationship $\bar{I}_\phi = \cos \phi$. A similar treatment of figure 14 in reference 8 yields similar results. With the best curve fit, a center intensity value of 164 mw/cm^2 measured at a distance $R = 6 \text{ feet}$, the axial radiance I_0 is:

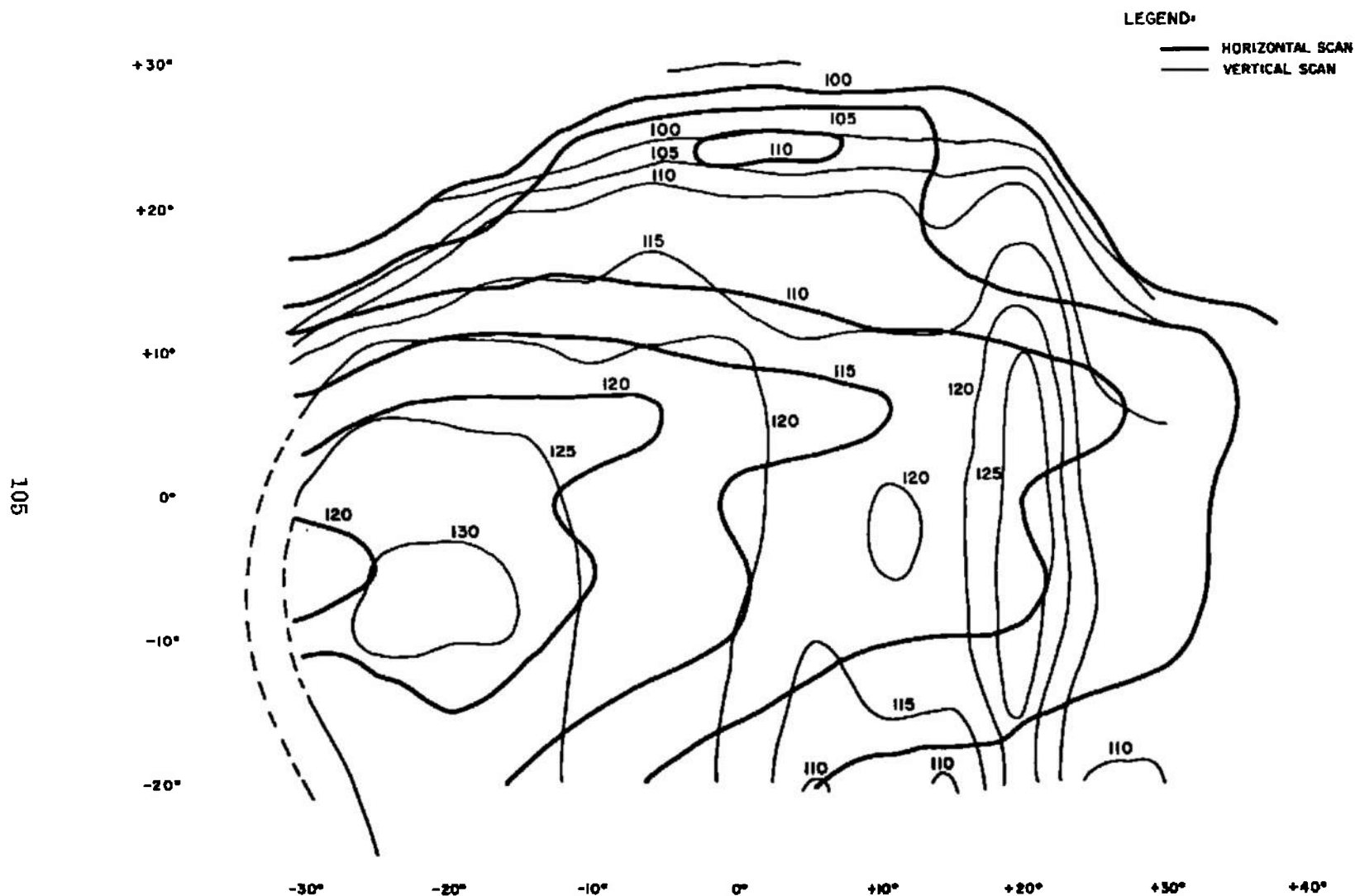


Figure 5-18. Superimposed Horizontal and Vertical Scans - Intensity in mw/cm^2 of 35-kw Unshielded Carbon Arc at Radius of 6 feet

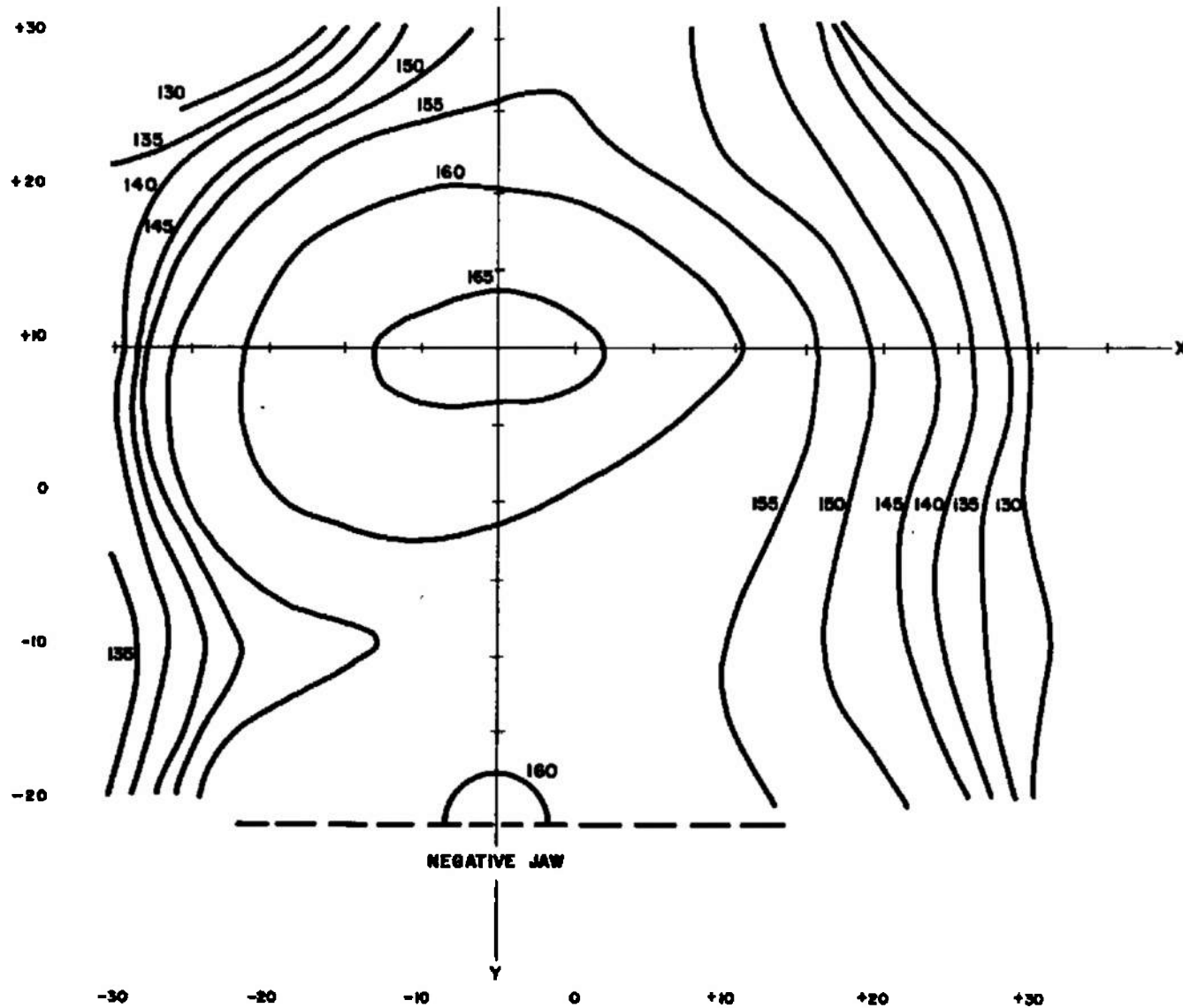


Figure 5-19. Intensity in mw/cm^2 of Shielded 75-kw Carbon Arc at Radius of 6 feet

$$I_o = ER^2 = \left(\frac{164}{1000}\right) (6 \times 12 \times 2.54)^2$$

$$= 5,480 \text{ watts/steradian}$$

whereby

$$I_\phi = 5480 \cos \phi \text{ watts/steradian} \quad (5-46)$$

This is the radiance function assumed for the 75-kilowatt carbon arc in all numerical calculations made in the study. It should be emphasized that this characterization is an approximation at best and, while it provides a relatively simple relationship very useful in a first order analysis, before further work is done toward the optical design of a solar radiation simulator to incorporate the High Intensity Carbon Arc, a far more comprehensive study must be made of its radiation characteristics.

5.2.3.2 Radiative Efficiency

Having defined (at least approximately) the radiance of the carbon arc, its effective radiative efficiency may now be calculated. For 75-kilowatt operation, this calculation proceeds as follows, starting from the basic relationship

$$P = \int I d\Omega \quad (5-47)$$

substituting for I from equation (5-46) and defining $d\Omega$ as

$$d\Omega = 2\pi \sin \phi d\phi$$

then

$$P = 2\pi (5480) \int_0^\Phi \sin \phi \cos \phi d\phi \text{ watts} \quad (5-48)$$

which upon integration yields

$$P = \pi (5480) \sin^2 \Phi \text{ watts} \quad (5-49)$$

where Φ is the maximum collection angle. Since virtually all of the useful radiation from the carbon arc is emitted into the forward hemisphere, an upper limit on Φ of 90° is indicated. Thus

$$P = 5480 \pi = 17,200 \text{ watts}$$

This yields a radiative efficiency η of

$$\eta = \frac{17,200}{75,000} \times 100 = 23\%$$

It is apparent that this figure is considerably lower, perhaps by one-half, than the value usually attributed to the carbon arc. The difference may be traced to two major contributing factors. First, the simplifying assumption of a cosine distribution may have introduced an error on the low side. If the actual average radiance function is more nearly spherical, a larger value of radiative power will result; in fact, for a perfectly spherical distribution, $I = 1$, the calculated radiative efficiency would be doubled. A second factor, which is undoubtedly the dominant reason for the relatively low radiative efficiency, is that the radiated power determined by evaluating equation (5-47) represents that power radiated which is useful to the optical system. In particular, the tail flame radiation has not been included. That tail flame radiation is a significant proportion of total arc radiation is verified by a comparison of data taken from the 75-kilowatt arc by a radiometer which was shielded from the tail flame radiation with that taken by an unshielded radiometer (figure 5-20). Warner and Nelms have estimated that tail flame radiation amounts to approximately 35% of the total radiation at 75-kilowatt operation. While analysis of the data represented by figure 5-59 is difficult because the axis of symmetry, if there is one, appears to be outside the solid angle within which scans were made, indications are that the radiation contribution from the tail flame may be even larger than this estimate.

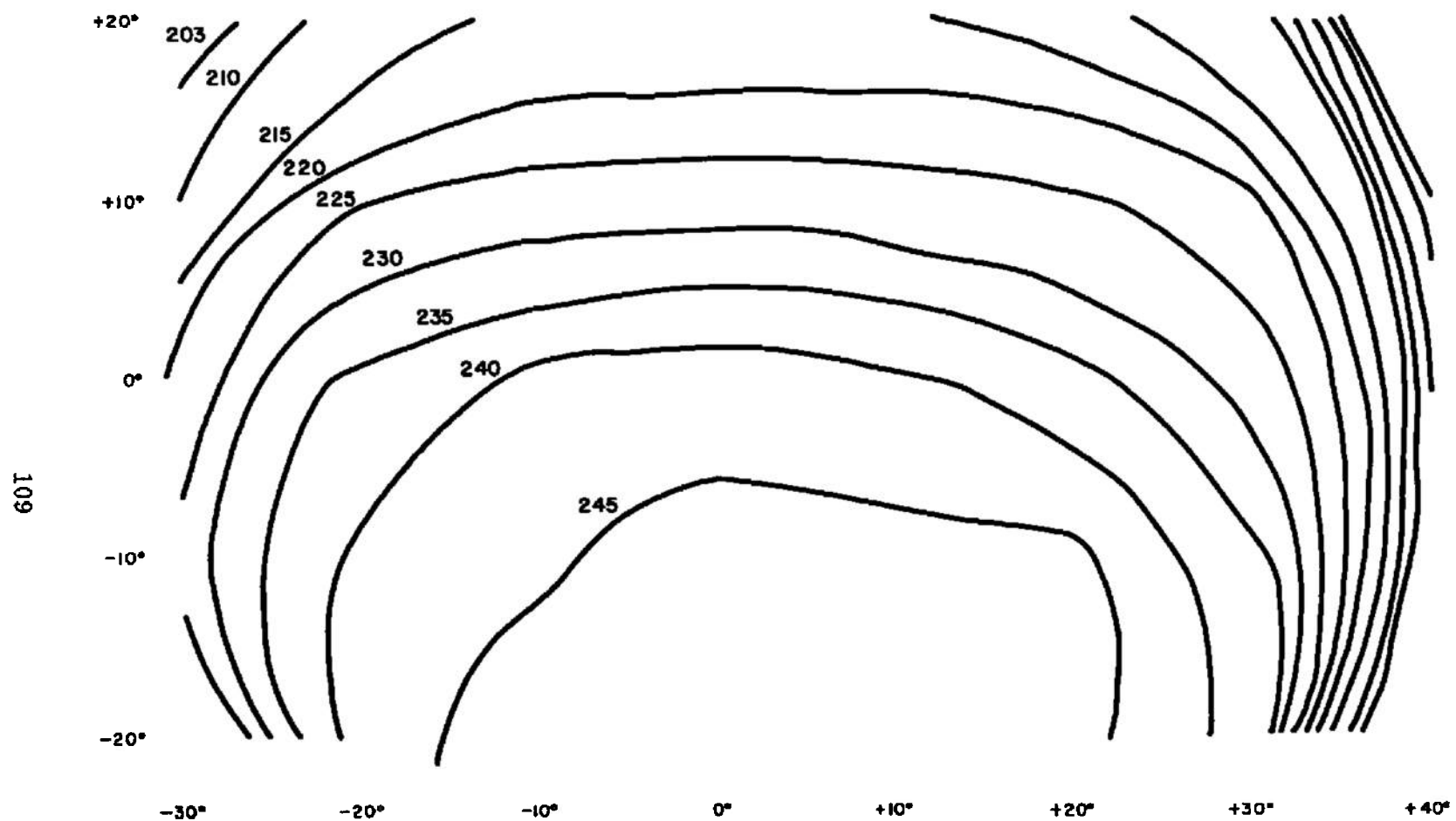


Figure 5-20. Intensity in mw/cm^2 of Unshielded 75-kw Carbon Arc at Radius of 6 feet

5.3 SPECTRAL ANALYSES

5.3.1 Criteria Used for the Spectral Analyses.

It was initially specified, as a design goal, that the solar spectrum, taken as the Johnson Curve, shall be matched within the following spectral range bands over the corresponding bands of the output spectrum of the solar radiation simulation system.

Spectral Criterion I

<u>Spectral Range</u> (Microns)	<u>Bandwidth</u> (Microns)	<u>Tolerance</u> (Per Cent)
Spectral Criterion IA		
0.2 to 3.0	0.02	±20
Spectral Criterion IB		
0.2 to 0.8	0.20	± 8
0.8 to 2.0	0.30	± 8
2.0 to 3.0	0.50	± 8

None of the spectral data furnished was adequate to permit the detailed analysis inherent in this criterion. The spectral data received for the Fluid Transpiration Arc covers only the range from 0.25 microns to 2.5 microns. The spectral data received for the High Intensity Carbon Arc covers only the range from 0.25 microns to 2.5 microns. The spectral data received for the Vortex Stabilized Radiation Source covers only the range from 0.25 microns to 1.05 microns and, additionally, was measured using a bandwidth of 0.10 microns. Further, the best data concerning the solar spectrum which was available¹ divides the solar spectrum as follows:

<u>Spectral Range</u> (Microns)	<u>Bandwidth</u> (Microns)
0.10 to 0.22	0.120
0.22 to 0.60	0.005

<u>Spectral Range</u> (Microns)	<u>Bandwidth</u> (Microns)
0.60 to 1.10	0.010
1.10 to 5.00	0.100

Since the data available, either for the solar spectrum or for the spectrums of the various radiation sources, did not permit the detailed analysis inherent in Spectral Criterion I, the following criterion was proposed for use as a guide for the spectral analyses:

Spectral Criterion II

1. The solar spectrum will be represented according to the data given in reference 9.
2. The output spectrum of the Solar Radiation Simulation System shall be matched to the solar spectrum (within the range for which data concerning the spectrum of each radiation source is available) within the spectral range bands, wavelength bandwidths, and tolerances indicated in the following table:

<u>Spectral Range</u> (Microns)	<u>Bandwidths</u> (Microns)	<u>Tolerance</u> (Per Cent)
------------------------------------	--------------------------------	--------------------------------

Spectral Criterion IIA

0.22 to 1.10	0.02	±20
1.10 to 3.00	0.10	±20

Spectral Criterion IIB

0.22 to 0.80	0.2	± 8
0.80 to 2.00	0.3	± 8
2.00 to 3.00	0.5	± 8

3. In those cases where the spectrum of the radiation source has been determined by dividing the spectrum into a series of non-overlapping wavelength bands and then measuring the energy within each band, the bandwidth used (or a multiple thereof) will be substituted for those bandwidths in the preceding table which it exceeds (or which are not a multiple thereof).

At this point, it is pertinent to ask how closely the output spectrum of a solar radiation simulator must match the solar spectrum and if it is truly necessary, for the application in question, to reduce or eliminate the line structure of the source spectrum throughout the entire range from 0.20 micron to 3.00 microns. The key to this problem lies in the phrase "the application in question" and, while not in a position to make a final judgement in this matter, the authors wish to suggest a criterion which it is believed, will be useful in making this determination. Since the criterion which is suggested can best be illustrated by applying it to a specific example, consider the case where the solar radiation simulator is to be incorporated into a space environmental facility which is to be used for thermal balance testing of various spacecraft. Consider further that the outer surface of these spacecraft will always be coated with one or more of the following materials: evaporated silver, evaporated gold, evaporated copper, evaporated aluminum, aluminum paint. The absorptances of these materials are plotted in figures 5-21 and 5-22. It is necessary and sufficient, in order to achieve the correct thermal balance condition, that the output spectrum of the solar radiation simulator be filtered to provide a close match to the solar spectrum only for those spectral ranges where the absorptances of the various materials vary rapidly and which also contain a significant fraction of the solar spectrum. Thus, if the solar spectrum is divided into approximately equal energy bands and these bandwidths are compared with the absorptance plots of figures 5-21 and 5-22, the spectral ranges noted below, within which the output spectrum of the solar radiation simulator should closely approximate the solar spectrum in terms of the energy contained within each range, are suggested. (These particular ranges were also chosen in order that the greatest possible use could be made of the spectral calculations generated prior to the definition of this criterion.) This tabulation also lists the percent of the solar energy contained within each bandwidth.

Spectral Criterion III

<u>Spectral Range</u> (Microns)	<u>Bandwidth</u> (Microns)	<u>Percent of Solar Energy in Wavelength Band</u> (Per Cent)
0.20 to 0.30	0.10	1.23
0.30 to 0.36	0.06	4.23
0.36 to 0.42	0.06	6.22
0.42 to 0.46	0.04	5.67
0.46 to 0.50	0.04	6.03
0.50 to 0.54	0.04	5.59
0.54 to 0.58	0.04	5.54
0.58 to 0.62	0.04	5.28
0.62 to 0.66	0.04	4.90

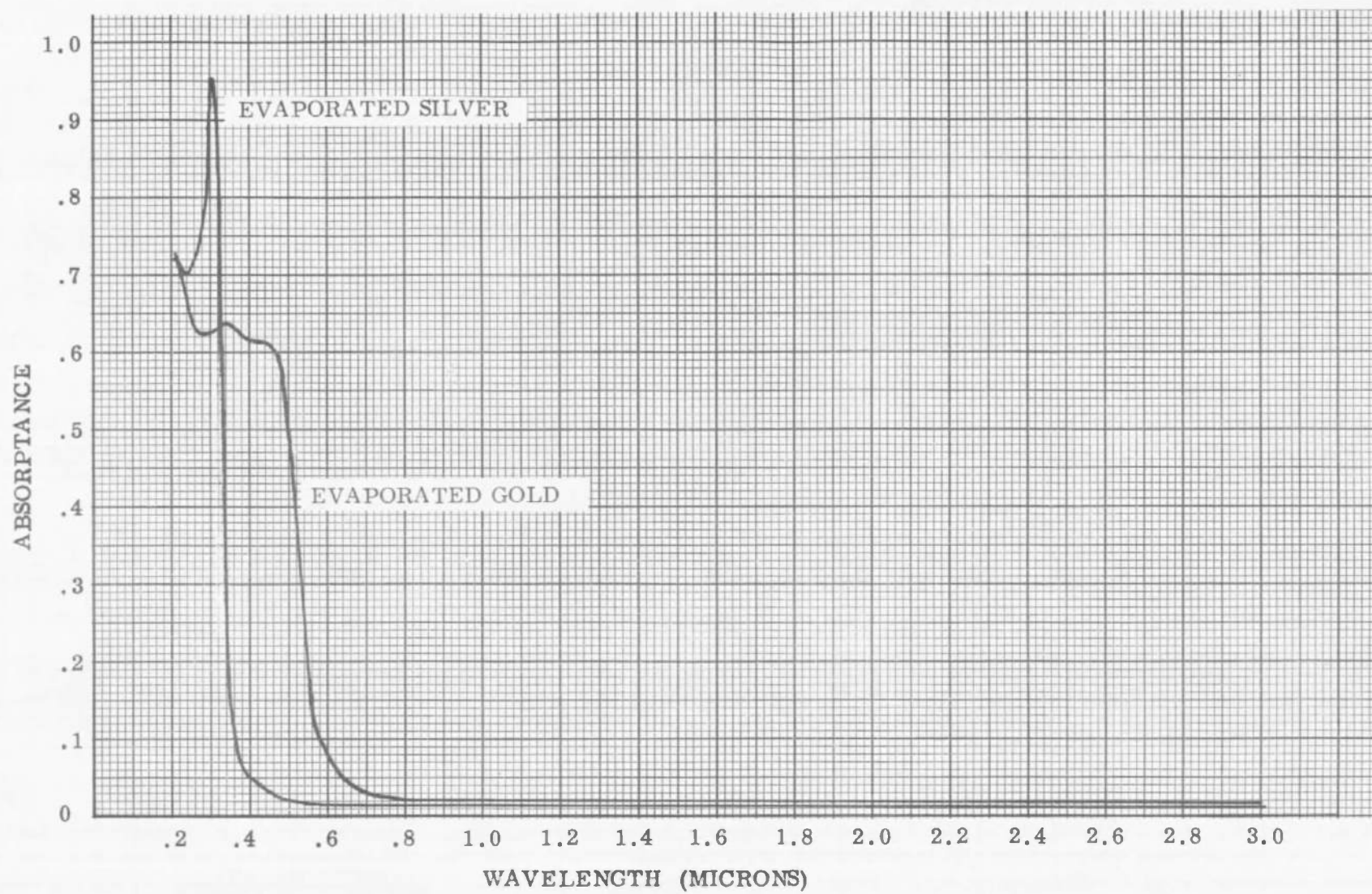


Figure 5-21. Absorptance of Evaporated Gold and Evaporated Silver

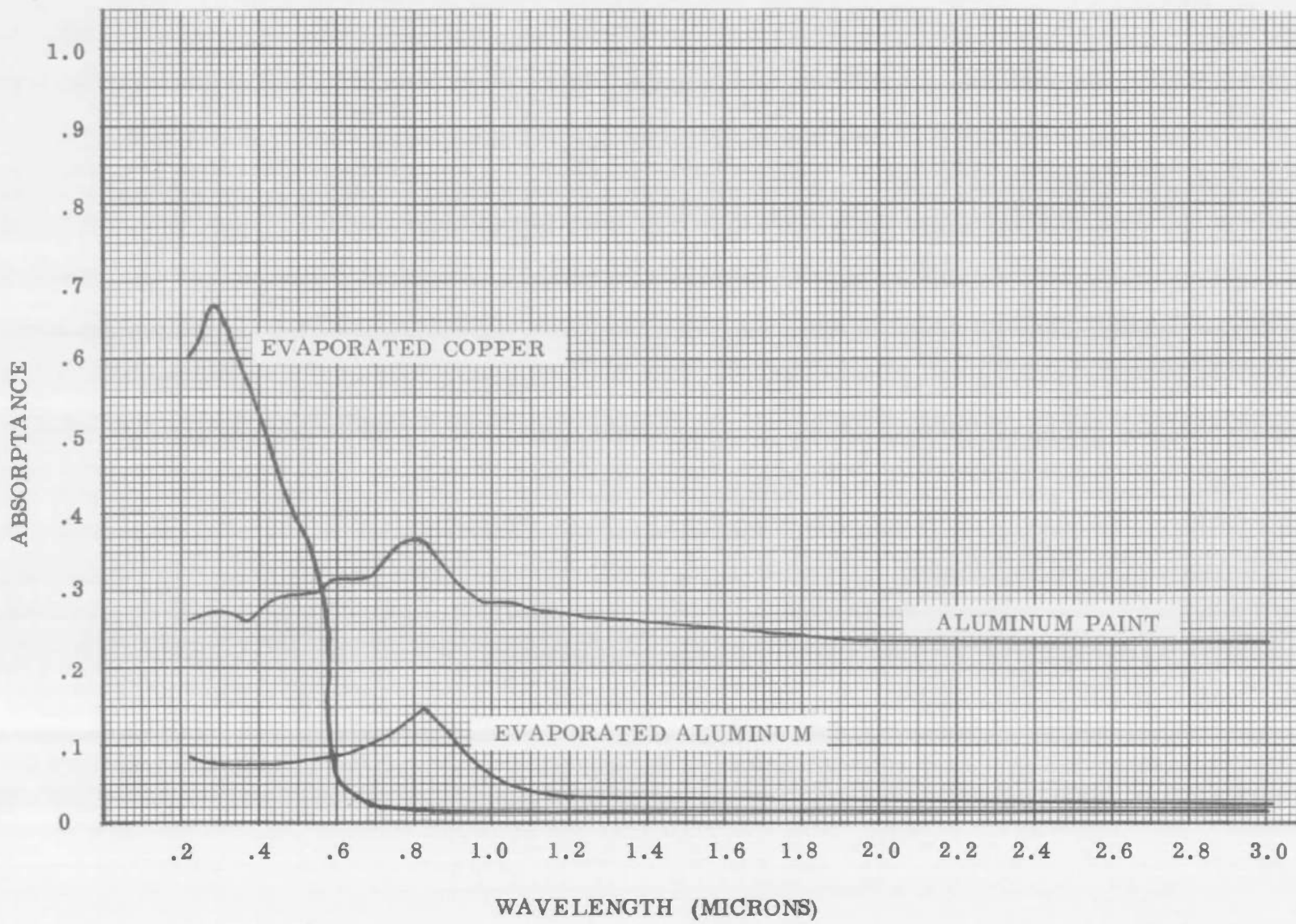


Figure 5-22. Absorptance of Evaporated Copper, Evaporated Aluminum and Aluminum Paint

<u>Spectral Range</u> (Microns)	<u>Bandwidth</u> (Microns)	<u>Percent of Solar Energy in Wavelength Band</u> (Per Cent)
0.66 to 0.70	0.04	4.46
0.70 to 0.76	0.06	6.07
0.76 to 0.82	0.06	5.27
0.82 to 0.90	0.08	5.98
0.90 to 1.00	0.10	6.03
1.00 to 1.10	0.10	4.75
1.1 to 1.3	0.2	6.82
1.3 to 1.6	0.3	6.04
1.6 to 2.3	0.7	5.90
2.3 to 3.0	0.7	2.04

Expressing a spectral match requirement in terms of equal energy bands rather than equal wavelength bands offers a distinct advantage in that it will result in a spectrum specification which requires the reduction or elimination of the spectral line structure only within narrow wavelength bands which contain significant fractions of the solar energy. However, the mere division of the spectrum into equal energy bands rather than equal wavelength bands does not eliminate the arbitrariness of any such specification. The accuracy of the representation is dependent upon the number, rather than the kind, of intervals into which the spectrum is divided; hence, the final choice of the number of these intervals and the tolerance assigned to each interval should not be made on an arbitrary basis. This latter point can best be illustrated by considering the spectrum of the Fluid Transpiration Arc in terms of Spectral Criterion II.A. In figure 5-23, it can be seen that the Fluid Transpiration Arc (37.5-kilowatt, 100% argon, 200 psig pressure) radiates a negligible portion of its energy between 0.90 and 0.92 micron which will be further decreased by passage through an optical system. The sun, however, radiates 1.30% of its energy into this wavelength band. Thus, the Fluid Transpiration Arc, when operated under those conditions which produce this spectrum, would have to be eliminated from further consideration if Spectral Criterion II.A were the required specification since the amount of special filtration required, even if possible, would result in an intolerable loss in efficiency.

To summarize, the preceding discussion has served to illustrate the following concerning the definition of a spectrum specification for use during the design of a solar radiation simulation optical system:

1. The solar spectrum should be considered in terms of energy bands rather than wavelength bands since this will result in a spectral specification which requires the reduction or elimination of this line structure in the output spectrum of the solar radiation simulator which contains significant portions of the solar energy.

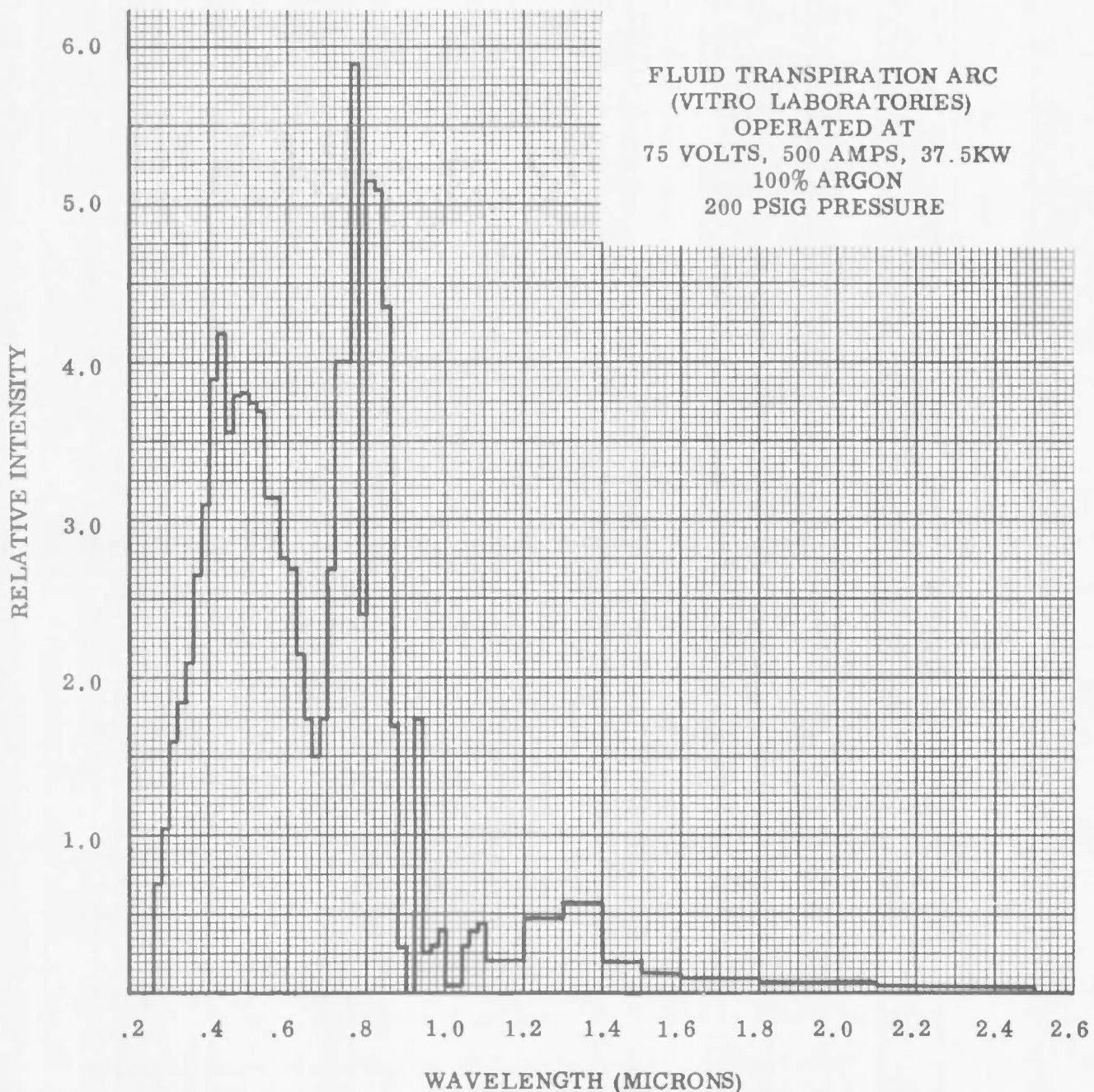


Figure 5-23. Spectrum of Fluid Transpiration Arc When Operated at 37.5 KW
(Spectral Criterion II A)

2. The choice of the number of intervals into which the spectrum is to be divided, the decision whether or not these intervals are each to contain equal fractions of the solar energy, and the tolerance specifications, should be made only after careful consideration of the testing requirements, and if possible should consider the source spectrum and variations therein as a function of time and of input power, and the resulting maximum spectral filtration efficiency.

Because of the technique used by Plasmadyne Corp. to measure and present the data concerning the spectrum of the Vortex Stabilized Radiation Source, it was necessary to define two additional methods of dividing the spectrum as follows:

Spectral Criterion IV

<u>Spectral Range</u> (Microns)	<u>Bandwidth</u> (Microns)
0.25 to 1.05	0.1

Spectral Criterion V

<u>Spectral Range</u> (Microns)	<u>Bandwidth</u> (Microns)
0.2 to 0.3	0.10
0.3 to 0.9	0.05
0.9 to 1.2	0.10

The optical materials analyses and source spectrum analyses were conducted in terms of the wavelength bands defined for Spectral Criteria II, III, IV and V.

5.3.2 Spectral Analyses of Optical Materials.

In order to generate spectral criteria for the choice of a radiation source and a combination of optical materials for use with this source, an analysis was performed to define idealized spectral curves, for various combinations of optical materials, which the spectrum of the radiation source must satisfy, after spectral filtration, if the source, optical-system, spectral-filter combination is to provide an output spectrum which matches the solar spectrum.

There are a number of refractive materials which transmit through the range from 0.2 micron to 3.0 microns. These are sapphire, calcium fluoride, lithium fluoride, sodium chloride, potassium bromide, and fused silica. However, except for fused silica, none of these materials are practical for use in a large solar radiation simulation system. Sapphire and lithium fluoride can be eliminated on the basis of high cost and limited size. Lithium fluoride is also hygroscopic and easily scratched. Potassium bromide can be eliminated on the basis of high cost and the fact that it is hygroscopic, soft, and easily scratched. Sodium chloride and calcium fluoride, though of moderate cost, are also hygroscopic and easily scratched. On this basis, the spectral analysis of optical materials was confined to four commercially available types of fused silica, these being Corning Fused Silica Code 7940 (manufactured by Corning Glass Works, Corning, N. Y.), Suprasil, Ultrasil, and Infrasil (manufactured by Amersil Quartz Division, Engelhard Industries, Inc., Hillsdale, N. J.). Evaporated aluminum was chosen as the most practical material for the reflective surfaces because of its high reflectivity throughout the spectral range from 0.2 micron to 3.0 microns, its low cost, and its resistance to corrosion. The combinations of optical components and optical materials studied are as follows:

1. Optical systems which incorporate three mirrors and four lenses were studied.
2. Optical systems which incorporate four mirrors and four lenses were studied.
3. The reflective surface of the mirrors was taken as evaporated aluminum which has been exposed to the atmosphere.
4. Each combination of optical components was studied for a total thickness of the refractive material of 4.0 inches, 6.0 inches, and 8.0 inches and for the following refractive materials:

Corning Fused Silica Code 7940

Suprasil

Infrasil

Ultrasil

If the assumption is made that the radiation is normally incident at each optical surface, the equation, which relates the energy E_i in a wavelength band $\Delta\lambda_i = \lambda_{i+1} - \lambda_i$ of the source spectrum after spectral filtration, is:

$$A_i = \frac{E_i}{R_i^m (e^{-\alpha_i t}) \left[1 - \left(\frac{n_i - 1}{n_i + 1} \right)^2 \right]^{2L}} = \frac{E_i}{T_i} \quad (5-50)$$

where

E_i = the energy within $\Delta\lambda_i$ in the solar spectrum

A_i = the energy required within $\Delta\lambda_i$ in the source spectrum after spectral filtration

m = the number of mirrors

R_i = the reflectance of evaporated aluminum within $\Delta\lambda_i$

L = the number of lenses

n_i = the refractive index of the refractive material within $\Delta\lambda_i$

α_i = The absorption coefficient of the refractive material within $\Delta\lambda_i$

t = the total thickness of the refractive material through which the radiation passes

T_i = transmittance of the optical system within $\Delta\lambda_i$

The dissipative efficiency k with which that portion of the radiation from each source, which is collected by each optical system, is transferred through the optical system is given by

$$k = \left(\frac{1}{n} \right) \frac{\sum_{i=1}^n E_i}{\sum_{i=1}^n A_i} = \left(\frac{1}{n} \right) \sum_{i=1}^n T_i \quad (5-51)$$

where n is the number of wavelength bands into which the spectrum is divided.

The source spectrum required (after spectral filtration), for each of the 24 cases, was calculated using equation (5-50). For these calculations, the parameters α , and n , for Corning Fused Silica Code 7940 were generated from data obtained from Corning Glass Works, Corning, N. Y., and for Suprasil, Ultrasil, and Infrasil from data obtained from Amersil Quartz Division, Engelhard Industries, Inc., Hillside, N. J. The reflectance, as a function of wavelength, of a freshly evaporated film of aluminum which has had no contact with the atmosphere, is plotted as the dotted curve of figure 5-24.⁹ From this curve, the solid curve of figure 5-24 was generated in order to compensate for degradation in the reflectance caused by exposure to the atmosphere, by specifying the mean reflectance between 0.22 microns and 1.00 microns as 85%. For the spectrum calculations, the values of the reflectance R , of an evaporated aluminum surface which has been exposed to the atmosphere were obtained from this latter curve.

The computer program, SOLAR (See Appendix I), written to evaluate equation (5-50), also calculated the relative intensity within each specified bandwidth of both the input and output spectrums and the dissipative efficiency of each optical system. For these calculations, the spectrums were divided as follows:

<u>Spectral Range</u> (Microns)	<u>Bandwidth</u> (Microns)
0.2 to 1.1	0.02
1.1 to 3.0	0.10

After equation (5-50) was evaluated for each case, the spectrum was divided into the following spectral ranges and bandwidths and a summary calculation was performed to determine the relative energy and intensity within each summary bandwidth.

<u>Spectral Range</u> (Microns)	<u>Bandwidth</u> (Microns)
0.2 to 0.8	0.2
0.8 to 2.0	0.3
2.0 to 3.0	0.5

These divisions were made in accordance with Spectral Criterion II.

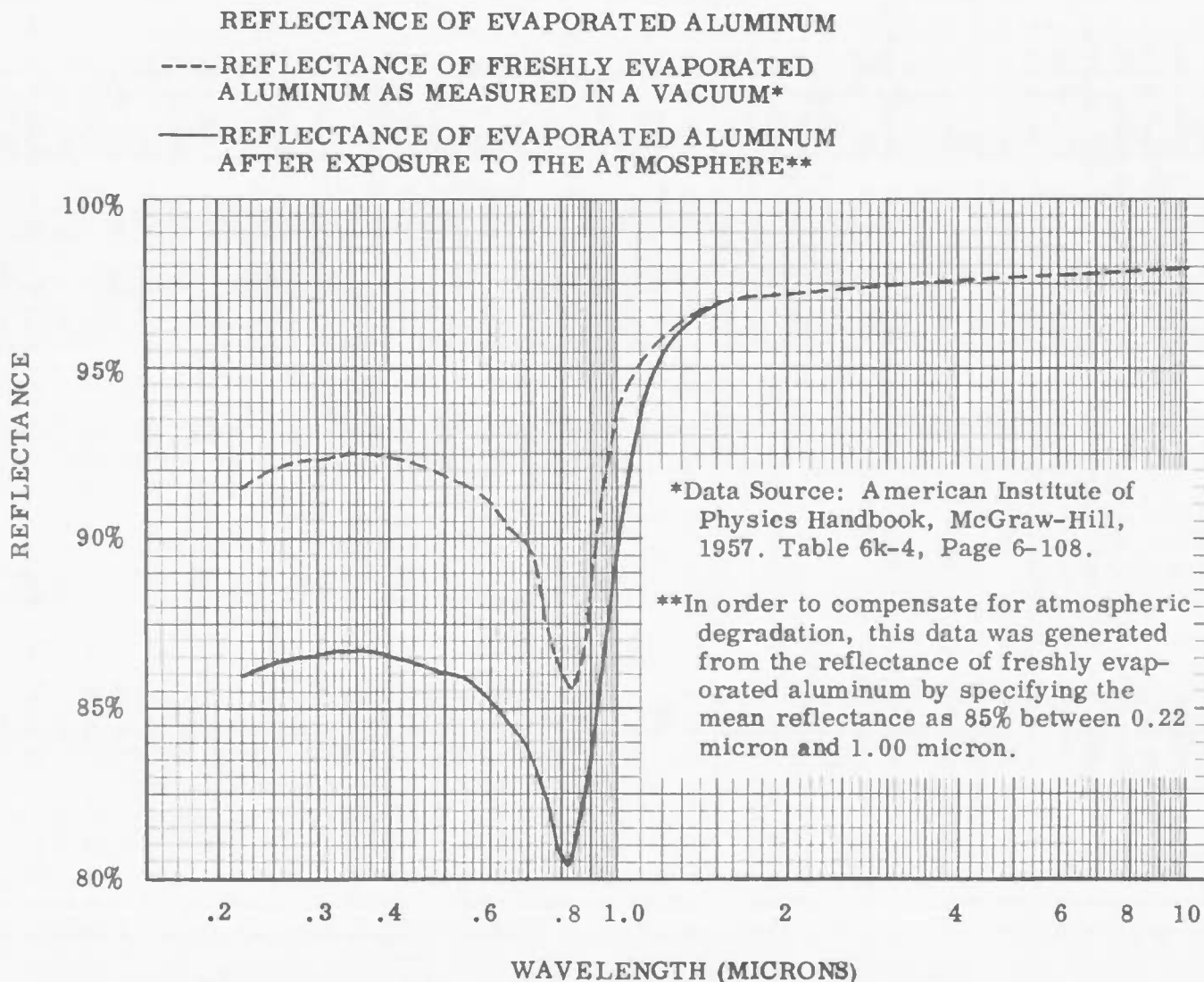


Figure 5-24. Reflectance As a Function of Wavelength for Evaporated Aluminum

The significance of these calculated spectrums lies in the fact that, in modifying the input source spectrum to provide the required output spectrum, the maximum total dissipative efficiency required of the optical system, spectral-filter combination is not affected by the location of the spectral filter within the optical train. That is, it makes no difference whether the source spectrum is filtered before, during, or after passage through the optical system since the transmittance of any optical system or spectral filter is a constant (and therefore independent of the source spectrum) within any given wavelength band. Therefore, if the output spectrum of a source, optical-system, spectral-filter combination is to match the solar spectrum within the required tolerances, it is necessary and sufficient that the source spectrum be filtered to match the calculated required source spectrum within these same tolerances.

The dissipative efficiencies of the 24 combinations of optical materials analyzed in accordance with Spectral Criterion II are listed in table 5-10. The source spectrums required for an optical system consisting of 3 mirrors, 4 lenses, and 4 inches of refractive material are plotted for Corning Fused Silica Code 7940, Suprasil, and Ultrasil in figure 5-25 and for Infrasil in figure 5-26. From table 5-10, figure 5-25, and figure 5-26, it can be seen that Infrasil is the only one of these four refractive materials which is suitable, from the standpoint of efficiency, for use in a solar radiation simulation system which is to reproduce the solar spectrum in accordance with Spectral Criterion II using the specified elements. Although all four of these materials have nearly identical transmission characteristics between 0.2 micron and 2.0 microns (as can be seen by comparing figures 5-25 and 5-26), Corning Fused Silica Code 7940, Suprasil, and Ultrasil have absorption bands between 2.0 microns and 3.0 microns which have, according to the manufacturer's data, been virtually eliminated for Infrasil. The transmittances, including surface reflections, of 1-centimeter thicknesses of Infrasil and Suprasil, which were used for the spectral calculations, are plotted in figure 5-27. The transmittance of Ultrasil is identical to that of Suprasil between 0.26 micron and 3.0 microns and lies between that of Suprasil and Infrasil between 0.2 micron and 0.26 micron. The transmittance of Corning Fused Silica Code 7940 is comparable to that of Ultrasil, being only slightly less in the ultraviolet and infrared regions of the spectrum.

The source spectrum required (after spectral filtration) in order to reproduce the solar spectrum in accordance with Spectral Criterion II when the source is used with an optical system consisting of 3 mirrors and 4 Infrasil lenses is plotted, for the initial calculation, in figure 5-28, and for the summary calculation, in figure 5-29. The summary calculations of the source spectrum required (after spectral filtration) in order to reproduce the solar spectrum when used with an optical system consisting of 4 mirrors and 4 Infrasil lenses are plotted, for thicknesses of Infrasil of 4 inches and 8 inches, in figures 5-30 and 5-31, respectively.

Table 5-10. Dissipative Efficiencies of the Various Optical System Configurations Studied as a Function of the Thickness of the Refractive Material (Spectral Criterion II).

			DISSIPATIVE EFFICIENCY (Per Cent)		
Number of Lenses	Number of Mirrors	Refractive Material	Thickness of Refractive Material		
			4 inches	6 inches	8 inches
4	3	Corning Fused Silica Code 7940	24.98	2.65	0.14
4	4	Corning Fused Silica Code 7940	22.88	2.57	0.14
4	3	Suprasil	26.95	3.01	0.16
4	4	Suprasil	24.58	2.91	0.15
4	3	Ultrasil	26.95	3.01	0.16
4	4	Ultrasil	24.57	2.91	0.15
4	3	Infrasil	48.51	47.89	47.27
4	4	Infrasil	42.03	41.50	40.97

98.05% of the energy in the solar spectrum is contained between 0.2μ and 3.0μ

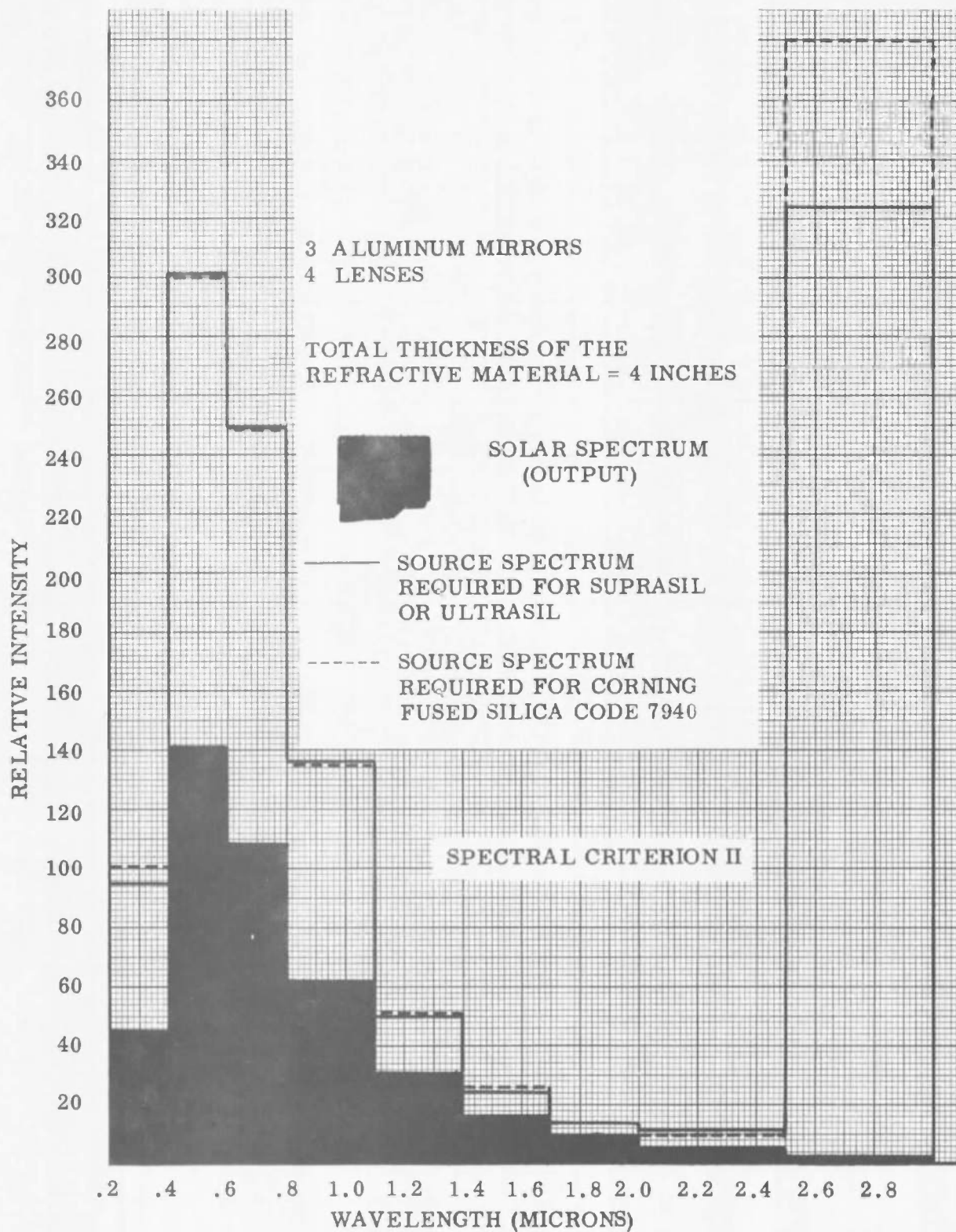


Figure 5-25. Summary Calculation of Source Spectrum Required for an Optical System of 3 Evaporated Aluminum Mirrors and 4 Lenses of Corning Fused Silica Code 7940, Suprasil, or Ultrasil (Total Thickness of 4 Inches)

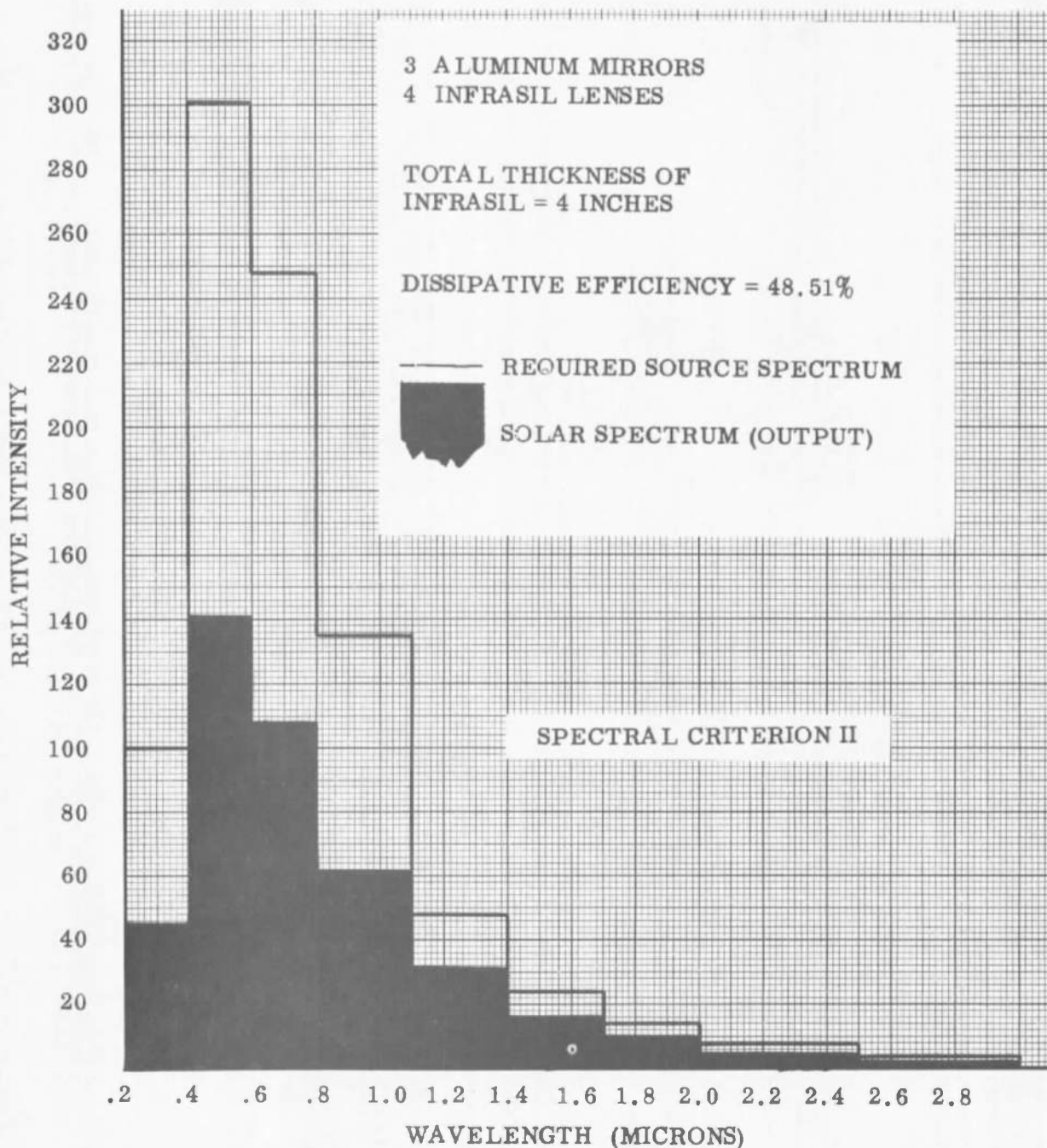


Figure 5-26. Summary Calculation of Source Spectrum Required for an Optical System of 3 Evaporated Aluminum Mirrors and 4 Infrasil Lenses (Total Thickness of 4 Inches)

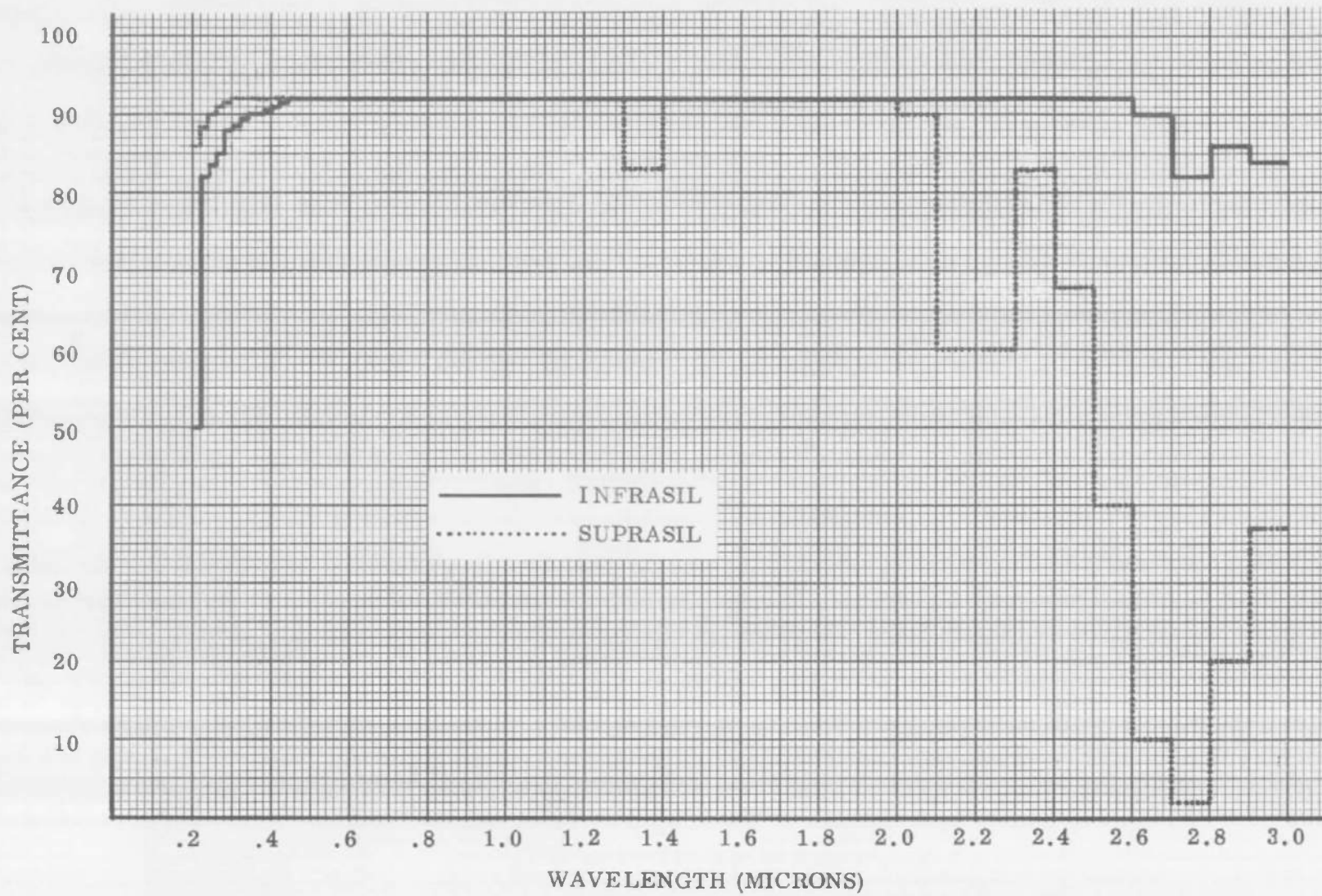


Figure 5-27. Transmittance, including surface reflections, of 1 cm thicknesses of Suprasil and Infrasil

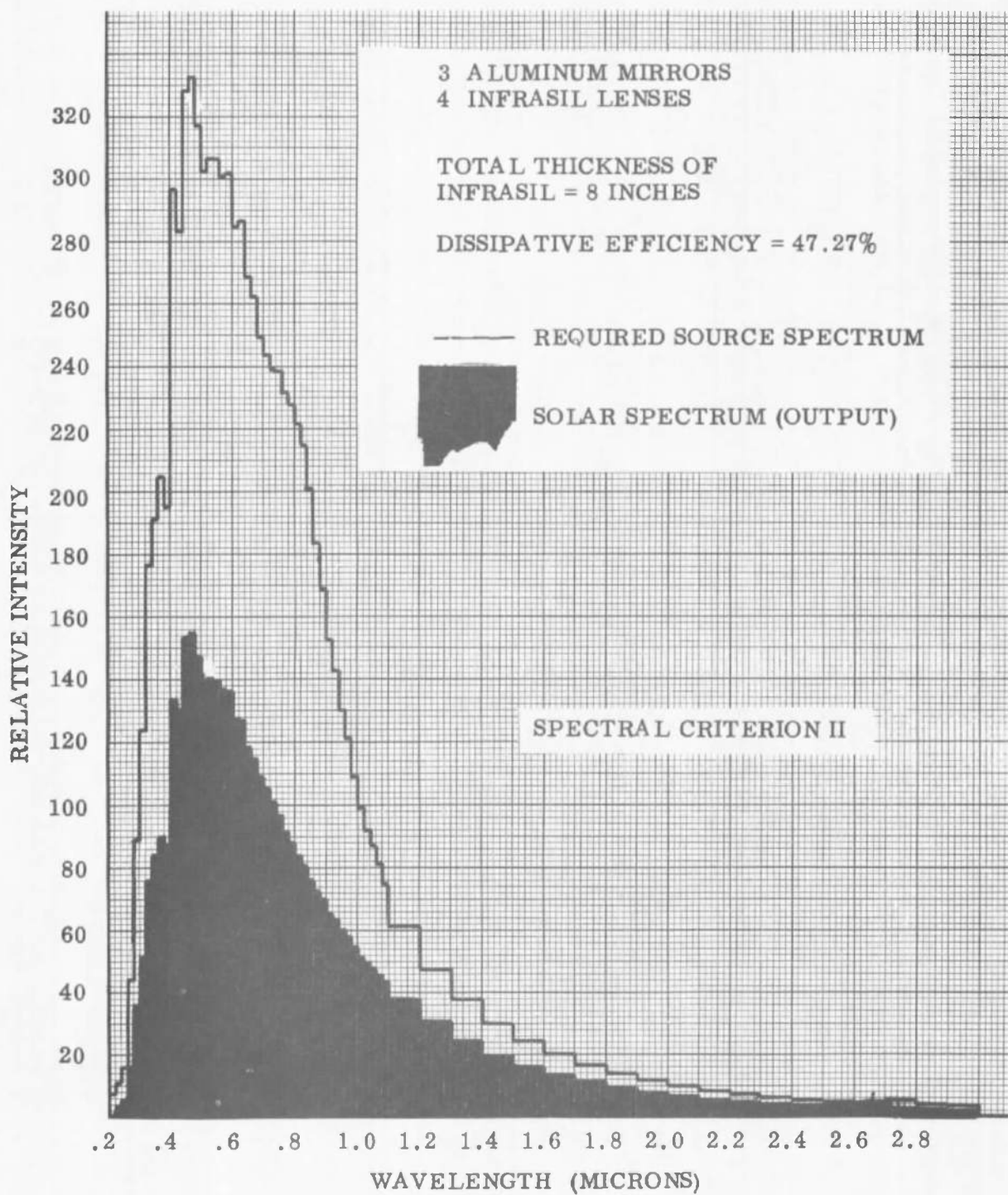


Figure 5-28. Initial Calculation of Source Spectrum Required for an Optical System of 3 Evaporated Aluminum Mirrors and 4 Infrasil Lenses (Total Thickness of 8 Inches)

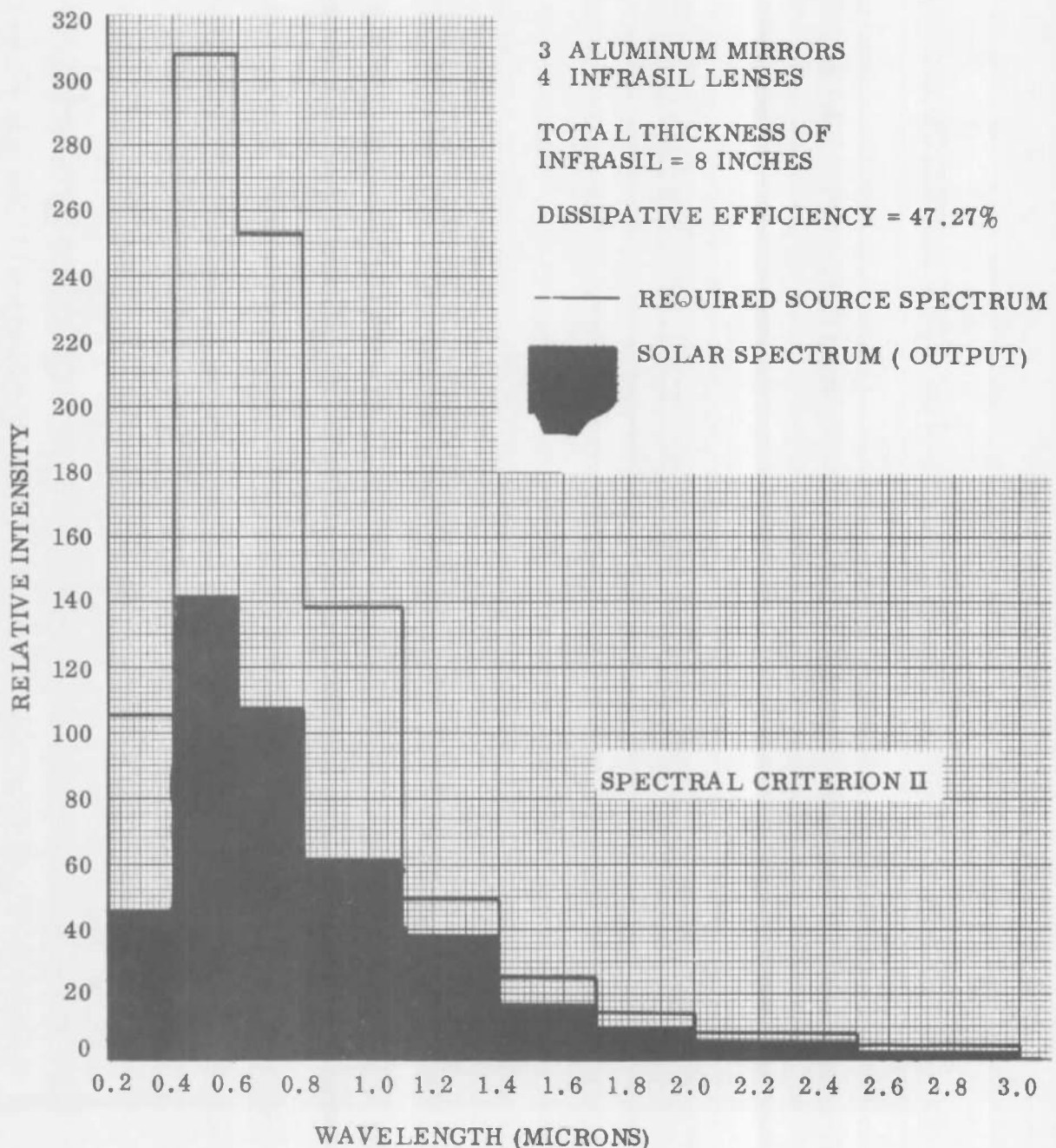


Figure 5-29. Summary Calculation of Source Spectrum Required for an Optical System of 3 Evaporated Aluminum Mirrors and 4 Infrasil Lenses (Total Thickness of 8 Inches)

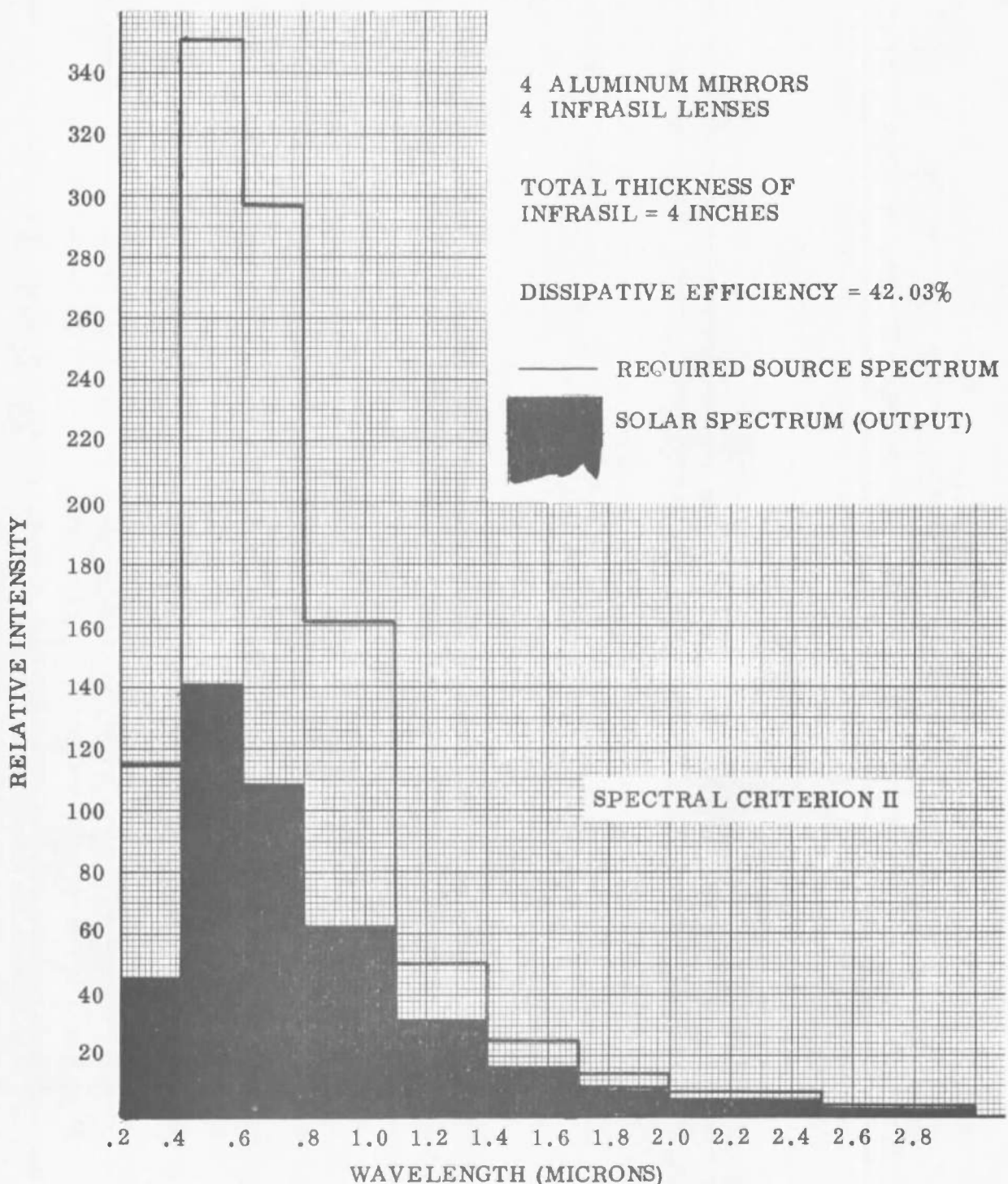


Figure 5-30. Summary Calculation of Source Spectrum Required for an Optical System of 4 Evaporated Aluminum Mirrors and 4 Infrasil Lenses (Total Thickness of 4 Inches)

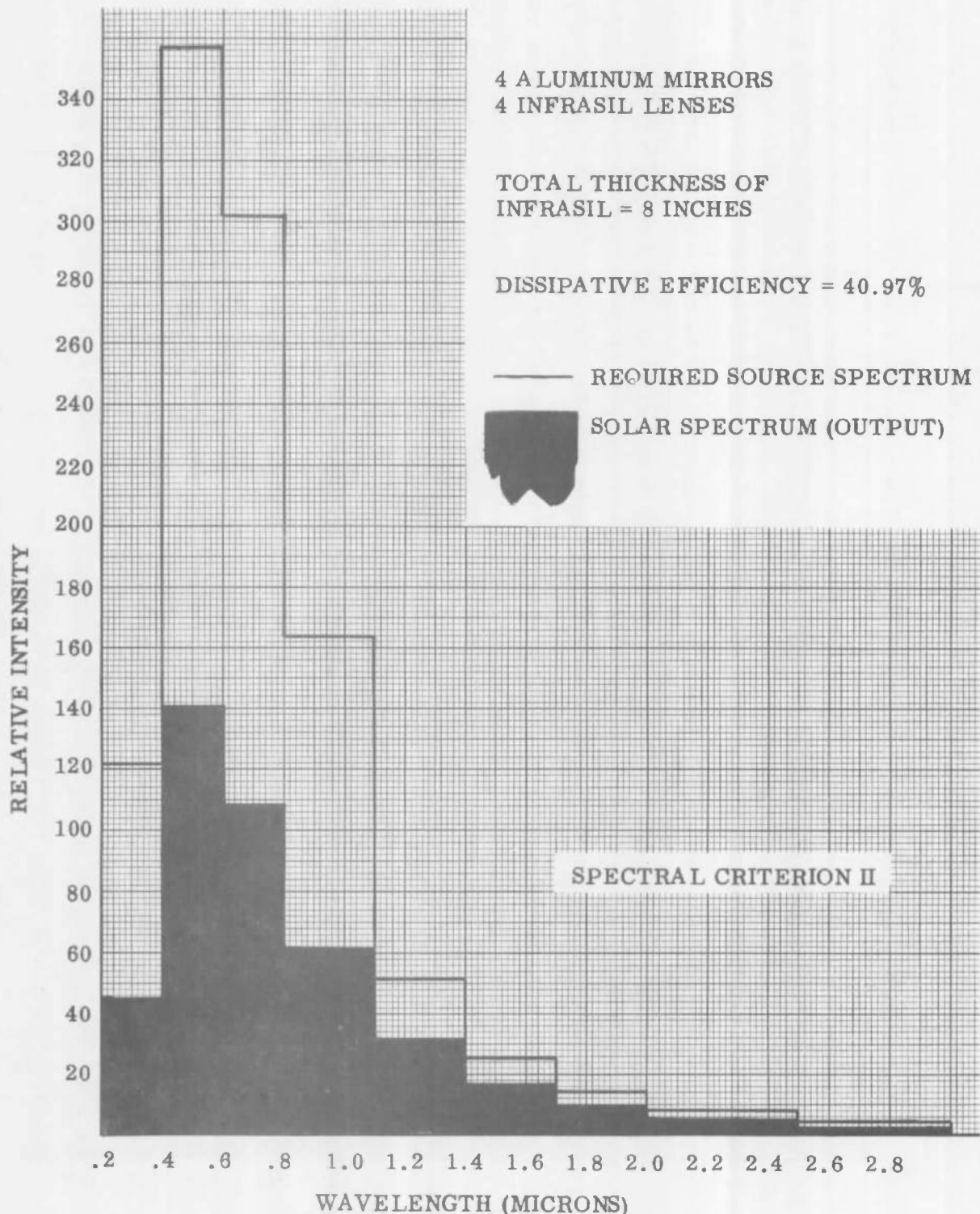


Figure 5-31. Summary Calculation of Source Spectrum Required for an Optical System of 4 Evaporated Aluminum Mirrors and 4 Infrasil Lenses (Total Thickness of 8 Inches)

In order to determine how the relative energy distribution in the required source spectrum is modified as the total thickness of Infrasil is increased, the required source spectrums calculated for the six cases studied for Infrasil were related by scaling each spectrum so that the relative energy in each, between 0.2 micron and 3.0 microns, was equal to 100. These scaled spectrums are plotted for an optical system consisting of 3 mirrors and 4 Infrasil lenses, in figure 5-32 and for an optical system consisting of 4 mirrors and 4 Infrasil lenses, in figure 5-33. From these plots, it can be seen that increasing the thickness of Infrasil in the optical system does not significantly alter the relative energy distribution within the required source spectrum. Comparable data (not included in this report) calculated for Corning Fused Silica Code 7940, Suprasil, and Ultrasil shows that this is not true for these materials and that, as the thickness of the refractive material increases, an increasing proportion of the energy is required in the infrared in order to compensate for the absorption.

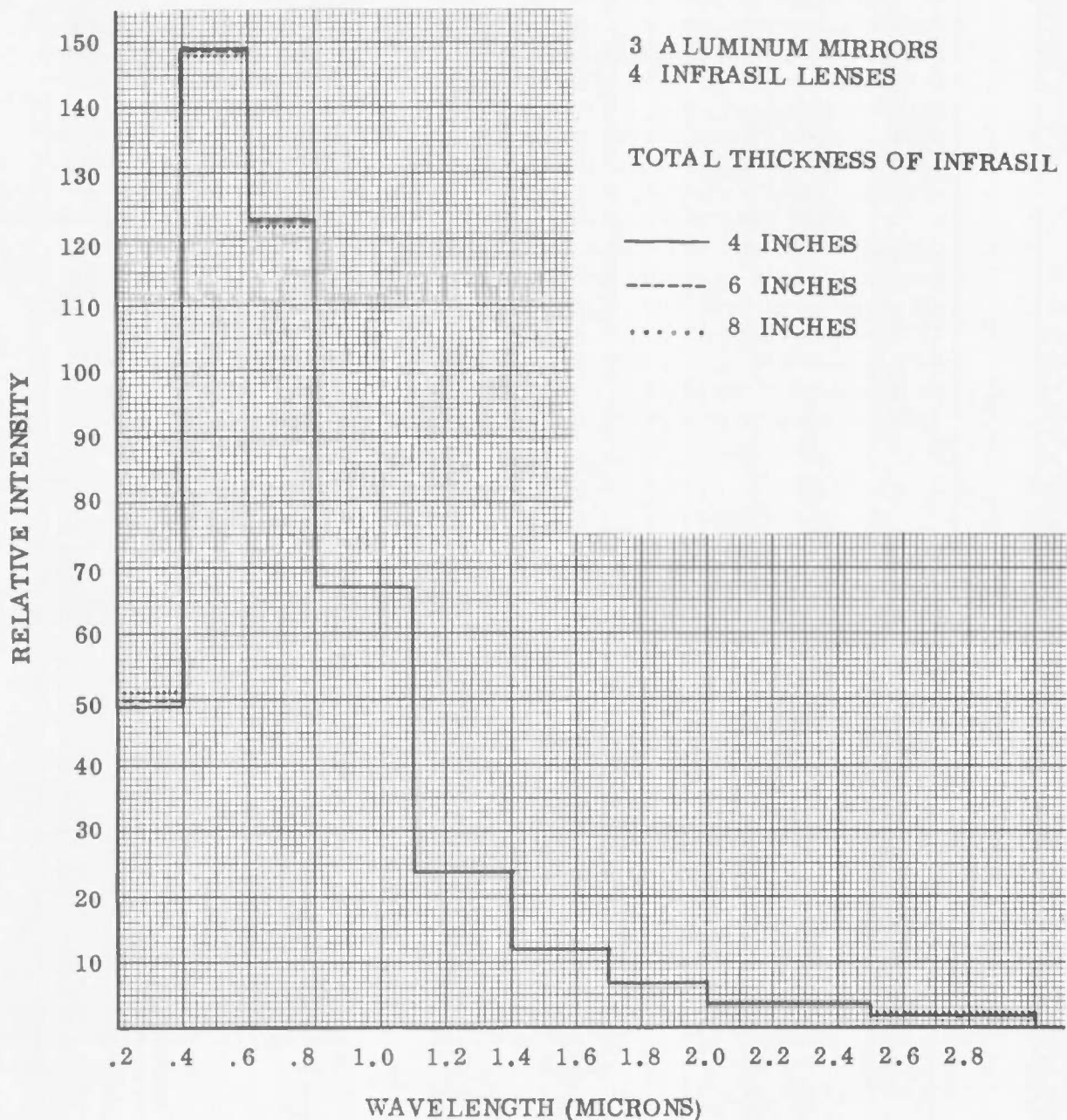


Figure 5-32. Variation, With Total Thickness of Infrasil, of the Source Spectrum Required for an Optical System of 3 Evaporated Aluminum Mirrors and 4 Infrasil Lenses (Spectral Criterion II B)

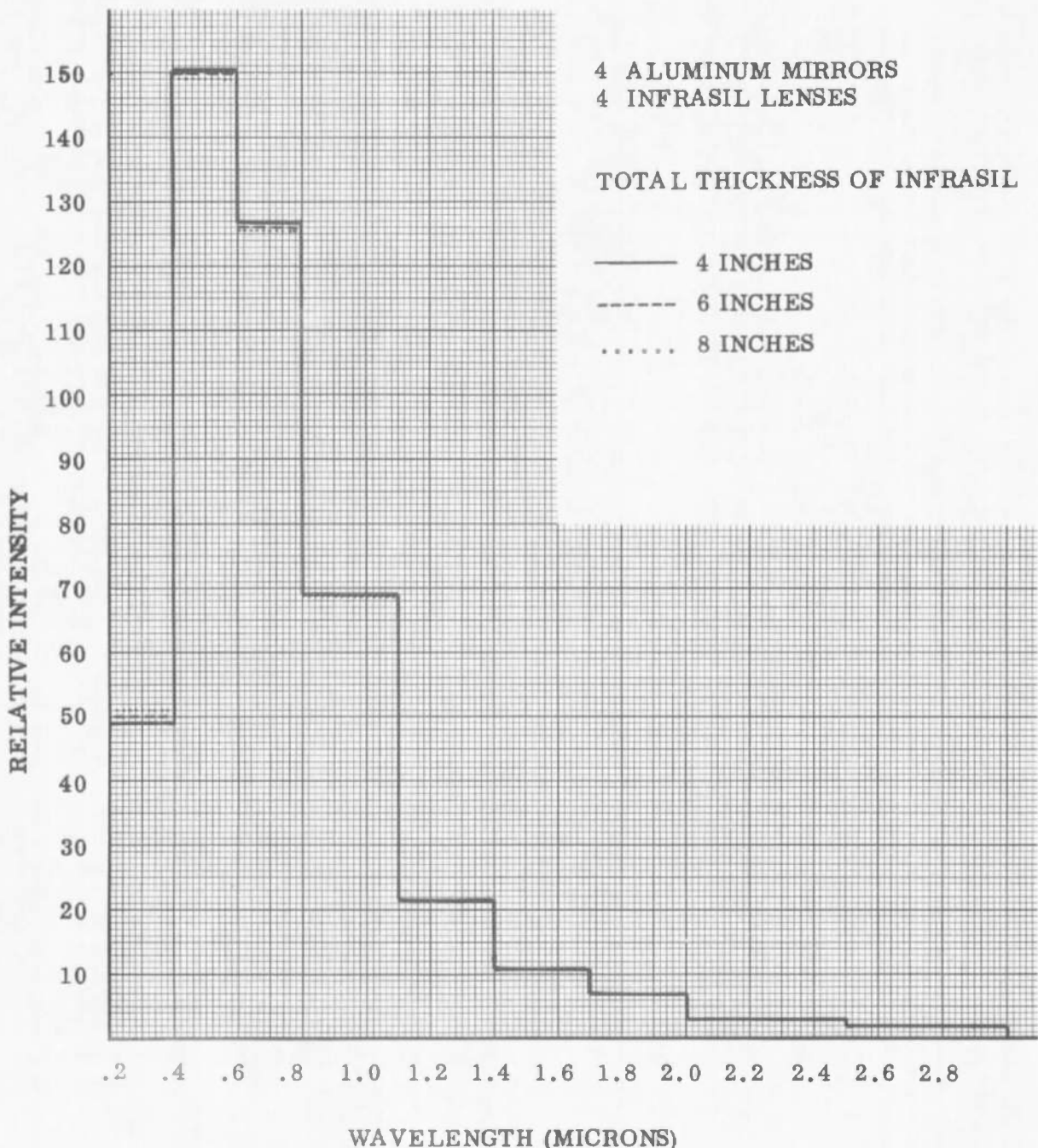


Figure 5-33. Variation, With Total Thickness of Infrasil, of the Source Spectrum Required for an Optical System of 4 Evaporated Aluminum Mirrors and 4 Infrasil Lenses (Spectral Criterion II B)

Dividing the spectrum in accordance with Spectral Criterion III, table 5-11 lists the percent of the solar energy contained within each bandwidth as well as the percent of the source energy required in each bandwidth, after spectral filtration, in order for the indicated optical system configurations to reproduce the solar spectrum. Table 5-12 lists the relative intensity (percent-per-micron) within each wavelength band for the solar spectrum and for the source spectrum required, after spectral filtration, for each of the indicated optical system configurations. The solar spectrum is plotted, in terms of these bandwidths, in figure 5-34 and the source spectrums required, after spectral filtration, are plotted in figure 5-35 for optical systems consisting of 3 aluminum mirrors and 4 Infrasil lenses and in figure 5-36 for optical systems consisting of 4 aluminum mirrors and 4 Infrasil lenses. Comparable data in terms of the bandwidths of Spectral Criterion IV is listed in tables 4-13 and 4-14 and is plotted in figures 5-37, 5-38 and 5-39. This data, expressed in terms of the bandwidths of Spectral Criterion V is listed in tables 5-15 and 5-16 and is plotted in figures 5-40, 5-41 and 5-42.

5.3.3

Spectral Analyses of the Various Sources.

The purpose of the spectral analyses conducted for the various sources was (1) to determine the maximum efficiency with which the source spectrum, as modified by optical systems fabricated of the various combinations of optical materials discussed previously, can be filtered to match the solar spectrum (see Appendix II) and (2) to estimate the probable transmittance (dissipative efficiency) of the various optical-system, spectral-filter combinations defined for each source.

Nine spectrums will be discussed; six for the Vortex Stabilized Radiation Source (data supplied by Plasmadyne), two for the Fluid Transpiration Arc (data supplied by Vitro Laboratories), and one for the High Intensity Carbon Arc (data supplied by AEDC). The spectral data supplied for the Vortex Stabilized Radiation Source (VSRS) was determined by dividing the wavelength range into a series of discrete, non-overlapping wavelength bands and measuring the energy within each bandwidth. The data for the Fluid Transpiration Arc (FTA) and the High Intensity Carbon Arc was supplied in the form of continuous scans. It is convenient, therefore, to divide this discussion into two sections, the first of which will deal with the VSRS and the second of which will discuss the FTA and the High Intensity Carbon Arc.

5.3.3.1

Spectral Analysis of the Vortex Stabilized Radiation Source.

Six spectrums were considered for the Vortex Stabilized Radiation Source (VSRS). These spectrums are identified in table 5-17 with respect to the conditions under which the VSRS was operating

Table 5-11. Percent of energy in each indicated wavelength band of the solar spectrum and of the source spectrums required, after spectral filtration, for each indicated optical system configuration (Spectral Criterion III)

Wavelength Band (Microns)	Solar Spectrum	Percent of Energy in Wavelength Band					
		Required Source Spectrum					
		3 Aluminum Mirrors and 4 Infrasil Lenses			4 Aluminum Mirrors and 4 Infrasil Lenses		
		4 Inches of Infrasil	6 Inches of Infrasil	8 Inches of Infrasil	4 Inches of Infrasil	6 Inches of Infrasil	8 Inches of Infrasil
0.20 - 0.30	1.23	1.46	1.53	1.62	1.46	1.53	1.62
0.30 - 0.36	4.23	4.61	4.68	4.74	4.60	4.67	4.74
0.36 - 0.42	6.22	6.63	6.68	6.72	6.63	6.68	6.73
0.42 - 0.46	5.67	5.93	5.91	5.89	5.94	5.92	5.90
0.46 - 0.50	6.03	6.32	6.30	6.27	6.35	6.33	6.30
0.50 - 0.54	5.59	5.92	5.89	5.87	5.97	5.94	5.92
0.54 - 0.58	5.54	5.90	5.88	5.86	5.97	5.94	5.92
0.58 - 0.62	5.28	5.70	5.68	5.66	5.79	5.77	5.75
0.62 - 0.66	4.90	5.39	5.37	5.35	5.51	5.49	5.47
0.66 - 0.70	4.46	4.97	4.96	4.93	5.10	5.08	5.06
0.70 - 0.76	6.07	7.01	6.99	6.97	7.29	7.26	7.24
0.76 - 0.82	5.27	6.61	6.59	6.57	7.06	7.04	7.02
0.82 - 0.90	5.98	7.45	7.43	7.41	7.95	7.92	7.90
0.90 - 1.00	6.03	6.36	6.34	6.33	6.42	6.40	6.39
1.00 - 1.10	4.75	4.20	4.19	4.18	4.00	4.00	3.98
1.10 - 1.30	6.82	5.28	5.27	5.26	4.81	4.80	4.80
1.30 - 1.60	6.04	4.47	4.47	4.47	4.02	4.02	4.01
1.60 - 2.30	5.90	4.26	4.26	4.27	3.80	3.80	3.81
2.30 - 3.00	2.04	1.53	1.58	1.63	1.36	1.40	1.45

Table 5-12. Relative Intensity in each indicated wavelength band of the solar spectrum and of the source spectrums required, after spectral filtration for each indicated optical system configuration (Spectral Criterion III)

Relative Intensity in Wavelength Band							
Wavelength Band (Microns)	Solar Spectrum	Required Source Spectrum					
		3 Aluminum Mirrors and 4 Infrasil Lenses			4 Aluminum Mirrors and 4 Infrasil Lenses		
		4 Inches of Infrasil	6 Inches of Infrasil	8 Inches of Infrasil	4 Inches of Infrasil	6 Inches of Infrasil	8 Inches of Infrasil
0.20 - 0.30	12.3	14.6	15.3	16.2	14.6	15.3	16.2
0.30 - 0.36	70.5	76.8	78.0	79.0	76.7	77.8	79.0
0.36 - 0.42	103.7	110.5	111.3	112.0	110.5	111.3	112.2
0.42 - 0.46	141.8	148.3	147.8	147.3	148.5	148.0	147.5
0.46 - 0.50	150.8	158.0	157.5	156.8	158.8	158.3	157.5
0.50 - 0.54	139.8	148.0	147.3	146.8	149.3	148.5	148.0
0.54 - 0.58	138.5	147.5	147.0	146.5	149.3	148.5	148.0
0.58 - 0.62	132.0	142.5	142.0	141.5	144.8	144.3	143.8
0.62 - 0.66	122.5	134.8	134.3	133.8	137.8	137.3	136.8
0.66 - 0.70	111.5	124.3	124.0	123.3	127.5	127.0	126.5
0.70 - 0.76	101.2	116.8	116.5	116.2	121.5	121.0	120.7
0.76 - 0.82	87.8	110.2	109.8	109.5	117.7	117.3	117.0
0.82 - 0.90	74.8	93.1	92.9	92.6	99.4	99.0	98.8
0.90 - 1.00	60.3	63.6	63.4	63.3	64.2	64.0	63.9
1.00 - 1.10	47.5	42.0	41.9	41.8	40.0	40.0	39.8
1.10 - 1.30	34.1	26.4	26.4	26.3	24.1	24.0	24.0
1.30 - 1.60	20.1	14.9	14.9	14.9	13.4	13.4	13.4
1.60 - 2.30	8.4	6.1	6.1	6.1	5.4	5.4	5.4
2.30 - 3.00	2.9	2.2	2.3	2.3	1.9	2.0	2.1

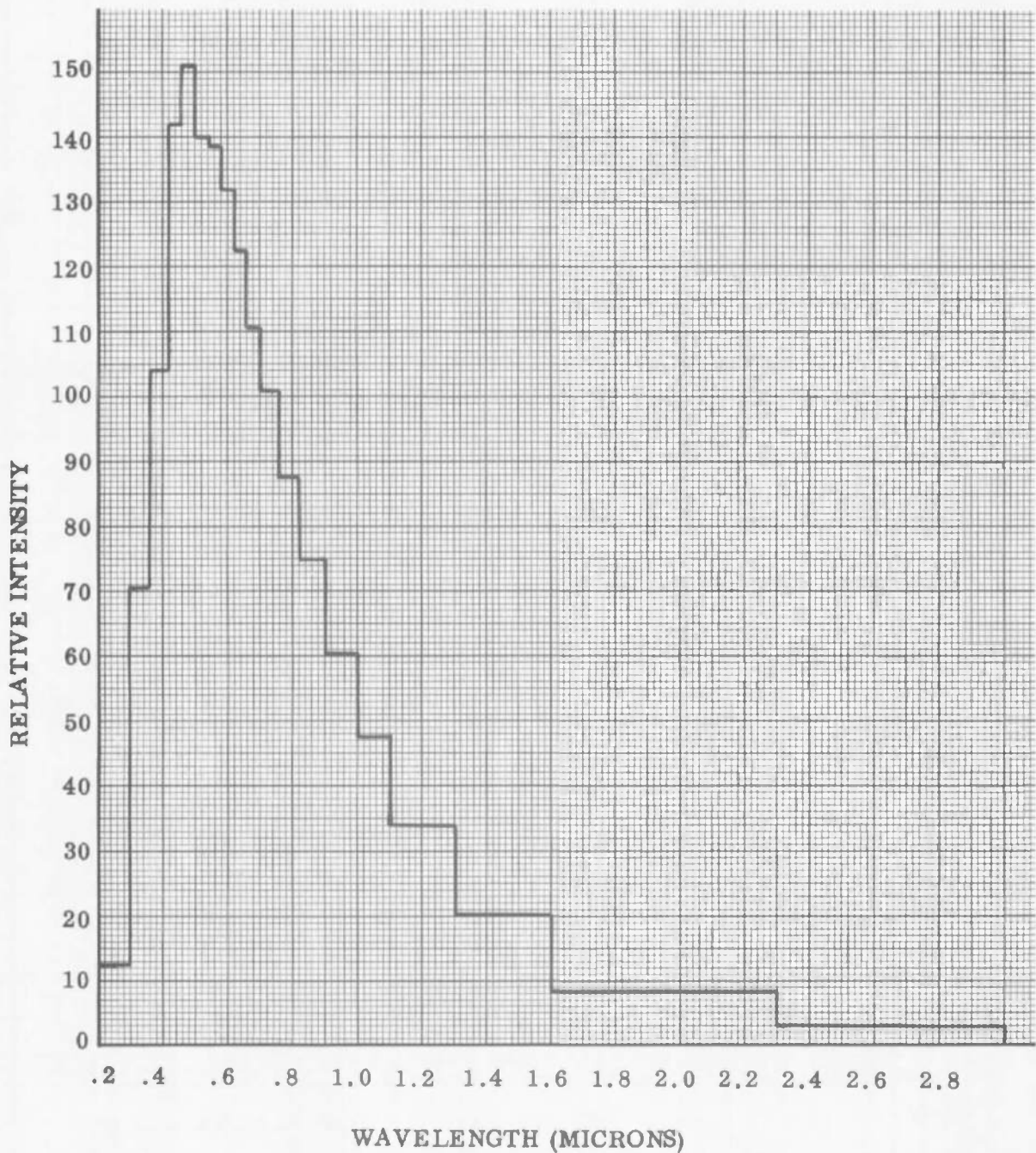


Figure 5-34. Solar Spectrum (Spectral Criterion III)

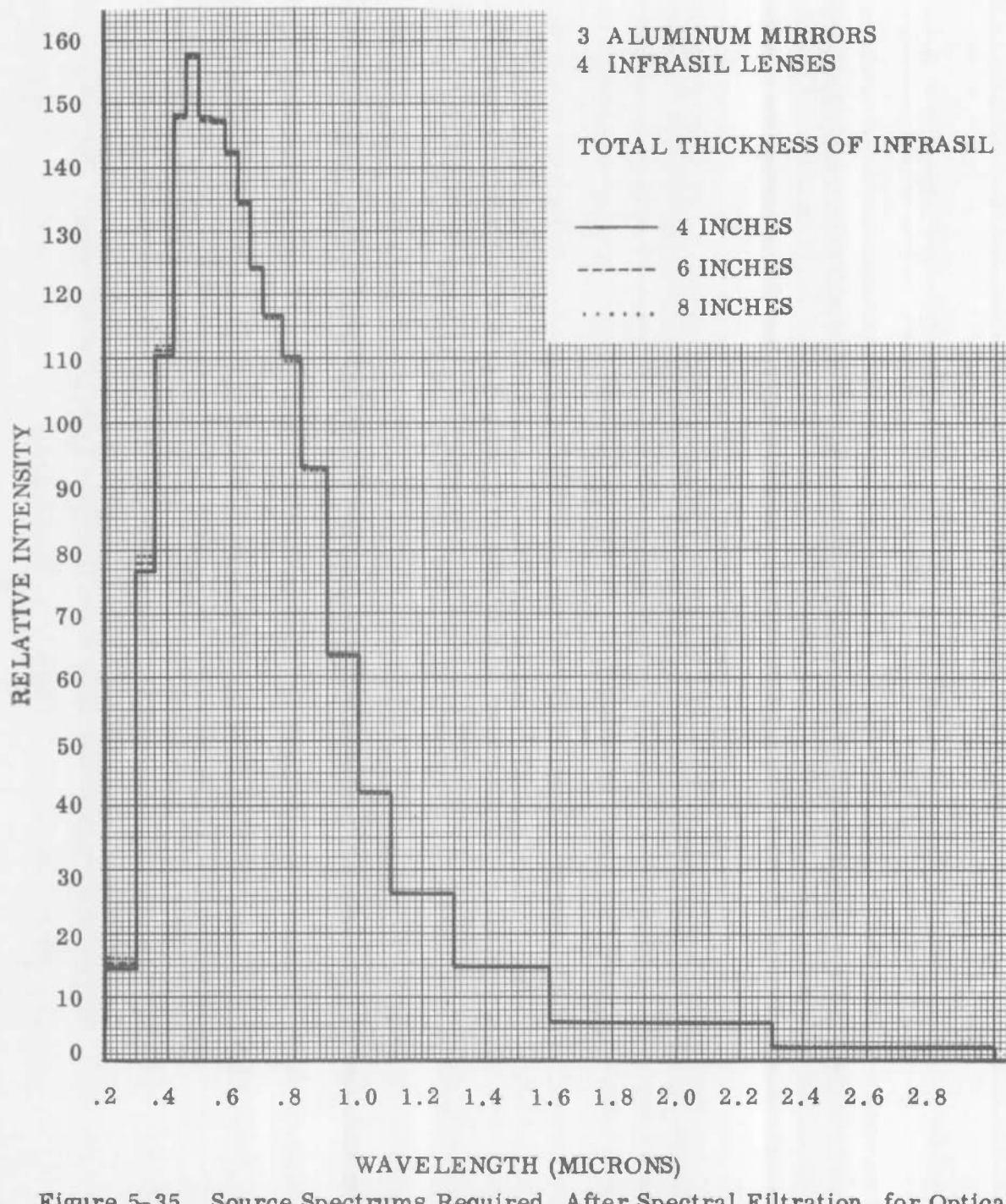


Figure 5-35. Source Spectrums Required, After Spectral Filtration, for Optical Systems Consisting of Three Aluminum Mirrors and Four Infrasil Lenses (Spectral Criterion III)

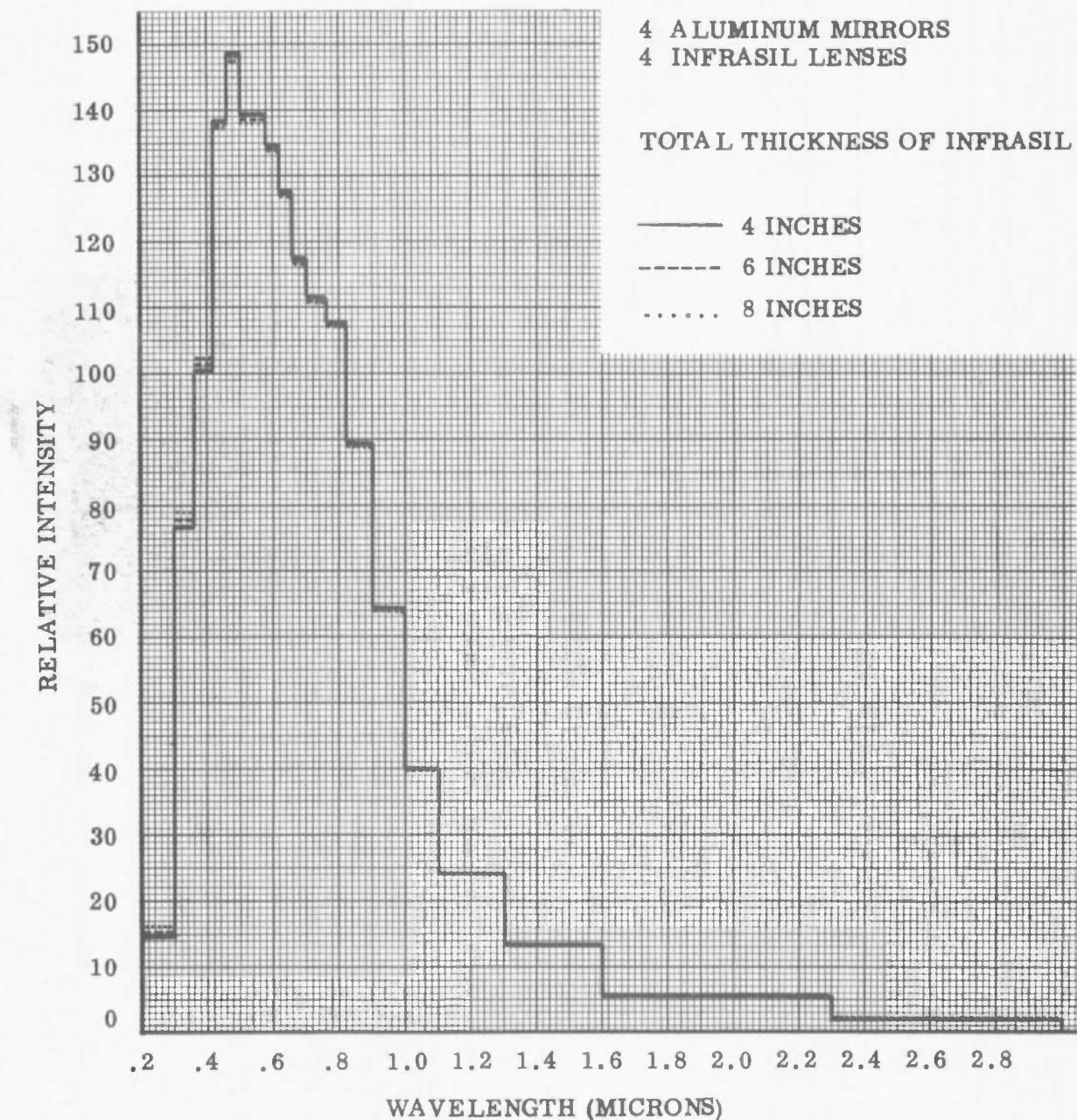


Figure 5-36. Source Spectrums Required, after Spectral Filtration, for Optical Systems Consisting of Four Aluminum Mirrors and Four Infrasil Lenses (Spectral Criterion III)

Table 5-13. Percent of Energy in each indicated wavelength band of the Solar Spectrum and the source spectrum required, after filtration, for each indicated optical system configuration (Spectral Criterion IV)

Wavelength Band (Microns)	Solar Spectrum	Percent of Energy in Wavelength Band					
		Required Source Spectrum					
		3 Aluminum Mirrors and 4 Infrasil Lenses			4 Aluminum Mirrors and 4 Infrasil Lenses		
		4 Inches of Infrasil	6 Inches of Infrasil	8 Inches of Infrasil	4 Inches of Infrasil	6 Inches of Infrasil	8 Inches of Infrasil
0.25 - 0.35	6.0	6.0	6.2	6.3	5.9	6.0	6.2
0.35 - 0.45	15.0	14.4	14.5	14.5	14.1	14.2	14.3
0.45 - 0.55	19.5	18.6	18.6	18.5	18.3	18.3	18.2
0.55 - 0.65	17.4	17.3	17.2	17.2	17.2	17.1	17.1
0.65 - 0.75	14.3	14.7	14.7	14.6	14.9	14.8	14.8
0.75 - 0.85	11.5	13.1	13.1	13.1	13.8	13.7	13.7
0.85 - 0.95	9.1	9.6	9.6	9.5	9.8	9.8	9.7
0.95 - 1.05	7.2	6.3	6.2	6.2	6.0	6.0	6.0

Table 5-14. Relative Intensity in each indicated wavelength band of the solar spectrum and of the source system required, after spectral filtration, for each indicated optical system configuration (Spectral Criterion IV)

Wavelength Band (Microns)	Solar Spectrum	Relative Intensity in Wavelength Band					
		Required Source Spectrum					
		3 Aluminum Mirrors and 4 Infrasil Lenses			4 Aluminum Mirrors and 4 Infrasil Lenses		
		4 Inches of Infrasil	6 Inches of Infrasil	8 Inches of Infrasil	4 Inches of Infrasil	6 Inches of Infrasil	8 Inches of Infrasil
0.25 - 0.35	60	60	62	63	59	60	62
0.35 - 0.45	150	144	145	145	141	142	143
0.45 - 0.55	195	186	186	185	183	183	182
0.55 - 0.65	174	173	172	172	172	171	171
0.65 - 0.75	143	147	147	146	149	148	148
0.75 - 0.85	115	131	131	131	138	137	137
0.85 - 0.95	91	96	96	95	98	98	97
0.95 - 1.05	72	63	62	62	60	60	60

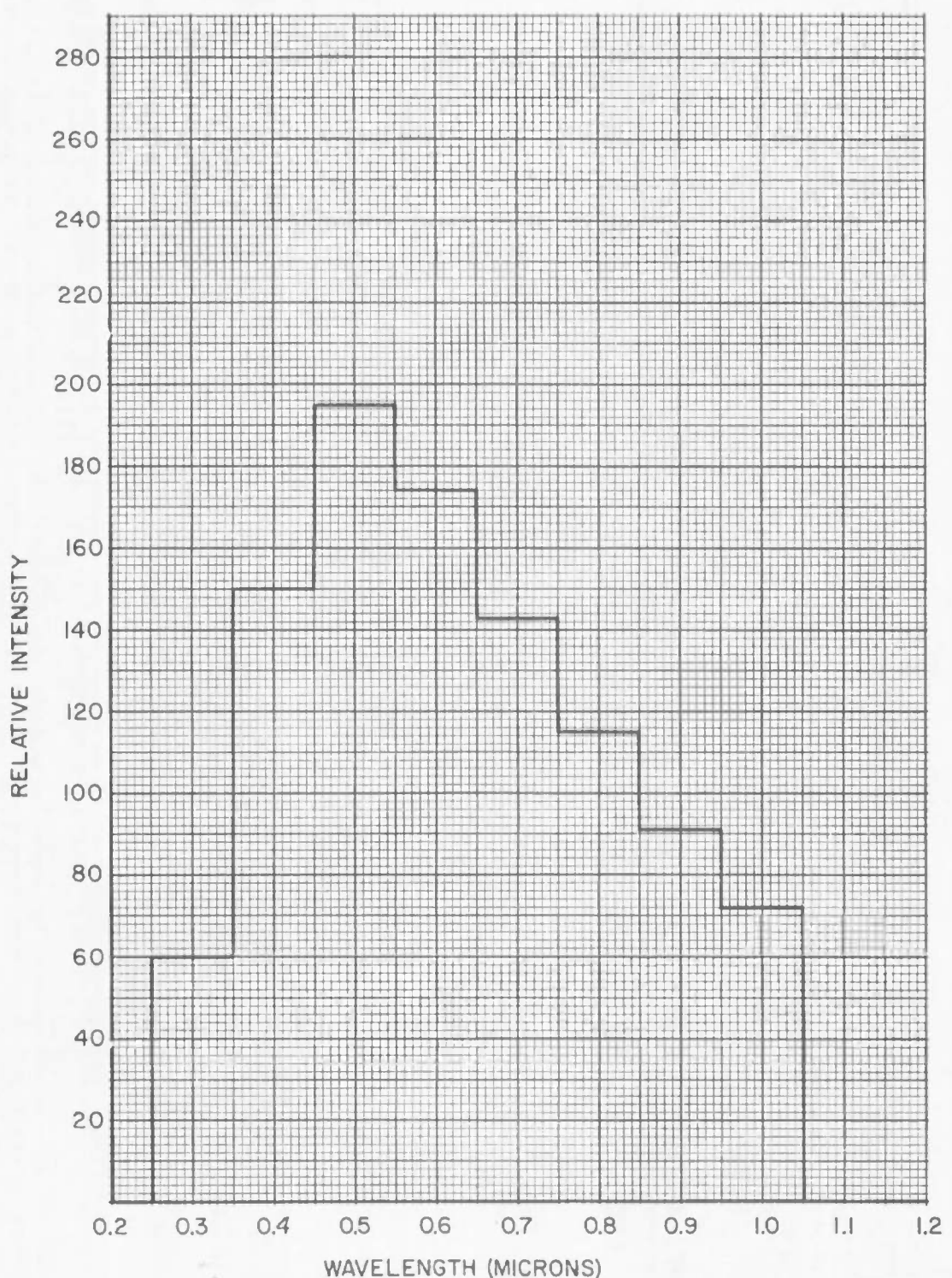


Figure 5-37. Solar Spectrum (Spectral Criterion IV)

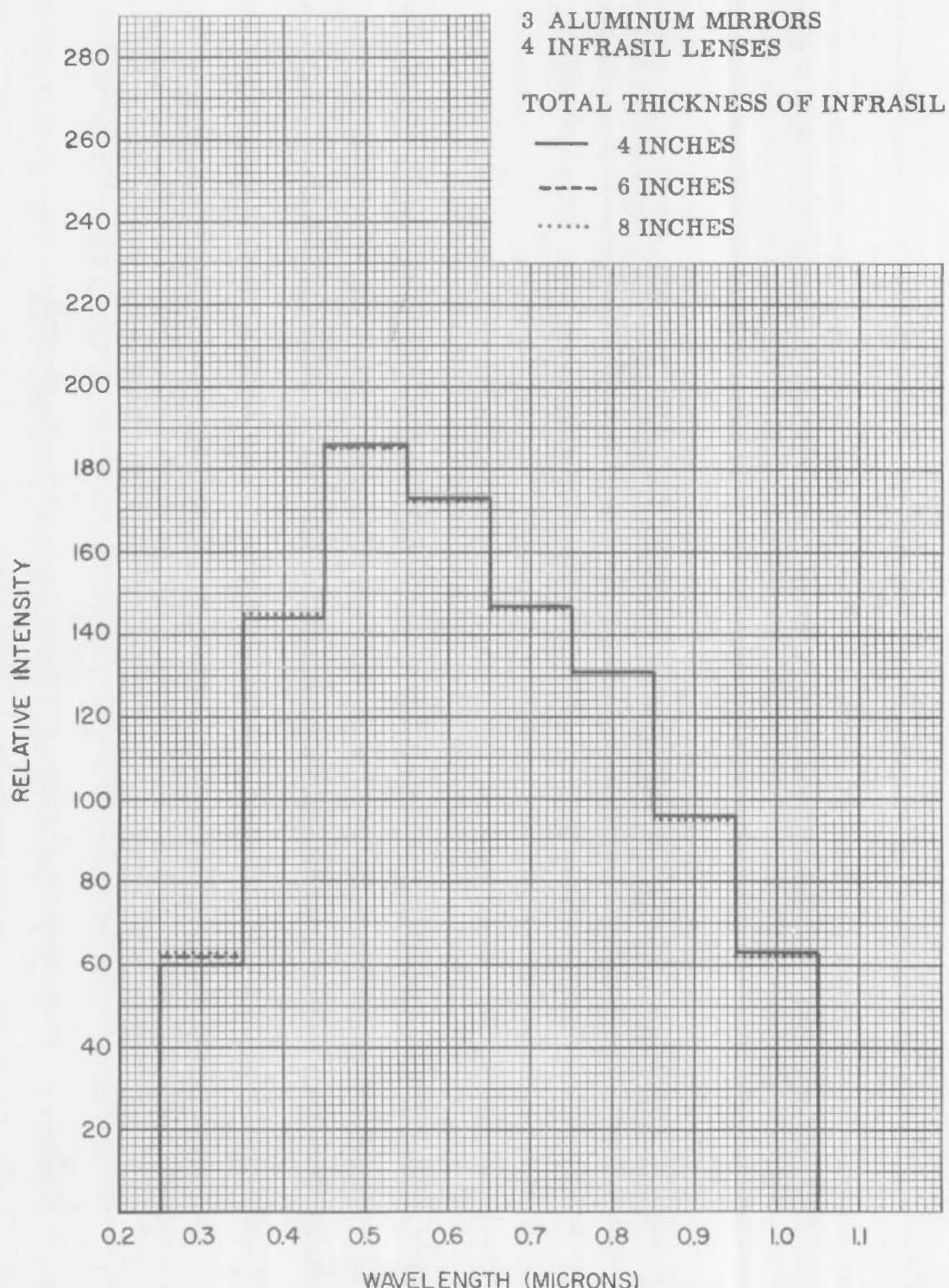


Figure 5-38. Source Spectrums Required, After Spectral Filtration, for Optical Systems Consisting of Three Aluminum Mirrors and Four Infrasil Lenses (Spectral Criterion IV)

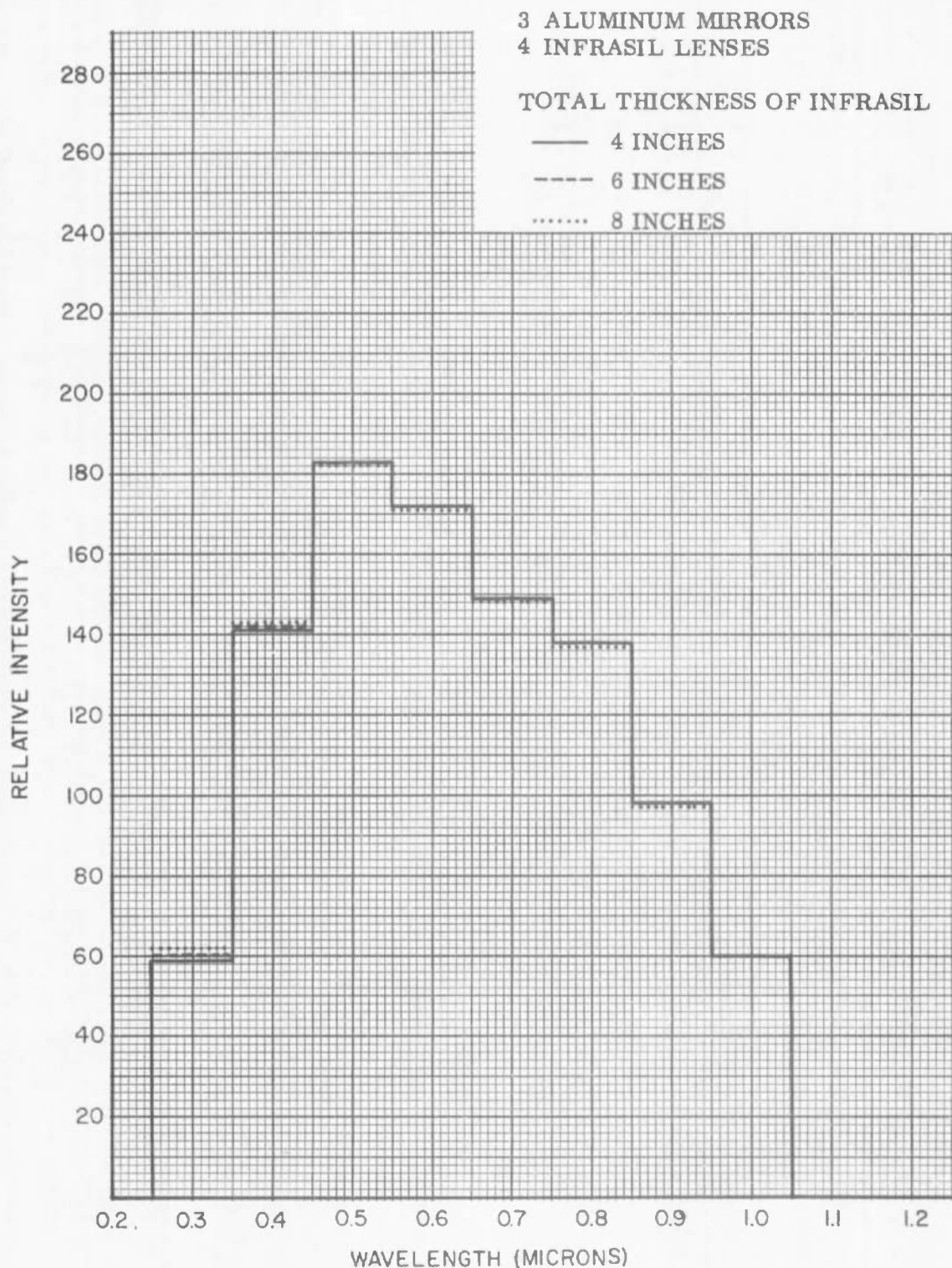


Figure 5-39. Source Spectrums Required, After Spectral Filtration, for Optical Systems Consisting of Four Aluminum Mirrors and Four Infrasil Lenses (Spectral Criterion IV)

Table 5-15. Percent of energy in each indicated wavelength band of the solar spectrum and of the source spectrum required, after spectral filtration, for each indicated optical system configuration (Spectral Criterion V)

Wavelength Band (Microns)	Solar Spectrum	Percent of Energy in Wavelength Band					
		Required Source Spectrum					
		3 Aluminum Mirrors and 4 Infrasil Lenses			4 Aluminum Mirrors and 4 Infrasil Lenses		
		4 Inches of Infrasil	6 Inches of Infrasil	8 Inches of Infrasil	4 Inches of Infrasil	6 Inches of Infrasil	8 Inches of Infrasil
0.20 - 0.30	1.50	1.67	1.75	1.84	1.65	1.73	1.83
0.30 - 0.35	4.19	4.28	4.30	4.37	4.17	4.24	4.31
0.35 - 0.40	5.43	5.37	5.42	5.48	5.29	5.35	5.40
0.40 - 0.45	8.40	8.20	8.21	8.21	8.09	8.10	8.10
0.45 - 0.50	9.37	9.06	9.03	8.99	8.96	8.92	8.89
0.50 - 0.55	8.64	8.47	8.44	8.41	8.42	8.39	8.36
0.55 - 0.60	8.43	8.40	8.38	8.35	8.38	8.35	8.32
0.60 - 0.65	7.65	7.84	7.82	7.80	7.88	7.86	7.83
0.65 - 0.70	6.97	7.17	7.15	7.13	7.25	7.23	7.21
0.70 - 0.75	6.28	6.69	6.68	6.66	6.84	6.82	6.80
0.75 - 0.80	5.62	6.42	6.40	6.40	6.72	6.70	6.68
0.80 - 0.85	5.01	5.95	5.94	5.93	6.32	6.30	6.29
0.85 - 0.90	4.45	5.02	5.01	5.00	5.24	5.23	5.21
0.90 - 1.00	7.47	7.27	7.26	7.24	7.23	7.22	7.21
1.00 - 1.10	5.90	4.80	4.80	4.79	4.50	4.50	4.49
1.10 - 1.20	4.68	3.40	3.40	3.40	3.07	3.07	3.06

Table 5-16. Relative Intensity in each indicated wavelength band of the Solar Spectrum and the source spectrum required, after spectral filtration, for each indicated optical system configuration (Spectral Criterion V)

Relative Intensity in Wavelength Band							
Wavelength Band (Microns)	Solar Spectrum	Required Source Spectrum					
		3 Aluminum Mirrors and 4 Infrasil Lenses			4 Aluminum Mirrors and 4 Infrasil Lenses		
		4 Inches of Infrasil	6 Inches of Infrasil	8 Inches of Infrasil	4 Inches of Infrasil	6 Inches of Infrasil	8 Inches of Infrasil
0.20 - 0.30	15.0	16.7	17.5	18.4	16.5	17.3	18.3
0.30 - 0.35	83.8	85.6	86.0	87.4	83.4	84.8	86.2
0.35 - 0.40	108.6	107.4	108.4	109.6	105.8	107.0	108.0
0.40 - 0.45	168.0	164.0	164.2	164.2	161.8	162.0	162.0
0.45 - 0.50	187.4	181.2	180.6	179.8	179.2	178.4	177.8
0.50 - 0.55	172.8	169.4	168.8	168.2	168.4	167.8	167.2
0.55 - 0.60	168.6	168.0	167.6	167.0	167.6	167.0	166.4
0.60 - 0.65	153.0	156.8	156.4	156.0	157.6	157.2	156.6
0.65 - 0.70	139.4	143.4	143.0	142.6	145.0	144.6	144.2
0.70 - 0.75	125.6	133.8	133.6	133.2	136.8	136.4	136.0
0.75 - 0.80	112.4	128.4	128.0	128.0	134.4	134.0	133.6
0.80 - 0.85	100.2	119.0	118.8	118.6	126.4	126.0	125.8
0.85 - 0.90	89.0	100.4	100.2	100.0	104.8	104.6	104.2
0.90 - 1.00	74.7	72.7	72.6	72.4	72.3	72.2	72.1
1.00 - 1.10	59.0	48.0	48.0	47.9	45.0	45.0	44.9
1.10 - 1.20	46.8	34.0	34.0	34.0	30.7	30.7	30.6

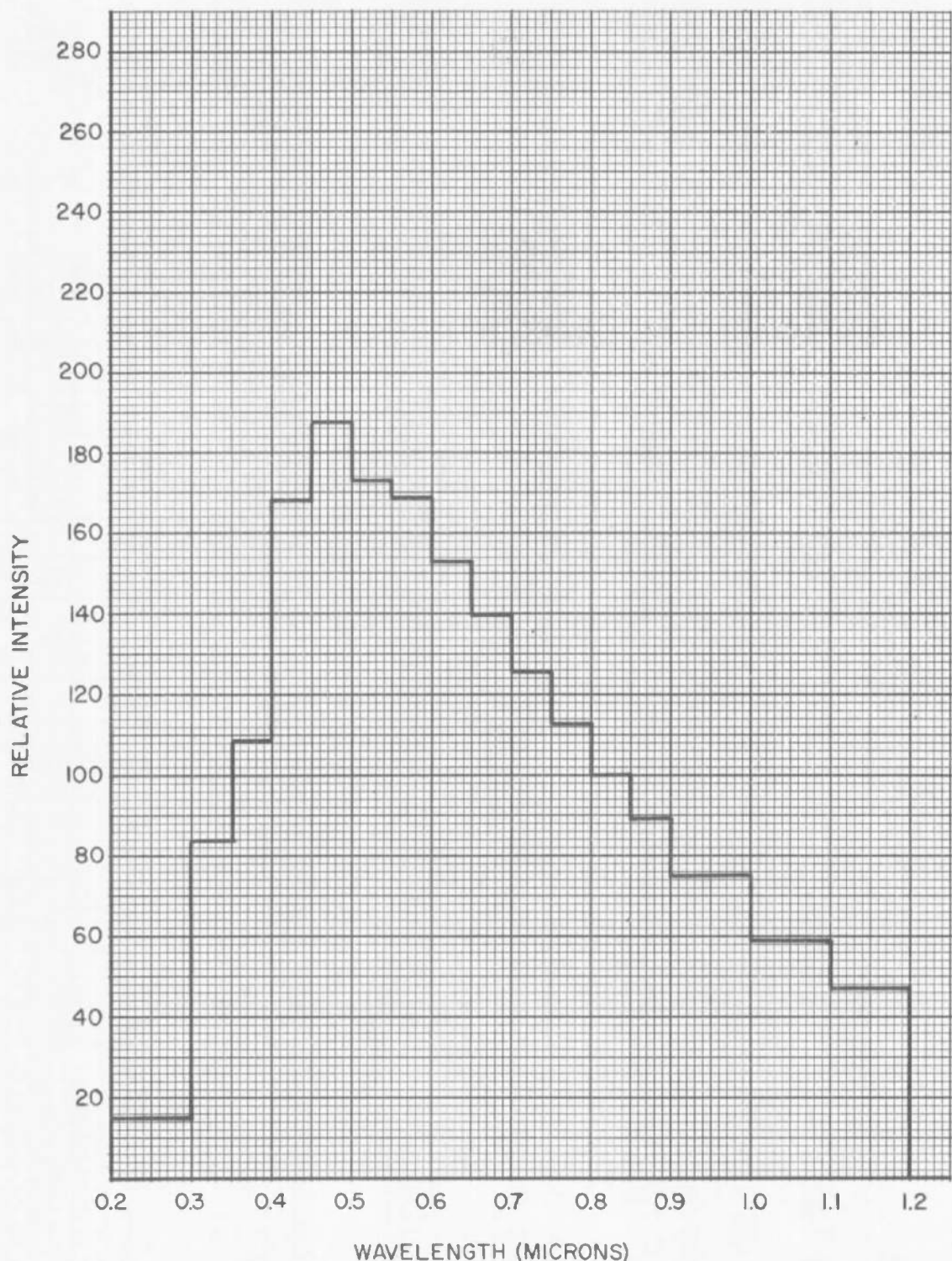


Figure 5-40. Solar Spectrum (Spectral Criterion V)

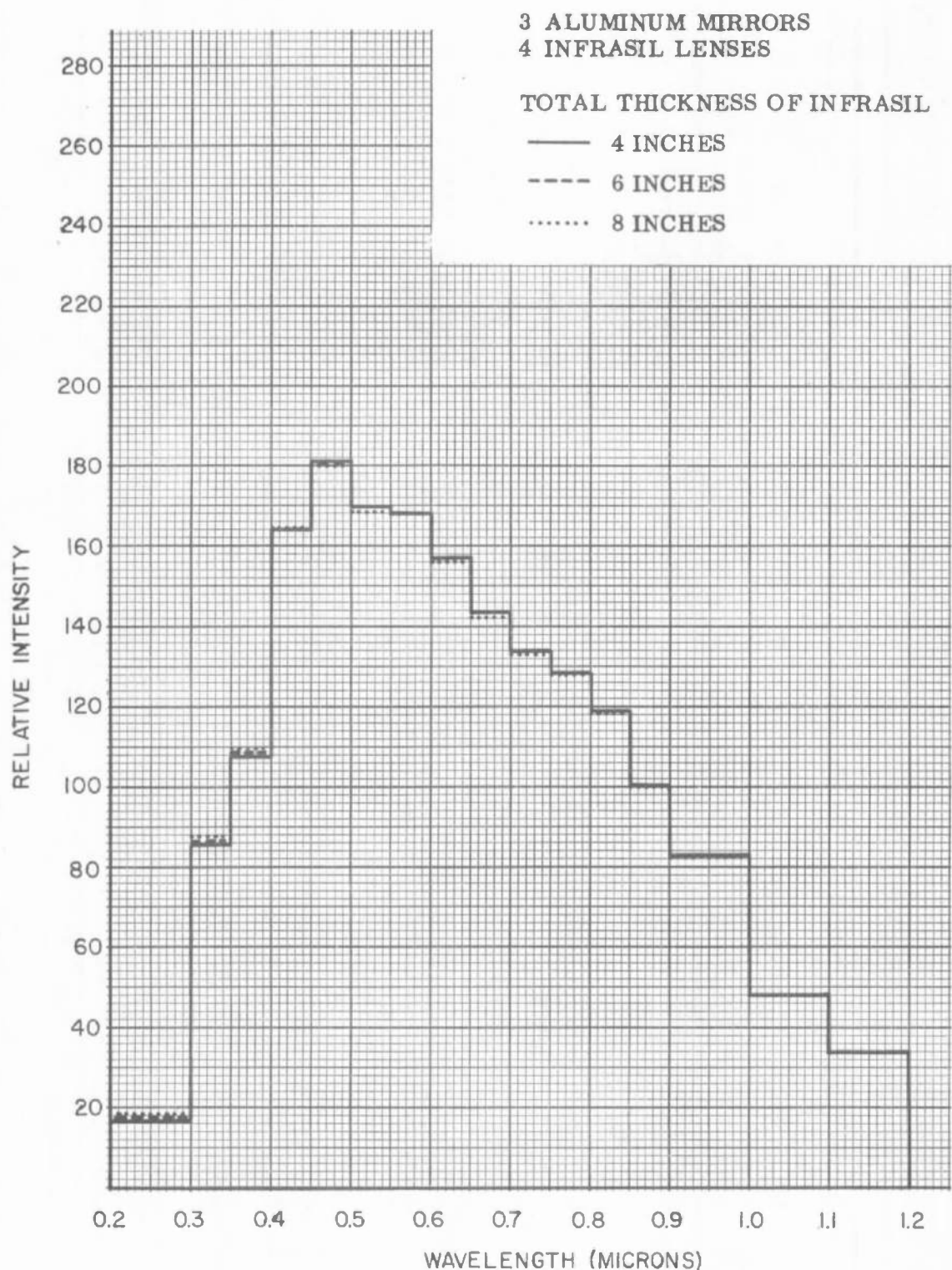


Figure 5-41. Source Spectrums Required, After Spectral Filtration, for Optical Systems Consisting of Three Aluminum Mirrors and Four Infrasil Lenses (Spectral Criterion V)

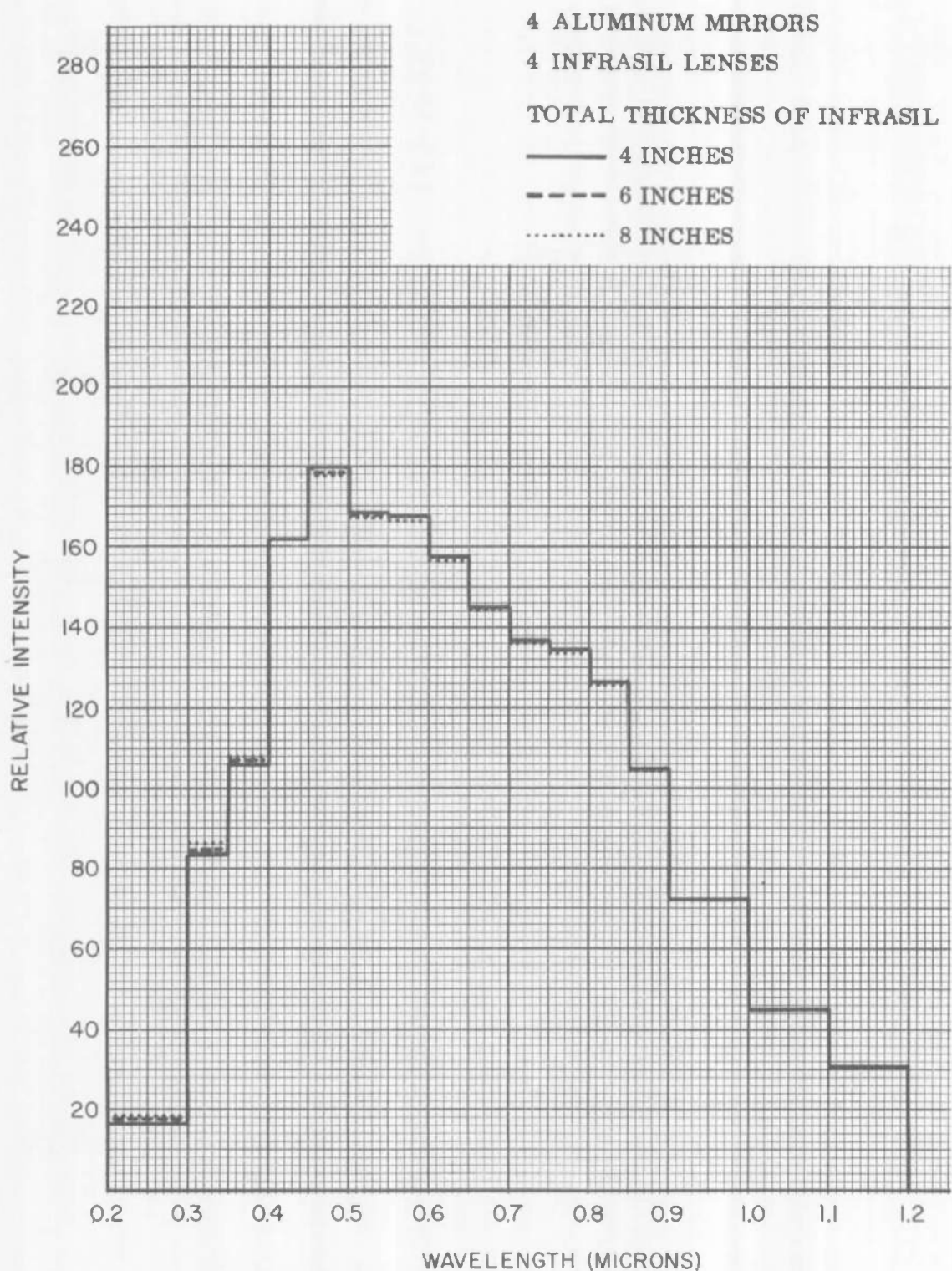


Figure 5-42. Source Spectrums Required, After Spectral Filtration, for Optical Systems Consisting of Four Aluminum Mirrors and Four Infrasil Lenses (Spectral Criterion V)

Table 5-17. Identification of the Various Spectrums considered for the Vortex Stabilized Radiation Source

Identification	Input Power	Gas	Pressure	Reference
Spectrum I	28.8 KW	100% Argon	10.0 Atmospheres	8MS113-1033, Figure 1
Spectrum IV	11.9 KW	100% Argon	10.0 Atmospheres	8MS113-1033, Figure 7
Spectrum V	17.4 KW	100% Argon	14.0 Atmospheres	11MS024-1033, Figure 7
Spectrum VII	17.0 KW	100% Argon	14.2 Atmospheres	AEDC-TDR-64-165, Figure 30
Spectrum VIII	21.0 KW	100% Argon	16.0 Atmospheres	AEDC-TDR-64-165, Figure 31
Spectrum IX	60.0 KW	100% Argon	19.0 Atmospheres	AEDC-TDR-64-165, Figure 31

when the spectral measurements were taken as well as the document from which the spectral data was obtained.

The data for Spectrums I, IV, V and VII was supplied between 0.25 micron and 1.05 microns in terms of 0.1 micron bandwidths (Spectral Criterion IV). This data, normalized with respect to the energy in this range, is tabulated in tables 5-18 and 5-19 and is plotted in figures 5-43, 5-44, 5-45, 5-46 and 5-47. The solid curve of figure 5-47 is the source spectrum required, after spectral filtration, to produce the solar spectrum with an optical system of three aluminum mirrors and four Infrasil lenses whose total thickness is 4.0 inches.

The data for Spectrums VIII and IX was supplied for the range between 0.20 micron and 1.20 microns in terms of 0.050 micron bandwidths. Because of the smaller bandwidths, it was possible to analyze this data on the basis of Spectral Criterion V, whose bandwidths were chosen to resemble more closely the bandwidths defined by Spectral Criterion III which was used to analyze the spectrums of the High Intensity Carbon Arc and the Fluid Transpiration Arc. The energy and intensity within each bandwidth defined by Spectral Criterion V are listed in tables 5-20 and 5-21 and these two spectrums are plotted in figures 5-48, 5-49 and 5-50. The solid curve on figure 5-50 represents the source spectrum required, after spectral filtration, to produce the solar spectrum with an optical system of three aluminum mirrors and four Infrasil lenses whose total thickness is 4.0 inches.

The maximum spectral filtration efficiency for each source-spectrum, optical-system, spectral-filter combination was determined (for Spectrums I, IV, V and VII) through a comparison with the data listed in tables 5-13 and 5-14, and plotted in figures 5-38 and 5-39; and (for Spectrums VIII and IX) through a comparison with the data listed in tables 5-15 and 5-16, and plotted in figures 5-41 and 5-42. The values thus determined are tabulated in table 5-22. It should be noted here, however, that the values of the maximum filtration efficiency for Spectrums I, IV, V, and VII are not directly comparable to those values determined for Spectrums VIII and IX since the bandwidths used are not the same. If the same 0.1 micron bandwidth is used to analyze Spectrums VIII and IX for an optical system of 3 aluminum mirrors and 4 Infrasil lenses whose total thickness is 4.0 inches, the maximum filtration efficiencies are 60.0% and 60.8%, respectively. The bandwidth of minimum filtration occurs between 0.55 micron and 0.65 micron for Spectrum VIII and between 0.65 micron and 0.75 micron for Spectrum IX.

The maximum efficiency k_{max} with which radiation collected from the Vortex Stabilized Radiation Source will be transferred, with

Table 5-18. Percent of Energy in each indicated wavelength band of the Solar Spectrum and Spectrums I, IV, V, and VII of the Vortex Stabilized Radiation Source (Spectral Criterion IV)

Wavelength Band (Microns)	Solar Spectrum	Percent of Energy in Wavelength Band			
		Vortex Stabilized Radiation Source			
		Spectrum I 100% Argon 28.8 KW 10 ATM	Spectrum IV 100% Argon 11.9 KW 10 ATM	Spectrum V 100% Argon 150 Amps 17.4 KW 14 ATM	Spectrum VII 100% Argon 200 Amps 17 KW 14.2 ATM
0.25 - 0.35	6.0	14.1	12.7	14.1	16.1
0.35 - 0.45	15.0	15.9	15.1	20.3	21.1
0.45 - 0.55	19.5	12.5	11.7	15.0	15.6
0.55 - 0.65	17.4	9.7	8.8	12.3	10.5
0.65 - 0.75	14.3	11.0	10.2	10.8	9.9
0.75 - 0.85	11.5	22.5	27.8	12.5	11.8
0.85 - 0.95	9.1	7.8	7.3	8.3	8.1
0.95 - 1.05	7.2	6.5	6.3	6.6	6.9

Table 5-19. Relative Intensity in each indicated wavelength band of the Solar Spectrum and Spectrums I, IV, V, and VII of the Vortex Stabilized Radiation Source (Spectral Criterion IV)

Wavelength Band (Microns)	Solar Spectrum	Relative Intensity in Wavelength Band			
		Vortex Stabilized Radiation Source			
		Spectrum I 100% Argon 28.8 KW 10 ATM	Spectrum IV 100% Argon 11.9 KW 10 ATM	Spectrum V 100% Argon 150 Amps 17.4 KW 14 ATM	Spectrum VII 100% Argon 200 Amps 17 KW 14.2 ATM
0.25 - 0.35	60	141	127	141	161
0.35 - 0.45	150	159	151	203	211
0.45 - 0.55	195	125	117	150	156
0.55 - 0.65	174	97	88	123	105
0.65 - 0.75	143	110	102	108	99
0.75 - 0.85	115	225	278	125	118
0.85 - 0.95	91	78	73	83	81
0.95 - 1.05	72	65	63	66	69

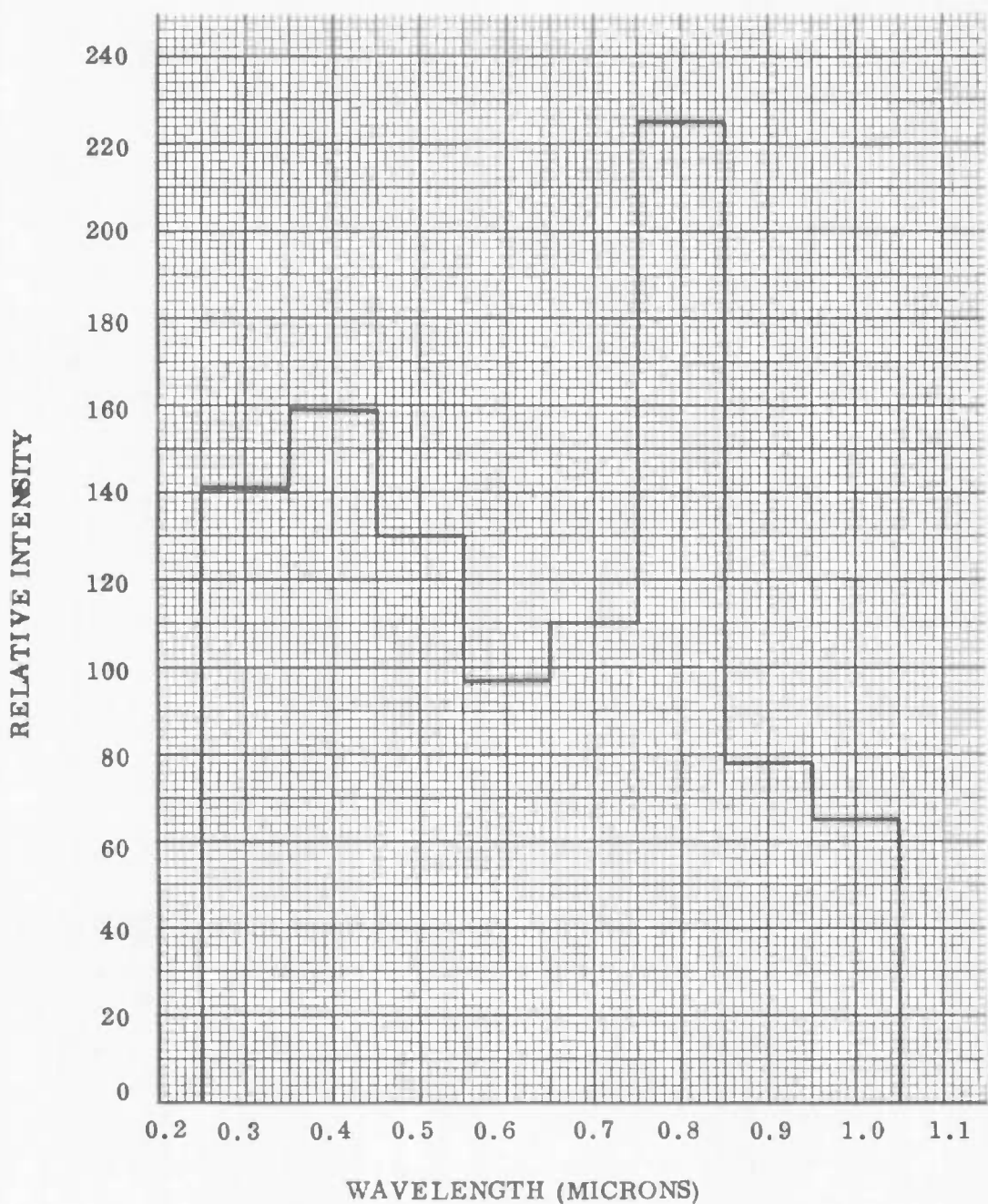


Figure 5-43. Spectrum I of the Vortex Stabilized Radiation Source
(Spectral Criterion IV)

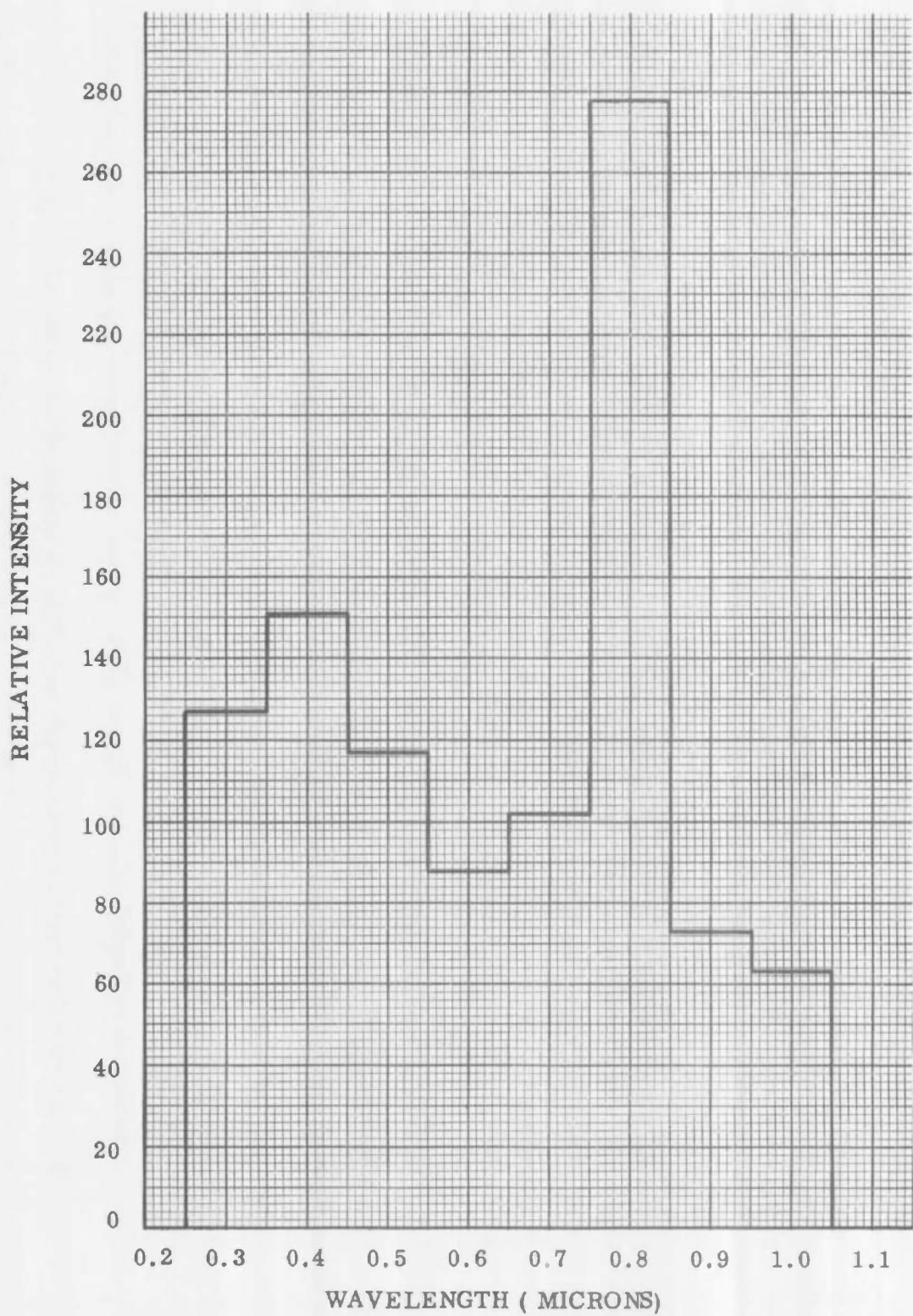


Figure 5-44. Spectrum IV of the Vortex Stabilized Radiation Source (Spectral Criterion IV)

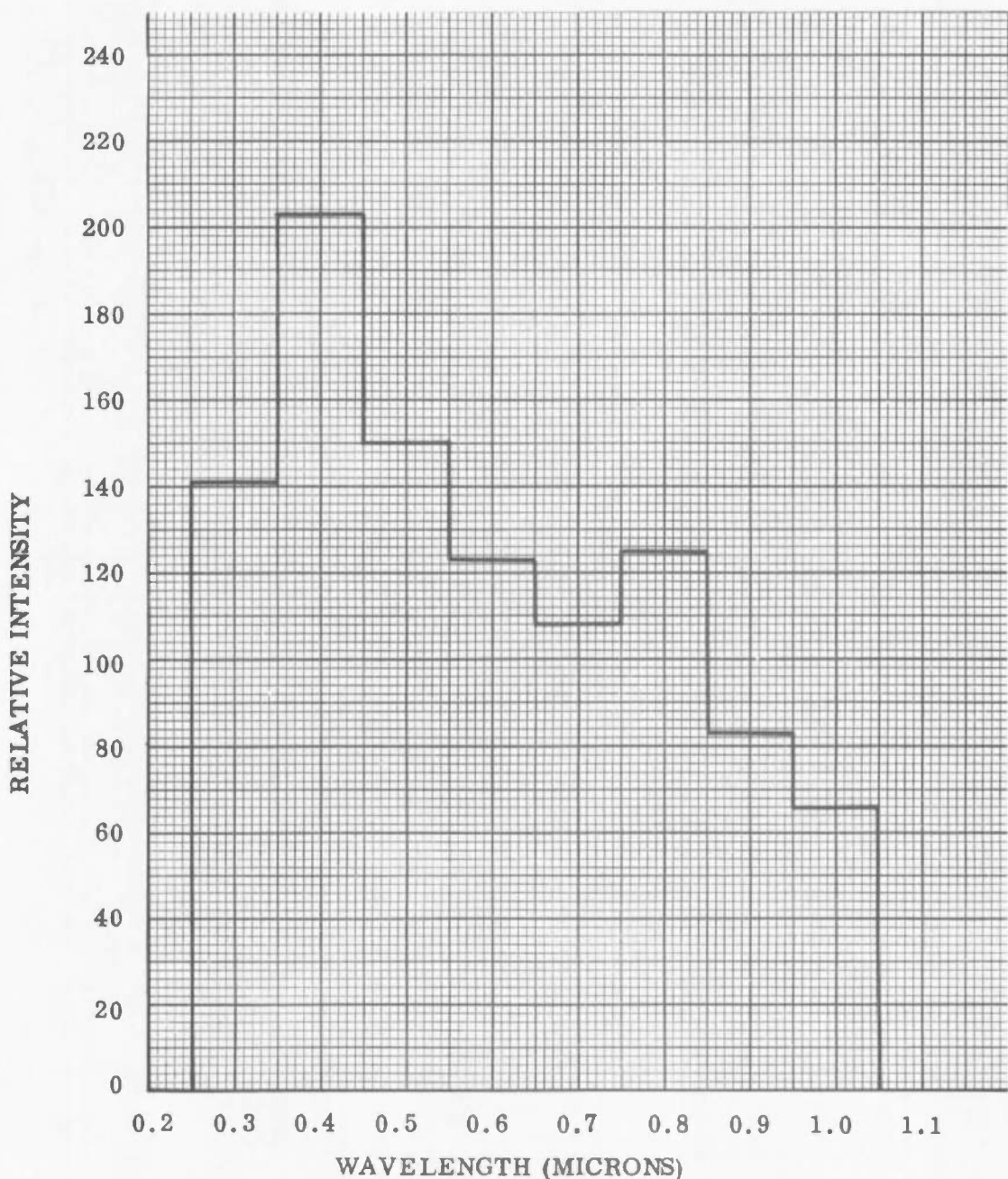


Figure 5-45. Spectrum V of the Vortex Stabilized Radiation Source (Spectral Criterion IV)

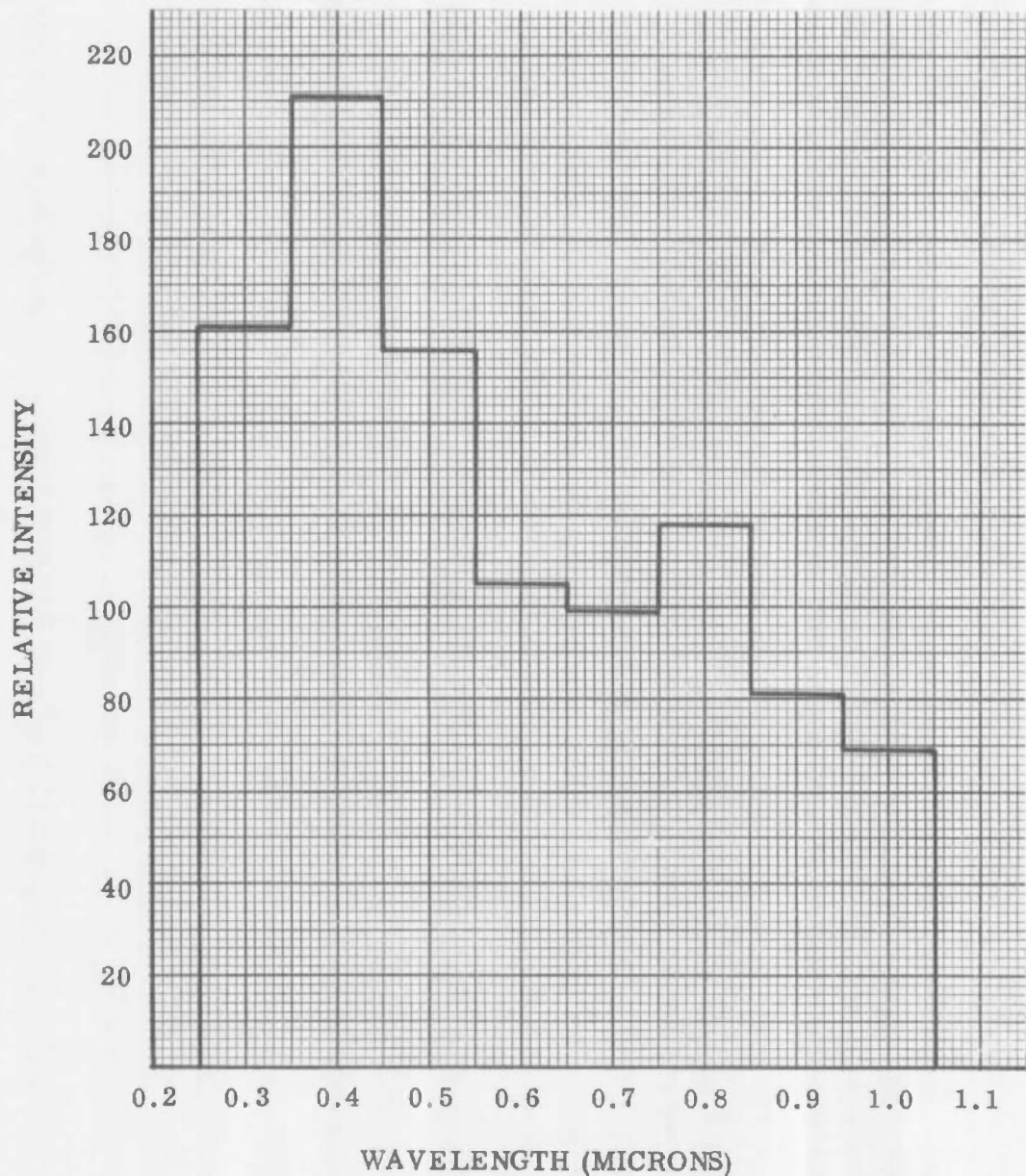


Figure 5-46. Spectrum VII of the Vortex Stabilized Radiation Source (Spectral Criterion IV)

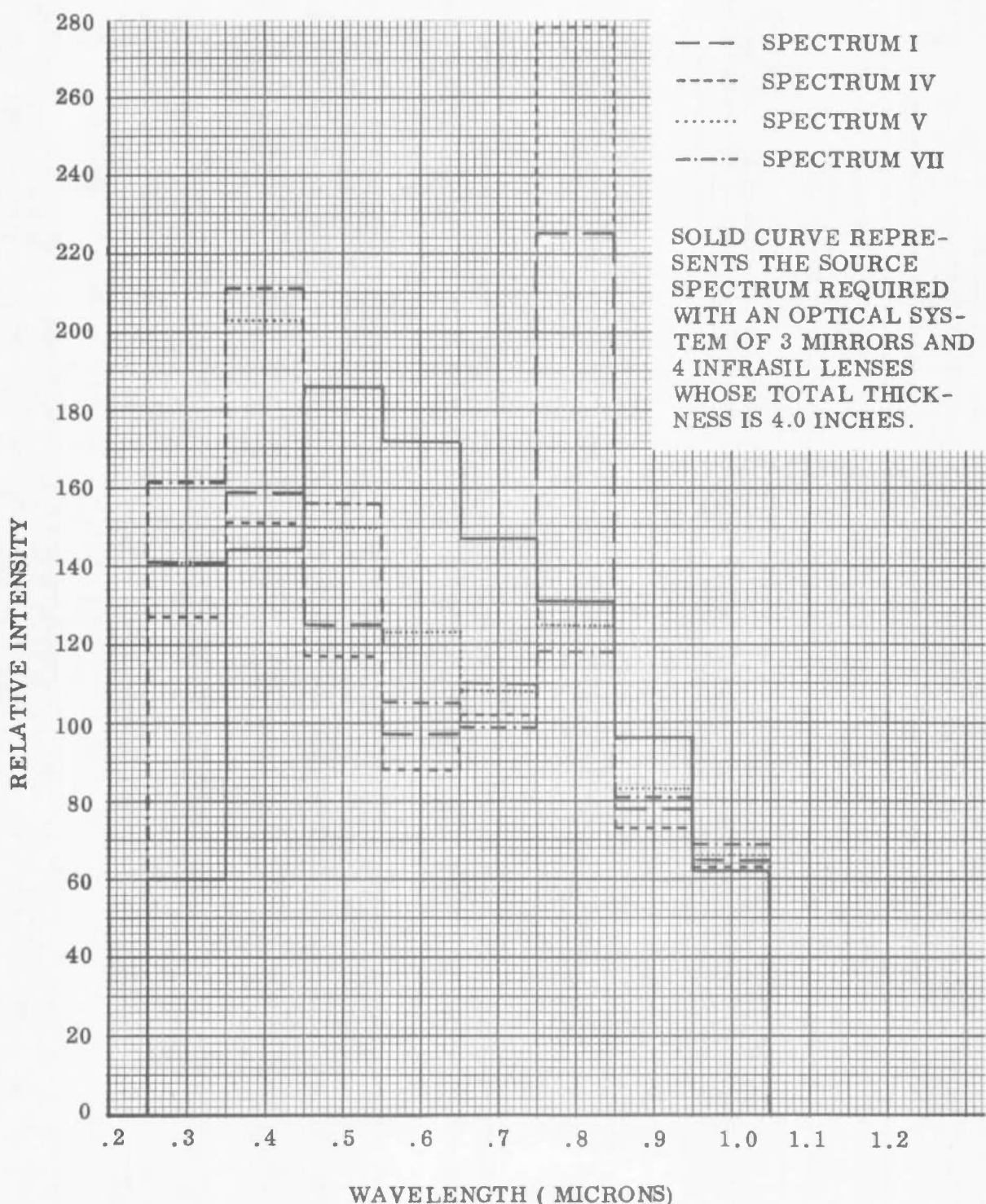


Figure 5-47. Spectrums I, IV, V, and VII of the Vortex Stabilized Radiation Source (Spectral Criterion IV)

Table 5-20. Percent of Energy in each indicated wavelength band of the Solar Spectrum and Spectrums VIII and IX of the Vortex Stabilized Radiation Source (Spectral Criterion V)

Wavelength Band (Microns)	Percent of Energy in Wavelength Band			
	Solar Spectrum	Vortex Stabilized Radiation Source		
		Spectrum VIII Argon 21 KW	16 ATM	Spectrum IX Argon 60 KW
0.20 - 0.30	1.50	5.90		5.56
0.30 - 0.35	4.19	7.61		8.01
0.35 - 0.40	5.43	8.98		9.75
0.40 - 0.45	8.40	9.32		10.07
0.45 - 0.50	9.37	7.70		8.75
0.50 - 0.55	8.64	6.42		7.12
0.55 - 0.60	8.43	5.39		6.04
0.60 - 0.65	7.65	4.36		4.88
0.65 - 0.70	6.97	4.11		4.48
0.70 - 0.75	6.28	4.62		3.95
0.75 - 0.80	5.62	5.22		4.32
0.80 - 0.85	5.01	6.16		4.96
0.85 - 0.90	4.45	5.73		4.96
0.90 - 1.00	7.47	7.96		7.25
1.00 - 1.10	5.90	5.56		5.48
1.10 - 1.20	4.68	4.96		4.43

Table 5-21. Relative Intensity in each indicated wavelength band of the Solar Spectrum and Spectrums VIII and IX of the Vortex Stabilized Radiation Source (Spectral Criterion V)

Wavelength Band (Microns)	Relative Intensity in Wavelength Band			
	Solar Spectrum	Vortex Stabilized Radiation Source		
		Spectrum VIII Argon 21 KW 16 ATM		Spectrum IX Argon 60 KW 19 ATM
0.20 - 0.30	15.0	59.0		55.6
0.30 - 0.35	83.8	152.2		160.2
0.35 - 0.40	108.6	179.6		195.0
0.40 - 0.45	168.0	186.4		201.4
0.45 - 0.50	187.4	154.0		175.0
0.50 - 0.55	172.8	128.4		142.4
0.55 - 0.60	168.6	107.8		120.8
0.60 - 0.65	153.0	87.2		97.6
0.65 - 0.70	139.4	82.2		89.6
0.70 - 0.75	125.6	92.4		79.0
0.75 - 0.80	112.4	104.4		86.4
0.80 - 0.85	100.2	123.2		99.2
0.85 - 0.90	89.0	114.6		99.2
0.90 - 1.00	74.7	79.6		72.5
1.00 - 1.10	59.0	55.6		54.8
1.10 - 1.20	46.8	49.6		44.3

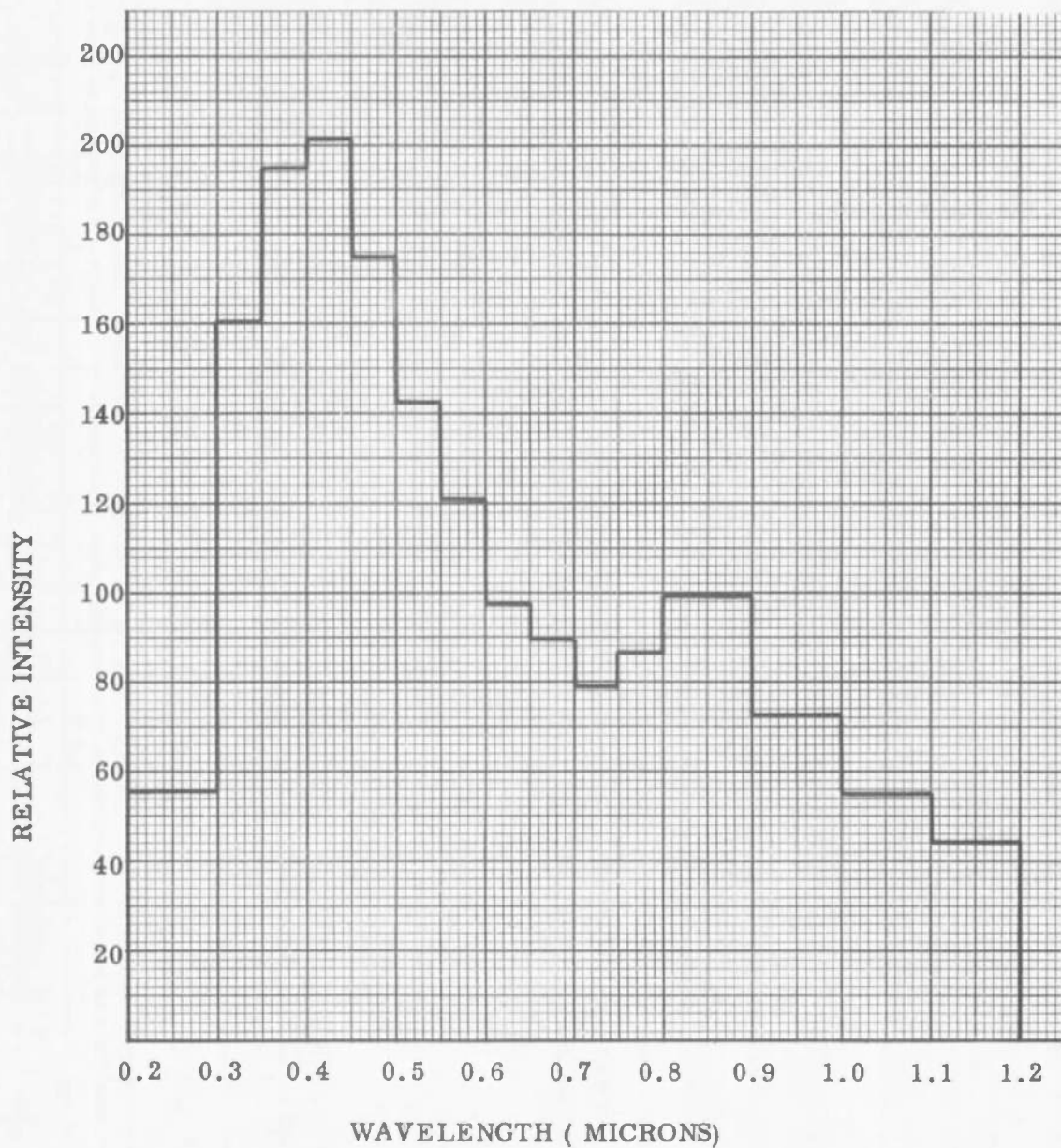


Figure 5-48. Spectrum IX of the Vortex Stabilized Radiation Source
(Spectral Criterion IV)

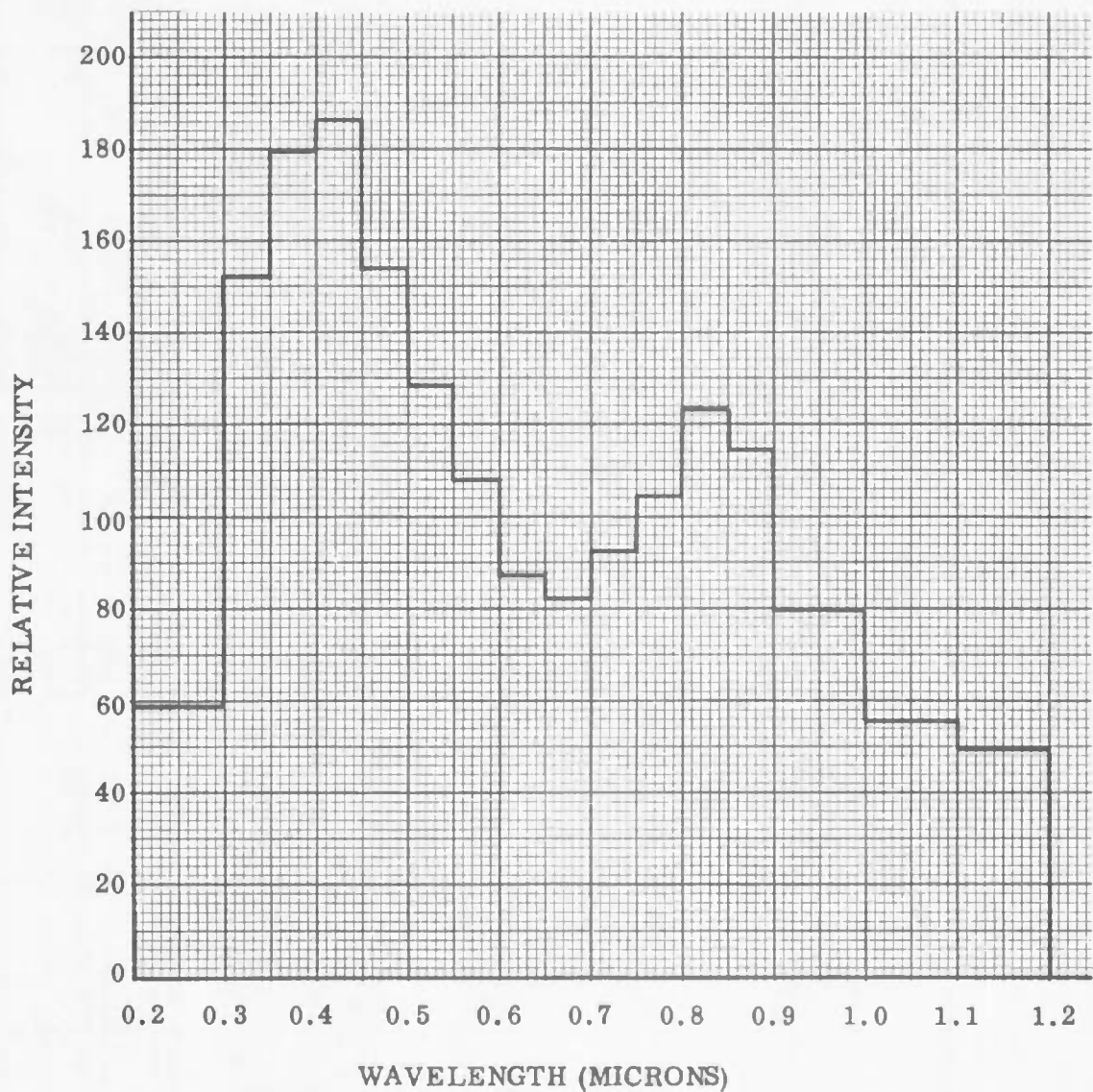


Figure 5-49. Spectrum VIII of the Vortex Stabilized Radiation Source
(Spectral Criterion V)

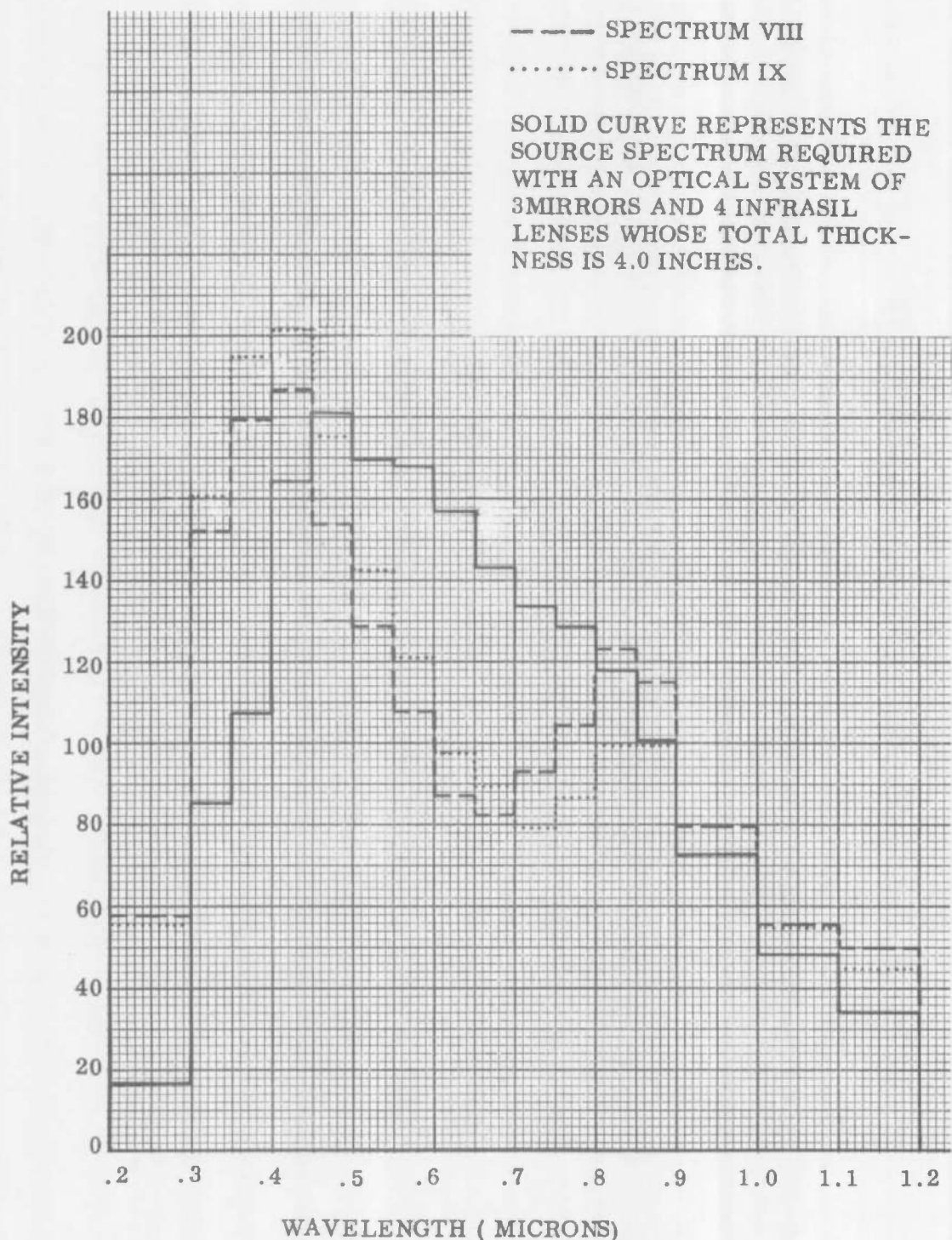


Figure 5-50. Spectrums VIII and IX of the Vortex Stabilized Radiation Source (Spectral Criterion V)

Table 5-22. For each indicated optical system configuration, the Maximum Efficiency with which Spectrums I, IV, V, VII, VIII, or IX of the VSRS can be filtered to match the source spectrums required, after spectral filtration, in order to match the Solar Spectrum

N = Number of Lenses

M = Number of Mirrors

T = Thickness of Infrasil (inches)

Bandwidth of minimum filtration = $0.55\mu - 0.65\mu$ except where noted

Optical System Configuration			Vortex Stabilized Radiation Source					
			Maximum Efficiency in Percent					
N	M	T	Spectrum I 100% Argon 28.8 kw 10 ATM	Spectrum IV 100% Argon 11.9 kw 10 ATM	Spectrum V 100% Argon 17.4 kw 14 ATM	Spectrum VII 100% Argon 17 kw 14.2 ATM	Spectrum VIII 100% Argon 21 kw 16 ATM	Spectrum IX 100% Argon 60 kw 19 ATM
4	3	4	56.1	50.9	71.1	60.7	¹ 55.6	² 59.0
4	3	6	56.4	51.2	71.5	61.0	¹ 55.8	² 59.1
4	3	8	56.4	51.2	71.5	61.0	¹ 55.9	² 59.3
4	4	4	56.4	51.2	71.5	61.0	¹ 55.3	² 57.7
4	4	6	56.7	51.5	71.9	61.4	¹ 55.5	² 57.9
4	4	8	56.7	51.5	71.9	61.4	¹ 55.7	² 58.1

¹ Bandwidth of minimum filtration = $0.60\mu - 0.65\mu$

² Bandwidth of minimum filtration = $0.70\mu - 0.75\mu$

appropriate spectral filtration, through each optical system configuration (again assuming that the refractive components are Infrasil) was determined by multiplying the various values of maximum spectral filtration efficiency (table 5-22) by the various values of dissipative efficiency (table 5-10) determined for the optical system configurations. The values of k_{\max} thus determined, together with the corresponding values of the k_{prob} (again determined by assuming a 10% safety factor) are listed in table 5-23.

5.3.3.2 Spectral Analysis of the Fluid Transpiration Arc and the High Intensity Carbon Arc

The spectrums, in terms of the bandwidths of Spectral Criterion IIA, Spectral Criterion IIB, and Spectral Criterion III, are plotted, for the High Intensity Carbon Arc in figures 5-51, 5-52 and 5-53, respectively; for the 37.5-kilowatt Fluid Transpiration Arc in figures 5-54, 5-55 and 5-56, respectively; and for the 29.1-kilowatt Fluid Transpiration Arc in figures 5-57, 5-58 and 5-59, respectively. The data from which figures 5-53, 5-56 and 5-59 were plotted is listed in table 5-24, and it is this data which was used to determine the maximum spectral filtration efficiency through a comparison with the data listed in tables 5-11 and 5-12 and plotted in figures 5-35 and 5-36. The maximum filtration efficiencies thus determined for the various source, optical-system, spectral-filter combinations are listed in table 5-25 together with the spectral range of minimum filtration. The range of minimum filtration is the bandwidth which establishes the filtering scale factor. Hence, the maximum filtration efficiency for the 37.5-kilowatt Fluid Transpiration Arc is due to the source spectrum energy deficiency between 1.00 and 1.04 micron (see figure 5-54) which has not been entirely obscured by the choice of a larger bandwidth of 1.00 to 1.10 micron (see figure 5-56). If the bandwidth is widened to include the energy between 1.0 and 1.3 micron, the bandwidth of minimum filtration occurs between 0.9 to 1.0 micron and results in a maximum spectral filtration efficiency of approximately 38%. Increasing the bandwidth to include the energy between 0.9 and 1.3 micron results in a maximum filtration efficiency of approximately 45% with the bandwidth of minimum filtration occurring between 0.9 and 1.3 micron.

The maximum efficiency k_{\max} with which radiation collected from the High Intensity Carbon Arc or Fluid Transpiration Arc will be transferred, with appropriate spectral filtration, through each optical system configuration (assuming that the refractive components are Infrasil) is tabulated for each source-spectrum, optical-system, spectral-filter combination in table 5-26. These values were determined by multiplying the various values of maximum spectral filtration efficiency (table 5-24) by the appropriate values of dissipative

Table 5-23. Maximum and Probable Dissipative Efficiencies of the indicated Source, Optical-System, Spectral-Filter Combinations:

N = number of lenses

M = number of mirrors

T = total thickness of Infrasil

k_{max} = Maximum Dissipative Efficiency (Percent)

$k_{prob} = 0.9 k_{max}$ = Probable Dissipative Efficiency (Percent)

Optical System Configuration			Vortex Stabilized Radiation Source Spectrum											
			I		IV		V		VII		VIII		IX	
N	M	T	k_{max}	k_{prob}	k_{max}	k_{prob}	k_{max}	k_{prob}	k_{max}	k_{prob}	k_{max}	k_{prob}	k_{max}	k_{prob}
4	3	4.0	27.2	24.5	24.7	22.2	34.5	31.1	29.4	26.5	27.0	24.3	28.6	25.7
4	3	6.0	27.0	24.3	24.5	22.0	34.2	30.8	29.2	26.3	26.7	24.0	28.3	25.5
4	3	8.0	26.7	24.0	24.2	21.8	33.8	30.4	28.8	26.0	26.4	23.7	28.0	25.2
4	4	4.0	23.7	21.3	21.5	19.4	30.0	27.0	25.6	23.1	23.2	20.9	24.3	21.9
4	4	6.0	23.5	21.1	21.4	19.2	29.8	26.8	25.5	22.9	23.0	20.7	24.0	21.6
4	4	8.0	23.2	20.9	21.1	19.0	29.5	26.6	25.2	22.7	22.8	20.5	23.8	21.4

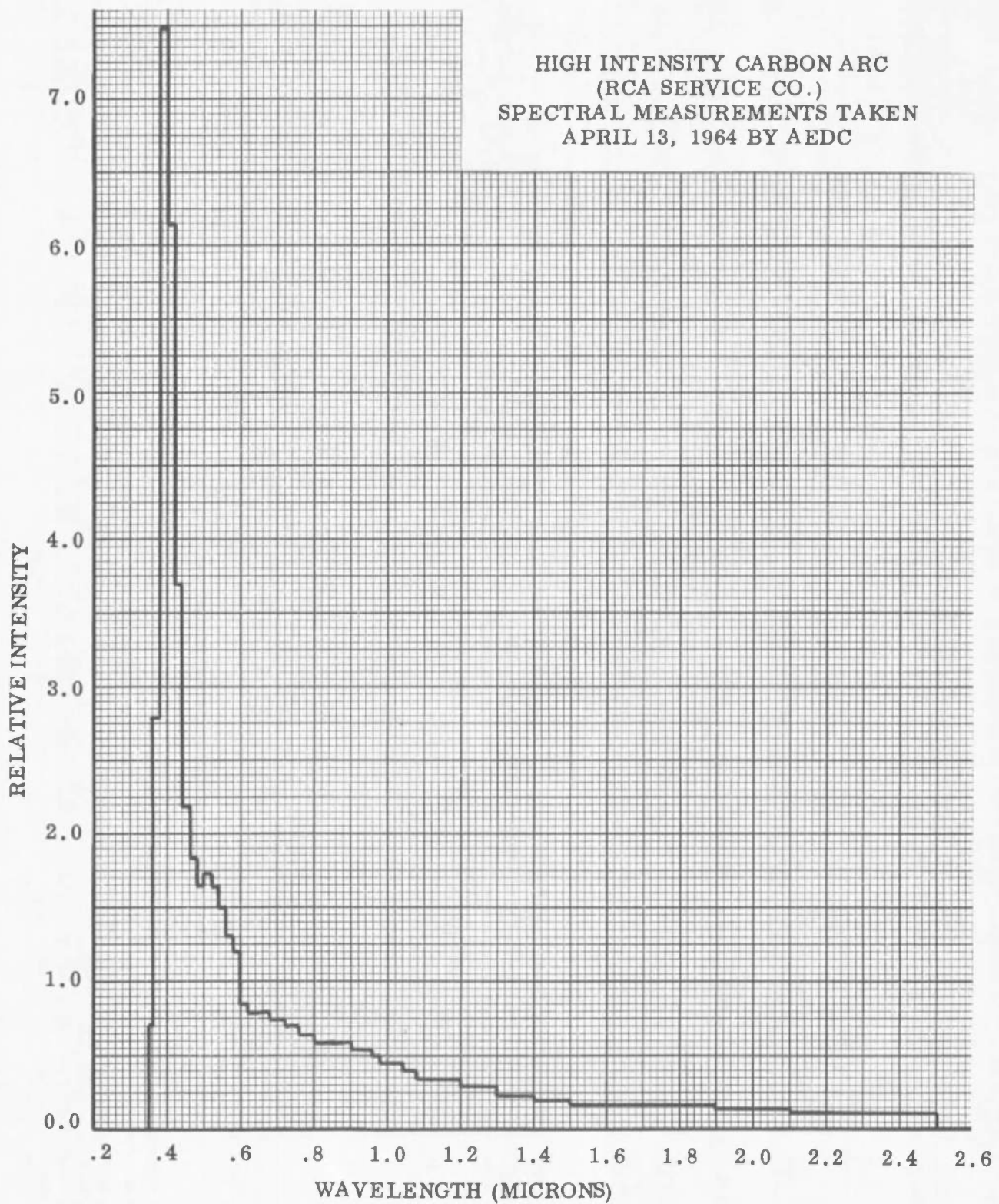


Figure 5-51. Spectrum of High Intensity Carbon Arc (Spectral Criterion IIA)

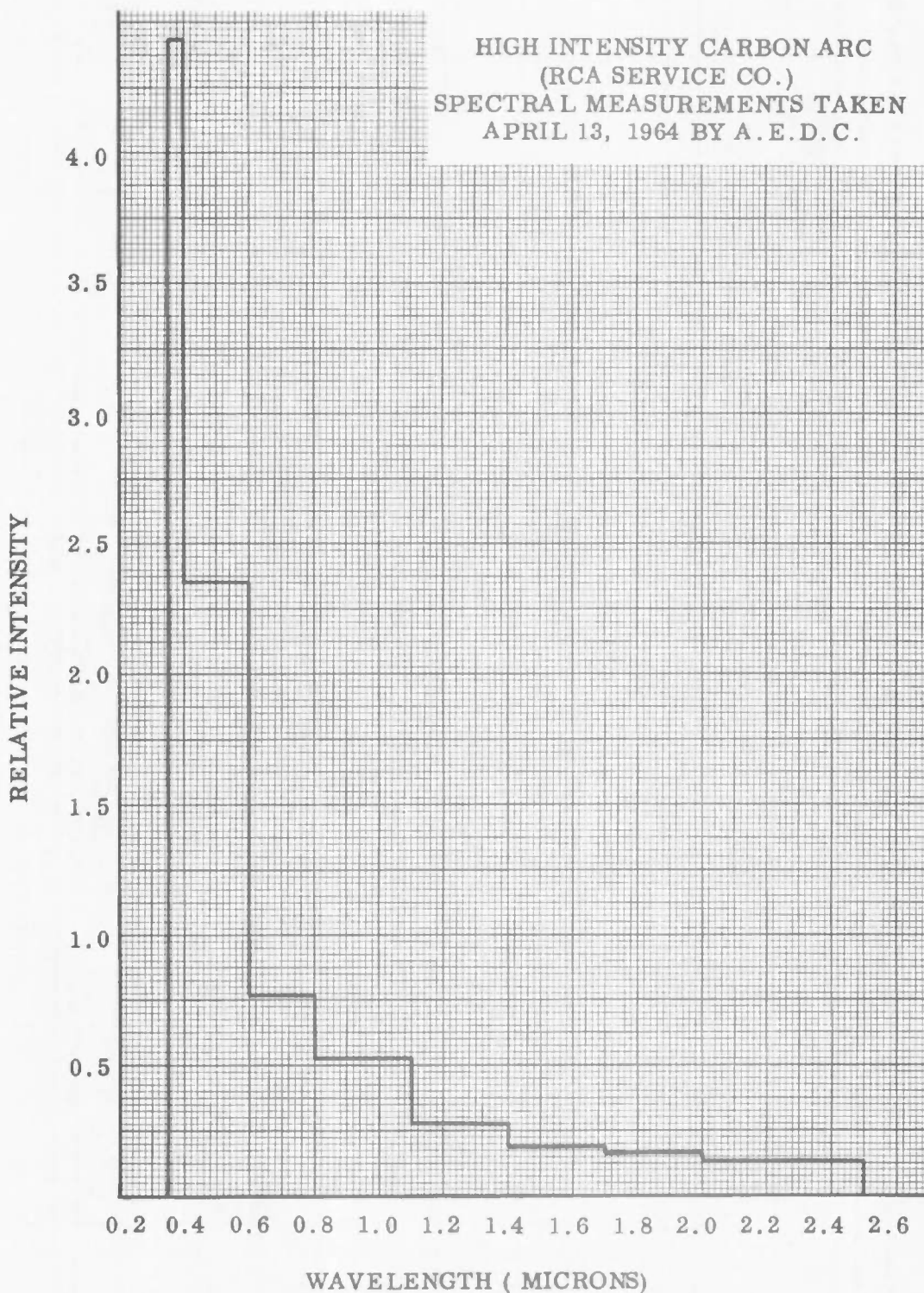


Figure 5-52. Spectrum of High Intensity Carbon Arc (Spectral Criterion II B)

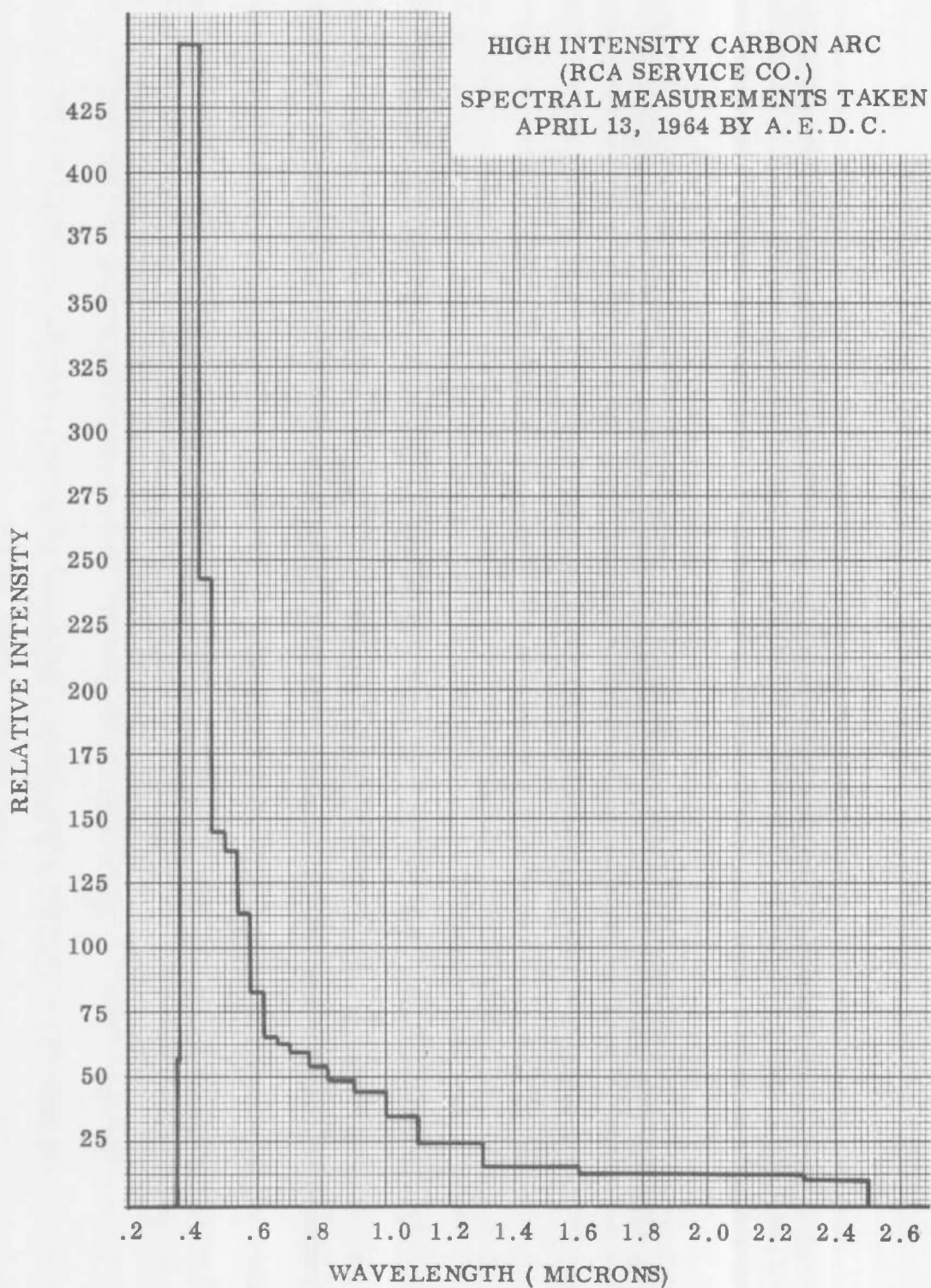


Figure 5-53. Spectrum of High Intensity Carbon Arc (Spectral Criterion III)

FLUID TRANSPERSION ARC
(VITRO LABORATORIES)
OPERATED AT
75 VOLTS, 500 AMPS, 37.5 KW
100% ARGON
200 PSIG PRESSURE

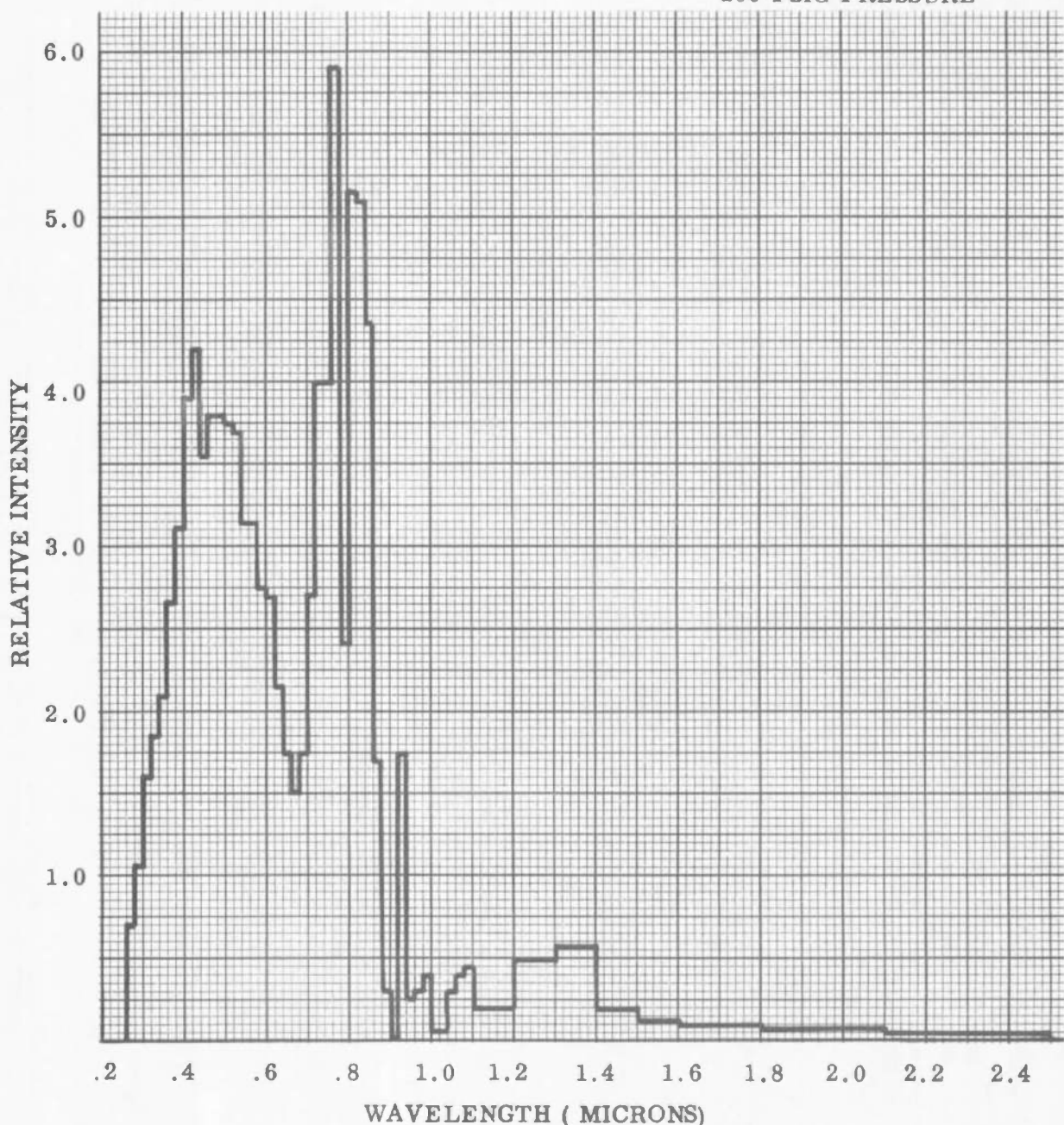


Figure 5-54. Spectrum of Fluid Transpiration Arc When Operated at 37.5 KW
(Spectral Criterion IIA)

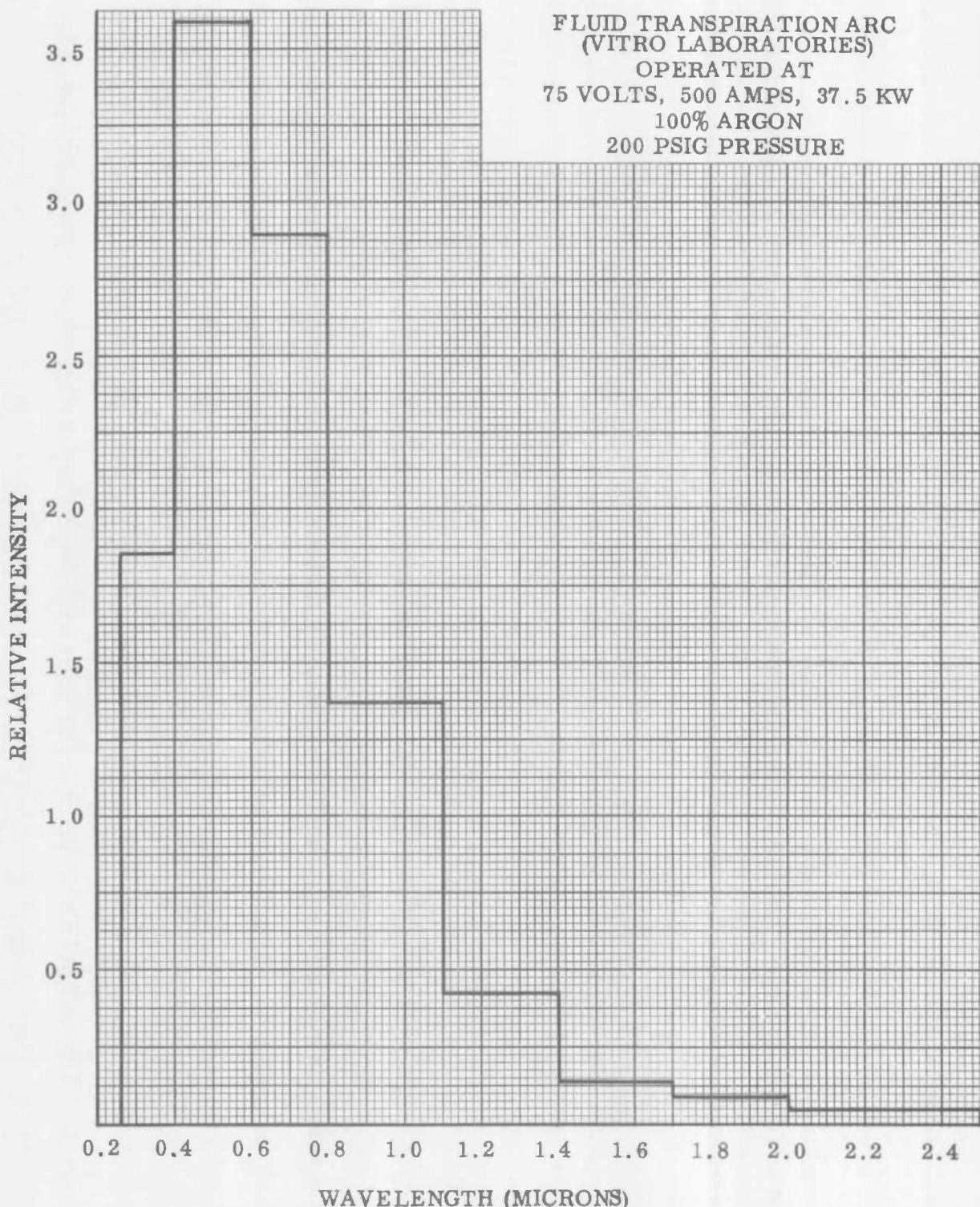


Figure 5-55. Spectrum of Fluid Transpiration Arc When Operated at 37.5 KW (Spectral Criterion IIB)

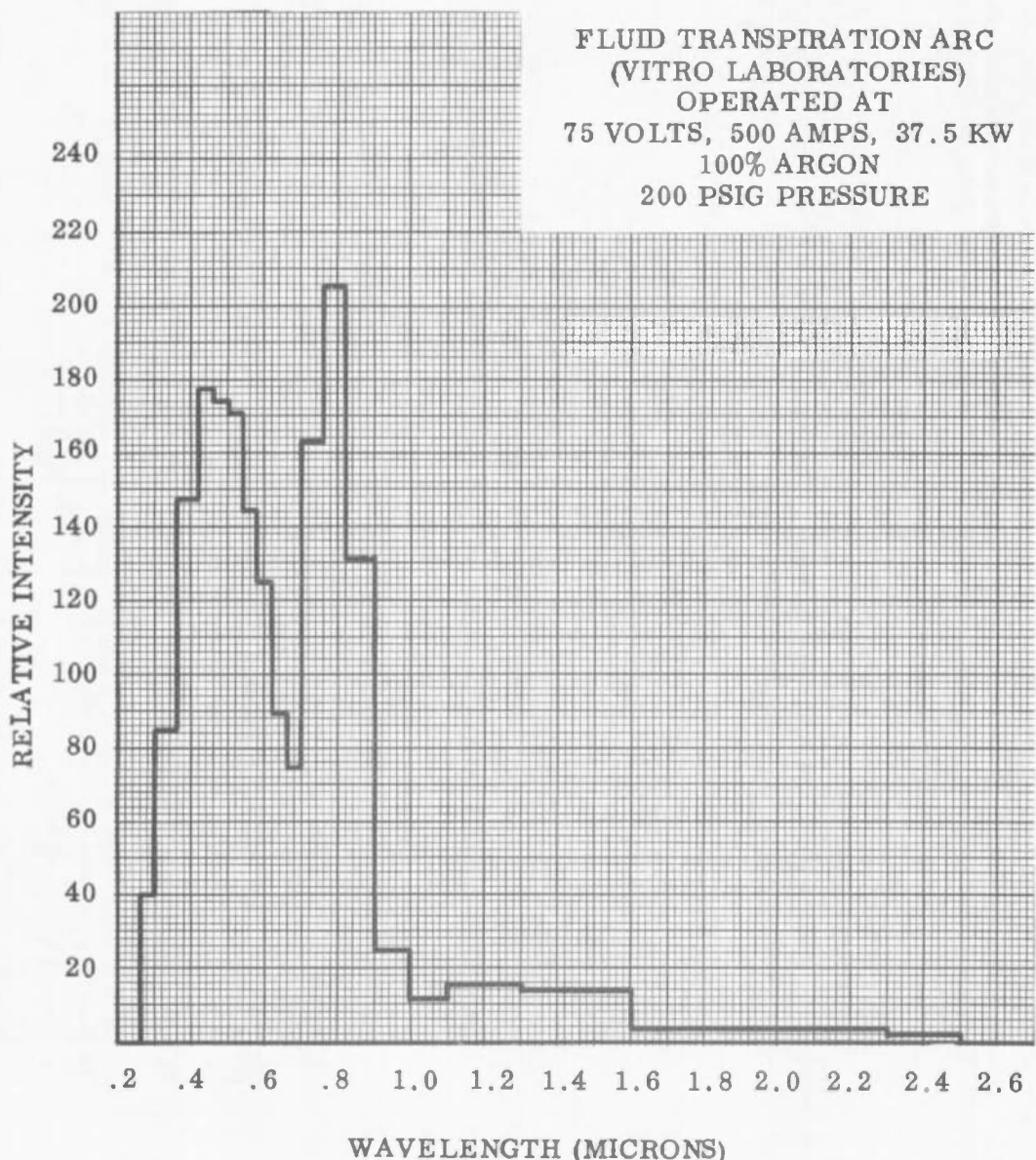


Figure 5-56. Spectrum of Fluid Transpiration Arc When Operated at 37.5 KW (Spectral Criterion III)

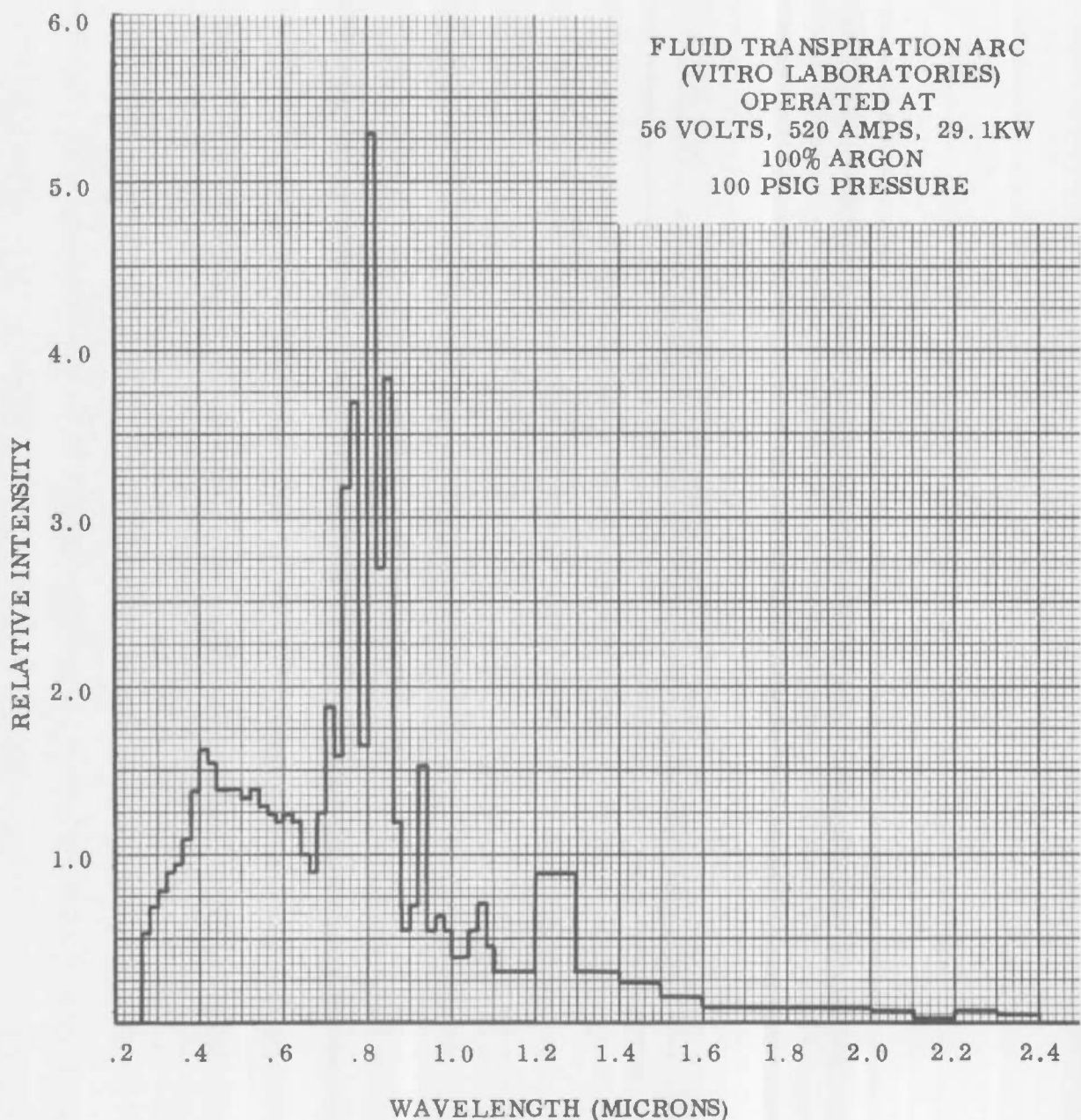


Figure 5-57. Spectrum of Fluid Transpiration Arc When Operated at 29.1KW
(Spectral Criterion IIA)

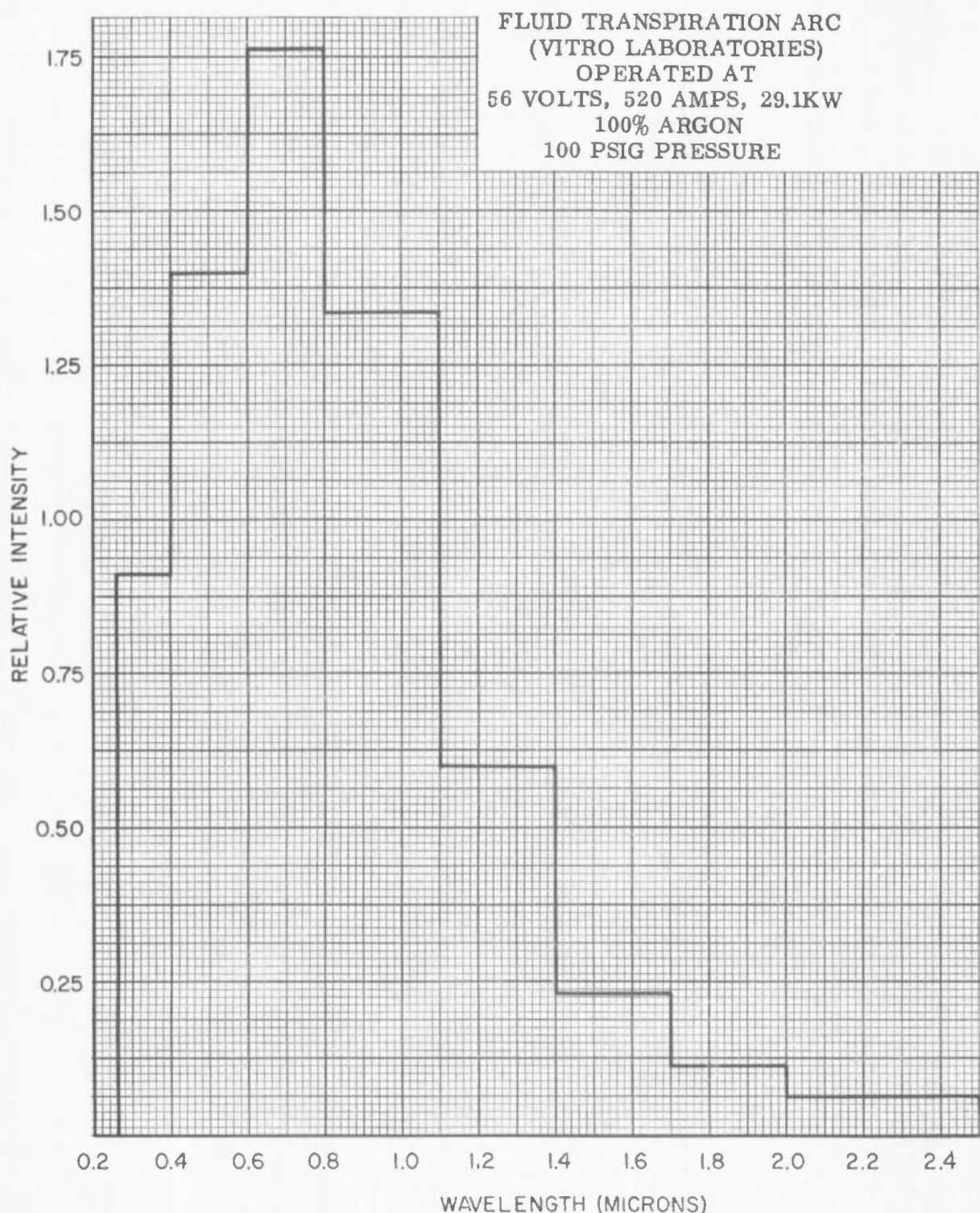


Figure 5-58. Spectrum of Fluid Transpiration Arc When Operated at 29.1 KW (Spectral Criterion IIB)

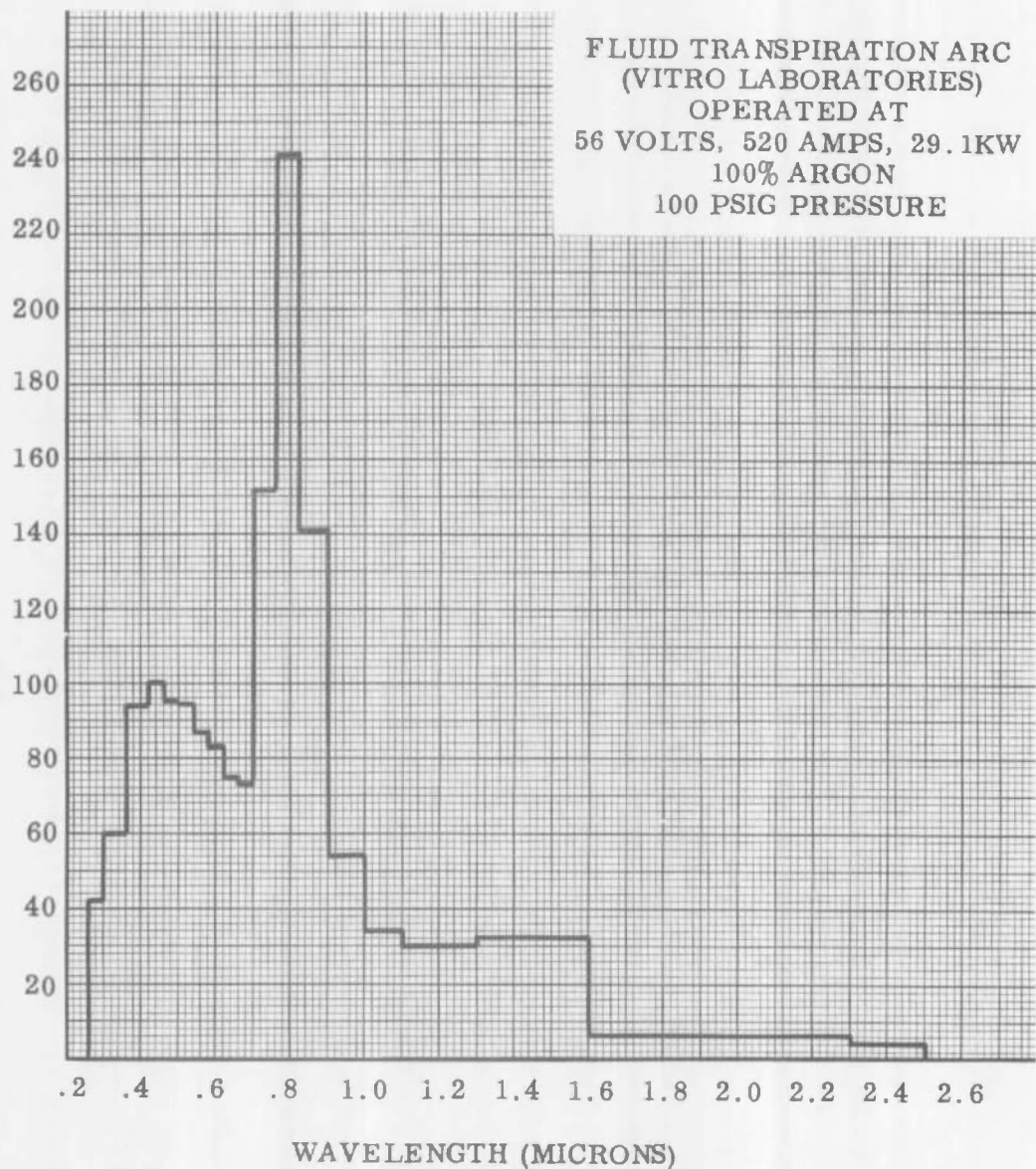


Figure 5-59. Spectrum of Fluid Transpiration Arc When Operated at 29.1KW
(Spectral Criterion III)

Table 5-24. Percent of Energy and Relative Intensity in Each Indicated Wavelength band of the Indicated Radiation Sources (Spectral Criterion III)

Wavelength Band (Microns)	Percent of Energy in Wavelength Band			Relative Intensity in Wavelength Band		
	Fluid Transpiration Arc		High Intensity Carbon Arc	Fluid Transpiration Arc		High Intensity Carbon Arc
	37.5 KW	29.1 KW		37.5 KW	29.1 KW	
0.26 - 0.30	1.60	1.70	No Data	40.00	42.50	No Data
0.30 - 0.36	5.08	3.60	0.57 *	84.67	60.00	57.00*
0.36 - 0.42	8.84	5.64	26.76	147.33	94.00	449.00
0.42 - 0.46	7.10	4.01	9.70	177.50	100.25	242.50
0.46 - 0.50	6.96	3.81	5.69	174.00	95.25	142.25
0.50 - 0.54	6.83	3.78	5.48	170.75	94.50	137.00
0.54 - 0.58	5.77	3.47	4.54	144.25	86.75	113.50
0.58 - 0.62	4.99	3.33	3.29	124.75	83.25	82.25
0.62 - 0.66	3.57	2.99	2.60	89.25	74.75	65.00
0.66 - 0.70	2.98	2.92	2.50	74.50	73.00	62.50
0.70 - 0.76	9.80	9.11	3.56	163.33	151.83	59.33
0.76 - 0.82	12.32	14.48	3.23	205.33	241.33	53.83
0.82 - 0.90	10.49	11.28	3.89	131.13	141.00	48.63
0.90 - 1.00	2.47	5.44	4.36	24.70	54.40	43.60
1.00 - 1.10	1.15	3.40	3.42	11.50	34.00	34.20
1.10 - 1.30	3.11	6.00	4.83	15.55	30.00	24.15
1.30 - 1.60	4.15	9.75	4.73	13.83	32.50	15.77
1.60 - 2.30	2.40	4.42	8.66	3.42	6.31	12.37
2.30 - 2.50	0.37	0.87	2.19	1.85	4.35	10.95

* 0.35μ-0.36μ wavelength band

Table 5-25. Maximum efficiency with which the spectrums of the indicated sources can be filtered to match the source spectrums required, after spectral filtration, for each indicated optical system configuration (Spectral Criterion III)

N = Number of lenses

M = Number of mirrors

T = Thickness of infrasil (inches)

$\Delta\lambda$ = Bandwidth of minimum filtration (microns)

η = Maximum filtration efficiency (percent)

Optical System Configuration			Fluid Transpiration Arc 100% Argon				High Intensity Carbon Arc	
			37.5 KW 200 PSIG Pressure		29.1 KW 100 PSIG Pressure			
N	M	T	$\Delta\lambda$	η	$\Delta\lambda$	η	$\Delta\lambda$	η
4	3	4.0	1.00 - 1.10	27.38	0.62 - 0.66	55.45	0.62-0.66	48.21
4	3	6.0	1.00 - 1.10	27.45	0.62 - 0.66	55.66	0.62-0.66	48.40
4	3	8.0	1.00 - 1.10	27.51	0.62 - 0.66	55.87	0.62-0.66	48.58
4	4	4.0	1.00 - 1.10	28.75	0.62 - 0.66	54.25	0.76-0.82	45.73
4	4	6.0	1.00 - 1.10	28.75	0.62 - 0.66	54.44	0.76-0.82	45.89
4	4	8.0	1.00 - 1.10	28.89	0.62 - 0.66	54.64	0.76-0.82	46.01

Table 5-26. Maximum and Probable Dissipative Efficiencies of the indicated Source, Optical-System, Spectral-Filter Combinations

N = Number of Lenses

M = Number of Mirrors

T = Total Thickness of Infrasil (inches)

k_{max} = Maximum Dissipative efficiency

$k_{prob} = 0.9 k_{max}$ = Probable Dissipative Efficiency (percent)

Optical System Configuration			Fluid Transpiration Arc				High Intensity Carbon Arc	
			37.5 KW - 200 PSIG Pressure		29.1 100 PSIG Pressure			
N	M	T	k_{max}	k_{prob}	k_{max}	k_{prob}	k_{max}	k_{prob}
4	3	4.0	13.28	11.95	26.90	24.21	23.39	21.05
4	3	6.0	13.15	11.83	26.66	23.99	23.18	20.86
4	3	8.0	13.00	11.70	26.41	23.77	22.96	20.66
4	4	4.0	12.08	10.87	22.80	20.52	19.22	17.30
4	4	6.0	11.93	10.74	22.59	20.33	19.04	17.14
4	4	8.0	11.84	10.66	22.39	20.15	18.85	16.97

efficiency (table 5-10) determined for the various optical system configurations. The parameter k_{prob} represents the probable dissipative efficiency of each source, optical-system, spectral-filter combination and was defined by assuming a 10% safety factor.

SECTION 6

OPTICAL SCHEMATA

6.1 SUMMARY OF MODULAR SCHEMATA TO BE STUDIED.

The various collection, transfer, and collimation subsystems which are the building blocks of all the optical system designs to be considered in this study are described in this section. A logical roadmap which connects these various concepts is illustrated in figure 6-1. In Section 7 the relative merits of various combinations of these several collector, transfer and collimator optical subsystems will be considered. Among the factors to be considered, in addition to the parameterization of the various combinations, are efficiency, adaptability to the three source types connected with this study, and the general practicability and functional utility of the optical design itself. Although every conceivable type of solar simulator optical system cannot be represented by combinations of the schemes to be presented, these nevertheless represent the major basic optical system concepts possible for utilization in a multi-modular array. Slight variations on these may be undertaken in any final design resulting from this study; however, most of the information gained in this study is applicable to the numerous possible minor alterations in detail design. Multiple source modules were not made a part of this study but consideration has been given to an array whereby one source serves more than one module in the discussion of uncollimated projection systems. Because of the exceptionally high power associated with the several light sources being evaluated, multiple source modules would become large scale solar simulators in themselves, making them impractical from the production standpoint; therefore, any discussion of such systems would be for reference only.

In addition to the uncollimated projector array, an array of simple paraboloids, each with a source mounted at its focus, and certain combinations of the optical subsystems to be described in this section will be treated in detail in Section 7. These include:

1. The basic conic section collector, relay, lens, and Cassegranian collimator
2. The same with the inclusion of the multifaceted relay lens
3. The pebble bed and paraboloidal collimator, simple relay lens and conic collectors
4. The source aperture subsystem using a multiaxis collection scheme with superimposed arc images
5. The first with the insertion of condenser lenses
6. The same with higher order correction terms on the Cassegrainian elements to control the distribution and reduce spherical aberration

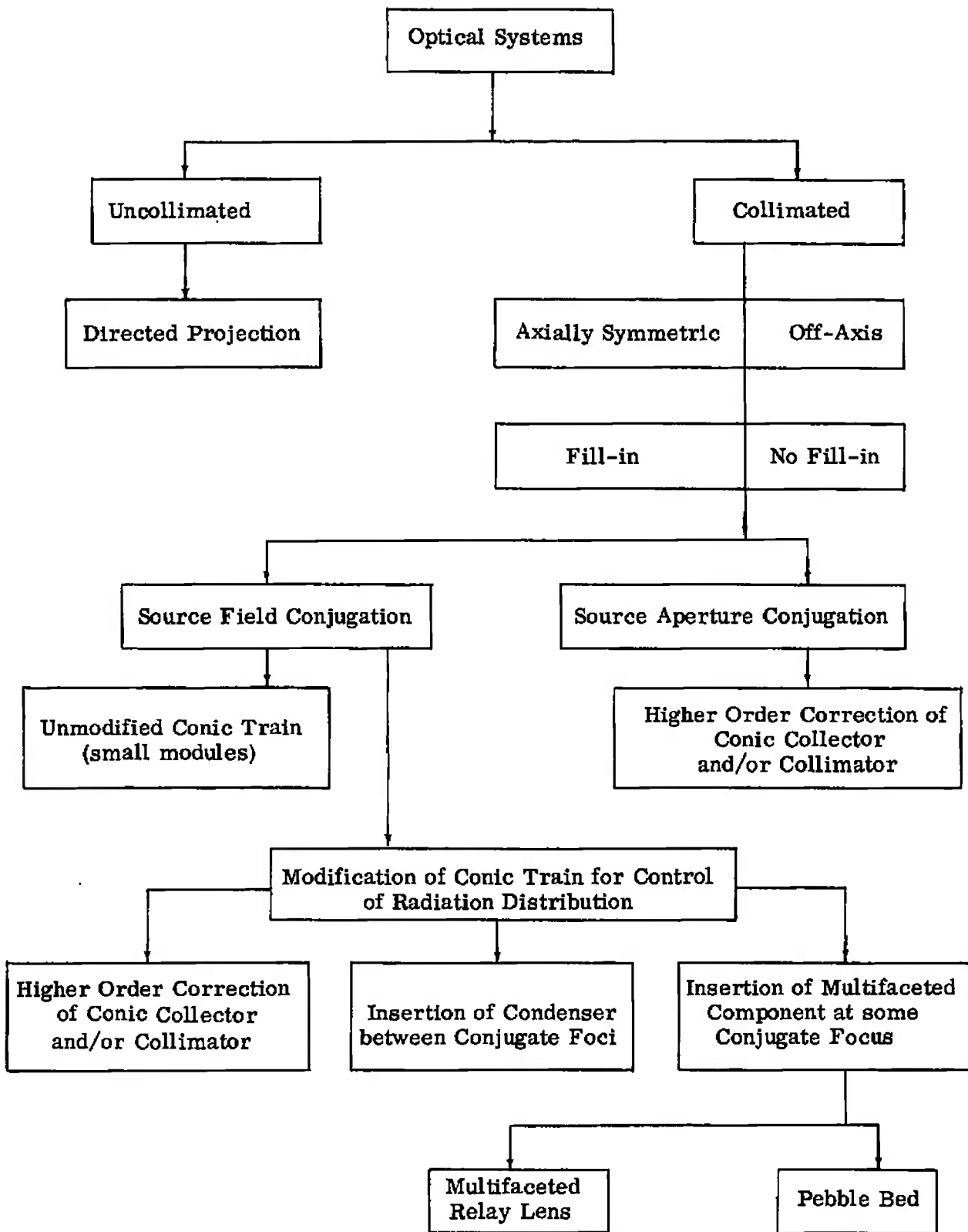


Figure 6-1. Optical System Concepts

7. The same again, with higher order terms on the collector conic sections as well
8. The sixth and seventh with the elimination of the condenser lenses.

Several collection schemes will be studied separately including the Fresnel collector, multiaxis collector with superimposed and separate images, and the various combinations of conic sections for single-ended arc collection. The integrated aspects of modular dynamics will be treated separately in the discussion of the simple paraboloid array using that array as a standard. The criteria for modular performance will be studied at that point.

6.2 UNCOLLIMATED SYSTEMS

It is possible to construct an array of modules which project uncollimated light in a manner analogous to ordinary theater projection equipment and achieve, under ideal conditions, the properties of invariant and directed field angle and uniform solar intensity. Such a radiation field, although it is truly uncollimated, does possess all the thermal-radiative influences and characteristics essential to thermal balance testing of a space vehicle. It could not, however, display the interference and/or polarization properties inherent in the solar or collimated radiation field. Since these effects are unimportant to environmental testing, it follows that the collimation specification found in every list of solar simulator requirements is not, of itself, a principal necessity. In fact, it is not even a sufficient condition, but merely parallels the manner in which uniformity of intensity is achieved in the actual environment over limited volumes at great distances. The characteristics of an array of uncollimated modules (projectors) will be treated at length in Section 7.

6.3 COLLIMATED SYSTEMS

6.3.1 General Characteristics.

The remainder of the optical systems to be discussed fall into the category of collimated systems. It was seen earlier (Section 4.1) how the property of collimation, in the context of the definition used herein, was a necessary condition for uniformity in depth for the general optical module. Since collimation is not required for the projection array, but is required for modules whose apertures cover the entire array, it might be well to discard this feature as a fundamental parameter and examine one which may be more universally applied. Such a parameter is the field angle of the system. Uniformity in depth can only be achieved by virtue of the invariance of total effective field solid angle throughout the volume in question. When the radiation exit pupil of the optical system is smaller than the aperture of the last optical element, then the property of collimation, or imaging an infinity, is the only way to achieve the required field solid

angle invariance in depth. It should be noted that, because of the optical aberrations, this condition is not guaranteed by collimation. On the other hand, as is shown in the treatment of projection-type modules, when the radiation exit pupil completely fills the module exit apertures, then the basic requirement for uniformity in depth is that the modular array simulate a Lambertian surface where the radiance falls off as the cosine of the angle to the local surface normal. This point will be proven later. When the apparent field is held fixed by appropriate masking of each module, then all of the necessary conditions are met without the requirement for collimation, on a theoretical basis as well as a practical one provided enough modules are seen within the field of view. The essential point to be made here is that, for collimated systems, the property of collimation is a necessary but not a sufficient condition. In the case of uncollimated systems, specially designed for the purpose, collimation is neither necessary nor sufficient.

Thus, with the understanding that the collimated system types to be discussed throughout most of what follows represents one branch of two possible concepts, the following analysis is made. Because a commitment to this approach elevates the property of collimation to the level of a fundamental requirement, the absence of spherical aberration also becomes an essential requirement. This is because collimation over the entire aperture is not possible in the presence of spherical aberration.

The basic definition of a collimated system can be stated, for all practical purposes, from a physical point of view as follows:

1. A lens or mirror is used as the last optical component to face the test volume and whose aperture or array of several apertures completely covers the projected surface facing the test volume.
2. This last component has a well-defined effective focal length corresponding to the principal focal position as defined by the condition that all rays emanating from this position are rendered mutually parallel after entering and leaving the collimating component. This implies that the collimator is properly free of spherical aberration.
3. The source must be located at the principal focal point and to satisfy the strict definition must have negligible extension along the optic axis. The source referred to here does not have to be the real source but could be a source image or some pseudo-source constructed from optical transfer of intermediate images. The source located at the collimator focus must, nevertheless, satisfy the requirement that each point, located within its boundaries, radiates to all points on the collimator.

6.3.2 Hexagonal Array of Paraboloidal Reflectors.

In the face of this operational definition of the collimator system, the simplest possible type would be to locate the real source at the focus of a collimating lens. For all practical purposes, this could also be a paraboloidal mirror. This basic collimating system has also been analyzed in section 7. An array of such paraboloids and sources constitutes the most basic of the collimated systems.

Although the simple paraboloid is a true collimating element, free from spherical aberration with respect to its principal focus, it still does not provide total compensation for nonuniformity of intensity throughout the target volume. It is quite difficult to realize high efficiency and good uniformity simultaneously. There is no guarantee that more complicated systems will yield a better result than that obtained with the simplest concept of a paraboloid array. Nevertheless, more sophisticated systems will be examined for the purpose of determining whether or not it is possible to obtain a somewhat higher level of performance than is realized with the simple paraboloidal collimator. Because the latter does not have any transfer optics, it is particularly difficult to provide for spectral filtration and, in some cases, this may be reason enough to consider systems with transfer optics in which spectral filtering components may be incorporated.

6.3.3 Optical Subsystems.

6.3.3.1 Subsystem Categories.

In spite of any additional complexities, ultimate collimation of some type of reference source is retained as a basic ingredient in all the optical systems in the collimated classification. It is possible to subdivide such systems into the following three subsystem categories.

1. Primary Collection Subsystem. These components serve to collect as much of the radiation from the lamp as possible and establish a reference beam which can be transferred into the collimation subsystem. They are the first components to face the source.
2. Illumination Transfer Subsystem. This subsystem collects the beam coming from the primary collection subsystem and, without vignetting, establishes the entrance pupil to the collimation subsystem through which it delivers the beam. This subsystem lies between the primary collection subsystem and the collimation subsystem. It acts also as a modifier between the two subsystems in order to produce uniformity and vignetting control.

3. **Collimation Subsystem.** This part of the system collimates the light coming from a reference entrance pupil located at the first principal focal point of the collimation subsystem. It is the last element of this subsystem which faces the test item in the chamber.

6.3.3.2 Collection Subsystems

Because of the size contemplated for the solar simulators which may be based upon this study, it is not thought feasible to consider totally refracting collecting lenses. The necessity of exacting the highest possible collection efficiency from these components is an additional reason for the use of reflecting components as the primary collector. Lenses cannot be designed with what amounts to an adequate numerical aperture (lens speed) compatible with the collection requirements of a solar simulation system.

There are basically five types of collection schemes to be studied. The division or classification is somewhat arbitrary and some overlap is possible; however, the radiation characteristics of the source itself (which derive from the electrode configuration) constitute the most fundamental distinction. A source which maintains the arc between two opposing electrodes shall be referred to as a two-ended or double-ended source. A source which maintains the arc directly in front of one electrode or the other with the remaining electrode removed from the direct radiation path shall be referred to as a single-ended source. The two-ended source radiates primarily about the equatorial plane with respect to the common axis of the two electrodes. There is no appreciable radiation within about 30° of this axis in either direction. The single-ended sources, on the other hand, radiate principally into the forward hemisphere with respect to the direction which the arc supporting electrode faces. There is little radiation passed beyond 90° from the axis of this electrode, i.e., in the backward direction. Because of this basic distinction in source radiation characteristics, there are two basic collector optical configurations. The five collector types, each adaptable to one-ended or two-ended sources are: (1) basic conic section, (2) higher order correction on conic section, (3) Fresnel collector, (4) multiaxis common collimator, (5) multiaxis multi-collimator or projector.

These basic collector types will be discussed in turn. One has, for the conic section, with the two-ended source, a simple ellipsoid, with the arc located at the focus nearest the vertex providing an image at the second focus. The single-ended configuration requires two conic section mirrors in order to bypass the supporting structure behind the arc-sustaining electrode. These can consist of two paraboloids facing each other with the source located close to the vertex of one and at the

focus of the other, and with the source image occupying a similar but reciprocal position. It is also possible to employ a concave ellipsoid in combination with a convex hyperboloid or a concave hyperboloid and a concave ellipsoid. These configurations are depicted in figure 6-2. Although it is possible to contrive far more complicated arrangements of conic sections for collection of the source radiation and subsequent image formation, those mentioned above represent the simplest choices consistent with the highest efficiency. The selection of a particular combination of conic sections is made to minimize the central hole in the beam and provide a convenient mechanical geometry. On a first order basis, all conic section collector designs are equivalent although there are some differences in higher order compensation. Therefore, there is little to choose between one design consisting of conic sections located in conjugate relationship to one another and any other conic section design similarly conceived. The detailed parameterization of the conic section subsystems selected for collection of the one-ended and two-ended arcs will be discussed later.

The second type of collection subsystem is actually based on the first in that it consists of higher order corrections on conic sections, involving deformation of the surfaces to control flux distribution. These deformations are introduced either in the form of a power series of aperture coefficients or as the solution of a defining differential equation. Spherical aberration is automatically introduced by this process and it is always necessary to deform a second reflecting surface in order to compensate. In the two-ended case, cancellation of spherical aberration must be provided either by the transfer optics or the collimator. In the single-ended case, having two reflecting collector components, spherical aberration can be totally compensated for in the collection elements alone, although this is not essential. The procedure for this will be demonstrated in Section 7.

The third type of collection subsystem is called a Fresnel collector because it is based upon the concept of individual zonal segments each physically separate from the other. Each zone is coaxial with the rest and all share common foci, both conditions also being properties of the radial zones of an ordinary conic surface of revolution. The principal difference is that the Fresnel mirror is made up of separate ring sections so placed as not to interfere with each other either physically or optically and so designed that the magnification of each zone is maintained within prescribed lower and upper bounds. This is accomplished by varying the eccentricity from one zone to the next and maintaining each zone in the form of a true ellipsoid. Spherical aberration is not introduced by the optical component, but compensation for flux distribution is obtained by altering the eccentricity of the conic section at discreet zones. The eccentricity of each zone is defined by the

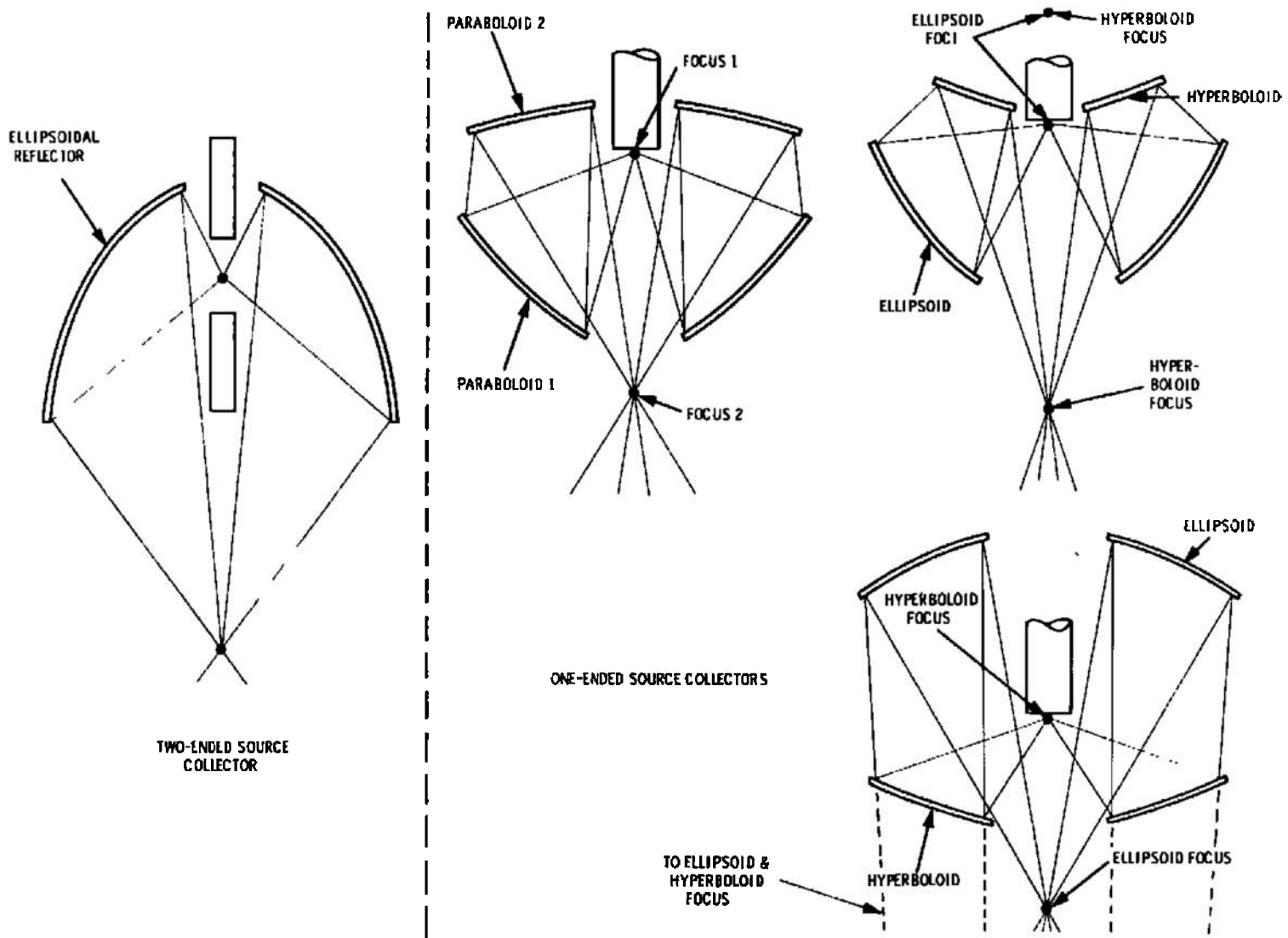


Figure 6-2. Basic Collector Types

magnification of that zone for its particular aperture radius. The purpose of this is the elimination of one of the most dominant effects leading to nonuniformity, namely coma, in the very fast collection optics. The Fresnel collector is illustrated schematically in figure 6-3. One of the most important considerations with regard to the Fresnel collector is its efficiency when weighed against the uniformity compensation obtained thereby. This problem will be handled quantitatively in Section 7. The Fresnel collector may be employed in other ways. With respect to the aperture transfer type of illumination transfer subsystem, the Fresnel zones may be used to form multiple source images as required at the field lens component in such a transfer system.

The fourth type of collection scheme consists of an array of many collector elements, each possessing its own optic axis. Such a collection scheme may consist of a combination of flat mirrors and either lenses or off-axis sections of ellipsoids surrounding the source, each forming its own source image. These source images are superimposed and transferred to a single collimator system. Such a collection concept is useful when used with the aperture transfer concept which requires multiple arc images at the field element. The details of this collection concept are illustrated in figure 6-4. The basic concept lies in establishing a number of virtual source images by the use of multiple flat mirror elements. These virtual images are then picked up by the appropriate optical component, either refracting or reflecting, and a secondary image formed thereby. Although this collection scheme may appear physically complicated, it has a number of distinct advantages which will be detailed in Section 7.

The fifth general category of collection optical subsystems also makes use of multiaxis collection optics; however, the secondary images formed by the separate collectors are not superimposed. They are rather delivered to separate collimator or projection optics. It will be seen that, in the case of the projection optics, this expedient is necessary in order to increase the number of modules without increasing the number of sources required. The large number of modules is required in order to smooth the distribution. The same device may also be employed with the simple collimation subsystem in order to reduce the required speed of the latter while maintaining total system efficiency at a high level. The whole concept of a single-source multimodular systems derives from the desire to maintain high efficiency while gaining uniformity through the use of more and smaller modules and correspondingly lower optical speeds.

In summary of the collection optical subsystem concepts, we find a basic consistency which runs throughout. This derives from the

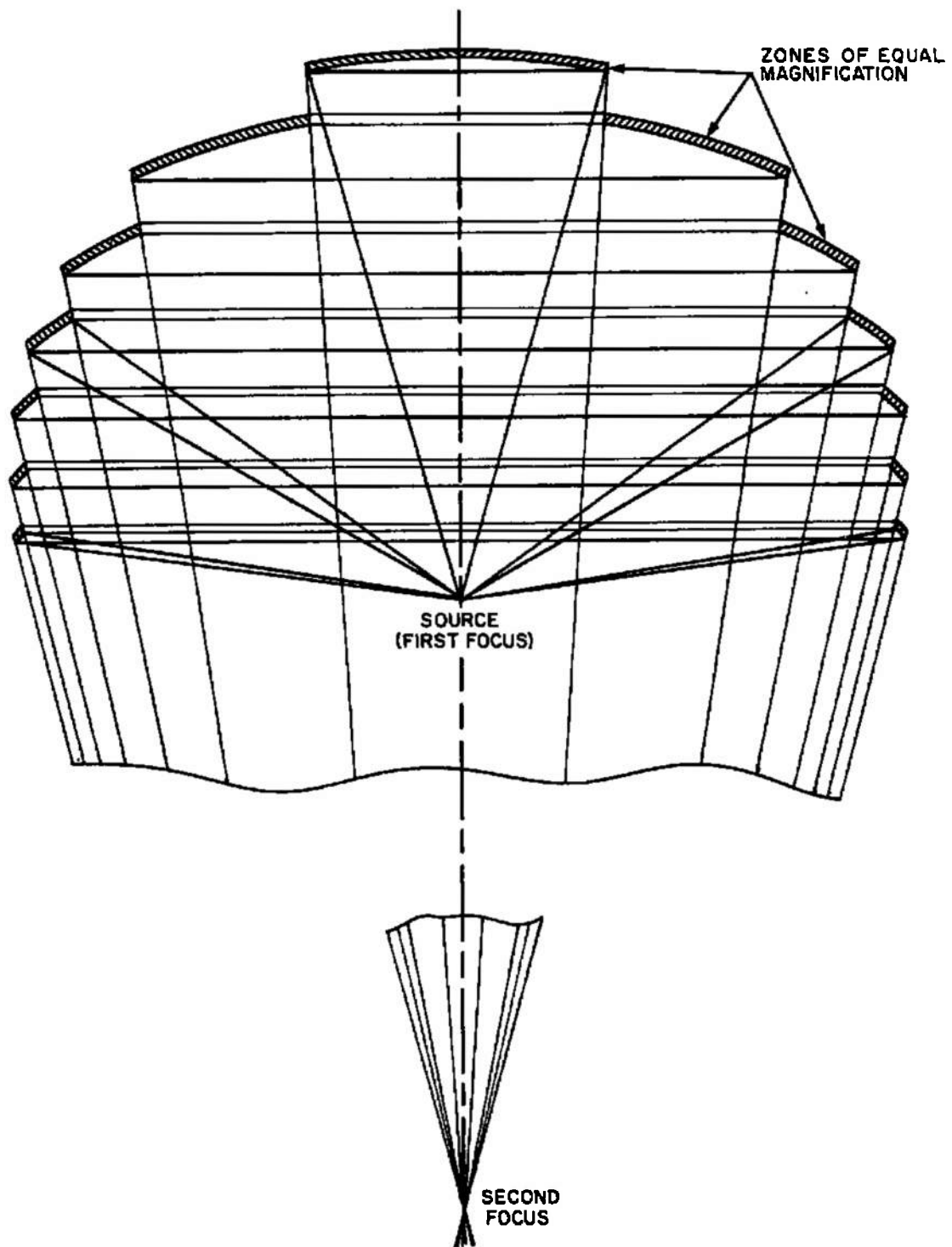


Figure 6-3. A Fresnel Collector

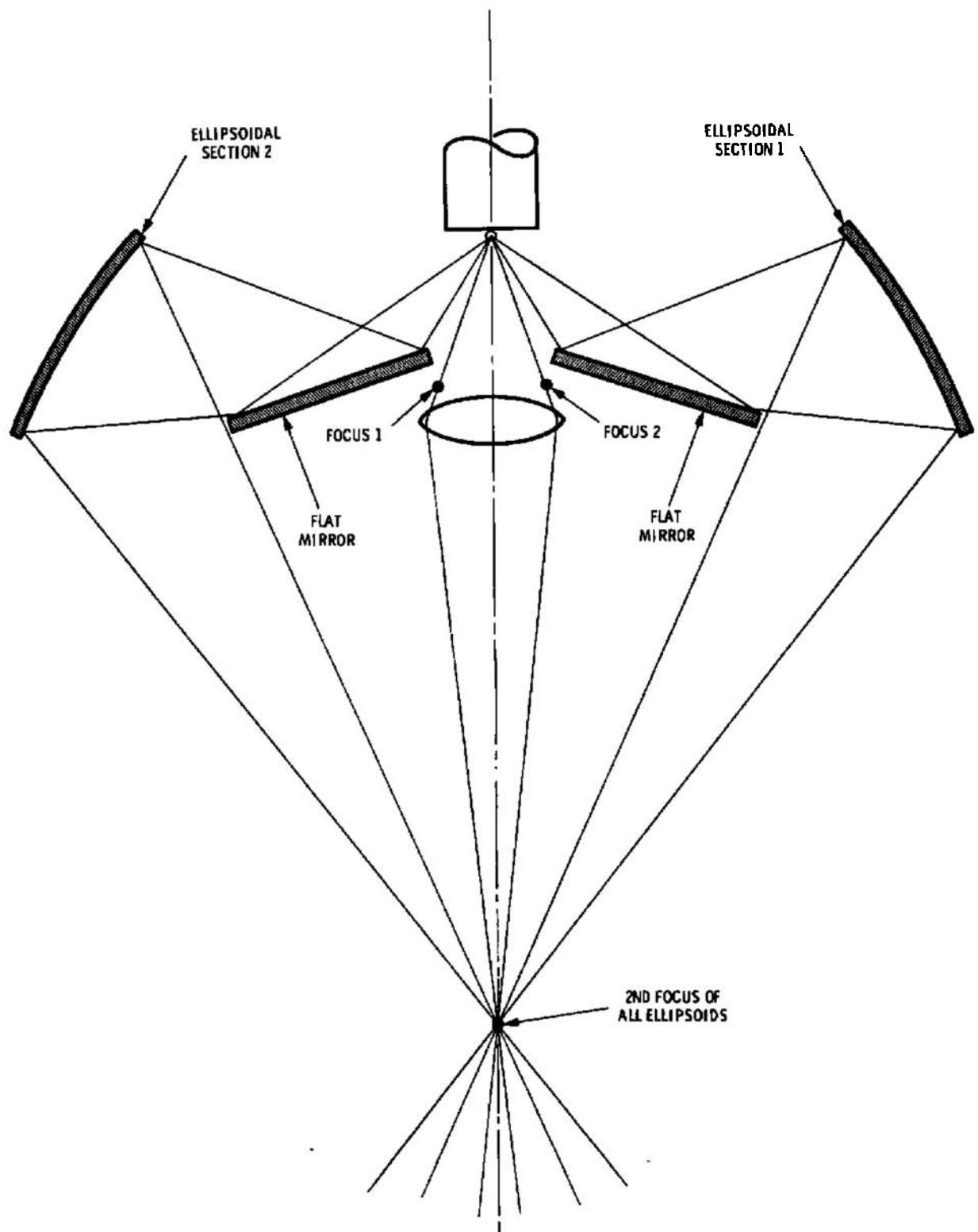


Figure 6-4. A Multifaceted Collector

essential purpose of the collection subsystem, namely to surround the source radiation, gather it and redirect it to a localized region in space or a finite number of localized regions in space. These regions we may refer to as secondary source images. The collection subsystem then acts much the same way as a condenser does in an ordinary projection system.

6.3.3.3 Transfer Subsystems.

The transfer subsystems, which we shall discuss in the following paragraphs, operate either at the secondary source image formed by the collector and the reference source position for the collimator simultaneously, or between these two positions in such a way that as much as possible of the light gathered by the collector is effectively used by the collimator. Thus, the purpose of the transfer subsystem is to form an isomorphic mapping of collector boundaries onto collimator boundaries, as well as to establish exit and entrance pupils with respect to these initial and final subsystems respectively.

Transfer optical subsystems may be divided into the two categories which were discussed previously in Section 4; (1) source aperture conjugation and (2) source field conjugation. There is only one optical design that need be considered with regard to source aperture conjugation, which involves a mapping of the source boundaries onto the aperture of the collimator subsystem. It should be noted that, for a number of reasons, such a subsystem is ineffective unless used with either a multiple bank of sources and collectors (which have been ruled out in the design of these modules), or with the multiaxis, single-collimator collection concept. This transfer subsystem uses a field element with respect to a projection lens in such a way that if the secondary source images are superimposed at the field element then the bank of collector optics is mapped onto the projection lens entrance pupil. The projection lens then projects the boundaries of the field element onto the aperture of the collimator. The projection lens itself acts as the reference source for the collimation system. A prescribed intensity distribution over the field element may be defined, which in conjunction with the projection lens, would produce a uniform intensity cross-section in the final beam for a given collimator. This problem will be treated analytically in Section 7. A schematic illustration of the source aperture transfer optics, as described herein, is shown in figure 6-5. This system has certain advantages by virtue of its indifference to the radiance distribution of the source, because each direction from the source is ostensibly superimposed upon every other by virtue of the superposition of source images. Thus, symmetry of the radiance distribution ceases to be an important question. On the other hand, one relies more heavily upon the basic smoothness and

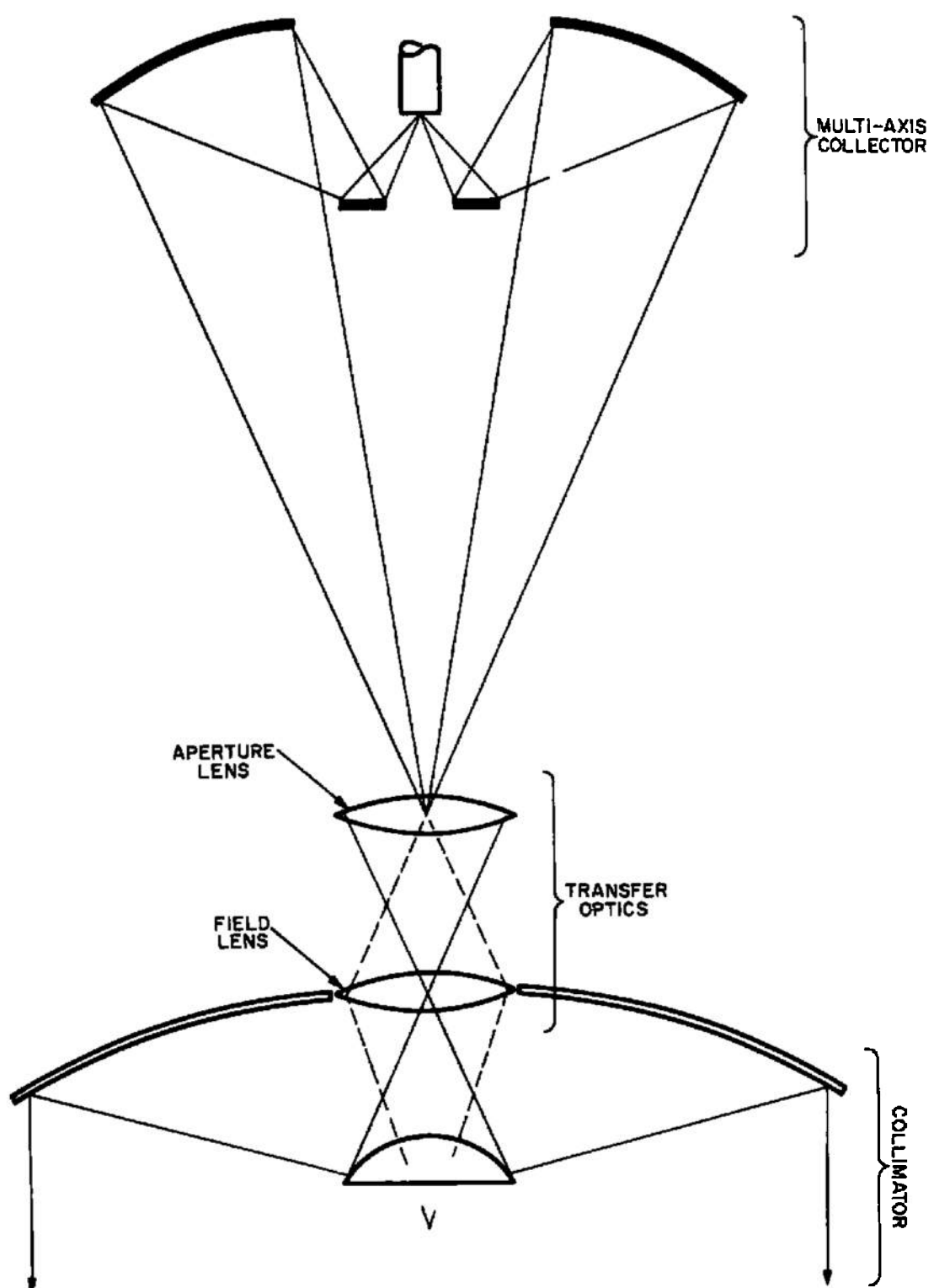


Figure 6-5. Source Aperture Transfer Optics

stability of the microbrightness distribution of the source itself. If the source image is superimposed many times upon itself in different orientations, even this factor becomes minimal. There are, therefore, significant advantages to such a system, its inherent complexities notwithstanding. These complexities derive from the fact that, although the distribution one obtains at the field element by virtue of superimposed arc images may be relatively stable, it may not be altogether a simple task to generate the appropriate intensity distribution across this element in order to effect the desired uniformity in the collimated beam. This question will be examined in greater detail in Section 7.

It is to be noted that with one exception, all transfer subsystem optics being proposed here consist of refracting elements as opposed to the reflecting components applied for the collection and collimation subsystems. The sole exception is the pebble bed hyperboloid which is a mirror transfer element to be discussed shortly. The remaining transfer optical subsystems to be covered fall in the category of source field conjugation in that it is the source or the source image which is ultimately imaged at infinity or collimated. Within this category four types of transfer optical subsystems will be considered. These are (1) condenser system and relay lens, (2) simple relay lens, (3) multi-faceted relay lens (optical integrator) (4) pebble bed, i.e., multi-faceted array of hyperboloids. With the source aperture conjugation subsystem, consisting of a field element and projection lens, this makes five possible transfer optical subsystems to choose from.

6.3.3.3.1 Condenser system and relay lens.

The features of the first of these source field conjugation transfer subsystems, namely the condenser and relay lens optical train, are as follows. The secondary source image is picked up by a condenser lens, which generally has more than one component. The numerical aperture of the condenser lens must match the exiting numerical aperture of the collector subsystem. The condenser lens forms a tertiary source image in a relay lens. The source image formed in the relay lens then constitutes the entrance pupil and reference source for the collimation subsystem. These condenser lens elements, which apparently do little more than transfer the secondary source image formed by the collection subsystem to another source image at the relay lens, serve to gain control of the radiation characteristics of the beam in order to effect a higher degree of uniformity than would otherwise be possible. This is best accomplished if the magnification required to enlarge the actual source size to match the dimensions of the collimator entrance pupil is divided between the collecting and condensing optical components. This technique reduces the required magnification (and therefore the coma) of the collector and allows for

compensating coma of an opposite sign to be designed into the condenser elements. The principal disadvantage of this concept is that highly restrictive design constraints must be placed upon the condenser element design in order to satisfy the requirements which lead to ultimate beam uniformity. These constraints make the optical design of the lenses difficult. A chief advantage of this concept is the high collection efficiency which it permits because of the exceptional degree of control one has over the transfer of the collected radiation, but on the other hand, the additional optical elements nearly nullify this efficiency advantage. The detailed parametric design of a condenser-relay subsystem will be demonstrated in Section 7. Examples of how design constraints bear on the lens design problem will also be given.

6.3.3.3.2 Simple relay lens.

The second transfer subsystem in the source conjugation category is the simple relay lens. In the last transfer subsystem type discussed, the relay lens served the purpose of defining the entrance pupil and reference source of the collimation system. It also serves to map the boundaries of the previous optical elements (in the last preceding case the condenser lenses) onto the aperture of the collimation subsystem whether that be the aperture of the hyperboloid for a Cassegrainian system or the aperture of the paraboloid for a simple parabolic reflector system. The simple relay transfer subsystem is nothing more than the previous subsystem with the removal of the condenser elements and the shifting of the secondary source image formed by the collection subsystem to the position of the relay lens. It must be pointed out that a considerable amount of control over the divergence of the beam formed at that image is immediately lost. The power exercised by the collection subsystem must be considerably higher and the corresponding coma is much more severe. This subsystem by itself would be very unsatisfactory with regard to uniformity if it were designed for the same level of collection efficiency as that which would be possible with the condenser elements. On the other hand, steps may be taken to compensate, by deformation of the collection or collimation optics, as will be discussed in Section 7, thereby regaining a certain degree of control over the distribution. One of the chief disadvantages, however, remains the exceptional burden placed upon the collection subsystem and the consequent enlargement of the secondary source image over that which would normally be obtained for the power level required. For example, if a magnification factor of 4 in the collection subsystem and a magnification factor of 4 in the condensers were required for a total magnification factor of 16 from the source to its image at the entrance pupil of the collimator subsystem, when the condensers are removed the total magnification factor of 16 must now be applied to the collection subsystem alone. Although this is only 4

times the magnification originally requested of the collection subsystem when the condensers were employed, the resulting secondary arc image size would be more than the expected 4 times its dimensions. This is due to the rapidly mounting aberrations for the more eccentric conic section collectors required. In an axially symmetric system this could work a considerable hardship because the size of the central hole would correspondingly grow out of proportion to the total aperture of the system, particularly for designs directed toward high efficiency.

It should be pointed out that, if the collection and collimation subsystems consist wholly of simple conic sections, a module using the simple relay transfer subsystem is nothing more than a string of conic section mirrors in series conjugate relation to one another. It will be shown later that all such systems, no matter how complex with regard to the string of conic sections and relay lenses at focal positions, are entirely equivalent in their radiative transfer properties to a simple paraboloid. Therefore, the analysis of such systems follows along the same lines as that for the array of parabolic mirrors. The simple relay transfer subsystem finds its real use when it is employed in conjunction with higher order deformations of the conic sections in either the collection or collimation subsystems or when employed with one of the other expedients to gain control over the flux distribution. It must be remembered that the simple relay lens is a basic component which is used in virtually every one of the optical transfer subsystems in one form or another. Its function as the reference source and entrance pupil to the collimation subsystem is augmented generally by its use as the window and vacuum seal for these optical systems. It is also a convenient location for the placement of spectral filters, since positions on the relay lens are integrated, by virtue of the nature of optical transfer from this component, over the entire collimator aperture.

6.3.3.3.3 Multifaceted relay lens (optical integrator)

A statistical approach which may be used to gain control of the flux distribution is to break up the relay lens into an array of multifaceted elements acting together. The multifaceted relay lens serves to break up the beam and to redistribute it, as a number of superimposed beams, at the collimator aperture. This process of division and integration has considerable influence upon the uniformity of the final collimated beam. It is one of the most effective methods of smoothing the distribution. The multifaceted relay lens serves the same purpose as the ordinary relay lens; it maps the previous aperture, in this case, the collection subsystem, onto the aperture of the collimator and serves as the reference entrance pupil and effective source for the collimator. In this case, all the little relay lens facets

perform this function together. One disadvantage of this approach could be in the mechanical difficulty of mounting such a multifaceted array in a sufficiently close packing to avoid exorbitant efficiency losses in the interstices. Absorption between the component lenses would raise the temperature of the metal parts, or the like, which hold the facets together and could easily deform the entire assembly. It must be remembered that the heat load at this point is staggering. One could certainly not use this element as the vacuum seal so readily as is possible with the simple relay lens. Other disadvantages are enlargement of the solar field by virtue of aberrations in the collection subsystem due to the increased magnification burden placed upon it, and further enlargement of the field due to its division into separate spots of light which appear to come from each facet in the multifaceted relay lens. The entire question of parameterization and efficiency of this subsystem will be taken up in Section 7.

6.3.3.4 Pebble bed

The pebble bed transfer subsystem, which consists of a multifaceted array of convex hyperboloids located at the focal point of the collimator, serves exactly the same purpose as the multifaceted relay lens. For the very same reasons it breaks up the beam into separate beam segments all subsequently superimposed at the collimator aperture. A statistical smoothing is realized thereby and uniformity becomes a relatively simple characteristic to achieve. The pebble bed, by virtue of its position, must exercise a demagnification in each hyperbolic facet in order that the total pebble bed be smaller than the collimator aperture. Indeed it must be considerably smaller in order not to occlude a major portion of the collimated beam. The details of the geometrical relationships will be worked out later. Because of the magnification relationships required of the pebble bed which are not necessarily present in the multifaceted relay lens, the enlargement of the solar field is considerably greater than that necessary for the multifaceted relay lens. This type of transfer subsystem uses a simple relay lens in its usual position behind the parabolic mirror and maps the collection aperture onto the pebble bed array. This array is located at the focal point of the paraboloid while each hyperbolic facet images the simple relay lens onto the aperture of the paraboloid. This type of transfer system may be particularly useful in off-axis designs where the solar field angle is not a critical specification and the pebble bed array may be located out of the direct collimated beam. The parameterization of the pebble bed used in conjunction with a simple relay and a parabolic collimator will be studied in Section 7. It should be noted that the mounting of the pebble bed of hyperboloid mirror elements, although not as difficult as the mounting of the multifaceted relay lens elements, still suffers from losses by

absorption at the interstices which could also throw the mirror elements out of alignment. Alignment is even more critical in the case of mirrors than in the case of lenses. It might be noted that, although the pebble bed transfer optical subsystem gives the appearance of a Cassegrainian collimation arrangement, it is not such a collimator type. The pebble bed array, just as does the multifaceted relay lens, forms what is essentially the reference source for the collimating paraboloid. In fact, each pebble forms what is ostensibly a source for the paraboloid so that the latter sees multiple sources in the vicinity of its principal focus. The relay lens serves in this case only to illuminate the pebble bed by mapping the collector boundaries onto the pebble bed boundaries.

6.3.3.4 Collimation Subsystem.

The collimation subsystem, as just defined, consists only of those final optical components contributing directly to the collimation of the reference source and excludes any components which comprise the reference source itself. As in the case of the collection subsystem, the size of solar simulator modules being considered in this study dictates against a totally refracting collimator. Therefore, attention will be centered upon reflecting-type collimators of which there are two basic types for our purpose. The first is the simple paraboloidal mirror. This mirror may be approximated in a number of ways, e.g., a sphere, a series of spherical segments each with the appropriate curvature and positioned on a parabolic locus, or a series of flat mirrors similarly positioned and properly oriented. Whichever way the mirror is approximated in fabrication, the paraboloid represents the ideal choice.

The second collimator type is a Cassegrainian mirror system consisting of a paraboloid and hyperboloid acting together. The principal difference from the simple paraboloid is the inclusion of a negative element, which serves to multiply the focal length of the paraboloid, leading to a greater collimator effective focal length. By virtue of this expedient the focal point may be located behind, rather than in front of the paraboloid. Although the paraboloid-hyperboloid combination is a distinct subsystem type, it nevertheless is subject to several variations which may prove particularly useful. In addition to the ramifications which derive from the alternative fabrication schemes indicated above for the simple paraboloid, it is possible to alter the basic shape of both the hyperboloid and paraboloid. Because of the mutually compensating effects of the Cassegrainian elements, the introduction of higher order terms can be employed to modify the flux distribution inherent in the collimator while simultaneously nullifying undesirable aberrations. This is done by cancelling errors in one component with errors of an opposite sign in the other. The form of these surfaces involves deformation coefficients of even powers of the aperture radius higher than the second, i.e., deformations with respect to conic sections.

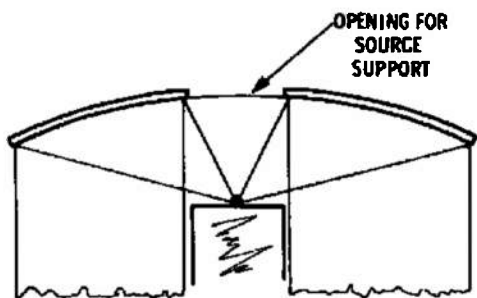
Thus, the two basic collimator types to be considered in this study are the simple paraboloid of one positive element and the Cassegrainian system of one positive and one negative element. Along with these, variations of the surfaces for reasons of fabrication or flux distribution control will be considered. Several representations of these two schemes are depicted in figure 6-6. Disregarding approximations to the desired surfaces for reasons of fabrication expediency, there are really three collimator types. They are the paraboloid, the Cassegrainian system, and the higher order modifications (deformations) of these.

The collimator orientation plays an important role in the modular geometry. If the collimator is axially symmetric, it is generally possible to arrange the modules on centers forming a hexagonal array with the collection and transfer optics behind the collimator sharing a common optic axis. When the collimator is taken as an off-axis section it is sometimes necessary to cant the axis of the collection and transfer system with respect to the optical axis of the collimator for greatest efficiency. This could preclude the possibility of employing a hexagonal array. A less efficient square array is always possible when interference prevents fitting the modules in a hexagonal close-packed lattice. Module orientation and off-axis design will be discussed in more detail later.

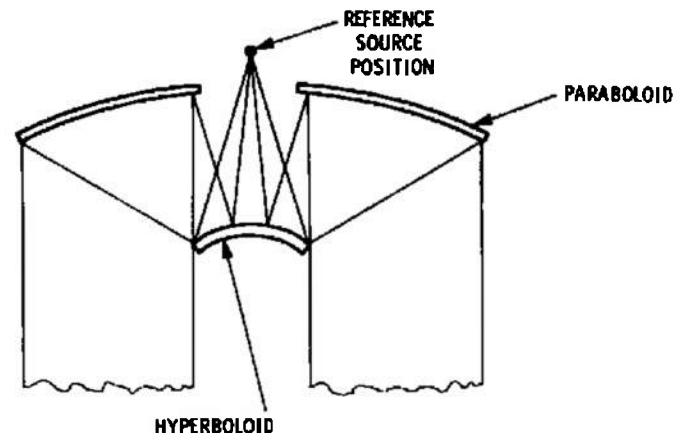
6.3.4 On-Axis versus Off-Axis Systems.

All of the collimated optical systems mentioned in paragraph 6.1 are amenable to collimator orientations which are either symmetrical about their respective axes or skewed in an off-axis manner. Figure 6-7 shows both arrangements using a reflective collimator as an example. It can be seen that the on-axis mirror is capable of returning energy directly back to the target area whenever the focal length of the mirror and the distance to the target are comparable. However, the figure shows that, in the case of the off-axis mirror, there is a zone bounded by the locus of normals to the edge of the mirror farthest from the axis which cannot be reached by reflected light. For unit structure systems (systems which employ one large collimator or section thereof) the size of the mirror, its focal length, and the distance to the test region are all comparable and the off-axis deflection of radiation returned from the target to the mirror is a necessity. An additional advantage of the off-axis configuration is the avoidance of the obstruction usually necessary in the beam of an on-axis system for placement of the collimator secondary mirror.

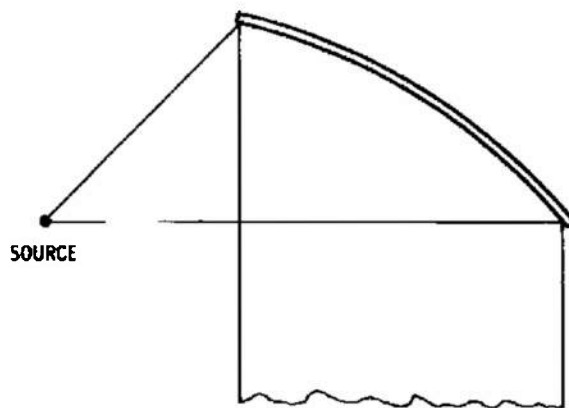
There are disadvantages in an off-axis system which should be mentioned. For example, the asymmetry which necessarily obtains causes mismatch of boundaries with an attendant spillover of energy.



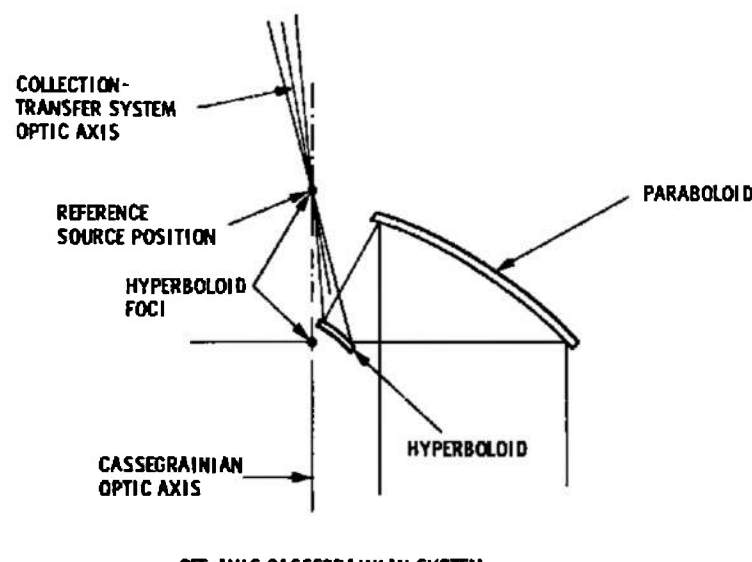
SIMPLE ON-AXIS PARABOLOID



ON-AXIS CASSEGRAINIAN SYSTEM



SIMPLE OFF-AXIS PARABOLOID



OFF-AXIS CASSEGRAINIAN SYSTEM

Figure 6-6. Basic Collimator Types

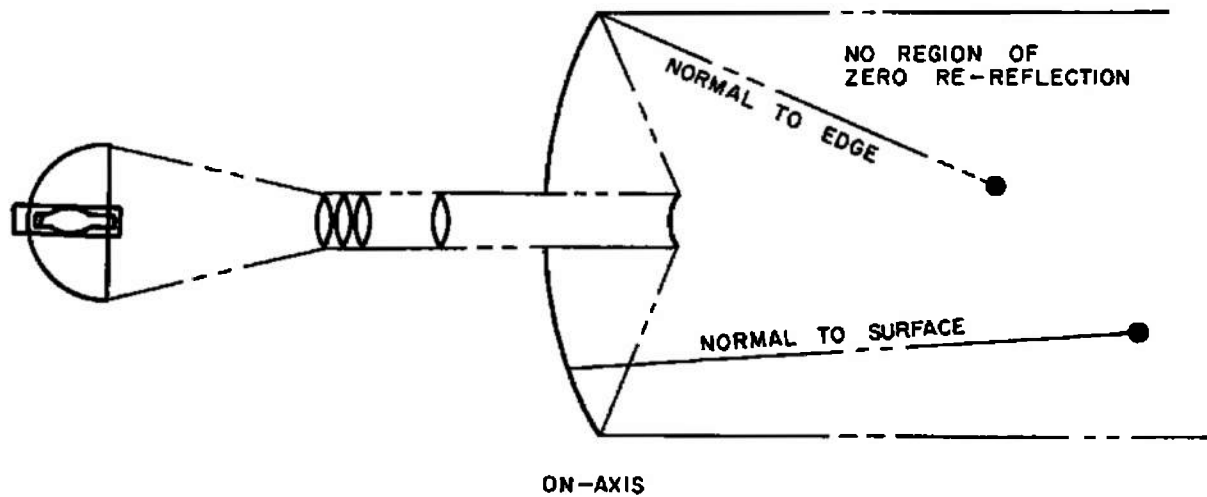
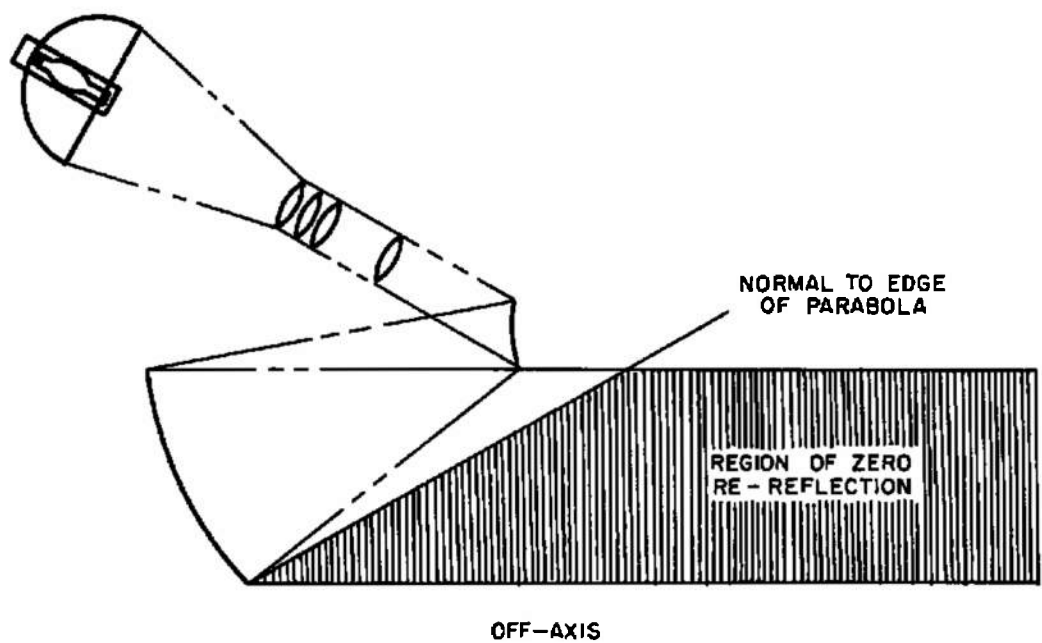


Figure 6-7. On- and Off-Axis Collimators.

With proper scaling, however, this loss of efficiency may be held to approximately 15% although it can be as high as 35%. An additional difficulty, perhaps more subtle, is the loss of uniaxial symmetry which exists in the symmetric module of a multimodular array. This creates difficulties in balancing aberrations between the components in the system and is a point which must not be overlooked when considering detailed design of the optical components. Another problem is that the off-axis section type collimator must be faster than the symmetrical collimator in terms of zonal radius to focal length ratio in order to effect the same equivalent speed of the collimator system as would be obtained in the symmetrical collimator. This creates some serious problems in design as well as manufacture. Although off-axis optical systems are commonplace today, the magnitude of the task of manufacturing such elements should not be underestimated. In spite of these drawbacks, the simple fact that an off-axis arrangement is truly the only way that re-reflection of radiation can be completely avoided and obstruction of the center of the beam of each module can be eliminated lends considerable weight to a recommendation for such a system.

6.3.5 Shadowing and Fill-In Systems.

6.3.5.1 Collecting Optics.

When the off-axis collimator is employed, a central fill-in system is generally unnecessary in the collimator components. A central dark spot may still persist, however, due to the axial gap in the collection subsystem components. It is not possible to collect completely to the optic axis for either the single-ended or two-ended arcs; however, in the case of the single-ended arc it may be possible to minimize the axial gap to a small angle. Depending upon transfer subsystem design, it may be possible to further minimize the effects of this central hole in the collected beam by the time it reaches the collimation subsystem. The two-ended arc necessarily has a hole in the beam near the axis due to electrode shadowing. Little can be done in terms of parametric design of the primary collection subsystem to minimize the effects of this lack of radiation near the axis. However, the transfer subsystem optics and those of the collimator may be so designed as to reduce the effect of this shadow or annihilate it completely by redistribution of the radiant energy. This occurs to some extent in the multifaceted relay lens and pebble bed type transfer subsystems; however, the integration or mixing of shadows over the entire collimator aperture is not truly affected by these devices. The only way that this particular difficulty can be completely circumvented is by use of the source aperture conjugation type transfer subsystem. Thus, whether or not an off-axis collimation subsystem is employed, it is likely to be necessary to fill in the central angles of the collected

beam if the shadows which they cast on the collimator aperture grow too large. In the case of the one-ended sources, all that is needed are some additional refracting elements which are symmetrical about the collection subsystem axis, and which feed the same transfer subsystem as the major part of the collection subsystem. There will be a discontinuity in the radiation beam caused by the boundary between the central refracting collection subsystem and the peripheral reflecting collection subsystem. The effects of this boundary should be minimal, however, and the shadows caused thereby should be far less than those obtaining by virtue of the lack of axial radiation. In the case of the two-ended source the fill-in system is not so simple because the axial radiation does not exist to be collected and transferred. Radiation must come from the extreme marginal zones of the main collection system itself. This radiation is redirected toward the axis of the collector in the form of an image of the source which would be formed there. This image is picked up by another axially mounted mirror to form a tertiary image of the source to be picked up by refracting condenser elements of the type mentioned for the single-ended source or by the transfer subsystem itself. The two types of collection fill-in optical systems are illustrated in figure 6-8.

In either case, the efficiency of the central fill-in collection system will be less than that of the principal collection subsystem particularly in the case of the two-ended source. Once the problem of the central collection fill-in optics is solved, care should be taken that these components are properly designed so that the images formed thereby and the divergence angles so established properly match those of the principal collection subsystem, in order that the same transfer subsystem optics may be used for both radiation components. Although this is not absolutely essential, a considerable saving can be realized by this expedient.

6.3.5.2 Collimation Optics.

The transfer subsystem, now possessing a complete radiation beam all the way to the axis, will require no additional fill-in system if it is feeding an off-axis collimator. On the other hand, if the collimator is a symmetrical one, then it must of necessity be either a Cassegrainian collimator or a simple paraboloid with a pebble bed reference source. In either case, the secondary mirror (hyperboloid in the case of the Cassegrainian collimator, or the pebble bed in the case of the simple paraboloid) may have to have a central hole. In this hole would be placed a field element which would become the source for a collimating lens placed behind either secondary component. It is possible, if these secondary components can be made small enough, that the expedient of a collimator fill-in can be avoided.

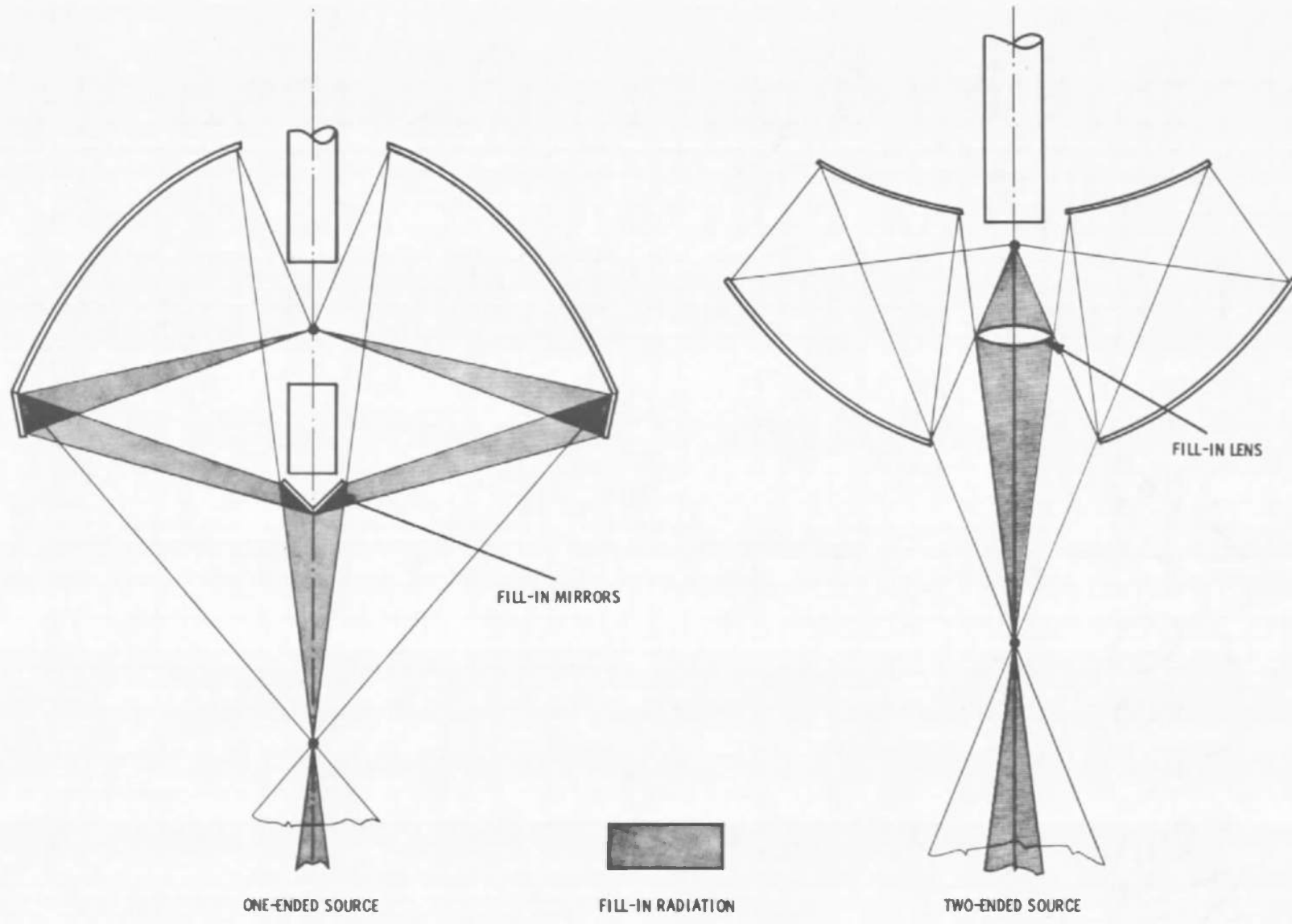


Figure 6-8. Collection Fill-In Optical Systems

entirely. In any case this simple fill-in concept is illustrated in figure 6-9. Because the fill-in system is relatively slow in optical speed by comparison to the main part of the solar simulator optics, the problem of design for the sake of uniformity across its own aperture is not a difficult one. The question of its delivering the requisite amount of total average energy across its aperture by comparison to the main optical system is a different question entirely.

6.3.6 Modular Arrangements.

A final aspect of the optical schemata has to do with the arrangement of the modules themselves. In the case of the axially symmetric collimators, the collimator axes will be located on centers forming a hexagonal array. The collimator apertures will be cut to hexagonal shapes with the corners of the hexagon rounded to a certain extent to provide access. The junctions of the rounded corners of the hexagons will leave a hole in the beam as does the central obscuration of the secondary collimator element (either the hyperboloid or the pebble bed). Therefore, the amount of corner rounding should be minimized. If the modules are mounted adjacent to one another it will probably be necessary to leave some space between the modules on the hexagonal flats. This, of course, will also cause some shadowing. Thus, the multimodular (contiguous) system, consisting of a group of axially symmetric optical systems placed in juxtaposition will necessarily have shadows, created by the boundaries separating the modules. The effect of these shadows will be minimized as the distance to the target increases. It is possible, by mounting the modules in a staggered arrangement as shown in figure 6-10 to overlap them in such a way that the beams emanating from them will add to each other without boundary shadows being present. Thus, the multimodular staggered array is a group of single unit modules which, if projected on a plane parallel to the simulator array, would appear adjacent with a small amount of overlap. This overlap prevents them from being placed in juxtaposition but has the advantage of preventing shadows in the beam due to edge effects. The amount of overlap is determined by the solar field angle in that the amount of projected overlap in each receding module must subtend the solar field half-angle from the edge of the module directly in front of it. When this is done it is seen that from any point in the target volume no line can be drawn within the solar field angle which does not intersect some portion of some module aperture. That is, the spaces between the modules within the solar field angle cannot be seen when the staggered module expedient is employed.

In the case of off-axis modular apertures, an off-axis section of a paraboloid is fed by either a hyperboloidal secondary mirror or a pebble bed which is located behind the peripheral margin of each

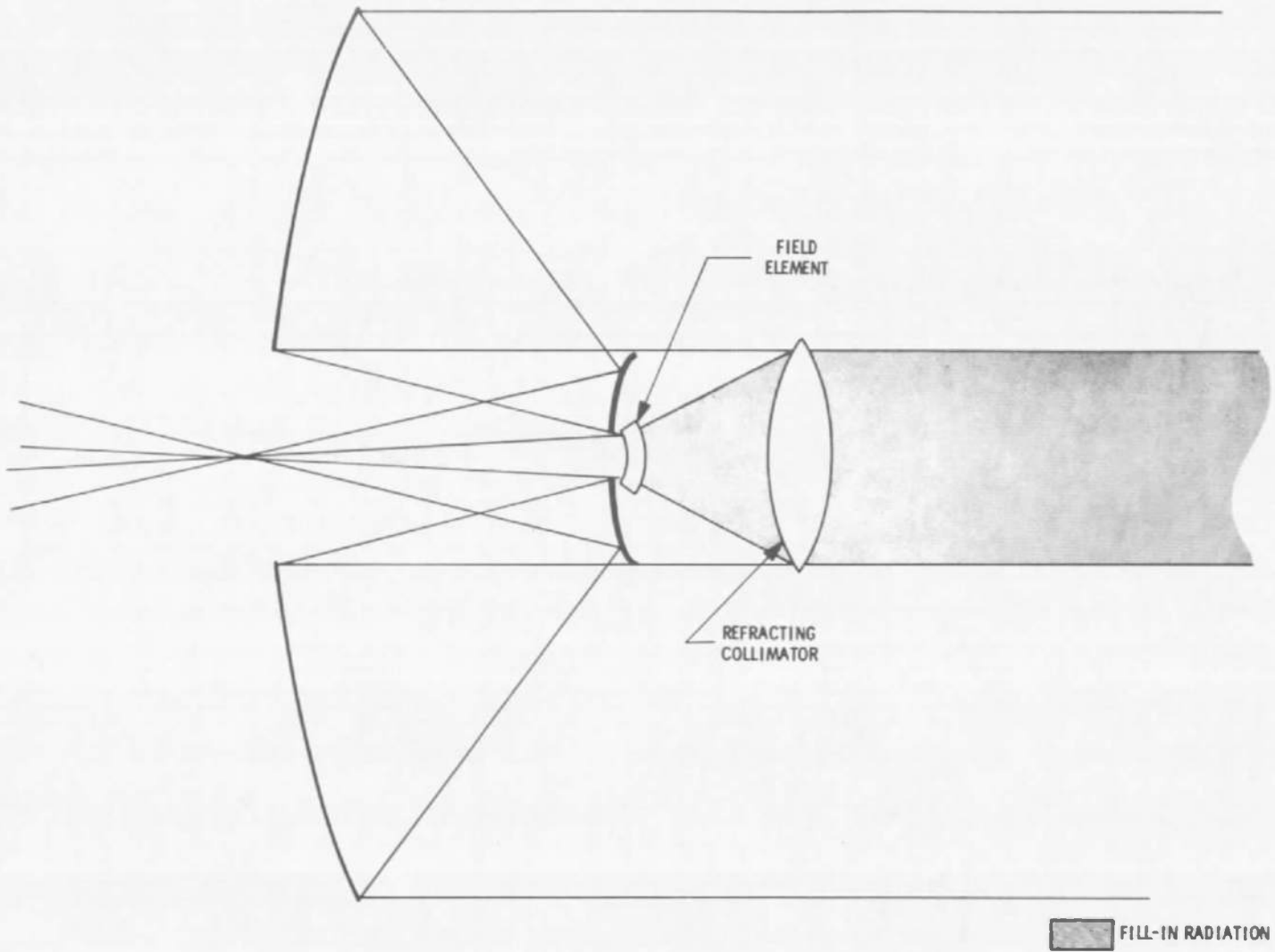


Figure 6-9. Collimator Fill-In Optics

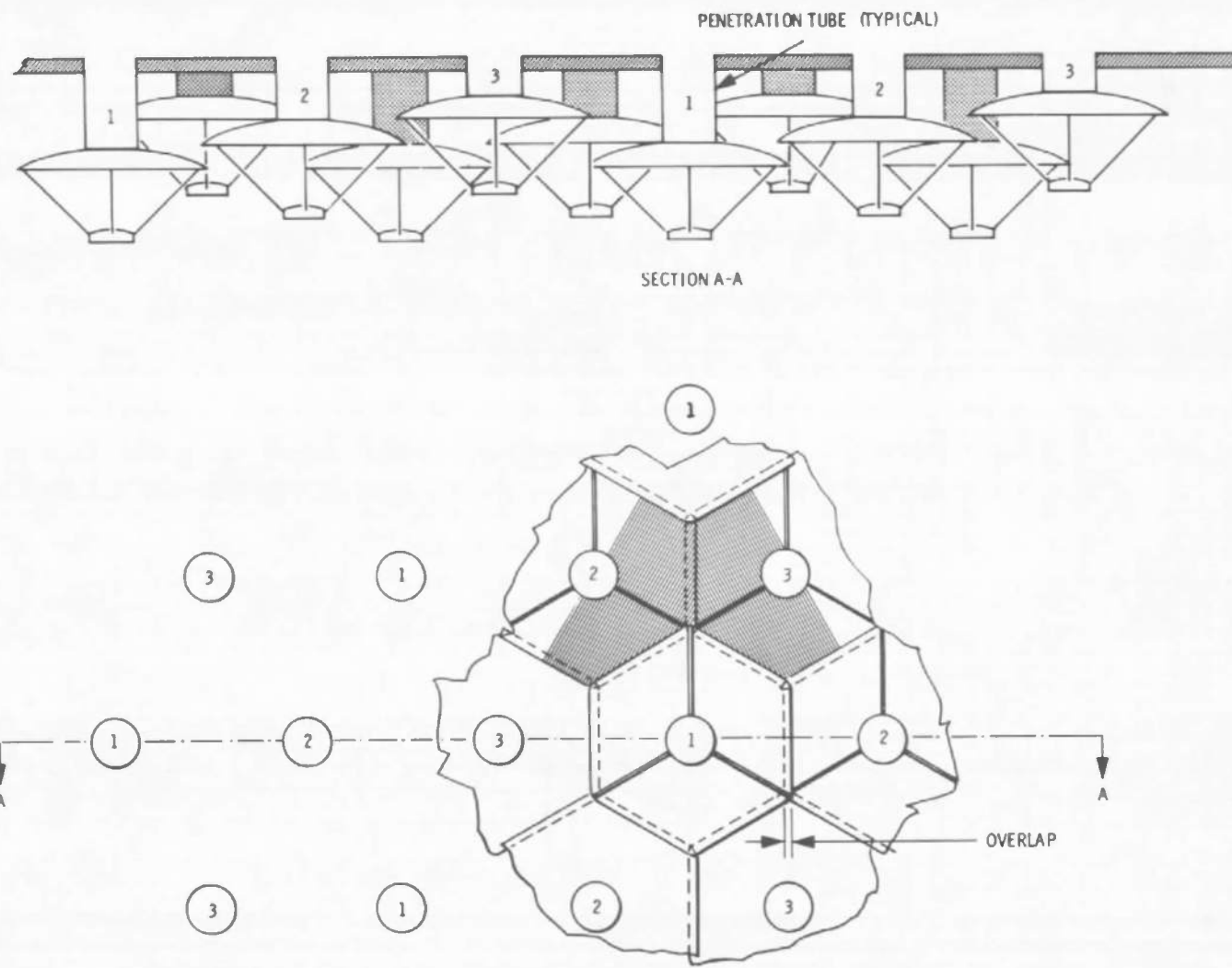


Figure 6-10. Staggered Array of Collimators

successive paraboloid. This modular array is necessarily of the staggered type. The amount of overlap, which is governed by the solar field half-angle, dictates the angle of skew of the collection and transfer optics, the magnification factor of the hyperboloidal secondary, and the speed of the primary paraboloidal collimator. This concept is illustrated in figure 6-11.

The foregoing has described, in broad outline, the nature of the optical systems to be discussed in detail in the Section 7 which follows. In Section 7 the parametric and radiant transfer characteristics of each optical system type and combination of subsystem schemes will be studied in detail. The behavior of these systems with regard to overall performance will be analyzed with regard to their uniformity, efficiency, and the general compatibility with the overall space environmental simulation requirements.

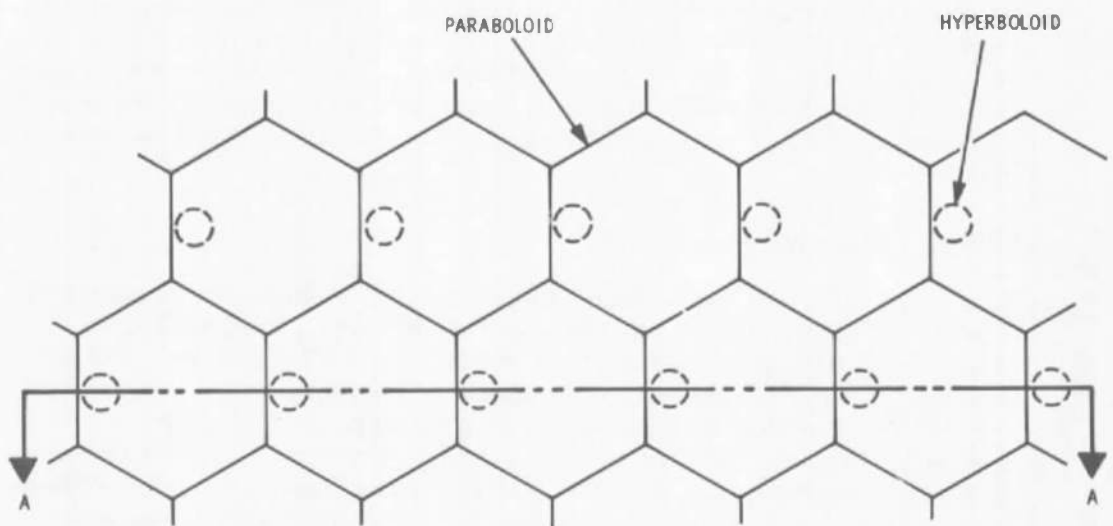
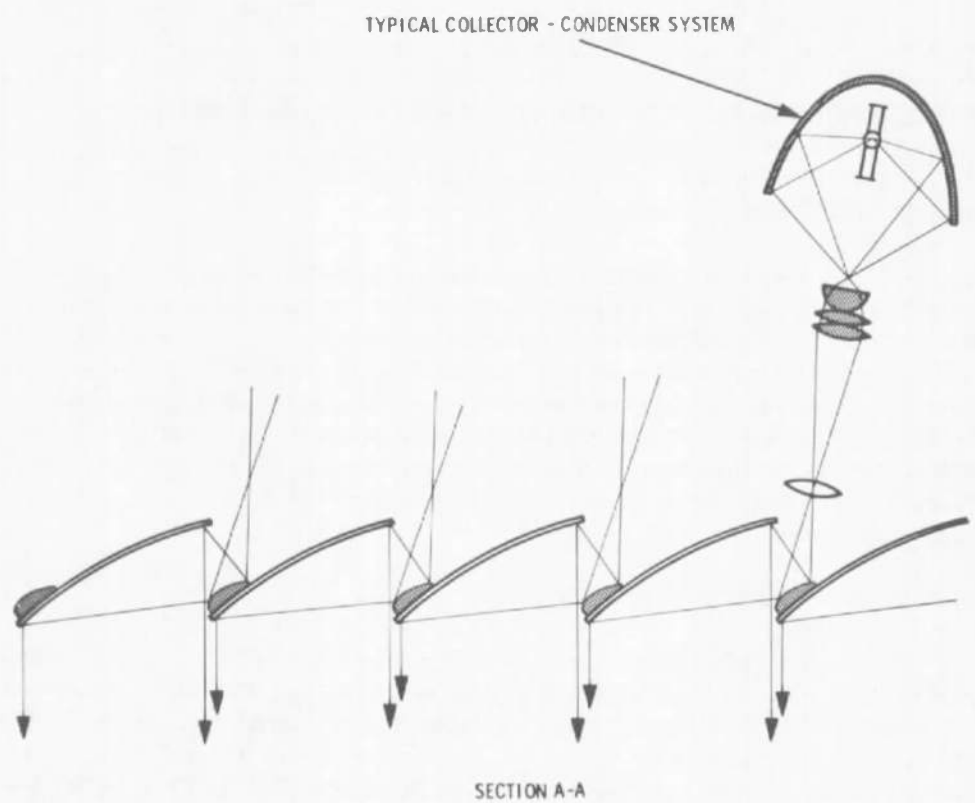


Figure 6-11. An Off-Axis Modular System

SECTION 7

BASIC ANALYSES OF THE VARIOUS OPTICAL SCHEMATA

7.1 INTRODUCTION

This section contains analyses, on a first order basis, of the performance characteristics of the several optical schemata described in section 6. Development of system parameters is carried through at least to the point at which it is possible to state with some confidence that the approach being considered is or is not feasible. Relative merit of those systems deemed feasible is also discussed, in order that the direction to be taken in a final design using any of the sources studied may be focused into a relatively narrow field of further investigation and refinement.

7.2 SOURCE REPRESENTATION

The criteria for source characterization depend primarily upon three radiometric parameters which affect intensity, uniformity and efficiency. In dealing with these parameters, they may be dealt with in the order of assigned priority. In order of the weight of their effects, these parameters are: (1) the radiance distribution about the source, (2) the source size and (3) the micro-brightness distribution. The first of these has to do with distribution of radiant energy about the source and is most conveniently expressed, in units of energy radiated per unit solid angle, in terms of a spherical coordinate system whose origin is centered within the source. (Radiance is analogous to candlepower when one is concerned with the visible or luminous output of a lamp.) The second is self-explanatory. The third has reference to the source brightness detail, i. e., the energy per unit area per unit solid angle emitted by or through any elemental area on the surface of the source.

7.2.1 Radiance Distribution

The nature of the source is such (namely, spontaneous emission in what is effectively thermodynamic equilibrium) that each element of volume within the plasma which comprises the source must emit isotropically for all directions in space. However, there is considerable self-absorption throughout the source volume, the result of which is a very irregular pattern of directionally-dependent brightness values which thereby comprise the effective source of light. It has been shown in section 4.5.1 that such a radiation field can be uniquely characterized by a vector intensity function on a single surface which surrounds the source. (This result is an immediate outgrowth of Huygens' principle and the superposition principle of electromagnetic propagation.)

Further, it has been shown that, since the radiance distribution of a Lambertian surface is by definition a function only of surface geometry, this representation can be reduced to a series of successively contained Lambertian surfaces, the radiation from each of which may propagate outward through successive surfaces but not inward through its own boundary. (Such surfaces, arranged similarly to the layers in an onion, may be considered Huygens' wave surfaces in every sense of the word.) Thus, the radiance distribution of a source may be represented as the sum of contributions from a series of successively-contained Lambertian surfaces, the magnitude of the individual contribution from each surface being determined by its shape and brightness.

Bearing the above in mind, the discussion will be restricted, for the moment, to collimating optical systems in which the source is located at or is optically conjugate to principal foci. Consider what information might be derived from a source which may be regarded as negligible in size and which has a prescribed axially symmetric radi-

ance function I_ϕ . It is convenient to define $\bar{I}_\phi = \frac{I_\phi}{I_0}$ as the normalized

radiance function where I_0 is the value of I_ϕ at $\phi = 0^\circ$. Regardless of whether the radiance distribution is a function of the source shape or other factors, the relative intensity distribution across the aperture of the collimator has been shown in section 4.4 to be

$$R = -2f^2 \frac{d(\cos \phi)}{d(r^2)} \bar{I}_\phi \bar{k}_\phi \quad (7-1)$$

where:

R = relative intensity at a point in the collimator aperture

f = effective focal length of the optical system

ϕ = angle at which a ray passing through the point in question enters the optical system

r = distance of the point in question from the optic axis

\bar{k}_ϕ = transmittance of the optical system

This expression referred to herein as the "Normal Illuminance Criterion" is restricted to axially symmetric systems and is an exact expression of the situation governing the value of R only when the source size is negligible. These restrictions do not invalidate the utility of the expression, however, for the value of an exact limiting case is not to be dismissed. Indeed, it is by virtue of this very

property that the fundamental relationship in equation (7-1) provides the first order evaluation of the flux distribution in the nearfield single module beam.

Several important points are to be noted, the first of which is the separability of the contributions defined by the optical parameters f^2 and $\frac{d(\cos \phi)}{d(r^2)}$, and the source parameter, \bar{I}_ϕ . (An immediate con-

clusion is that the actual intensity distribution due to a real source can be obtained by multiplying the radiance function I_ϕ of the real source by the result obtained from equation (7-1) evaluated for a source whose relative radiance function \bar{I}_ϕ is unity, i.e., a spherically symmetric source. This goes to the very core of the source philosophy adopted, and illustrates the dichotomy between source and optical characteristics.) Second, it is seen that the first order effects of the radiance distribution are divorced from a consideration of source size and/or detailed micro-brightness information, and thus the effects of these latter may be introduced separately, as required for subsequent refinements of the study. Finally, the radiance distribution (in absolute radiometric units) is the only information required in order to determine the total radiated power output of a source and the collection efficiency of the optical system to be used with the source.

To illustrate this latter point, consider the case of a source with an axially symmetric radiance function I_ϕ whose radiated power output is being collected by the optical system through an axially symmetric solid angle Ω given by

$$\Omega = 2\pi \int_0^\Phi \sin \phi \, d\phi \quad (7-2)$$

where ϕ is measured with respect to the axis of symmetry. Φ is the maximum value of ϕ . The power P radiated by the source into the solid angle Ω is given by

$$P = \int_0^\Phi I_\phi \, d\Omega = 2\pi \int_0^\Phi I_\phi \sin \phi \, d\phi \quad (7-3)$$

If Φ is set at the collection angle of the optical system, then equation (7-3) gives the total power collected P_c . If Φ is taken as $180^\circ = \pi$ radians, the total power radiated P_r is obtained. The collection efficiency η_c of the optical system is given by

$$\eta_c = \frac{P_c}{P_r} \quad (7-4)$$

Further, it can be shown that if E_o is the radiant intensity required in the collimator aperture at the optic axis, then the effective focal length f of equation (7-1) is given by

$$f = \sqrt{\frac{I_o}{E_o}} \quad (7-5)$$

where I_o is again the radiance I_ϕ at $\phi = 0^\circ$. It should be noted, however, that this equation gives no information concerning the intensity at any other position in the collimator aperture.

In the preceding, the absence of absorption has been tacitly assumed. This difficulty can, however, be easily circumvented by multiplying all values of the radiance function I_ϕ by the appropriate absorption constant k_o .

7.2.2 Source Size

As the next step in this analysis, let us consider the effect which source size alone has on performance characteristics. Although real sources can have various shapes, we may generalize this parameter by stipulating that source size refers to the dimensions of a sphere which can completely contain that volume of the source from which the energy is thought to be emanating. We therefore think of the source as being spherical and of a given diameter. By virtue of this source shape (excluding the effects of the micro-brightness distribution), the relative radiance function I_ϕ has a value of one for all values of ϕ , and the relative intensity distribution across the aperture of a collimating optical system, as defined by equation (7-1), is a function only of the optical system. However, because of the finite size of the source, the various optical aberrations come into play and begin to affect the intensity distribution across the aperture of the modules which could otherwise be calculated using equation (7-1).

With the single exception of spherical aberration, the various monochromatic optical aberrations, i.e., coma, astigmatism, curvature of field, and distortion, have no effect on the intensity distribution in the aperture of a collimating optical system for the limiting case of an infinitesimal source. Thus, since spherical aberration is not a function of source size and its effects can be studied using equation (7-1), it can be omitted from this discussion of the effect of finite source size.

All of the remaining aberrations, which are functions of source size, generally have a smoothing effect upon the distribution of intensity in the target volume, if for no other reason than by virtue of the increased spreading or divergence of the beam emanating from each module due to the influence of these aberrations. Thus, as source size is increased, beam divergence increases, not in linear proportion to the corresponding increment in field angle, but in an accelerated manner due to the effects of various aberrations. Near the axis these aberrations have little effect and the field remains circularly symmetric, subtending an angle 2Θ where

$$\Theta = \text{arc sin } \frac{D}{2f} \quad (7-6)$$

In this equation, D is the diameter of the spherical source and f is the effective focal length of the optical system. Thus, one must consider that the concept of source size encompasses all those factors affecting radiance light distribution in the target volume which arise from optical aberrations relating to a finite field angle and which cannot, therefore, be incorporated into the demesne of equation (7-1).

There are two additional things to consider when talking about the optical effects of source size on flux distribution. The first consideration applies, whether either a multi-modular array is the approach used or if there is but a single module to serve the entire target volume, and has to do with the size and shape of the aperture, properly termed the exit pupil, through which radiation must pass in order to be conveyed from the last element in the optical system (the collimator or paraboloid) to a particular point in the target region. This exit pupil, when properly delineated in space at the collimator, does not necessarily cover the entire collimator aperture, but rather is variable in size since the exit pupil as viewed from any point in the target volume always subtends the field angle. The foreshortening of the exit pupil, which one sees toward the edge of a paraboloid and which is basically a manifestation of a first order effect, would tend to be eliminated as the field began to cover larger sections of the middle zones and center of the mirror. Thus it is that, the larger the field, the greater is that portion of the collimator aperture over which the influence of the aberrations and first order optical effects are averaged; and since the exit pupil grows with distance from the module, the non-uniformities in the far field are less striking than those in the near field.

The second consideration which depends upon field size (and thus upon source size) involves the overlap of beams from adjacent modules in a multi-module array. Instead of the simple symmetry that obtains about the optic axis in the case of a single module, the multiple symmetry about the several optical axes of the contributing modules, as

well as that with respect to the conjoining boundaries of those modules, must be considered. When there are spaces between the modules, the rate of shadow fill-in is in direct proportion to the field angle. This composite of interrelated effects is a veritable miasma when an attempt is made to separate it into an articulate arrangement amenable to systematic analysis. It is, nevertheless, vitally important to a comprehensive study to be able to account for the increasing influence of these effects as one recedes from the array. This analysis can, unfortunately, only be performed on an integrated basis. For the purposes of this study, this analysis takes the form of a computerized energy trace.

7.2.3 Micro-Brightness

The final source characteristic, which has been ignored thus far in the discussion, is the micro-brightness distribution within the source itself. For the purposes of this study we shall continue to ignore it for two reasons. The first of these reasons has already been alluded to in the discussion concerning the radiance distribution, namely, that this particular characteristic can be represented by a series of Lambertian surfaces of constant brightness and of varied shapes with the ultimate distribution being cumulative with respect to their several contributions. Since it has already been shown that all of the effects which depend upon optical parameters can be accounted for on the basis of a spherical source representation, it then follows that a single spherical Lambertian surface is sufficient, thus eliminating any need for reference to micro-brightness detail. Secondly, although micro-brightness variations do have an effect upon the flux distribution, the optical system acts merely as a vehicle for their conveyance and does not affect their manifestation in a direct sense. (The last statement may be dangerously close to an oversimplification, but it is the quintessence of the arc philosophy which we have here expounded, i.e., the optical and arc determinants of intensity distribution in the target volume must be treated separately if a cogent evaluation of optical system properties is to be obtained.)

7.3 MODULAR ARRAY OF UNCOLLIMATED PROJECTION SYSTEMS

7.3.1 Introduction

This analysis will deal with the problem of achieving a uniform distribution of radiant energy within some finite volume (target volume) using as the source of the radiant energy a multi-modular array of Uncollimated Projection Systems as represented schematically in figure 7-1. Throughout this analysis, the array will be defined as consisting of a number of modules (projectors), so located that they are uniformly distributed over the surface (the array surface) defined by the locus of the apertures of the modules, with the radiation

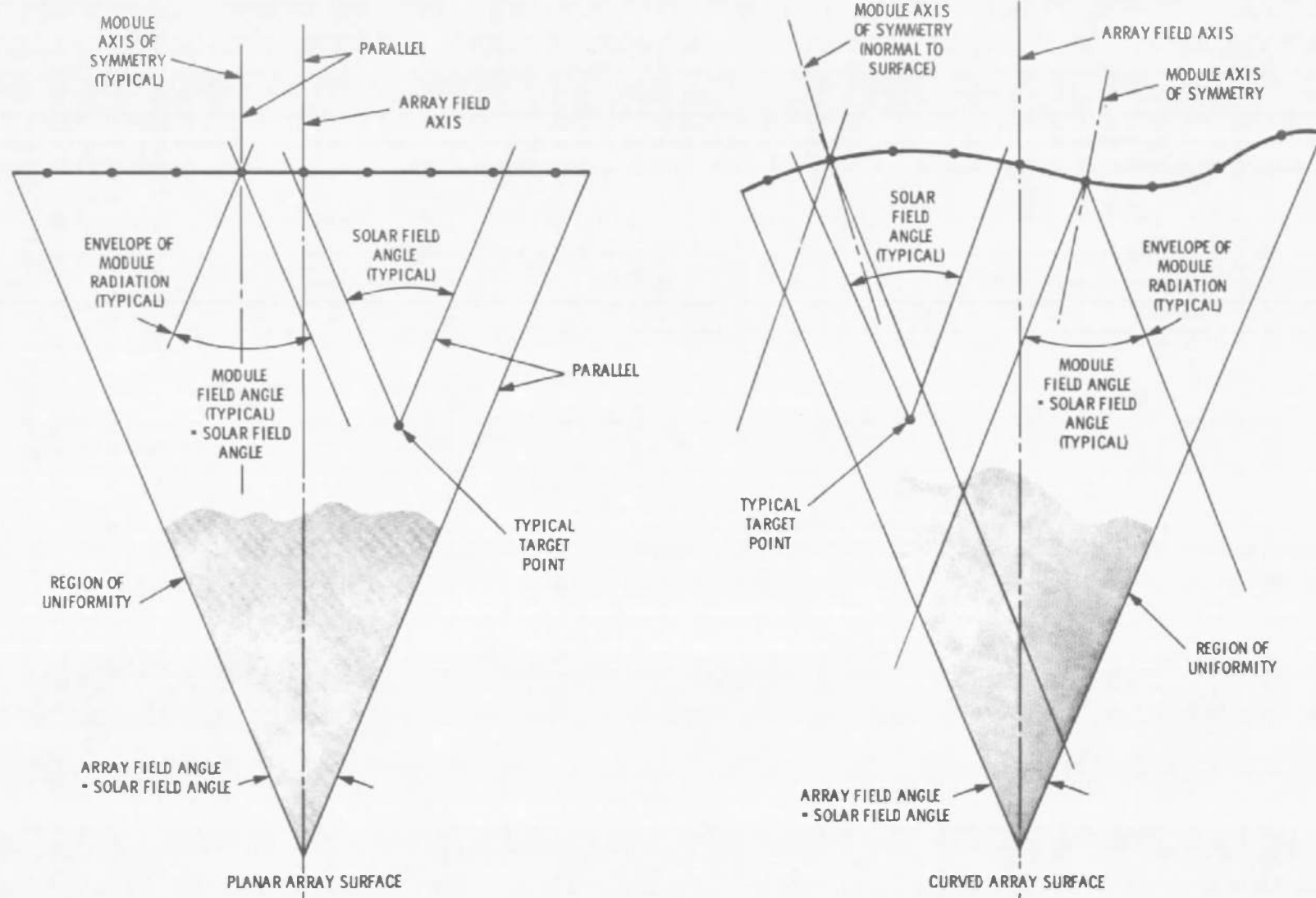


Figure 7-1. Projection Module Systems

emanating from each module being aimed at the target volume. It will be shown that, in order to achieve a uniform distribution of radiant energy throughout the target volume, the axis of symmetry (optic axis) of each individual module must be oriented normal to the array surface and the radiance function of all the modules, with respect to their individual optic axes, must be identical within such angular limits as may be dictated by field stops. It will also be shown that, if the array surface is other than a plane, there is a rigid theoretical requirement that the radiance distribution of each module must be a cosine function with respect to the optic axis of the module. Further, although the optic axis of the modules will not necessarily be mutually parallel if the array surface is other than a plane, it will be shown that the field of radiation from the array of modules must be symmetric about the direction of the array axis (the array axis passes through the center of the target volume) and the maximum angular divergence of radiation from each module with respect to the direction of the array axis must equal, within the target volume, a specified limit established for the angular divergence of radiation from the array (the array projection angle), which control is achieved through the use of appropriate field stops. Finally, it will be seen that, if the boundary of the array is circularly symmetrical about the array axis, the volume throughout which a uniform distribution of radiant energy will be achieved is bounded by the array surface and the surface of a right circular cone whose base is the array boundary, whose axis is coincident with the array axis, and whose apical angle is equal to the array projection angle. Thus, for uniformity, the angle subtended by the radiation incident upon any element of area in the target volume (the target field angle) is equal to the array projection angle.

In the analysis, it will first be assumed, for the purpose of continuity, that the module packing may be so close that one may pass to the limit of infinitesimal module size. The solution thus obtained is a smooth, continuous function within the volume. The analysis will then proceed to the case of finite module size and it will be seen that, in this case, the solution is an oscillatory function of the distance to the target position, the amplitude of whose undulations, with respect to the continuous solution obtained for the case of infinitesimal module size, is inversely proportional to the number of modules which can be seen within the target field angle and which approaches the continuous solution as an asymptotic limit. Also, since the number of modules which can be seen within the target field angle increases with the distance from the array to the target position, with the size of the target field angle, and with the packing density, all three of these parameters will be varied and their effects studied.

7.3.2 System Performance Analysis

To begin the analysis of the performance characteristics of a multi-modular array of uncollimated projection systems, consider the case, represented schematically in figure 7-2, where an array of identical modules of infinitesimal size has been located on a general surface Σ so that the module density N is uniform over the surface. Define a spherical coordinate system about some position in the target volume such that its polar axis (the z -axis of figure 7-2) is parallel to the array axis. The following relationships can be specified:

$$d\omega = \sin \phi d\phi d\theta \quad (7-7)$$

$$d\omega = \frac{\vec{dA} \cdot \hat{r}}{(R^2) \cdot (R^2)} = \frac{dA \cos \gamma}{R^2} \quad (7-8)$$

where

$d\omega$ = an element of solid angle taken in a direction (ϕ, θ)

ϕ = an angle measured with respect to the z -axis

θ = an angle measured in the xy -plane with respect to the x -axis

dA = an element of area on the surface Σ intercepted by $d\omega$

\vec{dA} = the normal to dA

\hat{r} = a unit vector defining the direction from the target position to dA .

R = the distance from the target position to dA

γ = the angle between \hat{r} and \vec{dA}

If I_γ is now defined as the radiance of each module on the element of area dA in the direction γ with respect to the array surface normal, then the element of flux d^2F incident on a target element of area dS oriented so that its surface normal lies in the direction $\phi = 0^\circ$ is

$$d^2F = (N dA) \left[\frac{I_\gamma dS \cos \phi}{R^2} \right] \quad (7-9)$$

where $N dA$ is the number of modules on dA . If dE is now defined as the element of intensity on dS , then

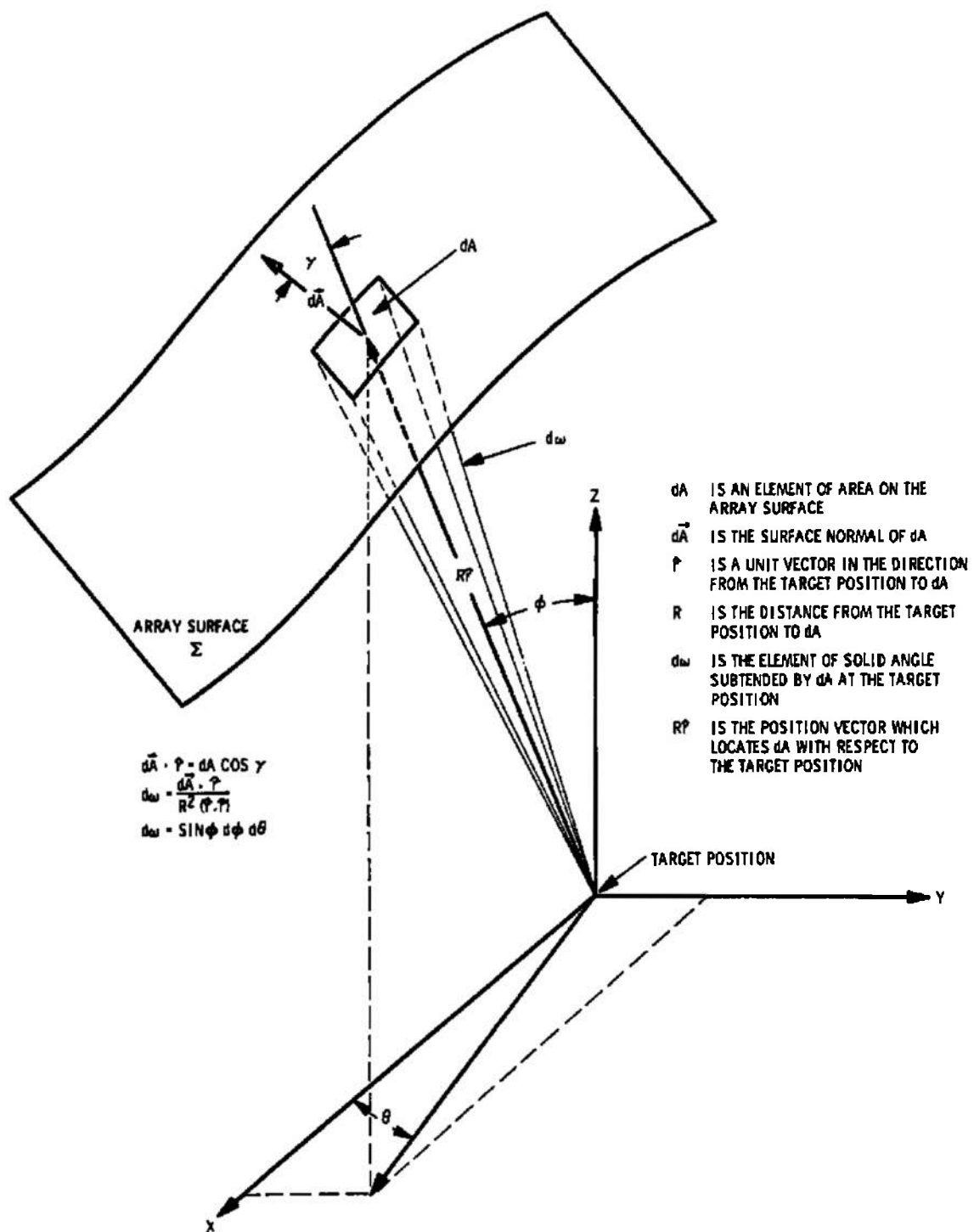


Figure 7-2. Schematic Representation of the Geometric Relationships which Govern the Transfer of Radiation from an Array of Projectors to a Target Position

$$dE = \frac{d^2F}{dS} = \frac{N dA I_\gamma \cos \phi}{R^2} \quad (7-10)$$

If equations (7-7) and (7-8) are combined and solved for dA ,

$$dA = \frac{R^2 \sin \phi d\phi d\theta}{\cos \gamma} \quad (7-11)$$

which, when substituted into equation (7-10) gives

$$dE = NI_\gamma \frac{\sin \phi \cos \phi}{\cos \gamma} d\phi d\theta \quad (7-12)$$

The very essence of the problem of providing uniform intensity throughout a target volume with an array of projectors, and the solution to this problem, is embodied in the integration of equation (7-12) from $\phi = 0^\circ$ to $\phi = \Phi$, where 2Φ is the target field angle (the angular subtense of radiation incident upon a target element of area). Since the target field is symmetrical about the polar axis, equation (7-12) may be integrated according to

$$E = \int_0^{2\pi} d\theta \int_0^\Phi \left[NI_\gamma \left(\frac{\sin \phi \cos \phi}{\cos \gamma} \right) \right] d\phi \quad (7-13)$$

For most surface geometries, an inherent non-uniformity of intensity within the target volume is imposed by the term $\cos \gamma$ of equation (7-13) by virtue of the fact that $\cos \gamma$ is dependent, not only upon ϕ and θ , but upon spatial position parameters which cannot be annihilated. The solution to this problem is to define the array so that the $\cos \gamma$ term is eliminated. In general, there is no way to define N (the module surface density) so as to cancel $\cos \gamma$ because N is a surface scalar quantity while $\cos \gamma$ is dependent, not only upon location, but also upon the orientation of the surface element with respect to the target position. However, if the radiance of each module is a symmetric function of γ , specifically

$$I_\gamma = I_0 \cos \gamma \quad (7-14)$$

where I_0 is the radiance in the direction of the surface normal $d\vec{A}$, then equation (7-13) becomes

$$E = NI_0 \int_0^{2\pi} d\theta \int_0^\Phi \sin \phi \cos \phi d\phi \quad (7-15)$$

Integrating equation (7-15) yields

$$E = NI_0 \pi \sin^2 \Phi \quad (7-16)$$

which has no dependence upon position parameters. Thus, placing no restrictions on the array surface geometry, this concept calls for aligning the module axes normal to the array surface and holding the values of N and I_0 invariant for all modules. Further, the radiance of each module must be a cosine function with respect to its axis ($\gamma = 0^\circ$) and the angular divergence of radiation from each module must be restricted, by using appropriate field stops, to within an angle Φ with respect to the array axis. (The array axis is parallel to the z -axis of figure 7-2.)

The power P radiated by a module into a solid angle Ω is given by

$$P = \int L_\gamma d\Omega \quad (7-17)$$

Each module must radiate into the same field as that which is subtended by the radiation incident upon the target element. Therefore

$$P = \int_0^{2\pi} d\theta \int_0^\Phi I_\gamma \sin \phi d\phi \quad (7-18)$$

Since, for uniformity, the radiance of the module must be a function of $\cos \gamma$, then equations (7-14) and (7-18) yield

$$P = I_0 \int_0^{2\pi} d\theta \int_0^\Phi \cos \gamma \sin \phi d\phi \quad (7-19)$$

If the axis of the module is not parallel to the array axis, ϕ and θ must be expressed with respect to the module axis before equation (7-19) can be integrated. If the axis of the module is parallel to the array axis, then $\gamma = \phi$ and equation (7-19) may be integrated to give

$$P = I_0 \pi \sin^2 \Phi \quad (7-20)$$

which, when combined with equation (7-16) yields

$$P = \frac{E}{N} \quad (7-21)$$

There is an additional way to eliminate the term $\cos \gamma$ of equation (7-13). From the geometry of figure 7-2, it can be seen that if the array surface Σ is taken as a plane perpendicular to the z -axis, then γ and ϕ are equal which, when substituted into equation (7-13) gives

$$E = N \int_0^{2\pi} d\theta \int_0^\Phi I_\gamma \sin \phi d\phi \quad (7-22)$$

Since combining equation (7-18) and (7-22) again yields equation (7-21), it can be seen that when the conditions are such that uniformity obtains, the power output required from each module whose axis is parallel to the array axis is a function only of the required intensity E and the surface density of the modules N . If the array surface is other than a plane, the power output required of those modules whose axes are not parallel to the array axis must be determined according to equation (7-18) and could be more or less than the P of equation (7-21) depending upon the shape of the array surface. If the array surface were curved somewhat about the target volume, some savings in power for the edge could be realized. A further saving could be achieved by designing the modules so as to minimize the power which each radiates away from the target volume. It is important to note that the axial radiance I_o is fixed by the parameters N , E and Φ . That is, for any I_γ , if we define a function G on the basis of equation (7-18) such that

$$P = I_o G \quad (7-23)$$

where

$$G = \int_0^{2\pi} d\theta \int_0^\Phi \frac{I_\gamma}{I_o} \sin \phi d\phi \quad (7-24)$$

then from equation (7-21)

$$I_o = \frac{E}{NG} \quad (7-25)$$

The significance of this equation lies in the fact that the axial radiance of all the modules must be identical, regardless of their orientation, and may thus be studied on the basis of modules whose axes are parallel to the array axis. Thus, if the radiance is a cosine function

$$\frac{I_\gamma}{I_o} = \cos \gamma = \cos \phi$$

and

$$I_o = \frac{E}{\pi N \sin^2 \Phi} \quad (7-26)$$

For a spherically symmetric radiance function $\left(\frac{I_\gamma}{I_o} = 1 \right)$

$$I_o = \frac{E}{2\pi N(1 - \cos \Phi)} \quad (7-27)$$

Thus, for either of these radiance distributions, the lower the module packing density N and the smaller the field half angle Φ , the higher is the minimum permissible axial radiance I_o . This is a constraint which cannot be ignored in the design of modules for this type of system. Further, each module must radiate into a field restricted to Φ with respect to the direction of the array axis. Finally, the radiating area A of the module (the area of the module aperture) is restricted to $A \leq \frac{1}{N}$, which restriction results from the requirements of N modules per unit area. Using these three constraints, it is then possible to fix a lower bound on the most fundamental of the module's radiometric parameters, namely, brightness B . The brightness of the module aperture as seen from positions along the module's axis is given by

$$B = \frac{I_o}{A} \quad (7-28)$$

For a given axial radiance I_o , the minimum brightness B_{\min} is given by

$$B_{\min} = \frac{I_o}{A_{\max}} = I_o N \quad (7-29)$$

Thus, for a module whose radiance is a cosine function

$$B_{\min} = \frac{E}{\pi \sin^2 \Phi} \quad (7-30)$$

Equation (7-30) is of paramount importance in the determination of a feasible field angle for such a system since it actually contains much more information than the mere fact that the source must be at least sufficiently bright so that the effective module brightness after absorption

is that given minimally by equation (7-30) as a function of E and Φ only. On the contrary, the source must be considerably brighter in order that A does not have to be so great as $1/N$; otherwise the entire purpose of the projection array has been defeated. For example, if $A = 1/N$, then the exit apertures of the modules must cover the entire array area and a straightforward collimation system might just as well be employed to do the same thing. Thus, from a practical standpoint, the ratio of module exit aperture area to available module area (the quantity AN) must be considerably less than one. The quantity AN is proportional to the square of the ratio of the module aperture diameter to the intermodule spacing. In what might be a realistic estimate, the latter would be approximately $1/10$, in which case AN would be on the order of $1/100$.

Equation (7-30) may be written, for a cosine radiator, in more general form as

$$B = \frac{E}{AN \pi \sin^2 \Phi} \quad (7-31)$$

From this it is seen that the effective source brightness required for the case where $AN = \frac{1}{100}$, must be 100 times the value required for a continuous optical system, all other things being equal.

Equation (7-31) must be interpreted as follows. Let Φ_0 be the field angle possible in a continuous aperture optical system, e.g., collimator, for a source brightness B and a desired intensity E . (For a continuous aperture optical system, $AN = 1$.) In a discontinuous system the field angle that must be used, for the same source and requirements, is seen from equation (7-31) to be

$$\sin \Phi = \frac{1}{\sqrt{AN}} \sin \Phi_0 \quad (7-32)$$

Since the angle subtended by the simulated solar field $\Theta = 2\Phi$, then for the case where $AN = \frac{1}{100}$, the angle subtended by the solar field simulated by the projector array must be approximately 10 times that required had the same source been used with a continuous aperture optical system such as the hexagonally arranged array of parabolic reflectors to be considered next. (For the three sources considered for use with the array of parabolic reflectors, the range of the field angle is from 0.75° to 2.32° . Thus if these same sources were used for a projector array for $AN = \frac{1}{100}$, the angle subtended by the simulated solar field would range from 7.5° to 23.2° .) As can be seen from equations (7-26) and (7-32), I_0 is diminished, for a given E , in proportion to the AN factor.

It is instructive to examine the parametric relationships for an optical system so defined that, when it is employed with a specific source, the output radiance is a cosine function. We shall assume that the source radiance \bar{I}_0 and the output radiance $I_\gamma = I_0 \cos \gamma$ are axially symmetric. Defining P_c as the source power collected within an initial collection angle α , k as the transmittance of the optical system, and P as the output power radiated within the field half-angle Φ , then

$$P_c = 2\pi \bar{I}_0 \int_0^\alpha \frac{\bar{I}_0}{\bar{I}_0} \sin \phi d\phi \quad (7-33)$$

$$P = 2\pi I_0 \int_0^\Phi \frac{I_\gamma}{I_0} \sin \gamma d\gamma = \pi I_0 \sin^2 \Phi \quad (7-34)$$

$$P = k P_c \quad (7-35)$$

It is convenient to define a parameter G so that

$$G = \int_0^\alpha \frac{\bar{I}_0}{\bar{I}_0} \sin \phi d\phi \quad (7-36)$$

Thus G is proportional to the collection efficiency of the optical system. Equations (7-33), (7-34), (7-35) and (7-36) give

$$I_0 \sin^2 \Phi = 2k \bar{I}_0 G \quad (7-37)$$

Now specify that the optical system must deliver radiation to its exit pupil so that the exit pupil appears uniformly bright as viewed from all directions within Φ of the axis. Further specify that this exit pupil is circular, of radius y , and of brightness B . Then

$$I_0 = B\pi y^2 \quad (7-38)$$

$$I_\gamma = B\pi y^2 \cos \gamma \quad (7-39)$$

Combining equations (7-37) and (7-38)

$$G = \frac{B\pi y^2 \sin^2 \Phi}{2k \bar{I}_0} \quad (7-40)$$

If \bar{B} is now defined as the source brightness, then B is related to \bar{B} through

$$B = k \bar{B} \quad (7-41)$$

since brightness is altered only by dissipative factors in the optical system. Therefore

$$G = \frac{\bar{B} \pi y^2 \sin^2 \Phi}{2I_0} \quad (7-42)$$

Thus a relationship has been established between the source parameters and certain geometrical parameters of the optical system. Now consider the behavior of equation (7-42) for several simple source configurations.

First, consider a flat disk of radius x and brightness B . By definition, the radiance of such a source is a cosine function. Therefore

$$\bar{I}_0 = \bar{B} \pi x^2 \quad (7-43)$$

$$\bar{I}_\phi = \bar{I}_0 \cos \phi = \bar{B} \pi x^2 \cos \phi \quad (7-44)$$

Then, from equations (7-36), (7-43) and (7-44)

$$G = \frac{1}{2} \sin^2 \alpha \quad (7-45)$$

(In this case G equals one half the collection efficiency)

Substituting equations (7-43) and (7-44) into equation (7-45) gives

$$x \sin \alpha = y \sin \Phi \quad (7-46)$$

The validity of the above procedure is seen in the fact that equation (7-46) is Abbe's sine condition for lateral magnification. In order to achieve an exit pupil of radius y which is uniformly bright as seen from all directions within Φ of the axis, then the lateral magnification m of the optical system which images the source at the exit pupil must be a constant within the collection angle α . Therefore

$$m = \frac{y}{x} = \frac{\sin \alpha}{\sin \Phi} = \frac{\sin \phi}{\sin \gamma} \quad (7-47)$$

where α and Φ are the maximum values of ϕ and γ , respectively. Combining equations (7-32), (7-45) and (7-46) gives

$$N = \frac{\sin^2 \Phi_0}{2 \pi x^2 G} \quad (7-48)$$

where Φ_0 again is the field angle possible if the source were used with a collimating optical system. Equation (7-47) can be used to define the optical system to be used with the source of radius x since, if one additional parameter (such as the exit pupil radius y or the parameter G) is specified, the remaining optical parameters are completely constrained.

Consider, as a second source, a uniformly radiating sphere of radius r and brightness B . The radiance function of this source is

$$\frac{\bar{I}_\phi}{\bar{I}_0} = 1 \quad (7-49)$$

If T is defined as the total power radiated by this source, then

$$T = 2 \pi \bar{I}_0 \int_0^\pi \sin \phi \, d\phi = 4 \pi \bar{I}_0 \quad (7-50)$$

The brightness \bar{B} is

$$\bar{B} = \frac{T}{(4\pi)(\pi r^2)} = \frac{\bar{I}_0}{\pi r^2} \quad (7-51)$$

From equation (7-36)

$$G = 1 - \cos \alpha \quad (7-52)$$

(In this case, G equals twice the collection efficiency)

Substituting equations (7-51) and (7-52) into equation (7-42) yields

$$\frac{y^2}{r^2} = \frac{2(1 - \cos \alpha)}{\sin^2 \Phi} = \frac{2(1 - \cos \phi)}{\sin^2 \gamma} = \text{constant} \quad (7-53)$$

which is the defining equation for the optical system to be used with a spherical source.

The last source to be considered here is a combination of the plane and spherical sources considered above. The radiance and brightness of the source are

$$I_\phi = I_0 (a + b \cos \phi) \quad (7-54)$$

$$\bar{B} = \frac{\bar{I}_0}{\pi x^2} \quad (7-55)$$

Therefore, from equation (7-36)

$$G = a(1 - \cos \alpha) + \left(\frac{b}{2}\right) \sin^2 \alpha \quad (7-56)$$

and, substituting equations (7-55) and (7-56) into equation (7-42), the defining equation for the optical system to be used with this combination source is

$$\frac{y^2}{x^2} = \frac{2a(1 - \cos \alpha) + b \sin^2 \alpha}{\sin^2 \Phi} = \frac{2a(1 - \cos \phi) + b \sin^2 \phi}{\sin^2 \gamma} = \text{constant} \quad (7-57)$$

If the array surface is specified as planar, the requirement that the output radiance be a cosine function no longer exists and a simple projection system of the type represented schematically in figure 7-3 may be used. In this system, the collector-condenser system serves to image the source into the aperture of the projection lens, collecting radiation through an angle α and projecting it through an angle β . The projection lens serves to image the exit pupil of the collector-condenser system at infinity. Certain relationships are immediate. First, $\beta = \Phi$ since it is the collector-condenser exit pupil which forms the field. Further, since the collector-condenser system produces an image of the source at the projection lens, then from Abbe's sine condition

$$r \sin \alpha = y \sin \beta = y \sin \Phi \quad (7-58)$$

where r is the source radius and y is the image radius. The parameter $\sin \alpha$ is known as the numerical aperture of the collector-condenser system and is important in determining the feasibility of designing such a system.

If it is assumed that the projector is a refractive optical system of four lenses, and that each lens has an average transmittance of 90%,

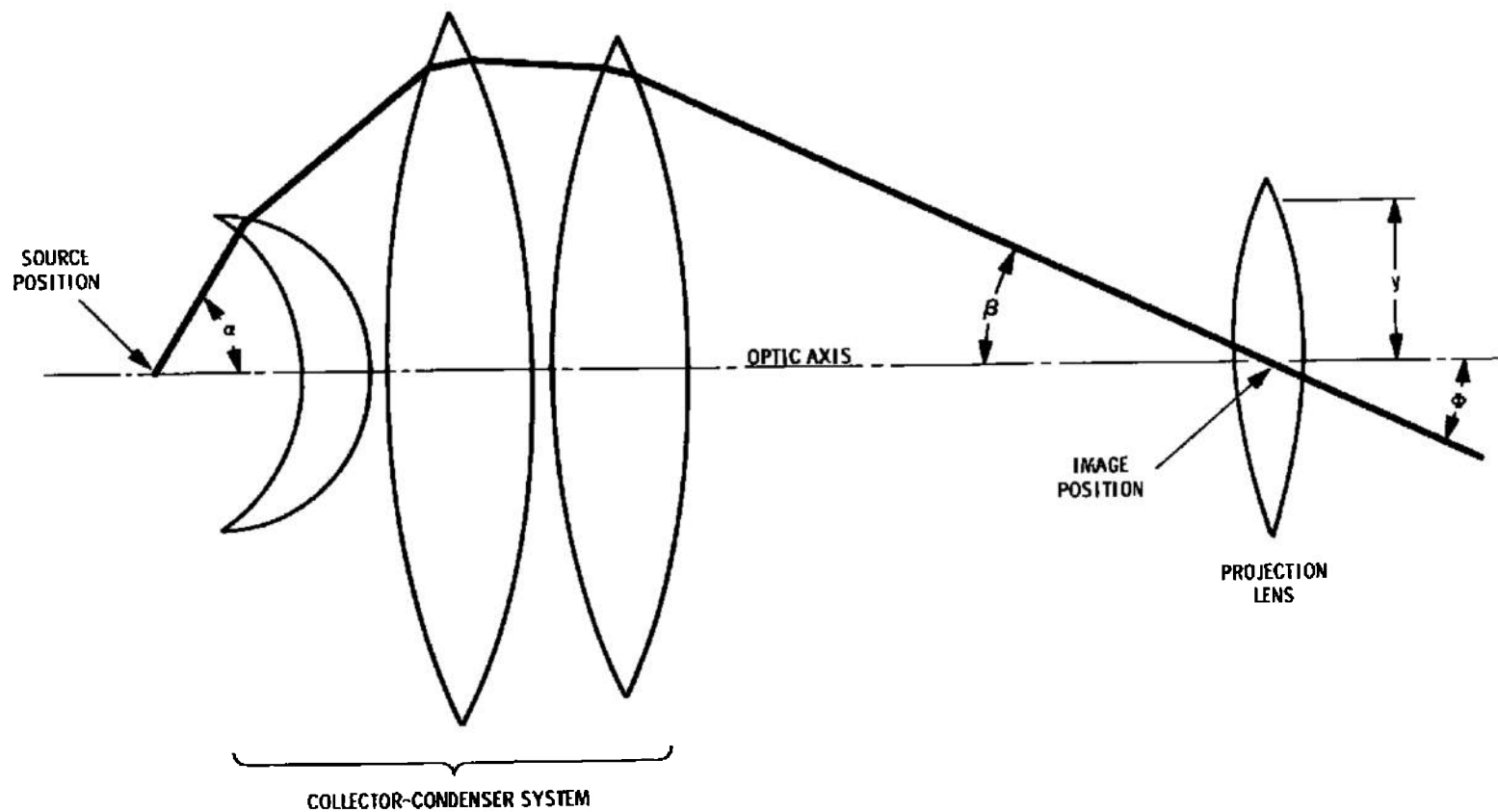


Figure 7-3. Schematic Representation of a Projector System

then the transmittance k of the optical system is 65.61%. Also, since it is extremely difficult to achieve a practical optical design for a refractive collector-condenser system for a numerical aperture which is much greater than 0.866, the initial collection angle shall be specified $\alpha = 60^\circ$. Now consider the performance characteristics of this system when it is used with the 37.5-kilowatt Fluid Transpiration Arc.

Available data indicates that radiance of the 37.5-kilowatt Fluid Transpiration Arc may be represented according to equation (7-54) where $I_0 = 1900$ watts-per-steradian, $a = 0.9236$ and $b = 0.0764$. The power P_c collected by the optical system within $\alpha = 60^\circ$ may be calculated by applying equations (7-33), (7-54), and (7-56), and is

$$P_c = \pi I_0 [2a(1 - \cos \alpha) + b \sin^2 \alpha] = 5850 \text{ watts}$$

The collection efficiency, with respect to the power radiated by the 37.5-kilowatt FTA (11482 watts) into a hemisphere is 51.0%. The power output is

$$P = kP_c = 3840 \text{ watts}$$

The density N of modules on the array surface required in order to achieve an intensity $E = 0.260$ watt-per-square-centimeter (solar intensity at the Venus orbit) is, from equation (7-21)

$$N = \frac{E}{P} = 0.0629 \text{ module-per-square foot}$$

There must, therefore, be one module for each 15.9 square feet of area on the array surface. If the modules are arranged in a hexagonal array and, if d is defined as the distance between the axes of adjacent modules,

$$A_{\text{HEX}} = \frac{3}{2} d^2 \tan 30^\circ = 15.9 \text{ square feet}$$

which, when solved for d yields

$$d = 4.28 \text{ feet}$$

The solid angle Ω into which the module radiates is equal to the solid angle through which radiation is incident upon a target element. If A_T is the area on the array surface which is seen to radiate with an average brightness \bar{B} , then the intensity at the target position is given by

$$E = \bar{B} \Omega = \bar{B} \pi \sin^2 \Phi \quad (7-59)$$

If \bar{B} is now defined as the average brightness across the apertures of each of the n modules which can be seen through the solid angle Ω then, again defining A as the aperture area of each module and N as the density of modules on the array surface,

$$\bar{B} = \frac{nA \bar{B}}{A_T} = AN \bar{B} \quad (7-60)$$

The radius r of the 37.5-kilowatt FTA is approximately 0.2 inch and its axial radiance \bar{I}_0 is 1900 watts-per-steradian. If Φ_0 is again defined as the field half angle which would result if the 37.5-kilowatt FTA were used with a collimating optical system of the same transmittance k in order to produce the required intensity E , then

$$E = \pi B \sin^2 \Phi_0 \quad (7-61)$$

$$\sin \Phi_0 = r \sqrt{\frac{E}{k \bar{I}_0}} = 0.007336 \quad (7-62)$$

Combining equations (7-59), (7-60) and (7-61) yields

$$AN \sin^2 \Phi = \sin^2 \Phi_0 \quad (7-63)$$

which may be rewritten as

$$\sin^2 \Phi = \frac{\sin^2 \Phi_0}{AN} \quad (7-64)$$

Combining equations (7-58), (7-62) and (7-64), an equation may be obtained for the radius of the module aperture y . Thus

$$y = \frac{r \sin \alpha}{\sin \Phi_0} \sqrt{AN} = \sin \alpha \sqrt{\frac{AN k \bar{I}_0}{E}} \quad (7-65)$$

Again specifying that $AN = 0.01$, then $\Phi = 4.2^\circ$, the aperture radius $y = 2.361$ inches, and the aperture area $A = 17.5$ square inches = 0.12161 square foot. Now, calculating a value for AN from the calculated values of A and N , yields $AN = 0.0076$. This discrepancy between the specified and calculated values of AN is a measure of the degree to which equation (7-58) and thus equation (7-65) is an approximation for a volumetric source. Had the values of A and y been determined directly from the calculated value of $N = 0.0629$ modules-per-square-foot and the specified value of $AN = 0.01$, then $A = 0.159$ square foot = 22.9 square inches and $y = 2.70$ inches.

Thus far, it has been determined, assuming infinitely dense module packing, that it is possible to achieve constant field angle, uniformity of intensity and prescribed solar intensity throughout a finite volume. To accomplish this it is required that the modules be masked so that their fields are all identically limited with respect to the same direction, the module axes be normal to the local array surface and the polar radiance with respect to the module axis must be a cosine function if the array surface is curved but is undefined if the array surface is flat. It was seen that for realistic module exit aperture sizes, it is necessary to enlarge the projection field and thereby the simulated solar field.

It is imperative, therefore, to examine the behavior of the system for finite module aperture sizes and spacing. The nature of the distribution of module apertures on the array surface is arbitrary, provided they cover the array surface with uniform packing density. In order to show that the specific nature of the distribution of modules is immaterial and also to develop a somewhat different approach to the calculation, consider a hexagonally arranged array on a flat surface (the closest packing arrangement possible in two dimensions).

Assume without loss of generality, that each module produces a uniform radiance within the angle Φ with respect to its axis. The symmetry axis of radiation from each module will be directed normal to the plane (the array surface). At a position a distance D from the array, calculate E on a surface element facing the plane modular array. Because of the geometry imposed, radiation can reach the target element only from modules located within the field angle $\Theta/2 = \Phi$ taken with respect to the target position. The intensity of the radiation from each module which is incident upon the surface element varies inversely with the square of the distance from the surface element to the module. Define the uniform radiance of the modules as

$$I = \frac{P}{\Omega} = \frac{P}{2\pi(1 - \cos \Phi)} \quad (7-66)$$

where Ω is the solid angle into which the modules radiate. The intensity at a distance L from a module, is

$$E \approx \frac{I}{L^2} \quad \text{where } L = \frac{D}{\cos \theta} \quad (7-67)$$

where θ is taken, with respect to the direction of the array surface normal, from the target position to the array and is the angle from that position to a ring of modules. Therefore, the intensity contributed at the target element from a module in the direction θ is

$$\Delta E = I \left(\frac{\cos^3 \theta}{D^2} \right) \quad (7-68)$$

The additional cosine factor is the view factor taken at the target surface element.

In a hexagonal array, the modules are arranged in nearly circular rows with $6n$ modules in the n th row. Defining A as the intermodule spacing; i.e., distance between the centers of adjacent modules, then the distance R , which is measured, in the plane of the array, from the perpendicular from the target point to the array to the n th row is $R = nA$. Also

$$R = D \tan \theta \quad (7-69)$$

$$dR = \left(\frac{D}{\cos^2 \theta} \right) d\theta \quad (7-70)$$

The number of rows in dR is $\frac{dR}{A}$ and the average number of modules in the rows at a distance R is $\left(\frac{R}{A} \right)$. Therefore, the number of modules within $d\theta$ at θ is

$$6 \left(\frac{R}{A} \right) \frac{dR}{A} = 6 \left(\frac{D \tan \theta}{A^2} \right) \left(\frac{D}{\cos^2 \theta} \right) d\theta = 6 \left(\frac{D^2 \tan \theta}{A^2 \cos^2 \theta} \right) d\theta \quad (7-71)$$

Multiplying this by the intensity contributed from each module and integrating gives

$$E = \int_0^\Phi \left(\frac{I \cos^3 \theta}{D^2} \right) \left(\frac{6D^2}{A^2} \right) \left(\frac{\tan \theta}{\cos^2 \theta} \right) d\theta \quad (7-72)$$

where the limit of integration is determined by the upper bound on the field angle (as explained above) and the equation is valid only within the region where these limits hold. This reduces to

$$E = \frac{6I}{A^2} \int_0^\Phi \sin \theta d\theta = \frac{6I}{A^2} (1 - \cos \Phi) \quad (7-73)$$

which from equation (7-66) is

$$E = \frac{3P}{\pi A^2} \quad (7-74)$$

It is seen that the flux density E is independent of D , which implies uniformity in volume as stated above, as long as the limits of integration remain intact. On the other hand, the number of modules within a radius R is the arithmetic sum of $\frac{6n(n+1)}{2}$ where $n = \frac{R}{A}$.

Thus, the number of modules N per unit area, is

$$N = \frac{3 \left(\frac{R}{A} \right) \left(\frac{R}{A} + 1 \right)}{\pi R^2} \quad (7-75)$$

If $\frac{R}{A}$ is large, then the approximation that $\frac{R}{A} = \left(\frac{R}{A} \right) + 1$ can be made. Therefore, $N = \frac{3}{\pi A^2}$. Combining this with equation (7-74) gives

equation (7-21), $E = PN$. This treatment is not strictly correct in the way in which the modules were integrated, in that the rows arrange themselves as the perimeter of a hexagon rather than as a circular ring. In order to sum the contributions of the modules properly and take into account the limited number of modules in any given field of view, the finite sum of the appropriate series must be evaluated. That this is worthwhile can be seen from the result above, where uniformity can be demonstrated as one approaches the infinite sum. The value $E = PN$ will also be the asymptotic limit of the series sum.

In evaluating the actual fluctuations in intensity on the target element as it recedes from such an array of modules, the contributions of radiation from each of the modules falling within the limits of integration are added. Since these contributions vary inversely with the square of the distance from the array, the same approach as was just used for the continuum of modules is now applied to each module individually.

It is assumed, again for convenience, that the polar radiance function, I , is constant. Figure 7-4 shows an array of modules centered at the origin of an x - y coordinate system and the following will show how to account for all those contained within a circle of radius R , representing the effective exit pupil of the array with respect to a given target point. If D is the perpendicular distance from the array to the point of observation then R must subtend the appropriate field value or

$$\frac{R}{D} = \tan \left(\frac{\theta}{2} \right) \quad (7-76)$$

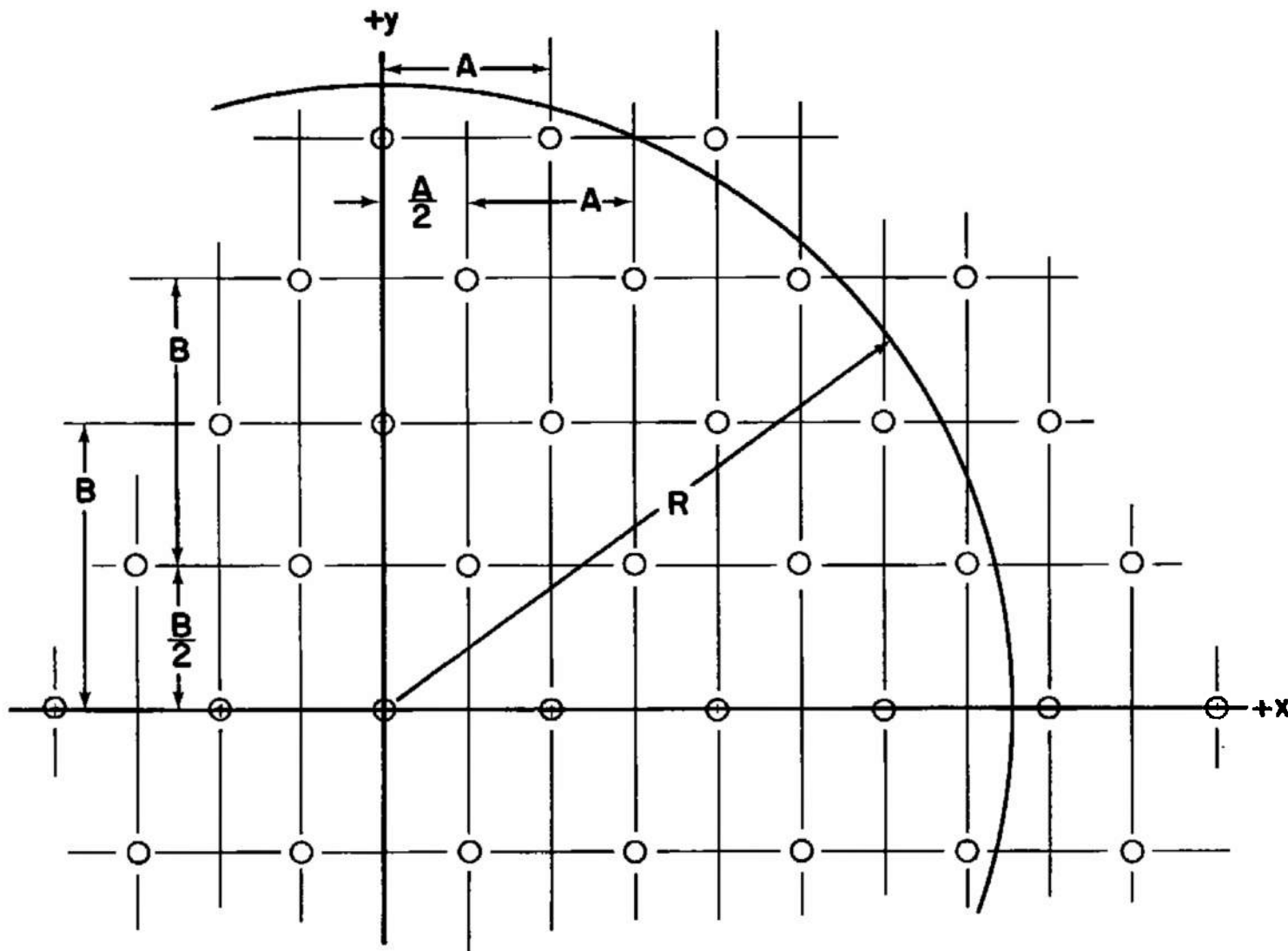


Figure 7-4. Hexagonal Array of Projectors

The contribution of each module ΔE is still given by equation (7-68). The field will be divided among the four quadrants of the x-y coordinate system. Thus, if A is again defined as the distance between the centers of the projection lens apertures of adjacent projectors, then the distance between projectors along the x-axis is A and the distance between projectors along the y-axis is $B = A\sqrt{3}$. The total intensity E on the target element is then defined as

$$E = E_c + E_x + E_y + E_{xy} \quad (7-77)$$

where

E_c = intensity contribution from the central projector

E_x = intensity contribution from projectors on the x-axis

E_y = intensity contribution from projectors on the y-axis

E_{xy} = intensity contribution from projectors on neither axis

Defining I , R , D , and θ as above, and

$$\alpha = \frac{R}{A} \quad (7-78)$$

$$\gamma = \frac{D}{A} \quad (7-79)$$

the intensity contributions are determined as follows. (Note: In the following equations, the quantities with an asterisk (*) in the exponent position are to be truncated to integers before proceeding with the computation.) From equations (7-68) and (7-79)

$$\Delta E = \frac{I \cos^3 \theta}{A^2 \gamma^2} \quad (7-80)$$

1. For the central projector, $\cos \theta = 1$. Therefore

$$E_c = \frac{I}{D^2} = \frac{I}{A^2 \gamma^2} \quad (7-81)$$

2. Define $2n$ as the number of projectors along the x-axis (excluding the central projector) that are contributing energy to the target element; all of the contributing projectors (spaced at intervals of length A) are contained within a circle of radius R and

$$n = \left(\frac{R}{A}\right)^* = \alpha^* \quad (7-82)$$

Defining i as an integer so that $1 \leq i \leq n$ then

$$\cos \theta_i = \frac{D}{\sqrt{D^2 + x_i^2}} = \sqrt{\frac{D^2}{D^2 + i^2 A^2}} = \sqrt{\frac{\gamma^2}{\gamma^2 + i^2}} \quad (7-83)$$

Therefore from equation (7-80)

$$E_x = 2 \sum_{i=1}^n \left(\frac{I}{A^2 \gamma^2}\right) \left(\frac{\gamma^2}{\gamma^2 + i^2}\right)^{\frac{3}{2}} \quad (7-84)$$

3. Define $2m$ as the number of projectors along the y -axis (again excluding the central projector) that are contributing energy to the target element; all of the projectors (spaced at intervals of length $B = 2A \cos 30^\circ = A\sqrt{3}$) are contained within a circle of radius R and

$$m = \left(\frac{R}{B}\right)^* = \left(\frac{R}{A\sqrt{3}}\right)^* = \left(\frac{\alpha}{\sqrt{3}}\right)^* \quad (7-85)$$

Defining j as an integer so that $1 \leq j \leq m$, then

$$\begin{aligned} \cos \theta_j &= \frac{D}{\sqrt{D^2 + y_j^2}} = \sqrt{\frac{D^2}{D^2 + j^2 B^2}} = \sqrt{\frac{D^2}{D^2 + 3j^2 A^2}} \\ &= \sqrt{\frac{\gamma^2}{\gamma^2 + 3j^2}} \quad (7-86) \end{aligned}$$

Therefore

$$E_y = 2 \sum_{j=1}^m \left(\frac{I}{A^2 \gamma^2}\right) \left(\frac{\gamma^2}{\gamma^2 + 3j^2}\right)^{\frac{3}{2}} \quad (7-87)$$

4. The remaining projectors in the array lie at coordinates x_h, y_k such that:

$$x_h = \frac{hA}{2} \quad (7-88)$$

$$y_k = kB - \delta B = A(k - \delta)\sqrt{3} \quad (7-89)$$

where

$$\delta = \frac{1}{2} \left[\left(\frac{h+1}{2} \right)^* - \left(\frac{h-1}{2} \right)^* \right] \quad (7-90)$$

The quantity δ is a positioning parameter and was determined, on the basis of the array geometry, so that when h is odd $\delta = \frac{1}{2}$ and when h is even $\delta = 0$. This formalism is designed for convenience of computer programming and is based upon the columnar symmetry of the hexagonal array. It is seen from figure 7-4 that every module center may be located on vertical columns (parallel to the y -axis) spaced at intervals of one half of the intermodule center distance A . Thus the horizontal parameter x_h is measured in integral units of $\frac{A}{2}$ and each column can be assigned a position number h . The vertical spacing between module centers along any given column is B . If the column h is odd, the first module ($k = 1$) is located a distance $\frac{1}{2}B$ from the x -axis while if the column number h is even, the first module ($k = 1$) is located a distance B from the x -axis. This is the purpose served by the parameter δ in equation (7-89) where the magnitude of δ is controlled by the column number h in accordance with equation (7-90).

Any given projector located at coordinates (x_h, y_k) contributes energy to the target element if and only if

$$R^2 \geq x_h^2 + y_k^2 \quad (7-91)$$

where from equations (7-88) and (7-89)

$$x_h^2 + y_k^2 = \frac{h^2 A^2}{4} + 3A^2 (k-\delta)^2 = \frac{A^2}{4} [h^2 + 12(k-\delta)^2] \quad (7-92)$$

If u is defined as the upper limit of h , then

$$R \geq x_u = u \left(\frac{A}{2} \right) \quad (7-93)$$

Therefore

$$u = \left(\frac{2R}{A} \right)^* = (2\alpha)^* \quad (7-94)$$

If v is defined as the upper limit of k for any value of h , then substituting v for k in equation (7-92):

$$R^2 \geq x_h^2 + y_v^2 = \frac{A^2}{4} [h^2 + 12(v-\delta)^2] \quad (7-95)$$

Solving this equation for v

$$v = \left(\sqrt{\frac{4\alpha^2 + h^2}{12}} + \delta \right)^* \quad (7-96)$$

The direction of view to a projector is given by

$$\begin{aligned} \cos \theta_{hk} &= \frac{D}{\sqrt{D^2 + (x_h^2 + y_k^2)}} = \sqrt{\frac{4D^2}{4D^2 + A^2 [h^2 + 12(k-\delta)^2]}} \\ &= \sqrt{\frac{4\gamma^2}{4\gamma^2 + h^2 + 12(k-\delta)^2}} \quad (7-97) \end{aligned}$$

It can therefore be seen that the intensity contribution from all of the projectors which lie neither on the x -axis nor the y -axis is

$$E_{xy} = 4 \sum_{h=1}^u \sum_{k=1}^v \left(\frac{I}{A^2 \gamma^2} \right) \left[\frac{4\gamma^2}{4\gamma^2 + h^2 + 12(k-\delta)^2} \right]^{\frac{3}{2}} \quad (7-98)$$

The total contribution is obtained by summing equations (7-81), (7-84), (7-87), and (7-98). The solution is expressed in terms of the normalized intensity parameter J as

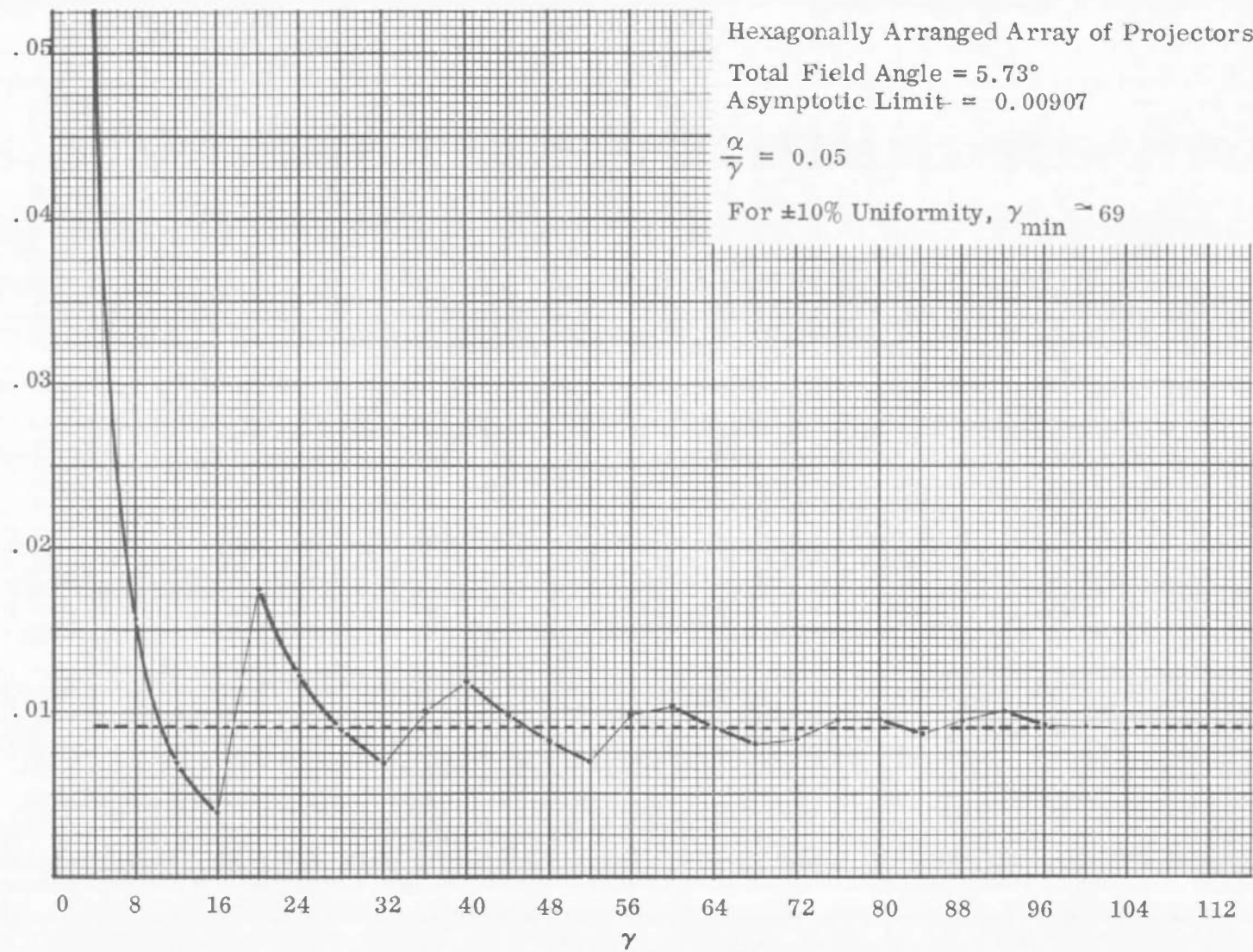
$$\begin{aligned}
 J = \frac{EA^2}{I} = & \left[\frac{1}{\gamma^2} + 2\gamma \sum_{i=1}^n \left(\frac{1}{\gamma^2 + i^2} \right)^{\frac{3}{2}} \right. \\
 & + 32\gamma \sum_{h=1}^u \sum_{k=1}^v \left(\frac{1}{4\gamma^2 + h^2 + 12(k-\delta)^2} \right)^{\frac{3}{2}} \\
 & \left. + 2\gamma \sum_{j=1}^m \left(\frac{1}{\gamma^2 + 3j^2} \right)^{\frac{3}{2}} \right] \quad (7-99)
 \end{aligned}$$

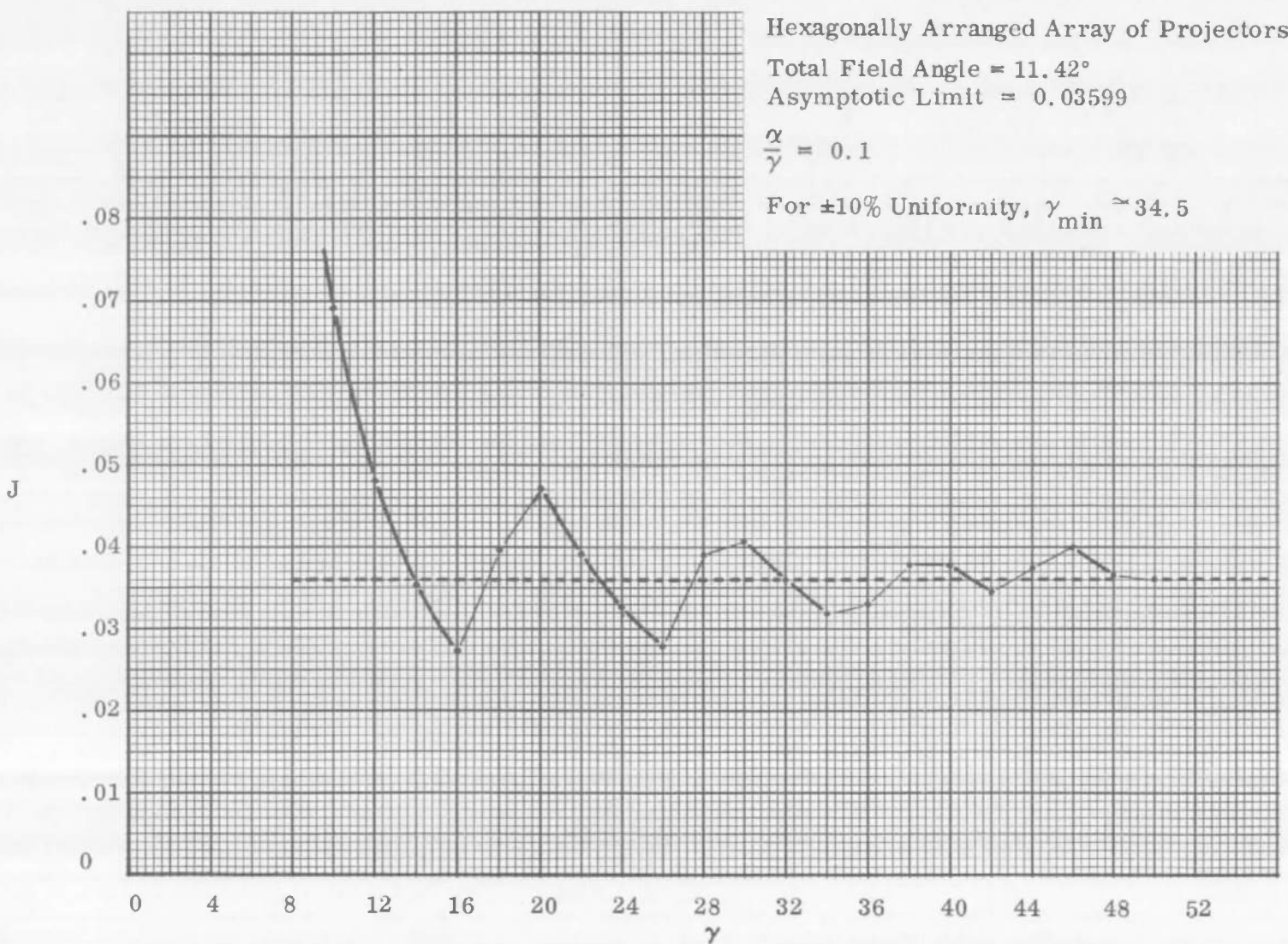
where the parameters n , m , u , v , and δ are given, respectively, by equations (7-82), (7-85), (7-94), (7-96), and (7-90).

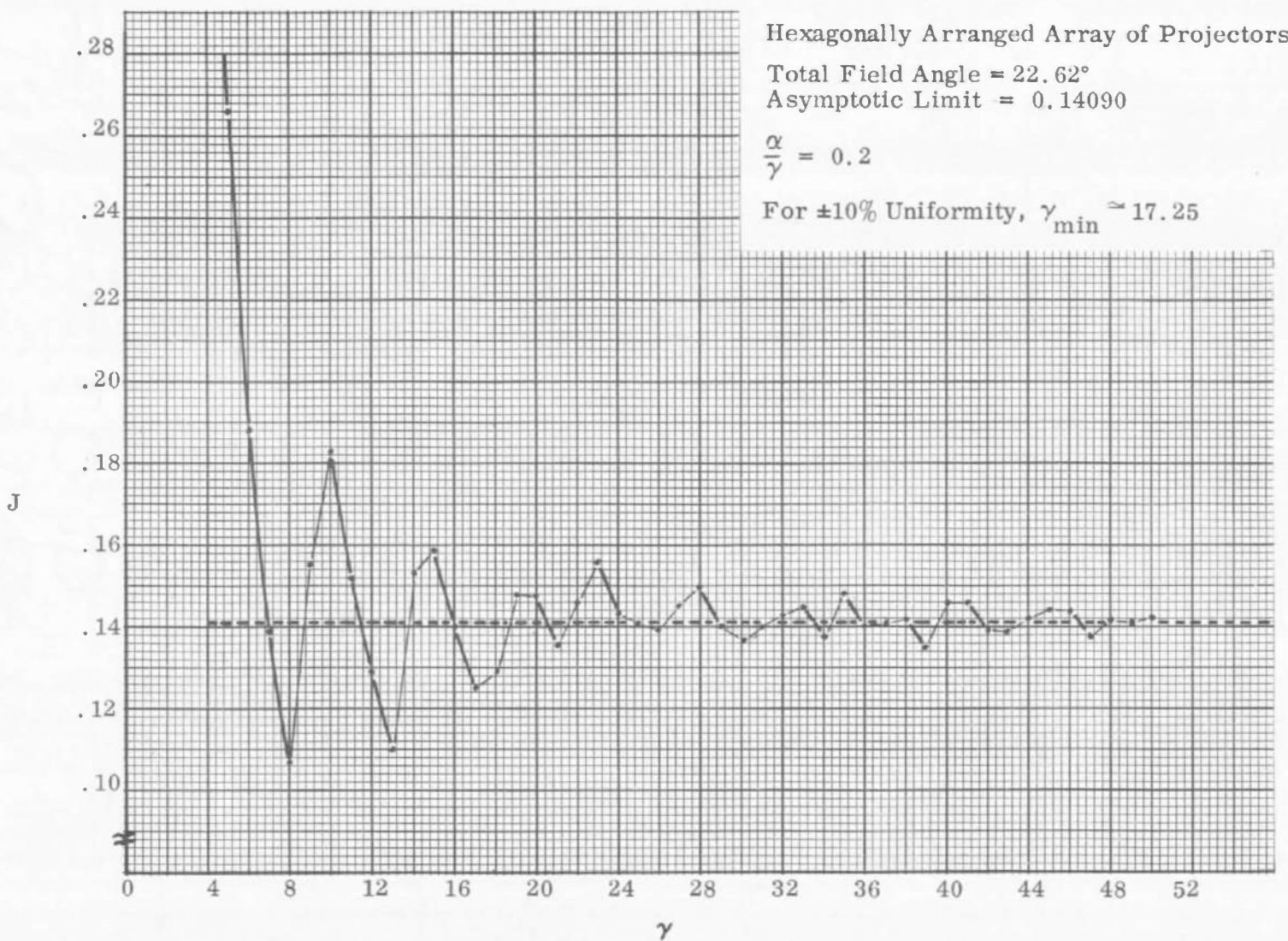
The normalized intensity parameter J is then calculated and plotted as a function of γ . The relative variation in J is a measure of the uniformity in depth which is possible. The only parameters which can affect the behavior of this function are field angle and packing density. It is clear that the greater each is, the smoother the distribution will be. Also, the farther from the array (higher γ) the smoother the distribution will become. All these things are displayed in the results obtained from the evaluation of equation (7-99). Both packing density and field angle are parameters which resolve to the single parameter α . The field angle, as defined by equation (7-76), is

$$\tan \frac{\Theta}{2} = \frac{R}{D} = \frac{\alpha}{\gamma} \quad (7-100)$$

The procedure, then, is to hold $\frac{\alpha}{\gamma}$ constant as γ is varied. When the amplitude of undulation of J is sufficiently small, we note the value of γ and calculate the value of α from equation (7-92) for the particular field Θ used. This provides a measure of the number of modules which must be included in the field for any given field angle to obtain an intensity distribution of any desired smoothness. A special purpose computer program (PROJT) was developed to solve equation (7-99) for J as a function of γ for a number of values of $\frac{\alpha}{\gamma}$. See Appendix I. The values of $\frac{\alpha}{\gamma}$ used were 0.05, 0.1, 0.2, and 0.5, which correspond to field angles Θ of 5.73° , 11.42° , 22.62° , and 53.13° , respectively. Figures 7-5 through 7-8 are plots of J vs. γ for these field values.

Figure 7-5. J versus γ for $\Theta = 5.73^\circ$

Figure 7-6. J versus γ for $\Theta = 11.42^\circ$

Figure 7-7. J versus γ for $\Theta = 22.62^\circ$

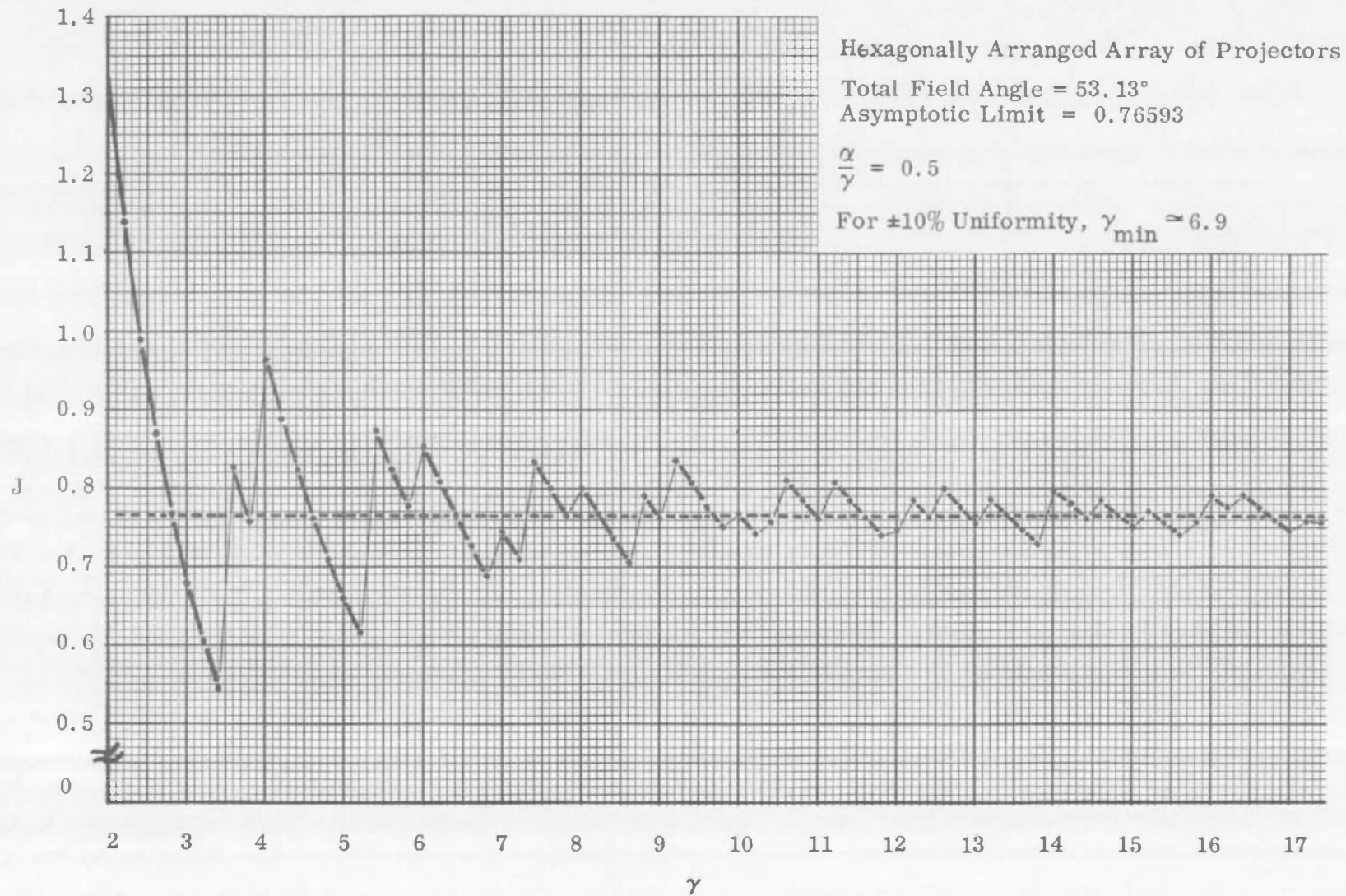


Figure 7-8. J versus γ for $\Theta = 53.13^\circ$

If \bar{J} is defined as the average value of J within the target volume, then J approaches \bar{J} as a limit as γ approaches infinity. For the case of a hexagonally arranged array of projectors whose output radiance I is uniform and contained within a solid angle Ω ,

$$\bar{J} = \lim_{\gamma \rightarrow \infty} J = \frac{2\Omega}{\sqrt{3}} = \frac{[4\pi - 1 - \cos(\frac{\Omega}{2})]}{\sqrt{3}} \quad (7-101)$$

The value of \bar{J} was determined for each case studied and was plotted as a dashed straight line on figures 7-5 through 7-8.

If it is now arbitrarily specified that the intensity distribution in the target volume must be uniform within $\pm 10\%$, this means that for all values of γ greater than γ_{\min} , J must range between $0.9 \bar{J}$ and $1.1 \bar{J}$. γ_{\min} thus represents the minimum relative distance between the array of projectors and the target volume. A study of the graphs of figures 7-5 and 7-8 indicates that, in all cases, J is uniform within $\pm 10\%$ when α is greater than approximately 3.45. (The value of γ_{\min} noted on each of these figures was determined by specifying that $\alpha_{\min} = 3.45$.) The density N of modules on the array surface is

$$N = \frac{2}{A^2 \sqrt{3}} \quad (7-102)$$

The area S on the array surface which contains all of the modules which are irradiating any given target position is

$$S = \pi R^2 = \pi \alpha^2 A^2 \quad (7-103)$$

Therefore, if n is defined as the minimum number of modules which can irradiate any position in the target volume, based on a requirement of $\pm 10\%$ uniformity, then from equations (7-99) and (7-103)

$$n = NS_{\min} = \frac{2\pi \alpha_{\min}^2}{\sqrt{3}} \cong 43 \text{ modules} \quad (7-104)$$

It was calculated earlier that, if the 37.5-kilowatt Fluid Transpiration Arc were used with a refractive projection system, the total angle into which such a module would radiate would be approximately 8.4° in which case $\frac{\alpha}{\gamma} = 0.07336$. Since the magnitude of α_{\min} is apparently a function only of the uniformity requirement, then for $\pm 10\%$ uniformity, $\alpha_{\min} = 3.45$ and thus $\gamma_{\min} = 47$. It was also calculated that spacing between adjacent modules in a hexagonally arranged array would be $A = 4.3$ feet. Therefore, from equation (7-79), the minimum distance

at which the intensity distribution produced by a hexagonal array of such modules would become uniform within $\pm 10\%$ would be approximately 202 feet from the array surface. Also, because of the 8.4° field angle, the diameter of the array surface would have to be about 30 feet larger than the diameter of the target volume at 202 feet from the array. Therefore, it must be concluded that this is a totally impractical design concept.

7.3.3

Analysis of Results

It has been shown that, on a theoretical basis, it is possible to obtain uniformity within a finite volume using the projection array design concept as described above. The conditions which must be met in order to achieve the proper average intensity were derived. It was shown further that this ideal solution is only an asymptotic limit, as the conditions of continuity are approached by an otherwise discrete set of values and, until a sufficient number of modules are included in the field of view, the deviation from the mean intensity is considerable. At high levels of input power the modules themselves are of such great size and intercenter distance that the dimensions involved are totally impractical. Further, the energy wasted at the edge of the array, because of a necessarily enlarged field angle and great throw distance, can be many times the energy actually used by the target volumes. For example if the target volume were 50 feet across, the array would have to be 80 feet across and the energy wasted outside the target volume would then be approximately 2.5 times that actually used.

There are only two conceivable ways to circumvent this difficulty. One is to use many more, much less powerful sources. However, if the power level were reduced by a factor of 10, assuming the same brightness (which is not likely), the intermodule dimensions would be reduced only by a factor of 3 (less for a source of lesser brightness). Thus the point of closest approach could be about 70 feet as opposed to the 202 feet. This is still a hopelessly defeating situation. If arc power were reduced even further, then the whole point of this study directed at high power solar modules is frustrated.

The only other expedient possible would be to allow one arc to act as a source for many projectors. The concept is a simple one. First note that the field angle will not be affected as it is determined by \sqrt{AN} [see equation (7-32)] which remains fixed, and the value of Φ_0 which is a function only of arc brightness, also unalterable. The AN ratio, or module aperture to intermodule spacing, is not changed because the energy delivered to the module determines its size and spacing by exactly reciprocal proportions.

Although it is not necessary to go into great detail here on how this concept might be effected, one approach, which could satisfy the essential requirements and still provide for practical overall system dimensions, is illustrated in figure 7-9. It consists of a ring of flat mirrors and off-axis ellipsoidal reflector segments positioned to provide a corresponding number of virtual images of the source. They are tilted in a manner which would locate the virtual images in a somewhat hexagonal array, perhaps, or some other convenient symmetrical distribution. In front of each ellipsoid, subsequent to the latter's reflection of the incident light, is positioned a condenser lens which images the arc, as seen in the mirror, into a projection lens. Except for the presence of the mirrors to break up the single arc into many arc images, the optical system is virtually the same as that discussed earlier. In order to realize a lower bound on approach distance of less than 25 feet (which can be thought practical for large space environmental chambers), the effective intermodule spacing would have to be not much greater than 6 inches. In such a case, excellent uniformity would be realized through most of the target volume but it will never be possible to improve the field angle characteristic by any significant factor. Finally, although it may be possible to obtain the desired aperture packing density, this can only be done at the expense of a considerably more complicated module design, particularly with regard to the number of components.

7.4 MODULAR ARRAY OF SIMPLE PARABOLOIDS

7.4.1 Statement of the Problem

It is not difficult to visualize an array of identical axially symmetric parabolic mirrors (each of which has a light source at its focus) whose apertures are hexagonal, whose axes are mutually parallel, and whose apices all lie in the same place on equally spaced centers corresponding to hexagonal closest packing. Unfortunately, the picture becomes a bit confusing with attempts to represent the multiplicity of radiant energy contributions to the target volume from such an array. The temptation to regard the radiant flux distribution as that which would result from a contiguous array of mutually exclusive "cylinders" of light whose respective boundaries are defined by the hexagonal aperture of each module can lead only to miscalculation. This is particularly true at large distances from the aperture plane of the array because of the divergent nature of the pencil of light emanating from each module. It is therefore necessary to consider a complex of overlapping beams at every level of the target volume. If this overlapping did not occur, it would be sufficient to know the radiant flux distribution across the aperture of a single module. (Theoretically, this can be closely approximated on the basis of wavefront curvature at each discontinuity if the field angle subtended by the incident radiation is considered to be small.) The overall distribution of radiant flux across any plane

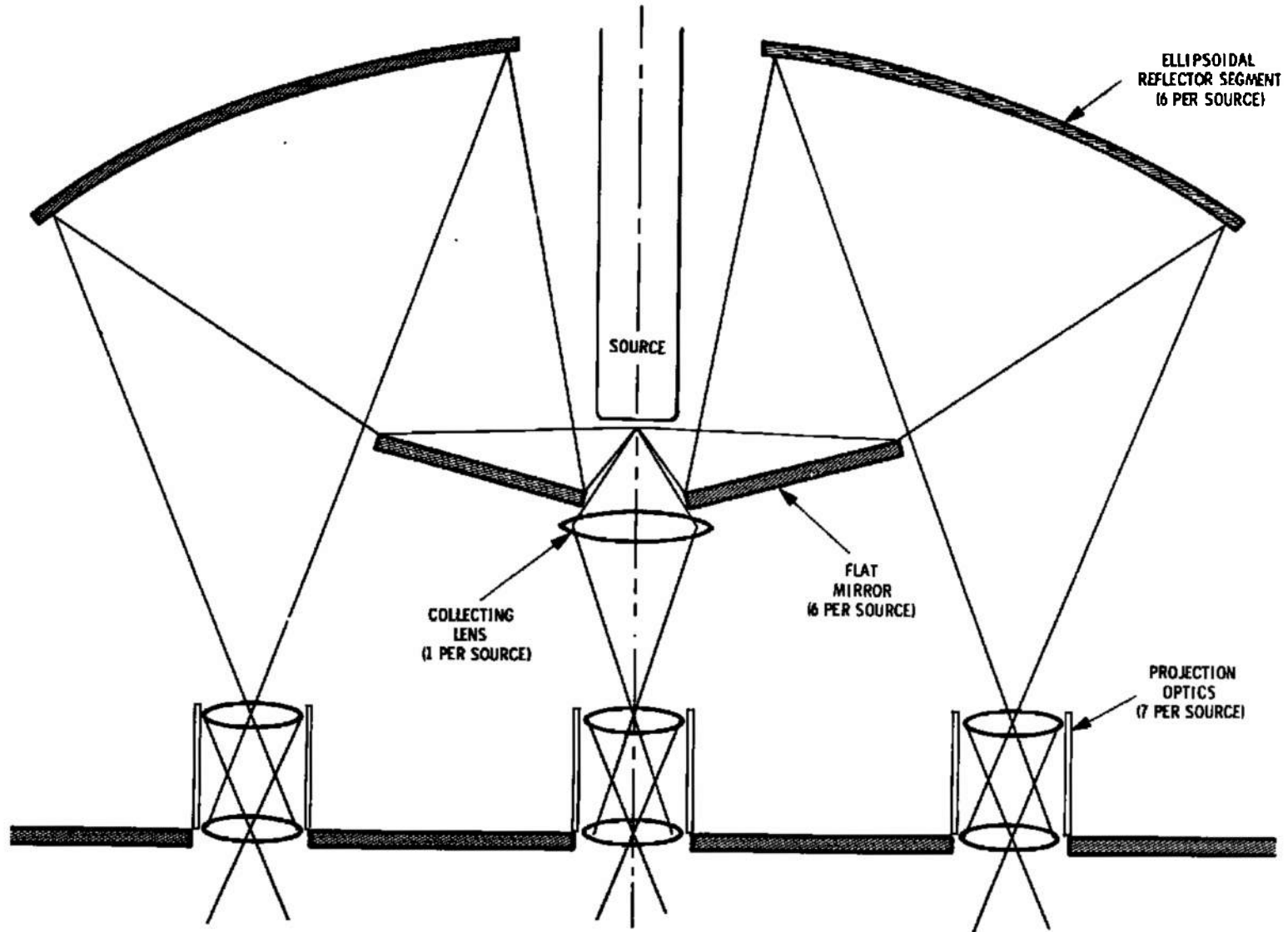


Figure 7-9. Projection Module Design Concept

through the target volume due to the array of modules could then be represented as a two-dimensional periodic continuation of the known distribution for a single module. This simple case does, however, represent a boundary condition, since it is valid at, and only at, the aperture plane of the array.

The pertinent technical problem is, therefore, one of calculating the radiant flux distribution in the target volume in terms of uniformity and total intensity and then relating these parameters to the system efficiency, to the field angle subtended by the incident radiation, and to the characteristic source parameters. It is also instructive to examine the boundary solution referred to above, even though its validity in depth is directly related to the proximity of the aperture plane of the array and the target plane in question, since it provides a convenient metric for expressing and comparing the general results with the values toward which they should converge at the aperture plane of the array.

7.4.2 The Near-Field Small Source Approximation

The Near-Field Small Source Approximation could easily be made merely by employing the computerized energy trace program (Appendix I) with a close target plane and a very small source diameter. It is instructive, however, to obtain this result analytically. This may be done using either equation (7-1) or the wavefront curvature technique. It will be shown that both concepts are equivalent and lead to useful parameters to which the nomography of the optical system study may be related in a convenient manner.

To this end consider figure 7-10 which depicts the relevant parameters pertaining to a paraboloid. A spherical wave which emanates from a source placed at the focus will strike the paraboloid with an intensity which diminishes as the square of the distance from its origin or center to the intercept point. This is a statement of the intensity law of geometrical optics, namely, the intensity of a wavefront is in inverse proportion to the square of its radius of curvature. After striking the mirror, a point of optical discontinuity, the wavefront is rendered plane, whereby there is no further decrease in wave amplitude or intensity, a well known property which derives from the definition of a parabolic surface. Since the resulting wavefront which emanates from the paraboloid is a plane which is normal to the axis of the paraboloid, the propagation vectors are everywhere parallel to that axis. It remains, then, to determine an expression which gives the square of the distance from the parabolic focus to any position on the surface of the paraboloid. With respect to the coordinate system referenced in figure 7-10, the paraboloid is defined as a surface which obeys

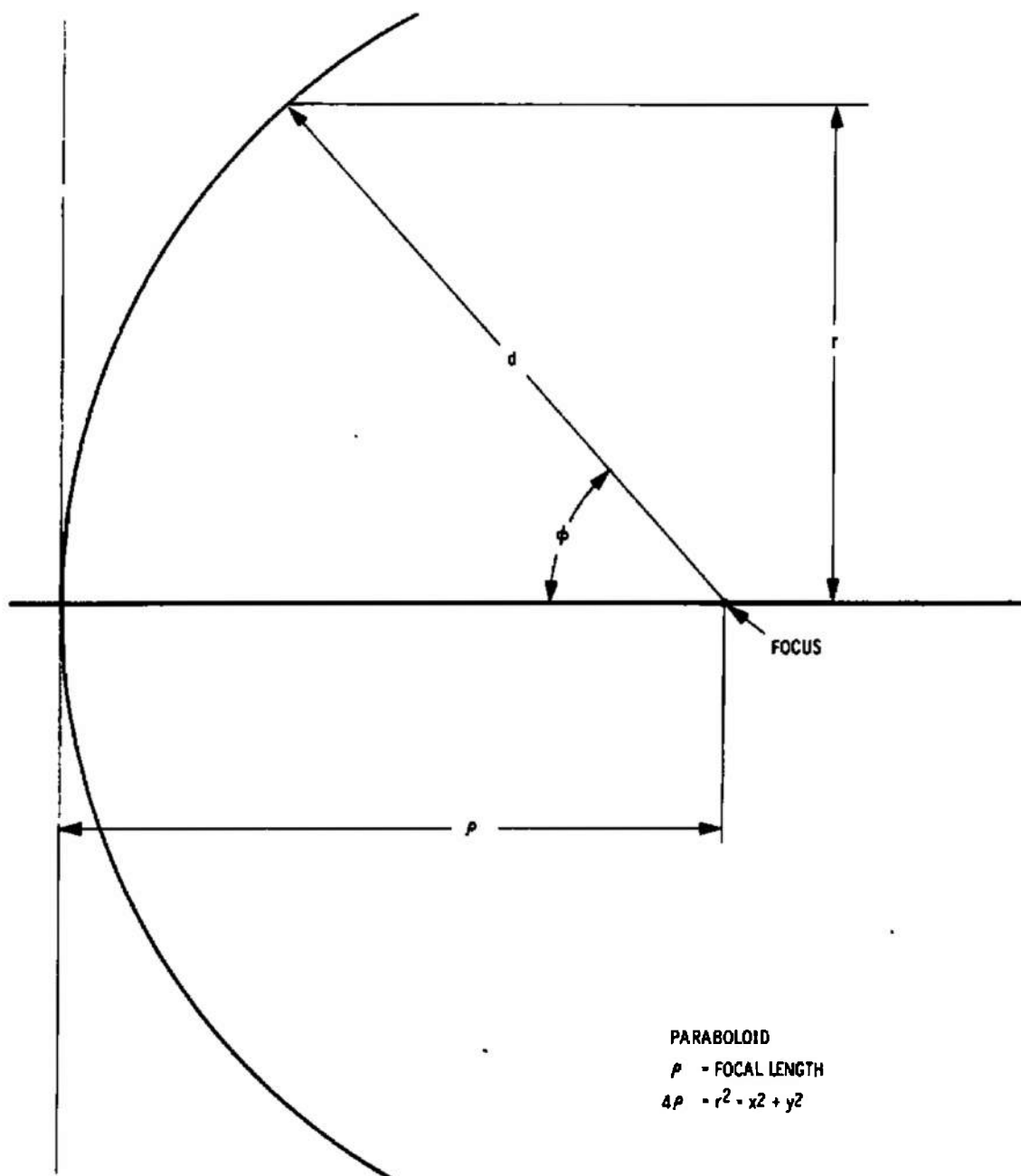


Figure 7-10. Schematic Representation of the Geometry of a Paraboloidal Reflector

$$z = \frac{x^2 + y^2}{4\rho} = \frac{r^2}{4\rho} \quad (7-105)$$

where the focal point lies a distance ρ from the origin along the z-axis. Defining d as the distance from the focus to a point on the paraboloid surface at a radius r from the axis

$$d^2 = r^2 + \left(\rho - \frac{r^2}{4\rho}\right)^2 = \left(\frac{4\rho^2 + r^2}{4\rho}\right)^2 \quad (7-106)$$

If I_ϕ is the radiance of the source, the radiant intensity E_r as a function of r is given by

$$E_r = \frac{I_\phi}{d^2} = I_\phi \left(\frac{4\rho}{4\rho^2 + r^2}\right)^2 \quad (7-107)$$

The last result may be translated into terms of collection efficiency by considering the initial collection angle ϕ . To this end, the standard trigonometric relationships may be written

$$\sin \phi = \frac{r}{d} = \frac{4\rho r}{4\rho^2 + r^2} \quad (7-108)$$

$$\cos \phi = \frac{\rho - \frac{r^2}{4\rho}}{d} = \frac{4\rho^2 - r^2}{4\rho^2 + r^2} \quad (7-109)$$

Solving the latter for r^2 as a function of $\cos \phi$

$$r^2 = \frac{4\rho^2 (1 - \cos \phi)}{1 + \cos \phi} \quad (7-110)$$

Inserting equation (7-110) into (7-107) and simplifying

$$E_r = \left(\frac{I_\phi}{\rho^2}\right) \frac{(1 + \cos \phi)^2}{4} \quad (7-111)$$

Where r and ϕ are zero, the intensity at the axis should be

$$E_0 = \frac{I_0}{\rho^2} \quad (7-112)$$

Again defining $\bar{I}_\phi = \frac{I_\phi}{I_0}$ as the relative radiance distribution of the source, the relative intensity R is given, as a function of r and ϕ respectively, by

$$R = \frac{E_r}{E_0} = \frac{\bar{I}_\phi}{\left(1 + \frac{r^2}{4\rho^2}\right)^2} = \frac{(1 + \cos \phi)^2}{4} \bar{I}_\phi \quad (7-113)$$

This equation could have been determined by applying equation (7-1) directly to equations (7-109) or (7-110). Thus

$$\frac{d(\cos \phi)}{d(r^2)} = \frac{-8\rho^2}{(4\rho^2 + r^2)^2} = \frac{-(1 + \cos \phi)^2}{8\rho^2} \quad (7-114)$$

Since, in this case, $f = \rho$, if equation (7-114) is substituted into equation (7-1), then

$$R = \frac{(1 + \cos \phi)^2}{4} \bar{I}_\phi \quad (7-115)$$

From this equation, by specifying $R = 1$, an expression is obtained for the source radiance distribution required in order to achieve a uniform distribution of energy across the aperture of a parabolic reflector. Thus, for absolute uniformity across the aperture of a parabolic reflector, the required source radiance is given by

$$\bar{I}_\phi = \frac{4}{(1 + \cos \phi)^2}$$

This function is plotted as the solid curve of figure 7-11. The dotted curve in this figure represents the same function normalized with respect to the radiance in the direction $\phi = 90^\circ$. In subsequent studies the general applicability of equation (7-1) will prove most useful, particularly when the relationship between the initial angle ϕ , and the final height r , is a complex one. (In fact, it will be shown that equation (7-115) is universally applicable to optical systems consisting entirely of conic section reflectors arranged in a series extension between their conjugate foci. The power embodied in this technique will be more fully appreciated when its application to the synthesis of optical systems has been demonstrated.)

Equation (7-115) provides considerable insight into the meaning of first and second order effects with regard to flux distribution for

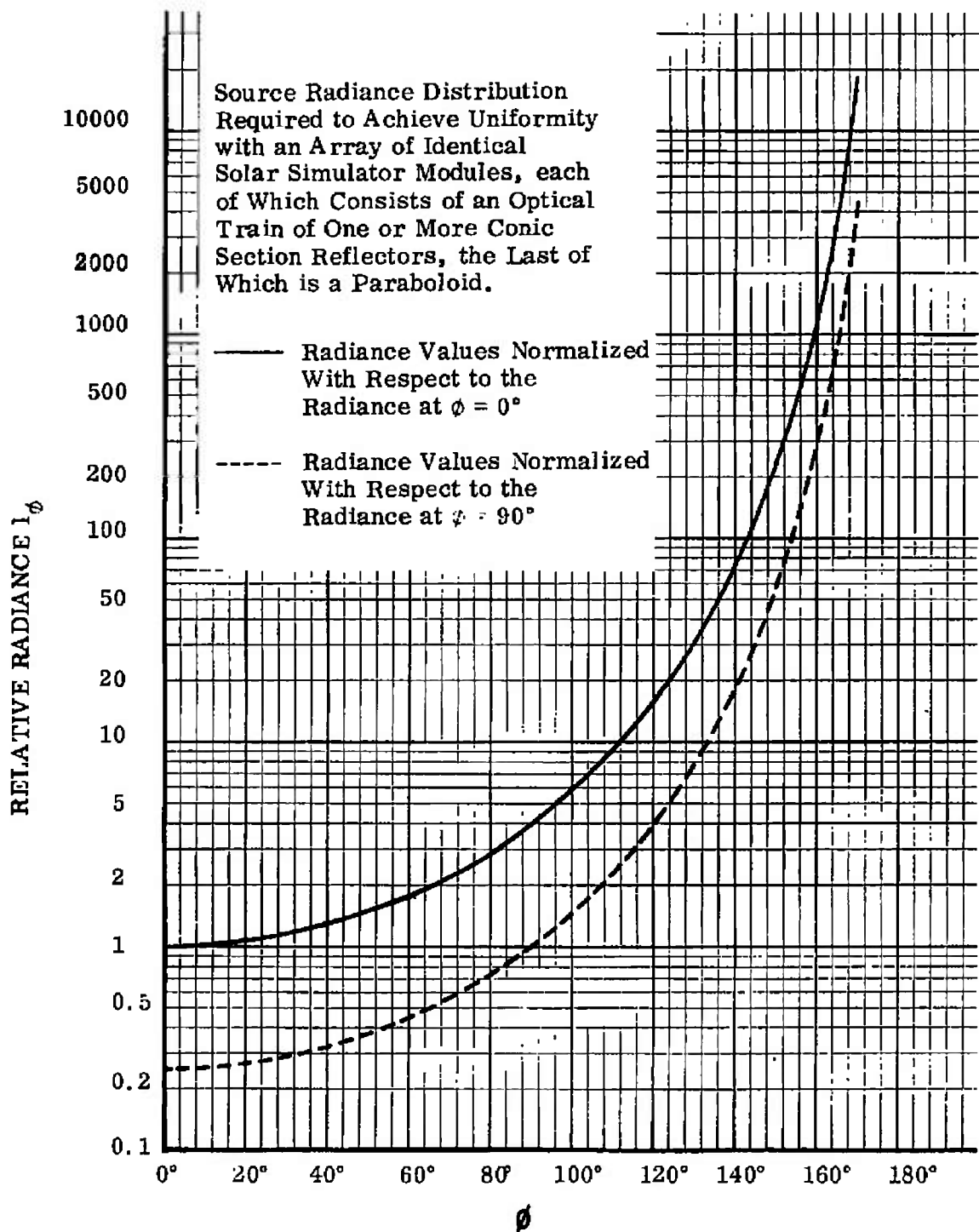


Figure 7-11. Source Radiance Distribution Required for Absolute Uniformity Across the Aperture of a Parabolic Reflector

this problem. For ordinary optical systems, light is rarely collected past an angle of $\phi = 30^\circ$, even when condenser lens systems are incorporated. In such a case the value of R at the margin of the system is approximately 0.87 or only 13% attenuated with respect to the center of the system. On the other hand, such optical systems are capable of handling fields of view as large as 30° to 60° or even higher. Thus, first order effects for ordinary systems, such as might be found in theater projection devices, relate, in the main, to the field angle determinants rather than the polar radiance relationships embodied in equation (7-1) and which comprise what could properly be termed second order effects for standard systems.

When such parameters as are encountered in solar simulation optics of the type being studied are considered, the situation is considerably different. Collection angles of $\phi = 120^\circ$ are not uncommon and the corresponding value of R is $1/16$. There can be no question but that this is the dominant effect, particularly when the field angle is at most 3° , a situation which is the reverse of that encountered in typical projection systems. Even in the face of the overwhelming importance of the polar radiance functions, the field size, although relegated to a second order effect, is still significant by virtue of the great throw distance to the target volume. As this throw distance is increased, finite field angle effects are progressively amplified.

7.4.3 Parameters and Nomography

In order to present the results of the computer study in the most meaningful form a set of parameters has been adopted which relate directly to two of the most essential desiderata governing solar simulation, namely, efficiency and uniformity.

The first is defined, assuming a source which radiates with a spherical polar radiance function $\bar{I}_\phi = 1$, so that the power collected is given by

$$P_c = I_o \int_0^{2\pi} d\theta \int_0^\Phi \sin \phi d\phi = 2\pi I_o (1 - \cos \Phi) \quad (7-116)$$

Since the total power radiated by the spherical source is $4\pi I_o$, the geometrical collection efficiency is given by

$$\eta_c = \frac{1}{2} (1 - \cos \Phi) \quad (7-117)$$

where Φ is the marginal limit of the initial angles through which radiation is collected by the optics directly from the source. Referring to

equation (7-109), equation (7-117) may be written

$$\eta_c = \frac{1}{\left(\frac{4p^2}{r^2}\right) + 1} \quad (7-118)$$

Now combine equations (7-113) and (7-118) and obtain the very interesting result that, for a source with a spherically symmetric radiance distribution ($\bar{I}_\phi = 1$)

$$R = (1 - \eta_c)^2 \quad (7-119)$$

which states that the marginal intensity decrement R , as a function of optical efficiency η_c , is independent of specific optical parameters. It is not very encouraging to note that when η_c is as low as 50%, R goes to 1/4 and for $\eta_c = 30\%$, which is about as low as could even remotely be considered, R is still only 1/2. It should be remembered, however, that this represents the solution for the close-in, small field approximation only.

The framework, nevertheless, has been set for a corresponding parametric description of the pivotal relationship between uniformity and efficiency. It would be of little use, for the purposes of this analysis, merely to present intensity plots set against a maze of associated optical and geometric parameters. Therefore a uniformity parameter, \bar{R} , is defined as the ratio of the intensity at some point in the field directly under the edge of the module, to that at a point the same distance away but under the center. These positions, when taken close to the module, lead to the identity $\bar{R} = R$. Otherwise, they are the corresponding positions projected parallel to the optical axis (the z -axis). Thus, regardless of the distance to the target plane, the intensity reference positions are, respectively, directly in front of the edge and center of the module. The edge may be regarded as being the flat or corner of the hexagon. Since it is generally found that the lowest intensity value obtains in front of the corner of the hexagon, the parameter \bar{R} , therefore, represents the maximum relative decrement in intensity with respect to the center where, in the absence of shadow considerations, the intensity maximum generally occurs. When these intensity values are obtained by energy trace calculations, the parameter \bar{R} includes the amalgamated influences of finite field and throw distance effects, and includes the contributions from all modules which irradiate a given target point. Using this metric for the performance of the system as a whole, there are two questions which are of immediate interest. The first question is "How does \bar{R} relate to the individual module collection efficiency?" Therefore, plots of \bar{R} versus

η_c will be studied. The second question, which is less obvious but equally important, is "How does the overall system uniformity parameter \bar{R} relate to the individual module uniformity R ?" The parameter R is a natural choice to characterize the unitary module uniformity, as it is affected only by the dominant first order optical properties of the module, and does not include the obfuscating influence of higher order effects. Therefore, plots of \bar{R} versus R will also be studied. While it is true that η_c and R are mutually dependent parameters, the information offered by plots of \bar{R} versus each is different. Plots of \bar{R} versus η_c reveal what module optical collection efficiency corresponds to a given degree of system uniformity. Plots of \bar{R} versus R , show approximately how uniform an individual module must be in order to achieve the desired system uniformity. It is in the plots of \bar{R} versus R that the deliberate separation of effects pays its biggest dividends, since it is a certainty that the system intensity profile will display smaller variations than are inherent in the contributing module intensity extremes. By placing this relationship on a quantitative basis, it then becomes possible to predict the required minimal module uniformity R requisite to the achievement of a desired system uniformity \bar{R} , regardless of how the former is obtained.

This concept has a number of interesting ramifications, one being a possible calculation of the radiance function required for a source which would be just adequate to achieve desired system uniformity. Another, perhaps more important, is the possibility of determining a tolerance band, related directly to module uniformity, which may then be translated into standards for acceptable stability of the source radiation characteristics and optical or geometric quality.

To summarize, the system performance will first be related to a uniformity metric R , which will then be plotted in terms of both the module collection efficiency η_c and the basic module uniformity metric R (analogous to \bar{R}). In order to study the behavior of these relationships as a function of the pertinent optical and geometrical parameters, the plots of \bar{R} versus η_c and \bar{R} versus R will be depicted as families of curves, one curve for each different throw distance from the array. There will be a set of such curves for each source representation used. Once an acceptable range for R has been determined, it is possible to obtain a corresponding upper bound value for ϕ or r by reading the value of η_c or R from the curves and using equations (7-115), (7-117), or (7-118) to calculate Φ or r . Thus:

$$\frac{r}{\rho} = 2 \sqrt{\frac{1}{\sqrt{R}} - 1} = 2 \sqrt{\frac{\eta_c}{1 - \eta_c}} \quad (7-120)$$

$$\cos \Phi = 2 \sqrt{R} - 1 = 1 - 2 \eta_c \quad (7-121)$$

By virtue of the fact that in this case $\rho = f$ and is fixed by equation (7-5) on the basis of source properties it would appear to be possible to immediately calculate the numerical value of r , the radius of the module aperture, from equation (7-120). This would be a dangerous error since equation (7-120) merely constrains a permissible range of values for $\frac{r}{\rho}$ and $\cos \Phi$, and if a value of r is chosen which is too large, the system could fail for lack of adequate total available power.

The module size is based upon the actual power available from the source as well as the constraints of equation (7-120). Thus, if I_ϕ is the radiance function of the source in absolute radiometric units and Φ is the marginal limit of collection, then the power radiated by the source which is then collected by the optical system is

$$P_c = 2\pi \int_0^\Phi I_\phi \sin \phi \, d\phi \quad (7-122)$$

The average radiant intensity in the aperture would then be given by

$$\bar{E} = \frac{kP_c}{\pi r^2} \quad (7-123)$$

where k is the transmittance of the optical system. The correct procedure would be to select the largest permissible value of Φ consistent with the constraints of equation (7-120) and then calculate P_c from equation (7-122). The required average intensity \bar{E} is then specified and equation (7-123) is used to calculate the value of r required which, in this case refers to the radius of a circle which circumscribes the hexagonal aperture of the module. Since, from equation (7-121)

$$\sqrt{R} = \frac{1 + \cos \Phi}{2} \quad (7-124)$$

a value for ρ may be calculated from equation (7-120)

$$\rho = \frac{r}{2\sqrt{\frac{1}{\sqrt{R}} - 1}} = \frac{r}{2\sqrt{\frac{\eta_c}{1 - \eta_c}}} \quad (7-125)$$

This value of ρ will necessarily be smaller than the value of $\rho = f$ which would be calculated using equation (7-5) for the following reasons. If the value of ρ determined using equation (7-5) is used, then

the intensity at the center of the module would be the E_0 inserted into the calculation. However, the intensity everywhere else in the aperture would be considerably different, due to both the first order intensity variation described by equation (7-115) and the natural vicissitudes of the source radiance function. The average intensity value would, therefore, not necessarily be E_0 . Since the value of E_0 at the module center is generally higher than would be found anywhere else, it must exceed the desired average E , thereby leading to a smaller ρ than that calculated directly using equation (7-5). It is, therefore, essential that the procedure just outlined for the determination of the parameters r , ρ , R , η_c , and P_c be precisely followed, based upon a prudent selection of Φ in the light of an examination of the relative source radiance function \bar{I}_ϕ (and the absolute radiometric value of that function). The selection of Φ must also include consideration of the ϕ -dependent relationship of equation (7-120). The parameters P_c , E , R , η_c and ρ are then obtained by sequential application of equations (7-122), (7-123), (7-124), (7-117), and (7-125). If the arc size is known, then the field angle Θ can be calculated from equation (7-6), using $f = \rho$.

The foregoing has tacitly assumed, and naively so, that commencing with what could be considered a reasonable value for the system uniformity metric \bar{R} , the procedure, as outlined, would lead to a successful or even internally consistent result. Unfortunately, the situation is so bad that it could very well be impossible to obtain a solution for a desired range of \bar{R} . Protection from these otherwise frustrating pitfalls is afforded by the information immediately apparent in the plots described above. Nevertheless, when confronted with this situation, it becomes necessary to reverse the logic and ferret out the value of \bar{R} which can be accommodated by the system or, alternatively, to establish the minimal source radiance characteristics requisite to the \bar{R} desired. In the interests of minimum confusion, this question will be taken up as needed in the discussion of results to follow.

Before proceeding further, it would be well to note the way in which the initial bifurcation and subsequent coadunation of optical and source radiative parametric determinants was employed. The latter was deleted from the equations by the expedient insertion of a spherical polar radiance function. This led to a definition of R and η_c which could later be modified by a real source polar radiance function. Thus the abscissa, R , of one of the above referenced plots, can be scaled (not linearly) up or down to correspond with the ratio of polar radiance values obtaining for the source in question. For example, if a source had twice the radiance at $\phi = 120^\circ$ as it had at $\phi = 0^\circ$, then where R at 0° is always 1 the R at 120° would have twice the value of that corresponding to a spherical source. The result is a plot specifically applicable to the particular source. Various aspects of the problem will require varied but analogous treatment, examples of which are to be found in the subsequent discussion of numerical results.

The actual efficiency must likewise undergo redefinition with respect to the real case. Thus if P_c is the collected power, as defined by equation (7-122), then the true collection efficiency $\bar{\eta}$ can be written

$$\bar{\eta} = \frac{P_c}{\pi \int_0^{2\pi} I_\phi \sin \phi d\phi} \quad (7-126)$$

Thus while the concepts remain the same, the tailoring of parameters to specific source characteristics is based upon the direct product coupling of the actual radiance function with the parameters defined on the basis of a spherical source. The crucial averaging process, by which a valid calculation of \bar{E} is obtained, is an example of this concept. Here the meaning of the average intensity value \bar{E} , which is a central part of the system specification, is retained by the proper combination of optical and source effects.

7.4.4

Numerical Results

It is convenient, for purposes of numerical analysis, to normalize all linear dimensions with respect to the paraboloid focal length ρ , which shall therefore be set equal to unity. The radius of the paraboloid aperture r was chosen to cover the range of optical speeds from $f/6$ to $f/0.25$. The total field angle, 2Θ , which the assumed spherical source subtends at the apex of the paraboloid, was taken as 1° , 2° and 3° . (The physical radius of the source is given by $\rho \sin \Theta$.) The target distances were chosen as multiples of the paraboloid aperture which, for a given arc power level, is a stable quantity. If a simple number had been used, then the throw distance parameter would have represented widely varying target distances with changes in system focal length since, even though the latter is always one, the dimensional unit it actually represents is highly variable in order to accommodate the more constant physical dimension of the module aperture. The parameters which were used as input data to the Energy Trace Program, (Appendix I) are summarized below.

1. Focal length of paraboloid = $\rho = 1$.
2. Radius of paraboloid aperture = $r = 1/6, 1/2, 3/4, 1, 2, 4$.
3. Field angle = $2\Theta = 1^\circ, 2^\circ, 3^\circ$.
4. Radius of the source = $\rho \sin \Theta = 0.00872654, 0.01745241, 0.02617695$.

5. Target distance = $D = 10r, 20r, 40r, 60r$.

The target distances chosen correspond to ranges of from 10 to 60 feet for a 2-foot diameter module or 20 to 120 feet for a 4-foot diameter module which should be sufficiently representative.

With ρ and \bar{I}_0 taken as one, the nomographic parameters given by equations (7-113) and (7-118) become:

$$R = \frac{16}{(4 + r^2)^2} \quad (7-127)$$

$$\eta_c = \frac{r^2}{4 + r^2} \quad (7-128)$$

In this analysis, where a generalized source representation in the form of a sphere has been chosen, there is little concern with the details of a more complex multiple surface source characteristic. However, since three field sizes ($1^\circ, 2^\circ, 3^\circ$) were used, it may be of interest to note the effect of the cumulative result for all three source surfaces taken simultaneously. As the surfaces grow progressively smaller, the source would have the appearance of growing correspondingly brighter toward its center, all the while maintaining a spherical radiance distribution. Although the information sought has to do with the behavior of the optical system as a function of field size, it is instructive to note how the various effects are weighted by the micro-brightness distribution, proving that it may not be ignored in the final evaluation.

Figures 7-12 through 7-19 depict the results obtained from the Energy Trace Program, which are tabulated for reference in table 7-1. Perusal of these curves indicates that the ratio of edge to center intensity \bar{R} drops to very low values for similar values of R in an almost linear fashion for small field angles, on the order of 1° , for all target distances considered. This condition also exists for larger field angles if restricted to shorter target distances. For larger field angles and longer throw distances, however, there is an increasing tendency for \bar{R} to fall off less rapidly with R , and even to reverse and increase for greater and greater ranges of R before a subsequent accelerated descent sets in.

Using $\pm 10\%$ as a criterion for \bar{R} , it appears that, for a 1° field (figure 7-12), the tolerable lower limit for R is 0.75 for throw distances of $10r$ to $60r$ but could be lowered to $R = 0.7$ for a restricted range of target distances from $20r$ to $60r$ or greater. For a 2° field, (figure 7-13), the throw distances spread the value of \bar{R} both above

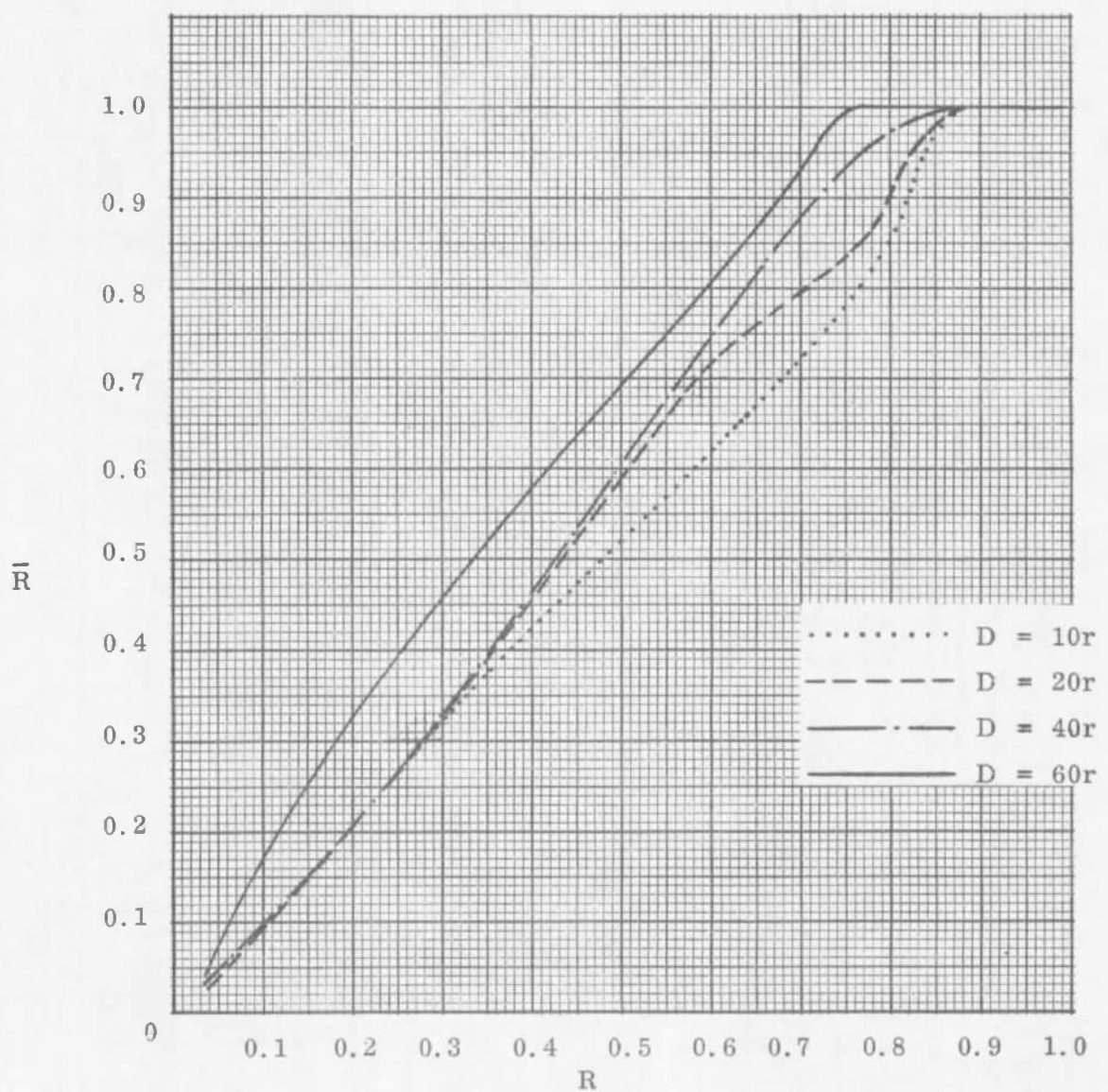


Figure 7-12. \bar{R} versus R for a Simple Spherical Source and a 1° Field Angle

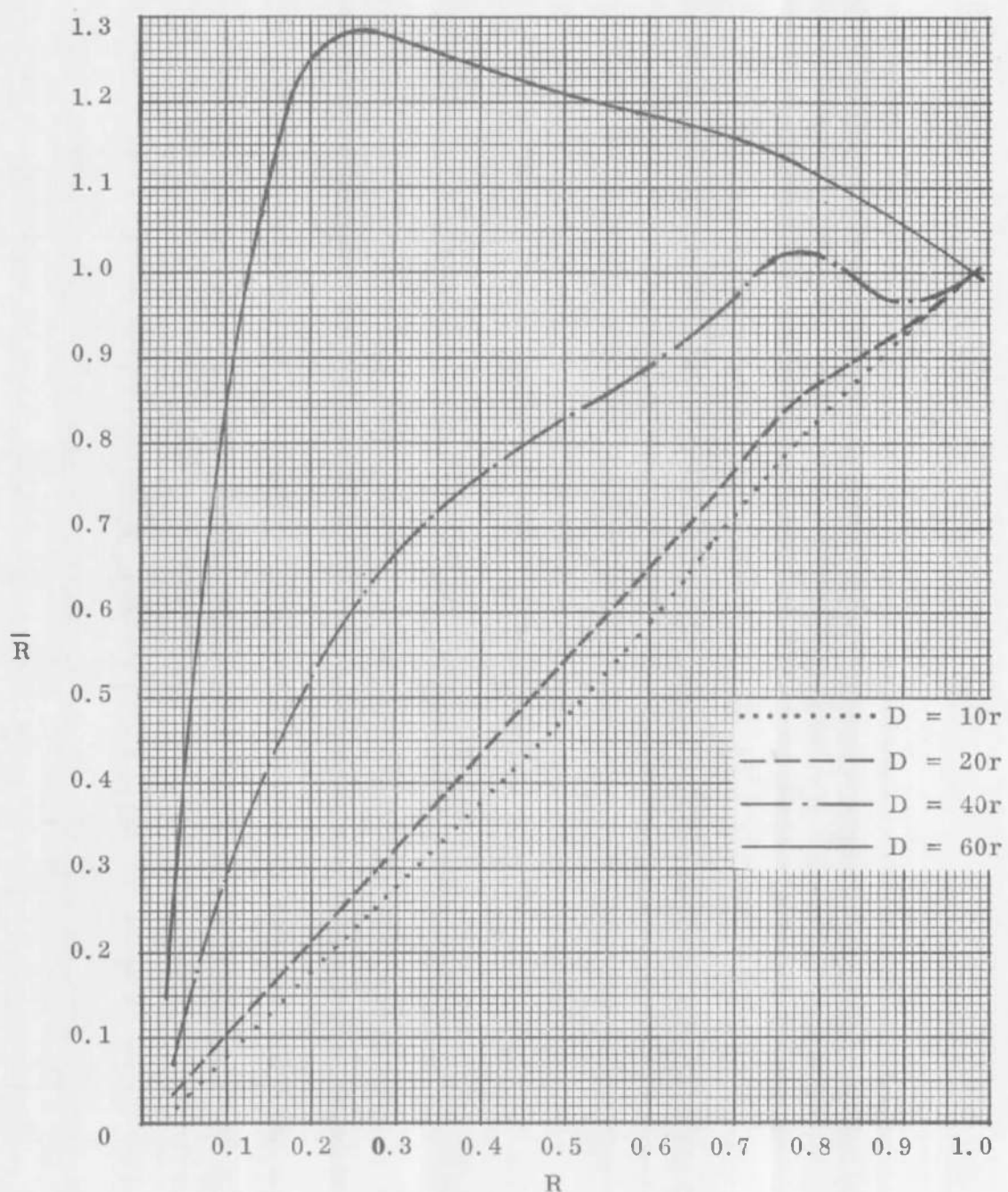


Figure 7-13. \bar{R} versus R for a Simple Spherical Source and a 2° Field Angle

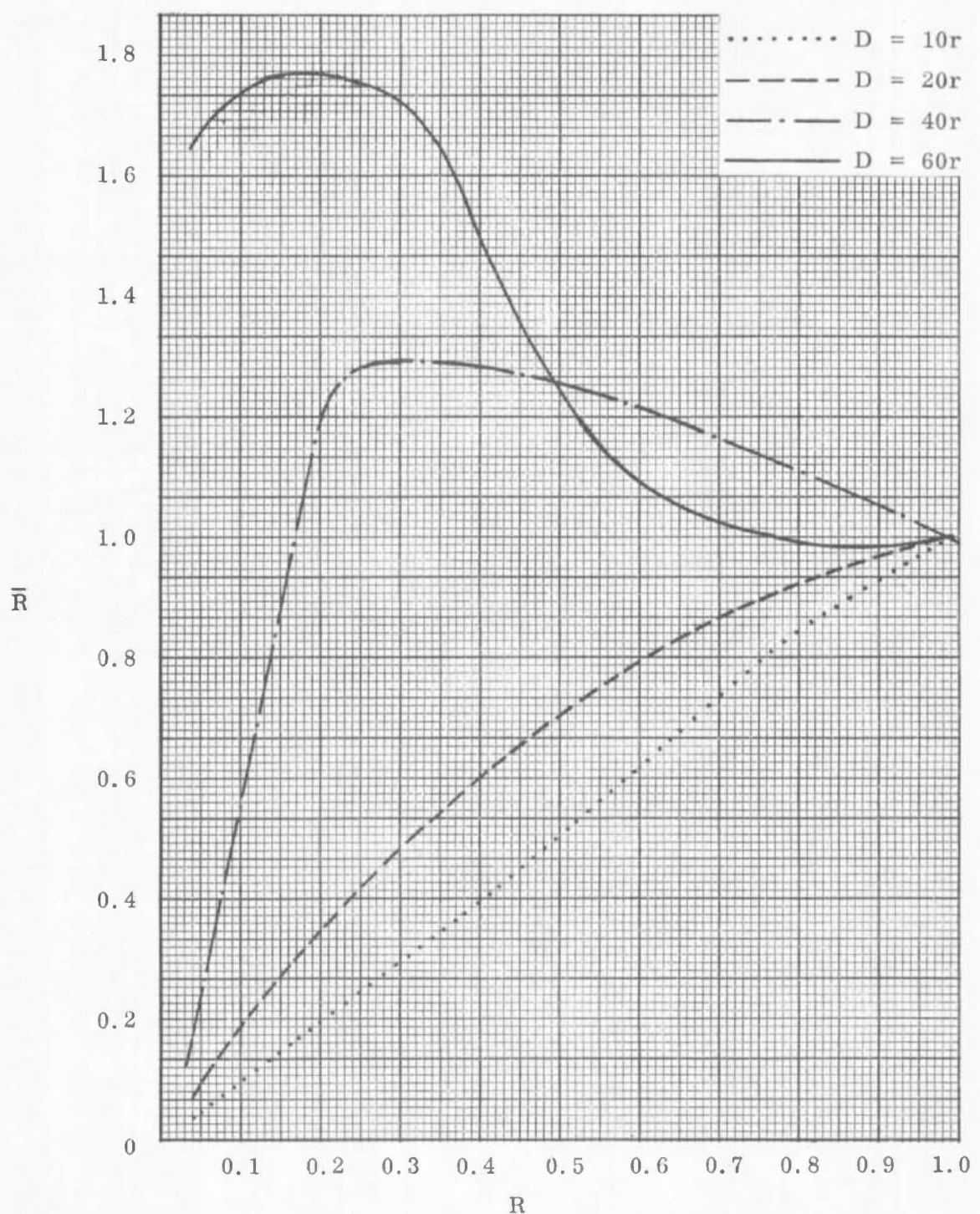


Figure 7-14. \bar{R} versus R for a Simple Spherical Source and a 3° Field Angle

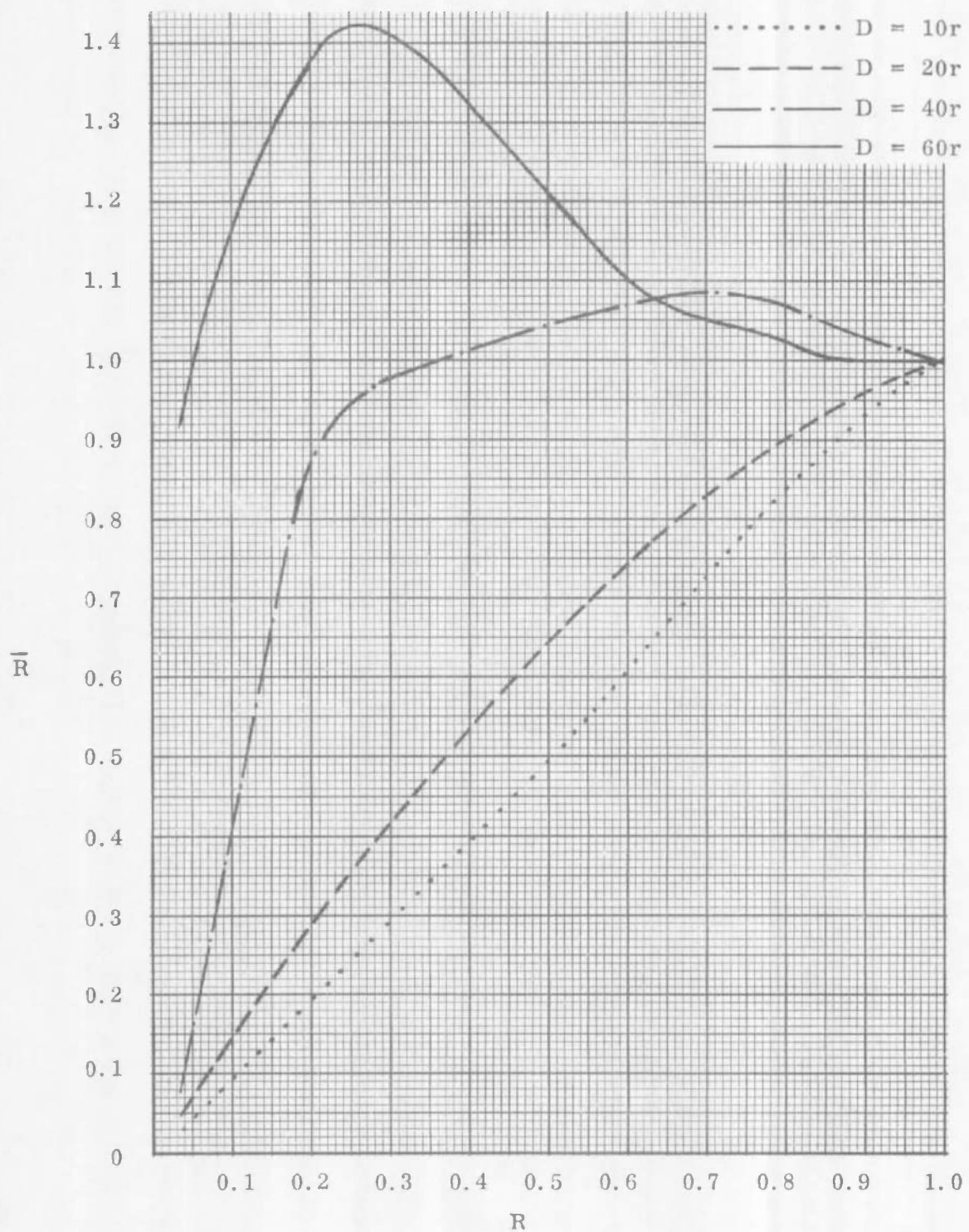


Figure 7-15. \bar{R} versus R for a Combination Source and a 3° Field Angle

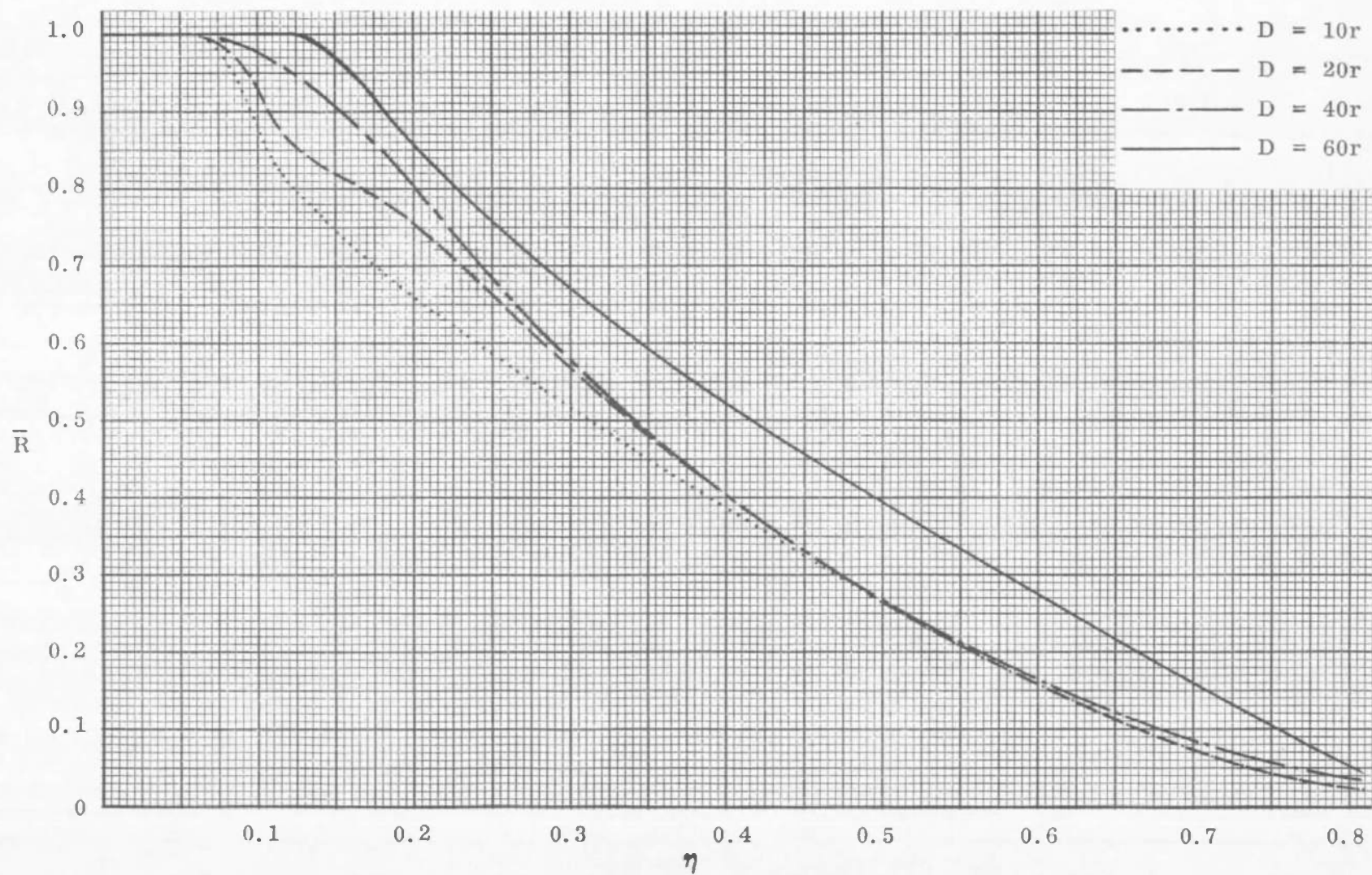


Figure 7-16. \bar{R} versus η_c for a Simple Spherical Source and a 1° Field Angle

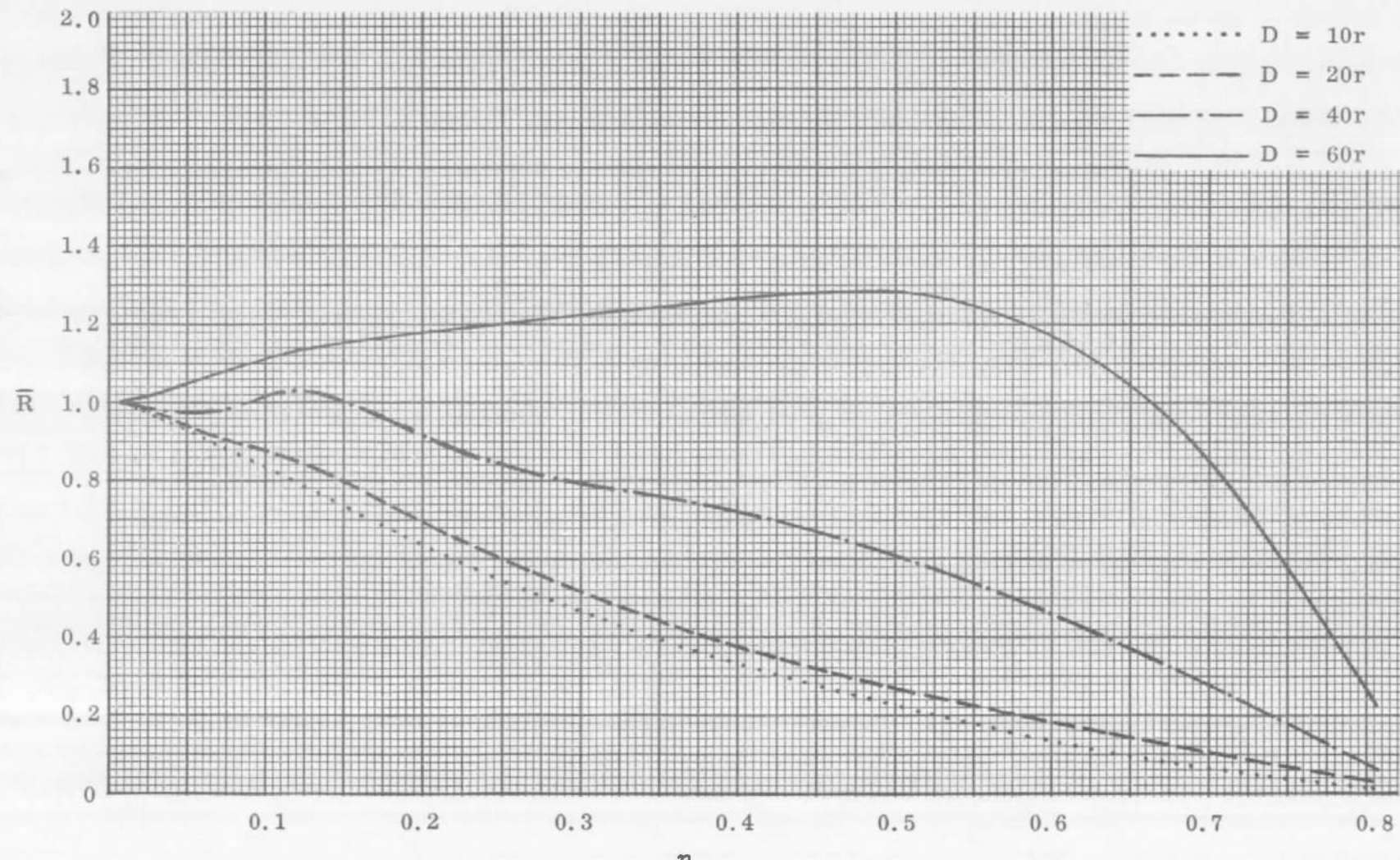


Figure 7-17. \bar{R} versus η_c for a Simple Spherical Source and a 2° Field Angle

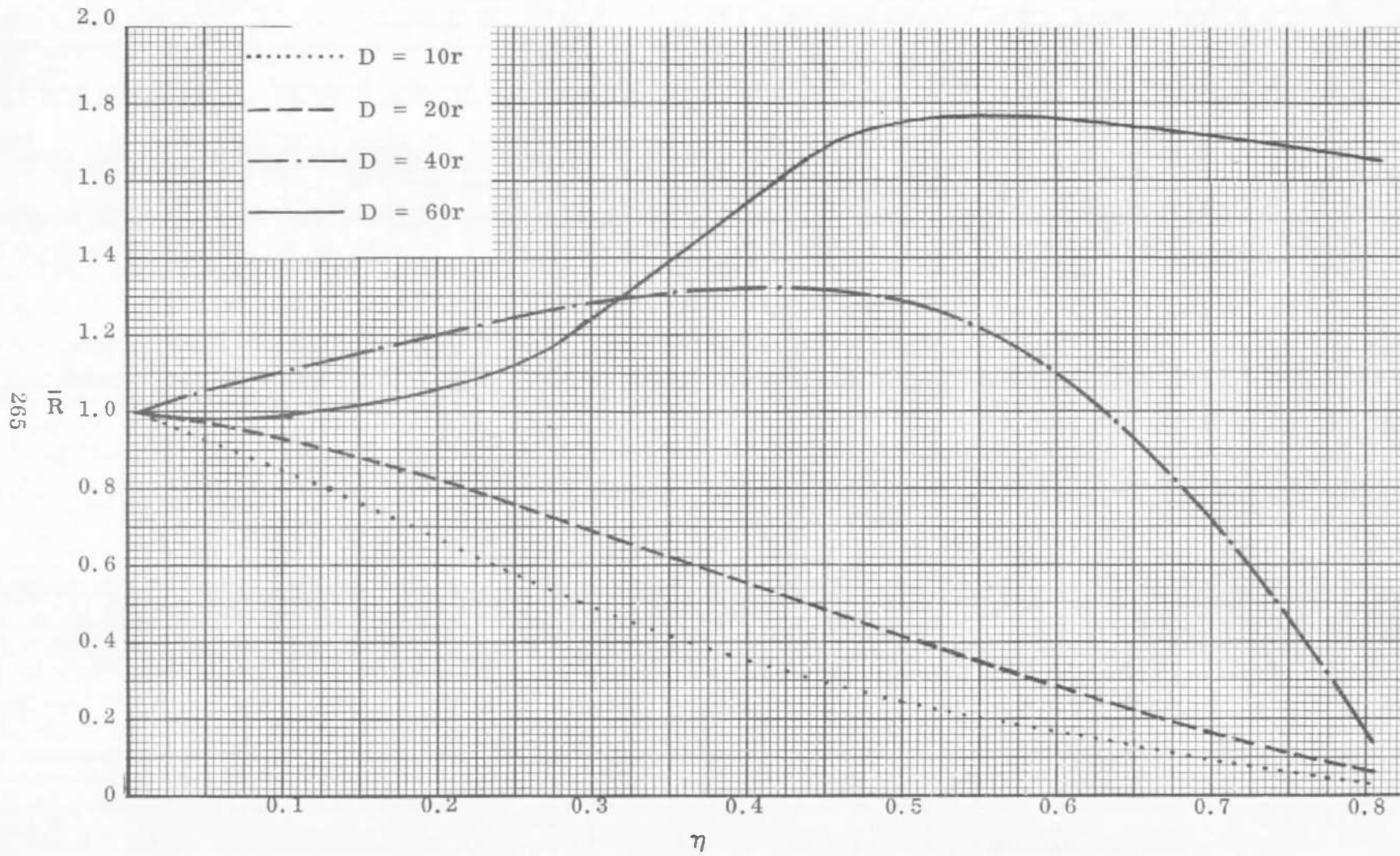


Figure 7-18. \bar{R} versus η_c for a Simple Spherical Source and a 3° Field Angle

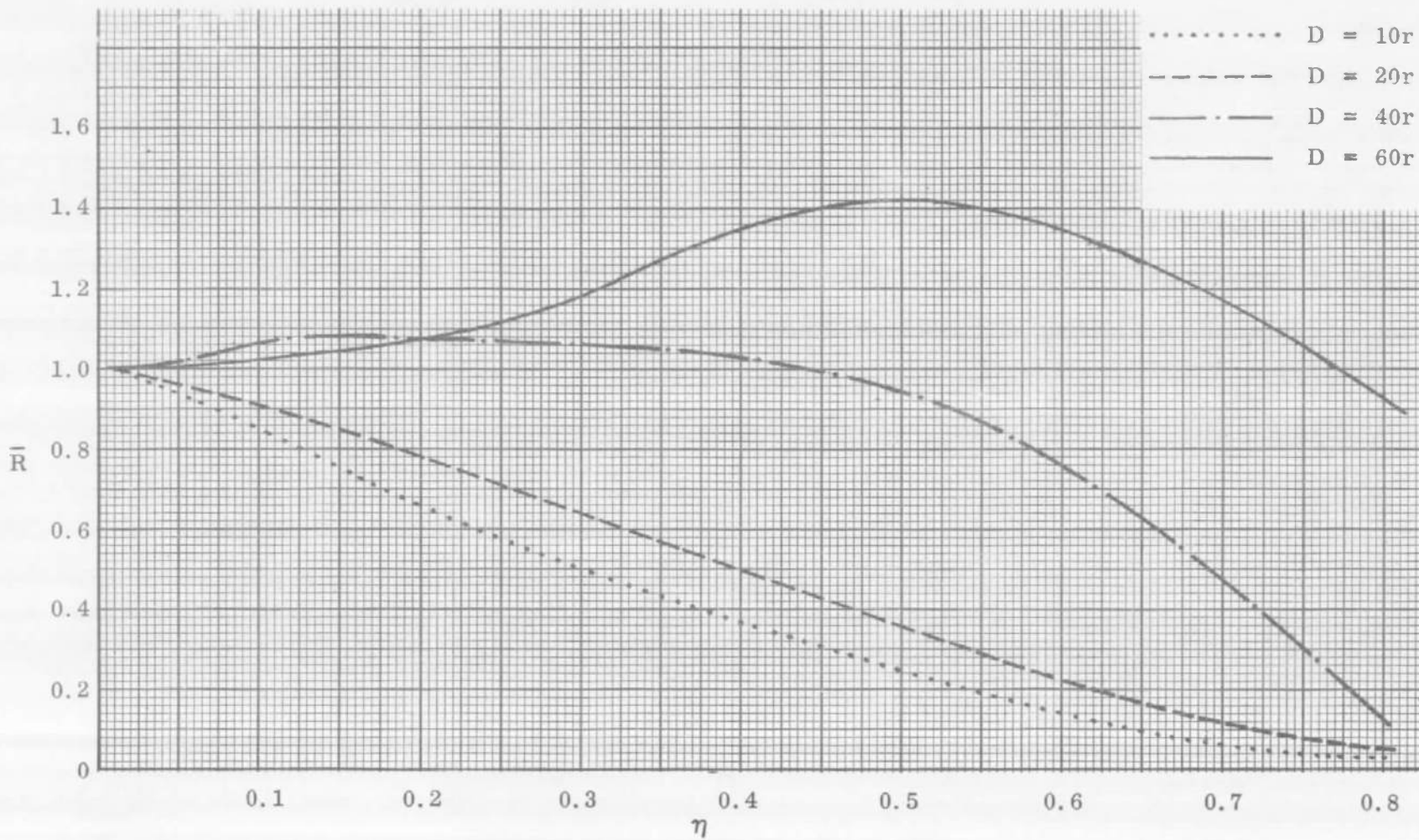


Figure 7-19. \bar{R} versus η_c for a Combination Source and a 3° Field Angle

Table 7-1. Uniformity Calculations for an Hexagonally Arranged Array of Parabolic Reflectors

$$D = \frac{\text{Target Distance}}{\text{Aperture Radius}}$$

$$R = \frac{\text{Corner Intensity}}{\text{Center Intensity}} \text{ at target plane}$$

$$\eta_c = \frac{r^2}{4 + r^2} = \text{geometrical efficiency}$$

$$r = \text{Aperture Radius}$$

$$R = \frac{16}{(4 + r^2)^2} = \text{uniformity decrement in aperture}$$

r	η_c	R	D	\bar{R}			
				Simple Spherical Source			Combination Source
				1° Field Angle	2° Field Angle	3° Field Angle	3° Field Angle
$\frac{1}{6}$	0.00689	0.9862	10	1.0	1.0	1.0	1.0
				20	1.0	1.0	1.0
				40	1.0	1.0	1.0
				60	1.0	1.0	1.0
$\frac{1}{2}$	0.0588	0.8858	10	1.0	0.9116	0.9185	0.9218
				20	1.0	0.9226	0.9658
				40	1.0	0.9668	1.0630
				60	1.0	1.0606	0.9800
$\frac{3}{4}$	0.1233	0.7686	10	0.8049	0.7901	0.8117	0.8051
				20	0.8536	0.8453	0.9058
				40	0.9512	1.0242	1.1223
				60	1.0000	1.1324	1.0000
1	0.2	0.64	10	0.6585	0.6354	0.6650	0.6561
				20	0.7561	0.6961	0.8241
				40	0.8049	0.9172	1.1973
				60	0.8536	1.1756	1.0578
2	0.5	0.25	10	0.2683	0.2265	0.2487	0.2434
				20	0.2683	0.2675	0.4147
				40	0.2683	0.6075	1.2856
				60	0.3939	1.2839	1.7554
4	0.8	0.04	10	0.0244	0.0191	0.0367	0.0301
				20	0.0244	0.0374	0.0687
				40	0.0370	0.0769	0.1682
				60	0.0526	0.2683	1.6501

and below one. Thus, with a target distance range bounded above and below by $60r$ and $10r$, respectively, the lower limit on R is 0.8. Restricting the target range from $10r$ to $40r$, however, permits a lowering of R to approximately 0.73. For a field of 3° , (figure 7-14), there are some very interesting reversals which allow a target range of $20r$ to $60r$, corresponding to a lower limit on R of about 0.75. When the effects of the sum of all these fields are considered, which in essence, amounts to considering a 3° field of a complex arc (figure 7-15) there are offsetting influences which provide a slightly improved situation. Thus, with a target throw restriction of about $30r$ to $60r$ the best range of data would permit a lower limit on R of about 0.6. This might be relaxed somewhat to extend the lower bound on target range to $20r$. In any case, it is apparent that, by proper selection of the appropriate ranges of parameters, it is possible to arrive at a relatively optimal condition. Whether the latter is adequate is a matter for engineering judgement when evaluated in the light of the total problem.

For the sake of the present discussion, assume the values stated for the combined case above, figure 7-15, although they are, perhaps, slightly optimistic. In addition, proceed with the understanding that the criterion of $\bar{R} = \pm 10\%$ employed may be only marginally adequate.

The same logic can be applied to the curves of figures 7-16, 7-17, 7-18 and 7-19 where \bar{R} is plotted against η_c , and from which a corresponding value of R could be obtained. The value of η_c which corresponds to $R = 0.6$ is $\eta_c = 0.225$. In other words, the geometrical optical efficiency is only 22.5% under optimum conditions. For the Fluid Transpiration Arc (FTA) whose polar radiance distribution appears to be roughly spherical, but which is confined primarily to the forward hemisphere, the real efficiency $\bar{\eta}$ would be double the geometric efficiency, hence about 40% of the total radiated power would be collected. Although this is not too encouraging, it is not to be dismissed at face value.

Since the radiance function for the FTA appears to be quite close to spherical, the discussion may be continued using this source as an example, without having to modify the numbers obtained above. Adhering to the concepts presented in the previous section, the value of Φ is established as the collection angle limit. Thus from equation (7-121)

$$\cos \Phi = 2\sqrt{0.6} - 1 = 0.549193$$

$$\Phi = 56^\circ 41'$$

In the analysis of the FTA in section 5 it has been shown (table 5-25) that its radiance function, in watts-per-steradian, is given by

$$I_\phi = I_0 (\bar{A} + \bar{B} \cos \phi) = I_0 (0.9236 + 0.0764 \cos \phi) \quad (7-129)$$

where for the 37.5-kilowatt arc the value of I_0 is 1900 watts-per-steradian. The magnitude of the radiance I_ϕ will be attenuated somewhat by absorption, for which a factor of 0.85 for a single mirror reflection will be assumed. (This method of analysis is also valid for a system of conic section reflectors, should such a system prove to be more desirable from a mechanical or system design standpoint, the only difference being a higher absorption constant.) From equations (7-122) and (7-129) the power collected from the 37.5-kilowatt FTA and reflected by the paraboloidal reflector is

$$P_c = 2\pi I_0 \int_0^\phi (\bar{A} + \bar{B} \cos \phi) \sin \phi d\phi = 5280 \text{ watts}$$

At this power level, it may prove desirable to achieve an intensity of two solar constants ($\bar{E} = 0.260$ watts-per-square-centimeter). From equation (7-123) assuming a transmittance $k = 0.85$,

$$r^2 = \frac{kP_c}{\pi \bar{E}} = \frac{4490}{0.260 \pi} = 5500 \text{ square centimeters}$$

Therefore:

$$r = 74.16 \text{ cm} = 29.2 \text{ inches} = 2.43 \text{ feet}$$

This corresponds to a module aperture diameter of approximately 5 feet, which could very well be near the upper limit on module size for practical fabrication reasons.

The physical collection efficiency $\bar{\eta}$, of this module is based upon the total radiated power P_r . From table 5-25 we have, for the 37.5-kilowatt FTA, $P_r = 11,482$ watts, and the radiative efficiency $\eta_r = 30.6\%$. The true collection efficiency, before absorption, is

$$\bar{\eta} = \frac{P_c}{P_r} = \frac{5280}{11482} = 46.0\%$$

and the total system efficiency is

$$\eta_t = \frac{kP_c}{37500} = 11.75\%$$

Now consider these efficiencies in the light of solar simulation standards. First, although the radiative efficiency of the 37.5-kilowatt FTA is not exceptional, neither is it very poor. Further, the overall total system efficiency is quite acceptable by comparison to most other systems. Unfortunately, the real collection efficiency η is actually a good deal lower than most systems could possibly employ and still function properly. In this case, the saving factors are the copious amount of power available and the exceptionally high transmission efficiency of the optical system due to the use of only one mirror, although it is still difficult to overlook the fact that over 50% of the radiant energy output of the FTA never even sees the solar simulator but is lost to surrounding space in the form of a spurious and definitely unwanted heat load. The reason this system appears to perform adequately is that the decrease of about 50% in the usual collection efficiency is balanced by an approximate doubling of the transmission efficiency.

What, then, could possibly be the advantage of using a more complex optical system which absorbs about as much additional energy as it collects from the source? The key to the answer lies in two areas, better uniformity and greater control. With respect to the first point, it should be remembered that the uniformity standard was a very loose one, namely $\pm 10\%$, and even this is barely met by the optimistic choice of parameters. It is easily seen that it would take a very large further sacrifice in efficiency to realize even a small improvement in the uniformity characteristics. The value selected above is actually a toe of a rather extended plateau, so that even a small increase in efficiency leads immediately to very large compromises in uniformity, while lowering the efficiency improves the situation very little. Further, the performance cited was restricted to target distances on the order of $20r$ to $60r$. Thus, for a module aperture diameter of 5 feet, the target volume would be restricted to between 50 feet and 150 feet from the aperture plane, which is not likely to be a practical range for most space simulation chambers although perhaps suitable for an extremely large one. All factors being equal, however, the output power of the source could be scaled down in proportion to the square of the target throw distance. Thus, if one cut the output power level by a factor of four (to about 3000 watts), then the module aperture diameter would become 2.5 feet and the target volume could extend from 25 feet to 75 feet. While this might be an acceptable short side distance, the long side could possibly abridge the specifications most suited to an especially large space chamber.

A second distinguishing factor, from which derives the principal justification for a more complex system, is the matter of gaining specific control over a number of functional factors, the most immediate and compelling of which is control over flux distribution. Thus, unless the additional components and complexities allow a degree of compensation adequate to the otherwise widely divergent flux concentration which results from the needed additional energy collected, there can be little reason for their inclusion. On the other hand, the relatively poor performance of the simple parabolic

array (using the FTA) at close-in distances, and the rigidly limited volume wherein reasonable uniformity performance is obtained with such an array, provides strong motivation to seek not a more efficient system but rather one which provides greater uniformity throughout a larger relative volume. Another example of the need for control over flux distribution is seen in the difficulty of making truly profitable use of the extraordinary power levels of the three sources considered in this study (the Fluid Transpiration Arc, the Vortex Stabilized Radiation Source, and the High Intensity Carbon Arc). For example, systems designed for what appear (for the moment) to be the most suitable target volumes, require only a 20-kilowatt power level input. This might be viewed as a golden opportunity to filter the spectrum of the 37.5-kilowatt FTA to match the solar spectrum (as defined by the Johnson curve) with a fidelity not otherwise possible. The only problem here is, with such a simple system, where are the filters to be placed? The matter of control thus becomes an even more poignant question. It should be noted here that, since the results obtained above also apply to any optical system consisting entirely of conic section reflectors arranged in a series extension between their conjugate foci (cf. section 7.5), two conic section reflectors may be used for initial collection (as in the RCA Solar Simulator) with the collected radiation then converging to a window or relay lens, and thence going to a Cassegrainian system for collimation. The filter may be placed at the window or relay lens. (Filters of adequate thermal stability are available.) However, since the collection angle of this more complicated system is still restricted to $\Phi = 56^\circ 41'$, the overall system efficiency will be reduced because of the lower transmission of the optical system. (Assuming that the reflectance of each mirror is 85% and assuming that the lens has a transmittance of 90%, the inclusion of one lens and three additional mirrors reduces the transmission by about 55% so that the 37.5-kilowatt FTA now appears, to the paraboloid, to be a 21-kilowatt source.)

These last few paragraphs are not intended to draw conclusions in favor of one approach over other, but serve rather to place the problem in its proper perspective and to outline the system of thought to be applied to its eventual evaluation and solution. It can be said, however, that if the additional complexity of the optical system can be justified for the sake of filtration, the degree of complexity needed to realize improved performance in other areas, which complexity may not be comparatively as great, can also be justified.

Returning to the parameterization of the parabolic array using the 37.5-kilowatt FTA, we may use equation (7-125) to calculate the paraboloid focal length (or what would also be the effective focal length of an optical system of conic section reflectors). Thus, taking $\eta_c = 0.225$ and $r = 29.2$ inches, then

$$p = 27.1 \text{ inches}$$

It is interesting to calculate the on-axis, close-in flux density E_o which is given by

$$E_o = \frac{I_o}{\rho^2} = 2.59 \text{ w/sq in} = 0.401 \text{ w/sq cm}$$

This is 1.54 times the Venus orbit solar constant (0.260 watt-per-square-centimeter) for which the system parameters were designed, and serves to demonstrate the higher central intensity value required in order to compensate the lower intensity value at the edge of the aperture and thus obtain the proper average intensity value of 0.260 watts-per-square-centimeter. The edge intensity, being 60% of the center intensity in the close-in small field approximation, is thus 93% of the Venus solar constant. The closer adherence to the desired average intensity at the edge compared to at the center is due to the proportionally larger amounts of area represented by the former. This initial intensity variation of approximately $\pm 25\%$ across the aperture will, when carried further down field, smooth out to the $\pm 10\%$ value. It is interesting to note that if equation (7-5) had been used to calculate ρ by specifying the center intensity $E_o = 0.260$ watts-per-square-centimeter thereby ignoring the effects of non-uniformity on the average intensity, then a value for ρ of 85.5 centimeters = 33.66 inches is obtained. Using this value of ρ to calculate r from equation (7-120) again taking $\eta_c = 0.225$, then $r = 36.27$ inches and the area of the aperture of the module $\pi r^2 = 4133$ square inches as compared to the 2680 square inches of aperture area which results when $r = 29.2$ inches as established by the previous design calculation. Thus, if the module aperture is sized to give the desired intensity at the center of the aperture, the average intensity over the aperture will actually be 65% of the desired intensity.

There is still one more parameter to be evaluated, namely, the field angle subtended by the FTA as seen from the target volume. Since this source very nearly displays the spherical radiance symmetry upon which the selection of R , and therefore Φ , was based, it also displays the increasing brightness toward the center, which led to relaxing R from 0.75 to 0.6 on the basis of a 3° field assumption. Now this assumption will be checked.

Data available concerning the Fluid Transpiration Arc indicates that, for the 37.5-kilowatt FTA, most of the energy emanates from within a plasma filled sphere of about 0.4 inch diameter. The field angle Θ subtended by a sphere of diameter $D = 0.4$ inch located at the focus of a paraboloid whose focal length $\rho = 27.1$ inches is given by

$$\Theta = 2 \arcsin \left(\frac{D}{2\rho} \right) = 0^\circ 51'$$

This is an excellent value by solar simulation standards and is very near to the $0^\circ 45'$ which the sun actually subtends at Venus. Although better simulation of the field angle could not be desired, it is most unfortunate from the standpoint of uniformity, since better uniformity is obtained as the size of the field angle increases. Even if one goes to the more complex system of conic section reflectors and includes a 50% filter factor, the focal length is cut only in half, thus increasing the field angle to only $1^\circ 45'$ which is not

large enough to allow the system to be parameterized on the basis of the relaxing influence of a 3° field angle.

At this point the reader may be growing somewhat impatient with the present exercise but it has served well as an illustration of just how difficult it is to push the parameters into the realm of practical utility and still achieve adequate performance. Thus, it is necessary that a value of R at about 0.75, corresponding to a field angle of 1° , be selected if a uniformity criterion of $\pm 10\%$ over a target range of from $10r$ to better than $60r$ is to be maintained. With these values the efficiencies and related parameters become:

$$\eta_c = 13.4\% = \text{Geometrical Collection Efficiency}$$

$$\Phi = 43^\circ = \text{Limiting Angle of Collection}$$

$$\bar{\eta} = 27.6\% = \text{True Collection Efficiency}$$

$$P_c = 3170 \text{ watts} = \text{Power Collected}$$

$$\eta_t = 7.19\% = \text{Total System Efficiency (Assuming one reflection)}$$

$$r = 22.6 \text{ inches} = \text{Aperture Radius}$$

$$p = 28.7 \text{ inches} = \text{Focal Length of Paraboloid}$$

$$\Theta = 0^\circ 48' = \text{Field Angle}$$

The target distance limitations for uniformity are from about 19 feet to more than 115 feet for an approximately 4-foot diameter module. Thus, it can be seen that this system differs considerably in efficiency from the previously defined system which results in the module aperture being somewhat smaller and the focal length of the paraboloid being slightly longer. The field angle is very close to that actually subtended by the sun ($0^\circ 45'$) at the Venus orbit. One major improvement is seen in the permissible target volume range. This system must be regarded as having only mediocre efficiency and uniformity by solar simulation standards. Nevertheless, a module (parabolic reflector) with an aperture diameter of 4 feet (no spectral filtration) or a module consisting of a system of conic section reflectors with an aperture diameter of 2 feet (assuming a dissipative efficiency including filters of 25%) is a workable system and will, using the 37.5-kilowatt FTA, yield a $0^\circ 48'$ field angle and $\pm 10\%$ uniformity in a 19 feet to 115 feet target range.

To summarize the results for the 37.5-kilowatt FTA, it is seen that the solar field angle for the Venus orbit forces the system performance curves for a field angle of 1° or less to be used. These curves display a linear \bar{R} vs. R characteristic with little or none of the recovery tendency

which can be seen in the curves for larger field angles. The result of all this is an approximate, but simple, relationship which states that the efficiency and the module aperture diameter are inversely proportional, respectively, to the uniformity criterion and to the square root of that criterion. Thus, since a uniformity criterion of $\pm 10\%$ yields a 7.19% efficient module whose aperture diameter is 45 inches, a $\pm 20\%$ uniformity requirement would result in a module which is approximately 12% efficient and whose aperture diameter is approximately 65 inches. The above also serves to illustrate a procedural basis upon which quantitative evaluations of system performance characteristics may be made for comparison purposes. The numerical calculations are, perhaps, somewhat optimistic in some cases but can be justified, to a certain extent, on the basis of certain offsetting influences when the total arc characteristic and the smoothing effect of finite area sensors are considered. Indeed, a $\pm 10\%$ point-by-point intensity distribution could appear to be uniform within $\pm 5\%$ if a sensor whose area is on the order of one square foot is used. It may, therefore, be concluded that the analysis contained herein is, as a first approximation, within the limits of accuracy required to make preliminary evaluations and determine whether system performance warrants further, more detailed study.

Now consider the two sources for which the assumption of a spherically symmetric radiance function does not apply, namely, the High Intensity Carbon Arc and the Vortex Stabilized Radiation Source (VSRS). In the case of the carbon arc, the available data indicates a very unsymmetrical situation. However, the data supplied for the 75-kilowatt carbon arc (taken with the detector shielded from most of the radiation which originates outside the anode crater) indicates that the axial radiance I_o is 5480 watts-per-steradian and that the radiance distribution is roughly a cosine function (within approximately $\pm 10\%$) although this is a tentative assumption, at best. Since this is the best that can be done with the information at hand, the discussion will proceed on that basis.

The first step would be to obtain an idea of the magnitude of the field angle by first applying equation (7-5) to determine the effective focal length f and then applying equation (7-6). However, knowing that the central intensity E_o will have to be significantly higher than the average intensity \bar{E} , it is advisable to first apply a safety factor to \bar{E} to define E_o . Thus, using a safety factor of 2,

$$E_o = 2\bar{E} = 0.520 \text{ watts-per-square-centimeter}$$

and

$$f = \sqrt{\frac{kI_o}{E_o}} = 94.5 \text{ centimeters} = 37.2 \text{ inches}$$

This calculation includes the 0.85 transmission coefficient. The predominant contribution of radiant energy from the carbon arc emanates from the anode crater. Further, the carbon arc may be treated as an approximately flat single-surface source oriented so that it is normal to the anode axis. Thus, the size of the anode determines the major dimension of the arc. For the 75-kilowatt carbon arc, the anode is 35 millimeters in diameter, and the field angle Θ may be approximated by

$$\Theta = 2 \arcsin \left(\frac{D}{2f} \right) = 2 \arcsin (0.0185) \cong 2^\circ$$

In view of the above, the performance curves for a 2 degree field may be used in performing the system analysis. Perusal of these curves indicates that it would be well to restrict the target volume rigidly to between $10r$ and $60r$ for optimum system parameterization. The constraints realized thereby take the form of an approximately linear R vs. R characteristic, represented by the $10r$ and $20r$ curves of figure 7-13. These restrictions should not be accepted at face value, however, as the modification required by the particular source radiance function must be imposed, as is illustrated in what follows.

It would appear that for the 2° field, a uniformity criterion of $\pm 10\%$ would allow a value of R of 0.73. This actually means that a marginal intensity decrement of 0.73 is permitted in the aperture of the module. Since part of this decrement is contributed by the radiance distribution of the source, the source radiance function I_ϕ must also be included in the calculation. Since the radiance distribution of the carbon arc has been assumed to be a cosine function, then $I_\phi = \cos \phi$. Thus, from equation (7-115)

$$R = \left[\frac{(1 + \cos \Phi)^2}{4} \right] \cos \Phi = 0.73$$

where Φ is again the limiting angle of collection. This equation has one real root and two conjugate complex roots for all positive real values of R . The one real root for $R = 0.73$ is approximately

$$\cos \Phi = 0.852 \quad \text{or} \quad \Phi = 31.5^\circ$$

The total radiated power is given in Section 5 as 17,200 watts. The power collected is

$$P_c = 2\pi \int_0^\Phi I_0 \cos \phi \sin \phi d\phi = \pi I_0 \sin^2 \Phi = 4700 \text{ watts}$$

With a collected power of 4700 watts, the true collection efficiency $\bar{\eta} = 27.3\%$ which, in spite of the small collection angle, is still comparable

to that determined for the FTA. In order to achieve an average intensity of $E = 0.260$ watt-per-square-centimeter (Venus orbit intensity) the radius of the aperture of the paraboloid must be (again assuming the transmittance $k = 0.85$)

$$r = \sqrt{\frac{kP_c}{\pi E}} = 70 \text{ centimeters} = 27.5 \text{ inches}$$

Thus, the target volume is limited to between 23 feet and 136 feet. The geometrical collection efficiency is, from equations (7-113) and (7-117) taking $\bar{I}_\phi = \cos \phi$

$$\eta_c = 1 - \sqrt{\frac{R}{\cos \Phi}} = 0.07436 = 7.436\%$$

The effective focal length (the focal length of the paraboloid) is, from equation (7-113)

$$p = \frac{r}{2} \sqrt{\frac{1 - \eta_c}{\eta_c}} = 48.5 \text{ inches}$$

and, from equation (7-6), taking the source diameter D as 35 millimeters, the field angle Θ is

$$\Theta = \arcsin \left(\frac{D}{2p} \right) = 1^\circ 40'$$

As compared to the system determined for the FTA, this system is less favorable for a number of reasons, not the least of which is the fact that the overall system efficiency is only 5.3% and this without any added complexities or spectral filtration. In addition, the very low collection angle coupled with the physical location of the electrodes, makes it extremely difficult to get any radiation past the source itself, a problem which also besets the FTA system, though not to so great an extent.

The results obtained here for the carbon arc are intended to provide a direct comparison to those for the FTA, treated previously, and the VSRs, to be considered next. The initial conditions and criteria have been deliberately selected the same for this purpose. Although it is seen, in each case, that parameters exist which will satisfy the conditions imposed, they should in no way be construed as a recommendation that the system is necessarily desirable or even practical. Such a decision must await complete information on all comparable systems and the relevant ratiocination concerning their relative merits from the perspective of total system requirements.

The VSRS presents several new problems concerning its analysis in the present scheme, the first of these being the fact that no radiation is emitted along its axis of symmetry. If this fact were incorporated into the definition of the parameters used above, they would immediately be rendered meaningless, for the ratio of a finite intensity to zero center intensity is infinite. This should not be considered an imponderable. In fact, an equivalent difficulty was ignored in the analysis of the FTA and carbon arc, since the occlusion caused by the presence of the arc hardware in the beam is no less serious than not having any central radiation at all. (It is assumed, of course, that the VSRS is mounted with its electrode axis colinear with the optical axis.) A second problem is that of representing the polar radiance function itself. The solution to both these problems, as far as this analysis is concerned, is simply to represent the central radiant intensity by a value to which the actual distribution is asymptotic for reference purposes only. A guide to this procedure is provided by considering what would be the most ideal source polar radiance function. Since the close-in, small field approximation gives a distribution in accordance with equation (7-115), it is evident that the compensating function is:

$$\bar{I}_\phi = \frac{4}{(1 + \cos \phi)^2} = \frac{I_\phi}{I_0} \quad (7-130)$$

Thus, any source which has a polar radiance function given by equation (7-130) would yield a theoretically uniform intensity distribution across the output beam both close-in and at a distance. Such a radiance distribution has a center radiance which is 87% of its radiance in the direction $\phi = 30^\circ$.

In view of this relationship, a radiance representation shall be adopted which, for ϕ greater than 30° , best fits the empirical data and, setting $I_0 = 0.87 I_{30^\circ}$, letting equation (7-130) represent the distribution between 0° and 30° . This expedient will circumvent the central reference difficulty, as well as provide a meaningful basis for calculating relative intensity parameters.

Referring to figure 16 of Reference 10, it appears that the radiance distribution of a 19-kilowatt Vortex Stabilized Radiation Source (VSRS), with a recessed plate anode and a 12-millimeter electrode gap, may be represented as a function of ϕ by two straight lines, with reasonable accuracy. Again defining I_ϕ as the radiance in watts-per-steradian in the direction ϕ measured with respect to the anode axis, the first of these straight lines defines the radiance distribution between 30° and 90° and was chosen so that it passes through the points $I_{30^\circ} = 200$ watts-per-steradian and $I_{90^\circ} = 600$ watts-per-steradian. Thus, for the following calculations, the radiance distribution of the 19-kilowatt VSRS between 30° and 90° will be represented by the function

$$I_{\phi} = \frac{20\phi}{3} \text{ watts/steradian} = 381.97 \phi' \text{ watts/steradian}$$

(7-131)

where ϕ is expressed in degrees and ϕ' in radians. The second of these straight lines defines the radiance distribution between 90° and 135° and is horizontal, thus making I_{ϕ} independent of ϕ in this region. Thus, for the following calculations, the radiance distribution of the 19kw VSRS between 90° and 135° will be taken as

$$I_{\phi} = 600 \text{ watts/steradian}$$

(7-132)

It was stated above that the radiance distribution between 0° and 30° will be represented according to equation (7-130). Since the curve thus defined must pass through the point $I_{30^\circ} = 200$ watts-per-steradian, then $I_0 = 174.1$ watts-per-steradian. Therefore, for the following calculations, the radiance distribution of the 19-kilowatt VSRS between 0° and 30° will be represented by the function

$$I_{\phi} = \frac{696.41}{(1 + \cos \phi)^2} \text{ watts/steradian}$$

(7-133)

The radiance distribution as defined by equations (7-131), (7-132) and (7-133) will, hereinafter, be denoted as the radiance distribution of the basic arc.

Figure 40 of reference 10 indicates that, if the cathode geometry is slightly modified and its surface made reflecting, the radiance distribution is so altered that it may be represented by extending the first straight line to 120° . (The use of this particular electrode design will not be questioned for the moment, and the distribution will be accepted as cited.) Thus, for the following calculations, this radiance distribution will be represented for ϕ from 0° to 30° by equation (7-133) and for ϕ from 30° to 120° by equation (7-131), and will be denoted, hereinafter, as the radiance distribution of the modified arc.

The size of the basic arc is approximately 12 millimeters as determined by the electrode gap. The data concerning the modified arc indicates that incorporation of a conical cathode reflecting surface increases the apparent length of the arc as viewed from directions ϕ greater than 90° , reaching a maximum apparent length, as seen from $\phi = 120^\circ$, which is 1.5 times its real length. The effect of foreshortening at the margins of the paraboloid at such extreme angles more than cancels the effect of this apparent growth in arc size. Because of the long narrow arc shape, the field angle is bound to be less than the value calculated on the basis of a 12-millimeter arc gap. (A precise value can only be obtained through a detailed energy trace evaluation using an accurate source representation as previously

described.) However, for the purposes of this calculation, an assumed source diameter $D = 10$ millimeters is an adequate approximation.

To begin, the field angle Θ will be approximated as was done in the case of the carbon arc. Thus, using a safety factor of 1.5 to define the central intensity E_0 with respect to the desired average intensity $\bar{E} = 0.260$ watts-per-square-centimeter and again assuming a transmittance of $k = 85\%$

$$E_0 = 1.5 \bar{E} = 0.390 \text{ watts-per-square-centimeter}$$

$$f = \sqrt{\frac{kI_0}{E_0}} = 19.12 \text{ cm} = 7.53 \text{ inches}$$

$$\Theta = 2 \text{ arc sin} \left\{ \frac{D}{2f} \right\} = 3^\circ$$

At this value for the field angle, the performance data and curves indicate a reversal in relative intensity between the edge and center for target distances of $40r$ or better. The appearance of the curves due to this apparent pileup of energy under the corners of the modules can be very misleading, as it is not immediately clear that such an increase must be at the expense of center intensity. When this fact is taken into account it is seen that, although the curve shows a relative value in excess of one, the actual value is not higher than, for example, the central intensity at a target distance of $10r$. Thus a $\pm 10\%$ criterion on uniformity corresponds to an approximately 20% variation of \bar{R} on either side of $\bar{R} = 1.0$, which indicates that between $10r$ and $60r$ at most, it is possible to realize a $\pm 10\%$ uniformity characteristic with an R of 0.76. Again, as was the case with the carbon arc, this refers only to the basic module uniformity for which the appropriate collection angle suited to the VSRS radiance distribution will now be determined.

The simplest procedure for determining the collection angles for the two VSRS radiance distributions being considered here is to plot the relative intensity R versus ϕ where, from equation (7-115)

$$R = \frac{(1 + \cos \phi)^2}{4} \quad (\bar{I}_\phi) \quad (7-134)$$

The relative radiance \bar{I}_ϕ is determined for each ϕ using equations (7-131), (7-132), and (7-133) as appropriate. The plots of R versus ϕ for the two VSRS configurations are shown in figure 7-20. Thus, for an R of 0.76, the collection angle for the basic arc is $\Phi_B = 93.5^\circ$, while that for the modified arc is $\Phi_M = 94.9^\circ$.

Perhaps it would be well to reiterate precisely what has been done up to this point. It was first decided, on the basis of relative intensity data for a 3° field, that an intrinsic module decrement of 0.76 was permissible in order to remain within a uniformity criterion of $\pm 10\%$ for a target space rigidly fixed, in this case, to from 10r to 60r. The values of Φ_B and Φ_M , calculated above, are the collection angles possible with a parabolic reflector, defined so that the marginal intensity is no less than 0.76 of the center intensity for either VSRS configuration.

The total power radiated by the basic 19-kilowatt VSRS is given in (reference 10) as 5,466 watts, giving a radiative efficiency of 28.8%. The collected radiation for this configuration is, substituting equations (7-131), (7-132) and (7-133) into equation (7-122), given by

$$P_{c_B} = 2\pi \left[\int_{0^\circ}^{30^\circ} \frac{696.41 \sin \phi \, d\phi}{(1 + \cos \phi)^2} + \int_{30^\circ}^{90^\circ} 281.97 \phi \sin \phi \, d\phi \right. \\ \left. + \int_{90^\circ}^{93.5^\circ} 600 \sin \phi \, d\phi \right] \quad (7-135)$$

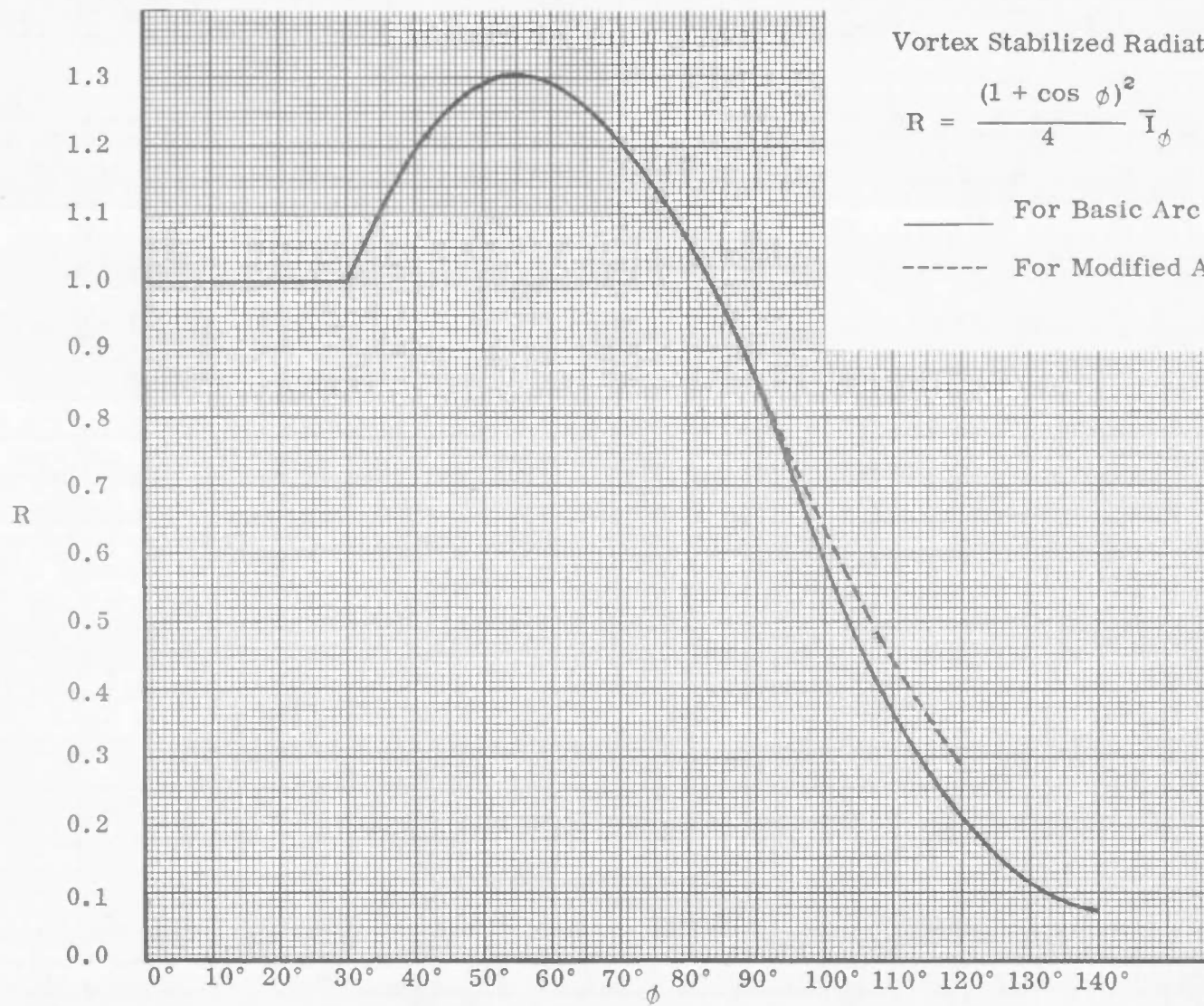


Figure 7-20. R versus ϕ for the Basic VSRS and the Modified VSRS (Approximate)

(In this equation, the limits have been expressed in degrees for convenience but must be converted to radians prior to integration and evaluation.) It is interesting to note what portion of the collected power is defined by each term of the above equation. Therefore, solving this equation term by term, the first term is

$$P_1 = 2\pi \int_{0^\circ}^{30^\circ} \frac{696.41 \sin \phi d\phi}{(1 + \cos \phi)^2} = 157 \text{ watts}$$

the second term is

$$P_2 = 2\pi \int_{30^\circ}^{90^\circ} 381.97 \phi \sin \phi d\phi = 2288 \text{ watts}$$

and the third term is

$$P_3 = 2\pi \int_{90^\circ}^{93.5^\circ} 600 \sin \phi d\phi = 230 \text{ watts}$$

Thus the total power collected from the basic arc is

$$P_{C_B} = P_1 + P_2 + P_3 = 2675 \text{ watts}$$

The total power collected from the modified arc can be determined by substituting equations (7-131) and (7-133) into equation (7-122). Thus

$$P_{C_M} = 2\pi \left[\int_{0^\circ}^{30^\circ} \frac{696.41 \sin \phi d\phi}{(1 + \cos \phi)^2} + \int_{30^\circ}^{94.9^\circ} 381.97 \phi \sin \phi d\phi \right] \quad (7-136)$$

(Again, the limits have been expressed in degrees for convenience, but must be converted to radians prior to integration and evaluation.) Since the first term of this equation is identical with that of equation (7-135) again $P_1 = 157$ watts. Evaluating the second term of equation (7-136), gives:

$$P_2 = 2\pi \int_{30^\circ}^{94.9^\circ} 381.97 \phi \sin \phi d\phi = 2619 \text{ watts}$$

and thus the total power collected from the modified arc is

$$P_{C_M} = P_1 + P_2 = 2776 \text{ watts}$$

The 5,466 watts radiated by the 19-kilowatt VSRS corresponds to a collection efficiency for the basic arc of $\bar{\eta}_B = 48.94\%$ and for the modified arc of $\bar{\eta}_M = 50.79\%$. The improvement in the collection efficiency of the modified arc as compared to that of the basic arc is not sufficient in these calculations to be considered significant. Further, the question of whether the reflectance of the cathode surface can be maintained constant in order to provide the needed stability in the modified radiance distribution has not really been settled experimentally. It therefore appears that, for this application, the improvement in system performance is not sufficient to warrant the use of the modified arc and the determination of the remaining system parameters shall consider only the basic VSRS electrode configuration. Thus, in order to achieve an average intensity $\bar{E} = 0.260 \text{ watt-per-square-centimeter}$ (Venus orbit intensity) the radius of the paraboloid must be (assuming an optical transmittance of $k = 0.85$)

$$r = \sqrt{\frac{kP}{\pi \bar{E}}} = 52.76 \text{ cm} = 20.77 \text{ inches}$$

From equation (7-110), the focal length of the paraboloid is

$$\rho = \frac{r}{2} \sqrt{\frac{1 + \cos \Phi_B}{1 - \cos \Phi_B}} = 24.82 \text{ cm} = 9.77 \text{ inches}$$

Again taking the source diameter $D = 10 \text{ millimeters}$, the field angle Θ is

$$\Theta = 2 \text{ arc sin} \left(\frac{D}{2\rho} \right) = 2.32^\circ$$

The total system efficiency is 12% and the permissible target distance ranges between approximately 17 feet and 104 feet.

The results obtained here for the VSRS are quite encouraging and some sacrifices in efficiency could be tolerated for the sake of improved uniformity.

Although it would be more appropriate, for refinements to achieve better than $\pm 10\%$ uniformity, to perform a detailed energy trace analysis using the proper source representation, the calculations just presented certainly indicate the level of performance which can be expected.

7.4.5 Summary

The preceding has served to treat the problem of simulating solar radiation using a hexagonally arranged array of parabolic reflectors, each of which has a source located at its focus. (This analysis is also applicable to hexagonally arranged arrays of identical optical systems, each of which consists of a system of conic section reflectors arranged in a series extension between their conjugate foci.) The intrinsic performance of the system, irrespective of the radiation characteristics of the source, was derived and a corresponding metric, upon which a uniformity criterion is based, was established. Three sources were considered, the Fluid Transpiration Arc (Vitro Laboratories), the High Intensity Carbon Arc (RCA Service Co.) and the Vortex Stabilized Radiation Source (Plasmadyne Corp.). Each source, parabolic-reflector system was defined and analyzed on the basis of an allowable intensity variation within the target volume of $\pm 10\%$, which choice appeared to be optimum for a 3° field. This uniformity criterion, though possibly sub-standard, was chosen in order to remain within the region where the calculated system performance curves are most significant since the reliability of these curves, with regard to uniformity, grows less as the range of intensity variations becomes lost in the tolerance band of the calculation. The purposes served by this study are:

- (1) to provide one basis for comparison of the various sources
- (2) to provide a means of evaluating the concept of using a hexagonally-arranged array of parabolic "spotlights" as a solar radiation simulator
- (3) to provide information concerning what intensity variations can be tolerated across the aperture of a collimating optical system in order that the radiant energy from a hexagonally-arranged array of such systems will be uniformly distributed (within a stated tolerance) throughout a stated target volume.

The results obtained for each source, parabolic-reflector system were based upon a design goal of achieving an average intensity equal to a Venus orbit intensity of 0.260 watts-per-square-centimeter with a maximum allowable intensity variation of $\pm 10\%$ of the mean intensity within the target volume. For each source, parabolic-reflector system, the paraboloid collection angle, focal length and aperture radius were determined and the basic optical collection and total system efficiencies were calculated. The probable field angle and the applicable range of target distances which define the target volume were also established to a good approximation. The geometrical and performance parameters of the parabolic reflector arrays defined for each source are summarized in table 7-2.

Table 7-2 - Geometrical and Performance Parameters of the Various Source, Parabolic-Reflector Systems which, when arranged in an hexagonal array, provide a mean intensity of 0.260 watts/sq. cm (Venus Orbit Intensity) and $\pm 10\%$ Uniformity

	Fluid Transpiration Arc	High Intensity Carbon Arc	Vortex Stabilized Radiation Source
P_i	37500 watts	75000 watts	19000 watts
R	0.75	0.73	0.76
Minimum Target Distance	10r (19.2 feet)	10r (22.7 feet)	10r (17.3 feet)
Maximum Target Distance	60r (115.4 feet)	60r (136.3 feet)	60r (103.9 feet)
Φ	43°	31.5°	93.5°
P_c	3170 watts	4700 watts	2675 watts
$\bar{\eta}$	27.6%	27.3%	48.94%
η_t	7.19%	5.3%	11.97%
r	22.6 inches	27.25 inches	20.77 inches
ρ	28.7 inches	48.5 inches	9.77 inches
Θ	0° 48'	1° 40'	2° 19'
Relative Aperture Area	0.688	1.000	0.581

Parametric Definitions:

- P_i = Input Power to the source
- R = Uniformity Decrement
- Φ = Limiting Angle of Collection with respect to the axis
- P_c = Radiant Energy Collected
- $\bar{\eta}$ = Collection Efficiency
- η_t = Total System Efficiency (Assuming an optical transmittance of $k = 0.85$)
- r = Aperture Radius
- ρ = Focal Length
- Θ = Field Angle

✓

The minimum target distance thus determined is probably quite reliable, but the maximum represents only an approximate position where there is an unfortunate accumulation of energy in some spots which exceeds the uniformity tolerance. Because of the general leveling of the distribution with distance, this effect is quickly dissipated as the target distance increases beyond the specified maximum and thus the intensity variation may actually not be as significant as is indicated by the curves of figures 7-12 through 7-19. The specified maximum limit on target distance does, nevertheless, represent a problem zone to which special attention should be paid in a more detailed study.

7.5 UNMODIFIED CONIC SECTION OPTICAL SYSTEMS

It has already been shown in equation (7-110), that, for a paraboloid, the height of an exiting ray in terms of the angle which the entering ray makes with the optic axis is given by

$$r^2 = 4p^2 \frac{(1 - \cos \phi)}{(1 + \cos \phi)} \quad (7-110)$$

Where p is the paraboloid focal length. It will now be shown that this relationship holds for any arbitrary string of conic sections joined through their conjugate foci as illustrated in figure 7-21. This applies when the effective focal length of the entire string, f , is substituted for the paraboloid focal length, p , and when the initial entrance angle ϕ_0 , is used in place of ϕ in equation (7-110). Thus,

$$r^2 = 4f^2 \frac{(1 - \cos \phi_0)}{(1 + \cos \phi_0)} \quad (7-137)$$

This conclusion is the essential reason for the assertion that all conic section systems are equivalent on a first order basis.

To demonstrate this, examine, for a conic section, some fundamental relationships between the entering and exiting angles of rays proceeding from one focus, and reflected by the surface toward the other focus. In the case of the ellipsoid, referring to figure 7-22,

$$\phi_1 = \alpha + \phi_1' \quad (7-138)$$

where ϕ_1 and ϕ_1' are the entering and exiting angles, respectively, with respect to the major axis, and α is the angle between the two corresponding rays. If T is the aperture radius of the point on the ellipsoid where the reflection occurs and S and S' are the path lengths of the two rays respectively, then:

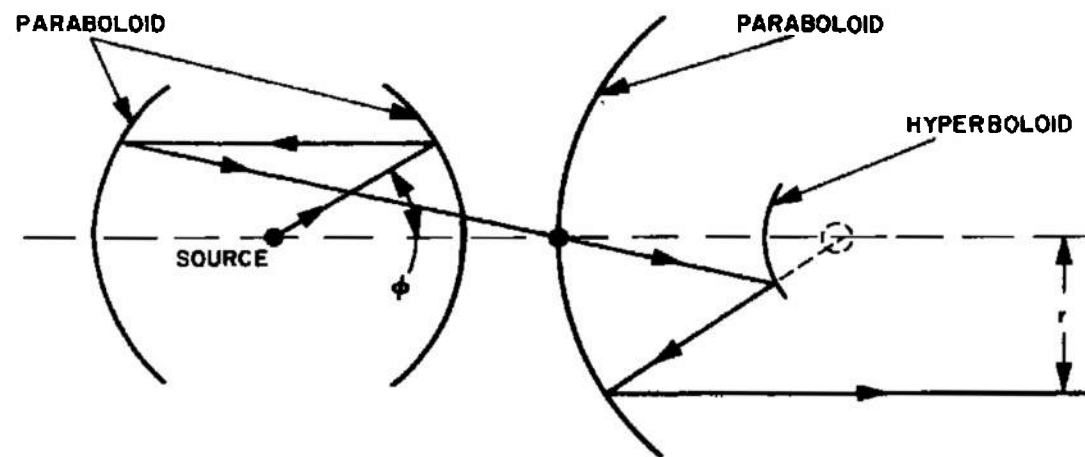
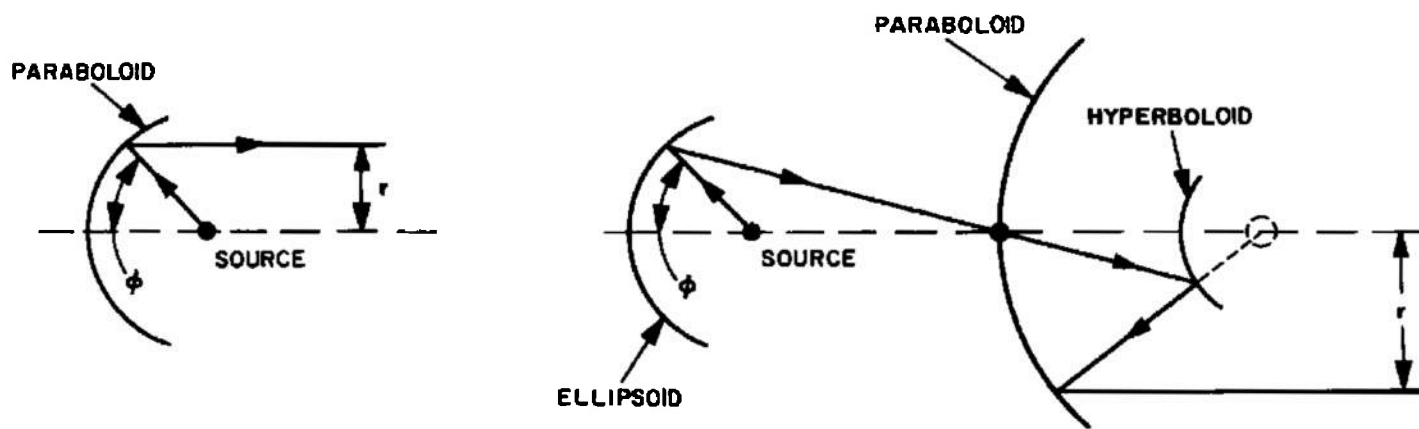


Figure 7-21. Conic Section Optical Systems

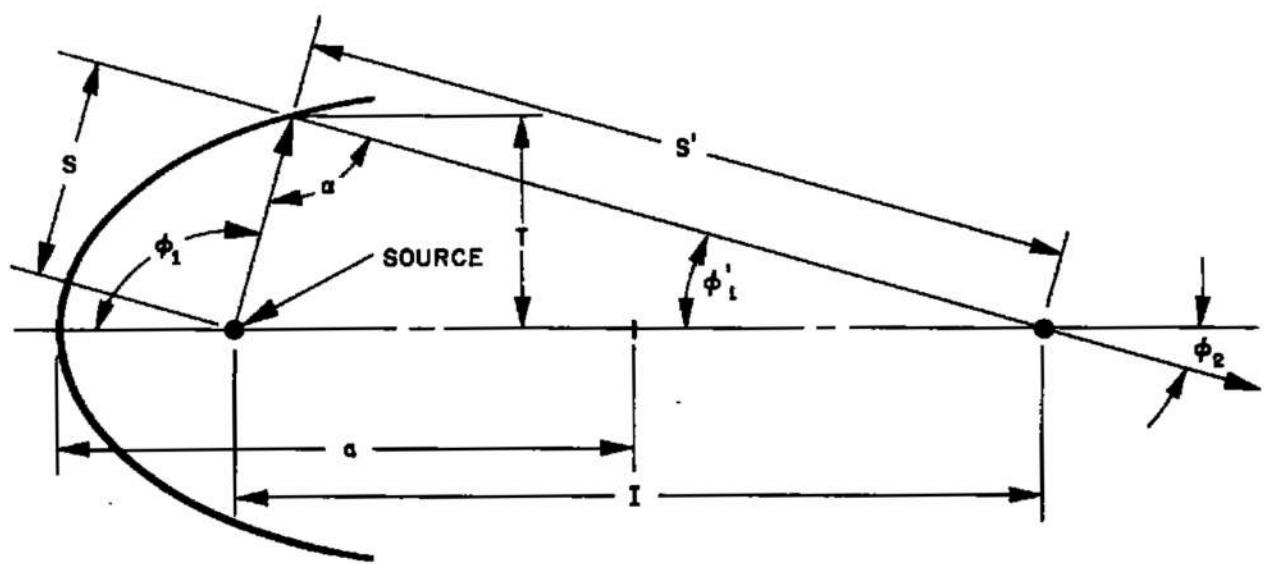


Figure 7-22. Ellipsoidal Reflector Parameters

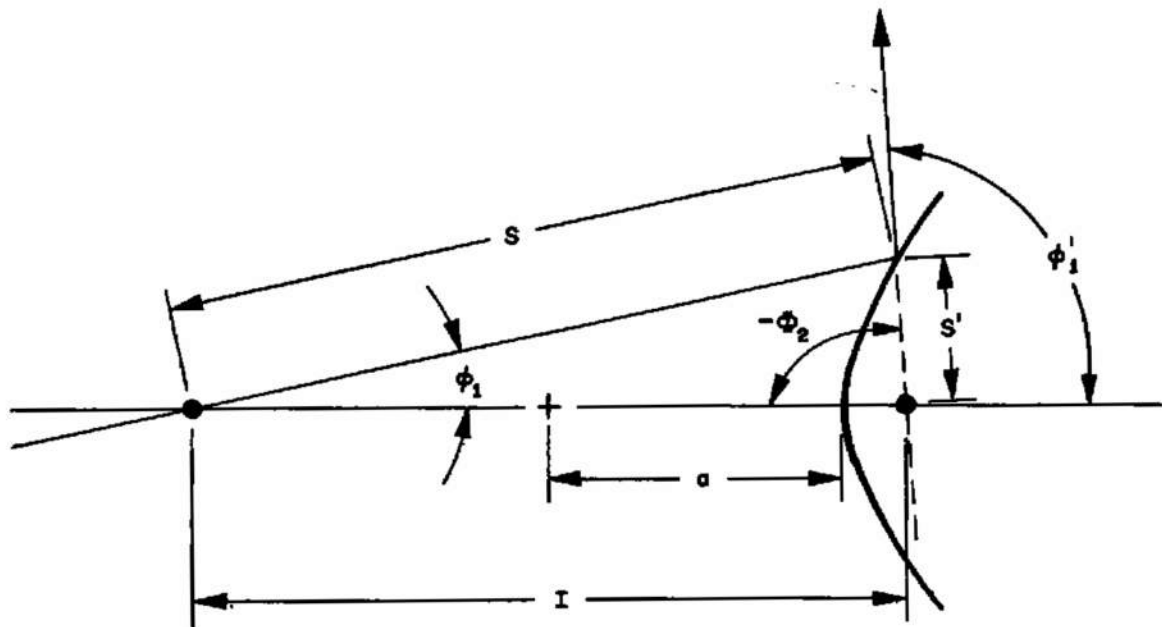


Figure 7-23. Hyperboloidal Reflector Parameters

$$\frac{T}{S} = \sin \phi_1, \quad \frac{T}{S'} = \sin \phi_1' \quad (7-139)$$

and

$$\frac{S'}{S} = \frac{\sin \phi_1}{\sin \phi_1'} \quad (7-140)$$

The definition of an ellipsoid requires that

$$S' + S = 2a \quad (7-141)$$

Where a is the semi-major axis. Further, by reason of the sine relationship for triangles

$$\frac{S}{\sin \phi_1'} = \frac{I}{\sin \alpha} = \frac{I}{\sin (\phi_1 - \phi_2)} \quad (7-142)$$

where I is the interfocal distance of the ellipsoid. Combining equations (7-140) and (7-141):

$$S \left(\frac{\sin \phi_1}{\sin \phi_1'} + 1 \right) = 2a \quad (7-143)$$

Combining equations (7-142) and (7-143):

$$\frac{\sin \phi_1'}{\sin (\phi_1 - \phi_1')} I \left(\frac{\sin \phi_1}{\sin \phi_1'} + 1 \right) = 2a, \quad \text{and}$$

$$\frac{\sin \phi_1 + \sin \phi_1'}{\sin (\phi_1 - \phi_1')} = \frac{2a}{I} \quad (7-144)$$

Since, by definition, the eccentricity of an ellipsoid, e , is given by $e = \frac{I}{2a}$, then

$$e = \frac{\sin (\phi_1 - \phi_1')}{\sin \phi_1 + \sin \phi_1'} \quad (7-145)$$

It should be noted that the principal defining parameter for the ellipsoid, i.e., eccentricity, is fixed by the angular relationship between one corresponding pair of entering and exiting rays. Similarly, it is possible to solve equation (7-145) for an explicit relationship between those two rays in terms of the eccentricity alone. Thus, equation (7-145) may be written

$$e = \frac{\sin \phi_1 \cos \phi_1' - \cos \phi_1 \sin \phi_1'}{\sin \phi_1 + \sin \phi_1'},$$

$$e (\sin \phi_1 + \sin \phi_1') = \sin \phi_1 \cos \phi_1' - \sqrt{1 - \sin^2 \phi_1} \sin \phi_1'$$

This reduces to

$$\left(\frac{1 + e^2 - 2e \cos \phi_1'}{\sin^2 \phi_1'} \right) \sin^2 \phi_1 - 2 \left[\frac{e(\cos \phi_1' - e)}{\sin \phi_1'} \right] \sin \phi_1 - (1 - e^2) = 0$$

Solving the quadratic and eliminating the extraneous root which gives a negative value for $\sin \phi_1$ corresponding to the opposite branch of the ellipsoid,

$$\sin \phi_1 = \left\{ \frac{e(\cos \phi_1' - e) + \sqrt{[e(\cos \phi_1' - e)]^2 + (1 - e^2)(1 + e^2 - 2e \cos \phi_1')}}{1 + e^2 - 2e \cos \phi_1'} \right\} \sin \phi_1'$$

Expanding the radical, this reduces to

$$\sin \phi_1 = \frac{1 - e^2}{(1 + e^2) - 2e \cos \phi_1'} \sin \phi_1' \quad (7-146)$$

Among other things the relationship expressed in equation (7-146) gives an explicit statement of the zonal magnification, m_e , of an ellipsoid as defined by Abbe; thus:

$$m_e = \frac{\sin \phi_1}{\sin \phi_1'} = \frac{1 - e^2}{(1 + e^2) - 2e \cos \phi_1'} \quad (7-147)$$

The paraxial magnification, M_e , may be obtained by allowing ϕ_1 and ϕ_1' to approach 0, whereupon $\cos \phi_1'$ goes to 1 and

$$M_e = \frac{1 - e^2}{(1 + e^2) - 2e} = \frac{1 + e}{1 - e} \quad (7-148)$$

For energy transfer calculations it would be more convenient to have equation (7-146) expressed in terms of the cosines of the angles. To this end it may be expanded thus:

$$1 - \cos^2 \phi_1 = \left[\frac{1 - e^2}{(1 + e^2) - 2e \cos \phi_1'} \right]^2 (1 - \cos^2 \phi_1')$$

$$\cos \phi_1 = \sqrt{1 - \left[\frac{1 - e^2}{(1 + e^2) - 2e \cos \phi_1'} \right]^2 (1 - \cos^2 \phi_1')}$$

$$= \sqrt{\frac{[(1 + e^2) - 2e \cos \phi_1']^2 - (1 - e^2)^2 (1 - \cos^2 \phi_1')}{(1 + e^2) - 2e \cos \phi_1'}}$$

The numerator expands as follows:

$$(1 + e^2)^3 - 4e(1 + e^2) \cos \phi_1' + 4e^2 \cos^2 \phi_1' - (1 - e^2)^2 + (1 - 2e^2 + e^4) \cos^2 \phi_1'$$

$$= 4e^2 - 4e(1 + e^2) \cos \phi_1' + (1 + 2e^2 + e^4) \cos^2 \phi_1'$$

$$= [(1 + e^2) \cos \phi_1' - 2e]^2$$

Inserting this result into the radical above yields finally:

$$\cos \phi_1 = \frac{(1 + e^2) \cos \phi_1' - 2e}{(1 + e^2) - 2e \cos \phi_1'} \quad (7-149)$$

$$\text{Defining } E = \frac{2e}{1 + e^2},$$

$$\cos \phi_1 = \frac{\cos \phi_1' - E}{1 - E \cos \phi_1'} \quad (7-150)$$

The last is a basic relationship which shall be used throughout the treatment of systems employing conic sections. A similar expression may be derived for the hyperboloid. Observing the sign convention for entrance and exit angles as labeled in figure 7-23, by definition of the hyperboloid

$$S - S' = 2a, \frac{S'}{S} = \frac{\sin \phi_1}{\sin(\pi - \phi_1')} = \frac{\sin \phi_1}{\sin \phi_1'}$$

also

$$\frac{S}{\sin \phi_1'} = \frac{I}{\sin(\phi_1' - \phi_1)}$$

Again

$$S \left(1 - \frac{\sin \phi_1}{\sin \phi_1'}\right) = 2a$$

and

$$\frac{\sin \phi_1'}{\sin(\phi_1' - \phi_1)} I \left(1 - \frac{\sin \phi_1}{\sin \phi_1'}\right) = 2a$$

The definition of the eccentricity, h , of a hyperboloid follows the same convention as that for an ellipsoid giving

$$h = \frac{\sin(\phi_1' - \phi_1)}{\sin \phi_1' - \sin \phi_1} \quad (7-151)$$

It is helpful to define the negative supplementary angle $-\Phi_2 = \pi - \phi_1'$. When this substitution is made in equation (7-151),

$$h = \frac{\sin[\pi - (\phi_1' - \Phi_2)]}{\sin[\pi - (-\Phi_2)] - \sin \phi_1} = - \frac{\sin(\phi_1 - \Phi_2)}{\sin \Phi_2 + \sin \phi_1}$$

or

$$-h = \frac{\sin(\phi_1 - \Phi_2)}{\sin \phi_1 + \sin \Phi_2} \quad (7-152)$$

It can be seen that equation (7-152) has precisely the same form as equation (7-145) with the substitution of h for $-h$ and ϕ_2 for Φ_2 . Therefore equations can be written corresponding to (7-146), (7-148), (7-149) and (7-150) for the hyperboloid by proceeding as follows:

$$\sin \phi_1 = \frac{1 - h^2}{(1 + h^2) + 2h \cos \Phi_2} \sin \Phi_2$$

The inverse transformation on Φ_2 yields

$$\sin \phi_1 = \frac{(h^2 - 1)}{(1 + h^2) - 2h \cos \phi_1'} \sin \phi_1' \quad (7-153)$$

As ϕ_1 goes to 0, ϕ_1' goes to $-\pi$, and $\cos \phi_1'$ becomes -1. Thus the paraxial magnification for the hyperboloid is

$$M_h = \frac{h - 1}{h + 1} \quad (7-154)$$

Similarly

$$\cos \phi_1 = \frac{2h - (1 + h^2) \cos \phi_1'}{(1 + h^2) - 2h \cos \phi_1'} \quad (7-155)$$

Defining $H = \frac{2h}{h^2 + 1}$

$$\cos \phi_1 = \frac{H - \cos \phi_1'}{1 - H \cos \phi_1'} \quad (7-156)$$

The inverse of equations (7-150) and (7-156) when written in terms of generalized successive angles are:

$$\cos \phi_1' = \frac{E + \cos \phi_1}{1 + E \cos \phi_1} \quad (7-157)$$

and

$$\cos \phi_1 = \frac{H - \cos \phi_1'}{1 - H \cos \phi_1} \quad (7-158)$$

In treating an arbitrary string of conic section reflectors which terminate in a paraboloid it is necessary to express the exiting ray height in terms of the initial angle. To do this the recursive formulae (7-157) and (7-158) are employed by successive substitution of the $\cos \phi_1'$ issuing from each preceding conic section for the $\cos \phi_1$ of the following conic section, since these angles must match by virtue of the ray crossover at the common foci between the two optical elements, as in figure 7-21. Thus, when equation (7-157) is substituted into equation (7-110),

$$\begin{aligned} r^2 &= 4p^2 \frac{\left(1 - \frac{E + \cos \phi_1}{1 + E \cos \phi_1}\right)}{\left(1 + \frac{E + \cos \phi_1}{1 + E \cos \phi_1}\right)} = 4p^2 \frac{1 + E \cos \phi_1 - E - \cos \phi_1}{1 + E \cos \phi_1 + E + \cos \phi_1} \\ &= 4p^2 \frac{(1-E) - \cos \phi_1 (1-E)}{(1+E) + \cos \phi_1 (1+E)} \end{aligned}$$

$$r^2 = 4p^2 \frac{(1 - E)}{(1 + E)} \frac{(1 - \cos \phi_i)}{(1 + \cos \phi_i)} \quad (7-159)$$

It is seen that the form of equation (7-159) is precisely that of equation (7-110) with respect to $\cos \phi_i$ so that successive application for any series of ellipsoids would give the same result. In the case of the hyperboloid, it is the supplementary angle, $\pi - \phi_i'$ from the previous element which must match the ϕ_i of the following one. Thus substituting $-\cos \phi_i'$ for $\cos \phi_i$ in equation (7-110) yields

$$r^2 = 4p^2 \frac{1 + H}{1 - H} \frac{(1 - \cos \phi_i)}{(1 + \cos \phi_i)} \quad (7-160)$$

From the expressions in (7-159) and (7-160)

$$\frac{1 - E}{1 + E} = \frac{1 - \frac{2e}{1 + e^2}}{1 + \frac{2e}{1 + e^2}} = \frac{(1 - e)^2}{(1 + e)^2} = \frac{1}{M_e^2} \quad (7-161)$$

and

$$\frac{1 + H}{1 - H} = \frac{1 + \frac{2h}{1 + h^2}}{1 - \frac{2h}{1 + h^2}} = \frac{(1 + h)^2}{(1 - h)^2} = \frac{1}{M_h^2} \quad (7-162)$$

On the basis of the expressions (7-159), (7-160), (7-161), and (7-162) where ϕ_0 is the initial angle to the first conic section, in general,

$$r^2 = \frac{4p^2}{M_1^2 M_2^2 \dots M_n^2} \frac{(1 - \cos \phi_0)}{(1 + \cos \phi_0)} \quad (7-163)$$

where the M_1 , M_2 , etc. refer to the paraxial magnifications of the various ellipsoids and hyperboloids employed in the system. The statement can also be generalized to include paraboloids, other than the terminal one which may be inserted into the system. It should be observed that when an intermediate paraboloid of focal length p_i is employed, it must be followed by another paraboloid of focal length p_{i+1} , if the string of conic sections is to be continued. Since the height of a ray reflected from the first after entering at an angle ϕ_i is the same as the height impinging upon the second to be reflected at an angle ϕ_{i+1} ; then, borrowing again from equation (7-110) for paraboloids gives:

$$4p_i^2 \frac{1 - \cos \phi_i}{1 + \cos \phi_i} = 4p_{i+1}^2 \frac{1 - \cos \phi'_{i+1}}{1 + \cos \phi'_{i+1}} \quad (7-163.1)$$

Equation (7-163.1) may be solved for $\cos \phi'_{i+1}$, giving

$$\cos \phi'_{i+1} = \frac{1 - \frac{p_i^2}{p_{i+1}^2} \frac{1 - \cos \phi_i}{1 + \cos \phi_i}}{1 + \frac{p_i^2}{p_{i+1}^2} \frac{1 - \cos \phi_i}{1 + \cos \phi_i}} \quad (7-163.2)$$

The paraxial magnification between the two paraboloids is given as well by the ratio of tangents as it is by the sines because of the equivalence of the two for small angles. Thus if r_i is the height of the ray between the two paraboloids, then

$$M_p = \frac{\frac{r_i}{p_i}}{\frac{r_{i+1}}{p_{i+1}}} = \frac{p_{i+1}}{p_i} \quad (7-164)$$

Referring to equation (4-68) it is seen that the system effective focal length f may be substituted for the quantity $\frac{p}{M_1 M_2 \dots M_n}$ in equation (7-164) yielding

$$r^2 = 4f^2 \frac{(1 - \cos \phi_0)}{(1 + \cos \phi_0)} \quad (7-137)$$

which is identical to equation (7-110) for the paraboloid and proves the assertion made earlier.

It is pointless to carry the analysis of simple conic section systems further on a first order basis because such an analysis would amount to a repetition of the analysis for the simple paraboloid from this point forward. Even the value of f in equation (7-137) must be exactly identical with p for the simple paraboloid because the effective focal length of the system is determined by thermodynamic principles as shown in section 4 and does

not depend on the nature of the optical system except for consideration of dissipative losses. Thus, from equation (4-43),

$$f = p = \sqrt{\frac{kI_0}{E}}$$

where:

f = paraxial focal length of the total conic system

p = paraxial focal length of simple paraboloid

k = dissipative efficiency

I_0 = axial source radiance

E = radiant intensity desired on axis.

The relative flux distribution for either the simple paraboloid or total conic system from equation (7-113), is

$$R = \frac{(1 + \cos \phi)^2}{4} \bar{I}_\phi, \text{ or } R = \left[\frac{4p^2}{4p^2 + r^2} \right]^2 \bar{I}_\phi$$

The gross analysis of these systems on a first order basis yields information so comprehensive that calculation of higher order effects pales by comparison. The relay lenses that would be inserted at each common focus between conic sections in any real design would not affect the first order analysis or gross flux distribution in any way. These display second order effects when distortion and field curvature are considered in the analysis of flux distribution profiles. However, relay lenses could not begin to overcome the precipitous attenuation in intensity level which occurs upon removal from the axis of conic section systems toward the marginal zones. Thus, of those systems which use the conic section scheme, with all sections joined together by relay lenses located at common conjugate foci, those used as marginal systems employing a separate refractive system for central fill-in suffer the worst possible performance. The central fill-in system may be adequate but the contribution of the outer conic section system is bound to degrade the overall performance if an attempt is made to utilize this part of the system to gain substantially higher efficiency as was shown in the analysis of the simple paraboloid.

Therefore, aside from noting that the conclusions already drawn in the analysis of the simple paraboloid as used with each arc also apply to any conic section system, any further discussion of these systems will be foregone and the examination of modifications for the purpose of gaining a more substantive control of the flux distribution will be undertaken.

7.6 MODIFIED CONIC SECTION OPTICAL SYSTEMS

7.6.1 Fresnel Collection Devices

Since coma introduced in the very fast collection optics is one of the primary sources of nonuniformity in conic section systems, a means of eliminating this aberration is very desirable. One approach to this problem is the use of a Fresnel reflector.

A typical Fresnel collection device (figure 6-3) consists of concentric rings of ellipsoidal sections arranged to collect the maximum source radiation. The concentric ellipsoidal sections all have the same conjugate foci and their eccentricities are chosen so that they all have approximately the same magnification. If the Fresnel collector is used in conjunction with a Cassegrainian collimation system, the intensity distribution in the collimated beam due to each collector section is given by equation (7-1) with respect to the axial intensity if that section were continued all the way to the axis. The axial intensity is given by equation (7-5) such that

$$E_0 = \frac{I_0}{f^2} \quad (7-165)$$

where f is the effective focal length of the total system. If F is the Cassegrainian focal length and M_{e_0} is the paraxial magnification of the ellipsoid section in question, then the paraxial magnification law, equation (4-68), and equation (7-165) give

$$E_0 = \frac{I_0}{F^2} \cdot M_{e_0}^2 \quad (7-166)$$

On the basis of equations (7-1) and (7-166) the actual intensity distribution for the ellipsoid section in question is given by

$$E = \frac{I_0}{F^2} \cdot M_{e_0} \cdot \frac{(1 + \cos \phi_1)^2}{4} \quad (7-167)$$

Stipulating E to be a solar constant, E_s ,

$$M_{e_0} = F \sqrt{\frac{E_s}{I_0}} \cdot \frac{2}{1 + \cos \phi_1} \quad (7-168)$$

Equation (7-148) gives

$$\frac{1 + e}{1 - e} = M_{e_0} = F \sqrt{\frac{E_s}{I_0}} \cdot \frac{2}{1 + \cos \phi_1} \quad (7-169)$$

When ϕ_1 is 0, for the axial section with eccentricity e_0 ,

$$\frac{1 + e_0}{1 - e_0} = F \sqrt{\frac{E_s}{I_0}} \quad (7-170)$$

so that, in general, for the eccentricity of any section at an initial collection angle, ϕ_1 :

$$\frac{1 + e}{1 - e} = \frac{1 + e_0}{1 - e_0} \frac{2}{1 + \cos \phi_1}$$

or

$$e = \frac{1 + e_0 \left(\frac{3 + \cos \phi_1}{1 - \cos \phi_1} \right)}{e_0 + \left(\frac{3 + \cos \phi_1}{1 - \cos \phi_1} \right)} \quad (7-171)$$

where e_0 is the eccentricity of the axial section. If sections of the Fresnel mirror, making an angle ϕ_1 , with the first focal point were designed with an eccentricity, e , as determined by equation (7-171) then the relative intensity distribution would be compensated in discrete steps, depending upon how many sections were used. The design procedure would be to plot a curve of e vs. ϕ_1 , and divide the total variation of e , for the full range of ϕ_1 desired, into as many equal intervals as the number of zonal sections planned. From the curve of e vs. ϕ_1 the corresponding values of ϕ_1 where each zone should be terminated are read. At the marginal point of each zone, a ray is drawn to the second focus, making an angle, ϕ_2 with the axis. The next zonal ring begins at its interior marginal intersection with the ray from the exterior margin of the previous inner zone. This is to avoid interference of each successive zone with the imaging rays of the previous zone (see figure 6-3). This will create gaps in the useful collection of radiation between each zone, and if such an ellipse configuration is plotted using various starting values of e_0 , it soon becomes apparent that a great deal of energy is lost between the Fresnel ring sections and that the whole array begins to fold back upon itself for angles beyond $\phi_1 = 90^\circ$. This provides not only inefficient collection but inefficient use of the energy that is collected as well. Therefore, this method of gaining control over intensity distribution for purposes of uniformity has been discarded.

7.6.2 Multifaceted Transfer Systems

Multifaceted components, that is, components consisting of many adjacent elements, each with individual optic axes, may be employed at the collection, transfer or collimation system level. Reference has been made to multifaceted multi-axis collectors which feed separate collimators or projectors. In the case of the aperture transfer concept which uses a field element and projection lens, the separately collected beams are superimposed at the field element. The multifaceted concept which shall be investigated here has to do with the transfer system. Specifically, either the relay lens at the entrance pupil of the collimator, or the hyperboloid of the Cassegrainian system, is broken up into many separate juxtaposed elements, with separate optic axes, such that the incident beam is divided into as many separate beams superimposed at the succeeding optical element. In each case the optical component so treated behaves as a multifaceted relay lens. Using several concepts derived from basic principles discussed earlier, the multifaceted transfer systems will be treated as another method of modifying the inherent distribution of a conic system. In dealing with a system which destroys the continuity of the field of radiation it is convenient to define a quantity which will be called average or reduced brightness. Thus, in a field which is broken up by dark spaces, by variations in brightness, or is otherwise unsymmetrical, a circular field of average brightness independent of direction within the field which delivers the same intensity to the target element as does the actual field of illumination will be considered. Thus, following the form of equation (4-18),

$$E = \oint B(\phi, \theta) \cos \phi d\Omega = \pi \bar{B} \sin^2 \bar{\Theta} \quad (7-172)$$

where \bar{B} is the average brightness and $\bar{\Theta}$ is the reduced field half angle. ϕ and θ are polar angles from the target element, while

$$\bar{B} = \frac{\oint B(\phi, \theta) d\Omega}{\int d\Omega} \quad (7-173)$$

Equations (7-172) and (7-173) will serve to define both \bar{B} and $\bar{\Theta}$. Now, if radiation of brightness B falls on a surface through an angle, θ , the intensity at the surface is

$$E = \pi B \sin^2 \theta = \pi \bar{B} \sin^2 \phi \quad (7-174)$$

where ϕ is the angle into which the radiation scattered by the surface emanates. This expression is based upon the assumption that the surface becomes the effective radiation source and the total flux is unaltered. If the surface were flat and specular then θ would equal ϕ and therefore \bar{B}

would equal B . If the surface were Lambert-diffuse then ϕ would be 90° and $B = E/\pi$ as derived earlier, and \bar{B} would equal $B \sin^2 \theta$. Thus the effective reduction in brightness due to a scattering surface is a function of the incident solid angle. If the surface were specular but curved, then equation (7-174) would not hold because the effective source would not be the surface itself but rather an image created by that surface, and B would be unaltered.

In the case of the pebble bed, consider figure 7-24 and the progression from one pebble, i.e., a hyperboloid, to many pebbles. Assuming that in (a) of figure 7-24 the field is appropriately fixed at a value Θ , then a radiant intensity under these conditions of one solar constant is given by

$$E_s = \pi B \sin^2 \Theta$$

The equivalent expression for many pebbles and a new field angle Θ' is

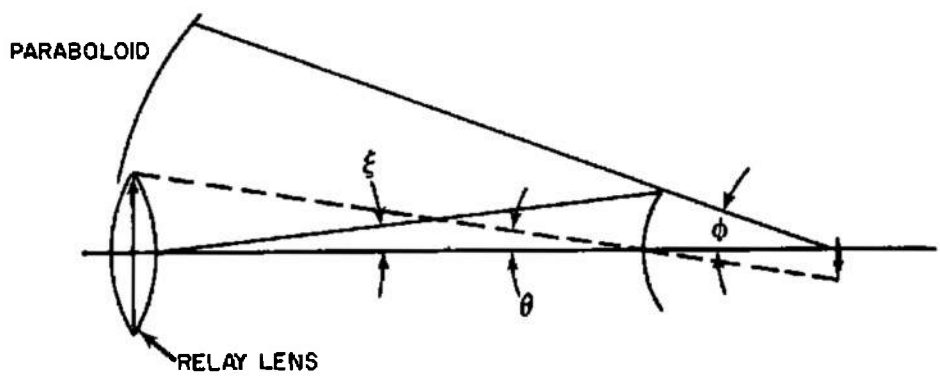
$$E_s = \pi \bar{B} \sin^2 \Theta'$$

Using equation (7-174) for B/\bar{B} the new field angle may be calculated in terms of the old as follows:

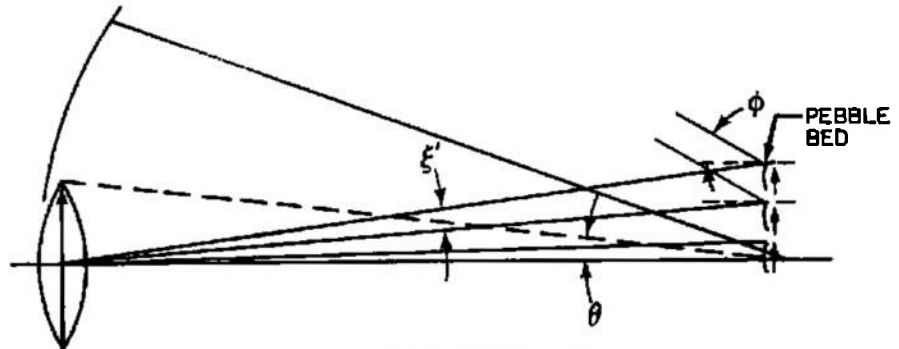
$$\sin \Theta' = \frac{\sin \phi}{\sin \theta} \sin \Theta \quad (7-175)$$

This shows that the effective field angle of the system must be enlarged if adequate intensity is to be obtained since $\sin \phi$ must always exceed $\sin \theta$. That is, the paraboloid must be larger than the relay lens in any practical system. It should be clear, then, that the smaller the relay lens which feeds the pebble bed and the larger the aperture of the paraboloid into which the pebbles must scatter the radiation, the greater will be the necessary increase in the field angle Θ . If the basic requirement of equation (7-175) is not observed and too small a field is designed, by virtue of too small a pebble bed, then it will be impossible to get enough energy into the system. Also, sufficient energy cannot be transferred to the pebble bed through the field lens unless the condition of equation (7-175) is adequately met.

The number of pebbles used makes no difference so long as they are closely packed and the total number subtends the field angle, Θ' . To prove this statement, figure 7-24 shows that the single hyperboloid subtends an angle, ξ , at the Cassegrainian secondary focus, which is the relay lens position. From Abbe's sine condition, the size of the image at the parabolic principal focus is proportional to $\sin \xi / \sin \phi$. If a pebble bed arrangement of hexagonal closest packing is assumed for the pebble array



A. ONE PEBBLE



B. MANY PEBBLES

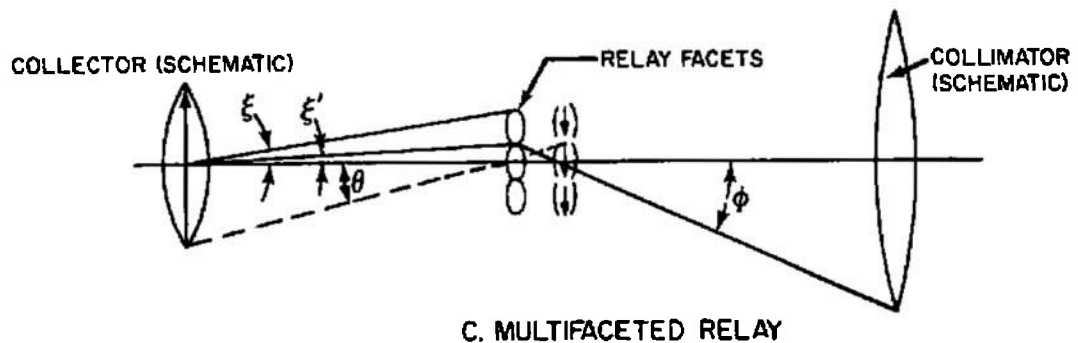


Figure 7-24. Multifaceted Concepts

then the angle ξ' for each pebble will be diminished in accordance with

$$\xi' = \frac{\xi}{2n-1} \quad (7-176)$$

where n is the number of circumscriptive rows of pebbles in the array. Thus the size of the image formed by each pebble is proportional to

$$\frac{\sin \xi}{2n-1} \sim \frac{1}{2n-1}$$

using the small angle approximation. The area of each image is therefore proportional to

$$A_n \sim \frac{1}{(2n-1)^2}$$

The number of pebbles, on the other hand, increases in an arithmetic progression as

$$N = \sum_{i=0}^n (1 + 6i) = 1 + 3n(n + 1)$$

The total effective area of the image behind the pebble bed is

$$A = A_0 \frac{1 + 3n(n + 1)}{(2n - 1)^2} \quad (7-177)$$

Where A_0 is the area of the image behind one pebble, i.e., a hyperboloid. In the limit, as n approaches infinity,

$$\lim_{n \rightarrow \infty} \frac{A}{A_0} = \frac{3n^2}{4n^2} = \frac{3}{4}$$

The fact that this ratio is not 1 is due to the packing factor which controls the number of pebbles one can fit into an inscribed hexagon within the angle, ξ . It means that, because of reduced efficiency due to vignetting by the interstices between the facets, the field angle will have to be enlarged by $\sqrt{4/3}$ or about 15% over that calculated in equation (7-175). The important fact is that the series converges to a finite limit proving the assertion that the number of pebbles used to gather the energy contained within the divergence ξ is unimportant. Ideally the total effective area of the image behind the pebble bed must equal A_0 if the intensity is to be preserved in the target region. This fact and the foregoing derivation may be used to prove the

validity of the assumptions made in the definition of B and the latter's use in obtaining equation (7-175). Thus the size of the effective source at the principal focus of the paraboloid approaches the actual size of the pebble bed for large values of n . Since the pebble bed subtends the angle ξ at the vertex of the paraboloid, the effective field half angle simply becomes

$$\Theta' = \xi \quad \text{or} \quad \sin \Theta' = \sin \xi \quad (7-178)$$

From the geometry in figure 7-28 it is seen that the basic field angle Θ is given by

$$\sin \Theta = \sin \theta \frac{\sin \xi}{\sin \phi}$$

Substituting equation (7-178) into this immediately yields equation (7-175) and thus the validity of the assumptions made in the definition of \bar{B} is established. Actually the field angle Θ' will have to be somewhat larger than ξ because the total image area behind the pebble bed is only $3/4$ that of the needed area. This requires a 15% increase in effective field angle which can be taken into account in efficiency considerations.

The multifaceted relay lens is basically identical to the pebble bed concept and the same equations apply. The only difference is that, with a refracting pebble arrangement, $\sin \theta$ may be allowed to approach $\sin \phi$ and, except for efficiency degradation due to vignetting by the interstices between the facets, the field angle increment may be held to no more than the 15% value. Thus, referring to figure 7-24, it is seen that each facet can be made to form an image its own size, thereby establishing an almost continuous field. This can be done when the collection element subtends the same angle as the collimator. At each image, formed by a pebble facet, of the collection unit it may be desirable to use another relay facet to image the first facet into the collimator aperture in order to avoid a large vignetting loss.

These two systems, then, (pebble bed and multifaceted relay) represent the best logical choices for effecting the concept of division and redistribution of the radiant field. That this device yields better uniformity than is possible with the ordinary conic section system upon which it is based is clear since it is, in effect, a number of such systems each of smaller effective aperture and all nearly superimposed one upon the other. It is the smaller effective aperture which makes the distribution of each more uniform and since the nature of the geometry tends to superimpose these beams, except for small displacements, one upon the other the net result is better uniformity. The amount of improvement depends upon the number of pebbles or facets, although perfect uniformity is not obtained in the limit of infinitesimal facets because the system is still subject to the off-axis effects, principally foreshortening, of the parabolic collimator. It might be noted that the condenser conic system to be described

below uses the source conjugate to the field while the multifaceted systems, although they can go either way, generally use the source conjugate to the aperture which is broken up and redistributed over the continuous collimator aperture.

The multifaceted element when used as a relay component in the optical train can be a very effective way of smoothing the distribution. It can be used as part of a conic system or in conjunction with higher order corrections to the latter which will be discussed below. In fact, the combined approach of multifaceted relay elements and specially designed mirror surfaces is a very effective way of controlling the distribution of relative flux level in the collimated beam.

7.6.3 Source Aperture Conjugation

Another application, although differing widely from the one just reviewed, is nevertheless one analog of the multifaceted concept. The principal comparison is that, while the previous concept divided the solar field and superimposed the several beams at the relay lens level, in the present case the solar field is divided at the collection level, with the several source images being superimposed at the so-called field lens, more properly termed aperture lens or aperture stop plane. It is the latter which is mapped by the subsequent projection lens onto the aperture of the collimator.

The projection lens becomes the entrance pupil for the collimator and delineates the solar field. It is an extended incoherent pseudo-source for the collimator wherein off-axis aberrations such as astigmatism and distortion have a considerable effect upon the flux distribution. These aberrations, and others, tend to shape and bend the source such as the bending of a plane around a sphere or the compressing of a sphere into an ellipse. It has already been seen what a profound difference is manifest in the final beam distribution by virtue of these various source shapes. What has been made apparent, then, is that not only the properties of the final collimating system (which, although it must be free of spherical aberration, can suffer from other aberrations) must be considered, but equally important are the imaging properties of the collection and transfer systems which must produce the source irradiance characteristics needed for the realization of ultimate uniformity. These source irradiance characteristics obtained by alterations or redistribution of the real source radiance function is what is meant by the pseudo-source. The optical system, in the present case, collects the radiation from the physical source and irradiates the pseudo-source, and consists of a multifaceted array of collection components which form secondary source images superimposed upon one another at the aperture stop plane. It is the object of this device to obtain a two-dimensional flux distribution at the aperture

stop plane which when mapped onto the collimator aperture will result in uniformity. There may be sufficient regularity in the brightness profiles of the sources themselves to allow for manipulation of the several source images to accomplish the purpose. On the other hand, the variations may be so severe (and even of a temporal nature) as to preclude their use unless the averaging effect is sufficient to reduce the vicissitudes to a tolerable level. In any case, the intensity function required at the aperture stop plane can be determined on the basis of the collimator characteristics and the optical properties of the projection lens.

To illustrate how this might be done, consider a hypothetical illumination system which both illuminates a pseudo-source and contains a plane (which is referred to as an aperture stop plane) that is conjugate to the target field, as illustrated in figure 7-25. If the aperture stop plane is mapped one-to-one onto the target space, then proper control of the flux in this plane will directly produce uniformity. This control can be brought about by careful design of the collection optics and by neutral density gradation in this plane. From the engineering standpoint, both might be needed but the less use of the latter the greater the efficiency.

As an example of how the aperture stop concept might be employed, consider a transfer function of the polar angles ϕ and θ taken from the pseudo-source as shown in figure 7-25. The transfer function, which could be tabulated, relates the energy radiated into an element of solid angle from the pseudo-source to the area which this solid angle subtends in the target space. The functions to be considered, therefore, are $dA/d\Omega(\phi, \theta)$. Whatever energy is contained in the solid angle $d\Omega$ will flow through the area dA and, as was pointed out previously, it is a basic theorem of radiative transfer that the continuous nature of $d\Omega$ can be preserved as it is traced through the optical system. Consider now that the illumination system which established the pseudo-source maps elements of area in the aperture stop plane uniquely onto the field of ϕ and θ , as shown in figure 7-25. Mathematically, the expression of the flux through an element of area in the target space can be written from equation (4-13) as follows:

$$dF = \bar{B} d\Omega |\vec{S} \cdot \hat{r}| \quad (7-179)$$

In the above, \vec{S} refers to equation (4-13) integrated over the pseudo-source. This is based on the assumption that for fixed values of ϕ and θ the brightness is constant over the entire pseudo-source surface. Simplifying equation (7-179) and introducing the parameter dA (See figure 7-25)

$$dF = \bar{B} \frac{1}{dA} dA |\vec{S}| \cos \psi \quad (7-180)$$

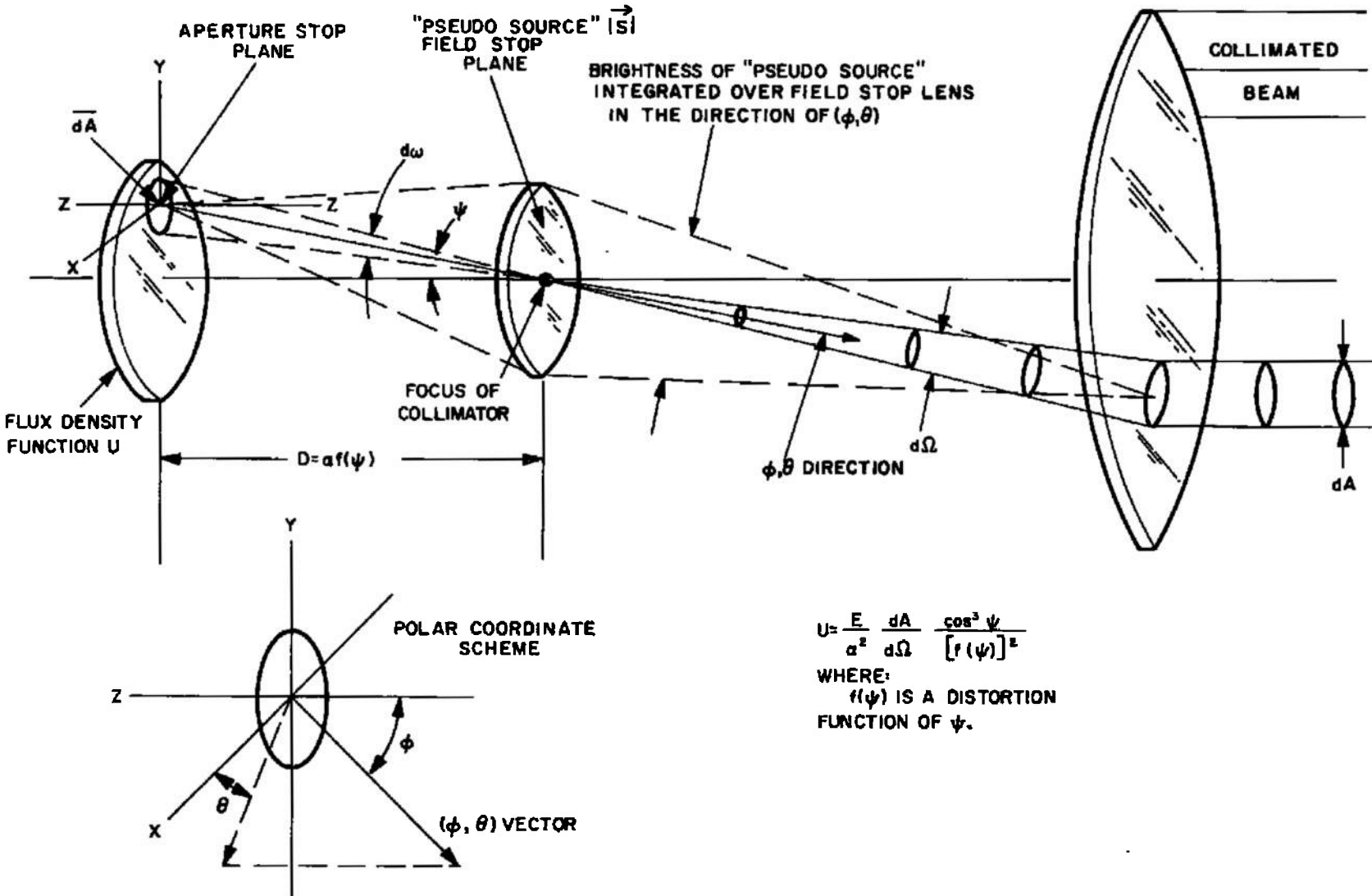


Figure 7-25. Aperture and Field Stop Mapping

The above includes the parameter $dA/d\Omega$ which is hypothesized as a unique mapping function from the pseudo-source to the target space over the field ϕ and θ . Ψ is the angle with respect to the normal to the surface $|S|$. This normal is also the optic axis of the illumination system. In the integration of equation (4-13) it is assumed that the parameter \bar{B} is averaged over the pseudo-source for particular values of ϕ and θ , and it remains to determine the dependence of \bar{B} upon those parameters. For this, the assumption of unique one-to-one mapping of positions on the aperture stop surface into the field ϕ , θ , is reasserted.

$$dF = \bar{B} d\omega |S| \cos \Psi \quad (7-181)$$

where $d\omega$ is now taken from an element on the aperture stop plane. Defining the flux density function, U , over the aperture stop surface and with the condition of complete containment of the divergence of energy from the element on the aperture stop surface by the pseudo-source

$$dF = U d\bar{A} \quad (7-182)$$

where $d\bar{A}$ is an element of the aperture stop surface.

Defining

$$\frac{d\bar{A}}{d\omega} = G(\Psi) \quad (7-183)$$

then combining (7-180), (7-181), (7-182), (7-183) and defining dF/dA equal to E , the flux density

$$U = E \frac{dA}{d\Omega} \left[G(\Psi) \right]^{-1} \quad (7-184)$$

The transfer function

$$\frac{dA}{d\Omega} \left[G(\Psi) \right]^{-1}$$

includes both the illumination system and the collimation system. It can be seen from equation (7-184) that the determination of the parameter $dA/d\Omega$ and the function $G(\Psi)$ is sufficient to establish a two-dimensional energy flux through the aperture stop surface to produce uniformity. It is a straightforward problem to trace a geometrical relation $dA/d\Omega$ through the optical system, as this is a parameter which depends only on the collimation system. The function $G(\Psi)$, on the other hand, which relates the field stop radiometry to that of the collimator system, depends upon the optical properties of the illumination system. It may be helpful

to examine the effect of certain aberrations of the illumination system on the transfer characteristics. Indeed, it would seem logical that certain gross aberrations would have a profound effect on the ultimate energy distribution.

One of the most important of these aberrations, because of its effect, is distortion or spherical aberration of the pupil planes. In order to show the effect of the action of distortion upon the G factor of the transfer function, consider the undeviated ray from an off-axis source point. This would be equivalent to considering the optical center of the system.

In any imaging system, there is a ray which makes the same angle with the optic axis before entering the lens system as it makes with the optic axis upon leaving the lens system. The optical system may be represented schematically as in figure 7-26, where the object is located at position A, the image at position B, and the cardinal points are at h_1 and h_2 . Point C is imaged at point D and point E is imaged at point F.

The ray from C to h_1 which makes an angle Ψ_c with the optic axis is the object ray. Upon leaving the lens system it passes through the point h_2 on the optic axis and is imaged at the point D making an angle Ψ_o with the optic axis. The ray from h_2 to D is the image ray.

As the point C moves from A to E, the point D moves correspondingly from B to F. If the object ray always passes through h_1 the image ray will always pass through h_2 and there will be no distortion. If, however, as C moves from A to E, the intersection of the image ray and the optic axis moves from h_2 to h_4 , the phenomenon known as pincushion distortion is introduced. The effect of this type of distortion on the imaging of a rectangular grid is shown schematically in figure 7-27.

Because the cardinal points h_1 and h_2 are the only positions at which the condition exists where the slope of the entering ray equals the slope of the exiting ray, the entering solid angle and the exiting solid angle must be referenced to those points. This is because, irrespective of the variation of the position of the cardinal points (i.e., continuous variation) in the limit of vanishingly small quantities an increment in the angle of the entrance ray is equal to an increment in the angle of the exiting ray.

Consider a lens system which exhibits pincushion distortion and investigate its energy transfer characteristics. Take an element of area $d\bar{A}$ at C, figure 7-28, such that the object ray makes an angle Ψ with the optic axis. The solid angle, $d\omega$, subtended at h_1 by the element of area, $d\bar{A}$, is given by the following equation:

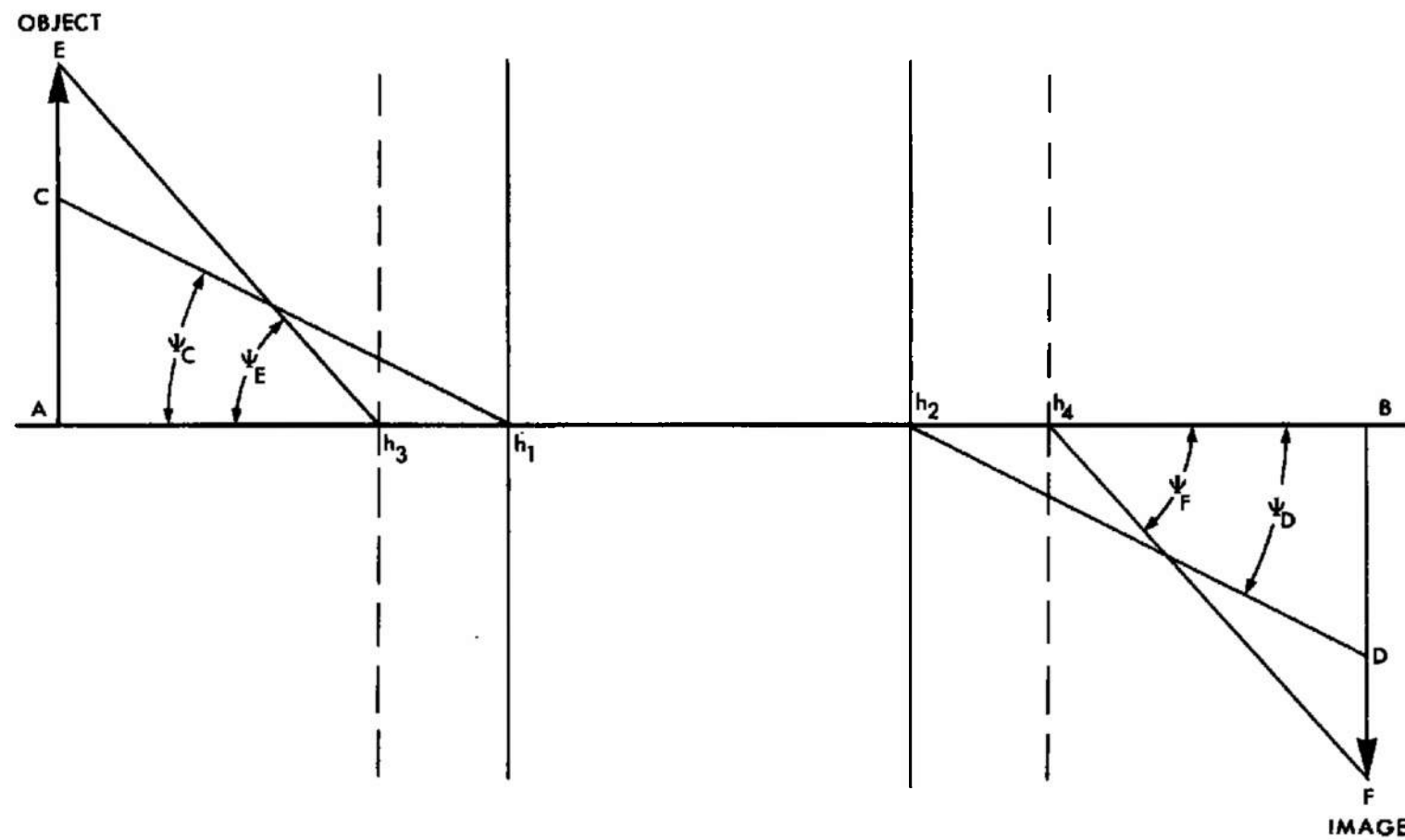
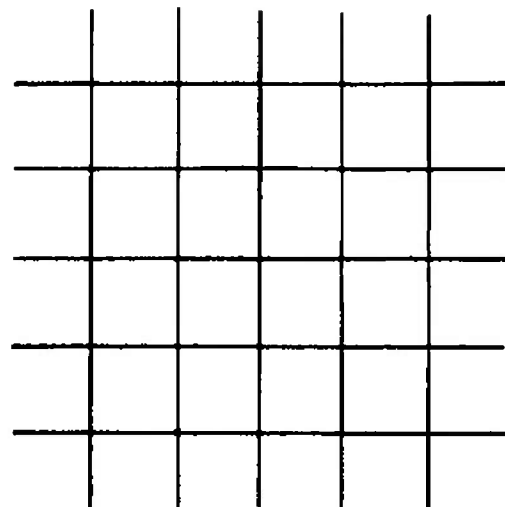
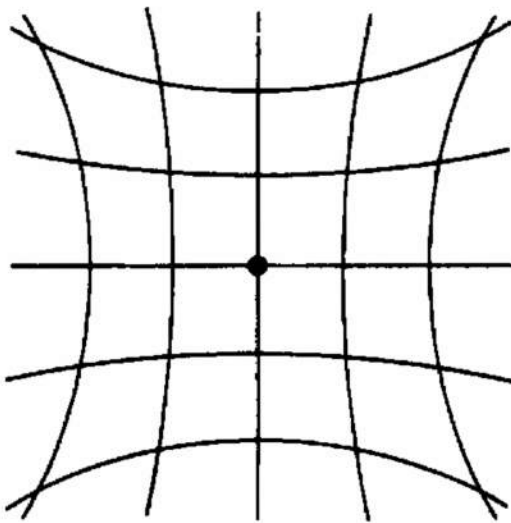


Figure 7-26. Spherical Aberration of the Pupil Planes (Distortion)



OBJECT



IMAGE

Figure 7-27. Pincushion Distortion.

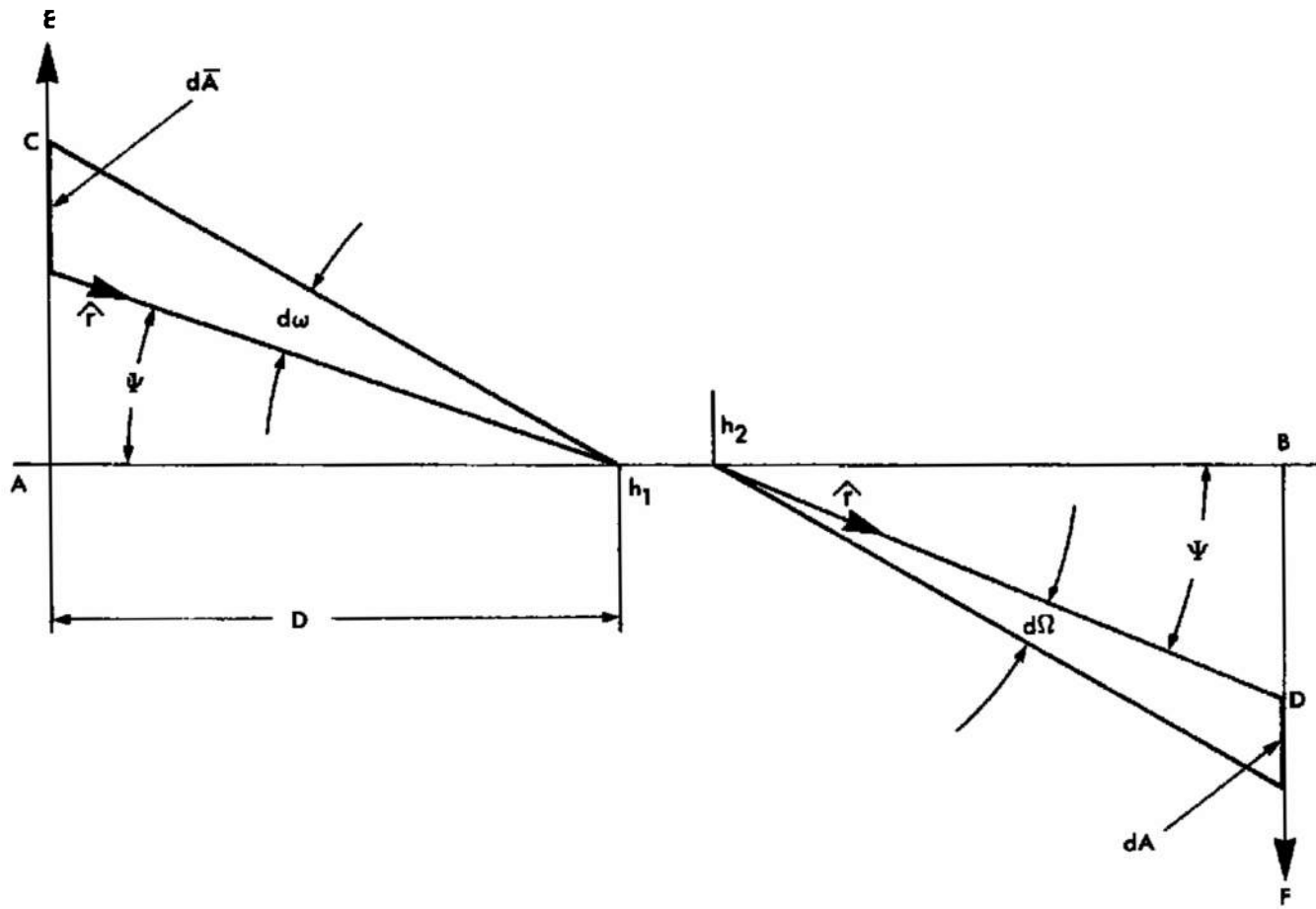


Figure 7-28. Solid Angle Transfer at Cardinal Points, Schematic

$$d\omega = \frac{d\bar{A} \cdot \hat{r}}{R^2} \quad (7-185)$$

where \hat{r} is the unit vector indicating the direction of the object ray and R is the distance from C to h_1 . From the geometry of the figure it is known that

$$R = \frac{D}{\cos \Psi} \quad (7-186)$$

$$d\bar{A} \cdot \hat{r} = d\bar{A} \cos \Psi \quad (7-187)$$

Combining equations (7-185), (7-186), and (7-187)

$$d\omega = \frac{d\bar{A} \cos^3 \Psi}{D^2} \quad (7-188)$$

If the special case of a particular form of pincushion distortion is assumed, such that the distance D from A to h_1 is a function of the angle Ψ as C moves from A to E , then

$$D = \alpha f(\Psi) \quad (7-189)$$

where α is the constant of proportionality.

It is possible to write, in this case, from equations (7-183), (7-188), and (7-189)

$$\frac{d\bar{A}}{d\omega} = G(\Psi) = \frac{\alpha^2 [f(\Psi)]^2}{\cos^3 \Psi} \quad (7-190)$$

If the above results are substituted into equation (7-184), then

$$U = \frac{E}{\alpha^2} \frac{dA}{d\Omega} \frac{\cos^3 \Psi}{[f(\Psi)]^2} \quad (7-191)$$

Thus it can be seen that distortion as well as the aberrations can be used to control energy distribution for a particular combination of projection and collimation optics. For the simple case assumed, either the prescribed distribution or neutral density filtration at the aperture stop surface is well defined and becomes the ultimate means for controlling uniformity in this case. If a conic type collimator is used, then from equation (7-137) :

$$\frac{dA}{d\Omega} = \frac{2\pi r dr}{2\pi \sin \Psi d\Psi} = \frac{4F^2}{(1 + \cos \Psi)^2} \quad (7-192)$$

where F is the collimator effective focal length. Equation (7-191) becomes

$$U = \frac{4EF^2}{\alpha^2} \frac{\cos^3 \Psi}{(1 + \cos \Psi)^2} \frac{1}{[f(\Psi)]^2} \quad (7-193)$$

The attempt may be made either to achieve the distribution, U , called for in equation (7-193) at the aperture stop plane or to design the projection lens with a degree of distortion $f(\Psi)$, such that equation (7-193) is satisfied with whatever distribution function U happens to exist for the case in question. Defining E_s as the solar constant, it is probably easiest to arrange the overlapping source images at the aperture stop plane so that U is a relatively uniform constant, U_0 , defined by

$$U_0 = \frac{E_s F^2}{\alpha^2} \quad (7-194)$$

The distortion function for the projection lens would then be defined by

$$f(\Psi) = \frac{2 \cos^{\frac{3}{2}} \Psi}{1 + \cos \Psi} \quad (7-195)$$

Such a distortion function, of the barrel type, is not entirely unreasonable for the design requirement of a projection lens. The most difficult requirement for this lens is actually to obtain reasonable mapping qualities from the aperture stop position to the collimator aperture, particularly with regard to the speed and field coverage which would be required of the projection lens for the efficiencies which are normally considered for solar simulator optical designs.

Although a one-to-one mapping by the projection lens of the aperture stop plane onto the collimator aperture is not a fundamental necessity, it is basic to the assumptions which make the foregoing analysis valid. That is, the distribution function U , is defined only to the degree that the mapping fidelity is maintained. Should the latter prove impossible to provide, U could only be adjusted on an empirical basis until uniformity is obtained in the output beam. This system is recommended only when a large number of sources are used per module, as would be

the case when a single module is used to cover a large area for a large scale solar simulator. This has the advantage of mixing and averaging the effects of many lamps. However, when the separate contributions to the aperture stop plane must be simulated by breaking up the collection from a single source with multiple collection units, the advantages to be gained do not warrant the additional complexities introduced.

7.6.4 Condenser Lens Assembly Analysis.

There are a number of ways to modify the distribution characteristics of conic systems. A method which has been found to work reasonably well in practice, although not necessarily the ideal solution, is to insert a refracting element (condenser lens) between two conjugate foci in place of a conic section which might otherwise occupy such a position. Figure 7-29 shows such an arrangement as a typical example and can be basically described as follows. A conic collection system forms an image of the arc in front of the condenser elements at their first conjugate focal point. The condensers form a secondary image at their second conjugate focus in the relay lens, whose exit pupil is the reference source for the conic collimation system which follows. The transfer angles, which illustrate how the successive apertures must be mapped onto one another, are shown in figure 7-29. In the analysis which follows, the effect of the relay lenses which must be located at each focus is omitted inasmuch as the source is assumed to be of negligible extension for first order calculations.

The design of such a system proceeds by first recognizing the following constraints:

1. The paraxial magnification of the condenser, must be equal, as required by the paraxial magnification law expressed in equation (4-68), to the focal length of the collimator, i.e., paraboloid divided by the effective focal length of the total system, calculated in equation (4-43), and the paraxial magnifications of all the other elements in the system, namely, the hyperboloid of the Cassegrainian collimator and the conic collector system.
2. The numerical aperture of the condensers is determined by the slope of the marginal existing ray from the conic collector which is in turn determined by the latter's collection efficiency and eccentricity, both of which are dependent upon the collimator aperture and focal length. These interrelationships will be examined in what follows.
3. The final consideration is the actual relationship between the entering and exiting angles to and from the condenser which must obtain over the latter's entire aperture in order to realize uniformity on a first order basis.

Consider first item 3, in general terms, as the results lead directly to consideration of items 1 and 2. To this end, consider the factors which influence uniformity in the collimated beam. The problem is one of synthesizing the system on the basis of the fundamental uniformity criterion expressed in equation (4-69). For this discussion assume a simple ellipsoidal collector and a Cassegrainian collimating system of effective focal length, F . If the paraboloid is of focal length ρ , and the hyperboloid has a magnification factor of M_h , then the paraxial magnification law gives

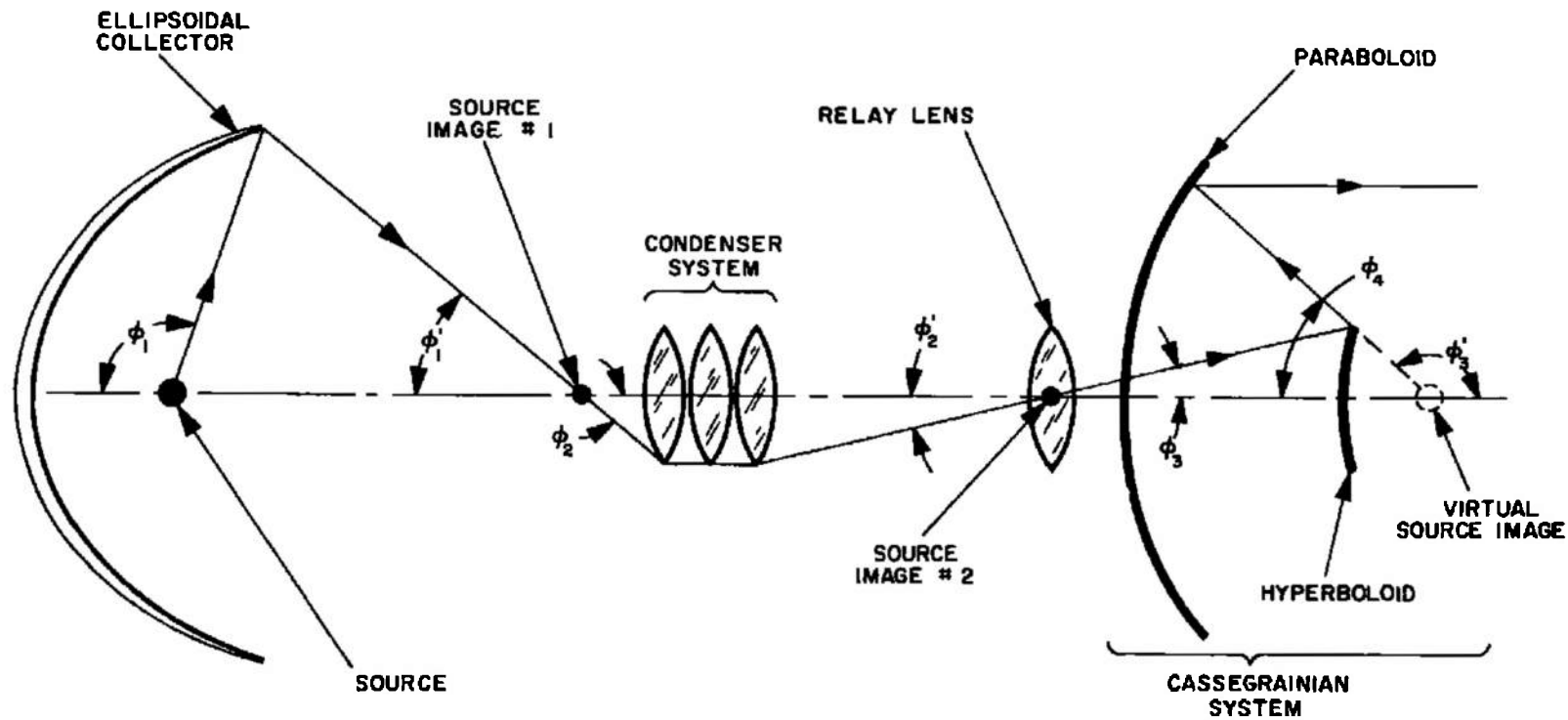


Figure 7-29. Conic Section Optical System with Condenser Lenses

$$F = \frac{\rho}{M_h}$$

The angle entering the collector is ϕ_1 while that leaving it is ϕ_1' . ϕ_1' must be equal in magnitude to ϕ_2 , the entering angle to the condenser. A similar relationship exists between ϕ_2' , the exiting angle from the condenser, and ϕ_3 , the entering angle to the collimator. ϕ_3 will be treated as equal to ϕ_2' and a relationship will be found between ϕ_2 and ϕ_3 to define the properties of the condenser lens. Equation (7-137) gives

$$r^2 = 4F^2 \frac{(1 - \cos \phi_3)}{(1 + \cos \phi_3)} = G_1 (\cos \phi_3) \quad (7-196)$$

and equation (7-157) gives

$$\cos \phi_1' = \frac{\cos \phi_1 + E}{1 + E \cos \phi_1} \quad (7-197)$$

or

$$\cos \phi_2 = \frac{E + \cos \phi_1}{1 + E \cos \phi_1} = G_2 (\cos \phi_1) \quad (7-198)$$

Equation (7-196) gives a relationship between r and ϕ_3 while equation (7-198) connects ϕ_1 and ϕ_2 . In order to relate ϕ_1 and r as required for a calculation of relative intensity in the collimated beam in accordance with equation (4-69), it is necessary to express ϕ_3 as a function of ϕ_2 . Define such a functional relationship as

$$\cos \phi_3 = \Psi(\cos \phi_2) \quad (7-199)$$

Thus the nature of the function Ψ may be tailored so that the ultimate relationship between r and ϕ_1 is such that the desired uniformity results. Combining equations (7-196), (7-198), and (7-199) in terms of implicit continued functions, r can be written in terms of $\cos \phi$ as follows:

$$r^2 = G_1 [\Psi(\cos \phi_2)] = G_1 \{ \Psi[G_2 (\cos \phi_1)] \} \quad (7-200)$$

The total differential of equation (7-200) is

$$d(r^2) = \frac{\partial G_1}{\partial (\cos \phi_3)} \frac{\partial \Psi}{\partial (\cos \phi_2)} \frac{\partial G_2}{\partial (\cos \phi_1)} d(\cos \phi_1) \quad (7-201)$$

The condition of uniformity can be described by virtue of equation (7-1) by the statement

$$R = -2 \bar{I}_\phi \frac{f^2 d(\cos \phi_1)}{d(r^2)} = 1 \quad (7-202)$$

where all angles are measured consistently from the same side of the axis, see figure 7-24. Thus, by setting R identically equal to 1, uniformity over the entire aperture is implied. Consistent with the general philosophy in the treatment of first order analyses of optical systems, assume a spherically symmetric source whereby \bar{I}_ϕ is also identically 1 for all angles ϕ_1 .

If the paraxial magnification of the condenser is defined as M_{cn} , then on the basis of equation (7-202)

$$\frac{d(r^2)}{d(\cos \phi_1)} = -2 \frac{F^2}{M_e M_{cn}} = -2f^2 \quad (7-203)$$

where M_e denotes the effective conic section collector paraxial magnification and F is the effective collimator focal length. Combining equations (7-203) and (7-201) gives

$$\frac{\partial \Psi}{\partial(\cos \phi_2)} = -2 \frac{F^2}{M_e^2 M_{cn}^2} = \frac{1}{\frac{\partial G_1}{\partial(\cos \phi_3)} \frac{\partial G_2}{\partial(\cos \phi_1)}} \quad (7-204)$$

Both partial derivatives in equation (7-204) can be calculated from equations (7-196) and (7-198) respectively and then solved for in terms of $\cos \phi_2$. Equations (7-204) then becomes the defining differential equation which determines the function Ψ . Thus,

$$\frac{\partial G_1}{\partial(\cos \phi_3)} = \frac{-8F^2}{(1 + \cos \phi_3)^2} \quad (7-205)$$

and

$$\frac{\partial G_2}{\partial(\cos \phi_1)} = \frac{1 - E^2}{(1 - E \cos \phi_1)^2} \quad (7-206)$$

From equation (7-198)

$$\cos \phi_1 = \frac{-E + \cos \phi_2}{1 - E \cos \phi_2} \quad (7-207)$$

so that equation (7-174) becomes

$$\frac{\partial G_2}{\partial(\cos \phi_1)} = \frac{(1 - E \cos \phi_2)^2}{1 - E^2} \quad (7-208)$$

By virtue of the definition of Ψ as expressed in equation (7-199), equation (7-205) may be written:

$$\frac{\partial G_1}{\partial(\cos \phi_3)} = -\frac{8F^2}{(1 + \Psi)^2} \quad (7-209)$$

Combining equations (7-204), (7-208), and (7-209) yields the linear differential equation

$$\frac{\partial \Psi}{\partial(\cos \phi_2)} = \frac{1}{4M_{cn}^2 M_e^2} \frac{(1 - E^2)(1 + \Psi)^2}{(1 - E \cos \phi_2)^2} \quad (7-210)$$

Integration of equation (7-210) leads to

$$\frac{1}{1 + \Psi} = \frac{E^2 - 1}{4 M_{cn}^2 M_e^2} - \frac{1}{E (1 - E \cos \phi_2)} + C \quad (7-211)$$

The undetermined constant, C , can be defined by the boundary condition that $\cos \phi_3$ must be 1 when $\cos \phi_2$ is 1, if the condenser lens is to be smoothly continuous at the optic axis. There is no fundamental requirement to this effect but most ordinary lenses are designed this way. When dealing with a two-ended source which does not provide any energy at the axis, the integration of equation (7-210) from the axis becomes impossible. This particular point will be taken up later. For the time being merely assume a continuous source, namely, $\bar{I}_\phi = 1$, all the way to the axis so that

$$\frac{1}{1 + 1} = \frac{-(1 - E^2)}{4 E M_{cn}^2 M_e^2} - \frac{1}{(1 - E)} + C = \frac{-(1 + E)}{4 E M_{cn}^2 M_e^2} + C$$

$$C = 1/2 + \frac{1 + E}{4 E M_{cn}^2 M_e^2} \quad (7-212)$$

When equations (7-211) and (7-212) are combined,

$$\Psi + 1 = \frac{4 M_{cn}^2 M_e^2}{1 + 2 M_{cn}^2 M_e^2 - \frac{\cos \phi_2 - E}{1 - E \cos \phi_2}}$$

or

$$\Psi = \frac{2 M_{cn}^2 M_e^2 - \left(1 - \frac{\cos \phi_2 - E}{1 - E \cos \phi_2}\right)}{2 M_{cn}^2 M_e^2 + \left(1 - \frac{\cos \phi_2 - E}{1 - E \cos \phi_2}\right)} \quad (7-213)$$

Equation (7-213) is the desired relationship between $\cos \phi_3$ and $\cos \phi_2$ in explicit form. It is particularly useful to have an expression of $m_{cn}^2 = \sin \phi_2 / \sin \phi_3$ for lens design purposes, thus

$$m_{cn}^2 = \frac{\sin^2 \phi_2}{\sin^2 \phi_3} = \frac{1 - \cos^2 \phi_2}{1 - \Psi^2}$$

$$= \frac{(1 - \cos^2 \phi_2) \left[2 M_{cn}^2 M_e^2 + \left(1 - \frac{\cos \phi_2 - E}{1 - E \cos \phi_2}\right) \right]^2}{8 M_{cn}^2 M_e^2 \left(1 - \frac{\cos \phi_2 - E}{1 - E \cos \phi_2}\right)} \quad (7-214)$$

A cross check of these results can be obtained by calculating the limit of m_{cn}^2 as ϕ goes to 0. The paraxial magnification M_{cn}^2 should be obtained, i.e.,

$$\lim_{\phi_2 \rightarrow 0} m_{cn}^2 = M_{cn}^2 \quad (7-215)$$

Since the limit of the expression in equation (7-214) is an indeterminate form it may be extracted by considering the first order zeros only, thus

$$\begin{aligned} \lim_{\phi_2 \rightarrow 0} m_{cn}^2 &= \lim_{\phi_2 \rightarrow 0} \frac{(1 - \cos^2 \phi_2)(2M_{cn}^2 M_e^2)^2}{8M_{cn}^2 M_e^2 \left(1 - \frac{\cos \phi_2 - E}{1 - E \cos \phi_2}\right)} \\ &= \lim_{\phi_2 \rightarrow 0} \frac{M_{cn}^2 M_e^2}{2} \frac{1 - E \cos \phi_2 - \cos^2 \phi_2 + E \cos^3 \phi_2}{E + 1 - \cos \phi_2 - E \cos \phi_2} \end{aligned}$$

Taking the derivatives of numerator and denominator with respect to $\cos \phi_2$ gives

$$\begin{aligned} \lim_{\phi_2 \rightarrow 0} m_{cn}^2 &\Rightarrow \lim_{\phi_2 \rightarrow 0} \frac{-E - 2\cos \phi_2 + 3E \cos^2 \phi_2}{-1 - E} \frac{M_{cn}^2 M_e^2}{2} \\ &= 2 \frac{1 - E}{1 + E} \frac{M_{cn}^2 M_e^2}{2} = \left(\frac{1 - E}{1 + E} M_e^2\right) M_{cn}^2 \end{aligned}$$

By virtue of equation (7-161) the statement expressed by equation (7-215) has been proven. Most important, there is a definite relationship, equation (7-213) which defines the lens design problem for the condensers. In the case where the source radiance function is not finite all the way to the axis, equation (7-209) may be integrated between fixed limits starting at some finite angle off the optic axis, provided the entrance angle ϕ_2 , to the condenser which corresponds to the inner edge of the radiation field collected by the ellipse is known. The corresponding exit angle ϕ_3 is then chosen to give the appropriate magnification so that

$$\frac{F}{M_e M_{cn}} = f$$

where the parameters are as defined above. If \bar{I}_ϕ is the actual polar radiance function between $\phi_{1,0}$, the initial collection angle, and some angle ϕ_1 ; then the corresponding initial angle $\phi_{2,0}$ is given by equation (7-157), and the defining integral equation based upon equation (7-211) becomes

$$\frac{1}{1 + \Psi} = \frac{1}{1 + \Psi_0} - \frac{1 - E^2}{4E} \frac{f^2}{F} \int_{\phi_{2,0}}^{\phi_2} \frac{\bar{I}_\phi}{1 - E \cos \phi} d\phi \quad (7-216)$$

If

$$M_{cn} = \frac{F}{M_e f}, \text{ where } M_e = M_{e,0}$$

and $m_{e,0}$ is given by equation (7-147), then from equation (7-214)

$$\frac{1 - \cos^2 \phi_{e,0}}{1 - \Psi_0^2} = m_{cn,0}^2 = M_{cn}^2 = \frac{F^2}{M_e^2 f^2}$$

which defines Ψ_0 .

This procedure has been tried on a design for a two-ended high pressure arc lamp. It leads to a number of difficulties in the actual design of the condenser lens, not the least of which is the fact that the boundary condition of $\phi_3 = 0$ when $\phi_2 = 0$ no longer holds. In other words, zero energy from the lamp at the axis forces the design of a conical lens. Since the design constraint so obtained is impossible to meet in any case, it is better to ignore the fact that energy does not exist at the axis of the lamp and extrapolate the polar radiance function of the source to the axis. The on-axis error can be compensated for by a fill-in system if necessary.

Typical design criteria for the condenser elements obtained on the basis of the above analysis is depicted in figures 7-30 through 7-32. It is seen in figure 7-30 that a compromise near the axis from the ideal case had to be made in order to secure a feasible lens design specification. On the basis of the results of this lens design, it is seen that the simplest expedient is to follow the design specification as an upper bound on zonal magnification, adhering as closely to it as possible without exceeding it or an arbitrary upper limit on magnification whichever is smaller. The arbitrary upper limit is based upon the largest field aperture the collimator can accept at its entrance pupil. When the magnification $m_{e,mcn}$ exceeds this limit, as it would toward the center of the system, then that value is ignored and either the fixed upper limit or the central fill-in system (which is a separate design) is used.

The only parameters to be determined are the values of e , F , and the aperture of the collimator and remaining components in the system. If the collimator is a symmetric Cassegrainian system, then ρ is made as small as possible in order to minimize the central hole. F is given by $\frac{p}{M_h}$ where M_h is the paraxial magnification of the hyperbola secondary. The latter is also determined on the basis of minimizing the central hole. This analysis is expounded later but is based upon equalization of the size of the hyperbola secondary and the center hole in the parabola as representing the condition for minimum central obscuration in the collimator elements. The value e , for the ellipse, is also based upon geometrical convenience, namely, that the inner rays should avoid hitting the source envelope. Once e and F are fixed, on the basis of geometrical convenience, all the remaining parameters described above can be determined.

- .14 SINE OF ENTRANCE ANGLE OF RAY
($\sin \phi_2$) vs. SINE OF EXIT ANGLE OF
RAY ($\sin \phi_3$)

- .13 THE SOLID CURVE REPRESENTS THE
EXACT THEORETICAL SOLUTION
- .12 REQUIRED FOR UNIFORMITY -- THE
DOTTED LINE REPRESENTS THE
DESIRED COMPROMISE SOLUTION
- .11 (DESIGN GOAL)

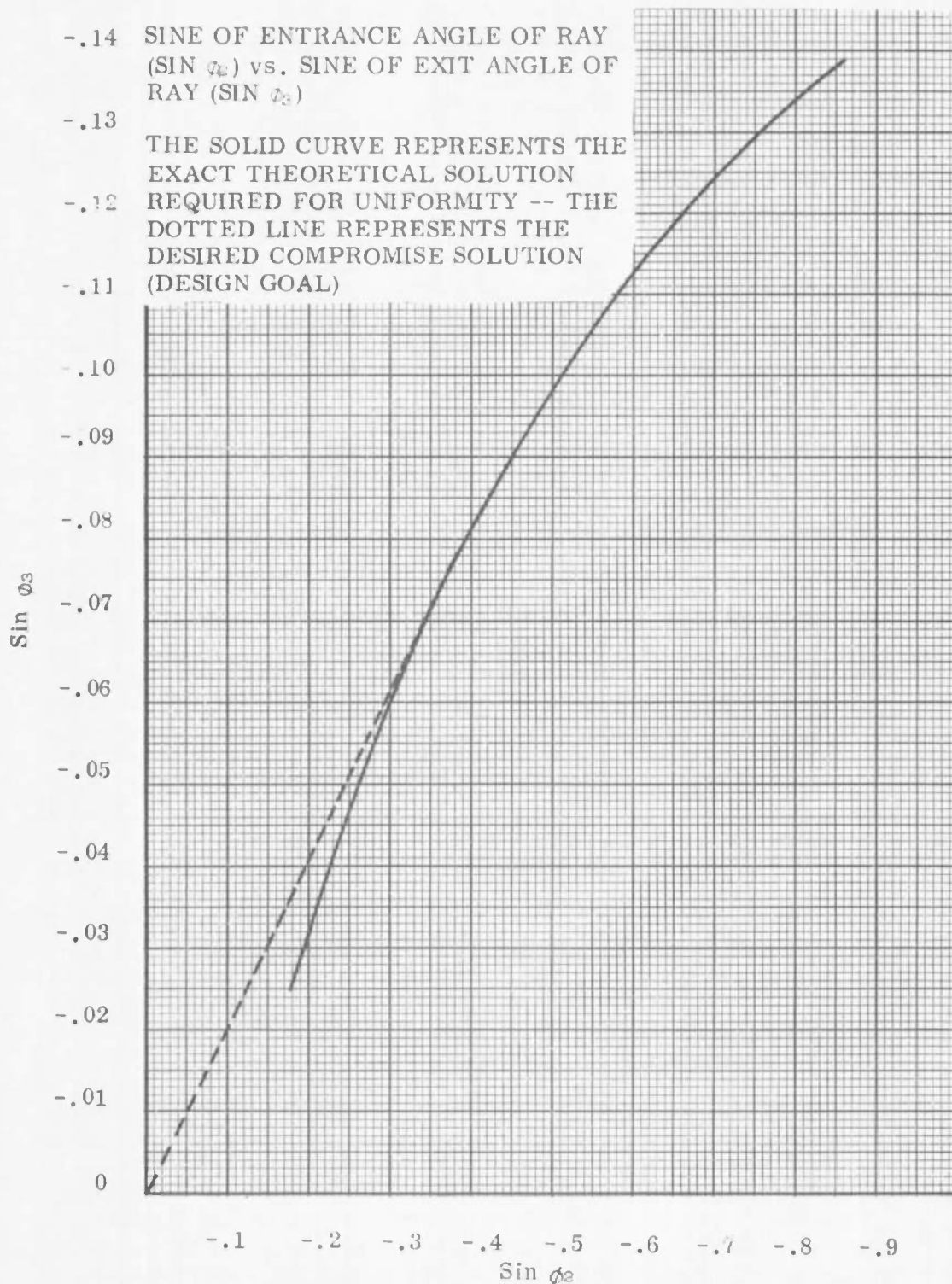


Figure 7-30. Theoretical and Compromise Relationships Between
 $\sin \phi_2$ and $\sin \phi_3$ for a Condenser Assembly Design.

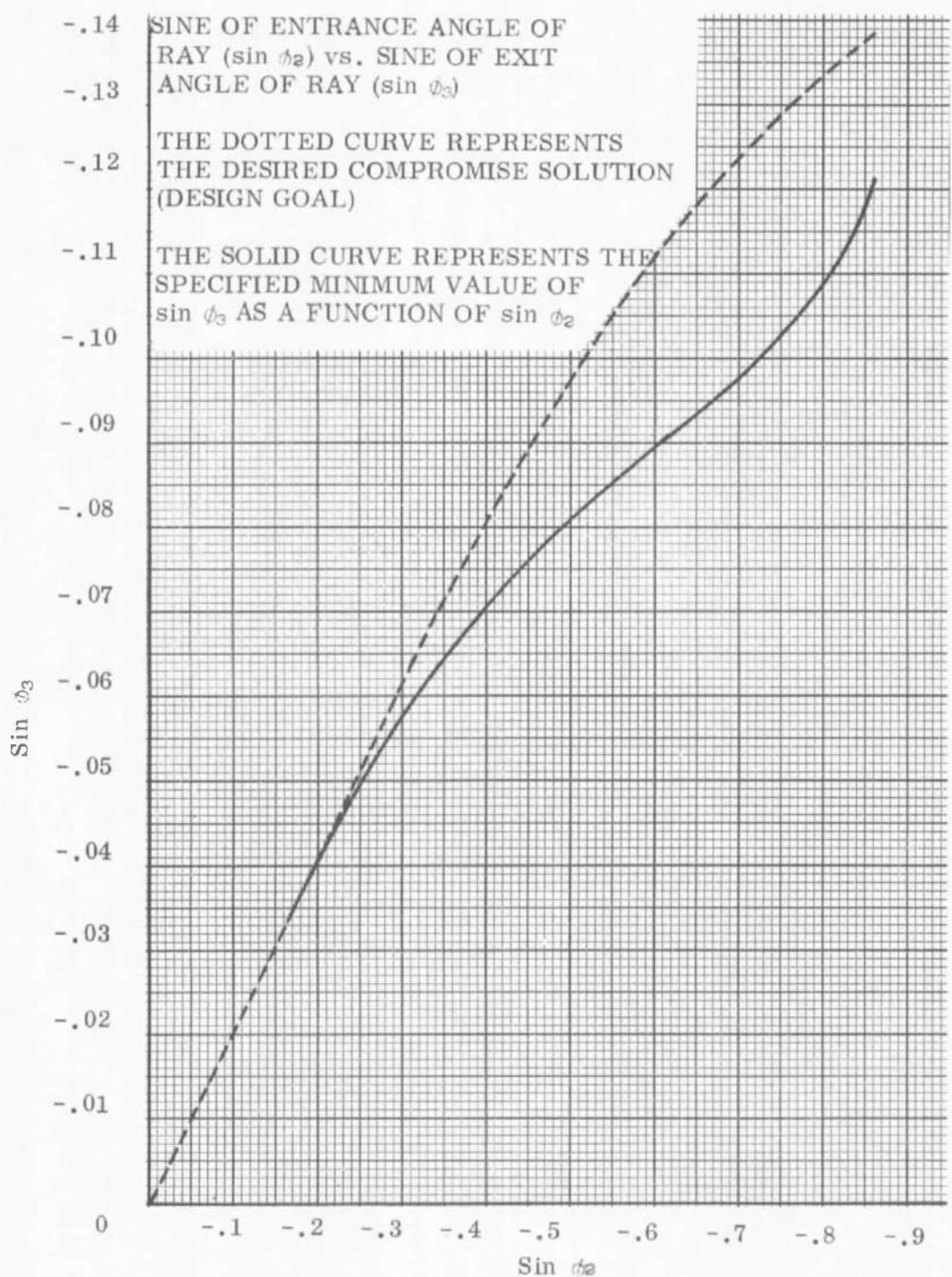


Figure 7-31. Desired Compromise and Specified Minimum Values of $\sin \phi_3$ as a Function of $\sin \phi_2$ for Condenser Assembly Design.

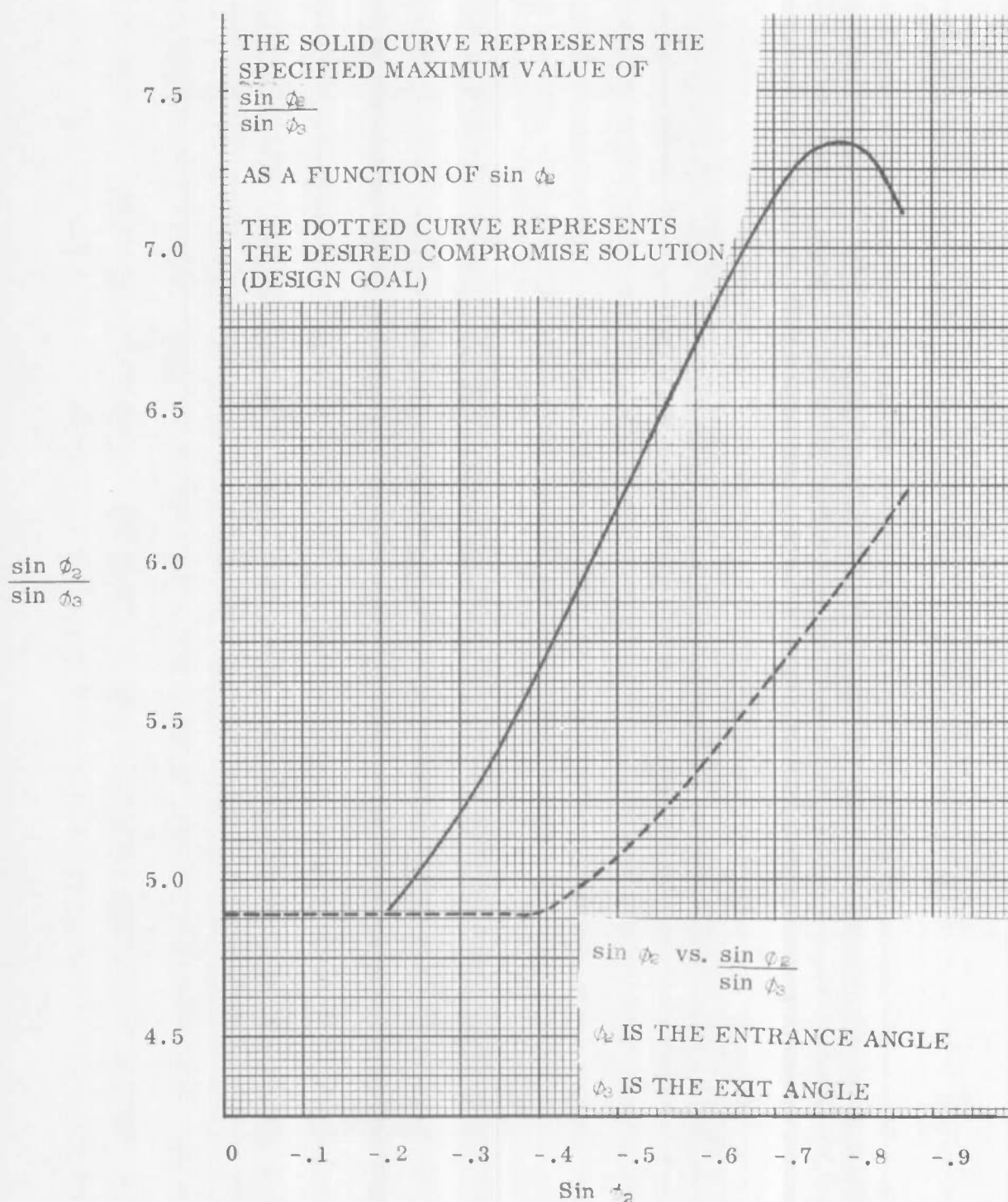


Figure 7-32. Desired Compromise and Specified Maximum Values of $\frac{\sin \phi_2}{\sin \phi_3}$ as a function of $\sin \phi_2$ for Condenser Assembly Design.

The system apertures are based upon the following:

1. Select the upper bound on $\phi_{1,1}$ into which the lamp radiates with adequate intensity: say $\phi_{1,1}$
2. Calculate, the total radiant power P_C collected

$$P_C = I_0 2\pi \int_0^{\phi_{1,1}} \bar{I}_\phi \sin \phi d\phi \quad (7-217)$$

where I_0 is the extrapolated axial source radiance value. The aperture radius R , of the parabolic collimator is then:

$$R = \sqrt{\frac{KP_C}{\pi E}} \quad (7-218)$$

where E is the final flux density desired.

Equation (7-157) will give the limiting entrance angle to the condenser based upon the selected marginal ray $\phi_{1,1}$ to the ellipse. This completes the essential parameteric determination of the system design constraints. The actual scaling of the components is based upon second order design considerations which would dictate that the paraxial magnification of the ellipse be as low as possible in order that the condenser entrance pupil field be small. However, a point of diminishing returns is reached here since this increases the numerical aperture. There is an optimum point which is selected principally on the basis of design experience.

In summary, it is seen that a design condition can be defined and imposed upon the condenser elements which, if realized, would completely satisfy the first order criterion for uniformity. The paraxial magnification of the condenser can be calculated on the basis of the system effective focal length, collimator focal length, and ellipse eccentricity, all of which can be determined as shown above. The apertures of the system are based upon the angular relationships derived above, the power available from the lamp within prescribed angular limits, and the flux level required in the collimated beam. Finally, it is seen that the actual lens design, which must be free from spherical aberration while it observes all the design conditions as well, is an extremely difficult one to realize. In fact, compromises must be made, particularly near the axis of the system. As there is no energy available from most lamps and collection schemes near the axis, this really becomes a separate problem, namely, that of fill-in. In view of the fact that total compensation for non-uniformities in this design is not readily possible, particularly for highly efficient choices of collection angles, it is desirable to look into alternative or auxiliary methods of flux distribution compensation.

7.6.5 Aconic Reflector(s) Analysis

7.6.5.1 Higher Order Corrections on Conic Sections Used with Condenser Lenses

In the last section it was found that the condition for first order uniformity, namely, a linear relationship between r^2 and $\cos \phi_1$, could not be fully realized by employing the expedient of an intermediate condenser lens alone. This was not due to the fact that a fundamental restriction exists but rather because of the practical difficulty in realizing a working lens design which both satisfied the design constraints over a large range of numerical aperture and was simultaneously free of the disastrous effects of spherical aberration. It is possible to approximate the lens design requirements, thereby coming considerably closer to the condition which provides ultimate uniformity, and a means will now be examined of completing the corrective efforts by exploiting higher order deformations of the Cassegrainian elements, the hyperboloid and paraboloid.

First, the best possible job is done with the condenser lens design and then a plot is made of the resultant r^2 versus $\cos \phi_1$. This should be a straight line with a slope equal to twice the square of the system effective focal length, f . The deviation of the plot from the straight line condition for various values of $\cos \phi_1$ is noted. There are a number of ways to proceed from this point. By means of a ray trace, the relationship between ϕ_1 and ϕ_3 in the system in question may be obtained. The theoretical relationship is obtained by combining equations (7-150) and (7-182) which gives the expression

$$\cos \phi_3 = \frac{2F^2 - f^2 (1 - \cos \phi_1)}{2F^2 + f^2 (1 - \cos \phi_1)} \quad (7-219)$$

The ideal solution of equation (7-171) is given by

$$r^2 = 2f^2 (1 - \cos \phi_1) \quad (7-220)$$

with the boundary condition defined by $\cos \phi_1 = 1$ when $r^2 = 0$. Thus, combining equations (7-219) and (7-220),

$$\cos \phi_3 = \frac{2F^2 - \frac{r^2}{2}}{2F^2 + \frac{r^2}{2}} \quad (7-221)$$

and

$$r^2 = 4F^2 \frac{1 - \cos \phi_3}{1 + \cos \phi_3} \quad (7-222)$$

This last expression is nothing more than equation (7-137), as it should be. The point is that Δr^2 versus $\cos \phi_3$ for the real case may be plotted, i. e., the change, Δr^2 , in r^2 required to satisfy the relationship expressed in equation (7-220) may be observed.

Referring to figure 7-33 it is seen that the normal to the hyperboloid surface makes an angle, α , with the axis given by

$$\alpha = \phi_3 + \frac{\phi_3^1 + (\pi - \phi_3^1)}{2} \quad (7-223)$$

where the normal bisects the exterior angle formed by ϕ_3 and ϕ_3^1 . The slope, m , of the surface is the negative reciprocal of $\tan \alpha$, i. e.,

$$m = \tan \left(\frac{\phi_3^1 + \phi_3}{2} \right)$$

or

$$m = \frac{\sqrt{1 - \cos \phi_3} \sqrt{1 + \cos \phi_3^1} + \sqrt{1 + \cos \phi_3} \sqrt{1 - \cos \phi_3^1}}{\sqrt{1 + \cos \phi_3} \sqrt{1 + \cos \phi_3^1} - \sqrt{1 - \cos \phi_3} \sqrt{1 - \cos \phi_3^1}} \quad (7-224)$$

When the slope of the surface is altered to produce an adjustment in the ray height, r , coming off the paraboloid, the effect is seen through a change in the value of $\cos \phi_3^1$. Since Δr^2 can be plotted against $\cos \phi_1$, equations (7-219) and (7-156) may be used to write

$$\cos \phi_3 = \frac{H - \cos \phi_3^1}{1 - H \cos \phi_3^1} = \frac{2F^2 - f^2 (1 - \cos \phi_1)}{2F^2 + f^2 (1 - \cos \phi_1)}$$

so that

$$\cos \phi_3^1 = - \frac{2F^2 (1 - H) - f^2 (1 - \cos \phi_1) (1 + H)}{2F^2 (1 - H) + f^2 (1 - \cos \phi_1) (1 + H)} \quad (7-225)$$

By virtue of equation (7-162) and the paraxial magnification law, equation (7-225) can be written

$$\cos \phi_3^1 = - \frac{2\rho^2 - f^2 (1 - \cos \phi_1)}{2\rho^2 + f^2 (1 - \cos \phi_1)} \quad (7-226)$$

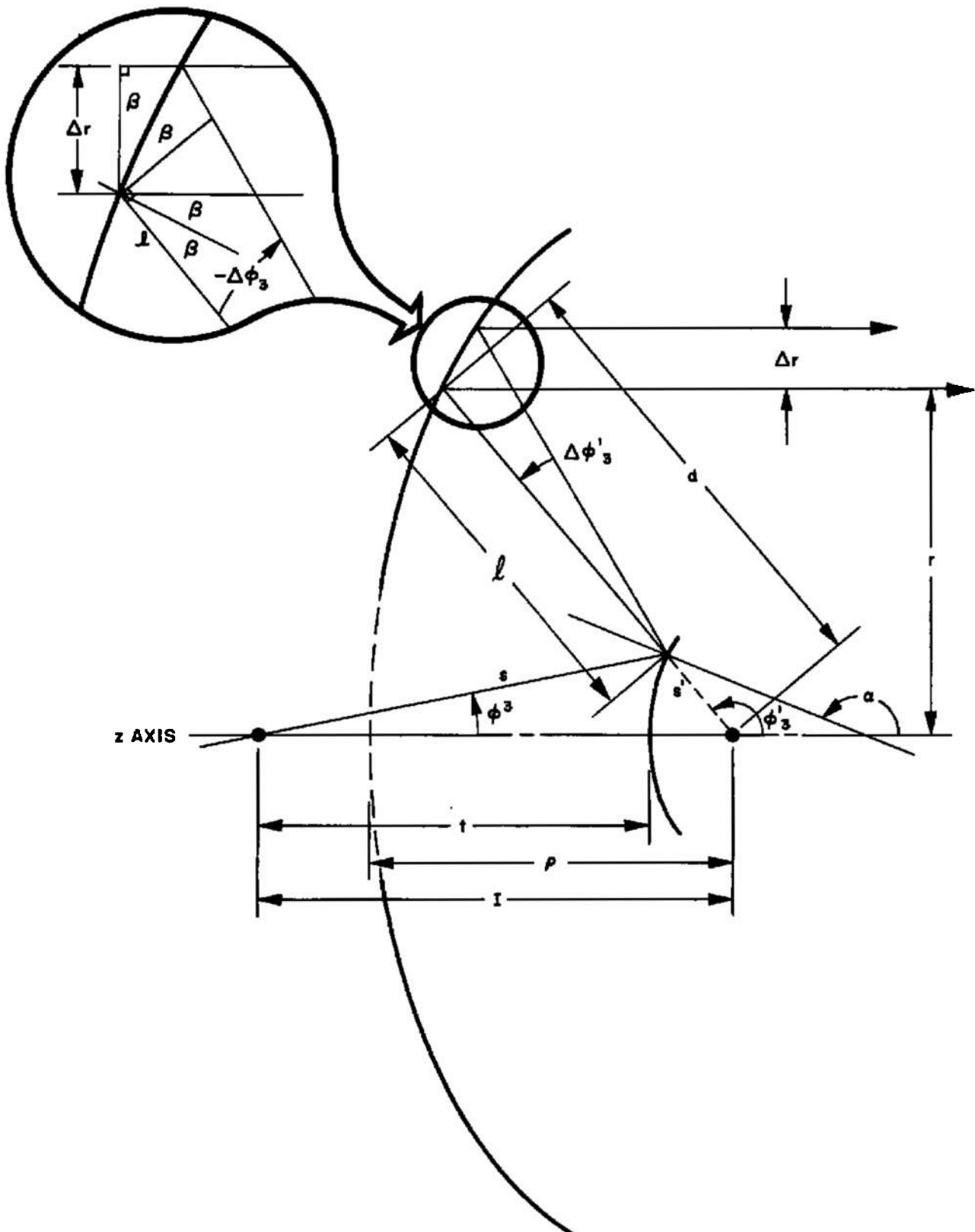


Figure 7-33. Parameters of a Modified Cassegrainian Collimator for a System Using Condenser Lenses

which has the same form as equation (7-219) with the sign indicating the proper sense of ϕ_3^1 . Thus it is again seen that a relationship between any pair of angles in a conic section system may be found from a similar relationship between another pair of angles simply by substituting the subsystem focal length associated with the angle in question and observing the proper sign by inspection of the sense of the angle. That is, ρ is to ϕ_3^1 as F is to $(7 - \phi_3^1)$. In any case, equation (7-226) is a means of generating a plot of Δr^2 vs. $\cos \phi_3^1$ from the information obtained in the plot of r^2 vs. $\cos \phi_1$. Alternatively, starting with Δr^2 versus r^2 ,

$$\cos \phi_3^1 = \frac{4\rho^2 - r^2}{4\rho^2 + r^2} \quad (7-227)$$

which can be obtained directly from equation (7-226) by means of equation (7-221). The important fact is that Δr^2 is easily related to the entrance angle to the paraboloid. The expression analogous to equation (7-222) may now be differentiated to obtain

$$\begin{aligned} \Delta r^2 &= \frac{-8F^2}{(1 + \cos \phi_3^1)^2} \Delta(\cos \phi_3^1) \\ &= \frac{8\rho^2}{(1 - \cos \phi_3^1)^2} \Delta(\cos \phi_3^1) \end{aligned} \quad (7-228)$$

All the expressions (7-219) through (7-228) have been shown to be completely interchangeable between the pairs $F, \cos \phi_3^1$ and $\rho, -\cos \phi_3^1$ for the following reason: the slope of the hyperboloid is corrected by forming a parametric relationship in terms of one of two possible scanning angles ϕ_3^1 or ϕ_3^2 . The choice between these two goes to the very heart of the method of correction. For example, if it is assumed that zero spherical aberration exists at the entrance pupil to the Cassegrainian collimator, i.e., $\cos \phi_3^1$ is always measured from the same focal point, then any modification of the slope of the hyperboloid would cause $\cos \phi_3^1$ to be measured from a different position along the axis as a function of ϕ_3^1 due to the spherical aberration introduced. Thus a small error would be encountered in the expression (7-228) as a function of ϕ_3^1 because the reflected ray from the hyperboloid crosses the axis at a position which is no longer constant and at a distance, ρ , from the paraboloid vertex. It would then be left to changes in the surface slope of the paraboloid to compensate for the spherical aberration so introduced. The principal difficulty, however, is in using ϕ_3^1 as a scanning angle from a fixed point for parametric evaluation of the $z-r$ coordinates of the modified hyperbolic surface. Thus, assuming no spherical aberration has been introduced by the collector-condenser system, ϕ_3^1 could be selected as the scanning angle since it is measured

from a fixed point, and the slope, m , in equation (7-224) should be expressed in terms of $\cos \phi_3^t$. On the other hand, spherical aberration could be introduced into the collector-condenser system of an amount equal and opposite to that experienced by virtue of changes in the hyperboloid surface so that slope changes in the paraboloid would be unnecessary. Under these conditions all ϕ_3 angles would appear to be measured from the same point, namely, the focus of the paraboloid. The ϕ_3 angles would be referenced at different points along the optic axis so that the scanning vector which parameterizes the modified hyperboloid surface would best be selected as ϕ_3^t in this case. If the correction is to be divided between both the collector-condenser system and the paraboloid with the hyperboloid acting as the pivotal component, then the required Δr can be cut so that one part, i.e. Δr_1 , is handled by the collector-condenser and the other, Δr_2 , is handled by changes in the paraboloid. The optimum might seem to be to split the necessary change so that $\Delta r_1 = \Delta r_2$ and $\Delta r_1 + \Delta r_2 = \Delta r$. However, it is best to avoid introducing spherical aberration in the collector-condenser system for two reasons. First, it tends to enlarge the entrance pupil to the collimator out of proportion to the size of the solar field, thereby causing even greater central shadowing (which may already be too large). Second, when spherical aberration is present at the position of the Cassegrainian entrance pupil, then the relay lens which must be placed there acts in a complicated manner as an additional condenser element to varying degrees over the aperture of the system as a whole. It therefore produces its own spherical aberration and would have to be incorporated into a condenser lens design which may already be too complicated. In any case it is an additional complexity on a first order level which is impossible to ignore and extremely difficult to treat.

Therefore, the attempt will be made to realize as much correction as possible by alterations in the hyperboloid-paraboloid system while designing the collection and transfer system for minimum spherical aberration. To this end the necessary slope change will be calculated by means of the corresponding change required in $\cos \phi_3^t$ to a first approximation. Thus, from equation (7-228)

$$\Delta (\cos \phi_3^t) = \frac{(1 - \cos \phi_3^t)^2}{8\rho^2} \Delta r^2 \quad (7-229)$$

The new value of $\cos \phi_3^t$, i.e., $\cos \bar{\phi}_3^t$ is

$$\cos \bar{\phi}_3^t = \cos \phi_3^t + \Delta (\cos \phi_3^t) \quad (7-230)$$

A somewhat better approximation to $\Delta (\cos \phi_3^t)$ would obtain from a measurement from the point on the hyperboloid surface in order to avoid the displacement error of the shifted intersection point along

the axis. Thus in accordance with figure 7-33 the increment in the angle, $\Delta(\pi - \phi'_3) = -\Delta\phi'_3$, may be calculated by computing the displacement over the optical path length from the hyperboloid surface to the paraboloid surface. Since the increment, Δr , makes an angle, β , (see figure 7-33), with the parabolic surface, the arc chord length is $\frac{\Delta r}{\cos \beta}$. However, since this element is projected in the ϕ'_3 direction, again making an angle, β , with that direction, then the increment, projected in the ϕ'_3 direction is $\left(\frac{\Delta r}{\cos \beta}\right) \cos \beta = \Delta r$. Therefore,

$$-\Delta\phi'_{3s} = \frac{\Delta r}{\ell} = \frac{\Delta(r^2)}{2rl} \quad (7-231)$$

where ℓ is the path length between the hyperboloid and paraboloid. From an earlier result, (equations (7-109) and (7-110)) the path length, d , from the parabolic focus to the parabolic surface is, since $\cos\phi'_{3s}$ (figure 7-33) is equal to $-\cos\phi$ (figure 7-10),

$$d = \frac{2\rho}{1 - \cos\phi'_3}$$

so that:

$$r = \frac{2\rho \sin\phi'_3}{1 - \cos\phi'_3}$$

and

$$-\Delta\phi'_{3s} = \frac{1 - \cos\phi'_3}{4\rho \sin\phi'_3} \frac{\Delta(r^2)}{\ell} \quad (7-232)$$

Equation (7-232) may be written

$$-\Delta(\cos\phi'_{3s}) = \frac{1 - \cos\phi'_3}{4\rho} \frac{\Delta r^2}{\ell} \quad (7-233)$$

Now if ℓ were merely taken as d , equation (7-233) would reduce immediately to the expression (7-229). However, for a more accurate result, subtract the path length, s' , from the parabolic focus to the hyperboloid surface from d to obtain an improved value for ℓ . Thus referring to figure 7-33,

$$s \cos\phi'_3 - s' \cos\phi'_3 = l$$

$$s - s' = 2a$$

and

$$\frac{I + s' \cos \phi_3'}{\cos \phi_3} - s' = 2a, \quad s' = \frac{I - 2a \cos \phi_3}{\cos \phi_3 - \cos \phi_3'} \quad (7-234)$$

$$s' = \frac{I}{h} \frac{h - \cos \phi_3}{\cos \phi_3 - \cos \phi_3'}$$

where from equation (7-158)

$$s' = \frac{I}{h} \frac{(h - H) + \cos \phi_3' (1 - hH)}{H + \cos \phi_3' (H \cos \phi_3' - 2)} \quad (7-235)$$

$$s' = \frac{I}{2h} \frac{(h^2 - 1) (h - \cos \phi_3')}{h - \cos \phi_3' (h^2 + 1 - h \cos \phi_3')} \quad (7-235)$$

$$s' = \frac{I}{2h} \frac{h^2 - 1}{1 - h \cos \phi_3'} \quad (7-235)$$

To a good approximation

$$s' \approx \frac{I}{2h} \frac{h^2 - 1}{1 - \cos \phi_3}$$

and

$$\ell \approx \left[2\rho - \frac{I(h^2 - 1)}{2h} \right] \frac{1}{1 - \cos \phi_3} \quad (7-236)$$

where the actual value of ℓ is less than or equal to the approximation in equation (7-236). This causes the correction to be on the generous side, i.e., overcompensation, to make up for the fact that subsequent correction of the paraboloid will remove some of the adjustment in Δr made by this process of modification of hyperboloid surface slope. Thus from equation (7-233):

$$\Delta(\cos \phi_3') = \frac{(1 - \cos \phi_3')^2}{4\rho \left[2\rho - \frac{I(h^2 - 1)}{2h} \right]} \Delta r^2 \quad (7-237)$$

Referring to equation (7-224) the new slope is given by:

$$\bar{m} = \frac{\sqrt{1 - \cos \phi_3} \sqrt{1 + \cos \phi_3'}}{\sqrt{1 + \cos \phi_3} \sqrt{1 + \cos \phi_3'}} + \frac{\sqrt{1 + \cos \phi_3} \sqrt{1 - \cos \phi_3'}}{\sqrt{1 - \cos \phi_3} \sqrt{1 - \cos \phi_3'}} \quad (7-238)$$

On the basis of equations (7-156), (7-230), (7-237), and (7-238) the slope m may be expressed as a function of $\cos \phi_3$.

It is now possible to set up the differential equation for the solution, in parametric form, of the surface of the corrected hyperboloidal mirror. Putting the center of a Cartesian coordinate system at the point on axis from which the angle ϕ_3 is measured, as in figure 7-33,

$$\cos \phi_3 = \frac{z}{\sqrt{z^2 + r^2}}, \sin \phi_3 = \frac{r}{\sqrt{z^2 + r^2}} \quad (7-239)$$

where (z, r) defines a point on the new surface. Taking the differential of $\sin \phi_3$,

$$\begin{aligned} d(\sin \phi_3) &= \frac{(z^2 + r^2)^{\frac{1}{2}}}{z^2 + r^2} dr - r(z^2 + r^2)^{-\frac{1}{2}} (zdz + rdr) \\ &= \frac{z^2 dr - z r dz}{(z^2 + r^2)^{\frac{3}{2}}} \end{aligned}$$

which gives

$$\frac{d(\sin \phi_3)}{\sin^3 \phi_3} = \frac{\left(\frac{z}{r}\right)^2 - \left(\frac{z}{r}\right) \left(\frac{dr}{dz}\right)^{-1}}{r} dr \quad (7-240)$$

Since $z/r = \cot \phi_3$ and $\left(\frac{dr}{dz}\right)^{-1} = (\bar{m})^{-1}$,

$$\frac{dr}{r} = \frac{d\phi_3}{\sin^2 \phi_3 \left(\cot \phi_3 - \frac{1}{\bar{m}}\right)} \quad (7-241)$$

A similar process yields

$$\frac{dz}{z} = \frac{-d\phi_3}{\cos^2 \phi_3 (\tan \phi_3 - \bar{m})} \quad (7-242)$$

Since \bar{m} has already been derived in terms of $\cos \phi_3$, integration of equation (7-241) or (7-242) can be used to determine the surface loci. Since integration from the axis, i.e., $r = 0$, is the likely starting point, one would use equation (7-242) which does not have an indeterminacy at this limit. The initial conditions at $\phi_3 = 0$ are $r = 0$ and $z = t$ (figure 7-33), where

$$M_h = \frac{h-1}{h+1} = \frac{I-t}{t} , \text{ or } t = I \frac{h+1}{2h} \quad (7-243)$$

Thus

$$\int_t^z \frac{dz}{z} = \int_0^{\phi_3} \frac{-d\phi}{\cos^2 \phi (\tan \phi - \bar{m})}$$

and

$$z = t \exp \left\{ \int_0^{\phi_3} \frac{-d\phi}{\cos^2 \phi (\tan \phi - \bar{m})} \right\} \quad (7-244)$$

$$r = z \tan \phi_3$$

Equation (7-244), along with the previous determination of \bar{m} yields the surface form for the corrected secondary mirror of the Cassegrainian collimator. It is not likely, however, that the integrand in equation (7-244) is an exact differential of any standard, not to mention algebraic, function even if Δr is expressible in a simple form; which is equally unlikely. Δr can be expressed in either tabular form or by an analytic approximation using least squares or finite difference techniques in order that equation (7-244) can be integrated on a computer by successive increments.

One of the greatest difficulties with this technique is not in the determination of the $r-z$ coordinates of the surface but rather in the ray tracing of an optical system into which such a surface is incorporated. A technique which yields the accuracy required is to generate an even power series of aperture coefficients which approximates the calculated curve. Thus is formed

$$z = a_0 + a_1 r^2 + a_2 r^4 + a_3 r^6 + \dots + a_n r^{2n} \quad (7-245)$$

If R is the maximum aperture radius over which the surface is to be specified then r_i is defined as

$$r_i = i \frac{R}{2n}, \text{ where } i = 0, 1, 2, \dots, 2n \text{ and} \quad (7-246)$$

where $n+1$ is the number of constant coefficients in the expansion, equation (7-245). Further,

$$z_i = z(r_i) \quad (7-247)$$

The z_i values can be generated from interpolation tables using the solution derived from equations (7-244). Based upon finite difference techniques the values of a_i can be obtained as follows:

$$a_0 = A, \text{ and}$$

$$a_i = \left(\frac{2n}{R}\right)^{2i} \sum_{j=0}^{2i-1} (-1)^{[i-(j+1)]} \frac{z_j}{(2i-j)! j!} \quad (7-248)$$

If it is desired to avoid taking equal intervals in r in order to circumvent the necessity of interpolation in z there are numerous methods for the purpose, although perhaps they are somewhat more lengthy. The pertinent interpolation formulae to be used in generating the (z_i, r_i) values from the $[z(\phi_3), r(\phi_3)]$ parametric determination are stated for reference as

$$z_i = \sum_{m=0}^{2n} \left[\sum_{\substack{l=0 \\ l \neq m}}^{2n} \frac{(r_l - r_i)}{(r_m - r_l)} z_m \right] \quad (7-249)$$

where the r_m and z_m are paired values taken from the computed curves for the corrected secondary mirror of the Cassegrainian collimator.

This entire process, which is suitable only for computer analysis, is adequate for the determination of the intersection point on the higher order surface using the form of equation (7-245) and standard ray tracing procedure. However, for the actual calculation of the reflection slope the procedure which determines the coefficients in equation (7-245) leaves a great deal to be desired. Once the $r-z$ intersection is known then ϕ_3 can be obtained from equation (7-244) where

$$\tan \phi_3 = \frac{r}{z}$$

and

$$\cos \phi_3 = \frac{z}{\sqrt{r^2 + z^2}}$$

Of course, z is measured from the position on the entrance pupil to the Cassegrainian collimator from which ϕ_3 is measured. Thus, instead of using the normal ray trace procedure to calculate the surface slope from the form in equation (7-245), \bar{m} may simply be computed

from the calculated value of $\cos \phi_3$, equations (7-238), (7-156), (7-230) and (7-237), and the same analytic expression for Δr which was used to calculate the surface originally. Tracing one ray off of the higher order surface may appear to be a monumental computation task and indeed it is relatively involved. However, the operations are purely algebraic and cycle very quickly on a large computer. The most important thing is that the slope errors which introduce very erratic ray trace results have been suppressed by virtue of direct reference to the slope condition which defined the surface in the first place. The slight position errors which necessarily obtain from the approximation of equation (7-245) have very little effect upon the ray trace result. It is true, however, that such a formulation of the surface approximation could produce a function which oscillates closely about the desired surface but, because of its repetitive position corrections, never displays the actual surface slope to a good approximation.

A direct method for determining the coefficients in equation (7-245), although less precise and lacking the detailed calculation of surface slope which equations (7-244) provide, would be to compare slope values directly. Thus, as is usually done in ray tracing aspheric surfaces, the slope, \bar{m} , of the curve is given by the derivative of equation (7-245):

$$(\bar{m}_j)^{-1} = \frac{dz}{dr} = 2 a_1 r_j + 4a_2 r_j^3 + 6a_3 r_j^5 + \dots \quad (7-250)$$

where, with the range of r being from 0 to R as in equation (7-246); the a_i 's are determined thus:

$$a_i = \frac{1}{2i} \left(\frac{2n}{R}\right)^{2i-1} \sum_{j=0}^{2i-1} (-1)^{i-(j+1)} \frac{(\bar{m}_j)^{-1}}{(2i-j)!(j-1)!} \quad (7-251)$$

where, using ray tracing information, the \bar{m}_j are determined just as before by equation (7-238) with

$$(\cos \phi_3)_j = \frac{z_j}{\sqrt{r_j^2 + z_j^2}}$$

where

$$z_j = \frac{I}{2} + \sqrt{\frac{I^2}{4h^2} + \frac{r_j^2}{h^2 - 1}} \quad (7-252)$$

The values of z_j , determined in equation (7-252), are based on the intersection of the ray with the original hyperboloid. This process provides the necessary coefficients for ray tracing purposes without first requiring the generation of detailed information about the surface itself. Since the basic \bar{m} may still be used for ray slope calculations it is probably nearly as accurate as the previous method which involved point-by-point integration for the exact surface coordinates.

Finally, a still shorter method which may be used to make final adjustments when the solution has been closely approached is an approximation based entirely on a ray tracing procedure. Rays are traced through the optical system, noting the height at which they strike the paraboloid and the path length from the hyperboloid to the paraboloid. The latter is printed out in most standard ray trace formats.

The Cassegrainian secondary is entered into the program in terms of corrections to the original hyperboloid surface. Thus the z coordinate measured from the hyperboloid vertex is given by

$$z = \frac{Cr^2}{\sqrt{1 + 1 + C^2 (h-1) r^2}} + a_1 r^2 + \dots + a_n r^{2n} \quad (7-253)$$

Where the first term gives the surface position of the original hyperboloid where vertex curvature is C . The additional terms whose coefficients are the a_i 's are entered as corrections to the original surface. The change in slope is therefore entirely due to these terms and is given by

$$(\Delta m)^{-1} = \frac{dz}{dr} = 2a_1 r + \dots + 2na_n r^{2n-1} \quad (7-254)$$

The change in the slope of the normal is

$$(\Delta N) = - \frac{1}{\Delta m}$$

and the change in the slope of the ray is twice that of the normal with the opposite sign, thus

$$-2(\Delta N) = \frac{\Delta r}{\ell} = 4a_1 r + \dots + 4na_n r^{2n-1} \quad (7-255)$$

where Δr is the ray height adjustment needed at the paraboloid as figured from the uniformity criterion applied to the particular ray traced, and ℓ is the path length read from the ray trace. The process would then be to trace n rays, noting Δr , r and ℓ each time. It is then possible to set up n simultaneous equations for the solution of the a_i . This procedure is good only for fine adjustments, because if too large an alteration to the surface slope is attempted by this process, the lack of precision may lead to divergent solutions,

not to mention the waviness which would be induced by the point fitting process.

When equation (7-255) is used as a corrective procedure the values obtained for the a_i may be added to those already existing as a description of the surface. Since the corresponding coefficients for each corrective step are linearly additive the solution may be approached by a series of successive approximations. Care, must be taken however, not to allow the values lying between the points for which the coefficients are calculated to drift too far out of line. The important point to be made is that a solution which can be bounded on both sides and bridged at discrete intervals must necessarily exist in a smooth form, provided the more detailed techniques discussed earlier are employed. This is a matter for final design should such a system be selected for that purpose.

Upon correction of the hyperboloidal surface with higher order terms it becomes necessary to impart a similar correction to the paraboloid in order to compensate for the spherical aberration so induced. For this purpose one could again use the ray trace technique just discussed where, for the paraboloid

$$z = \frac{r^2}{4p} + a_1 r^3 + \dots + a_n r^{2n} \quad (7-256)$$

The angle which the ray makes with the z-axis after reflection from the paraboloid is noted. If this angle is δ , then

$$\frac{\delta}{2} = 2a_1 r + \dots + 2na_n r^{2n-1} \quad (7-257)$$

From n such equations, the surface correction coefficients, a_i , may be found algebraically. However, it is important to insure that the curve described by the function (7-257) is smooth between the n points for which it is fitted. This may be done by a least squares technique which would not require n equations such as (7-257) but could use fewer or more, the latter being preferred. Thus

$$\Delta_j = a_1 r_j + 2a_2 r_j^3 + \dots + na_n r_j^{2n-1} - \frac{\delta_j}{4} \quad (7-258)$$

where Δ_j is the residual between the value of $\frac{\delta_j}{4}$, computed in accordance with equation (7-257), and the actual desired value, $\frac{\delta_j}{4}$. In accordance with the least squares principle it is desirable to minimize

$$\sum_{j=1}^m \Delta_j^2 = \sigma \quad (7-259)$$

Therefore, in general it may be written

$$\frac{\partial \sigma}{\partial a_\ell} = 0 \quad (7-260)$$

and n simultaneous equations may be formed in this manner. Based upon equations (7-258), (7-259), and (7-260).

$$\frac{1}{2} \frac{\partial \sigma}{\partial a_\ell} = \sum_{j=1}^m \left[\left(\sum_{i=1}^n i a_i r_j^{2i-1} \right) - \frac{\delta_j}{4} \right] \ell r_j^{2\ell-1} \quad (7-261)$$

Which yields n equations of the type

$$\sum_{i=1}^n \left[\sum_{j=1}^m r_j^{(2i-1)(2\ell-1)} \right] i a_i = \sum_{j=1}^m \frac{\delta_j}{4} r_j^{(2\ell-1)} \quad (7-262)$$

where ℓ goes from 1 through n . The coefficients of the a_i , namely:

$$i \sum_{j=1}^m r_j^{(2i-1)(2\ell-1)} = c_{\ell i} \quad (7-263)$$

form the coefficient determinant, $c_{\ell i}$, and the nonhomogeneous terms form the vector, \vec{v}_ℓ :

$$\vec{v}_\ell = \sum_{j=1}^m \frac{\delta_j}{4} r_j^{(2\ell-1)}$$

The a_i components of the vector formed by the coefficients in the surface equation (7-245) may be obtained from the standard solution of the matrix equation

$$\sum_i c_{\ell i} a_i = \vec{v}_\ell$$

namely

$$a_i = \sum_\ell c_{\ell i}^{-1} \vec{v}_\ell$$

Since $c_{\ell i}$, as defined by equation (7-263), is a symmetric matrix when each column is divided by i ; that is

$$\left| \left(c_{\ell i} \right) \right| = n! \left| \left(\frac{c_{\ell i}}{i} \right) \right|$$

and

$$\frac{c_{\ell i}}{i} = \frac{c_{i\ell}}{\ell}$$

Then the inverse of $c_{\ell i}$, namely $c_{\ell i}^{-1}$, must exist and in fact is

$$c_{\ell i}^{-1} = \frac{1}{n!} \left(\frac{c_{\ell i}}{i} \right)^{-1}$$

Thus, when the solution for the a_j is obtained, equation (7-256) provides the form for the modified paraboloid.

Corrections to the hyperboloid, using equation (7-255), and to the paraboloid using a straight algebraic solution of n equations of the type (7-248) were made for the optical system containing the condensers whose design criteria were shown earlier in figures 7-30 through 7-32. Figure 7-34 is a plot of r versus $\cos \phi$ for both the original and modified designs, while figure 7-35 shows the uniformity, R , across the module aperture for each case, both with a spherically symmetric source and with a source having the radiance distribution of the VSRS. It will be seen that use of a source such as the VSRS results in considerable improvement in the uniformity for this optical system. The final residual spherical aberration which was obtained both before and after correction is plotted in figure 7-36. It is seen that corrections were excellent for specific positions on the aperture but the deviations between these points are stronger than desired. It has been demonstrated that the solution exists on both sides and can be bridged at an arbitrary number of points. In the final design process the more lengthy least squares approach would be used, eliminating the nonuniform convergence problem.

This procedure has demonstrated the feasibility of designing an optical system employing a conic collector, a condenser and a Cassegrainian collimator with higher order correction terms, which satisfies the first order uniformity criterion and is free of residual third order spherical aberrations. This has been accomplished for collection angles as high as 120° from the axis. The result is generally quite smooth up to about 90° to 100° and the remainder can be adjusted with the appropriate smoothing techniques outlined above. This means that, as far as collection is concerned, virtually all the radiation from any of the sources which is contained within those regions where the radiance values are reasonably close to the average can be used. This system is therefore adjudged to be generally feasible although not

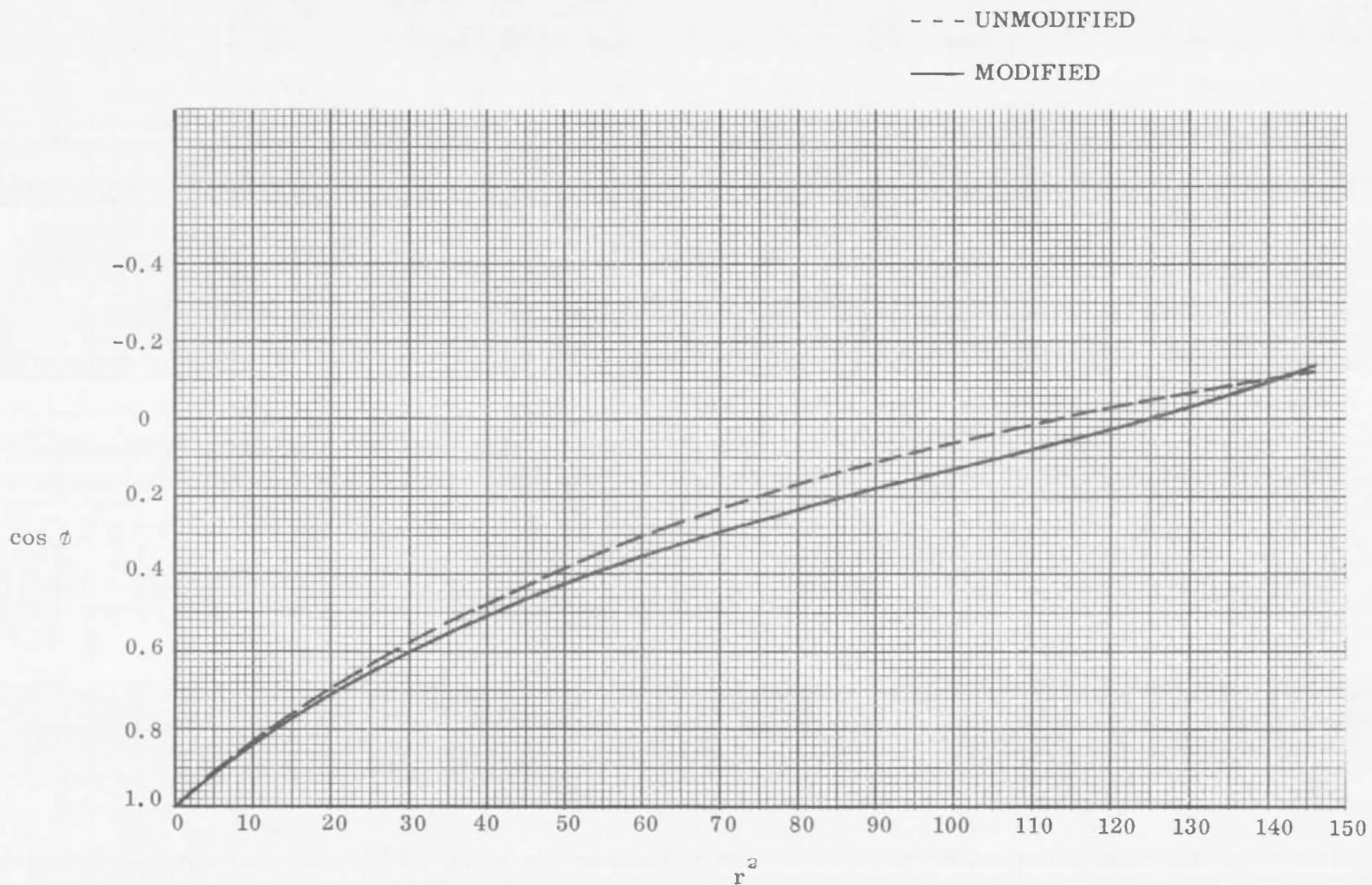


Figure 7-34. Plot of r^2 vs. $\cos \phi$ for Original and Modified Optical Systems

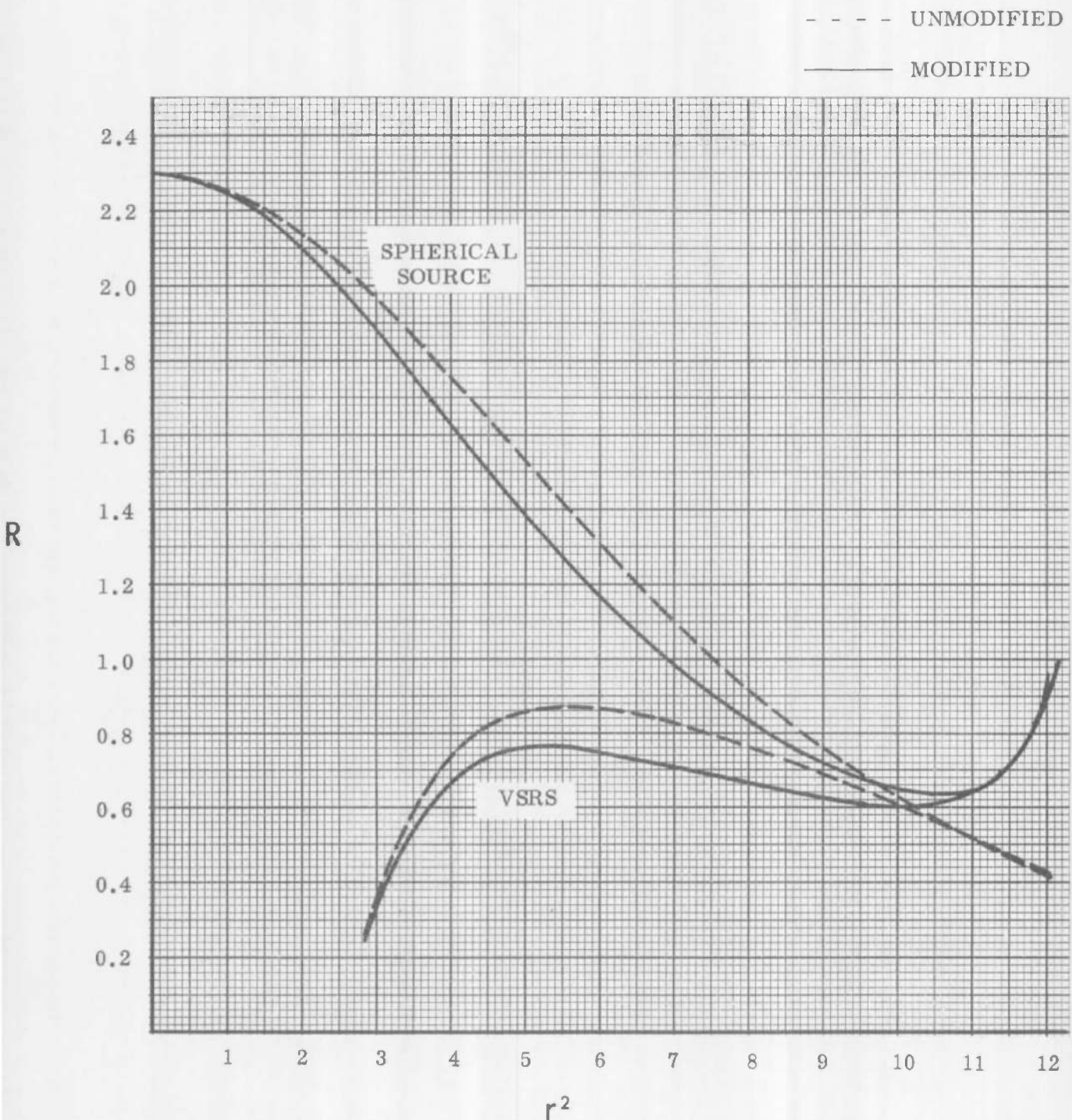


Figure 7-35. Uniformity vs. Aperture Radius for Original and Modified Design

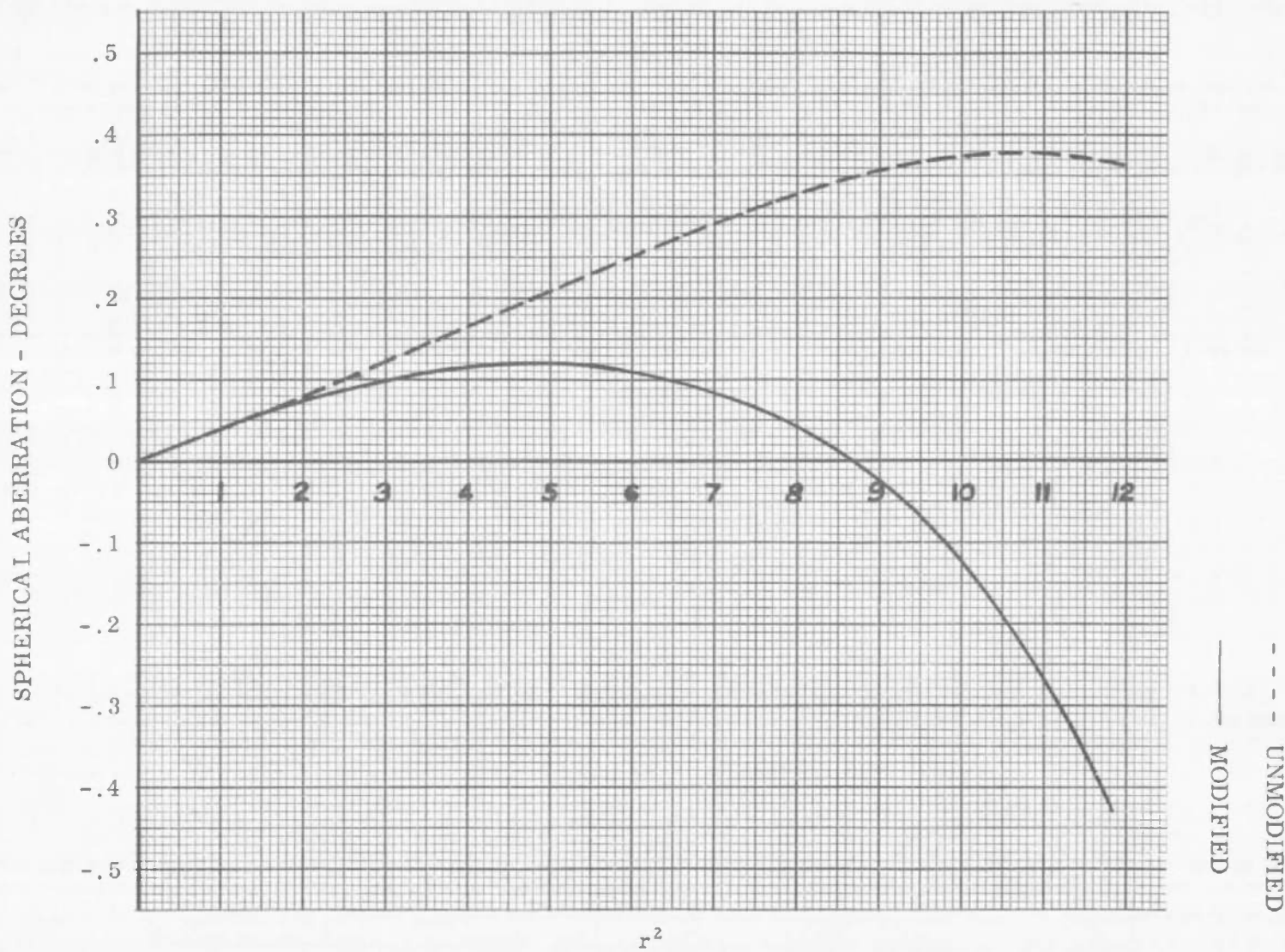


Figure 7-36. Residual Spherical Abberation in a Corrected Optical System

necessarily more efficient than the simple paraboloid design because of the additional optical components. The uniformity can, however, be brought under better control and the ultimate non-uniformities would be due primarily to vicissitudes in lamp output, manufacturing and alignment errors in the system, and shadows caused by central obstructions and edge effects. These will be treated separately later.

In the actual final design the specific radiance function for the source in question would be incorporated into the equations and their solution. Thus the solution expressed in equation (7-220) which summarizes the ray-height, initial-angle relationships for a spherical radiance function would take the more general form

$$r^2 = 2f^2 \int_0^{\phi_1} \bar{I}_\phi \sin \phi d\phi \quad (7-264)$$

and the Δr^2 would be computed on this basis. The remainder of the analysis is the same as for the spherical source. That is, equation (7-222) relates r^2 to $\cos \phi_3$ and equation (7-157) relates $\cos \phi_3$ to $\cos \phi_1$, so with the solution of (7-264) on either a numerical or analytical basis, $\cos \phi_3$ and $\cos \phi_1$ may be related as before for purposes of the condenser lens design. This would then be followed by direct application of equation (7-264) for the evaluation of Δr^2 from ray tracing and the subsequent design of the Cassegrainian elements as outlined above.

Because I_ϕ for the Vortex Stabilized Radiation Source is a monotonically increasing function of ϕ over that region of ϕ which one would normally use for collection of the bulk (better than 90%) of the emitted radiation, the amount of compensation required in the condensers and modified Cassegrainian collimator is correspondingly reduced by comparison to the spherically symmetric source. This is particularly true when the electrodes incorporate the specially designed conical cathode configuration which augments the rate at which I_ϕ increases with ϕ to the point where the amount of correction by comparison to the spherical radiance example is reduced by a factor greater than two.

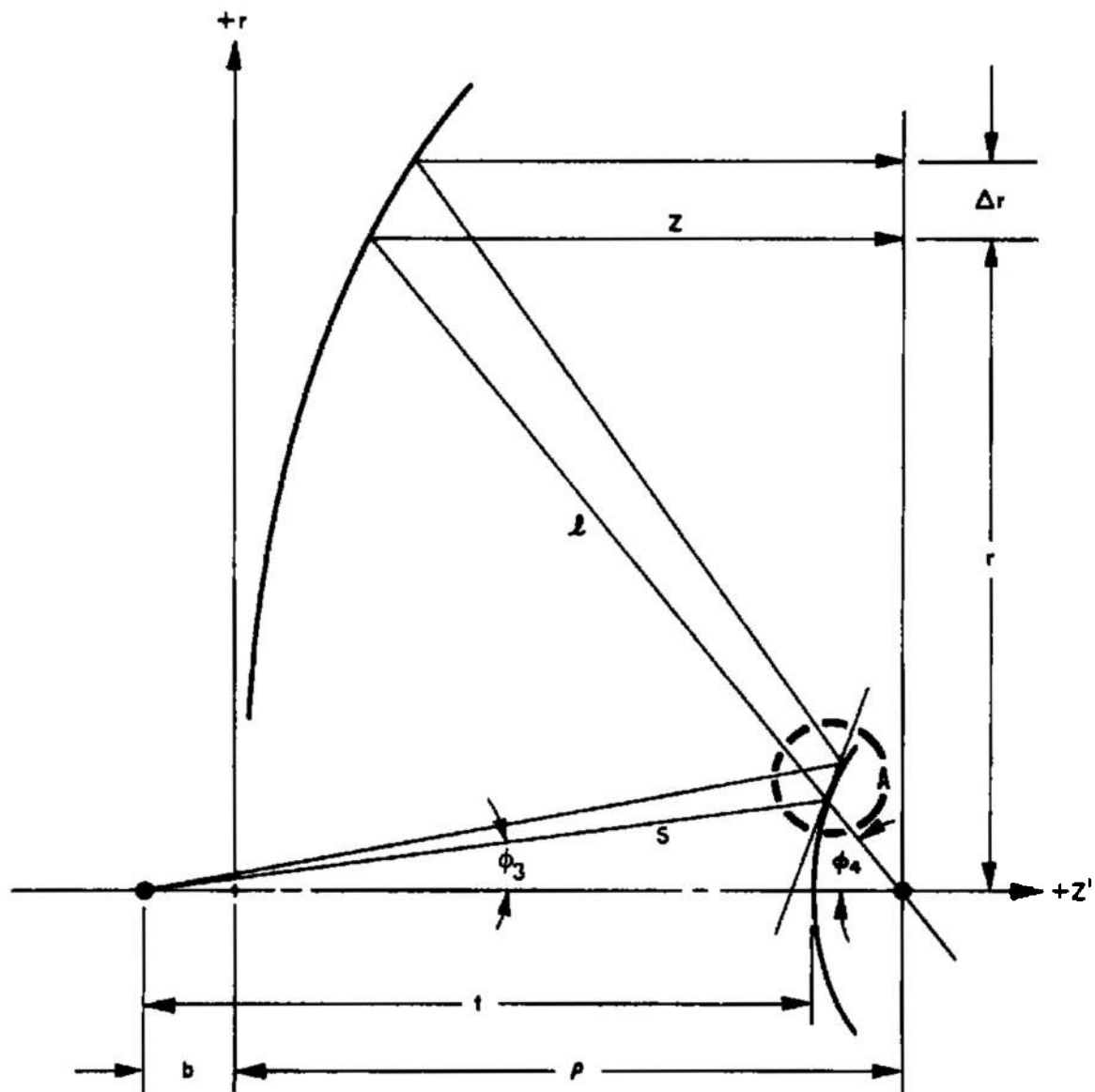
With respect to the FTA source the analysis of the spherical example would apply almost directly while, for the High Intensity Carbon Arc, additional correction beyond what was attempted numerically in this study would be required. Every indication points to the fact that it would be possible to realize this additional correction but the design surfaces become increasingly complex and difficult to fabricate.

7.6.5.2 Higher Order Corrections on Conic Sections used without Condenser Lenses

The analysis above has demonstrated the manner in which an optical system can be compensated to an arbitrary degree of accuracy for first order uniformity when an intermediate condenser system is used in the transfer optics. This correction for the dominant degrading effect in designs which operate at high optical speed or collection efficiency is the principal one pursuant to ultimate uniformity across the modular aperture. Additional adjustments or fine tuning, as required to a greater or lesser extent depending upon the size of the solar field, may be made by control of off-axis aberrations such as field curvature and distortion, both of which may be corrected at the relay lens position. In view of this it is desirable to examine the possibility of realizing the essential first order correction for distribution without the use of condensers, but rather with analogs to conic sections in the form of such surface types with higher order terms designed into them. Should this prove to be feasible, the final adjustments for distribution may be made at the relay lens by control of Petzval field curvature and distortion through lens bending and position factors.

The fundamental problem here is to define the Cassegrainian surface shapes so that a ray entering the entrance pupil at an angle, ϕ_s , figure 7-37, exits from the pseudo-paraboloid aperture at a prescribed height r which shall be defined later. For the moment a target plane shall be placed at the paraxial focal position for the primary parabolic-type element of the Cassegrainian collimation system, a distance ρ , from the origin. The entrance pupil is located a distance b , behind the primary mirror whose vertex is at the origin. The paraxial interfocal distance, I , is $\rho + b$.

A ray which enters the system at an angle, ϕ_s , strikes the secondary mirror after traveling an optical path length equal to s . It is then reflected toward the primary Cassegrainian mirror which it strikes after spanning the distance l between the two mirrors in the direction of the proper course of the ray. Upon its encounter with the primary mirror it must be reflected in a direction parallel to the forward z -axis. After traversing the distance, Z , it intersects the reference target plane, located at $z = \rho$, at a height equal to r which will be specified as a function of the original angle ϕ_s . The latter, of course, will also be specified, in terms of the collection angle ϕ_1 , as a function dependent upon the type of collection system used. In the present case the collection system will be composed of either an ellipse or combination of two conic sections, depending upon whether the double- or single-ended sources are used, respectively.



DETAIL A

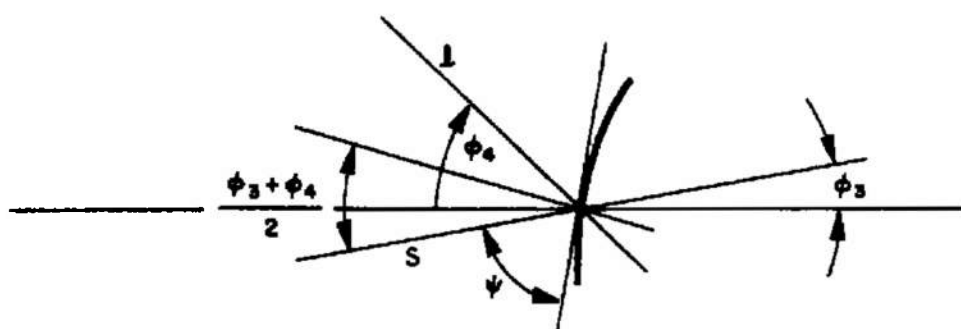


Figure 7-37. Modified Cassegrainian Collimator for a System without Condenser Lenses

The total optical path, p , travelled by the ray upon entering the collimation system and striking the reference target plane is

$$p = s + l + z \quad (7-265)$$

Assume a coherent wave front, which leaves the focal point located at the entrance pupil, and is transformed into a plane wave front upon leaving the collimator, so that the wave front is normal to the axis of the collimator, as required by the definition of the symmetric collimator. Then all ray path lengths, p , must be invariant and independent of the angle ϕ_3 or the height, r , on the normal target plane. In other words, p must be a constant in order to represent the proper solution of the eikonal or wave front equation which describes the propagation of radiation as required herein. This is consistent with Fermat's extremum principle which stipulates that a ray which follows a path between two points must represent a relative extremum in time of flight. The proof is as follows:

1. Consider two rays, one starting at ϕ_3 and striking the target plane at a height r , and the other starting at $\phi_3 + \Delta\phi_3$ and terminating at $r + \Delta r$, both in accordance with the requirements above which call for their respective path lengths to be fixed at the constant value, p .
2. Now, if some path could be defined such that the path lengths for a ray starting at ϕ_3 and striking at $r + \Delta r$ and a ray starting at $\phi_3 + \Delta\phi_3$ and striking at r are both greater than p , then it would establish the path length p to be a relative minimum with respect to the change $\Delta\phi_3$.
3. The last is done simply by noting that if either ray in item 1 is followed to the Cassegrainian primary, unaltered, but then is made to strike the plane wave front at the other's height, then the path length, which would otherwise have been p , is now greater than p as it no longer includes the shortest or perpendicular distance to the plane wave, Q. E. D.

Conversely the equality of all path lengths as defined above means that all rays from a plane wave front striking the Cassegrainian primary will be in phase to define the focus. Then it follows that equation (7-265) is a necessary and sufficient condition to define the optical requirements for the surfaces in question with assurance that the imaging properties desired will follow as a consequence. Thus, in accordance with figure 7-37,

$$\begin{aligned} t^2 &= [(s \cos \phi_3 - b) - (p - Z)]^2 + (r - s \sin \phi_3)^2 \\ t^2 &= (Z + s \cos \phi_3 - I)^2 + (r - s \sin \phi_3)^2 \end{aligned} \quad (7-266)$$

Combining equations (7-265) and (7-266)

$$\begin{aligned} (1 - \cos \phi_3) s Z + (I - p) Z + (r \sin \phi_3 + I \cos \phi_3 - p) s \\ + \frac{1}{2} (p^2 - I^2 - r^2) = 0 \end{aligned} \quad (7-267)$$

By virtue of equation (7-267) the parameters s and Z may be expressed in terms of each other as follows:

$$s = \frac{(p - I) Z - \frac{1}{2} (p^2 - I^2 - r^2)}{Z(1 - \cos \phi_3) + (r \sin \phi_3 + I \cos \phi_3 - p)} \quad (7-268)$$

$$Z = \frac{(p - r \sin \phi_3 - I \cos \phi_3) s - \frac{1}{2} (p^2 - I^2 - r^2)}{s(1 - \cos \phi_3) + (I - p)} \quad (7-269)$$

From figure 7-37 the angle ψ between the ray, s , and the tangent to the surface of the Cassegrainian secondary is related to the derivative of s in terms of the parametric relationship

$$\frac{ds}{d\phi_3} = s \cot \psi \quad (7-270)$$

The angle between the incident and reflected ray is the external angle, $\phi_3 + \phi_4$, and from the laws of reflection, the angle between the incident ray and surface normal is $(\phi_3 + \phi_4)/2$. Therefore, the angle ψ is given by

$$\psi = \frac{\pi}{2} - \frac{\phi_3 + \phi_4}{2} \quad (7-271)$$

From standard half angle formulae

$$\cot \psi = \frac{1 - \cos(\phi_3 + \phi_4)}{\sin(\phi_3 + \phi_4)} \quad (7-272)$$

Thus, from equations (7-270) and (7-272)

$$\frac{ds}{d\phi_3} = s \frac{\frac{1}{\cos \phi_4} - \cos \phi_3 + \sin \phi_3 \tan \phi_4}{\sin \phi_3 + \cos \phi_3 \tan \phi_4} \quad (7-273)$$

Since, from figure 7-37 and equation (7-265)

$$\frac{1}{\cos \phi_4} = \frac{p - (Z + s)}{Z + s \cos \phi_3 - I} ,$$

and

$$\tan \phi_4 = \frac{r - s \sin \phi_3}{Z + s \cos \phi_3 - I}$$

then

$$\frac{ds}{d\phi_3} = s \left[\frac{p - (Z+s) - \cos \phi_3 (Z + s \cos \phi_3 - I) + \sin \phi_3 (r - s \sin \phi_3)}{\sin \phi_3 (Z + s \cos \phi_3 - I) + \cos \phi_3 (r - s \sin \phi_3)} \right] \quad (7-274)$$

From equations (7-274) and (7-269)

$$\frac{ds}{d\phi_3} = \frac{\left\{ s - \frac{1}{2} \left[(p - I) + r \cot \frac{\phi_3}{2} \right] \right\}^2 (2s \tan \frac{\phi_3}{2})}{\frac{1}{2} [(p - I)^2 - r^2] + (p - I)r \cot \phi_3 - \left[(p - I) - r \tan \frac{\phi_3}{2} \right] s} \quad (7-275)$$

Similarly

$$\frac{dZ}{d\phi_3} = \frac{dZ}{dr} \frac{dr}{d\phi_3} \quad (7-276)$$

dZ/dr is the slope of the normal to the surface of the Cassegrainian primary and $dr/d\phi_3$, which we shall call r' , can be calculated from

the expression for r . Since, in this case, the reflected ray is parallel to the axis, it makes an angle ϕ_4 , with the incident ray so that the surface normal makes an angle $\phi_4/2$ with the axis. Thus

$$\frac{dZ}{dr} = \tan \frac{\phi_4}{2} = \frac{\frac{1}{\cos \phi_4} - 1}{\tan \phi_4} \quad (7-277)$$

which, using equation (7-269) and the previous expressions for $\frac{1}{\cos \phi_4}$ and $\tan \phi_4$ leads to

$$\frac{dZ}{dr} \frac{dr}{d\phi_3} = \frac{r - s \sin \phi_3}{(p - I) - s(1 - \cos \phi_3)} r' = \frac{dZ}{d\phi_3} \quad (7-278)$$

Differentiating equation (7-269)

$$\frac{dZ}{d\phi_3} = \frac{As^2 + Bs + Cs' + (I - p) rr'}{[s(1 - \cos \phi_3) - (p - I)]^2}, \quad (7-279)$$

where

$$A = [(1 - \cos \phi_3)(r - r' \sin \phi_3) - (p - I) \sin \phi_3]$$

$$B = \frac{\sin \phi_3}{2} [(p - I)^2 - r^2](p - I)(r \cos \phi_3 + r' \sin \phi_3) + (1 - \cos \phi_3) rr'$$

$$C = -\frac{[(p - I)(1 + \cos \phi_3) - r \sin \phi_3]^2}{2(1 + \cos \phi_3)}$$

The expressions for $dZ/d\phi_3$ in equations (7-278) and (7-279) may now be equated, using equation (7-275) for the expression for s' . This yields a quartic equation in s in terms of the angle ϕ_3 alone, provided a function of r versus ϕ_3 is given. The latter may be any arbitrary function which satisfies the basic differential equation governing uniformity as derived earlier. The particular form of $r(\phi_3)$ will depend upon the collection and transfer optics and the radiance function of the source. In general s may be solved for and then equation (7-269) returned to for a solution for Z . The particular value of s to be chosen out of the four possible solutions defined by these equations is that which is closest to the original hyperboloid with respect to which the modifications are made. Thus R_h , Z_h and R_p , Z_p , the coordinates of the pseudo-hyperboloid and pseudo-paraboloid with respect to their respective vertices, are given by

$$\left. \begin{aligned} R_p &= r \\ Z_p &= \rho - Z = \rho - \frac{r(I - s \cos \phi_3)}{s \sin \phi_3} \end{aligned} \right\} \quad (7-280)$$

and

$$\left. \begin{aligned} R_h &= s \sin \phi_3 \\ Z_h &= s \cos \phi_3 - \frac{I}{M_h + 1} \end{aligned} \right\} \quad (7-281)$$

where M_h is the paraxial magnification of the pseudo-hyperboloid element. M_h is defined in the same manner as the ordinary hyperboloid in the limit as ϕ_3 goes to zero. Thus in accordance with figure 7-37, where t is the distance from the secondary mirror's vertex to the entrance pupil of the Cassegrainian collimator (which is the secondary focal position in the Cassegrainian arrangement), the paraxial magnification for the secondary, analogous to that of the hyperboloid which it replaces, is given by

$$M_h = \frac{I - t}{t} \quad (7-282)$$

Now suppose that the modified Cassegrainian system as defined by equations (7-280) and (7-281) is fed by an ellipsoidal collector which forms an image of the arc at the entrance pupil to the collimator. The determination of r as a function of the initial collection angle ϕ_1 is still the same as in equation (7-220) for the spherical arc or equation (7-264) for an arc with arbitrary normalized polar radiance function, \bar{I}_ϕ . In either case, when the ellipsoidal collector is employed the restriction must be observed that

$$f = \frac{\rho}{M_e M_h}$$

where $M_e = \frac{1+e}{1-e}$ for the ellipsoid which is used.

In case where the source radiance function is spherical and equation (7-220) applies

$$r^2 = 2f^2 (1 - \cos \phi_1)$$

and from equation (7-150) for the ellipse,

$$r^2 = 2f^2 \left(1 - \frac{\cos \phi_3 - E}{1 - E \cos \phi_3} \right)$$

or

$$r^2 = 2f^2 (1 + E) \frac{1 - \cos \phi_3}{1 - E \cos \phi_3} \quad (7-283)$$

From equation (7-283)

$$rr' = \frac{(1 - E^2) f^2 \sin \phi_3}{(1 - E \cos \phi_3)^2} \quad (7-284)$$

and

$$r' = \frac{(1 - E^2) \sin \phi_3}{\sqrt{2(1 + E) (1 - \cos \phi_3) (1 - E \cos \phi_3)^2}} f \quad (7-285)$$

The expressions (7-284) and (7-285) may be inserted into equations (7-278) and (7-279) for the determination of s in terms of the parameter ϕ_3 . The solution is now an explicit one where f is a basic parameter and ρ and M_h are selected for convenience and minimization of central shadowing. E is then determined and equation (7-283) may be used in conjunction with equations (7-280) and (7-281) for a complete determination of the surface coordinates for the Cassegrainian components. It should be noted that this system is completely free of residual spherical aberration and satisfies the first order uniformity criterion exactly.

It is well to underscore the significance of this result in that it truly represents the ultimate solution for any reasonable source radiance function provided the surfaces called for are practical from the fabrication standpoint. Although complete numerical solutions of these equations are beyond the scope of this report, it is possible to examine their behavior for typical optical parameters. These may be normalized with respect to the nominal parabolic paraxial focal length ρ . Thus

$$\rho = 1, M_h = 0.2 \text{ and } f = 0.5$$

These require an M_e of 10 and an e of 0.818, which correspond to the normalized values of a typical optical system. For values of ϕ_3 as high as 12° which correspond to collection angles somewhat better than $\phi_1 = 90^\circ$ the equations are still well behaved and there is no reason to expect surfaces too exceptional to permit fabrication.

These results point up the fact that major compensation for distribution can be effected for the VSRS and the FTA to the point that virtually all the useful radiation can be collected and utilized. Optical compensation for the VSRS would not have to be so great as that for the FTA by virtue of the unique radiance distribution associated with the VSRS, namely its tendency to increase with increasing values of the initial collection angle, ϕ_1 . With the conical cathode the radiance distribution may be approximated as before in accordance with

$$\bar{I}_\phi = 1 \text{ between } 0^\circ \text{ and } 30^\circ = \phi_{1,0}$$

while

$$\bar{I}_\phi = a\phi_1 \text{ for } \phi_1 \text{ greater than } \phi_{1,0}$$

The solution for the surfaces between 0° and 30° is the same as that given above. From that point on, in accordance with equation (7-264),

$$r^2 - r_0^2 = 2f^2 \int_{\phi_{1,0}}^{\phi_1} a\phi \sin\phi d\phi \quad (7-286)$$

Thus

$$r^2 = r_0^2 + 2f^2 a [(\sin \phi_1 - \phi_1 \cos \phi_1) - (\sin \phi_{1,0} - \phi_{1,0} \cos \phi_{1,0})] \quad (7-287)$$

where

$$r_0^2 = 2f^2 (1 - \cos \phi_{1,0}) \quad (7-288)$$

Since equation (7-150) gives the expression for ϕ_1 in terms of ϕ_3 , equation (7-287) is sufficient to provide the needed relationships. The starting angle for ϕ_3 in this case, corresponding to $\phi_{1,0}$, is 3° . The surfaces need only be solved for starting at this point since the remainder of the solution (toward the axis) will be devoted to a fill-in system if required. It should be noted that the only thing to be changed in the determination of the surfaces for a different source radiance function is the expression for r ; otherwise the technique remains the same. The results for the 19-kilowatt VSRS arc with $a = \frac{6}{\pi}$ are not materially different from the spherical case which corresponds to the FTA, as far as the reasonable numerical behavior of the equations is concerned. The limiting collection angles are somewhat greater,

however, and collection up to $\phi_1 = 120^\circ$ is entirely feasible, representing almost total collection of available radiation.

In the case of the FTA, the solution of the spherical case would apply to a good approximation and, since collection to $\phi_1 = 90^\circ$ is entirely feasible, there should be no difficulty in utilizing nearly all the radiated power of the FTA as well. The singular difference is in the fact that the collection scheme must consist of at least two conic sections for the single-ended source. If, for example, a concave hyperboloid followed by a concave ellipsoid are used, as in figure 6-2, then successive applications of equations (7-158) and (7-157) yield:

$$\cos \phi_1 = \frac{\frac{E - H}{1 - EH} + \cos \phi_3}{1 + \frac{E - H}{1 - EH} \cos \phi_3} \quad (7-289)$$

If the parameter, Q , is defined such that

$$Q = \frac{H - E}{1 - EH}, \text{ then } \cos \phi_1 = \frac{\cos \phi_3 - Q}{1 - Q \cos \phi_3} \quad (7-290)$$

and an expression exactly analogous to equation (7-156) has been obtained, with the understanding that ϕ_1 as used here is the interior collection angle to the first concave hyperboloid. The total magnification of the collection system, M_{cl}^2 , is given by

$$M_{cl}^2 = \frac{1 - Q}{1 + Q} \quad (7-291)$$

just as in equation (7-162). Checking equation (7-291) against equations (7-161) and (7-162) yields

$$M_{cl}^2 = \frac{1 - EH - E + H}{1 - EH + E - H} = \frac{1 - E}{1 + E} \frac{1 + H}{1 - H} = \frac{1}{M_e^2} \frac{1}{M_h^2}$$

which is the proper relationship since the hyperboloid and ellipsoid are used in the reverse sense to that which defined M_e and M_h . In any case M_{cl}^2 for the FTA collection must be the same as M_h^2 for the VSRS collection in order to satisfy the effective focal length requirements, assuming of course, the same ratio of effective focal length to ρ is desired in both cases for comparison purposes. In any case, on the basis of equation (7-290) it is clear that the solution already given for the spherically symmetric polar radiance case is applicable irrespective of the exact nature of the conic section system. Specifically,

for the collection system illustrated, Q for the combined conics must be equal to $1/E$ for the ellipsoid used in the previous calculation where M_e was 10.

In the case of the High Intensity Carbon Arc the same logic applies to the collection scheme as in the case of the FTA since the carbon arc is also a single ended source. For the High Intensity Carbon Arc, however, the source radiance function follows, approximately, a cosine fall off with respect to the anode axis. Thus in accordance with equation (7-264)

$$r^2 = 2f^2 \int_0^{\phi_1} \cos \phi \sin \phi d\phi \quad (7-292)$$

$$r^2 = f^2 \sin^2 \phi_1 = f^2 (1 - \cos^2 \phi_1)$$

With $\cos \phi_1$ given as in equations (7-150) or (7-290), the corrected surfaces for the Cassegrainian elements may be determined. It is seen that the situation begins to deteriorate rapidly as $\phi_1 = 60^\circ$ is approached, but this limiting collection angle includes the bulk of the arc radiation, although perhaps not as much as in the case of the VSR or FTA sources. Somewhat more radiation may be collected and utilized at the sacrifice of some first order uniformity compensation. However, at angles above $\phi_1 = 60^\circ$ the fall-off begins to accelerate to an extent that makes significant additional collection most difficult.

7.6.5.3 Higher Order Correction of the Conic Collection Elements

Before leaving the subject of higher order corrections to conic mirror elements we shall take up the question of such modifications applied to the collection components. It is instructive to first examine the nature of the radiance distribution obtaining at the image of the source formed by a collection system when the radiance distribution of the source is known and given by \bar{I}_0 . Assume the existence of a continuous functional relationship between the initial collection angle ϕ_1 and the angle ϕ_3 exiting from the collection system and proceeding to the arc image which may or may not be well defined. Further, the paraxial magnification of the collector, M_{cl} , is defined as

$$M_{cl} = \lim_{\phi_1 \rightarrow 0} \frac{\sin \phi_1}{\sin \phi_3} \quad (7-293)$$

The radiance distribution at the image of the collector is \bar{E}_{ϕ_3} which can be determined indirectly as follows: Assume, as in figure 7-38, that the collection system is feeding a simple paraboloid of focal length, ρ . The relative flux distribution emanating from such a system is given by

$$R = \frac{(1 + \cos \phi_3)^2}{4} \bar{E}_{\phi_3} \quad (7-294)$$

It may also be given by

$$R = -2f^2 \frac{d(\cos \phi_1)}{d(r^2)} \bar{I}_\phi$$

By the chain differentiation rule,

$$R = -2f^2 \frac{d(\cos \phi_1)}{d(\cos \phi_3)} \frac{d(\cos \phi_3)}{d(r^2)} \bar{I}_\phi \quad (7-295)$$

Since

$$r^2 = 4\rho^2 \frac{1 - \cos \phi_3}{1 + \cos \phi_3}$$

and

$$d(r^2) = \frac{-8\rho^2}{(1 + \cos \phi_3)^2} d(\cos \phi_3) \quad (7-296)$$

combining equations (7-294), (7-295), and (7-296) we have for \bar{E}_{ϕ_3} , where $\frac{\rho}{M_{cl}} = f$,

$$\bar{E}_{\phi_3} = \frac{\bar{I}_\phi}{M_{cl}^2} \frac{d(\cos \phi_1)}{d(\cos \phi_3)} \quad (7-297)$$

In the case where the collector is a simple ellipsoid and

$$\cos \phi_1 = \frac{\cos \phi_3 - E}{1 - E \cos \phi_3}$$

$$d(\cos \phi_1) = \frac{1 - E^2}{(1 - E \cos \phi_3)^2} d(\cos \phi_3)$$

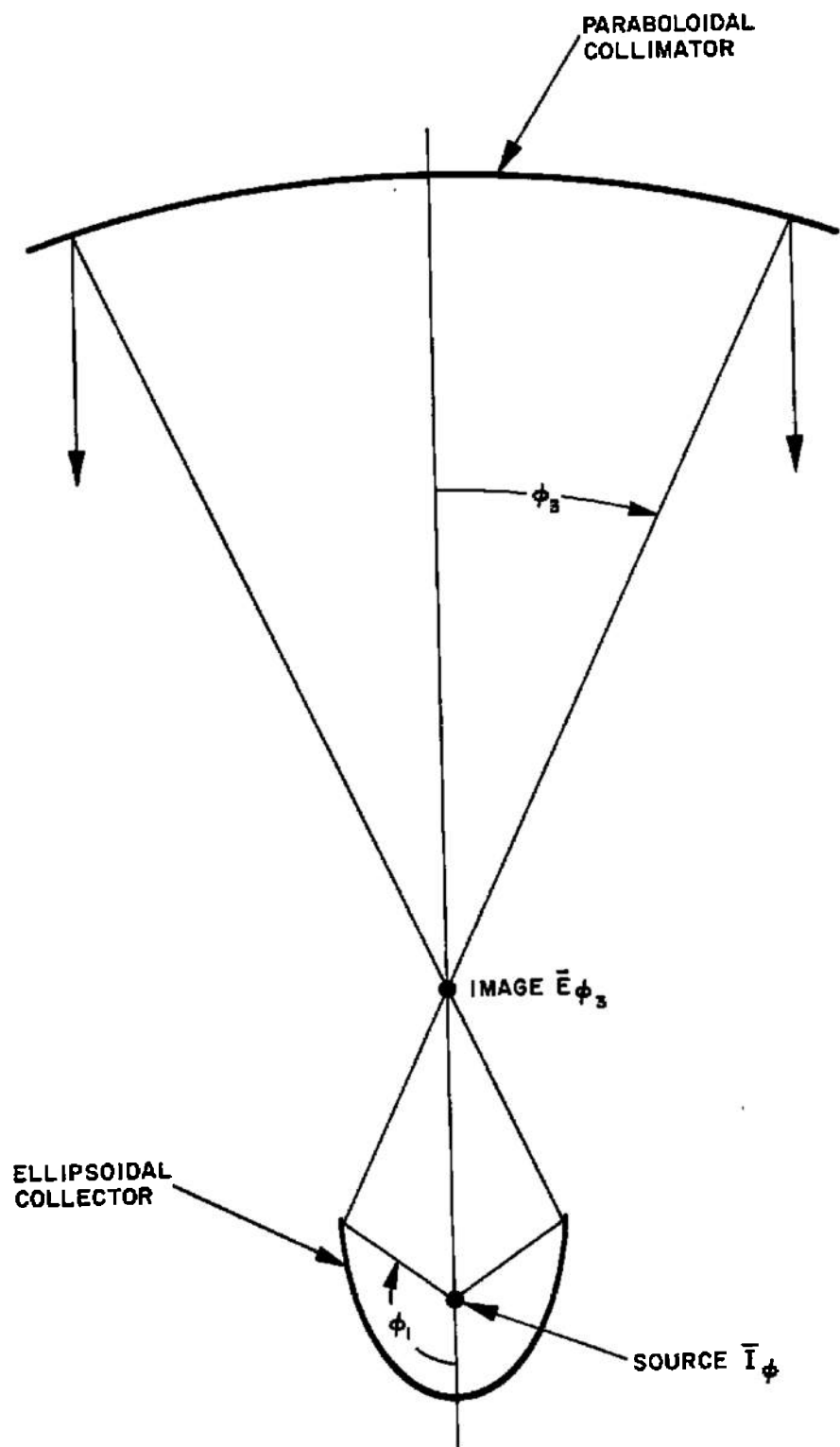


Figure 7-38. Collector and Paraboloid

so that

$$\bar{E}_{\phi_3} = \frac{1 - E^2}{M_{cl}^2} \frac{\bar{I}_{\phi}}{(1 - E \cos \phi_3)^2} = \frac{(1 - E)^2}{(1 - E \cos \phi_3)^2} \bar{I}_{\phi} \quad (7-298)$$

where

$$M_{cl}^2 = M_e^2 = \frac{1 + E}{1 - E}$$

Thus the natural distribution from an ellipsoid has a strong fall-off as a function of ϕ_3 even when a spherical arc is used such that $\bar{I}_{\phi} = 1$.

In the case of the High Intensity Carbon Arc where $\bar{I}_{\phi} \approx \cos \phi_1$, the distribution from a simple ellipsoid would be

$$\bar{E}_{\phi_3} = \frac{(1 - E)^2 (\cos \phi_3 - E)}{(1 - E \cos \phi_3)^3} \quad (7-299)$$

which is an even steeper fall-off. It was seen in the case where $\bar{I}_{\phi} = 1$ that the distribution of equation (7-298) could be compensated by higher order corrections to the Cassegrainian elements up to collection angles of about 90° so that most of the radiation from the FTA, for example, could be utilized. However, the High Intensity Carbon Arc distribution which leads to equation (7-299) for the resulting radiance function at the image of an ellipsoidal collector could not be compensated entirely by corrections to the Cassegrainian elements alone. Some improvement could be effected generally for both cases if all the burden for correction were not placed entirely upon the Cassegrainian elements but were shared to a certain extent by the collector elements. There is no fundamental criterion for assessing the division of the total required correction between collection and collimation elements. It is rather a matter of practical judgement to be exercised in the final design process after quantitative results have been carefully scrutinized. The following, therefore, will set the framework upon which such a design procedure is based and will establish the feasibility of the design concept.

It was shown earlier that if a system is free of coma, that is, if

$$\frac{r}{\sin \phi} = f,$$

then a radiance distribution of

$$\bar{E}_{\phi} = \cos \phi$$

will provide uniformity in the target beam. With a Cassegrainian design where $F = \frac{r}{\sin \phi_3}$ and $\bar{E}_{\phi_3} = \cos \phi_3$ the design relationship for the collector system would have to be

$$M_{cl} \cos \phi_3 d(\cos \phi_3) = \bar{I}_{\phi} d(\cos \phi_1) \quad (7-300)$$

The requirement set upon the Cassegrainian collimator design of freedom from coma is probably an excellent choice as such designs are known to exist for very fast operating speeds. Whether or not this still puts too heavy a burden upon the collector design, however, by virtue of equation (7-300), remains to be seen. In any case the latter yields an explicit relationship between ϕ_1 and ϕ_3 which in the case of a spherical arc, upon integration from the axis, is:

$$\cos \phi_1 = 1 - \frac{1}{2} M_{cl}^2 \sin^2 \phi_3 \quad (7-301)$$

When \bar{I}_{ϕ} is a cosine relationship the same process yields

$$M_{cl} \sin \phi_3 = \sin \phi_1 \quad (7-302)$$

which is nothing more than a statement that the zonal magnification of the collection must also be free of coma for all angles ϕ_1 . This is not surprising, as the source was a cosine radiator and, if such a relationship is to be preserved, constant angular magnification is a necessity. It merely proves that no matter where a cosine radiator is placed in the system the remainder of the system must be free of coma for uniformity to be preserved. It is easy to satisfy equation (7-302) when M_{cl} is unity, which amounts to employing a sphere and imaging the arc back upon itself. Whether a design which obeys equation (7-302) for values of M_{cl} greater than one is possible is not readily apparent and it may be necessary to incorporate more correction into the Cassegrainian elements than was assumed for this case. Equation (7-301), on the other hand, can probably be satisfied more easily for values of M_{cl} on the order of 10 or greater.

Having seen how a design relationship is established between the entrance and exit angles ϕ_1 and ϕ_3 , respectively, of the collection system, now undertake the problem of designing a system which will be free of residual spherical aberration as would be generally required for optimum performance. The elimination of spherical aberration is particularly important since the exit pupil of the collector system is placed at the entrance pupil of the collimator, and it is undesirable to enter the relay lens with residual spherical aberration upon which it

could act in a disastrous manner. The approach for determination of the appropriate collector surfaces follows along the same principles as that for the Cassegrainian elements with a few additional complications. Thus, referring to figure 7-39 the basic relationship exists:

$$S + L + S' = P \quad (7-303)$$

The nature of P in terms of the other parameters chosen for the system will be discussed later. For the present the distance between the two foci, I , is needed. In addition, assume that ϕ_3 is a known function of ϕ_1 , to be determined by choosing the optimum functional dependence of E_{ϕ_3} upon ϕ_3 for the particular source in question as discussed earlier.

In accordance with figure 7-39

$$L^2 = (S \cos \phi_1 + S' \cos \phi_3 - I)^2 + (S' \sin \phi_3 - S \sin \phi_1)^2 \quad (7-304)$$

$$L^2 = (S^2 + S'^2 + I^2) + 2SS' \cos(\phi_1 + \phi_3) - 2I(S \cos \phi_1 + S' \cos \phi_3)$$

Combining equations (7-303) and (7-304)

$$\begin{aligned} & [1 - 2\cos(\phi_1 + \phi_3)] SS' + 2(I \cos \phi_1 - P)S \\ & + 2(I \cos \phi_3 - P)S' + (P^2 - I^2) = 0 \end{aligned} \quad (7-305)$$

From figure 7-39 an expression for the slopes of the respective surfaces also exists;

$$\frac{dS}{d\phi_1} = S \tan \frac{\phi_1 + \phi_3}{2} = S \frac{\sec \phi_3 - \cos \phi_1 + \sin \phi_1 \tan \phi_3}{\sin \phi_1 + \cos \phi_1 \tan \phi_3}$$

$$\begin{aligned} \frac{dS'}{d\phi_3} &= S' \tan \frac{\phi_3 - \phi_2}{2} \\ &= S' \frac{\sec \phi_3 - \cos \phi_3 - \sin \phi_3 \tan \phi_2}{\sin \phi_3 - \cos \phi_3 \tan \phi_2} \end{aligned} \quad (7-306)$$

The geometry of the figure also yields

$$S \cos \phi_1 + S_1 \cos \phi_3 - I = L \cos \phi_2$$

So that

$$\sec \phi_2 = \frac{P - (S + S')}{S \cos \phi_1 + S' \cos \phi_3 - I} \quad (7-307)$$

$$\tan \phi_2 = \frac{S' \sin \phi_3 - S \sin \phi_1}{S \cos \phi_1 + S_1 \cos \phi_3 - I}$$

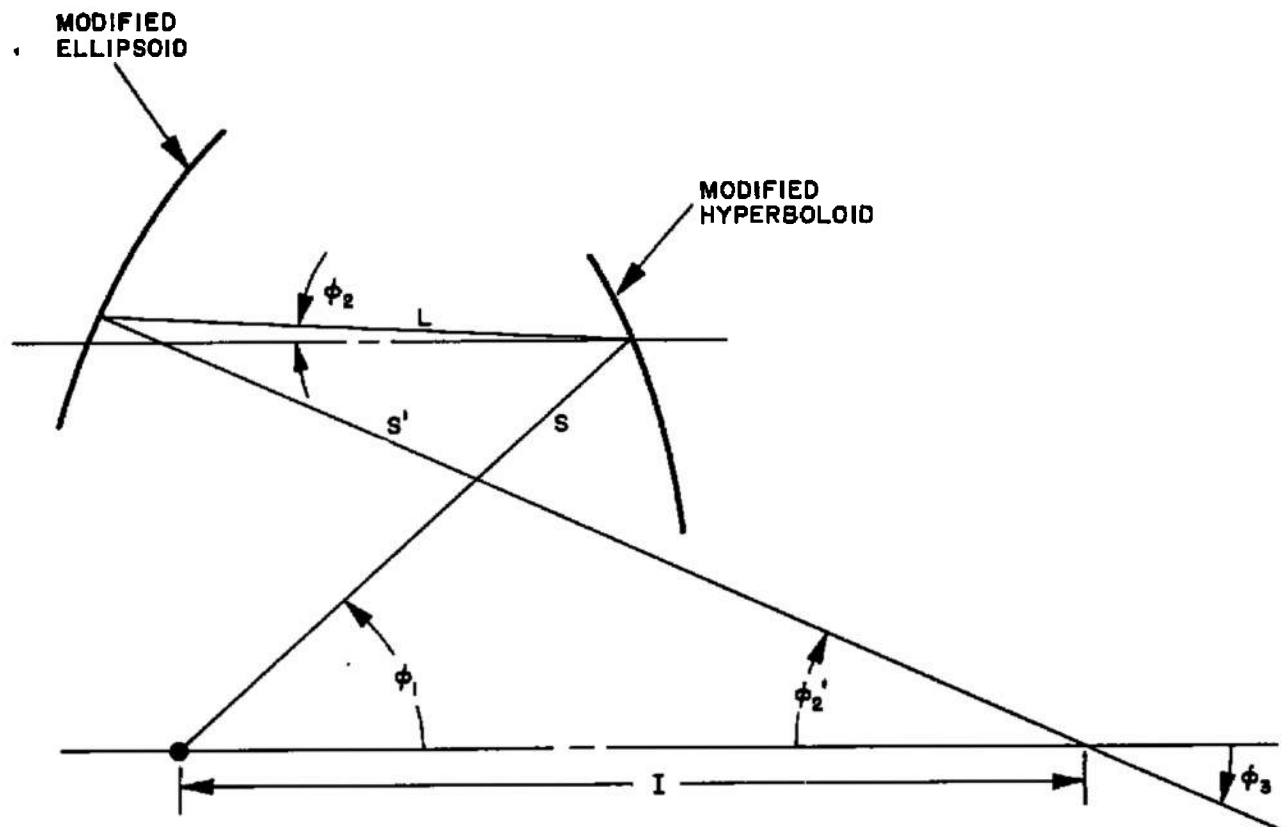


Figure 7-39. Parameters of a Two-Element Collector

From equation (7-305) an explicit expression of S' in terms of S and ϕ_1 , and hence, the derivative of S' in terms of the variables, $\frac{dS}{d\phi_1}$, and $\frac{d\phi_1}{d\phi_3}$ may be obtained. $\frac{dS'}{d\phi_3}$ so obtained is then equated to the second of the equations (7-306). Substitution of an expression for S' in terms of S , obtainable from equation (7-305), yields an explicit equation for S and the variable ϕ_1 , where ϕ_3 is a known function of ϕ_1 . After solving for S equation (7-305) may be reverted to for the solution of S' in terms of ϕ_3 . From such information the surfaces may be plotted. The details of this procedure follow along the same lines as in the case of the determination for the Cassegrainian elements. The algebra is quite involved and will not be included in this report. It should be noted however, that it would be desirable to maintain the spherical radiance distribution of the FTA source which requires the relationship of equation (7-297) to hold, where both \bar{I}_{ϕ} and \bar{E}_{ϕ_3} are identically 1. This case requires that

$$(1 - \cos \phi_1) = (1 - \cos \phi_3) M_{cl}^2 \quad (7-308)$$

Should this prove too much of a strain on the collection optics from 0° to 90° then the requirement could be relaxed somewhat so that the output distribution \bar{E}_{ϕ_3} would fall off as a cosine function such that $\bar{E}_{\phi_3} = \cos \phi_3$ and from equation (7-297)

$$M_{cl}^2 \int_0^{\phi_3} -\cos \phi \sin \phi d\phi = \int_1^{\cos \phi_1} d(\cos \phi) \quad (7-309)$$

$$M_{cl}^2 \sin^2 \phi_3 = 1 - \cos \phi_1$$

Appendix III gives an example of the design of a single surface collector which converts a spherical input to a cosine output. It is believed that neither expression (7-308) which would retain the spherical radiance distribution of the FTA in the collected output nor equation (7-309) which would convert it to a cosine fall-off at this point would be too severe a requirement for the determination of S and S' in the previous equations. The former is to be desired because a spherical polar output at the secondary focus of the collector would allow tilting of the collector optics with respect to the collimator optics, (as would be required in off-axis designs) without affecting the distribution significantly. The Cassegrainian elements can be designed for a spherical input distribution at ϕ_3 merely by observing the requirement of equation (7-264) which in this case stipulates that

$$r^2 = 2F^2 (1 - \cos \phi_3) \quad (7-310)$$

where F is the Cassegrainian effective focal length. In the case where the FTA input radiation to the Cassegrainian system is a $\cos \phi_3$ function, then equation (7-264) merely yields the condition of freedom from coma, namely:

$$\frac{r}{\sin \phi_3} = F \quad (7-311)$$

In the case of the High Intensity Carbon Arc where $\bar{I}_\phi = \cos \phi_1$ to a good approximation the best that can be hoped for is to preserve this relationship in the output. By virtue of equation (7-297)

$$M_{cl}^2 \int_0^{\phi_3} \cos \phi \sin \phi d\phi = \int_0^{\phi_1} \cos \phi \sin \phi d\phi$$

or

$$\frac{\sin \phi_1}{\sin \phi_3} = M_{cl} \quad (7-312)$$

This is nothing more than a statement that the collection elements must be free of coma, which applies as well for the Cassegrainian system in this case. Equation (7-311) would govern the design of the latter. In other words the entire system must be free of coma for the High Intensity Carbon Arc.

In the case of the VSRS where $\bar{I}_\phi \approx a \phi_1$, it would be desirable to convert this to a spherical distribution for angles greater than the $\phi_{1,0}$ referred to earlier in equation (7-286). Again, in the face of equation (7-297)

$$M_{cl}^2 \int_{\phi_{3,0}}^{\phi_3} d(\cos \phi_3) = \int_{\phi_{1,0}}^{\phi_1} a\phi d(\cos \phi) \quad (7-313)$$

where $\phi_{3,0}$ is determined in terms of $\phi_{1,0}$ on the basis of equation (7-308) for spherical input to spherical output relationships. Thus

$$\cos \phi_{3,0} = 1 - \frac{1 - \cos \phi_{1,0}}{M_{cl}^2} \quad (7-314)$$

The latter, combined with the solution of equation (7-313) yields

$$M_{cl} (\cos \phi_3 - 1) = a [(\phi_1 \cos \phi_{1,o} \cos \phi_{1,o}) \\ - (\sin \phi_1 - \sin \phi_{1,o})] - (1 - \cos \phi_{1,o})$$

This relationship between ϕ_3 and ϕ_1 would be used to design the collection optics for the VSRS between the initial angle $\phi_{1,o}$ and a ϕ_1 of about 120° . The design criterion for the Cassegrainian system would then be governed by equation (7-310) for the spherical input with respect to ϕ_3 .

The evaluation of the path length, P , is dependent upon the initial conditions, where $\phi_1 = 0$, since the surfaces are calculated with respect to a nominal conic section system at the axis. If, for example, the initial value of S were to a concave hyperboloid proceeding therefrom to a concave ellipse (see figure 7-39) then the value of P is given from the geometry of figure 7-39 by

$$P = 2S_o + 2S'_o - I \quad (7-316)$$

If h is the eccentricity of the first hyperboloid and e is the eccentricity of the subsequent ellipse then standard conic section formulae yield

$$\left. \begin{aligned} S_o &= \frac{I}{2} \left(1 - \frac{1}{h} \right) = \frac{I}{M_h + 1} \\ S'_o &= \frac{I}{2} \left(\frac{1}{e} - 1 \right) = \frac{I}{M_e - 1} \end{aligned} \right\} \quad (7-317)$$

so that combining equations (7-316) and (7-317)

$$P = \frac{\frac{3M_{cl} - M_h + \frac{1}{M_e} + 1}{M_h - M_{cl} - \frac{1}{M_e} + 1} I}{\frac{3M_{cl} - M_h + \frac{1}{M_e} + 1}{M_h - M_{cl} - \frac{1}{M_e} + 1} I} \quad (7-318)$$

where $M_{cl} = M_h/M_e$, since the magnification of the ellipse is used in the reverse sense. Defining the quantity $X = M_h M_e$, which is the ratio of the hyperboloid to ellipsoid magnifications in the sense in which they are used, equation (7-318) takes the form

$$P = \frac{\frac{3M_{cl}}{\sqrt{\frac{M_{cl}}{X}}} \frac{(X-1)+1}{(X-1)-M_{cl}+1} I}{\sqrt{\frac{M_{cl}}{X}} \frac{(X-1)-M_{cl}+1}{(X-1)+1} I} \quad (7-319)$$

where M_{cl} is the predetermined value of the effective collector magnification based upon the required effective focal length of the system f and the chosen focal length of the Cassegrainian element F , such that

$$M_{cl} = \frac{F}{f}$$

The parametric analysis discussed in the foregoing applies generally to single-ended sources or to two-ended sources when two reflecting components are employed in the collector. In any case, if M_{cl} represents the paraxial magnification of the collector system, then the central collecting lens for fill-in, if needed, should also be designed for this magnification. If it is, the position of the lens will automatically turn out correctly in accordance with figure 7-40.

It is seen that the lens position is such as to just gather all the energy not collected by the mirror collection system. It is further seen that the collection angle of the fill-in system is controlled by the size and position of the secondary source image which is located at the apex of the first mirror in order to minimize the hole size. Thus, the larger the collector mirrors, holding their eccentricities and the like constant, the smaller will be the central collection angle since the secondary image size is fixed by the eccentricities only. The value of X , or ratio of collector mirror magnifications, is arbitrary and adjusted by the necessary hole size around the source hardware.

In summary it may be said that modifications to conic sections in accordance with the equations outlined above constitute a singularly desirable solution to the solar simulator optical design problem based upon a multi-modular concept.

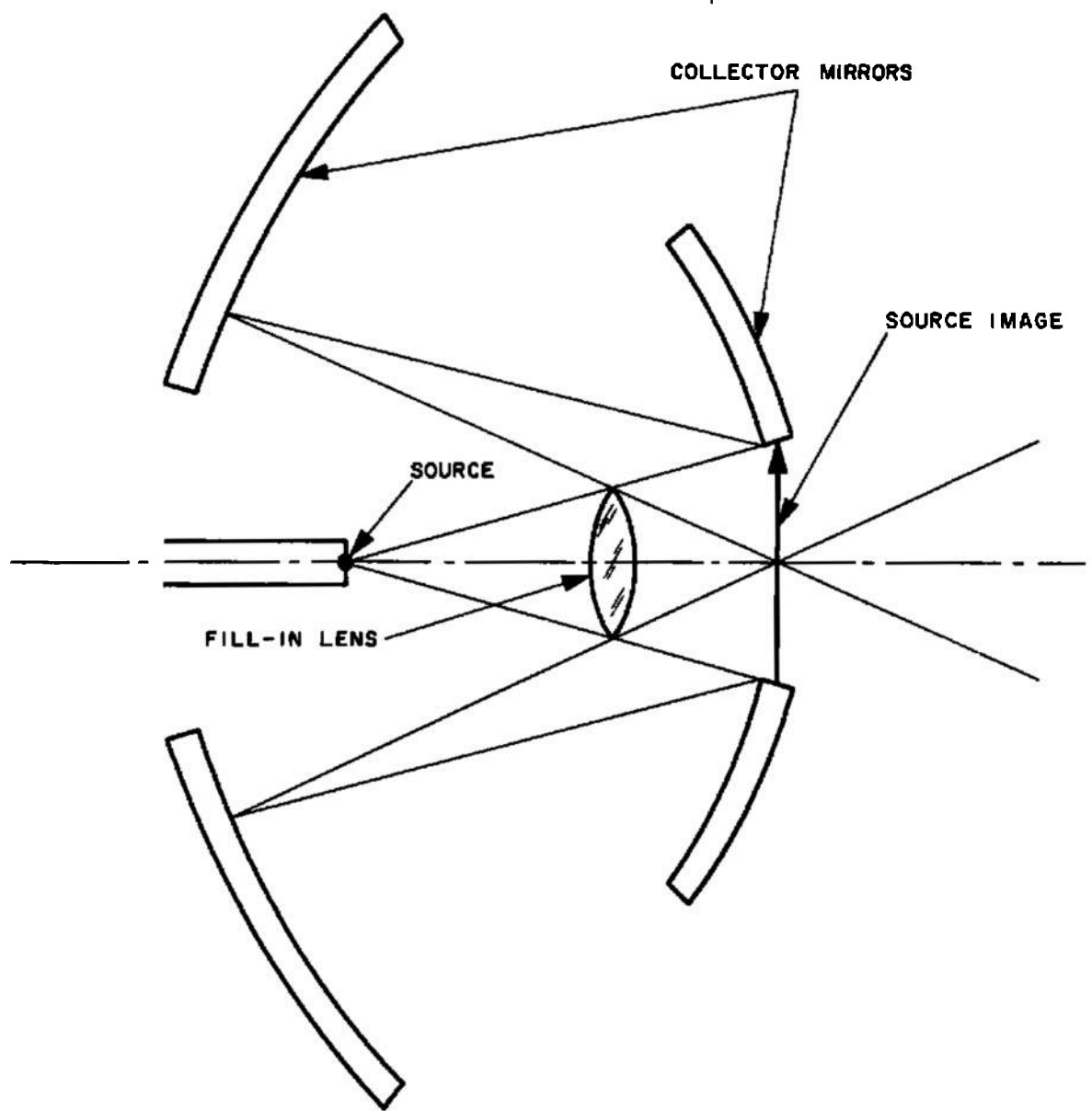


Figure 7-40. Collector Fill-in System

7.7 RE-REFLECTION ANALYSIS.

7.7.1 Off-Axis Collimators

The following paragraphs discuss what radiant flux density variations may result from flux being reflected from a test object back to the paraboloid and then re-reflected by the paraboloid into the test volume. Flux density variations in the test volume due to re-reflection by the paraboloid-hyperboloid combination of a Cassegrainian collimator will also be considered. It is shown that with proper geometry there is no re-reflection of radiation into the test volume from off-axis paraboloids and only minor re-reflection problems for Cassegrainian systems employed in a multi-modular array.

Case 1 — Re-Reflection of Radiation from an Off-Axis Paraboloidal Reflector.

For the purpose of analyzing the problem of re-reflection of radiation from the paraboloidal reflector, consider the graphical raytrace illustrated in figure 7-41. If the surface that is the locus of all normals to the edge of the paraboloid is formed, the line AB lies on that surface and is the normal with the largest slope. If the test volume is located outside of the surface as shown, then any ray originating within the test volume and incident upon the paraboloidal reflector will be reflected away from the test volume with the obvious result that the paraboloidal reflector alone cannot cause flux density variations due to re-reflection of radiation.

Case 2 — Re-Reflection of Radiation from an Off-Axis Paraboloid-Hyperboloid Combination.

Re-reflection of radiation into the test volume from the paraboloid-hyperboloid combination is most likely to occur when the test item occupies the region of the test volume closest to the paraboloidal reflector. To analyze the effects of this type of reflection, the imaging properties of the paraboloid must first be considered. As can be seen from figure 7-42, which illustrates a graphical raytrace to determine the imaging properties of the paraboloid, the lines AB and CD are imaged in a continuous manner along the lines A'B' and C'D', respectively. This property of the paraboloid allows easy definition of those rays from the test item which are incident upon the hyperboloid after re-reflection by the paraboloid.

To determine the rays originating in the test volume that would be re-reflected into the test volume by the paraboloid-hyperboloid combination (if any), a detailed graphical ray trace was constructed and is illustrated in figure 7-43. In order to ensure that the most extreme

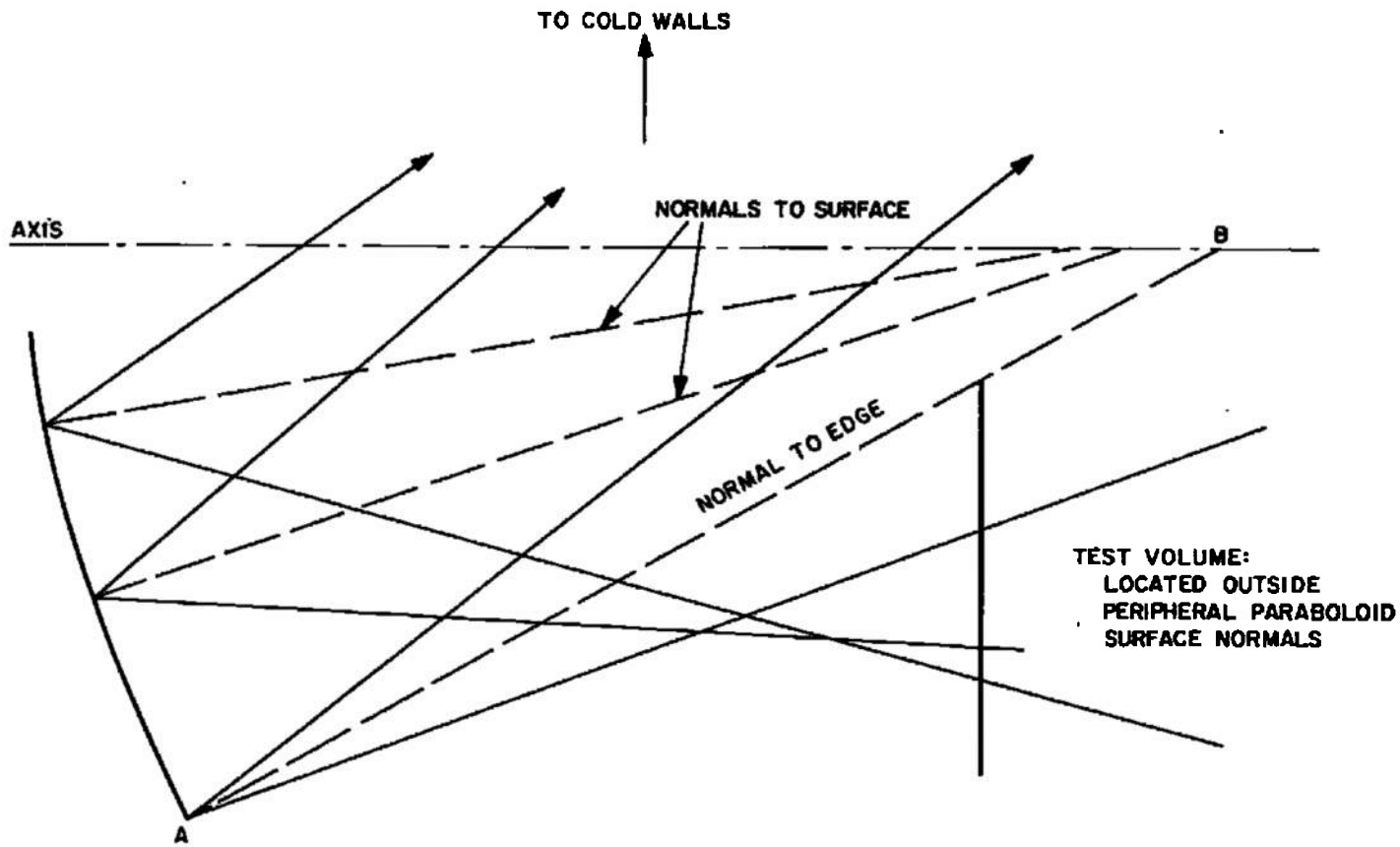


Figure 7-41. Graphical Ray Trace of Re-Reflection by Paraboloidal Reflector Module

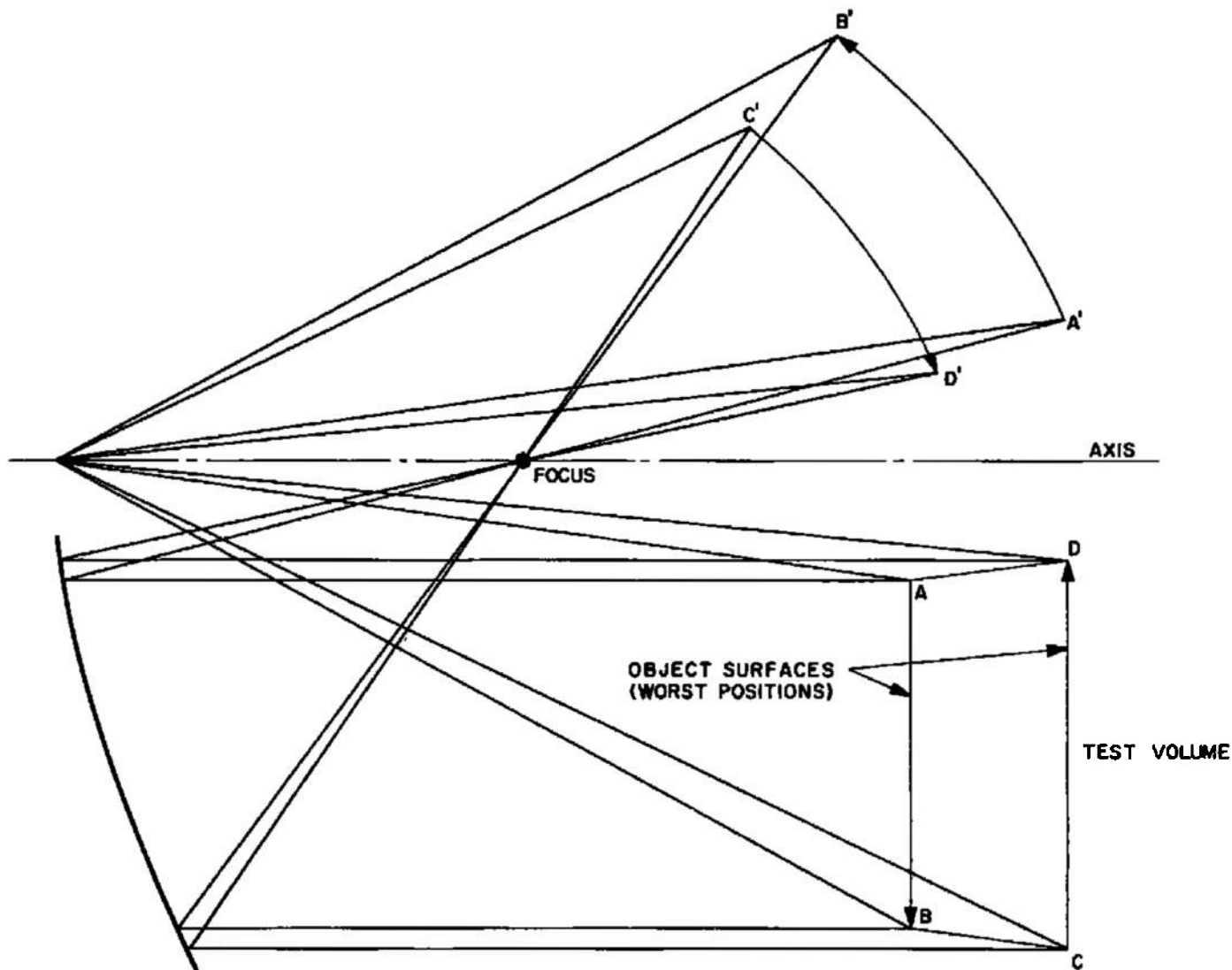


Figure 7-42. Graphical Ray Trace of Images of Object Surfaces in the Test Volume as Formed by a Paraboloidal Reflector

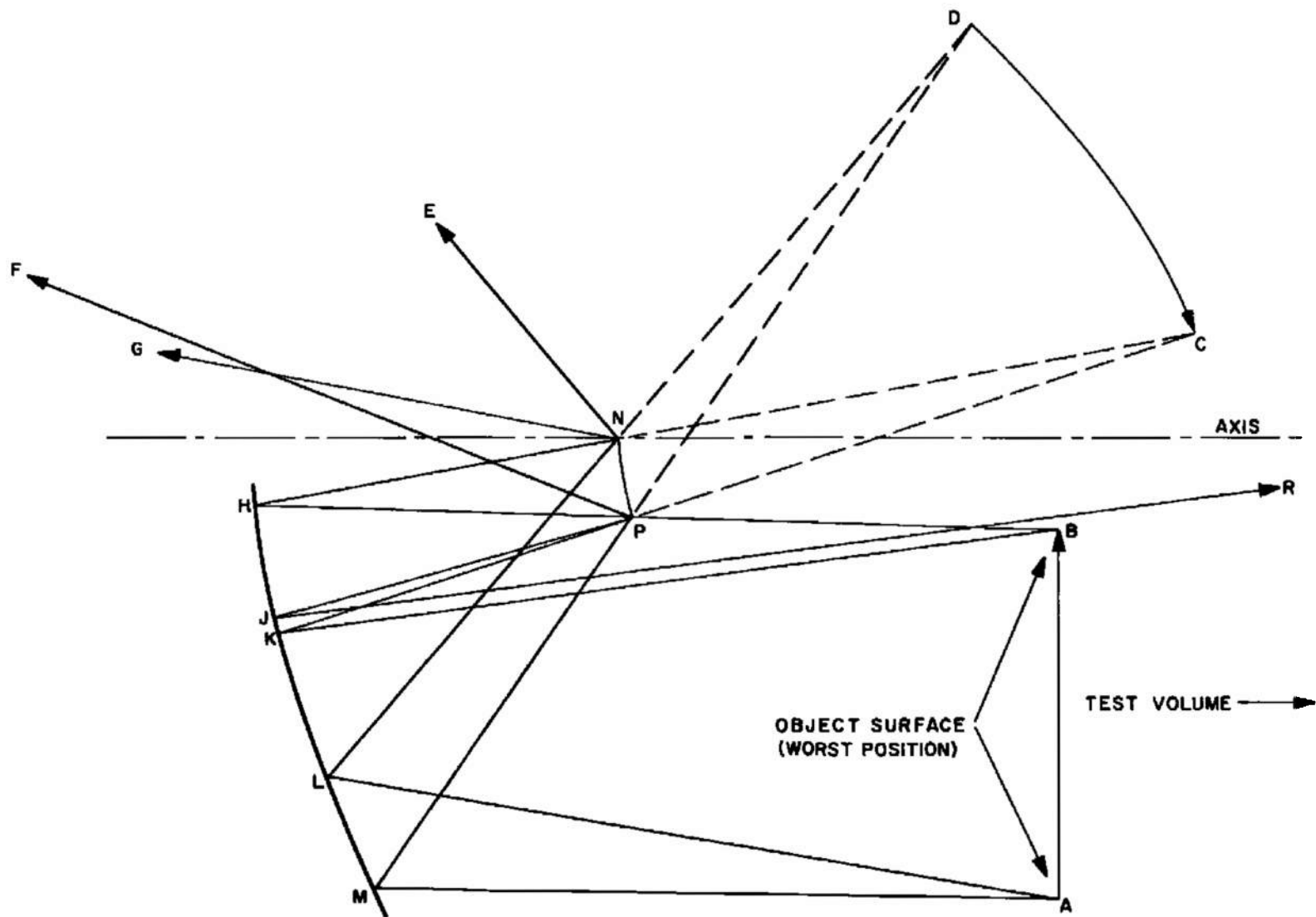


Figure 7-43. Graphical Ray Trace of Re-Reflection by a Cassegrainian System Module

cases of this type were considered, rays were traced from points A and B which are slightly outside of the test volume. These points are imaged at points D and C, respectively.

In the case where light is reflected from the point A to the paraboloid (figure 7-43), only those rays between the rays AMPF and ALNE will be incident upon the hyperboloid. Because both of these rays are then reflected away from the paraboloid toward the walls of the test chamber, it is apparent that no radiation from the point A can be returned to the test volume.

The two extreme rays from the point B incident on the hyperboloid follow the paths of rays BHNG and BKPJR. It can be seen from these ray paths that part of the radiation from B is re-reflected to the paraboloid by the hyperboloid with the remainder reflected toward the walls of the test chamber. That part which is re-directed after striking the paraboloid a second time can enter the target volume in a multi-module array. However, these paths, if they exist at all, are limited to the very edges of the hyperboloidal reflectors and can contribute only negligible re-reflected energy since most of the latter is vigneted by the hyperboloid itself.

It is reasonable to conclude that little, if any, measurable radiation can be returned to the test volume by off-axis Cassegrainian modules from virtually any source of light originating in that volume. Although it is possible to select some very limited extreme cases which provide possible return paths for the radiation, from and to the test volume, the energy which could be channeled through these very narrow limits is quite negligible.

7.7.2 On-Axis Collimators

The following treats the question of what flux-density variations may result from flux being reflected from a test object back to one of an array of on-axis paraboloids, and then being re-reflected by the paraboloid to a spot within the test volume. It is shown that neither a purely diffuse nor a purely specular object offers a significant problem provided the ratio of the target distance to paraboloid focal length is substantial, e.g., greater than 20; and it is concluded that partially specular objects will not offer a problem.

Case 1. Diffuse Object — Figure 7-44.

From the Paraboloid. If the test object is a Lambertian reflector its brightness is independent of the viewing angle, and hence its effect on secondary reflections is independent on the form of the surface. That is, a spherical segment or a plane of the same projected contour

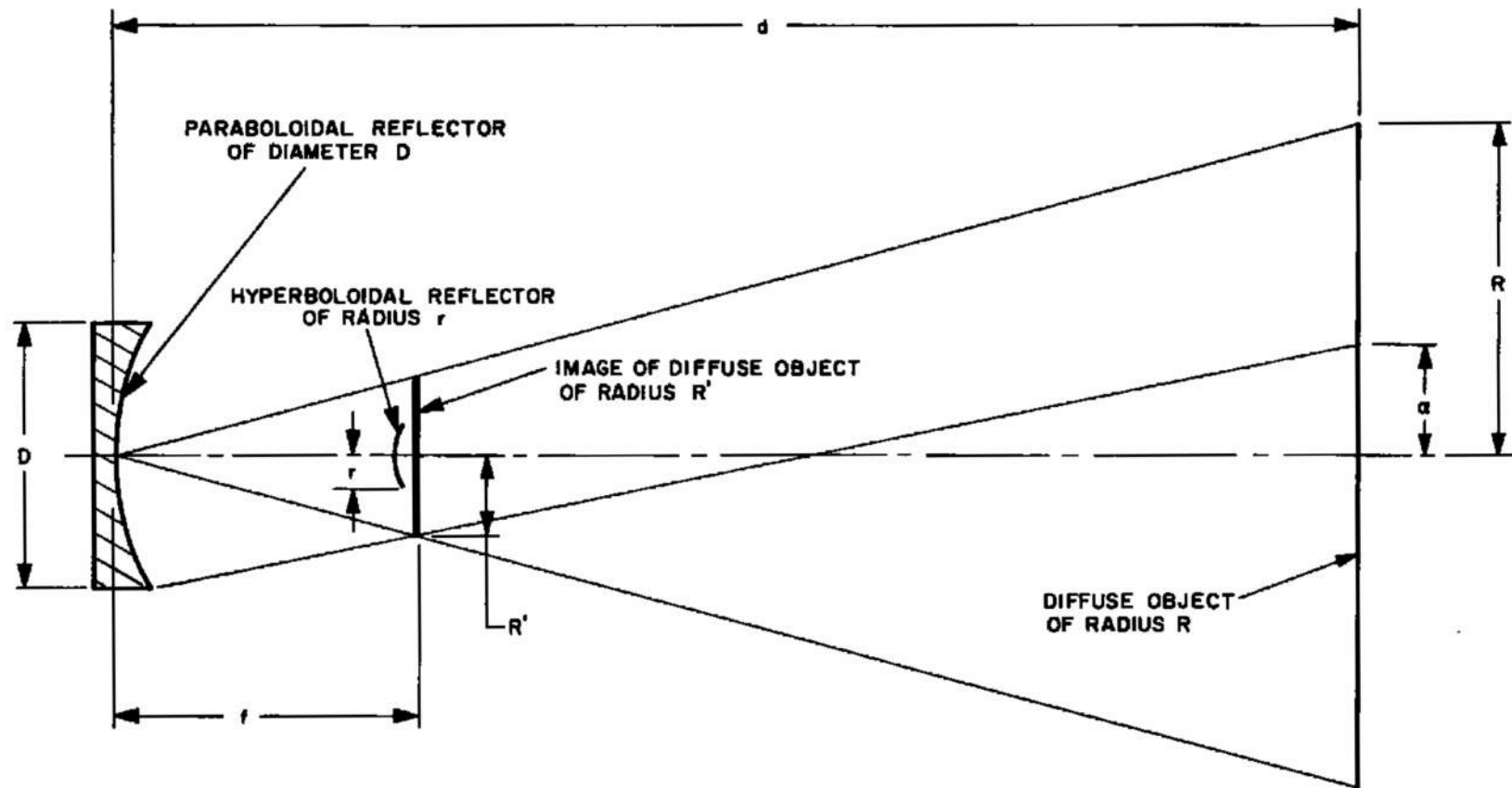


Figure 7-44. Case 1 - Diffuse Object

will have exactly the same effect so long as the sagitta of the spherical segment is small with respect to the distance to the solar simulator.

Consider a flat circular object of radius R , reflectivity k_1 , and distance d from a given module. If it is illuminated with a flux density E watts-per-square-foot, its apparent brightness as seen from above is

$$B = \frac{k_1 E}{\pi} \frac{\text{watts}}{\text{ft}^2 \times \text{steradian}} \quad (7-320)$$

The object appears to the paraboloid of a given module as a prime radiator of brightness B , and will be imaged near the focal plane of the paraboloid, as a disc of radius

$$R' = \frac{f}{d} R \quad (7-321)$$

where f is the focal length of the paraboloid. The flux will pass through the image and back into the test volume. For simplicity the effects of the obscuration by the hyperboloid and the hole in the paraboloid are neglected in the following treatment. The results are therefore on the pessimistic side in that respect.

Within a circular area of radius a at the test plane, each point receives energy from every point in the image. Thus, the flux density returned to the object is

$$E'' = B' \Omega \quad (7-322)$$

B' is the brightness of the real image which in turn is equal to the object brightness reduced by the absorption k_2 of the paraboloid.

$$B' = \frac{k_1 k_2 E}{\pi} \quad (7-323)$$

The solid angle is

$$\Omega = \frac{\pi R'^2}{(d - f)^2} = \frac{\pi f^2 R^2}{d^2 (d - f)^2} \quad (7-324)$$

Thus the flux density returned to the area under discussion is

$$E'' = \frac{k_1 k_2 f^2 R^2}{d^2 (d - f)^2} E \quad (7-325)$$

in a typical case, with $d = 21$, $R = 10$, $f = 1$, and a $k_1 k_2$ of 0.7

$$E'' = 0.0004E$$

(7-326)

Outside the area of radius a there is a penumbra in which the returned energy is less. With respect to a multi-modular array, the effect just calculated for a module directly in front of the target point, may be observed to a diminishing degree in modules farther removed from this position. Because of the combined effects of vignetting and foreshortening, it is not unreasonable to assume that the size of the virtual image is in inverse proportion to the number of modules displaced from the center module, at least for the first several rows. Beyond these rows, the effect of foreshortening diminishes the size of the virtual image, and thus the energy returned, to an even greater degree.

For an order of magnitude calculation, suppose the third circular row from the center module diminished the apparent re-reflected image due to vignetting and foreshortening by a factor of about $1/3$ which is a reasonable assumption. The first row factor would then be about $7/9$, the second row, $5/9$, the third, $3/9$, the fourth $1/9$, etc. The energy delivered would then follow roughly the sequence $3/4, 1/3, 1/10, 1/100$ --. The first row has six modules and therefore multiplies the effect by a factor of four. The second row has twelve modules and therefore also adds in another factor of four. The third row has 18 modules and therefore contributes a factor of 1.8, the fourth has 24 modules and a factor of 0.24 and so on. The sum is convergent to a value of approximately 10 and it is logical to conclude that the effect calculated for one module must be multiplied by a factor of about 10 for the entire modular array. On the basis of the previous result, it may be concluded that the returned energy from the array from a diffuse target is given by

$$E'' = 0.004E$$

From the Hyperboloid. In this situation equations (7-322) and (7-323) still hold, however the solid angle is that which is subtended by the hyperboloid at the paraboloid. This is because the paraboloid images the diffuse target at or near the hyperboloid which therefore contributes negligible optical magnifying power. This also limits the field so that this effect can only be observed in those modules or that module directly in front of the target point in question. The hyperboloid of radius r , which is near the focal point of the paraboloid, then becomes the target for reimaging by the paraboloid. Thus, with an r/f of about 0.2 (again taking $k_1 k_2 = 0.7$) one has

$$\Omega = \frac{\pi r^2}{f^2} = 0.126$$

(7-327)

and

$$E'' = \frac{k_1 k_2 r^2}{f^2} \quad E = 0.028E \quad (7-328)$$

Case 2. Specular Object — Figure 7-45

From the Paraboloid. In the case of a specular object, first consider a flat object tilted so that it reflects energy originating at module A to module B. Since the energy is initially collimated and the object is flat, module B forms an image of the original object at its focal plane. This image has a brightness $B' = kB$ and a radius R' , equal to the size of the virtual image of the hole in the paraboloid formed behind the hyperboloid. It is equal to the tangent of the collimation half angle times the focal length of the paraboloid.

The flux density received by the test object initially was

$$E = B\Omega \quad (7-329)$$

where Ω is established by the finite size of the source, (i.e., the total angle in the collimated beam). Assuming a solar field half angle of about 2° ;

$$E = \pi B (0.035)^2 \quad (7-330)$$

With the secondary reflection the solid angle is

$$\Omega' = \frac{\pi R^2}{(d - f)^2} \quad (7-331)$$

then

$$E'' = k_1 k_2 B \cdot \frac{\pi R^2}{(d - f)^2} \quad (7-332)$$

or

$$E'' = k_1 k_2 \frac{R^2}{(d - f)^2 (0.035)^2} E$$

With an R' of approximately 0.03 feet, and a $(d-f)$ of 20, with $k_1 k_2 = 0.7$ as before,

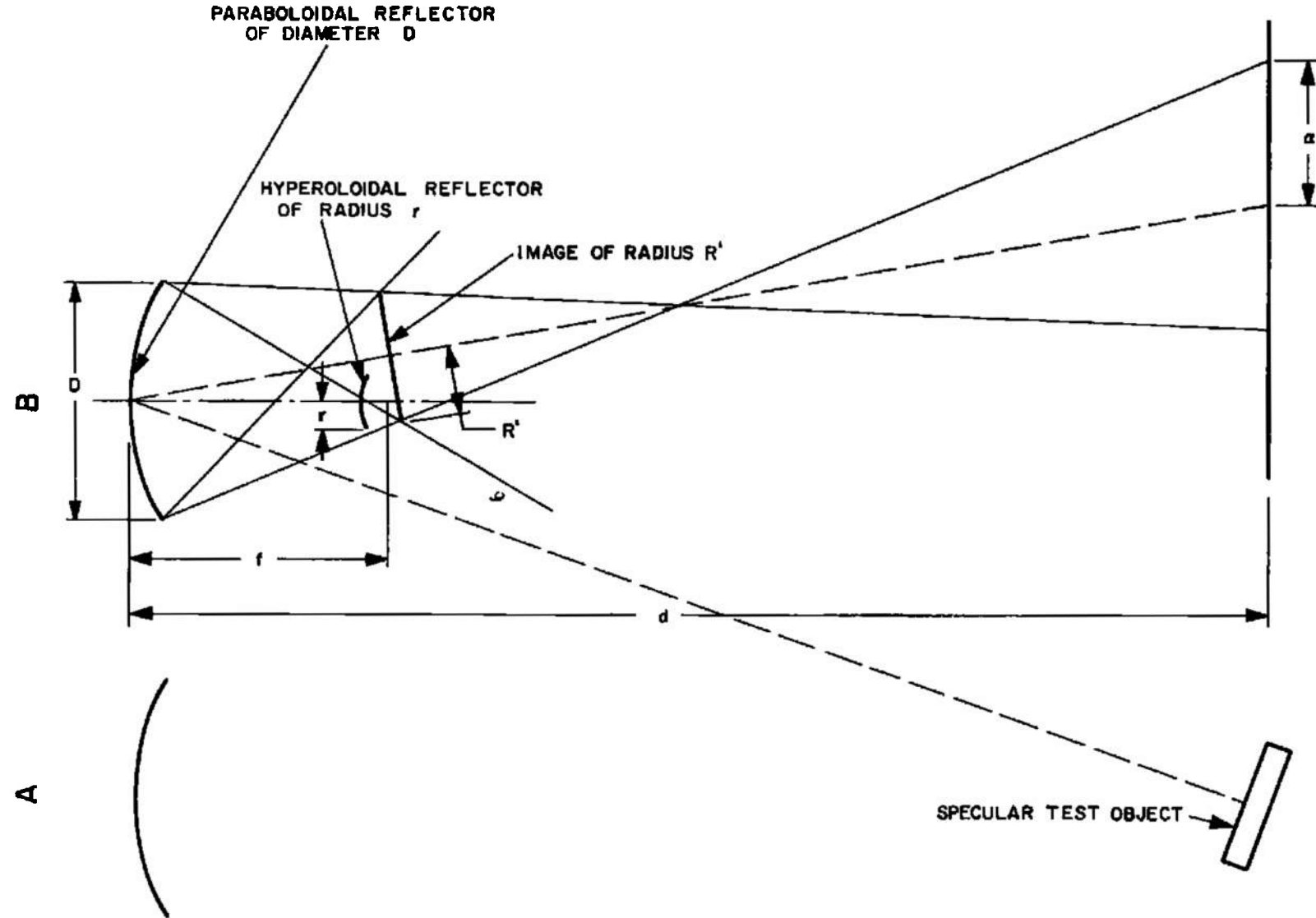


Figure 7-45. Case 2 - Specular Object

$$E'' = \frac{0.7 \times 0.0009}{400 \times 0.00123} E = 0.00126E$$

In this case the same effect could be observed from the paraboloids alone of a multi-modular array as was seen in the diffuse case. It would, therefore, again be a fair approximation to the real case to multiply the result just obtained by about 10, giving the result

$$E'' = 0.0126E$$

From the Hyperboloid. In this case the paraboloid will form the same image as in the previous case; however, it is now interrupted by the hyperboloid. Therefore the hyperboloid will reimagine the hole in the paraboloid back onto the paraboloid. Since the latter contributes no power when the image is at its surface, the solid angle subtended by the re-reflection is the same as that subtended by the hole in the paraboloid.

The result is nearly the same as above except that

$$\Omega' = \frac{\pi r^2}{d^2} \quad (7-333)$$

$$E'' = k_1 k_2 k_3^2 \frac{r^2}{d^2 (0.035)} E \quad (7-334)$$

and the dissipation is greater by the absorption at two reflections. Then the k products will be about 0.54. Then if $r = 0.0278$, figure 7-45,

$$E'' = \frac{0.54 \times 0.0278}{440 \times 0.00123} E = 0.0277E$$

The only danger from overlap would be in the diffuse case. This would still be negligible for reflections off the paraboloid. However, in reflections from the hyperboloid it may be possible to see two or three modules reflecting light from their respective hyperboloids when the line of sight lies on the boundary between the modules. In any case, when this happens the reflections seen will be so vignetted that the total appearance will be little more than that of one module. The returned energy may then go as high as 3 or 4 percent.

It is concluded that the ratio of throw distance to primary collimator focal length must be 20 or better in order to reduce the returned energy from any target to less than about 3 or 4 percent for on-axis collimators. In the case of off-axis collimators, the returned energy is either negligible or non-existent when it is sufficiently far off-axis that the module edge normals lie outside the target region. Although

the average return of energy to the target volume may be only a few percent for a throw factor of 20, it may still be possible to experience a local accumulation of energy due to considerable non-uniformity of the returned radiation. This may possibly result in re-reflection "spots" as high as 10% of the primary radiation intensity, assuming accumulations of a factor of 3 over the average returned intensity. It is believed that this represents the worst possible situation for these parameters.

SECTION 8

CONCLUSIONS

8.1 SOURCE DATA ANALYSES

8.1.1 Radiance

8.1.1.1 Vortex Stabilized Radiation Source (Giannini Scientific Corp.)

Using the coordinate system defined in Figure 5-1, the relative radiance, I_ϕ , of the VSRS may be considered circularly symmetric about the polar axis (i.e., independent of θ). It may be expressed to a good approximation as a function of ϕ by a series of straight line segments

as follows, where $\bar{I}_\phi = \frac{I_\phi}{I_{90^\circ}}$, and ϕ is expressed in degrees:

For the basic VSRS:

$$\bar{I}_\phi = \frac{0.07}{3} (\phi - 23.5714), \quad 30^\circ \leq \phi \leq 45^\circ$$

$$\bar{I}_\phi = \frac{0.1}{9} \phi, \quad 45^\circ < \phi \leq 90^\circ$$

$$\bar{I}_\phi = \frac{0.007}{3} (\phi - 338.5714), \quad 90^\circ < \phi \leq 135^\circ$$

For the modified VSRS (conical reflecting cathode):

$$\bar{I}_\phi = \frac{0.07}{3} (\phi - 23.5714) \quad 30^\circ \leq \phi \leq 45^\circ$$

$$\bar{I}_\phi = \frac{0.1}{9} \phi \quad 45^\circ < \phi \leq 100^\circ$$

$$\bar{I}_\phi = 0.015 (\phi - 26) \quad 100^\circ < \phi \leq 120^\circ$$

8.1.1.2 Fluid Transpiration Arc (Vitro Laboratories).

The relative radiance, \bar{I}_ϕ , of the Fluid Transpiration Arc as a function of the angles ϕ and θ (see figure 5-1) is rough hemispherical, i.e., independent of both ϕ and θ within a hemispherical volume. To a closer approximation, the relative radiance for the FTA may be considered independent of θ (circularly symmetric about the polar axis)

and may be described within the hemisphere as a function of ϕ by

$$\bar{I}_\phi = 0.9236 + 0.0764 \cos \phi$$

where $\bar{I}_\phi = \frac{I_\phi}{I_0}$ and ϕ is expressed in degrees.

8.1.1.3 High Intensity Carbon Arc (RCA Service Co.)

As a rough approximation, the relative radiance, \bar{I}_ϕ , of the High Intensity Carbon Arc may be considered to be independent of θ and to vary with ϕ according to

$$\bar{I}_\phi = \cos \phi$$

where $\bar{I}_\phi = \frac{I_\phi}{I_0}$

8.1.2 Radiative Efficiency

All three sources operate with approximately the same radiative efficiency (ranges between approximately 20% and 30% as a function of input power).

8.1.3 Spectral Distribution

8.1.3.1 Optical Materials.

In order for the output spectrum of the solar radiation simulation system to match with reasonable efficiency the solar spectrum between 0.2 micron and 3.0 microns in accordance with Spectral Criterion II, the reflective surfaces in the optical system should be evaporated aluminum and the refractive components of the optical system should be fabricated of Infrasil or equivalent. (Information received from General Electric's Willoughby Quartz Plant, Willoughby, Ohio, indicates that they manufacture two types (105, 106) of optical grade fused quartz whose transmittance is comparable to that of Infrasil.) This conclusion is based on the close spectral match required by Spectral Specification II A between 2.00 and 3.00 microns, which specification, in effect, prohibits the use of other types of fused silica because of the absorption bands which occur in the vicinity of 2.20 and 2.80 microns. However, consideration of these same materials in terms of Spectral Criterion III (which was defined on the basis of approximately equal energy bands in the solar spectrum) leads to the conclusion that a spectral specification based on a consideration of such energy bands, will relax the requirements between 2.00 and 3.00 microns since only 5.78% of the energy in the solar spectrum occurs

at wavelengths larger than 2.00 microns. In this case, the refractive components could be fabricated of any type of optical grade fused silica (fused quartz) without greatly affecting the dissipative efficiency, so long as the transmittance in the ultraviolet is maintained and the type chosen does not discolor when subjected to intense ultraviolet radiation.

8.1.3.2 Source, Optical-System Configurations.

The unfiltered spectral distribution of none of the source, optical-system configurations evaluated meets the spectral match criterion adopted for this study (See Spectral Criterion III, Section 5.3.1), however spectral filtration to achieve a match to this criterion is feasible for any of the sources studied. The penalty, in increased system complexity and cost, and in reduced efficiency, is a direct function of the spectral criterion adopted. This penalty increases rapidly as the percentage deviation allowable is decreased, or as the number of bandwidths into which the spectrum is divided and within which the average deviations are to be calculated, is increased. Using the criterion adopted for this study, in which the match to the "Johnson Curve" is specified to be within 8% for any of nineteen contiguous wavelength bands between 0.2 and 3.0 microns, all of which contain approximately equal fractions of solar energy, the maximum efficiency with which the source spectrums can be filtered to provide approximate spectral match ranges from 46% to 49% for the 35-kilowatt Carbon Arc; from 54% to 56% for the 29.1-kilowatt Fluid Transpiration Arc; and from 27% to 29% for the 37.5-kilowatt Fluid Transpiration Arc. The data provided for the Vortex Stabilized Radiation Source does not permit analysis in terms of Spectral Criterion III. Maximum efficiencies with which the 100% Argon VSRS can be filtered to provide spectral match to the sun vary from 51% to 72% depending on the input power level and operating pressure. These efficiency figures, however, are not directly comparable to those given here for the High Intensity Carbon Arc and the FTA because of the differences in the spectral criterion applied. (See text, Section 5.3.3 for details).

8.2 OPTICAL SYSTEM CONCEPTS

8.2.1 Hexagonal Array of Projectors

It is theoretically possible to obtain, in a finite volume, a prescribed level and uniformity of intensity using modules of the uncollimated projection type, if a number of definite conditions are rigidly observed. The degree of uniformity is a function of the number of modules which illuminate a given target point. However, the insertion of numerical values into the defining equations indicates that, for the sources studied, the field angle and intermodule spacing required to

achieve the desired average intensity with a reasonable aperture size results in both an unrealistically large separation between the target and the array and an overly large array diameter, if sufficient modules are to be seen from the target volume to produce reasonable uniformity. One expedient which may reduce array and test chamber dimensions to acceptable values, at the expense of increased modular complexity, is to have each source serve a number of projectors, thereby reducing the intermodule spacing and, hence, the array-target separation required for uniformity.

8.2.2

Hexagonal Array of Paraboloids or Modules Consisting of Conic Section Reflectors.

Both the simple paraboloid module and a train of conic section reflectors possess an inherent non-uniformity characteristic which grows with basic module efficiency. This non-uniformity is mitigated somewhat as the distance to the target increases. It is possible to compensate, to a certain extent, the inherent intensity distribution in the module aperture by using a source which has an appropriate radiance function. Conversely, the situation will be worsened if the radiance distribution is opposite to the desired characteristic. A spherically symmetric radiance distribution is neutral in this respect. The results for the High Intensity Carbon Arc are (because its radiance is approximately a cosine function) relatively poor and eliminate it from further consideration in optical systems of this simplicity. The Fluid Transpiration Arc (FTA) appears to provide a reasonably acceptable set of parameters but leaves little or no room for improvement upon a $\pm 10\%$ uniformity tolerance criterion. It may be expected that this source could provide average performance on all counts except field angle, where its match to that actually subtended by the sun is exceptionally good. However, due to the physical geometry of the FTA and the supporting apparatus which must accompany it, it is not likely that the FTA can be employed with an optical system consisting of a simple parabolic reflector since it would tend to block a great deal of the collimated radiation. It may, however, be used with an appropriate series of conic section reflectors, so defined as to minimize the central hole and to provide optimum collection and transfer of the radiation, which will result in performance characteristics comparable to those determined for a simple parabolic reflector except for a compromise factor of about 55% in transfer efficiency. It may be concluded then that if the performance cited herein were acceptable, further detailed study would be justified and a workable system could be designed.

The Vortex Stabilized Radiation Source has displayed singular meliority in its application to a system of either single parabolic reflectors or modules consisting of trains of conic section reflectors.

The tendency for its radiance to increase in magnitude with angle from the axis is advantageous to this design, from the uniformity standpoint, and makes it the best of the three sources for use in this type of system. The relatively high efficiency of the VSRS, when used with a simple parabolic reflector, makes it possible to consider certain sacrifices in efficiency in order to improve the uniformity. However, the extent to which this is possible must be determined by further, more detailed study (which certainly seems to be indicated in this case), provided consideration of other factors would also warrant such action, such factors having to do with the desirability of operating a lamp inside the vacuum vessel, taking into account such things as heat load, mechanical convenience, operational factors, lamp exchange, repairs and others as may occur in a total system problem review.

8.2.3 Modified Conic Section Systems

8.2.3.1 Fresnel Collector.

Use of a Fresnel ellipsoid as a means of eliminating coma in the very fast collection optics is not feasible because of its grossly inefficient collection of the source radiation.

8.2.3.2 Multi-faceted Transfer Systems.

Multi-faceted transfer systems of the reflecting (pebble bed) or refracting (multi-faceted relay lens) type, are effective ways of smoothing the distribution of radiation from a solar simulator by breaking up the radiant field and redistributing it over the aperture of the collimator. For this purpose the multi-faceted relay lens is preferable to the pebble bed reflector. Insertion of a multi-faceted component does result in a loss in efficiency, as well as an increase in the field angle subtended by the simulated "sun".

8.2.3.3 Source Aperture Conjugation.

This concept, in which the contributions of many sources, or one source broken up into many pieces, are combined at a single aperture stop plane to illuminate a pseudo-source which is then mapped onto the collimator, is theoretically feasible. It is best used, however, in systems where many sources are used per module to cover large areas of the target field. The complexities involved in breaking up and recombining the radiation from each source of a one-source-per-module system are not warranted by the advantages to be gained.

8.2.3.4 Insertion of Intermediate Condenser Lenses.

Significant improvements in uniformity, with modest gains in efficiency, may be obtained by use of intermediate condensing lenses with the basic conic section system. However, the optimum lens design is extremely difficult to realize, and requires compromises, particularly near the axis of the system, and does not readily permit total compensation for non-uniformities.

8.2.3.5 Aconic Reflector Systems.

The most promising optical system concept by far, from the standpoint of both compensation for uniformity of intensity in the target volume and total system efficiency, is one consisting of aconic (modified conic section) reflectors used in conjunction with a single relay lens. This system is capable of meeting all performance requirements with any of the sources studied. For the three sources studied, this concept would in all likelihood take the following forms:

VSRS - Single modified ellipsoidal collector, simple relay lens, and a modified Cassegrainian collimator.

FTA and High Intensity Carbon Arc - Two-element collector consisting of two modified conic section reflectors, a relay lens, and a modified Cassegrainian collimator.

It appears that the aconic mirror surfaces required are as amenable to fabrication as the conic section reflectors which they replace. Collection is possible through the same, or nearly the same angles as is possible with any other expedient. Elimination of an intermediate condenser lens system would increase the overall module efficiency by better than 40% since such condensers generally require at least three components. Solar simulation modules using condenser lens systems and short arc lamps have achieved efficiencies as high as 15% while realizing nominal uniformity performance. With the elimination of the condensers, a system of aconic reflectors designed for use with a short arc lamp could realize an efficiency on the order of 21%, a level unprecedented in solar simulator optical designs. Similarly increased efficiency would result for systems designed for use with other sources. A further advantage lies in the fact that this type of optical system can be designed, for any given source, to exactly satisfy the theoretical requirements for uniformity.

8.2.4

Comparison of Efficiencies of Various Optical Systems

Although much of this has already been discussed in the several sections on each system type, there are a number of points which may be reviewed for emphasis and clarity. To do this, consider the basic conic system as one containing several mirror elements and one lens, as opposed to the single parabolic reflector which may be considered an oversimplification in the practical sense. The latter was capable of reasonably high efficiency for some particularly suitable lamps with certain attendant compromises in uniformity specification. For example, the VSRS with a nominal $\pm 10\%$ uniformity provided an efficiency somewhat above the 10% using the single-mirror simple conic concept.

In a practical system, however, at least three reflective surfaces and one lens would be required. Assuming 85% reflectivity for mirrors and 90% transmission for lenses, the VSRS would, after consideration of transmission efficiency, provide a system efficiency lowered to about 6.6%. Thus, the number and nature of the components begins to mean a great deal as far as operating efficiency is concerned.

Much of the sacrifice in total system efficiency for the simple conic system is due to the limited collection, held down by uniformity considerations. Although this is not borne out in practice, it would appear theoretically possible to obtain a similar level of uniformity performance with the added advantage of almost total collection when condenser lenses are inserted in the optical train. Taking the VSRS again as an example, four lenses and three mirrors would be required. A collection efficiency of about 85% and approximately 40% transmission efficiency may be assumed. With the typical electrical conversion efficiency of 28%, the total system efficiency is about 9.5%. An arbitrary safety factor of about 90% for other losses, including vignetting which, of course, must be minimized, brings the value to 8.55%. This is not much better than the basic practical conic section system itself. The efficiency improvement for the FTA and High Intensity Carbon Arc would be somewhat better in the last calculation since the basic conic section system is considerably less efficient for these sources than for the VSRS. However, the collection improvement for these single-ended arcs, using condensers, would be about the same as for the VSRS. Thus, the insertion of condenser lenses brings the system efficiencies for the FTA and VSRS to about the same level by really improving the FTA and leaving the VSRS the same. The electrical conversion efficiency for the High Intensity Carbon Arc, considering only the useful part of the arc radiation, is about the same as for the other sources (23%). However, in the High Intensity Carbon Arc, a collection factor of about 75% would be the maximum achievable on a practical basis. With four mirrors and four lenses one might obtain a 34% transmission efficiency and therefore, 25.5% optical efficiency. This indicates a total system efficiency for such a system utilizing the High Intensity Carbon Arc of about 5.9%.

Now, if the use of a multi-faceted relay lens instead of the condensers is considered, then a transmission factor (72%) of three lenses is eliminated. Assuming that the advantage in basic collection efficiency is the same for both the condenser and pebble bed or multi-faceted alternatives, then only their respective transmission values need be considered. It was seen that the condensers impose a transmission factor of 72%. A multi-faceted lens, aside from its glass transmission factor which we shall assign to the relay transmission already included,

has numerous interstices which further block the light. Assuming the lens is made oversize to be certain of catching all the light that can fall within its boundaries, it still must consist of individual circular lenses bound together in some manner. They would form a hexagonal array for closest packing. The radius of a circle inscribed in a hexagon is:

$$r = \frac{a}{2} \cot\left(\frac{180^\circ}{6}\right)$$

where a is the length of a side. The area of the hexagon is:

$$A = \frac{3}{2} a^2 \cot\left(\frac{180^\circ}{6}\right)$$

Thus, the ratio of area of the lens to that of the space it occupies is:

$$\frac{\pi}{6} \cot 30^\circ = 0.91$$

There would have to be some space between the lenses for mounting and they would necessarily have a finite edge thickness, introducing vignetting losses at each lens boundary; the former is a factor of at least 95% and the latter must be at least 90%. This brings the transmission total to about 77%. The latter is an optimistic estimate, at best, and is little improvement over the condenser alternative.

The multi-faceted lens has the added advantage over the condenser design that it does not introduce chromatic aberration, as do the condensers to a serious degree. The multi-faceted lens could, however, be difficult to construct for the heat loads required. A second relay lens would be required for the vacuum seal, bringing the transmission of the lenses down to about 69% which would then be somewhat under the condenser lens alternative. In any case, because of the severe chromatic aberration which a condenser system will introduce, resulting in spectral inhomogeneity in the final beam, it is possible that the multi-faceted approach is to be preferred if it can be realized in practice for large scale simulators.

The greatest improvement in efficiency is provided by the system of aconic reflectors. Here the greatest collection efficiency can be obtained and utilized. Also, the condenser lenses or vignetting multi-faceted lenses are eliminated, thereby immediately realizing a 30% to 40% improvement in optical efficiency. Since the aconic optical system is a three-mirror, one-lens system for the two-ended source, and a four-mirror, one-lens system for the single-ended sources, the predicted system efficiencies for the three sources using this system are:

VSRS - $(0.85)^3 (0.9) (0.85) (0.28) (0.9)$ = 11.8%

FTA - $(0.85)^4 (0.9) (0.85) (0.30) (0.9)$ = 10.8%

High Intensity Carbon Arc -
 $(0.85)^4 (0.9) (0.75) (0.23) (0.9)$ = 7.3%

8.2.5 On-Axis versus Off-Axis Collimators

The specification of an on-axis or off-axis collimator for the desired solar module is largely a matter of application. For any of the systems described above, an on-axis design would be more straightforward and economical to design and fabricate; however, with an off-axis collimator type of module, re-reflections to the test volume are much less significant and can, in fact, be eliminated entirely, if sufficient target throw distance is available. If the application requires that these re-reflections be reduced to an absolute minimum for any test item configuration, then an off-axis design is dictated. On the other hand, if re-reflections of the order of 2% to 3% of the incident intensity level for certain worst case test item configurations can be tolerated, then an on-axis design will perform adequately and well.

8.3 RECOMMENDATIONS.

Regardless of the choice of source, the aconic optical system (in which compensation is achieved wholly through modifications to conic section reflectors) will provide the optimum in performance, and is therefore strongly recommended. Data provided concerning the radiation and operational characteristics of the three sources are insufficient to permit a conclusive objective recommendation of one source over another, although from the limited data available, the radiation characteristics of the VSRS and the FTA make them appear somewhat more desirable than the High Intensity Carbon Arc.

Because the recommended optical system concept may be equally well adapted to any source whose radiance distribution is reasonably stable and axially symmetric, the selection of a source may be made virtually independent of optical design considerations. It is, therefore, recommended that the source selection be based on such factors as stability of operation, reliability, availability, maintainability, and cost, both of production and operation. Once an evaluation of these factors has permitted the selection of a source, it is recommended that additional effort be invested in a comprehensive study of the characteristics of the chosen source, following the procedures delineated in Section 5. This study should be completed before any significant effort is spent on a detailed optical system design.

Finally, and also prior to initiation of a detailed optical system design, it is recommended that the performance requirements be carefully reviewed with potential users of the facility. The objective would be to establish specifications which define performance to a level at least adequate for all foreseeable tests, but which avoid the demand of performance to a level which significantly increases the cost without a comparable increase in usefulness of the facility. The area of spectral distribution is one where such a consideration is especially important.

REFERENCES

1. U.S. Air Force, Handbook of Geophysics, MacMillan, 1960, Table 16-8, "Spectral Irradiance Normal to the Sun's Rays Outside the Atmosphere", Page 16-16.
2. Max Planck, The Theory of Heat Radiation, New York: Dover Publishers, 1959, article 98.2 and Chapter IV.
3. Max Born and Emil Wolf, Principles of Optics, London, New York: Permagon Press, 1959, Chapter 3, 1.2.
4. W.W. Wallin, "Design of Special Projector Illuminating Systems", Journal of the SMPTE, October 1962 (Vol 71).
5. Francis A. Jenkins and Harvey E. White, Fundamentals of Optics, New York: McGraw-Hill Publishing Company, 1957, page 135, equation (9k)
6. Arthur C. Hardy and Fred H. Perrin, The Principles of Optics, New York: McGraw-Hill Publishing Company, 1932, Chapter 19, Section 146, "The Distribution of Light in Optical Systems" also, Francis A. Jenkins and Harvey E. White, Fundamentals of Optics, page 111, Equation (7k).
7. Murphy L. Dalton, "Slit Introduced Errors in Pressure Broadened Line Measurements", Applied Optics, Nov. 1963, Vol 2, page 1195.
8. Richard M. Warner and F. Nelms, Radiation Characteristics of a High Power Level Carbon Arc, Technical Documentary Report No. AEDC-TDR-64-202, October 1964.
9. American Institute of Physics Handbook, New York; McGraw-Hill Publishing Company, 1957 Ed., Table 6k-4, page 6-108.
10. D.G. Van Ornum, Study of Radiation from Vortex Arcs, Technical Documentary Report No. AEDC-TDR-64-165, August 1964.
11. Francis A. Jenkins and Harvey E. White, op. cit., page 152, 9.11.

APPENDIX I

COMPUTER PROGRAMS FOR OPTICAL DESIGN AND ANALYSIS

Several computer programs were utilized during the study described herein. The function which each program served and a brief discussion of the basic principles under which each operates is given below.

General Optical Raytrace Program (RAYTRACE)

One of the most basic tools of optical design and analysis is the geometrical raytrace. Much information can be gained concerning the behavior of an optical system by applying this procedure and it has been used as the basis of many of the analytic techniques which have been formulated. Therefore, a computer program (RAYTRACE) has been developed which will compute the path of a skew ray through a generalized optical system in accordance with the following considerations:

1. A given ray is specified by the coordinates x_o , y_o , z_o) of a point through which the ray passes and by its direction cosines $(\alpha_o, \beta_o, \gamma_o)$ in a reference coordinate system.
2. Each optical surface may be specified as being of one of the following types:
 - a. Paraboloid
 - b. Hyperboloid
 - c. Hemi-ellipsoid of revolution about major axis
 - d. Hemi-ellipsoid of revolution about minor axis
 - e. Hemisphere
 - f. Aicon (cone of revolution)
 - g. Toric
 - h. Cylinder

The program also contains a provision for specifying departures (deformations from these forms in order to accomodate the general aspheric case.

3. Each optical surface may be specified, with relative ease, in any arbitrary position and orientation.
4. At each surface, the ray may undergo reflection or refraction.
5. New surface types can be incorporated without making major modifications in the logical structure of the program.

6. As output, the program provides the coordinates (x_f, y_f, z_f) of the intersection of the ray with the last surface of the optical system, its final direction cosines $(\alpha_f, \beta_f, \gamma_f)$ in the coordinate system of the last optical surface, and the total optical path length of the ray from (x_o, y_o, z_o) to (x_f, y_f, z_f) . Alternatively, if the ray is vignetted somewhere in the optical system, the program provides the appropriate information.

Energy Trace Program (ENERGY)

To facilitate the analysis of the performance characteristics of specific solar radiation simulator designs, a computer program (ENERGY) has been developed, in accordance with the technique of energy tracing discussed previously, which serves to calculate the relative flux density at arbitrarily specified positions due to a finite extended incoherent light source in a generalized optical system. In making this computation, the source is represented (as discussed previously) as a series of successively contained Lambertian surfaces, the radiation from each of which may propagate outward through successive surfaces but not inward through its own boundary, and the General Optical Raytrace Program is used as a subroutine in order to generate the optical system.

ENERGY calculates the relative flux density at each specified position in the optical system by numerically evaluating equation (4-105). For this calculation, equation (4-105) is expressed as

$$E = \sum_{i=1}^s \sum_{j=1}^m \sum_{k=1}^n B_i \sin^2 \phi_j \sin \theta_k \Delta\phi \Delta\theta$$

where E is the relative flux density on an element of area at the specified position, B_i is the relative brightness of the i^{th} surface of the source representation, s is the number of surfaces of the source representation which are intersected by a ray traced from the specified position in the direction (ϕ_j, θ_k) , and m and n are, respectively, the number of increments of $\Delta\phi$ and $\Delta\theta$ into which the specified ranges of ϕ and θ are divided. ϕ and θ are the direction angles of a spherical coordinate system (ϕ being measured with respect to the polar axis) which is centered at the specified target position and whose polar axis lies in the plane of the target element of area (θ being measured with respect to this plane). The ranges of ϕ and θ must be specified such that the solid angle defined by these ranges includes all of the radiant energy from the source which is incident upon the target element of area. Within their respective ranges, ϕ and θ are incremented so that

$$\phi_{j+1} = \phi_j + \Delta\phi$$

$$\theta_{k+1} = \theta_k + \Delta\theta$$

ENERGY also plots the brightness distribution seen across the field subtended by the source at the specified target position.

If the optical system is free of chromatic aberration, the source parameters may be defined on the basis of the spectrally integrated relative brightness distribution. Since the energy transfer characteristics of the optical system are, in this case, independent of spectral considerations, the program output data represents the spectrally integrated relative intensity distribution. When the optical system is subject to chromatic aberration, the program output data represents the relative monochromatic intensity distribution and an additional analysis is required in order to determine the spectrally integrated relative flux density at each point. Such an analysis must take into account variations in the monochromatic brightness distributions of the source and spectral variations due to absorption and scattering by the optical system. The spectrally integrated relative intensity values may then be converted to absolute intensity values (watts-per-square-foot) through an efficiency analysis.

Special Purpose Computer Programs

Three special purpose computer programs (PROJT, SPECT, and SOLAR) were developed especially for use in this study. These programs were developed in accordance with the following considerations.

1. PROJT - This program serves to calculate the relative intensity J at various distances D from a hexagonal array of projectors as described in section 7.3. Defining θ as the field half angle into which each projector radiates, R as the radius of the circle in the plane of the array which contains all of the projectors which radiate to a given target element and A as the distance between adjacent projectors in the array, the parameter J is calculated according to the following equation (see equation 7-99)

$$\begin{aligned}
 J = & \left\{ \frac{1}{\gamma^3} + 2\gamma \sum_{i=1}^n \left(\frac{1}{\gamma^2 + i^2} \right)^{\frac{3}{2}} \right. \\
 & + 32\gamma \sum_{h=1}^u \sum_{k=1}^v \left[\frac{1}{4\gamma^2 + h^2 + 12(k - \delta)^2} \right]^{\frac{3}{2}} \\
 & \left. + 2\gamma \sum_{j=1}^m \left(\frac{1}{\gamma^2 - 3j^2} \right)^{\frac{3}{2}} \right\}
 \end{aligned}$$

where

$$R = D \tan \theta$$

$$\gamma = \frac{D}{A}$$

$$\alpha = \frac{R}{A}$$

$$n = \left(\frac{R}{A}\right)^* = \alpha^*$$

$$m = \left(\frac{R}{A\sqrt{3}}\right)^* = \left(\frac{\alpha}{\sqrt{3}}\right)^*$$

$$u = \left(\frac{2R}{A}\right)^* = (2\alpha)^*$$

$$v = \left(\sqrt{\frac{4\alpha^2 + h^2}{12}} + \delta\right)^*$$

$$\delta = 1/2 \left[\left(\frac{h+1}{2}\right)^* - \left(\frac{h-1}{2}\right)^* \right]$$

In the above equations, the quantities with an asterisk (*) in the exponent position are truncated to integers before proceeding with the computation.

2. SPECT and SOLAR - These computer programs were used (a) to calculate the transmittance of various combinations of optical materials and (b) to generate data from which the maximum efficiency with which each source spectrum can be filtered to match the solar spectrum could be determined. Making the assumption that the radiation is normally incident at each optical surface, both SPECT and SOLAR calculate the transmittance T_i of a given combination of optical materials within a wavelength band $\Delta\lambda_i = \lambda_{i+1} - \lambda_i$ according to

$$T_i = R_i^m \left(e^{-\alpha_i t} \right) \left[1 - \left(\frac{n_i - 1}{n_i + 1} \right) \right]^{2L}$$

where

m = the number of mirrors

R_i = the reflectance of the reflective material within $\Delta\lambda_i$

L = the number of lenses

n_i = the refractive index of the refractive material within $\Delta\lambda_i$

α_i = the absorption coefficient of the refractive material within $\Delta\lambda_i$

t = the total thickness of the refractive material through which the radiation passes.

It is convenient to define A_i as the energy within $\Delta\lambda_i$ of the source (or input) spectrum and E_i as the energy within $\Delta\lambda_i$ of the output (or simulated solar) spectrum. For a given source spectrum and a given combination of optical materials, SPECT calculates the spectrum of the output radiation by evaluating the equation

$$E_i = T_i A_i$$

For a given combination of optical materials, SOLAR calculates what input spectrum is required in order that the spectrum of the output radiation match the solar spectrum by evaluating the equation

$$A_i = \frac{E_i}{T_i}$$

APPENDIX II

SPECTRAL FILTRATION

The optimum technique for achieving the required spectral filtration while simultaneously maximizing the system efficiency is that of parallel filtration. Briefly, the technique of parallel filtration consists of inserting a pattern of small filters at some position in the optical train, the position and pattern geometry being dictated by the final optical system design. Each filter will consist of one or more layers of various materials, the choice of materials, film thicknesses, filter size, etc., being dependent upon the spectral filtration requirements. To illustrate the concept involved, consider the case of a solar radiation simulator whose collimation subsystem is a Cassegrainian system and which has a simple relay lens located at the principal focus of the Cassegrainian system. The "sun" seen from any position in the test volume will be contained within the image of the relay lens seen in the paraboloidal reflector from the same position in the test volume. It may therefore be specified that the filter pattern is to be deposited on the relay lens. Consider further that there are n multi-layer interference filters available, several of which have a transmittance of at least 90% in the bandwidth of minimum filtration. Specify, for the purpose of determining the spectral filter configuration, that the spectrum is to be divided into m wavelength bands, where m is less than n . It is convenient to make the following definitions.

A = A unit of area on the surface of the lens which is so chosen that the intensity of the incident radiation may be assumed to be constant.

F_i = The fraction of the area A upon which filter i is to be deposited.

S_j = Energy in wavelength band j of the solar spectrum.

E_j = Energy in wavelength band j of the source spectrum after being modified by passage through the optical system.

$T_{i,j}$ = Transmittance of filter i in wavelength band j .

F_u = The fraction of the area A upon which no filter is to be deposited and through which unfiltered radiation passes.

k = The number of filters to be deposited within each area A .

By definition:

$$AF_u = A - \sum_{i=1}^k AF_i \quad (II-1)$$

Since A has been chosen small enough that the intensity of the incident radiation may be assumed constant, then the amount of filtration performed by a filter is proportional to its area as well as its transmittance. Therefore, for each wavelength band j ,

$$S_j = E_j \left(F_u + \sum_{i=1}^k F_i T_{i,j} \right) \quad (II-2)$$

Combining equations (II-1) and (II-2) gives the equation

$$Q_j = \frac{S_j}{E_j} = \left[1 - \sum_{i=1}^k F_i (1 - T_{i,j}) \right] \quad (II-3)$$

where Q_j is the fraction of the incident radiation in wavelength band j which must be transmitted. Since the spectrum is divided into m wavelength bands, then there are m independent conditions Q_j which must be satisfied. These m independent conditions may be expressed in terms of m independent parameters (a necessary condition for a solution) by specifying that $k = m$. Then, by applying equation

(II-3) there may be generated $N = \frac{n!}{m! (n-m)!}$ different sets of m equations in m unknowns, one set for each combination of m of the n available filters. It is then possible to perform an analysis to determine which combination(s) of filters will provide the required spectral filtration with maximum transmittance of energy within the bandwidth of minimum filtration. For example, if it is specified that the filter pattern must transmit 90% of the energy in the bandwidth of minimum filtration, this automatically sets the relationship between S_j and E_j (and thus Q_j) for all m wavelength bands of the spectrum. The N sets of m equations can then be solved to determine the conditions under which each (if any) combination of filters must be used to provide the required spectral filtration. Using this technique, it is probable that a filter pattern can be defined whose spectral filtration efficiency is at least 90% of the maximum spectral filtration efficiency.

The term maximum spectral filtration efficiency refers to the condition when the source spectrum, after being modified by passage through the optical system, is filtered to exactly match the solar spectrum in all m bandwidths without removing energy from the bandwidth of minimum filtration. In order to estimate the maximum efficiency with which the spectrum of a given source can be filtered so that a given source, optical-system, spectral-filter combination will reproduce the solar spectrum, it is only necessary to determine, for each source, optical-system combination, a scale factor which, when multiplied by the relative intensity within each bandwidth of the source spectrum, results in a scaled relative intensity value for every bandwidth which is greater than or equal to the relative intensity within the corresponding bandwidth of the required source spectrum calculated for the given optical system configuration. This scale factor relates the energy in the source spectrum to the energy in the filtered spectrum (assuming minimum spectral filtration) and the maximum spectral filtration efficiency is, therefore, the reciprocal of this scale factor.

One immediate objection which can be raised to using the technique of parallel filtration as illustrated by the above example is that neither the filtered nor unfiltered portions of the beam match the solar spectrum. The fact that this objection is not really valid in the case of a solar radiation simulator, provided the pattern of filters deposited upon the relay lens contains many small filters, can be seen by considering the appearance of the "sun" as seen from the test volume. Since the filters will have been deposited in a pattern of many small filters, the relative energy distribution across the aperture of the collimator will not be affected by the insertion of the filter. The "sun", as seen from any position in the test volume, will appear as a disk which subtends the correct field angle and whose surface is covered with many small multi-colored spots. However, since any position in the test volume will see the complete solar disk, and since the correct balance between the energy levels of the filtered and unfiltered spectrums has been achieved by the filter, the spectrum of the energy incident at any position in the test volume will match the solar spectrum, both in intensity and distribution.

In the preceding example of parallel filtration, the filter pattern was located at the primary focus of the collimation subsystem in order to illustrate the fact that, even if an image of the filter pattern could be seen from the test volume, the integrated radiation output would have the correct spectral distribution although a multi-colored sun would result. An integrated spectral distribution could be achieved across the surface of the "sun" by locating the filter pattern at an alternative position in the optical train such that its image, as seen from the test volume, was in an out-of-focus condition.

The techniques necessary for the design and fabrication of multi-layer interference filters of the required precision and thermal stability have been defined by a number of companies, including Honeywell. As noted above, each

filter will consist of one or more layers of various materials, with the transmittance of each filter being dependent upon the combination of materials and the film thicknesses. After a specific combination of filters and a filter pattern have been defined according to the above techniques, the spectral filter may be fabricated through the use of a photographic-like process as follows:

1. The surface upon which the filter is to be deposited is coated with a light-sensitive gelatin emulsion.
2. The pattern in which the first layer of material is to be deposited is plotted so that the areas of the pattern where the material is to be deposited are black and the remainder of the area is white.
3. Locating the emulsion at the image plane of a camera, the pattern is photographed (correct magnification and orientation of the image must, of course, be provided).
4. The emulsion is "developed" to remove the gelatin from the unexposed areas of the surface.
5. The first layer of material is deposited uniformly over the surface to the required thickness, using a vacuum deposition process.
6. The remainder of the gelatin emulsion and its overcoating of material are then removed, leaving the desired pattern of material on the surface.
7. Steps 1 through 6 are followed repetitively for each layer of material.

APPENDIX III

SINGLE SURFACE COLLECTOR FOR COSINE OUTPUT FROM A SPHERICAL INPUT

A numerical example has been obtained to illustrate the nature of a single surface which provides an $\bar{E}_{\phi_3} = \cos \phi_3$. This surface cannot be simultaneously corrected for spherical aberration and it is instructive to examine the extent of the latter under the circumstances. Equation (7-309) applies in this case which, when ϕ_1 is measured with respect to the positive z-axis in figure III-1 gives

$$\sin^2 \phi_3 = \frac{2}{M^2 c l} (1 + \cos \phi_1) \quad (\text{III-1})$$

In accordance with equations (7-244) the solution for the surface coordinates r and Z is

$$r = r_0 \exp \left[\int_{\phi_0}^{\phi} \frac{d\phi}{\sin^2 \phi (\cot \phi - \frac{1}{m'})} \right] \quad \left. \right\} \quad (\text{III-2})$$

$$Z = \frac{r}{\tan \phi_1}$$

where m' is the slope of the surface defined by $r = m(Z)$. In accordance with figure III-1 the angle, α , made by the surface tangent with the z-axis is given by

$$\alpha = \frac{\pi}{2} - \left[\phi_3 + \frac{\pi - (\phi_1 + \phi_3)}{2} \right] = \frac{\phi_1 - \phi_3}{2} \quad (\text{III-3})$$

and

$$m' = \tan \alpha = \frac{1 - \cos (\phi_1 - \phi_3)}{\sin (\phi_1 - \phi_3)}$$

or

$$m' = \frac{1 - \cos \phi_1 \cos \phi_3 - \sin \phi_1 \sin \phi_3}{\sin \phi_1 - \cos \phi_1 \tan \phi_3}$$

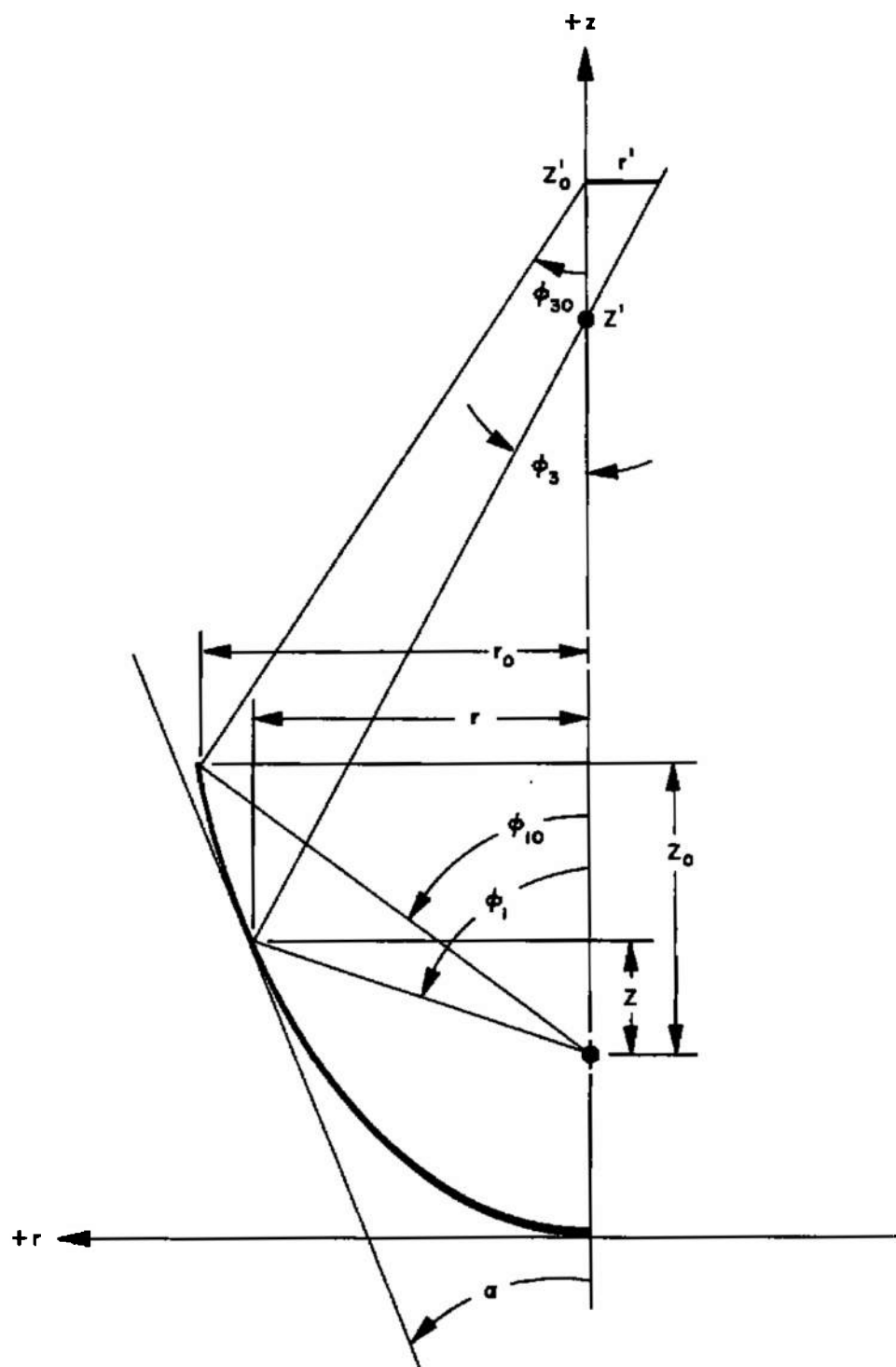


Figure III-1. Parameters of a Single-Surface Collector

$$m' = \frac{\sec \phi_3 - \cos \phi_1 - \sin \phi_1 \tan \phi_3}{\sin \phi_1 - \cos \phi_1 \tan \phi_3} \quad (III-4)$$

By virtue of equation (III-1)

$$\sec \phi_3 = \frac{1}{\sqrt{1 - \frac{2}{M_{cl}^2} (1 + \cos \phi_1)}} \quad (III-5)$$

$$\tan \phi_3 = \frac{2(1 + \cos \phi_1)}{\sqrt{M_{cl}^2 - 2(1 + \cos \phi_1)}} \quad (III-5)$$

The insertion of equations (III-5) into (III-4) yields an expression for m' in terms of ϕ_1 alone so that equation (III-2) may be integrated numerically on a computer.

Define Z'_o to be where the marginal ray crosses the axis. Then,

$$\frac{r_o}{Z_o - Z'_o} = -\tan \phi_{3,o}$$

and

$$\frac{r_o}{\tan \phi_{3,o}} + Z_o = Z'_o \quad (III-6)$$

The blur circle at Z'_o is determined in accordance with

$$\frac{r - r'}{Z - Z'_o} = -\tan \phi_3 \quad (III-7)$$

$$r' = (Z - Z_o) \tan \phi_3 + r$$

Where in each case $\tan \phi_3$ is given by equation (III-5). The range of r' is a measure of the spherical aberration introduced by the collector surface deformations. Numerical calculations were made for initial angles of $\phi_{3,o} = 65^\circ$ and $\phi_{1,o} = 40^\circ, 45^\circ, 50^\circ, 55^\circ, 60^\circ, 65^\circ$, and 70° . It is seen that these correspond to values of M_{cl} determined by

$$M_{cl} = \frac{\sqrt{2(1 + \cos \phi_{1,0})}}{\sin \phi_{3,0}} \quad (III-8)$$

The resulting surface coordinates are plotted in figure III-2 through III-8. The ray producing maximum spherical aberration is plotted in each case. Although the spherical aberration is generally severe, pointing up the necessity of a second compensating surface, the result does indicate the practical behavior of a surface which satisfies one of the possible design objectives of a collector scheme, namely, to transform the spherical input polar distribution to a cosine output polar distribution. The surfaces shown in figures III-2 through III-8 could not in themselves be used although it is seen that for collection angles of ϕ_1 as high as 110° to 120° the spherical aberration and image blur circle are not unreasonably severe. There can be little question that the inclusion of a second surface which could eliminate the spherical aberration would lead to a practical mirror shape in this case. It is likely that a design which preserves the spherical polar distribution in the output would also be practical.

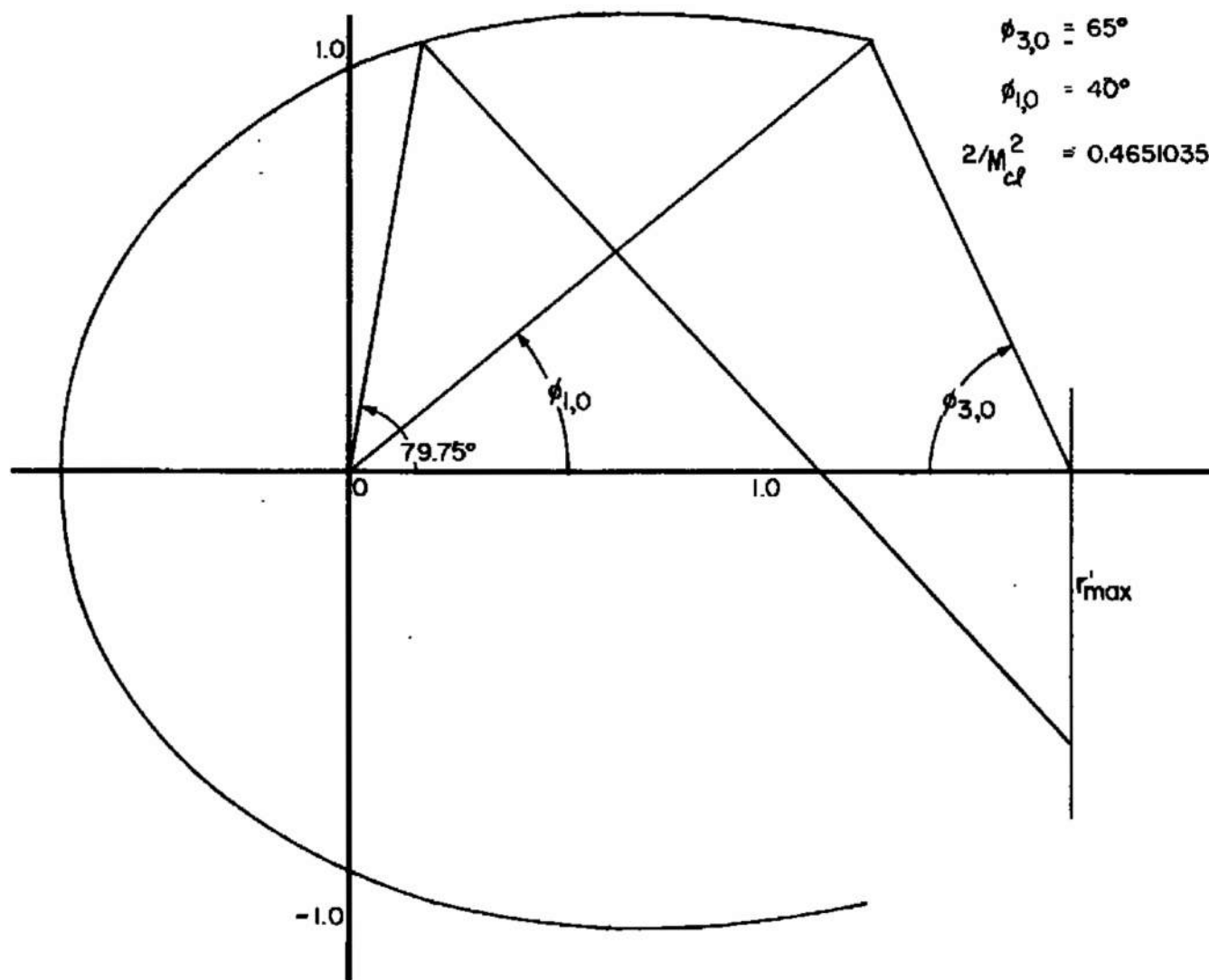


Figure III-2. Schematic Representation of a Collector Which Collects Radiation Between 40° and 180° of the Axis and Whose Output Radiance Distribution is a Cosine Function Within 65° of the Axis

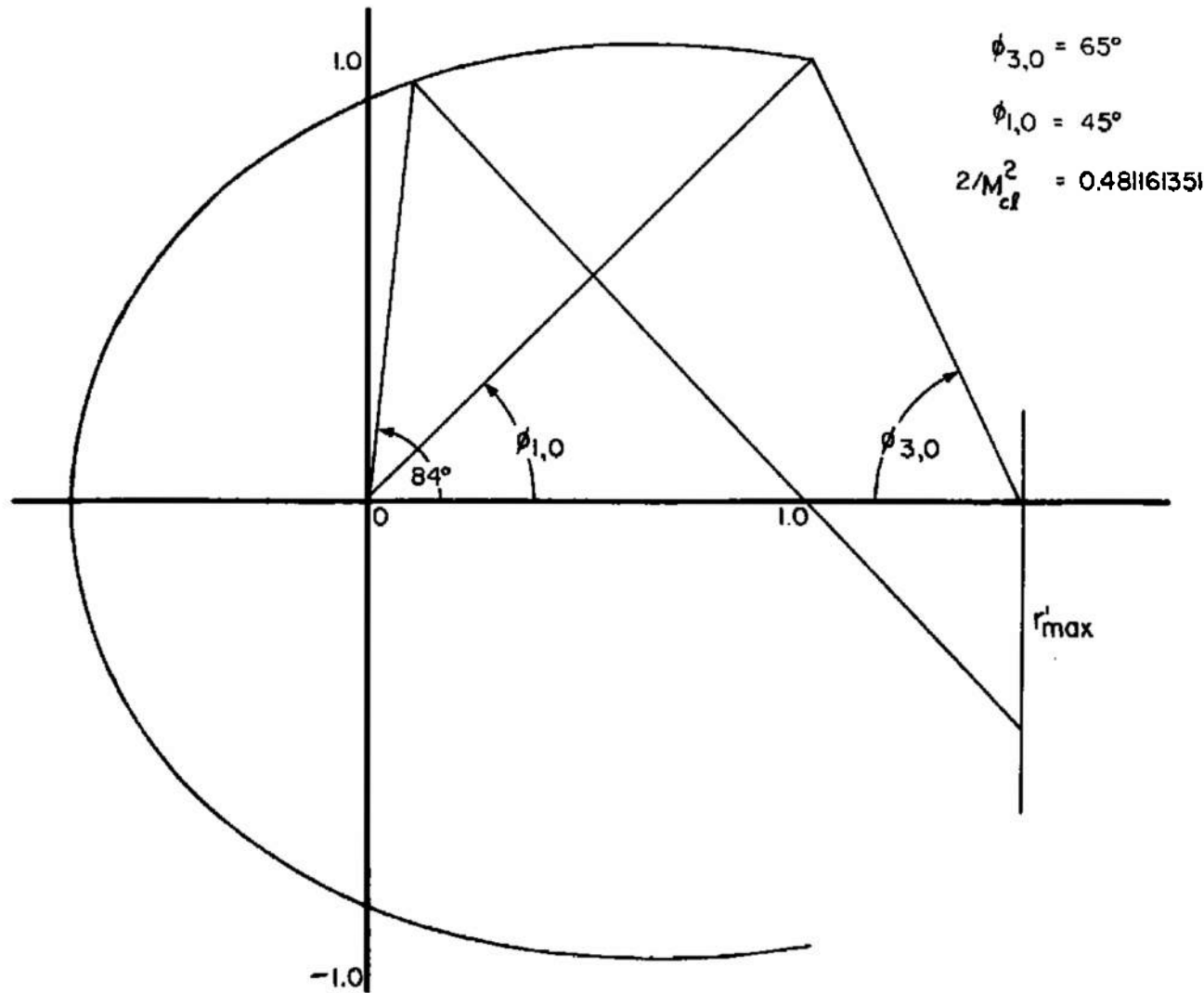


Figure III-3. Schematic Representation of a Collector Which Collects Radiation Between 45° and 180° of the Axis and Whose Output Radiance Distribution is a Cosine Function Within 65° of the Axis

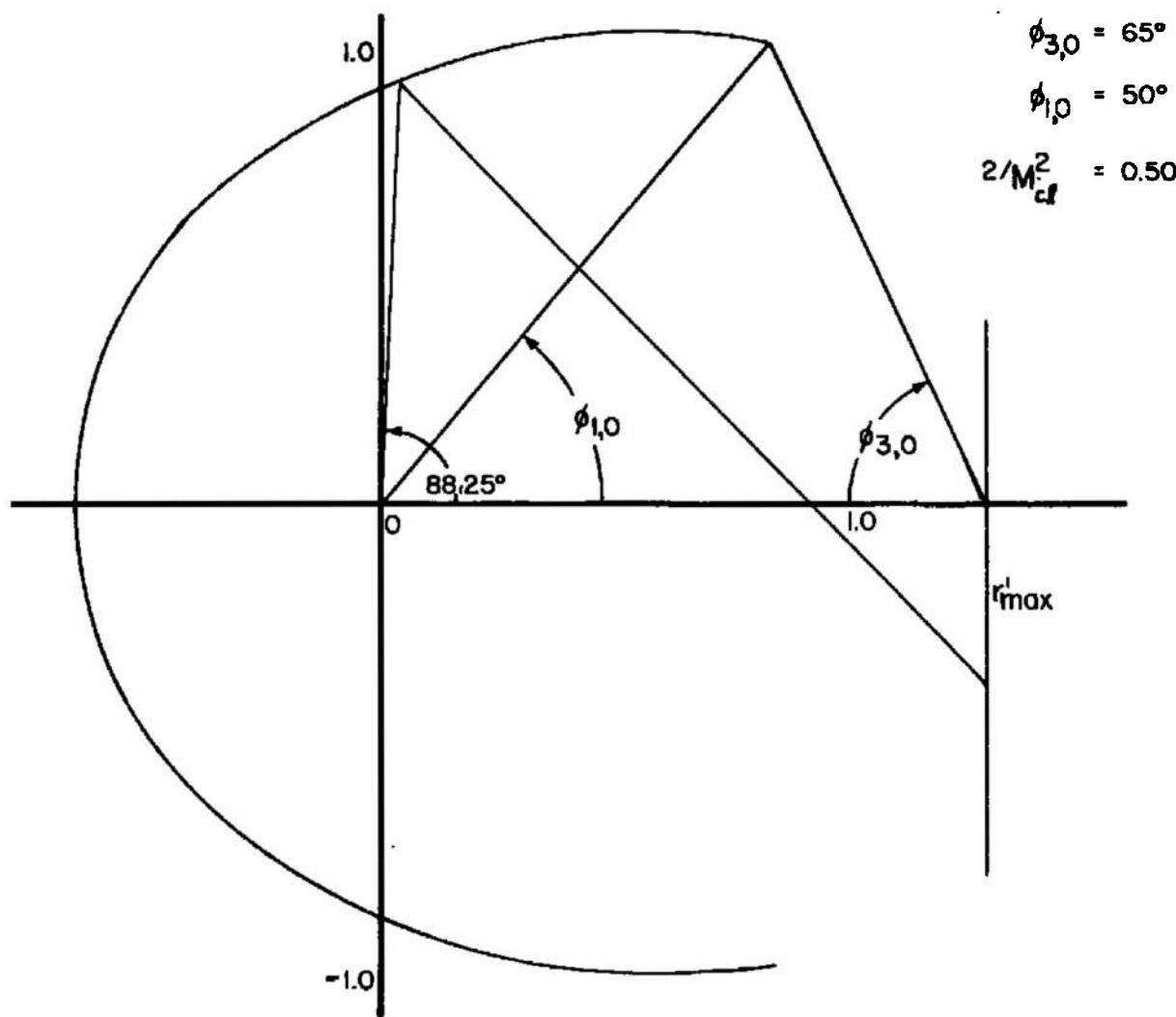


Figure III-4. Schematic Representation of a Collector Which Collects Radiation between 50° and 180° of the Axis and Whose Output Radiance Distribution is a Cosine Function Within 65° of the Axis

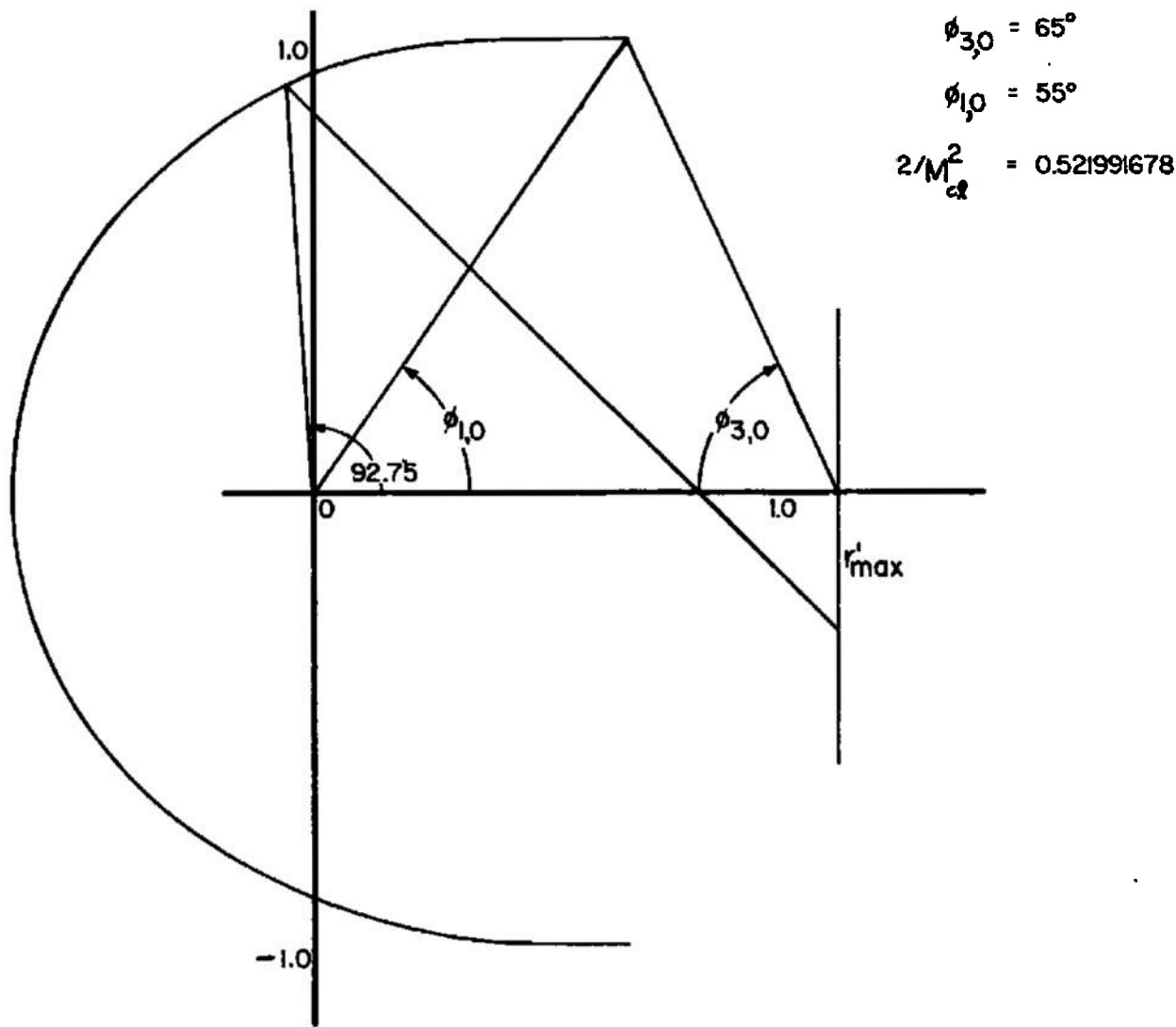


Figure III-5. Schematic Representation of a Collector Which Collects Radiation Between 55° and 180° of the Axis and Whose Output Radiance Distribution is a Cosine Function Within 65° of the Axis

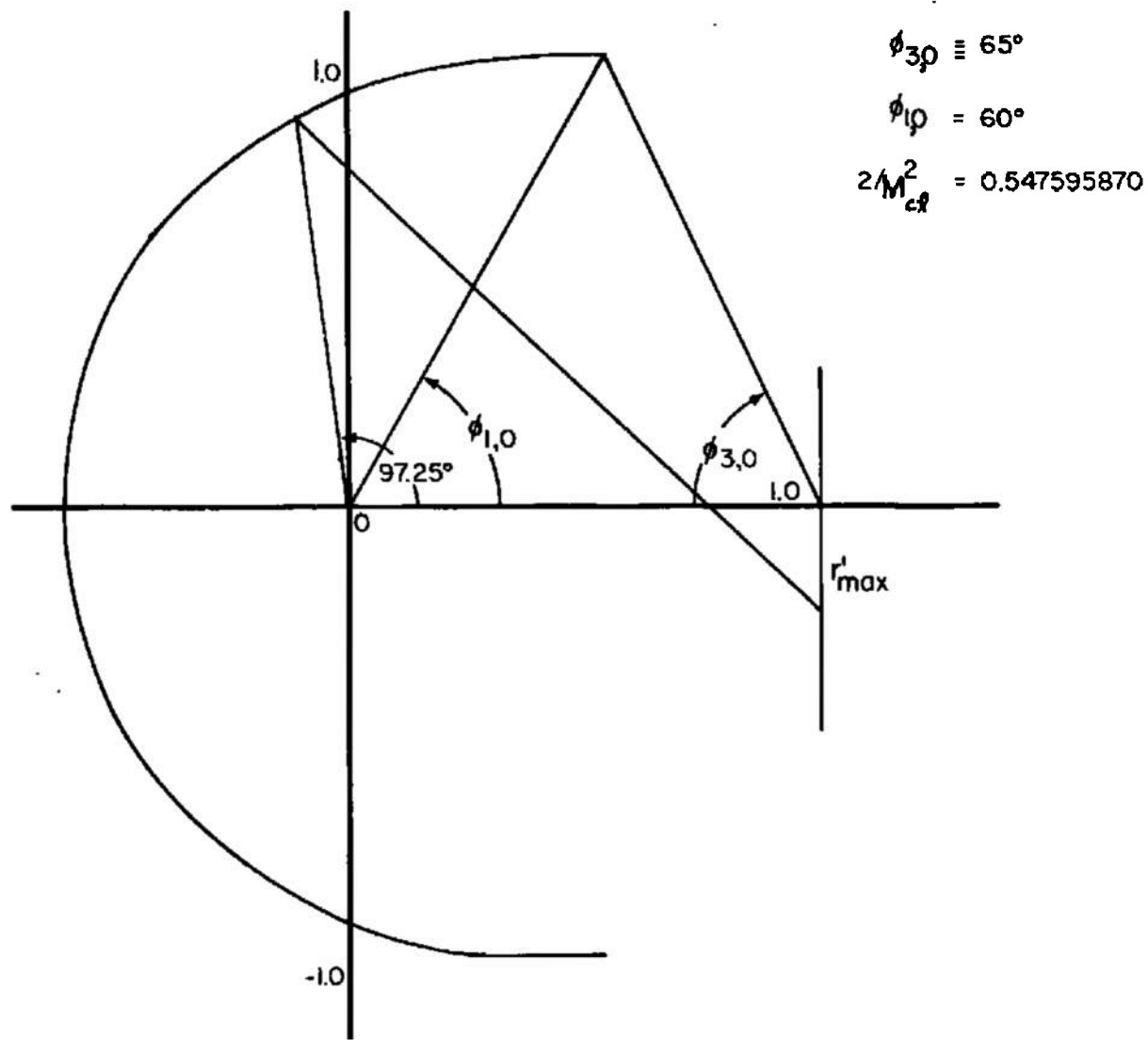


Figure III-6. Schematic Representation of a Collector Which Collects Radiation Between 60° and 180° of the Axis and Whose Output Radiance Distribution is a Cosine Function Within 65° of the Axis

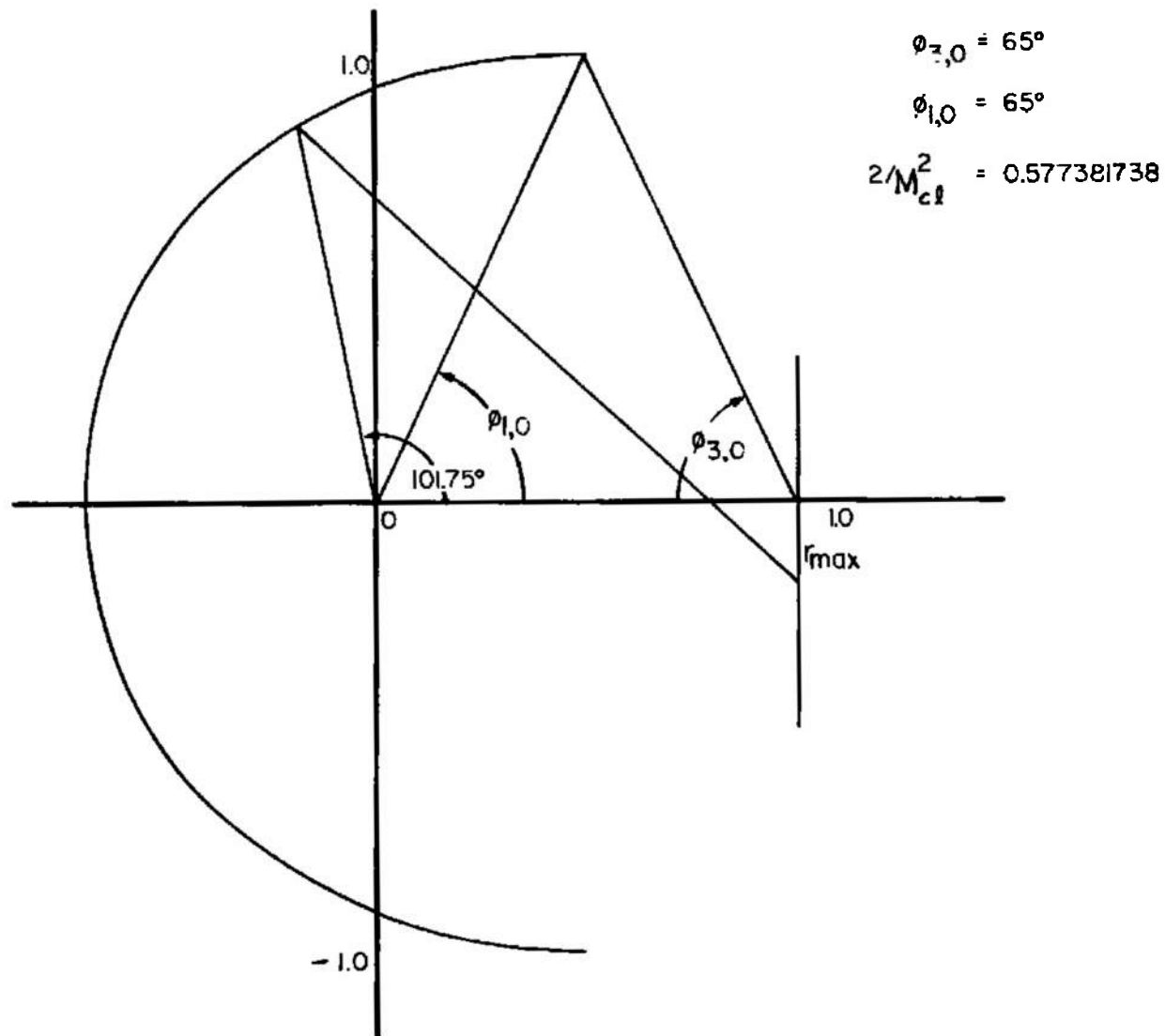


Figure III-7. Schematic Representation of a Collector Which Collects Radiation Between 65° and 180° of the Axis and Whose Output Radiance Distribution is a Cosine Function Within 65° of the Axis

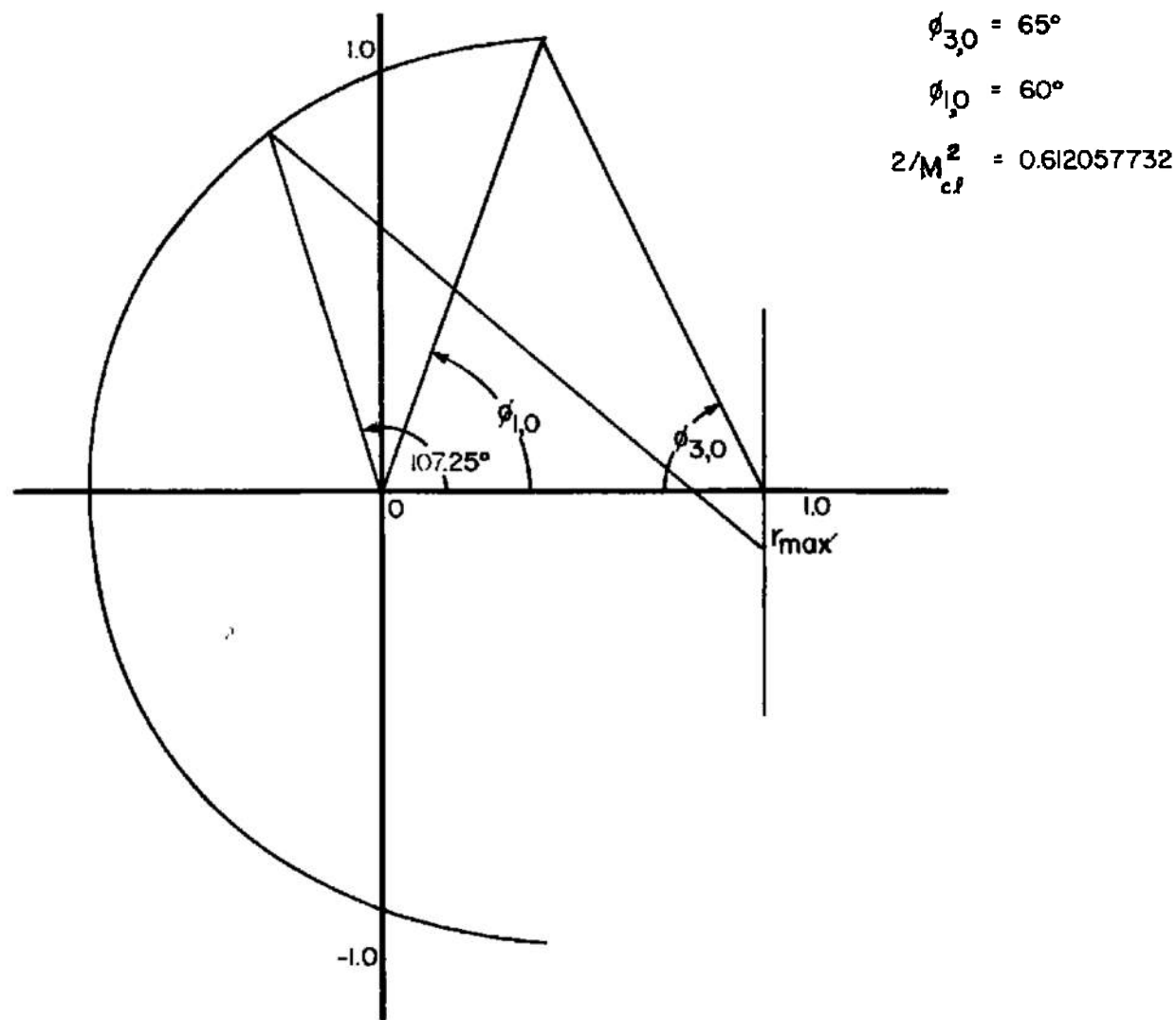


Figure III-8. Schematic Representation of a Collector Which Collects Radiation Between 70° and 180° of the Axis and Whose Output Radiance Distribution is a Cosine Function Within 65° of the Axis

UNCLASSIFIED

Security Classification

DOCUMENT CONTROL DATA - R&D

(Security classification of title, body of abstract and indexing annotation must be entered when the overall report is classified)

1. ORIGINATING ACTIVITY (Corporate author) Honeywell California Ordnance Center West Covina, California		2a. REPORT SECURITY CLASSIFICATION UNCLASSIFIED
		2b. GROUP N/A
3. REPORT TITLE A STUDY OF OPTICAL SYSTEM CONCEPTS AND HIGH INTENSITY LIGHT SOURCES FOR SOLAR RADIATION SIMULATION		
4. DESCRIPTIVE NOTES (Type of report and inclusive dates) N/A		
5. AUTHOR(S) (Last name, first name, initial) Fischel, Halbert (Messinger Consultants Company) and Hughes, Roger R. (Honeywell, Inc.)		
6. REPORT DATE May 1965	7a. TOTAL NO. OF PAGES 425	7b. NO. OF REFS N/A
8a. CONTRACT OR GRANT NO. AF 40(600)-1069	9a. ORIGINATOR'S REPORT NUMBER(S) AEDC-TR-65-117	
b. PROJECT NO. 8952	9b. OTHER REPORT NO(S) (Any other numbers that may be assigned this report) Honeywell Technical Document No. H-6152-19	
c. Program Element 62405334		
d. Task 895211		
10. AVAILABILITY/LIMITATION NOTICES Qualified requesters may obtain copies of this report from DDC.		
11. SUPPLEMENTARY NOTES N/A	12. SPONSORING MILITARY ACTIVITY Arnold Engineering Development Center, Air Force Systems Command, Arnold Air Force Station, Tennessee	
13. ABSTRACT The study described herein has been made to evaluate three new high-powered arc sources as possible radiation sources for a large modular solar simulator. The three sources are (1) the Vortex Stabilized Radiation Source developed by Giannini Scientific Corp. (Plasmadyne); (2) the Fluid Transpiration Arc developed by Vitro Laboratories; and (3) the High Intensity Carbon Arc developed by RCA Service Co. From data supplied by Arnold Engineering Development Center (AEDC), the radiation characteristics of the sources have been studied to determine the spectral properties of the radiation from each source, and to permit derivation of mathematical expressions for the radiance distribution of each source. A careful review of the nature of solar radiation and of the theory of energy transfer in optical systems has been conducted. On the basis of this review and the source radiance functions derived in the source study, several optical system concepts for solar radiation simulation have been synthesized and analyzed for use with each source. The optical concepts studied range from simple parabolic collimators and uncollimated projection modules to systems consisting of trains of conic section reflectors and modifications thereto.		

UNCLASSIFIED

Security Classification

14.	KEY WORDS	LINK A		LINK B		LINK C	
		ROLE	WT	ROLE	WT	ROLE	WT
	solar simulation						
	arc sources						
	radiation						
	optics						

INSTRUCTIONS

1. ORIGINATING ACTIVITY: Enter the name and address of the contractor, subcontractor, grantee, Department of Defense activity or other organization (corporate author) issuing the report.

2a. REPORT SECURITY CLASSIFICATION: Enter the overall security classification of the report. Indicate whether "Restricted Data" is included. Marking is to be in accordance with appropriate security regulations.

2b. GROUP: Automatic downgrading is specified in DoD Directive 5200.10 and Armed Forces Industrial Manual. Enter the group number. Also, when applicable, show that optional markings have been used for Group 3 and Group 4 as authorized.

3. REPORT TITLE: Enter the complete report title in all capital letters. Titles in all cases should be unclassified. If a meaningful title cannot be selected without classification, show title classification in all capitals in parenthesis immediately following the title.

4. DESCRIPTIVE NOTES: If appropriate, enter the type of report, e.g., interim, progress, summary, annual, or final. Give the inclusive dates when a specific reporting period is covered.

5. AUTHOR(S): Enter the name(s) of author(s) as shown on or in the report. Enter last name, first name, middle initial. If military, show rank and branch of service. The name of the principal author is an absolute minimum requirement.

6. REPORT DATE: Enter the date of the report as day, month, year; or month, year. If more than one date appears on the report, use date of publication.

7a. TOTAL NUMBER OF PAGES: The total page count should follow normal pagination procedures, i.e., enter the number of pages containing information.

7b. NUMBER OF REFERENCES: Enter the total number of references cited in the report.

8a. CONTRACT OR GRANT NUMBER: If appropriate, enter the applicable number of the contract or grant under which the report was written.

8b, 8c, & 8d. PROJECT NUMBER: Enter the appropriate military department identification, such as project number, subproject number, system numbers, task number, etc.

9a. ORIGINATOR'S REPORT NUMBER(S): Enter the official report number by which the document will be identified and controlled by the originating activity. This number must be unique to this report.

9b. OTHER REPORT NUMBER(S): If the report has been assigned any other report numbers (either by the originator or by the sponsor), also enter this number(s).

10. AVAILABILITY/LIMITATION NOTICES: Enter any limitations on further dissemination of the report, other than those

imposed by security classification, using standard statements such as:

- (1) "Qualified requesters may obtain copies of this report from DDC."
- (2) "Foreign announcement and dissemination of this report by DDC is not authorized."
- (3) "U. S. Government agencies may obtain copies of this report directly from DDC. Other qualified DDC users shall request through . . ."
- (4) "U. S. military agencies may obtain copies of this report directly from DDC. Other qualified users shall request through . . ."
- (5) "All distribution of this report is controlled. Qualified DDC users shall request through . . ."

If the report has been furnished to the Office of Technical Services, Department of Commerce, for sale to the public, indicate this fact and enter the price, if known.

11. SUPPLEMENTARY NOTES: Use for additional explanatory notes.

12. SPONSORING MILITARY ACTIVITY: Enter the name of the departmental project office or laboratory sponsoring (paying for) the research and development. Include address.

13. ABSTRACT: Enter an abstract giving a brief and factual summary of the document indicative of the report, even though it may also appear elsewhere in the body of the technical report. If additional space is required, a continuation sheet shall be attached.

It is highly desirable that the abstract of classified reports be unclassified. Each paragraph of the abstract shall end with an indication of the military security classification of the information in the paragraph, represented as (TS), (S), (C), or (U).

There is no limitation on the length of the abstract. However, the suggested length is from 150 to 225 words.

14. KEY WORDS: Key words are technically meaningful terms or short phrases that characterize a report and may be used as index entries for cataloging the report. Key words must be selected so that no security classification is required. Identifiers, such as equipment model designation, trade name, military project code name, geographic location, may be used as key words but will be followed by an indication of technical context. The assignment of links, rules, and weights is optional.

UNCLASSIFIED

Security Classification